Roger G. Barry

Mountain Weather
and Climate

THIRD EDITION

This page intentionally left blank

Mountain Weather and Climate
Third Edition

Mountains and high plateau areas account for a quarter of the Earth's land surface. They give rise to a wide range of meteorological phenomena and distinctive climatic characteristics of consequence for ecology, forestry, glaciology and hydrology. *Mountain Weather and Climate* remains the only comprehensive text describing and explaining mountain weather and climate processes. It presents the results of a broad range of studies drawn from across the world.

Following an introductory survey of the historical aspects of mountain meteorology, three chapters deal with the latitudinal, altitudinal and topographic controls of meteorological elements in mountains, circulation systems related to orography, and the climatic characteristics of mountains. The author supplies regional case studies of selected mountain climates from New Guinea to the Yukon, a chapter on bioclimatology that examines human bioclimatology, weather hazards and air pollution, and a concluding chapter on the evidence for and the significance of changes in mountain climates.

Since the first edition of this book appeared over two decades ago several important field programs have been conducted in mountain areas. Notable among these have been the European Alpine Experiment and related investigations of local winds, studies of air drainage in complex terrain in the western United States and field laboratory experiments on air flow over low hills. Results from these investigations and other research are incorporated in this new edition and all relevant new literature is referenced.

ROGER G. BARRY is Distinguished Professor of Geography at the University of Colorado and Director, World Data Center for Glaciology and the National Snow and Ice Data Center, Boulder.

MOUNTAIN WEATHER AND CLIMATE

THIRD EDITION

ROGER G. BARRY

University of Colorado, Boulder, USA

CONTENTS

FIGURES

TABLES

PREFACE TO THE THIRD EDITION

Research into mountain weather and climate has gained momentum over the 15 years that have elapsed since the publication of the second edition. Studies of the meteorology and climatology of mountains regions of Central Asia and South America, in particular, have provided material for new sections in Chapter 5, with shorter sections on the equatorial mountains of East Africa and the Southern Alps of New Zeeland. The high ice plateaus of Greenland and Antarctica are also included. There has also been more attention paid to changes in mountain environments, as part of the widening concern over global warming and through the International Panel on Climate Change (IPCC) for its second (1995), third (2001), and fourth (2007) assessment reports. Accordingly, the scope of the material in Chapter 7 has expanded. Research in mountain meteorology has benefited from projects such as the Mesoscale Alpine Program (MAP) and other more local individual endeavors in different parts of the world. Improvements in instrumentation, data recording and transmitting, and new satellite, airborne and ground-based remote sensing, are all changing the ways in which data can be collected. Data analysis, combined with higher resolution numerical modeling, is also becoming increasingly common.

The basic structure of the book remains unchanged, and apart from updating throughout, and corrections where appropriate, most of the original text has been retained. I believe firmly in recognizing important early contributions to the subject, as well as the latest advances. Some recent references incorporated in the bibliographies are not discussed in the text.

ACKNOWLEDGMENTS

1 MOUNTAINS AND THEIR CLIMATOLOGICAL STUDY

1.1 INTRODUCTION

It is the aim of this book to bring together the major strands of our existing knowledge of weather and climate in the mountains. The first part of the book deals with the basic controls of the climatic and meteorological phenomena and the second part with particular applications of mountain climatology and meteorology. By illustrating the general climatic principles, a basis can also be provided for estimating the range of conditions likely to be experienced in mountain areas of sparse observational data.

In this chapter we introduce mountain environments as they have been perceived historically, and consider the physical characteristics of mountains and their global significance. We then briefly review the history of research into mountain weather and climate and outline some basic considerations that influence their modern study.

1.1.1 Historical perceptions

The mountain environment has always been regarded with awe. The Greeks believed Mount Olympus to be the abode of the gods, to the Norse the Jötunheim was the home of the Jotuns, or ice giants, while to the Tibetans, Mount Everest (Chomo Longmu) is the "goddess of the snows." In many cultures, mountains are considered "sacred places;" Nanga Parbat, an 8125 m summit in the Himalaya, means sacred mountain in Sanskrit, for example. Conspicuous peaks are associated with ancestral figures or deities (Bernbaum, 1998) – Sengem Sama with Fujiyama (3778 m) in Japan and Shiva-Parvati with Kailas (6713 m) in Tibet – although at other times mountains have been identified with malevolent spirits, the Diablerets in the Swiss Valais, for example. This dualism perhaps reflects the opposites of tranquility and danger encountered at different times in the mountain environment. Climatological features of mountains, especially their associated cloud forms, are represented in many names and local expressions. On seeing the distant ranges of New Zealand, the ancestral Maoris named the land Aotearoa, "the long white cloud." Table Mountain, South Africa, is well known for the "tablecloth" cloud that frequently caps it. Wind systems associated with mountains have also given rise to special names now widely applied, such as föhn, chinook and bora, and others still used only locally.

Today, the majestic scenery of mountain regions makes them prime recreation and wilderness country. Such areas provide major gathering grounds for water supplies for consumption and for hydroelectric power generation, they are often major forest reserves, as well as sometimes containing valuable mineral resources. Mountain weather is often severe, even in summer, presenting risks to the unwary visitor and, in high mountains, altitude effects can cause serious physiological conditions. Concerns over sanctity and safety explain why mountains remained largely unexplored, except by hunters or mineral and plant collectors for much of human history. Scientific exploration of mountains began in earnest in the late-eighteenth century.

Despite their environmental and societal significance, and the fact that mountain ranges account for about 25 percent of the Earth's land surface, the meteorology of most mountain areas is little known in detail. Weather stations are few and tend to be located at conveniently accessible sites, often in valleys, rather than at points selected with a view to obtaining representative data.

Climatic studies in mountain areas have frequently been carried out by biologists concerned with particular ecological problems, or by hydrologists and glaciologists interested in snow and ice processes and melt runoff, rather than by meteorologists. Consequently, much of the information that does exist tends to be widely scattered in the scientific literature and it is often viewed only in the context of a particular local problem.

1.2   CHARACTERISTICS OF MOUNTAIN AREAS

Definitions of mountain areas are unavoidably arbitrary (Messerli and Ives, 1997, p. 8). Usually no qualitative, or even quantitative, distinction is made between mountains and hills. Common usage in North America suggests that 600 m or more of local relief distinguishes mountains from hills (Thompson, 1964). Such an altitudinal range is sufficient to cause vertical differentiation of climatic elements and vegetation cover. Finch and Trewartha (1949) propose that a relief of 1800 m can serve as the criterion for mountains of "Sierran type." Such a range of relief also implies the presence of steep slopes. In an attempt to provide a rational basis for definition, Troll (1973) delimits *high mountains* by reference to particular landscape features. The most significant ones are the upper timberline, the snow line during the Pleistocene epoch (which gave rise to distinctive glacial landforms) and the lower limit of periglacial processes (solifluction, etc.). It is apparent that each of these features is related to the effects of past or present climate and to microclimatic conditions at or near ground level.

On the basis of Troll's criteria, the lower limit of the high mountain belt occurs at elevations of a few hundred meters above sea level in northern Scandinavia, 1600–1700 m in central Europe, about 3300 m in the Rocky Mountains at 40° N, and 4500 m in the equatorial cordillera of South America (see Figure 1.1). In arid central Asia, where trees are absent and the snow line rises to above 5500 m, the only feasible criterion remaining is that of relief.
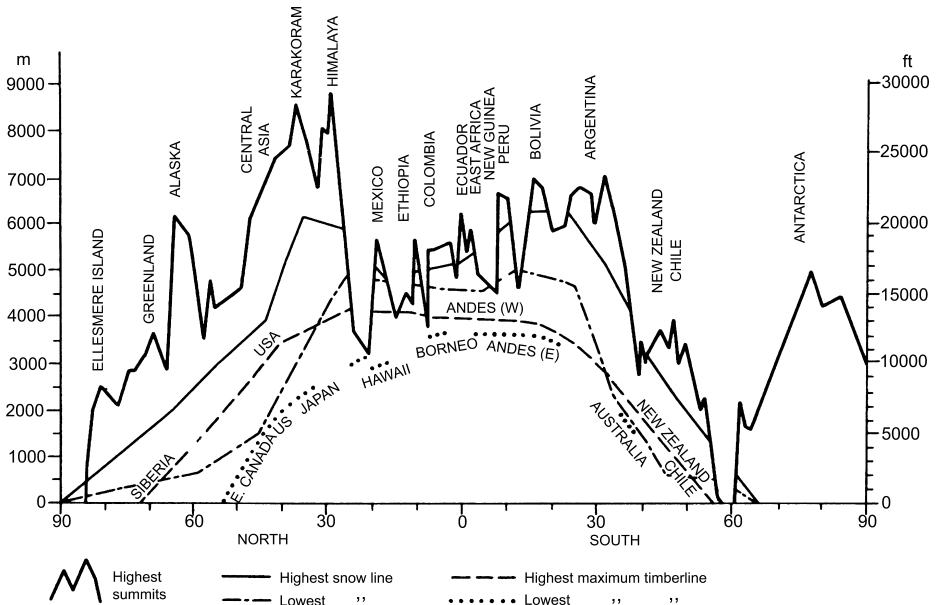
Fig. 1.1 Latitudinal cross-section of the highest summits, highest and lowest snow lines, and highest and lowest upper limits of timberline (from Barry and Ives, 1974).

Troll's approach derives from the German distinction between *Hochgebirge* (high mountains), such as the Alps and Tatra, and the lower and gentler ridges of the *Mittelgebirge*, which include the Riesengebirge and Vosges. It is not altogether suitable from the climatological standpoint since, although the altitudinal limit varies with latitude in such a way as to define *alpine* areas and their biota (cf. Barry and Ives, 1974), it is the altitudinal and slope effects, which cause many of the special features of mountain climates. It is worth noting in passing that "alpine" denotes above tree line, although in some mountains this may be ambiguous due to the absence of tree species at high elevation. A climatologically predictive use of tree line altitude (disregarding land use, fire, and a few special genus-specific effects) has been demonstrated by Körner and Paulsen (2004). Data they collected at 46 mountain sites between 42° S and 68° N show that the growing season mean 10-cm soil temperature at the climatic tree line averages 6.7 °C, with only small departures in different climatic zones (5–6 °C at equatorial tree lines and 7–8 °C in mid-latitudes and the Mediterranean zone). The alpine zone gives way to the *nival* zone where vascular plants are largely absent. An alternative terminology uses *eolian* zone, where wind plays a major role; this zone may be seasonally affected by nival (snow-related) conditions and processes, but also has extensive rock cover or rock and snow patches. These characteristics are important for biology and geomorphology, as well as for microclimates, but need not concern us further here.

Table 1.1 The global area of mountains and high plateaus.

	Mountains	Plateaus (10^6 km^2)	Mountains/land surface (%)[a]
3000 m[b]	– 6 –		4.0
2000–3000 m	4	6	2.7
1000–2000 m	5	19	3.4
0–1000 m	15	92	10.1
Total	30	117	20.2

[a] The total land surface is about 149 million km^2, oceanic islands covering 2 million km^2 are not included in the listed areas.
[b] All land above 3000 m.
Source: after Louis (1975).

Table 1.2 Mountain relief based on roughness classes, and the degree of dissection, both shown as percent of the land surface excluding Greenland and Antarctica.

(Very)/high mts	4.4%	(Very)/high plateaus	1.0%
Middle mts	10.1	Middle plateaus	3.3
Low mts	10.5	Low plateaus	8.3
Hills	8.6	Platforms	14.3
Rugged lowlands	3.2	High/middle plains	10.9
		Plains, lowlands	25.4
Extremely dissected	0.4%		
Highly dissected	5.8	Plateaus/plains	25%
Low/mod. dissection	32	Flat/very flat	37

Source: after Meybeck *et al.* (2001).

    The treatment in this book emphasizes high mountain effects, due to altitude, although since airflow modifications that arise at even modest topographic barriers can cause important differences between upland and lowland climates, such effects are also discussed.

    The geomorphologist H. Louis (1975) estimated that the land surface occupied by mountains is about 20 percent. His simple breakdown is shown in Table 1.1. A recent calculation based on the degree of dissection and altitude range has been made using 1-km digital terrain data for non-glacierized areas of the world aggregated to 30′ × 30′ cells (Meybeck *et al.*, 2001); Antarctica, Greenland and the Caspian and Aral seas are excluded. Relief roughness (RR) is defined as maximum minus minimum elevation in a cell divided by half the cell length (in units of m/km or ‰). Mountains are defined as having RR > 20‰ for a mean elevation 500–2000 m and RR > 40‰ at higher elevation. Their results (Table 1.2) indicate that mountains make up 25 percent of the land area. Mountains are also shown to provide 32 percent
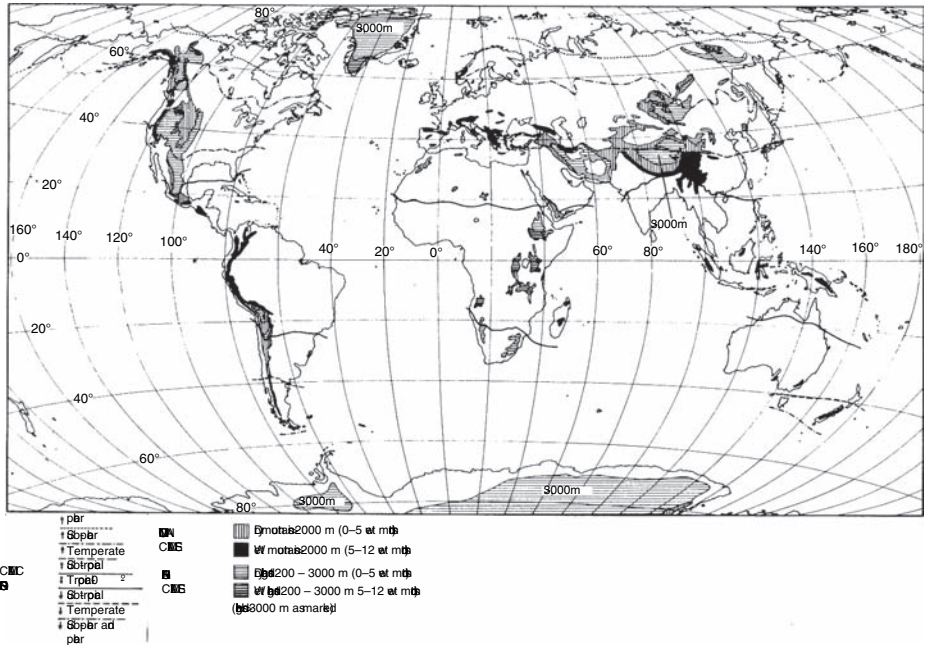
Fig. 1.2 **Alpine and highland zones and their climatic characteristics (after N. Crutzberg, from Ives and Barry, 1974).**

of global runoff; appropriately they have been dubbed "water towers of the twenty-first century" (Mountain Agenda, 2002). Moreover, 26 percent of the world's population lives in mountain and high plateau regions.

The locations of the major mountain ranges and highland areas of the world and their climatic zonation are shown in Figure 1.2. The most latitudinally extensive mountain chains are the cordilleras of western North and South America. The most extensive east–west ranges are the Himalaya and adjoining ranges of central Asia. Reference should also be made to the vast highland plateau exceeding 4000 m in Tibet and the even larger ice plateaus of Greenland and Antarctica. All of these regions have major significance for weather and climate at scales up to that of the general circulation of the atmosphere. In contrast, major, but isolated, volcanic peaks that occur in east Africa and elsewhere, have their own distinctive effects on local weather and climate.

1.3 HISTORY OF RESEARCH INTO MOUNTAIN WEATHER AND CLIMATE

Intensive scientific study of mountain weather conditions did not begin until the mid-nineteenth century although awareness of the changes in meteorological elements with altitude came much earlier. The effect of altitude on pressure was proved in September 1648 when Florin Périer, at the request of his brother-in-law

Blaise Pascal, operated a simple Torricelian mercury tube at the summit and base of the Puy de Dôme in France. In August 1787, H. B. de Saussure (1796), who was a keen mountaineer, made observations of relative humidity during an ascent of Mont Blanc using the hair hygrometer, which he had developed. His instruments are on display in Geneva (Archinard, 1980, 1988). In July 1788, he and his son maintained two-hourly meteorological observations on the Col du Géant (3360 m) near Mont Blanc while comparative observations were made at Chamonix (1050 m) and Geneva (375 m). Carozzi and Newman (1995) give information on these ascents and de Saussure's other journeys around Mont Blanc, including his observations about snow and glaciers. From these data, de Saussure was able to study temperature lapse rate and its diurnal variation, obtaining an estimate close to that of Julius von Hann a century later. His writings discussed eighteenth-century theories of the reason for low temperatures in the mountains and he came closer to modern views than most physicists of his day (Barry, 1978). De Saussure also attempted to measure altitudinal variations of evaporation and sky color and was fascinated by numerous other mountain weather phenomena and human response to high-altitude conditions. He can rightfully be regarded as the "first mountain meteorologist."

In the 1850s, meteorological measurements begin to be made systematically on high mountains, often in association with astronomical studies, as on the Peak of Tenerife (Canary Islands) (Smyth, 1859). In the United States, the earliest extensive observations were those made in the summers of 1853 to 1859 on Mt. Washington, New Hampshire (1915 m) (see Stone, 1934). The establishment of observatories by the US Signal Service soon followed on Mt. Washington in 1870 and on Pike's Peak, Colorado (4311 m) in 1874 (Rotch, 1892). Observations were also made on Mt. Mitchell, North Carolina (2037 m) in the summer of 1873 (Howgate and Sackett, 1873). In Europe, similar developments took place following a suggestion made by J. von Hann at the second International Meteorological Congress in Rome, in 1879. The major European countries established observatories (Rotch, 1886; Roschkott, 1934), particularly in the Alps, where many of these stations are still operating. The impressive location of the Sonnblick Observatory, Austria (Böhm, 1986; Auer et al., 2005) is shown in Figure 1.3. A summary of the location and periods of operation of the major observatories/weather stations is given in Table 1.3.

After the initial enthusiasm for mountain weather data in the United States, a number of problems led to a decline in interest in maintaining mountain observatories (Stone, 1934). On the technical side, the telegraph lines were hard to maintain, while a suitable basis for incorporating the data into the synoptic weather-map analyses, then based almost solely on surface weather observations, did not exist. Both Mt. Washington and Pike's Peak were closed by the Weather Bureau in the 1890s, and in Scotland the same fate befell the Ben Nevis Observatory in 1904, due to a lack of funds (Roy, 1983). The value of such observatories in connection with upper air studies was raised again in the 1930s when aerological

Fig. 1.3   The Sonnblick Observatory in April 1985 (R. Boehm).

networks were first being established (Bjerknes *et al.*, 1934). Mt. Evans, Colorado, for example, was used as a site for ozone measurements and new determinations of ultraviolet radiation (Stair and Hand, 1939). Mountain stations can operate in any weather conditions and collect data for 24 hours of the day, whereas soundings are made only twice per day and may be restricted by weather conditions. Partly as a result of such concerns, the Mount Washington Observatory was re-established during the International Polar Year 1932–33 and continues in operation (Smith, 1964, 1982). The only recent development is the establishment of Mauna Loa Observatory (Price and Pales, 1963), which has assumed major importance as a bench mark monitoring station for solar radiation and atmospheric gases. The Zugspitze Observatory in Germany has served as a base for aerosol, atmospheric electricity and radioactivity studies (Reiter, 1964) and the Weissfluhjoch in Switzerland for snow research (*Winterberichte No 15*, 1950).

In other areas of the world, mountain weather data were primarily collected by survey parties, such as those in the Himalaya (Hill, 1881), or by expeditions like those from Harvard University to the Peruvian Andes between 1893 and 1895 (Bailey, 1908). There were many such scientific expeditions, some specifically for meteorological purposes. These included early attempts to determine the extra-terrestrial solar radiation (see p. 35). In addition, climatic records have been collected from many second-order or auxiliary stations in mountain regions around the world. For long-term records (with published climatic mean data for 1931–60), there are about twenty stations around the world located above 2000 m according to Lauscher (1973). However, some of these are situated on high plateaus, in

Table 1.3 Principal mountain observatories.

Name	Country/state	Location	Elevation[a](m)	Records	References
Asia					
Mt. Fuji	Japan	35° 21′ N, 138° 44′ E	3716	1888–1931 (summers) 1932–	Fujimara (1971)[b]; Solomon (1979); Ohmura and Auer (2004)
O Mei Shan	China	29° 28′ N, 103° 41′ E	3383	1932–3	Lauscher (1979b)
Europe					
Fanaräken	Norway	61° 31′ N, 7° E	2062	1932–[d]	Spinnangr and Eide (1948); Manley (1949)[b]
Haldde	Norway	69° 56′ N, 22° 58′ E	893	1902–26	Brekke (2004)
Ben Nevis	Scotland	56° 48′ N, 5° 0′ W	1343	1893–1904	Buchan and Omond (1890–1910)[b]
Brocken	Germany	51° 48′ N, 10° 37′ E	1142	1895–[d]	Pleiss (1961)[b]
Fichtelberg	Germany	50° 26′ N, 12° 57′ E	1213	1891–	Hellman (1916)
Sniezka (Schneekoppe)	Poland	50° 44′ N, 15° 44′ E	1603	1881–→[d]	Grunow et al. (1957)[b]; Lauscher (1981)
Hohenpeissenberg	Germany	47° 48′ N, 11° 01′ E	989	1781–[c]	
Zugspitze	Germany	47° 25′ N, 10° 59′ E	2962	1900–[c]	Hauer (1950)[b]
Sonnblick	Austria	47° 03′ N, 12° 57′ E	3106	1886–[c]	*Jahresbericht des Sonnblick – Vereines* (1892–); Steinhauser (1938); Böhm (1986); Auer et al., 2005
Hoch Obir	Austria	46° 30′ N, 14° 29′ E	2044	1847–1943[c]	Lukesch (1952)
Rudolfshuette	Austria	47° 08′ N, 12° 38′ E	2315	1960–7. 1967– summers, 1980– synoptic	Slupetsky (2004).

Station	Country	Coordinates	Elevation (m)	Period	Reference
Villacher Alp	Austria	46° 34′ N, 13° 39′ E	2140	1929–(1971). 1994– AWS	Boehm (2004)
Säntis	Switzerland	47° 15′ N, 9° 20′ E	2500	1882–[c]	Maurer and Lütschg (1931)[b]
Jungfraujoch	Switzerland	46° 33′ N, 7° 58′ E	3577	1923–[c]	
Davos Weissfluhjoch	Switzerland	46° 50′ N, 9° 49′ E	2540	1936–[d]	Winterberichte (1950–); Zingg (1961)
Lomnicky Stit	Slovakia	49° 12′ N, 20° 13′ E	2635	1940, 1996– AWS, 2000– synoptic	Nieplovo and Pindjak (1992); Stasny (2004)
Moussala	Bulgaria	42° 11′ N, 23° 35′ E	2925	1932–	Tzenkova-Bratoeva (2004)
Kredarica	Slovenia	46° 23′ N, 13° 51′ E	2514	1897–1912 (climate data), 1954–	Cegnar (2004)
Bjelasnica	Yugoslavia	43° 42′ N, 18° 15′ E	2067	1895–1915	Forster et al. (1919); Muminovic (2004)
Mont Blanc	France	45° 50′ N, 6° 52′ E	4359	1887–93 (summers)	Vallot (1893–98); Hann (1899) Tutton (1925)[b]
Pic du Midi de Bigorre	France	42° 56′ N, 0° 08′ E	2860	1881–[d]	Klengel (1894); Bücher and Bücher (1973)
Puy de Dôme	France	45° 47′ N, 2° 57′ E	1467	1878–	Woeikof (1892)
Monte Rosa	Italy	45° 56′ N, 7° 53′ E	3560	1927–39, 1952–8	Mercalli (2004)
Plateau Rosa	Italy	45° 56′ N, 7° 12′ E	3480	1951–2000	Mercalli (2004)
Monte Cimone	Italy	44° 12′ N, 10° 43′ E	2165	1887–(discontinuous until 1945)	Mercalli (2004)
Mt. Etna	Italy	37° 44′ N, 15° 0′ E	2950	1892–1906	Obermayer (1908)
Izana	Tenerife	28° 18′ N, 16° 30′ W	2367	1915–[c]	Tzchirner (1925); Lauscher (1975); Cuevas (2004)
Mt. Olympus	Greece	40° 03′ N, 22° 21′ E	2817	1963– (summers)	Livadas (1963) Kyriazopoulos (1966)

Table 1.3 (cont.)

Name	Country/state	Location	Elevation[a](m)	Records	References
North America					
Mt. Washington	New Hampshire	44° 16′ N, 71° 18′ W	1914	1890–2; 1932–	Stone (1934)[b]; Smith (1964), (1982); Leitch, (1978); Mount Washington Observatory (1959); Grant et al. (2005)
Pike's Peak	Colorado	38° 50′ N, 105° 02′ W	4311	1874–88; 1892–4	US Army, Chief Signal Officer (1889)
Lick Observatory (Mt. Hamilton)	California	37° 20′ N, 121° 38′ W	1283	1880–	Reed (1914)[b]
Mauna Loa	Hawaii	19° 32′ N, 155° 35′ W	3399	1959–	Price and Pales (1963); Miller (1978)[b]
South America					
El Misti	Peru	16° 19′ S, 71° 23′ W	5822	1893–5	Bailey (1908)[b]
Corrido de Cori	Argentina	25° 06′ S, 68° 20′ W	5100	1942	Miller (1976)
Cristo Redentor	Argentina	32° 50′ S, 70° 05′ W	3800	1935–[c]	Prohaska (1957)
Collahuasi	Chile	21° 0′ S, 68° 45′ W	4810	1914–15	Lauscher (1979a)
Chuquicamata	Chile	21° 07′ S, 68° 31′ W	2710	1914–15	Lauscher (1979a)

[a] The largest published station reference height is given where possible. Elevations may differ by a few meters in different sources; sometimes this is due to reference to the corrected barometer height.

[b] These references generally describe the site and the history of the installation. They also include data tabulations in most cases.

[c] Annual values for these stations are contained in World Weather Records (Clayton 1944a, b, 1947; US Dept of Commerce 1959, 1966, 1968

[d] Annual values for these stations are contained in Meteorological Office (1973) which also lists sources (in most cases for the period 1931–60).

mountain passes, or in high valleys. There are also more than 200 high stations with shorter periods of record.

The best-known mountain ranges, in meteorological terms, are undoubtedly the European Alps (e.g. Bénévent, 1926; Fliri, 1974, 1975), while the least known (in English-language literature) are the mountain systems of central Asia and the Andes. Brief summaries of the climatic conditions in mountain regions of the world, with an ecological focus, are contained in Burga *et al.* (2004). In recent years, meteorological research has been carried out in areas as diverse as the Caucasus, the Mt. St Elias Range (Yukon), Mt. Wilhelm (Papua New Guinea), the tropical and subtropical Andes, and Tibet–Himalaya. Meetings on alpine meteorology have been held biennially in Europe since 1950 (Lauscher, 1963; Obrebska-Starkel, 1983, 1990) and other symposia have focused on special topics of mountain weather and climate (Reiter and Rasmussen, 1967; World Meteorological Organization, 1972; Reiter *et al.*, 1984). The intense interest in airflow phenomena in and around the Alps – lee cyclogenesis, local winds, mountain drag, and differential heating effects – led to the design of an Alpine Experiment (ALPEX) as part of the Global Atmospheric Research Programme (Kuettner, 1982; Smith, 1986) and similar interest in the influence of the Tibetan Plateau has developed (Xu, 1986).

1.4 THE STUDY OF MOUNTAIN WEATHER AND CLIMATE

The study of mountain weather and climate is hampered in three respects. First, many mountain areas are remote from major centers of human activity and tend, therefore, to be neglected by scientists. This problem is compounded by the difficulty of physical access, inhibiting the installation and maintenance of weather stations. Second, the nature of mountain terrain sets up such a variety of local weather conditions that any station is likely to be representative of only a limited range of sites. Third, there are serious difficulties to be faced in making standard weather observations at mountain stations. Some aspects of the last two problems are worth elaborating.

The conventional approach to climatic description involves long-term observation records spanning 30 years or more at a site selected to represent the "regional" environment. Stations are usually located in open terrain, away from the influence of buildings and other obstacles to airflow. In the mountains, however, we are dealing with at least three types of situation – summit, slope, and valley bottom – apart from considerations of slope orientation, slope angle, topographic screening, and irregularities of small-scale relief. These factors necessitate either a very dense network of stations or some other approach to determining mountain climate. In the future, the use of ground-based and satellite remote sensing combined with intensive case studies of particular phenomena may provide the best solution. The measurement problem is due to the generally severe nature of mountain weather with, in many localities, frequent strong winds and a high proportion of the precipitation occurring as snow. In this respect the problems are analogous to
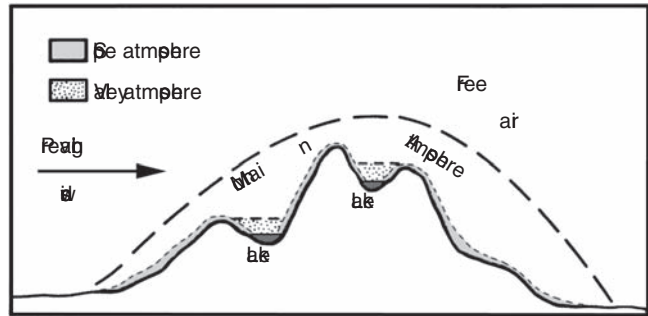
those encountered in polar regions, but special problems may arise, for example, due to the frequent occurrence of cloud at station level leading to rime build-up on the instruments with subzero temperatures. Local topography may also cause observations to be unrepresentative, at least for certain elements and for particular wind directions. Küttner (1949) and Reichel (1949) debated this question in the case of the Zugspitze Observatory.

Ekhart (1936, 1948) suggests that the atmosphere over mountains can be separated into the slope atmosphere – a few hundred meters thick, a valley atmosphere dominated by thermally included circulations and, in extensive mountain ranges, an enveloping mountain atmosphere where the airflow and weather systems are subject to major modification (Figure 1.4). Outside the latter is the "free air." In the case of isolated peaks, however, there is considerable mixing of the slope air with the free atmosphere, and the broader "mountain atmosphere" may be nonexistent. Moreover, the degree to which Ekhart's divisions are identifiable changes with season and, more especially, with the large-scale synoptic pressure field. In light pressure gradients, with clear weather, the valley and slope atmospheres may be decoupled from the surrounding atmosphere, whereas in strong airflows and cloudy conditions the only distinctive features tend to be those associated with mechanical sheltering effects.

Yoshino (1975) has attempted to develop a similar *climatic* regionalization for areas with hilly terrain. His scheme interposes a mesoclimatic scale between local (topoclimate) and macroclimate and the uplands are distinguished from the lowlands at this scale in the hierarchy. However, the gradation of altitudinal effects suggests that this is probably an unworkable division, and furthermore, the use of mesoclimate in this context is potentially misleading. It seems preferable to restrict its use to the climatology of mesometeorological scale weather systems. An attempt to summarize the identifiable levels of climatic divisions in major mountain areas, based partly on Yoshino's ideas, is shown in Figure 1.5. The mountain climate of isolated peaks or smaller features is perhaps best regarded as a topoclimatic variant of the particular regional (macro-) climate.

In most climate classifications, mountain areas are ignored, or regarded as undifferentiated "highland." Greenland *et al.* (1985) analyzed vegetation and

Note: The boundary between the orographically-modified macroclimates R1A and R3A will vary seasonally and synoptically.
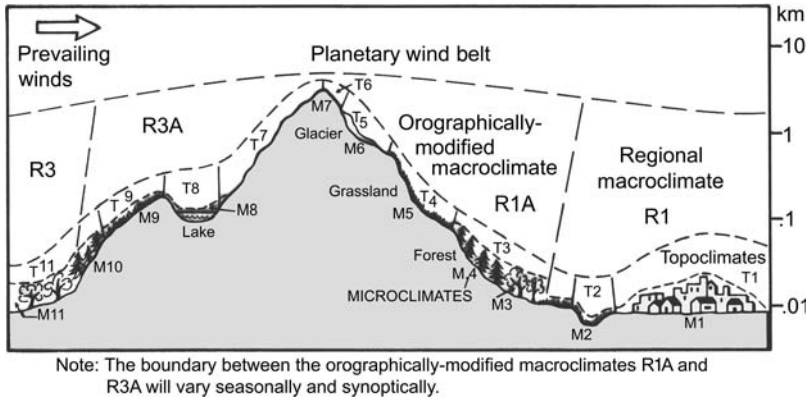
Fig. 1.5 **Scales of climatic zonation in mountainous terrain (after Yoshino, 1975). R, regional macroclimate; T, topoclimate; M, microclimate.**

climate zones on the east slope of the Colorado Front Range. They show that standard climate classifications are of limited applicability. For example, Niwot Ridge (3749 m) is variously classed as polar tundra (Köppen), perhumid tundra (Thornthwaite), or arid subpolar/alpine (Holdridge). Greenland *et al.* suggest that more appropriate bioclimatic variables are summer mean temperature, growing season soil moisture deficit, and the ratio of growing season thawing degree days to growing season precipitation. All three indices show consistent altitudinal gradients. For New Zealand mountains, Coulter (1973) proposes a threefold classification: (1) high annual precipitation (> 2500 mm) with long periods of cloud, fog and precipitation as on the west coast of South Island or the North Island volcanoes; (2) low annual precipitation (1000–1500 mm), high wind speeds, and low temperatures with short frost-free periods, as at higher altitudes of central Otago; (3) moderate annual precipitation, higher temperatures than category (2) and periods of strong drying conditions, as on the eastern ranges of both islands (see also McCracken, 1980). On a global scale, additional categories are undoubtedly necessary. The key variables that need to be considered include incoming solar radiation, mean temperatures of the warmest and coldest months, duration of the frost-free season and growing season, annual precipitation, snow cover duration, and wind speed.

A description of mountain climate rests on two considerations. What is the purpose of any particular characterization? What can feasibly be investigated in terms of the available technology and resources, including existing knowledge? In the present context, the characterization of mountain climates is in terms of the special meso- and micro-scale meteorological phenomena that occur in mountain areas. In other words, the concern is with the ways in which mountains give rise to distinctive weather and climatic regimes and their nature. Local contrasts of slope angle and orientation give rise to such large variation in local climatic conditions that it seems doubtful whether the concept of a "regional mountain climate" has much validity or value. It is more meaningful to describe the typical range of

climatic elements produced in particular topographic situations, according to the type of airflows that occur, bearing in mind the major controls of altitude, latitude, and continental location.

Mountains have three types of effect on weather in their vicinity. First, there is the substantial modification of synoptic weather systems or airflows, by dynamic and thermodynamic processes, through a considerable depth of the atmosphere. Second, there is the recurrent generation of distinctive regional weather conditions, involving dynamically and thermally induced wind systems, cloudiness and precipitation regimes and so on. Both of these major effects require that the mountain ranges be extensive in width and height and uninterrupted by deep transverse valleys and passes in their long dimension. Both also contribute to shaping the year-round character of the mountain climate, although each occurs with particular types of synoptic situation. For example, thermal wind regimes are best developed with light pressure gradients and clear skies. The third type of mountain effect is a result of slope and aspect variations. It operates primarily at the local scale of tens to hundreds of meters to form a mosaic of topoclimates. In the case of slope and valley wind systems in particular, however, it can operate on a regional scale causing recurrent patterns in the climatic distributions in major mountain systems such as the Himalaya.

The question as to what can feasibly be studied has both a practical and a conceptual aspect. The usual networks of reporting stations are designed to describe synoptic weather systems and regional climatic conditions (on a scale of 100 km or more) but, in the mountains, synoptic systems are greatly modified by the topography. The recommended spacing of weather stations (Brooks, 1947) on the plains (and mountains), respectively, is: one station per $26\,000\,km^2$ ($1300\,km^2$) for temperature, wind velocity and radiation; one station per $13\,000\,km^2$ ($1300\,km^2$) for precipitation; and one station per $6500\,km^2$ ($500\,km^2$) for snow data. These station densities exist in only a few mountain areas such as the Alps. Highlighting this issue are the results of an empirical assessment of station separation effects on temperature and precipitation data for the Great Alpine Region of Europe. Auer et al. (2005) show that the decorrelation distance (where $r < 0.5$) for annual values is 993 km for annual temperature and 149 km for annual precipitation; the corresponding distances for daily values are 533 km for temperature and only 42 km for precipitation. Such spacing is seldom realized. In the Rocky Mountains, the correlation for monthly temperatures at Niwot Ridge ($40.1°$ N, $105.6°$ W) and Berthoud Pass ($39.8°$ N, $105.8°$ W), some 40 km apart in the Colorado Rocky Mountains, is around 0.7–0.8 in most months but falls below 0.5 in July and November.

1.4.1 Advances in instrumentation

Until recently, meteorological measurements in remote mountain locations were greatly limited by the absence of electric power. Solar panels and telemetry systems can now resolve this difficulty, although in some countries vandalism of equipment

Fig. 1.6   **Automatic weather station in the Andes (D. Hardy).**

is a further problem. Miniaturization of equipment can reduce this threat and it also enhances portability to remote high altitude locations. Since the 1990s, several long-term mountain observatories in Europe have ceased to be manned on a regular basis and automatic weather stations are installed. The data acquired are appropriate for weather analysis and forecasting, but inhomogeneity and discontinuities introduced into the records may present problems for purposes of climate monitoring. The utility of high-altitude stations has become more widely recognized over the last decade. Measurements of solar and ultraviolet radiation, ozone and other chemical species have been expanded to address questions of global environmental change and physiological studies have been carried out to increase the safety of mountain climbers and sports enthusiasts.

Two different illustrations of the sophistication of modern field programs and instrumentation deserve mention. One is the use of automatic weather stations (AWS) on high mountains in the Tropics. For example, a University of Massachusetts group has operated such stations on Mt. Sajama (6542 m) in the Bolivian Andes, and Mt. Kilimanjaro (5794 m), Tanzania, providing previously unavailable information on these unique environments. Figure 1.6 shows the AWS that was operated in the Andes. The results of this work are included in Chapter 5.

The second is the "Foehn in the Rhine valley during the MAP" (FORM) sub-program of the Mesoscale Alpine Program (MAP) (Richner *et al.*, 2006). This took place during September–November 1999 and it involved some 50 surface stations, up to nine radiosondes, two wind profilers, four Doppler sound detection and ranging (SODAR) devices, two scintillometers (scintillation anemometers), one scanning and one back-scatter light detection and ranging (LIDAR) devices, tethered balloons, constant volume balloons for trajectories, an instrumented

cable car, an instrumented automobile, and research aircraft flights. Ground-based, airborne and satellite remote sensing has added new dimensions to mountain meteorological investigations. Neff (1990) details various ground-based remote sensing devices, including SODAR, LIDAR, and clear-air radar that are used in studies of airflow and other boundary-layer phenomena in complex terrain. FORM and related research is described in Chapters 3 and 5. The observations performed during the MAP included 6800 radiosonde launches, research radar and lidar measurements, research aircraft with dropsondes, and enhanced ground networks, during 35 days in 17 intensive observation periods (IOPs) (Bougeault *et al.*, 2001).

The following two chapters discuss the controls on mountain weather and climate from the standpoint of the geographical determinants of the meteorological elements, and then in terms of the dynamic and thermodynamic effects of mountain barriers on weather systems and airflow. Chapter 4 reviews the characteristics of the main climatic variables in mountain and then these are discussed for mountain regions of the world where substantial information is available. Chapter 6 examines altitude effects on people and other biometeorological considerations. Finally, changes in mountain climates and environments are discussed.

BIBLIOGRAPHY

Archinard, M. (1980) *L'apport genevois à l'hygrométrie*. Geneva: Musée d'histoire de sciences de Genève. 31 pp.

Archinard, M. (1988) Les instruments scientifiques d'Horace-Bénédict de Saussure. *Le Monde alpin et Rhodanien.*, no.1–2, 1988, 151–64.

Auer, Y., *et al.* (2005) A new instrumental precipitation dataset for the Greater Alpine Region for the period 1800–2002. *Int. J. Climatol.*, **25**(2), 139–66.

Bailey, S. I. (1908) Peruvian meteorology: Observations made at auxiliary stations, 1892 1895. *Ann Astron. Obs. Harvard Col.*, **49**(2), 104–232.

Barry, R. G. (1978) H. B. de Saussure: the first mountain meteorologist. *Bull. Am. Met. Soc.*, **59**, 702–5.

Barry, R. G. and Ives, J. D. (1974) Introduction. In J. D. Ives and R. G. Barry, (eds), *Arctic and Alpine Environments*. London: Methuen, pp. 1–13.

Bénévent, E. (1926) *Le Climat des Alpes Françaises*. Mémorial de I'Office National Météorologique de France. p. 14.

Bernbaum, E. (1998) *Sacred Mountains of the World.* Berkeley, CA: University of California Press, 191 pp.

Bjerknes, J., *et al.* (1934) For mountain observatories. *Bull. Am. Met. Soc.*, **15**, 993–4.

Böhm, R. (1986) *Der Sonnblick. Die 100 jährige Geschichte des Observatoriums und seiner Forschungstätigkeit*. Vienna: Osterreichischer Bundesverlag.

Böhm, R. (2004) Die Bergstationen Obir und Villacheralpe: Eineinhalb jahr-hunderte Klimamessungen Beobachtung in den Suedalpen. In *100. Jahresbericht der Sonnblick-Vereines fuer das Jahr 2002*. Vienna: Sonnblick-Verein, pp. 52–3.

Bougeault, P., *et al.* (2001) The MAP Special Observing Period. *Bull. Amer. Met. Soc.*, **82**, 433–62.

Brekke, A. (2004) The Haldde Observatory. In *100. Jahresbericht der Sonnblick-Vereines fuer das Jahr 2002*. Vienna: Sonnblick-Verein, pp. 8–11.

Brooks, C. F. (1947) Recommended climatological networks based on the representativeness of climatic stations for different elements. *Trans. Amer. Geophys. Union*, **28**, 845–6.

Buchan, A. (1890) The meteorology of Ben Nevis. *Trans. R. Soc. Edinb.*, **34**.

Buchan, A. and Omond, R. (1902) The meteorology of the Ben Nevis observatories, Part II. *Trans. R. Soc. Edinb.*, **43**.

Buchan, A. and Omond, R. (1905) Part III. *Trans R. Soc. Edinb.*, **43**.

Buchan, A. and Omond, R. (1910) Parts IV and V. *Trans. R. Soc. Edinb.*, **44**.

Bücher, A. and Bücher, N. (1973) La température au sommet du Pic du Midi de Bigorre. *La Météorologie*, **5**(28), 19–50.

Burga, C., Kloetzli, F. and Grabherr. G. (eds). (2004) *Gebirge der Erde. Landschaft, Klima, Pflanzenwelt*. Stuttgart: E. Ulmer, 504 pp.

Carozzi, A. V. and Newman, J. K. (1995) Horace-Bénédict de Saussure: Forerunner in glaciology. *Mémoires Soc. Phys., Histoire naturelles de Geneve*. Geneva: Éd. Passé Présent, 48: 149 pp.

Cegnar, T. (2004) Kredarika Observatory. In *100. Jahresbericht des Sonnblick-Vereines fuer das Jahr 2002*. Vienna: Sonnblick-Verein, pp. 61–2.

Cegnar, T. and Roskar, J. (2004) *Meteorolska postaja Kredarica 1954–2004*. Ljubljana: Ministry Okolje, Prostor, Energijo, Slovenia, 40 pp. (in Slovenian).

Clayton, H. H. (1944a) World weather records. *Smithson. Misc. Coll.*, 79.

Clayton, H. H. (1944b) World weather records. 1921–1930, *Smithson. Misc. Coll.*, 90.

Clayton, H. H. (1947) World weather records. 1931–40, *Smithson. Misc. Coll.*, 105.

Coulter, J. D. (1973) Ecological aspects of climate. In G. R. Williams (ed.), *The Natural History of New Zealand*. Wellington: A. H. and A. W. Reed.

Cuevas, E. (2004) Izaña Observatory. In *100. Jahresbericht der Sonnblick-Vereines fuer das Jahr 2002*. Vienna: Sonnblick-Verein, pp. 81–2.

de Saussure, H. B. (1779–96) *Voyages dans les Alpes, précédés d'un essai sur l'histoire naturelle des environs de Geneve*. Vol. 2, Chapters XXXV and LIII 1786, and Vol. 4, Chapters V–IX 1796, Neuchatel: L. Fauche-Borel.

Dessens, J. (2004) Meteorological observations since 1882 at the Pic du Midi, central Pyrenees. In *100. Jahresbericht des Sonnblick-Vereines fuer das Jahr 2002*. Vienna: Sonnblick-Verein, pp. 16–18.

Diot, E. and Diot, R. (2004) Observatoire météorologique du Mont Aiugoual. In *100. Jahresbericht des Sonnblick-Vereines fuer das Jahr 2002*. Vienna: Sonnblick-Verein, pp. 13–14.

Ekhart, E. (1936) La classification des Alpes au point de vue météorologique. *Geofis. pura appl.*, **17**, 136–41.

Ekhart, E. (1948) De la structure thermique et de l'atmosphère dans la montagne. *La Météorologie* (Ser. 4), **9**, 3–26. (Translated as On the thermal structure of the mountain atmosphere. In C. D. Whiteman and E. Dreiseitl (eds) (1984) *Alpine Meteorology*, PNL-5141, ASCOT-84–3; pp. 73–93, Richland, WA: Battelle, Pacific Northwest Laboratories.)

Finch, V. C. and Trewartha, G. T. (1949) *Elements of Geography*. New York: McGraw-Hill.

Fliri, F. (1975) *Das Klima der Alpen im Raume von Tirol*, Innsbruck: Universitätsverlag Wagner.

Fliri, R. (1974) Niederschlag und Lufttemperatur in Alpenraum, *Wiss. Alpenvereinshefte*, 24.

Forster, A., Hann, J. and Harisch, O. (1919) Das meteorologische Observatorium auf der Bjelasnica (2067 m) bei Sarajevo. *26–28 Jahresbericht des Sonnblick-Vereines für die Jahre 1917–18*. Vienna: pp. 12–18.

Fujimara, I. (1971) The climate and weather of Mt Fuji. In *Fujisan-sôgô-gakujutsuchôsa-hôkoku (Mt Fuji, Scientific Report)*, pp. 215–304. Tokyo: Fujikyuko Co. Ltd. (In Japanese; English summaries: 293–6, 343–5, also figure and table captions.)

Grant, A. N., Pszenny, A. A. P. and Fischer, E. V. (2005) The 1935–2003 air temperature record from the summit of Mount Washington, New Hampshire. *J. Climate*, **18** (21), 4445–53.

Greenland, D. E., *et al*. (1985) The bioclimates of the Colorado Front Range. *Mountain Res. Devem.*, **5**, 251–62.

Grunow, J., Greve, K. and Heigel, K. (1957) Das Observatorium Hohenpeissenberg 1781–1955. *Berichte d. Deutschen Wetterdienstes*, **5**(36).

Hann, J. (1899) Einige Ergebnisse der meteorologischen Beobachtungen am Observatorium Vallot auf dem Montblanc (4359 m). *Met Zeit.*, **16**, 198–204.

Hauer, H. (1950) Klima und Wetter der Zugspitze. *Berichte d. Deutschen Wetterdienstes in der US-Zone*, 16.

Hellman, G. (1916) Das meteorologische Observatorium auf der Schneekoppe. 24 *Jahresbericht des Sonnblick-Vereines für das Jahr 1915*. Vienna: pp. 6–9.

Hill, S. A. (1881) The meteorology of the North-West Himalaya. *Indian Met. Mem.*, **1** (vi), 377–429.

Howgate, H. W. and Sackett, D. H. (1873) Report of meteorological observations made at Mount Mitchell during the months of May, June, July, August and part of September. 1873. *Annual Rep., US Army Signal Corps*, Washington, DC, Paper no. 16, 770–947.

Ives, J. D. and Barry, R. G. (eds) (1974) *Arctic and Alpine Environments*. London: Methuen, 999 pp.

Klengel, F. (1894) Die Resultate der meterologischen Beobachtungen am Pic du Midi. 2860 meter, *Met. Zeit.*, **11**, 53–64.

Koener, C. and Paulsen, J. (2004) A world-wide study of high-altitude treeline temperatures. *J. Biogeog.*, **31**, 713–32.

Küttner, J. P. (1949) Messprobleme auf Bergstation. *Met Rdsch.*, **2**, 37–41.

Küttner, J. P. (1982) An overview of ALPEX. *Ann Met.*, **19**, 3–12.

Kyriazopoulos, B. D. (1966) The meteorological observatory of Ayios Antonios Peak of Mount Olympus. *Meteorologika*, **8**.

Lauscher, F. (1963) Wissenschaftliche Ergebnisse der Alpin-Meteorologischen Tagungen. *Geofis, Met.*, **11**, 295–303.

Lauscher, F. (1973) Neues von Höhenstation in vier Kontinenten, *68–69 Jahresbericht des Sonnblick-Vereines für die Jahre 1970–71*. Vienna: pp. 65–7.

Lauscher, F. (1975) Naturforschung auf den Kanarischen Inseln von Humboldt bis zur Gegenwart. *72–73 Jahresbericht des Sonnblick-Vereines für die Jahre 1974–75*. Vienna: pp. 61–75.

Lauscher, F. (1979a) Ergebnisse der Beobachtungen an den nordchilenischen Hochgebirgsstationen Collahuasi und Chuquicamata. *74–75 Jahresbericht des Sonnblick-Vereines für die Jahre 1976–77*. Vienna: pp. 43–66.

Lauscher, F. (1979b) Schnee in China. *Wetter u. Leben*, **30**, 148–64.

Lauscher, F. (1981) Hohenpeissenberg 1781–80. *Wetter u. Leben*, **33**, 239–48.

Leitch, D. C. (1978) Air temperatures on Mount Washington, New Hampshire, and Niwot Ridge, Colorado. *Mt. Washington Observatory Bull.*, **19**, 50–4.

Livadas, G. C. (1963) The new Mt. Olympus Research Center *Geofis. Met.*, **11**, 234.

Louis, H. (1975) Neugefasstes Höhendiagramm der Erde. *Bayer. Akad. Wiss.* (*Math.– Naturwiss. Klasse*), 305–26.

Lukesch, J. (1952) Die Geschichte des meteorologischen Observatoriums auf dem Hochobir. 2041 m, *48 Jahresbericht des Sonnblick-Vereines für das Jahr 1950*. Vienna: pp. 25–30.

McCracken, I. J. (1980) Mountain climate in the Craigieburn Range, New Zealand. In U. Benecke and M. R. David (eds), *Mountain Environments and Subalpine Growth*. Wellington: Tech. Paper, No. 70, Forest Res. Inst., New Zealand Forest Service, pp. 41–59.

Manley, G. (1949) Fanaråken: the mountain station in Norway, *Weather*, **4**, 352–4.

Maurer, J. and Lütschg, O. (1931) Zur Meteorologie und Hydrologie des Jungfraugebietes. *Jungfraujoch Hochalpine Forschungstation*, 33–44.

Mercalli, L. (2004) Hochalpine meteorologische Observatorien in Italien. In *100. Jahresbericht des Sonnblick-Vereines fuer das Jahr 2002*. Vienna: Sonnblick-Verein, pp. 67–68.

Mercalli, L., Beltrano, M. C. and Mangianiti, F. (1993) Gli osservatori Meteorologici del Monte Rosa: storia e risultati. *Nimbus*, **1**, 18–21

Messerli, B. and Ives, J. D. (1997) *Mountains of the World: A Global Priority*. Camforth: Parthenon, 495 pp.

Meteorological Office (1973) *Tables of Temperature, Relative Humidity, Precipitation and Sunshine for the World*, Pt. III. Europe and the Azores (MO 856c). London: HMSO.

Meybeck, M., Green, P. and Vorosmarty, C. (2001) A new typology for mountains and other relief classes. *Mountain Res. Devel.*, **23** (4), 34–45.

Migala, K. and Czerwinski, J. (2004) Das Observatorium auf der Schneekoppe (Sniezka) im Riesengebirge (Karkonosze). 1603 m, westliche Sudeten, Polen. In *100. Jahresbericht des Sonnblick-Vereines fuer das Jahr 2002*. Vienna: Sonnblick-Verein, pp. 24–6.

Miller, A. (1976) The climate of Chile. In W. Schwerdtfeger (ed.), *Climates of Central and South America*. Amsterdam: Elsevier, pp. 113–45.

Miller, J. (ed.) (1978) *Mauna Loa Observatory: a 20th Anniversary Report*. Boulder, CO: NOAA Environmental Research Laboratories. US Dept. of Commerce.

Mountain Agenda. (2002) *Mountains – Water Towers of the 21st Century*. Bern, Switzerland: Institute of Geography, University of Bern.

Mount Washington Observatory (1959) *News Bulletin*, Gorham, NH v. 1–.

Muminovic, M. (2004) Bjelasnica meteorological observatory. In 100 *Jahresbericht des Sonnblick-Vereines fuer das Jahr 2002*. Vienna: Sonnblick-Verein, p. 65.

Neff, W. D. (1990) Remote sensing of atmospheric processes over complex terrain. In W. D. Blumen (ed.), *Atmospheric Processes over Complex Terrain*. Meteorol. Monog. 23(45), Boston, MA: American Meteorological Society, pp. 173–228.

Nieplová, E. and Pindják, P. (1992) Fuenfzig Jahre meterologische Beobachtunen auf dem Lomnicky stít. In *88–89. Jahresbericht des Sonnblick-Vereines fuer das Jahr 2002*. Vienna: Sonnblick-Verein, pp. 37–48.

Obermayer, A. von (1908) Das Observatorium auf dem Atna. *16 Jahresbericht des Sonnblick Vereines für das Jahr 1907*. Vienna: pp. 3–11.

Obrebska-Starkel, B. (1983) Progress in research on Carpathian climate. *J. Climatol.*, **3**, 199–205.

Obrebska-Starkel, B. (1990) Recent studies on Carpathian meteorology and climatology. *Int. J. Climatol.*, **10**, 79–88.

Ohmura, A. and Auer, I. (2004) High mountain observatories in Japan. In *100. Jahresbericht des Sonnblick-Vereines fuer das Jahr 2002*. Vienna: Sonnblick-Verein, p. 83.

Pleiss, H. (1961) Wetter und Klima des Fichtelberges. *Abhand. Met. Hydrol. Dienst. der DDR*, **8**(62).

Price, S. and Pales, J. C. (1963) Mauna Loa Observatory: the first five years. *Mon. Weather Rev.*, **91**, 665–80.

Prohaska, F. (1957) Uber die meteorologischen Station der Hohen Kordillere Argentiniens. In *51–53 Jahresbericht des Sonnblick-Vereines für die Jahre 1953–55*. Vienna: pp. 45–55.

Rancourt, K. L. (2004) The Mount Washingtom Observatory 1917 m. In *100. Jahresbericht des Sonnblick-Vereines fuer das Jahr 2002*. Vienna: Sonnblick-Verein, pp. 75–77.

Reed, W. G. (1914) Meteorology at the Lick Observatory. *Mon. Weather Rev.*, **42**, 339–45.

Reichel, E. (1949) Zur der Messungen auf Gipfelstationen. *Met. Rdsch.*, **2**, 41–2.

Reiter, E. R. and Rasmussen, J. L. (eds) (1967) *Proceedings of the Symposium on Mountain Meteorology*. Atmos, Sci. Paper No. 122. Fort Collins, CO: Colorado State University.

Reiter, E. R., Zhu, B.-Z. and Qian, Y.-F. (eds) (1984) *Proceedings of the First Sino-American Workshop on Mountain Meteorology*. Boston, MA: American Meteorological Society, 699 pp.

Reiter, R. (1964) *Felder, Ströme und Aerosole in der unteren Troposphäre nach Untersuchungen in Hochgebirge bis 3000 m NN* (Wissenschaftliche Forschungsberichte 71. Darmstadt: D. Steinkopf.

Richner, H., *et al.* (2006) Nonstationary aspects of foehu in a large valley. Part I: operational setup, scientific objectives and analysis of the cases during the special observing period of the MAP subprogramme FORM. *Met. Atmos. Phys.*, **92**, 225–84.

Roschkott, A. (1934) Die Höhenobservatorien in internationalen Wetterdienst. In *42 Jahresbericht des Sonnblick-Vereines für das Jahr 1933*. Vienna: pp. 51–3.

Rotch, A. A. (1886) The mountain meterological stations of Europe. *Am. Met. J.*, **3**, 1524.

Rotch, A. L. (1892) The mountain meteorological stations of the United States. *Am. Met. J.*, **8**, 396–405.

Roy, M. G. (1983) The Ben Nevis meteorological observatory. 1883–1904. *Met. Mag.*, **112**, 118–29.

Slupetsky, H. (2004) Die Rudolfshuette (2,304 m) in den Hohen Tauern -die zweithöch-steständig bezetze Synopstation in Oesterreich. In *100. Jahresbericht des Sonnblick-Vereines fuer das Jahr 2002*. Vienna: Sonnblick-Verein, pp. 48–51.

Smith, A. A. (1964) The Mount Washington Observatory. *Weather* **19**, 374–9, 384–6.

Smith, A. A. (1982) The Mount Washington Observatory – 50 years old. *Bull. Amer. Met. Soc.*, **623**, 986–95.

Smith, R. B. (1986) Current status of ALPEX research in the United States. *Bull. Amer. Met. Soc.*, **67**, 310–18.

Smyth, C. P. (1859) Astronomical experiments on the Peak of Teneriffe. *Phil. Trans. R. Soc., London*, **148**, 465–533.

Solomon, H. (1979) Air temperatures on Mount Fuji. 1951–1960. *Mt. Washington Observatory Bull.*, **20**, 55–60.

Sonnblick Verein. (2004) *100. Jahresbericht des Sonnblick-Vereines fuer das Jahr 2002*. Vienna: 127 pp.

Spinnangr, F. and Eide, O. (1948) On the climate of the lofty mountain region of Southern Norway. *Met. Ann.*, **2**(13), 403–65.

Stair, R. and Hand, I. F. (1939) Methods and results of ozone measurements over Mount Evans. Colorado. *Mon. Weather Rev.*, **67**, 331–8.

Stastny, P. (2004) Meteorological observatory at Lomnicky Stit. In *100. Jahresbericht des Sonnblick-Vereines fuer das Jahr 2002*. Vienna: Sonnblick-Verein, pp. 58–9.

Steinhauser, F. (1938) *Die Meteorologie des Sonnblicks. 1. Teil*. Beiträge zu Hochgebirgs-meteorologie nach Ergebnissen 50-jähriger Beobachtungen des Sonnblick-Observatoriums. 3106 m, Vienna: Springer.

Stone, R. G. (1934) The history of mountain meteorology in the United States and the Mount Washington Observatory. *Trans. Am. Geophys. Union*, **15**, 124–33.

Thompson, W. F. (1964) How and why to distinguish between mountains and hills. *Prof. Geogr.*, **16**, 6–8.

Troll, C. (1973) High mountain belts between the polar caps and the equator: their definition and lower limit. *Arct. Alp. Res.*, **5**(3, Part 2), A19-A27.

Tutton, A. E. H. (1925) The story of the Mont Blanc observatories. *Nature*, **115**, 803–5.

Tzchirner, B. (1925) Ergebnisse der Temperaturregistrierungen in drei Höhenstationen auf Tenerifa. In *33 Jahresbericht des Sonnblick-Vereines für das Jahr 1924*, pp. 19–22, Vienna.

Tzenkova-Bratoeva, A. (2004) The meteorological observatory Moussala. In *100. Jahresbericht des Sonnblick-Vereines fuer das Jahr 2002*. Vienna: Sonnblick-verein, p. 63.

US Army, Chief Signal Officer (1889) Meteorological observations made on the summit of Pike's Peak, Colorado. January 1874 to June 1888, *Ann. Astron. Obs. Harvard Coll.*, 22.

US Dept. of Commerce (1959) *World Weather Records 1941–50*. Washington, DC: Weather Bureau.

US Dept. of Commerce (1966) *World Weather Records, 1951–60*, Vol. 2, Europe. Washington, DC: ESSA.

US Dept. of Commerce (1968) *World Weather Records, 1951–60*. Vol. 6, Africa, Washington, DC: ESSA.

Vallot, J. (1893–8) *Annales de l'Observatoire de Mont Blanc*, Vol. 1 (1893). 1–45; Vol. 2 (1896), 5–67; Vol. 3 (1898), 1–43; Paris: Steinheil.

von Hann, J. (1912) The meteorology of the Ben Nevis observatories. *Q.J.R. Met. Soc.*, **38**, 51–62.

Wanner, H., Salvisberg, E., Rickli, R. and Schüepp, M. (1998) 50 years of Alpine weather statistics. *Meteorol Zeit.*, **7** 99–111.

Wege, K. (2004) Das Observatorium auf der Zugspitze. In *100. Jahresbericht des Sonnblick-Vereines fuer das Jahr 2002*. Vienna: Sonnblick-Verein, pp. 29–33.

Winterberichte, Eidgenössische Institut für Schnee und Lawinenforschung, Nos. 1–25, Davos Platz, Switzerland; Nos. 26–39, Bern; No. 40–, Weissfluhjoch/Davos. (No. 1 contains meteorological data for 1936/37 to 1945/46; subsequent numbers give an annual tabulation.)

Woeikof, A. (1892) Klima des Puy de Dôme in Centralfrankreich. *Met. Zeit.*, **9**, 361–80.

World Meteorological Organization (1972) *Distribution of Precipitation in Mountainous Areas*. WMO Tech Note no. 326, Vol. 1 and Vol. 2. Geneva: World Meteorological Organization.

Xu, Y-G. (ed.) (1986) *Proceedings of the International Symposium on the Qinghai-Xizang Plateau and Mountain Meteorology*. Beijing: Science Press; Boston, MA: American Meteorological Society. (1036) pp.

Yoshino, M. M. (1975) *Climate in a Small Area: An Introduction to Local Meteorology*. Tokyo: University of Tokyo Press. 549 pp.

Zingg, Th. (1961) Beitrag zum Klima von Weissfluhjoch. *Schnee und Lawinen in den Schweizeralpen*, **24** (Winter 1959/60), 102–27.

PROCEEDINGS OF ALPINE METEOROLOGY CONFERENCES

I1950   (Milan and Turin) *Geofis. Pura appl.* 17(3–4), 81–245 (1950).

II1952   (Obergurgl) *Wetter u. Leben*, 5, 1–54 (1953).

III1954   (Davos-Platz) *Wetter u. Leben*. 6, 187–211 (1954).

IV1956   (Chamonix) *La Météorologie*, 4(45–6), 111–377 (1957).

V1958   (Garmisch-Partenkirchen) *Ber. Dtsch, Wetterdienstes*, 8(54) (1959).

VI1960   (Bled) VI *Internationale Tagung für alpine Meteorologie, Bled, Jugoslawien, 14–16 September 1960*, Institut Hydro-Meteorologique Federal de la Republique Populaire Federative de Yougoslavie, Beograd (1962).

VII1962   (Sauze d'Oulx-Sestrière) *Geofis. Met.*, 11 (1963).

VIII1964   (Viliach) *Carinthia 11*, Sonderheft 24 (1965).

IX1966   (Brig and Zermatt) *Veröff. Schweizer. Meteorol. Zentralanstalt*, No. 4, 366 (1967).

X1968   (Grenoble-St. Martin d'Hères) *X Congres International de Métérologie Alpine, La Météorologie*, Numéro Spécial (1969).

XI1970   (Oberstdorf) *Ann. Met.* NF 5 (1971).

XII1972   (Sarajevo) *Zbornik Met. Hydrol. Radova, 5* (1974).

XIII1974   (Saint Vincent, Valle d'Aosta) *Alti del Treolidesimo Congresso Internationale di Meteorologia Alpina, Riv. Geofis. Sci. Alpini, 1 (Speziale)* (1975).

XIV1976   (Rauris, Salzburg) *Veröff. Met. Geophys. Zentralanstalt*, Publ. No. 227, 1 Teil; Publ. No. 228, 2 Teil. (*Arbeiten, Zentralanst. f. Met. Geodynan.*, Vienna, L. 31, 32), 1978.

XV1978   (Grindelwald) *Veroff. Schweiz. Met. Zentr.*, 40, 1 Teil (1978); 41, 2 Teil (1979).

XVI1980   (Aix-les-Bains). *Contributions, XVIème Congrès International de Météorologie Alpine*. Société Météorologique de France, Boulogne (1980).

XVII1982   (Berchtesgaden). *Annal. Met.* No. 19. Deutscher Wetterdienst, Offenbach (1982).

XVIII1984   (Opatija). *Zbornik Met. Hidrol., Radova* 10. Beograd (1985).

XIX1986   (Rauris) *19th International Tagung für Alpine Meteorologie. Tagungsbericht*. Österreich. Gesellschaft fuer Meteorologie, Vienna (1987).

XX1988   (Sestola) *Cima '88. 20° Congresso Internazionale di Meteorologia Alpina*. (3 vols.). Servizio Meteorologico Italiano (1990).

XXI1990   (Engelberg) *Veröff. Schweizer Meteorol. Anstalt*. No. 48 (1990), No. 49 (1991).

1992:   (Toulouse) 22ieme Conference Internationale de Meteorologie Alpine. Societe Meteorologique de France, 452 pp; *La Meteorologie* 7 Serie, 45: 1–64.

1994:   (Lindau. Germany) 23 Internationale Tagung fuer Alpine Meteorologie. *Annalen Meteorol*. Nr. 30, 370 pp.

1996:   (Bled, Slovenia) *Proceedings of the 24th International Conference on Alpine Meteorology*, ICAM 96. Hydrometeorological Institute of Slovenia. Ljubljabna, 462 pp.

1998:   (Turin, Italy) *Proceedings of the 25th Conference on Alpine Meteorology*, CIMA

2000.   (Innsbruck) *Proceedings, of the 26th International Conference on Alpine Meteorology*. Österreichische Beiträge zu Meteorologie und Geophysik 23; Central Institute for Meteorology and Geodynamics, 392 pp.

2002:   *(D a v o s)   26th International Conference on Alpine Meteorology and MAP -SANW*. Publ. No. 66, Swiss Academy of Sciences.

2004.   (Brig, Switzerland) Proceedings of the 27th International Conference on Alpine Meteorology and MAP-Meeting 2003. *Meteorol Zeit*.13.

2005.   (Zadar, Croatia) *28th International Conference on Alpine Meteorology (ICAM) and the Annual Scientific Meeting of the Mesoscale Alpine Meteorology*.

Carpathian Meteorology Conference

1980   Tagung Gebirgsmeterologie (8 Internat. Conf. Karpatenneteorologie, Freiburg 1977). *Abhand. Met. Dienst*. DDR, XVI(124), Akad. Verlag, Berlin.

2 GEOGRAPHICAL CONTROLS OF MOUNTAIN METEOROLOGICAL ELEMENTS

This chapter examines the controls on mountain weather and climate from the standpoint of the geographical determinants of the meteorological elements – radiation, temperature, air pressure, vapor pressure and wind. The geographical factors that most strongly influence these elements and hence mountain climates are latitude, continentality, altitude, and the topography.

2.1 LATITUDE

The influence of latitude on the climate of different mountain systems shows up in a variety of ways. First, solar and net radiation and temperature broadly decrease with increasing latitude and, as a result, the elevations of the tree line and of the snow line decrease polewards. This means that the belt of alpine vegetation (above tree line) and the nival belt of permanent snow and ice are represented on much lower mountains in high latitudes than in the tropics (see Figure 1.1, p. 3). Second, the latitude factor is apparent in the relative importance of seasonal and diurnal climatic rhythms. This is determined by the seasonal trend in the daily Sun path at different latitudes (Figure 2.1). Seasonal changes of solar radiation, day length and temperature are basically small in low latitudes, whereas the diurnal amplitude of temperature, for example, is relatively large. Thus, Hedberg (1964) characterizes the equatorial mountains of East Africa as experiencing "summer every day and winter every night." Insufficient data exist to determine the diurnal range on these mountains reliably, but at 3480 m on Mt. Wilhelm (5° 40′ S), Papua New Guinea, it is about 7–8 °C throughout the year, compared with a seasonal range of 0.8 °C for mean monthly temperatures (Hnatiuk *et al.*, 1976). In middle and higher latitudes seasonal effects greatly exceed diurnal ones. At 3750 m on Niwot Ridge, Colorado, for example, the seasonal amplitude of mean temperature range is 21 °C compared with a daily range of 6–8 °C (Barry, 1973). If hourly data are available, the diurnal and seasonal temperature regimes can be conveniently illustrated by a *thermoisopleth* diagram (Troll, 1964). This is demonstrated in Figure 2.2 for Pangrango, Java, and for the Zugspitze, Germany. Lauscher (1966) discusses latitudinal differences in diurnal temperature range in detail.

Figure 2.3 shows the linear decrease of mean diurnal temperature range versus latitude for exposed mountain sites. In mountain valleys or on high plateaus, the range at low and middle latitudes is considerably larger than on mountain summits due to less mixing of the air with that of the free atmosphere.

(a)
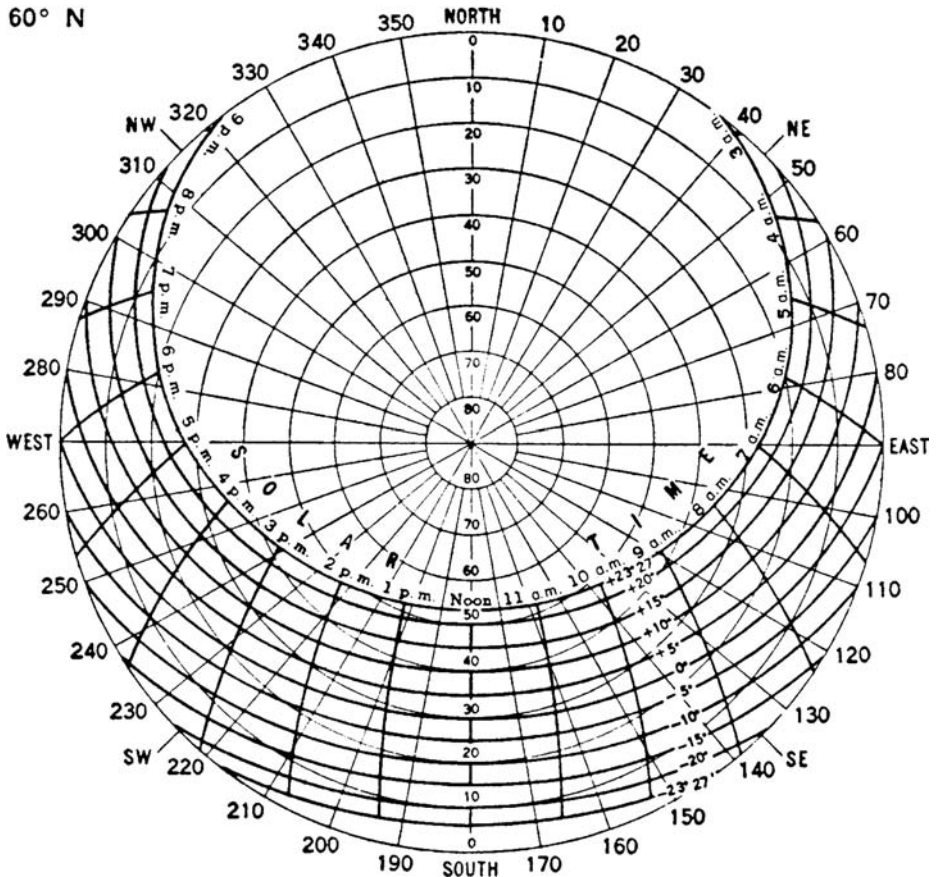
Fig. 2.1   (a) and (b) Daily Sun paths at latitudes 60° N and 30° N (from *Smithsonian Meteorological Tables*, 6th edn).
Approximate dates of the indicated declination angles are:

+23° 27′	June 21
+10°	April 16, August 28
0°	March 21, September 23
−10°	February 23, October 20
−23° 27′	December 23

These latitudinal differences in temperature regime also have an effect on the precipitation characteristics. On equatorial high mountains, above about 4000 m, snow may fall on any day of the year, particularly over-night. In middle and higher latitudes there is a well-marked and prolonged winter season. In the European Alps, for example, there is typically an average of 350 days per year with snow cover at 3000 m (Geiger *et al.*, 2003). Here, snowfall accounts for 80 percent or more of total annual precipitation (Lauscher, 1976), a higher proportion than at many arctic stations where much of the precipitation occurs as summer rains.

(b)

30° N

Fig. 2.1   (cont.)

Other latitudinal differences in mountain climates arise due to characteristics of the global atmospheric circulation. Tropical mountains are within the easterly trade wind regime; mid-latitude mountains are within the westerlies. The tropical easterlies decrease with height, whereas the westerlies increase steadily. Associated with these differences in the global wind belts, precipitation systems are primarily convective and small-scale in low latitudes, but cyclonic and generally large-scale in middle and higher latitudes.

2.2   CONTINENTALITY

The long-term average difference in mean temperature between the warmest and coldest months is termed the (true) annual temperature range (ATR). In general, over land in middle and high latitudes, the extreme months are July and January due to the approximately 1-month lag of temperatures behind solar radiation.

(a)

Fig. 2.2   **Thermoisopleth diagrams of mean hourly temperatures (°C) at (a) Pangrango, Java, 7° S, 3022 m (after Troll, 1964) and (b) Zugspitze, Germany, 47° N, 2962 m (after Hauer, 1950).**

However, it should be noted that the warmest month is not July in some locations affected by cold coastal currents, or by midsummer monsoon rains. The difference in mean July–January temperatures is termed the apparent range (Geerts, 2002) and this value is the one usually analyzed. It depends primarily on latitude and distance from a coastline in the prevailing upwind direction. Geerts (2002) shows that it peaks around 65° N and polewards of 70° S, with values in excess of 30 °C. In the equatorial zone it is less than 5 °C. The latitudinal gradient of ATR over land area between 5–65° N is just over 0.5 °C per degree latitude, although it is higher in East Asia and lower in western North America (Geerts, 2002).

The effect of distance upwind to an ocean is complicated by the seasonality of winds regimes in many regions, the actual length of the overland track of the air, and the time taken to reach a given location. Geerts (2002) shows that in western North America, the ATR from west to east along 46° N can be approximated by:

Fig. 2.2   (cont.)

Fig. 2.3   Mean daily temperature range versus latitude for a number of high valley and summit stations (after Lauscher, 1966).

Table 2.1 Measures of continentality at selected mountain stations.

Station	Latitude	Altitude (m)	Warmest month (°C)	Coldest month (°C)	Mean annual temperature range (°C) and percent of that at Verkhoyansk	Hygric continentality (deg)
Mt. Wilhelm/Pindaunde Papua New Guinea	6° S	3480	12.0	10.9	1.1 (2%)	46
Mucubaji (Sierra Nevada de Merida) Venezuela	5° S	3550	5.9	4.7	1.2 (2%)	74
Ski Basin (Craigieburn Range) New Zealand	43° S	1550	9.7	−1.4	11.1 (17%)	44
Mt. Fuji, Japan: Summit	35° N	3776	5.9	−19.5	25.4 (38%)	–
SW Slope, Taroba	35° N	1300				15
Ben Nevis, Scotland	57° N	1343	5.0	−4.5	9.5 (14%)	18
Niwot Ridge, Colorado	40° N	3749	8.2	−13.2	21.4 (32%)	76
Sonnblick, Austria	47° N	3105	1.2	−12.9	14.1 (22%)	64

$$\text{Annual Temperature Range (K)} = 0.14\phi \, (d + 15)^{0.2}$$

where ϕ is the latitude (degrees) and d is the zonal distance downwind (km) from the Pacific coast. In Europe (48–51° N) the ATR is proportional to $d^{0.18}$ downwind from the Atlantic coast as far east as Ukraine, and then becomes $d^{0.20}$ further eastward. Mountains have little immediate effect on the range, but downwind of the Rocky Mountains the range jumps about 3 K as a result of cold northerly airflows in winter. These general relationships can be modified if there are ocean areas, or inland seas, to the north or south of a given location. With increasing elevation, there is generally a decrease in the ATR. In Switzerland it is 2.2 K km^{-1} according to Geerts (2002) while Hess (1968) reports 1.7 K km^{-1} in the western Carpathians. However, in the Front Range of Colorado there is no change between the foothills and 3750 m (Barry, 1973). Within mountain ranges, the annual temperature range in valleys and basins may be 5 K larger than on summits of comparable elevation as a result of cold air ponding in the valleys.

The degree of continentality/oceanicity of a climatic region is most commonly expressed by the annual range of mean monthly temperatures. Various indices of continentality have been devised (W. Gorczynski, N. Ivanov); most of these incorporate a weighting of the annual temperature amplitude (by the inverse of the sine of the latitude angle) to standardize for the latitudinal effects on seasonality discussed above. Such adjustments are not essential, however, since it is only a relative measure. A simple measure proposed by Matullo *et al.* (2005) is the ATR at a given location expressed as a percentage of the ATR value (66 °C) observed at Verkhoyansk in eastern Siberia, the so-called "cold pole" of the northern hemisphere. Such values are included in Table 2.1.

The basic cause of continental effects is the well known difference in the heat capacity of land and water. Typically, the heat capacity of a sandy soil is $\times 1/2$ (wet) to $\times 1/3$ (dry) that of water, for unit volumes. As a result of this factor, and the deeper vertical transfer of heat by turbulent mixing in the upper ocean compared with the limited heat conduction of soils, the annual and diurnal ranges of surface and air temperature are much larger in continental climates than over the oceans. The predominance of maritime air masses in west coast mountain ranges extends the oceanic influence inland.

The amplitudes of ATR for similar latitudes and elevations at maritime and continental mountain stations are illustrated in Table 2.1. In addition to the smaller temperature range in maritime mountain ranges, the months of maximum and minimum values tend to lag the solar radiation maximum and minimum by up to 2 months, compared with only 1 month in continental interiors. Overall, continentality effects are more pronounced in the northern hemisphere than the southern, due to the 2 : 1 ratio of their respective land areas.

Oceanic versus continental conditions associated with these basic physical processes of surface heating and air mass transfer are also apparent in terms of cloud and precipitation regimes. Mid- and high-latitude west coast ranges have a high frequency of cyclonic activity, stratiform cloud and overcast skies, as in British Columbia and Alaska. Precipitation is usually greater in the winter half year, but there are no dry months. Conversely, in the interiors of the northern continents, cold anticyclones dominate the winter season, while heat lows and convective storms are typical in summer. There are generally low total amounts of cloud in winter and predominantly convective cloud regimes in summer. These contrasts apply in some degree to coastal versus continental mountain ranges.

Hygric continentality is a term introduced by Gams (1931) in his studies of vegetation in the Alps. He demonstrated that the distribution of forest types is related to the ratio of a station's altitude (m) to its annual precipitation (mm), Z/P. The index may be expressed as $\tan^{-1}(Z/P)$, which is $45°$ when $Z/P = 1$. Aulitsky *et al.* (1982) show values ranging from about $65°$ ($Z/P = 2.1$) at the tree line in Poschach Obergurgl, Austria (2072 m) and Stillberg, Switzerland, in the central Alps to only $31°$ ($Z/P = 0.6$) at Lunz-Dürnstein (1860 m). Figure 2.4 illustrates how forest types are related to hygric continentality, snow cover duration and annual temperature range. For example, larch and stone pine (*Pinus cembra*) woods occur on sites with relatively low annual precipitation (high hygric continentality), but modest annual temperature range and long-lasting snow cover; beech–oak woods occur at the opposite extremes, with larch–spruce woods on intermediate sites. On a global scale, values of hygric continentality range up to $75°$ on mountains in Colorado and Venezuela and as low as $15–20°$ in maritime locations such as western Scotland and Japan (Table 2.1).

Extensive mountain massifs and high plateaus set up their own large-scale and local-scale circulations. Such large-scale effects on diurnal and seasonal circulations ("plateau monsoons") have recently been demonstrated for the Tibetan
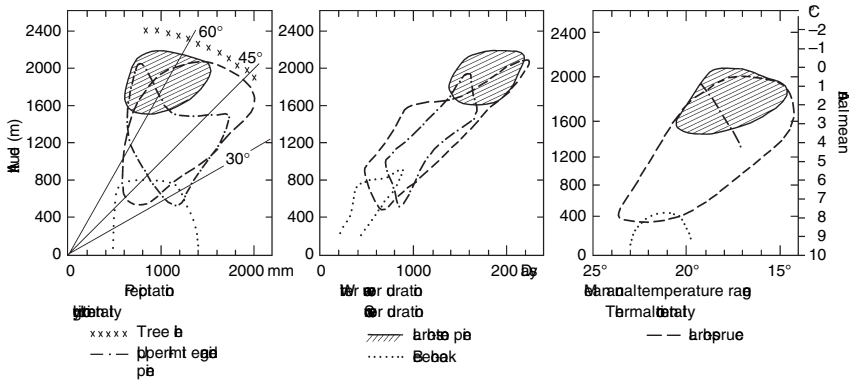
Fig. 2.4   Examples of the relations with altitude of hygric continentality, winter snow cover duration and thermal continentality, and tree species in Austria (after Aulitsky *et al.*, 1982).

Plateau and the plateaus and mountain ranges of the south-western United States (Tang and Reiter, 1984; Reiter and Tang, 1984). For example, the summer-time plateau wind circulation in the Great Basin area of the south-western United States reverses diurnally over a depth of 2 km. Gao and Li (1981) show that the Tibetan Plateau (30–38° N, 70–100° E) creates a lateral boundary layer that enlarges its effective dimensions to 22–43° N, 62–115° E in summer, and 27–40° N, 70–105° E in winter.

High mountains also protrude into the middle troposphere where the atmospheric circulation may differ considerably from that at sea level. For these reasons, mountain ranges located in a semi-arid macroclimatic zone, for example, may have distinctly different climatic characteristics and vegetational assemblages from the adjacent lowlands.

In view of the complexity of the effects of continentality in mountain areas, generalizations are of little value. Some particular aspects of continentality are discussed in the regional case studies (Chapter 5), in the following sections on meteorological elements, and in Chapter 4 on climatic characteristics of mountains.

2.3   ALTITUDE

The effect of altitude on climatic elements is of such primary importance that it is considered under several subheadings. First, its general effects on the atmospheric state variables of pressure, density, and vapor pressure are examined. Then, processes that determine the altitudinal variations of the radiation components, air temperature, and wind velocity are reviewed. Components of the energy and moisture budgets are discussed in Chapter 4 since their distribution in mountain areas involves the interaction of airflow with the topography on several scales, as well as direct effects of altitude.

Table 2.2 **The standard atmosphere.**

Z' (gpm)	P (mb)	T (°C)	ρ (kg m^{-1})
0	1013.25	15.0	1.2250
1000	898.8	8.5	1.1117
2000	795.0	2.0	1.0581
3000	701.2	−4.5	0.90925
4000	616.4	−11.0	0.81935
5000	540.5	−17.5	0.78643
6000	472.2	−24.0	0.66011

Z' = geopotential (gp) altitude. The difference between geopotential and geometric (Z) altitude is within 0.3% to 6000 m. $Z' < Z$ in low and middle latitudes; $Z' > Z$ in polar latitudes.
Source: COESA (1962).

2.3.1 Air pressure and density

The relationship between altitude and pressure was first demonstrated more than three centuries ago. It is the most precisely documented aspect of altitudinal influence on meteorological elements, although the mean condition is of little direct significance for weather phenomena. It is short-term departures from the average state that are important in this respect.

In an ideal incompressible fluid, the pressure at any depth (h) can be expressed as $p = g\rho h$, where p is the pressure, g is gravity and ρ is the air density. Where the air density also changes with height (z) we have $dp/p = -gdz/RT$ where R = the specific gas constant for dry air, T = temperature. The relationship between p, ρ, and z is often defined for a *standard atmosphere* where mean sea-level pressure = 1013.25 mb, surface temperature = 288 K and $dT/dz = 6.5$ K km^{-1} to an altitude of 11 km (see Table 2.2). The standard atmosphere represents a hypothetical state approximating the annual conditions in middle latitudes. The concept was first developed in France during the mid-nineteenth century in connection with ballooning and mountaineering (Minzer, 1962).

In the tropical atmosphere, pressure is about 15 mb greater at 3000 m, and 20 mb greater at 5000 m, than at the same levels in middle latitudes (Prohaska, 1970). This is due to higher virtual temperatures in the tropical atmosphere. Virtual temperature is the temperature for which dry air at the same pressure would have the same density as the air sample, $T_v = T/(1 - 0.375\,e/p)$, where e is the vapor pressure. Thus, pressure levels are some 200–300 m higher in the tropics than the levels given by the standard atmosphere in Table 2.2.

The effects of reduced pressure and density with height are of particular importance in connection with radiation conditions, as discussed, on p. 39 and for human bioclimatology (see pp. 444–7).

2.3.2   Vapor pressure

This is the partial pressure exerted by water vapor as one of the atmospheric gases. It is typically about 1 percent of the sea level pressure. The air temperature determines the limiting vapor pressure, known as the saturation value. Since temperatures at high altitudes are low, vapor pressures in mountain areas are also low, and the decrease is proportionately greater in the lower layers. For Mt. Fuji, Japan, the vapor pressure averages 3.3 mb at 3776 m compared with 11 mb at 1000 m and 14.5 mb at sea level (Fujimara, 1971, cited by Yoshino, 1975: 203).

Humidity data are less commonly available than most other standard meteorological variables. Glassy and Running (1994) note that National Weather Service stations in the western United States reporting humidity data have a density of < 1 station per $100\,000\,\mathrm{km}^{-2}$. However, the daily minimum temperature can be used as a surrogate for dew point temperature from which the vapor pressure can be determined.

Few specific studies of vapor pressure in mountain regions have been made, although most mountain stations record it, and there is extensive information for the free air from radiosonde soundings. Various empirical formulae have been developed to express the general exponential form of vapor pressure decrease with altitude. For example,

$$e_z = e_0 \exp(-\beta z),$$

where e is in $\mathrm{kg\,m}^{-2}$, e_0 denotes vapor pressure at the surface, z is the height (km). According to Reitan (1963), β is approximately $0.44\,\mathrm{km}^{-1}$. Kuz'min (1972) gives:

$$e_z = e_0 \times 10^{-az}$$

where $a = 0.20$ for the free air, $= 0.159$ for the mountain areas of central Asia. These empirical coefficients denote the vertical diffusion of water vapor, which must vary in efficiency both regionally and seasonally. On a daily basis the moisture profile is strongly determined by synoptic and meso-scale vertical motion.

For Sonnblick, Austria (3106 m) the July mean is about 6.5 mb, compared with 13.5 mb at Salzburg (430 m). Corresponding January averages are 1.8 mb and 4.9 mb, implying a slight increase here in the seasonal range with altitude (Steinhauser, 1936). On Sonnblick there is a moderate diurnal variation in summer of 1.2 mb, with a maximum at about 1400 h and a minimum at about 0500 h (Steinhauser, 1938). In winter, the variation is of similar phase, but negligible amplitude (0.1 mb), and this is also apparent from relative humidity data (Rathschuler, 1949).

Interesting data for the tropical Andes are provided by Prohaska (1970), in units of absolute humidity. Seasonal ranges in moisture content are large, but diminish with altitude (Figure 2.5). Even so, dry season values in these tropical high deserts (e.g. Imata) considerably exceed those in winter on summits in the Alps. Figure 2.5 also demonstrates that moisture contents in the Andean highlands are larger than

Fig. 2.5   Annual averages and range of monthly means of absolute humidity (g m^{-3}) as a function of altitude in tropical South America (after Prohaska, 1970). Station data, free air radiosonde values, and gradients calculated from Linke's equation are shown.
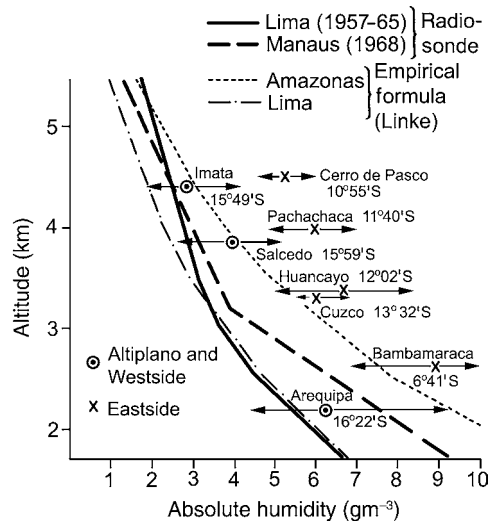
those at the same altitudes in the free air. Storr (1970) notes that this is generally the case up to at least 4 km, based on studies by Khrgian (1965) in the Caucasus and his own investigations at Marmot Creek in the Rocky Mountains near Calgary. At 1200 m, the excess in summer averages 2 mb at Marmot Creek and 2.5 mb in the Caucasus. Khrgian attributes it to evapotranspiration, but Storr notes that the seasonal and diurnal occurrence of the excess does not fully support this view. He suggests that daytime up valley and upslope air circulation is likely to carry moister valley air to higher elevations, with local variations in the strength and duration of these winds causing additional variability. However, this hypothesis is not fully in accord with Storr's finding that the excess was greater at 0500 LST than at 1700 LST at half of the sites in June and July 1967. Further studies of this problem are still needed. In mountains with permanent snow and ice cover, the slope–free air difference in vapor content will decrease above the zone of glacier ablation – the firn line – since there is no longer a moisture source (Kuz'min, 1972: 122).

Vapor pressure is important climatically in three ways. First, it reduces the transmission of infrared radiation and, to a lesser extent, solar radiation. Second, it influences the saturation deficit (the difference between the saturation and actual vapor pressure), which is an index of bioclimatic significance sometimes termed the "drying power" of the air. Third, it affects the total air density inversely, and this may also be important biologically in terms of the hypoxic effects of oxygen deficiency at high altitudes.

The fact of a vapor pressure excess in the mountain atmosphere should act to lower the condensation level, other factors remaining constant. It will also tend to reduce the transmission of infrared radiation, by comparison with the free air, thereby leading to higher atmospheric temperatures (Storr, 1970).

2.3.3   Solar radiation

Mountain observatories were of special importance in early studies of solar radiation and the *solar constant* – the average flux of solar radiation received on a surface perpendicular to the solar beam outside the Earth's atmosphere at the mean distance of the Earth from the Sun. In 1875, J. Violle made the earliest mountain-top measurements on Mont Blanc and Langley (1884) made actinometer observations on a special expedition to Mt. Whitney, California, in 1881, but their estimates of the solar constant were considerably higher than the currently assumed value of 1368 W m^{-2}. Dorno (1911) initiated long-term spectral measurements at Davos (1560 m).

Before examining observational results, the nature of atmospheric effects on solar radiation will be briefly reviewed. Detailed theoretical treatments may be found in the texts of Sivkov (1971), Kondratyev (1969) and others. We first consider a pure, dry atmosphere. In this case, solar radiation is affected by molecular (Rayleigh) scattering and by absorption by the atmospheric gases.

The path length of the solar beam through the atmosphere is expressed in terms of optical air mass, m

$$m = \frac{1}{\sin \theta}$$

where θ is the solar altitude.

For most practical purposes, this formulation is sufficiently accurate when $\theta > 20°$. At sea level, the relationship between optical air mass and solar altitude is: for $m = 1$, $\theta = 90°$, $m = 2$, $\theta = 30°$, and $m = 4$, $\theta = 14°$. For comparative radiation calculations at different altitudes, the absolute optical air mass $M = m(p/p_0)$, where p is the station pressure and $p_0 = 1000$ mb, is used to allow for the effects of air density on transmission. Thus at 500 mb a value of 2 for M corresponds to $m = 4$ and $\theta = 14°$. For an ideal (pure, dry) atmosphere, the direct solar radiation received at the 500 mb level (approximately 5.5 km) is 5–12% greater, according to solar altitude, than at sea level (Table 2.3). This corresponds to an average increase of 1–2 percent km^{-1}.

Table 2.3 **Altitude effect on (direct) solar radiation in an ideal atmosphere (W m^{-2}).**

	Optical air mass (m)			
	1	2	3	6
	Corresponding solar altitude (θ)			
Level	90	30	19.3	9.3
Extra-terrestrial	1370	1359	1350	1335
500 mb	1299	1238	1183	1162
750 mb	1269	1188	1123	985
1000 mb	1244	1146	1073	922

Source: modified from Kastrov (1956).

The depletion of the direct solar beam irradiance by atmospheric absorption and backscatter is referred to as the relative opacity of the atmosphere or its *turbidity*. Some indices of turbidity are defined for all wavelength radiation, others are for monochromatic visible radiation, used for studies of particulate aerosol loading. There are various indices of turbidity due to A. Ångstrøm, Schüepp (1949) and others (see Lowry, 1980b; Valko, 1961). Valko (1980) shows that the turbidity at Swiss mountain stations is typically four to five times less than that in the lowlands. Beer's Law for the direct flux through an atmospheric layer can be expressed:

$$S = S_0 \exp(-\tau M)$$

where S_0 and S are the fluxes at the top and bottom of the layer, respectively, τ is a transmissivity coefficient (< 1.0), and M is the absolute optical air mass to the level of S. An analogous all-wavelength expression is

$$S = S_0(\tau)^M$$

Total optical depth represents the sum of the effects due to Rayleigh scattering, ozone absorption, water vapor absorption and aerosol scattering and absorption (Bruegge *et al.*, 1992). Measurements of Rayleigh optical depth for the band 0.27 to 0.53 μm at Cuzco (13.5° S. 3400 m) and Quelccaya Base Camp (5150 m), Peru, in June–July 1977 gave values of 0.211 and 0.170, respectively, with corresponding values for the total optical depth of 0.28 and 0.10 (Hastenrath, 1997). There is little aerosol in the highland atmosphere in contrast with coastal Lima.

A useful index, K, developed by Lowry (1980b) for zenith path transmissivity (τ_p) can be defined as

$$K = -d(\ln \tau_p)/dp$$
$$\text{where } (\ln S - \ln S_p) = \ln(\tau_p)$$

For a clean, dry atmosphere, at $p = 1$ (where $p = \text{mb}/1000$)

$$\ln(\tau_p) = Kp(\ln 0.906)$$
$$\text{or } \tau_p = (0.906)^{Kp}$$

The lines indicating values of K in Figure 2.6 represent the amounts of depletion of direct beam zenith flux through an atmosphere with homogeneously distributed absorption and scattering, relative to clean dry air ($K = 1$). Figure 2.6 illustrates schematic soundings for a clean dry atmosphere with ozone (2.5 percent absorption), a clean moist atmosphere, and a moist dirty atmosphere. Note that the zenith path transmissivity at the surface ($p = 1$) is approximately 0.7.

For a real atmosphere, the effects of absorption of radiation by water vapor and of attenuation by aerosol scattering (Mie scattering) must be taken into account, in addition to absorption by the atmospheric gases and molecular scattering. Ozone absorption is strongly wavelength dependent, occurring primarily below 0.34 μm. Molecular scattering is also inversely dependent on wavelength, giving rise to the

Fig. 2.6   **Profiles of zenith-path transmissivity for a clean, dry atmosphere with ozone, a clean, wet atmosphere and a dirty, wet atmosphere; profiles of the theoretical transmissivity index (*K*) of W. P. Lowry are also shown for *K* = 1, 2, and 4 (after Lowry, 1980b).**
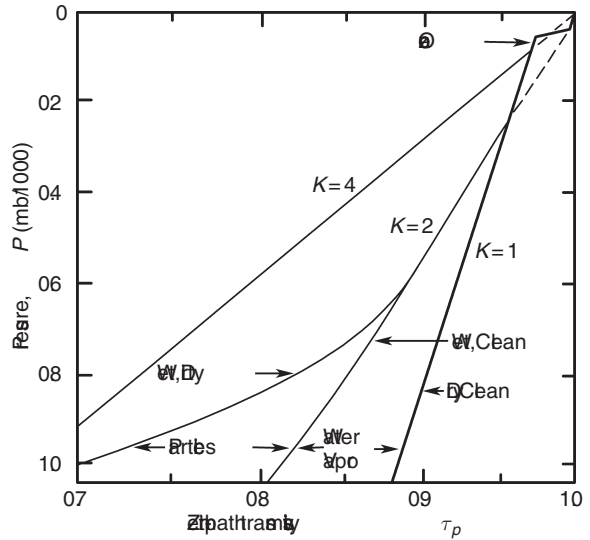
blue color of the sky (more scattering at shorter wavelengths), whereas aerosol scattering and absorption of solar radiation change only slightly in the visible and UV wavelengths. Generally, in mountain areas, however, the aerosol content tends to be low and most of the atmospheric water vapor is below about 700 mb, diminishing these effects.

Aerosol concentrations decrease by about an order of magnitude between the lowlands ($3–5 \times 10^3$ cm^{-3}) and summits at about 3 km in Europe ($10^{2\text{-}3}$ cm^{-3}), for example. This is a prime reason for the generally good visibility in mountain regions.

Water vapor influences atmospheric transmissivity through refraction effects but, since it is concentrated in the lowest 2–3 km of the atmosphere, the effect on the optical mass is negligible according to Sivkov, except where $m > 6$ (Sivkov, 1971: 28). Drummond and Ångstrøm (1967) show that under cloudless skies at 3380 m on Mauna Loa, Hawaii, the water vapor absorption accounts for about 90 W m^{-2} at noon. The same is true for aerosols, except with high turbidity at very low solar altitudes. Ångstrøm and Drummond (1966) show turbidity effects to be negligible, at high altitude stations between 16° and 36° N, for wavelengths > 0.7 μm; these wavelengths account for 50 percent of all solar radiation. For the Alps, P. Volko (cited by Körner, 2003) shows the atmospheric turbidity at 0.5 μm on Jungfraujoch (3500 m asl) is most commonly around 0.015 compared with 0.03 at Davos (1590 m) and 0.042 at Locarno-Monti (380 m).

Early estimates of the solar constant were obtained by extrapolating actinometer (later pyrheliometer) measurements of integrated solar radiation, made at different path lengths, to a theoretical zero value of *m*. The alternative technique of spectro-bolometry, pioneered by S. P. Langley on Mt. Whitney (4420 m), California, in 1881, was gradually perfected by C. G. Abbott and his associates. This involves

Table 2.4 Direct radiation on a perpendicular surface at 47° N, as a percentage of the extraterrestrial total.

	Altitude (m)				
	200	1000	2000	3000	Extra-terrestrial total (W m^{-2})
15 December	37	48	58	61%	488
15 June	51	58	67	72%	865

Source: after Steinhauser (1939).

observations of *relative* intensity in narrow spectral bands at different solar angles. Transmission coefficients are thereby determined for each ray. These results are then scaled by absolute pyrheliometer measurements of total solar radiation. Following new spectrobolometer measurements with ultraviolet filters on Mt. Whitney in 1909–10, Abbott and Fowle (1911) estimated a mean solar constant of 1343 W m^{-2}. Pyrheliometer data obtained 30 years later by the US Weather Bureau on Mt. Evans, Colorado, gave 1349 W m^{-2} (Hand *et al.*, 1943), both estimates within 2 percent of the modern value derived from satellite measurements (see note 1, p. 108). High mountain sites continue to be useful for radiation studies. Drummond and Ångstrøm (1967) repeated earlier measurements of direct beam solar radiation normal to the surface at solar noon and found that, for cloudless skies, there is an almost constant maximum value of 1174 W m^{-2} when corrected to mean solar distance. This was in close agreement with results of K. Ångstrøm (1900), Abbott and Fowle (1911) and Bishop *et al.* (1966). The difference between this value and the solar constant is accounted for by upper atmosphere absorption.

Some of the most extensive studies of altitudinal effects on solar radiation have been made in the European Alps. Steinhauser (1939) analyzed the direct radiation, on a surface normal to the beam, and showed that, as a percentage of the extra-terrestrial radiation, there is a rapid increase up to about 2000 m, after which the rate of increase declines (Table 2.4). In fact, based on observations from many high mountain stations, the increase is broadly exponential (Figure 2.7), due to the concentration of water vapor in the lower troposphere. This effect is pronounced by comparison with the theoretical distribution for an ideal (pure, dry) atmosphere.

Empirical expressions for direct beam radiation under cloudless skies versus altitude were originally developed by Klein (1948) and Becker and Boyd (1957). Lowry (1980a) proposes a more physically realistic approach relating zenith transmissivity to "standard atmosphere" pressures and a turbidity index. Lowry's (1980b) physically based models for atmospheric depletion show an improvement in the explained variance over the regression formulation of Klein for the same data. The best fit is obtained with

$$\ln (0.975 - \tau_p) = \ln M + NP$$

Table 2.5 Relationships between clear-sky direct beam transmissivity of solar radiation (τ_p) with pressure level (p) and turbidity (K).

Pressure level p (mb/1000)	Moist atmosphere[a]		Dry atmosphere[b]	
	τ_p	K	τ_p	K
1	0.678	3.937	0.757	2.820
0.9	0.758	3.119	0.806	2.418
0.8	0.817	2.559	0.844	2.148
0.7	0.860	2.183	0.873	1.966
0.5	0.914	1.822	0.914	1.822

[a] $\tau_p = 0.975 - 0.0127 \exp(3.1529p)$.
[b] $\tau_p = 0.975 - 0.0171 \exp(2.5468p)$
Source: after Lowry (1980b).

Fig. 2.7 Direct solar radiation versus altitude in an ideal atmosphere for $m = 1$ (after Kastrov, in Kondratyev, 1969; p. 262) and as observed at mountain stations (based on Abetti, 1957; Kimball, 1927; Pope, 1977).
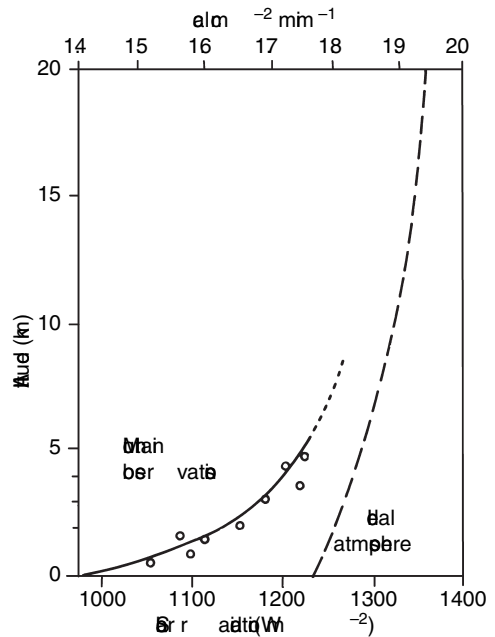
where M and N are constants for the moist and dry atmospheres of the data. Lowry (1980b) proposes standard relationships between clear sky direct beam transmissivity with pressure level and turbidity, which are summarized in Table 2.5.

Measurements made at the Jungfraujoch, Sonnblick and Zugspitze observatories have provided a wealth of material for analysis (Sauberer and Dirmhirn, 1958). Table 2.6 shows that for cloudless conditions the global solar radiation is 32 percent greater at 3000 m than at 200 m in December, 25 percent greater in

Table 2.6 Altitude and cloudiness effects on global solar radiation in the Austrian Alps (W m^{-2}).

Altitude (m)	Cloud cover					
	December			June		
	0/10	5/10	10/10	0/10	5/10	10/10
200	63	43	14	335	241	75
1000	73	51	19	362	262	100
2000	80	59	26	387	290	142
3000	83	63	36	404	314	196
		March			September	
200	187	126	41	216	146	43
1000	208	150	58	237	161	55
2000	226	172	87	256	179	75
3000	234	187	122	270	193	96

Source: after Sauberer and Dirmhirn (1958).

Table 2.7 Solar radiation on a horizontal surface, under clear skies, based on data from many sources at high mountain stations in the Alps for December and June (after Mueller, 1984, tables 3 and 4, pp. 138–41). Midday values are in W m^{-2} and daily totals MJ m^{-2}. Gradients (% km^{-1}) refer to daily totals between the successive elevation intervals.

Elevation (m)	December			June		
	12.00	Daily total	Gradient	12.00	Daily total	Gradient
1500	323	5.86		921	28.97	
2000	338	6.18	9.2	960	30.42	9.0
2500	350	6.43	6.8	992	31.71	7.6
3000	360	6.62		1018	32.84	
4000	374	6.94	4.7	1064	34.75	5.6

March and September and 22 percent greater in June. This implies an increase of 7–10 percent km^{-1}, which, as noted by Lauscher (1937), is far greater than the rate of increase for direct radiation in an ideal atmosphere. For overcast conditions the global solar radiation increased by 9–11 percent km^{-1} in all months. The ratio of global radiation for overcast to cloudless skies increases considerably with altitude, from about 0.22 at 200 m, in all seasons, to about 0.40 at 3000 m in winter and fall and about 0.50 in summer and spring (Sauberer and Dirmhirn, 1958). The higher ratios indicate that cloud cover has a smaller influence on the radiation conditions.

Mueller (1984, 1985) also provides data on the altitudinal variation of solar radiation in the Alps based on earlier literature and his own calculations. Table 2.7 illustrates the variation with altitude of clear-sky solar radiation on a horizontal surface in December and June. The vertical gradient between 1500–2500 m, 2000–3000 m and 3000–40 000 m decreases from around 9 to 5 percent km^{-1}.
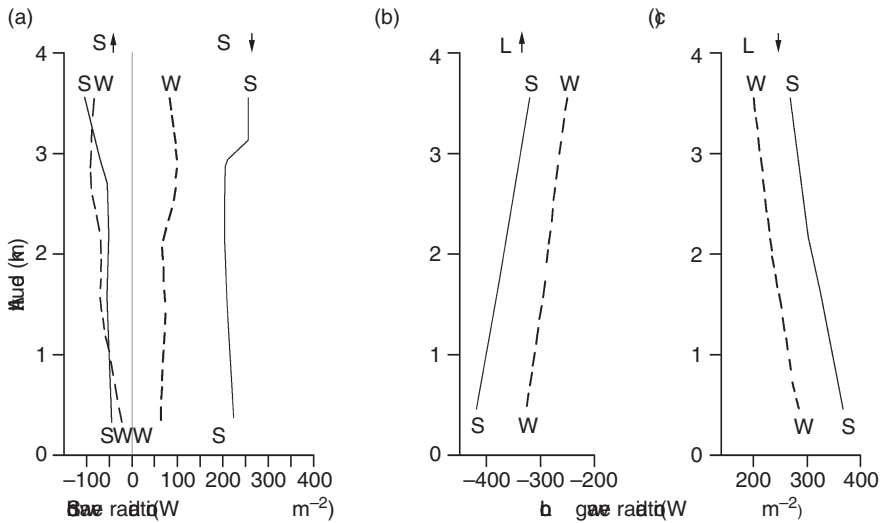
Fig. 2.8 Altitudinal variation of seasonal mean values (W m^{-2} km^{-1}), of (a) all-sky shortwave radiation; (b) upward longwave (infrared) radiation; and (c) downward longwave radiation measured at ASRB stations in the Swiss Alps (adapted from Marty *et al.*, 2002).

Even though the albedo is highest in winter and lowest in summer for all stations, the largest amount of reflected radiation for stations above 1500 m is in spring (March, April, May) due to solar elevation angle. Therefore, for stations where the snow cover starts in October and ends in May–June, the annual reflected shortwave radiation is larger than the winter or summer values.

An alpine surface radiation budget (ASRB) network of nine mountain stations and two lowland ones was established in 1994 between 370 and 3580 m altitude in Switzerland (Marty *et al.*, 2002). Pyranometers and pyrgeometers, with a shading band to cast a uniform shadow on both instruments at solar noon, are used to measure the diffuse shortwave radiation and the true down-welling longwave radiation (Philipona *et al.*, 1996). For cloud-free conditions, global solar radiation increases by 7 W m^{-2} km^{-1} in winter and 27 W m^{-2} km^{-1} in summer. All-sky global radiation increases by 13 W m^{-2} km^{-1} for annual mean values. However, in summer, the gradient at stations below 2000 m is slightly negative as a result of convective cloud cover at the lower stations. Above 2800 m, multiple reflections between clouds and snow-covered alpine slopes produce a vertical increase in solar radiation (see Figure 2.8a). Mueller (1984; p. 112–13) shows theoretically calculated variations in albedo for the Alps in summer months; there are few observational data sets. For a region with mountain snow and ice cover, for example, the albedo in July might increase from 0.25 at 2000 m to 0.60 at 3500 m.

Dirmhirn (1951) made in-depth studies of the effect of altitude on diffuse (sky) radiation. Under cloudless skies, the sky radiation decreases with altitude owing to the reduction in air density and therefore in scattering, but multiple reflections from adjacent peaks may obscure this to some extent, especially when there is snow

Table 2.8 Altitude effects on sky radiation in the Austrian Alps (W m^{-2}).

Altitude (m)	December		June	
	Cloudless	Overcast	Cloudless	Overcast
200	13.9	14.5	48	75
1000	12.2	18.5	41	100
2000	10.4	26.0	34	142
3000	9.3	36.5	30	196

All radiation data in this and other tables have been uniformly converted to W m^{-2} for convenience of comparisons, using the conversions appropriate for the particular time unit. Source: after Sauberer and Dirmhirn (1958).

Table 2.9 Mean daily totals of diffuse radiation in the Alps with overcast conditions (W m^{-2}).

	December	March	June	September
Vienna (202 m)	10	42	73	45
Rauris (950 m)	20	57	110	73
Davos (1600 m)	40	93	136	75
Sonnblick (3106 m)	38	124	202	98

Source: after Dirmhirn (1951).

cover. Table 2.8 summarizes her results for cloudless and overcast skies. With overcast conditions, sky radiation is much greater on the mountains owing to the generally shallower cloud layers overhead. Table 2.9 compares diffuse radiation for stations at several elevations in the Alps and shows a 280 percent increase in December at the Sonnblick, and a 175 percent increase in June compared with Vienna. However, it should be noted that an analysis of the actual mean values of diffuse radiation at these stations shows increases of only 119 percent in December and 128 percent in June at the Sonnblick, compared with Vienna (Neuwirth, 1979). The diffuse component represents 50–55 percent of the global radiation on an annual basis in Austria. For the Sonnblick, this figure ranges from 70 percent in May to 32 percent in October, which is usually a sunny month.

The effect of cloud cover on solar radiation as a function of altitude is complex and, again, the most detailed results are available from the Alps (Sauberer and Dirmhirn, 1958; Thams, 1961a,b). In June and December there is a nearly linear relationship between global solar radiation and cloud amount in the mountains at 3000 m, whereas at lower elevations thicker clouds cause a sharper decline for conditions of overcast (Figure 2.9). A generalized relationship between diffuse radiation and cloud amount at four elevations is shown in Figure 2.9. The diffuse radiation increases up to a limiting value of cloud amount that varies according to

Fig. 2.9 **Global solar radiation versus cloud amount at different elevations in the Austrian Alps in June and December (based on Sauberer and Dirmhirn, 1958).**
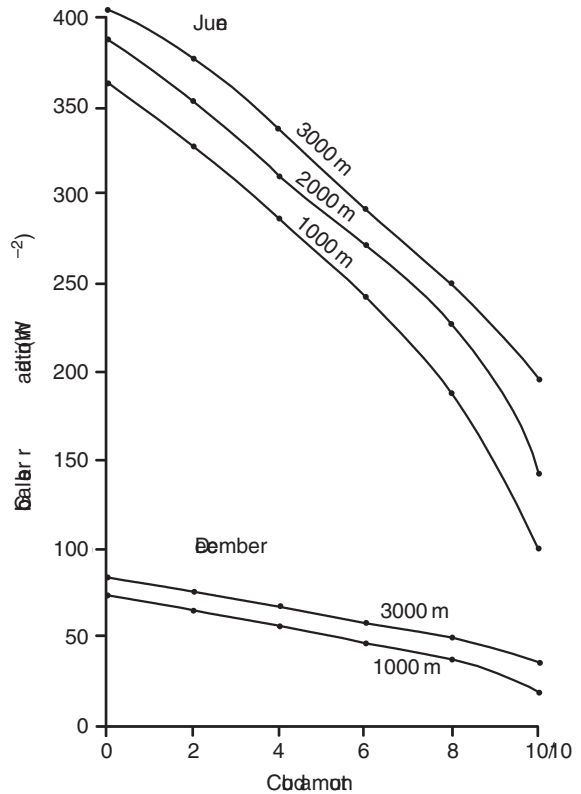
altitude. This limit is about 6/10 cloud over the lowlands, but increases to 9/10 at about 2000 m. This effect represents the predominance of thinner cloud layers at the higher stations (Thams, 1961b; Bener, 1963) as well as multiple reflections between snow cover and cloud layers. Observations by Thams (1961a) at Locarno (380 m) confirm the general shape of the curve for lowland stations in Figure 2.10, although his graph peaks at about 5/10 cloud cover where diffuse radiation contributes 260 (280) percent of the amount for cloudless skies in winter (summer), respectively.

Klein (1948) estimated the altitudinal dependence of the ratio of diffuse to global solar radiation for cloudless skies. For a solar elevation of 65°, the ratio is around 0.16 near sea level and 0.08 at 4400 m (Mt. Whitney, California). The ratio increases at lower solar altitudes. Flach (1966) also shows a decrease in diffuse radiation with increased atmospheric transparency at higher elevations.

2.3.4 Ultraviolet radiation

At the top of the atmosphere 8.3 percent of total solar radiation is in the ultraviolet (UV) wavelengths. The standard wavelength divisions for UV radiation are: 200–280 nm (UV-C), 280–315 nm (UV-B) and 315–380 nm (UV-A), where
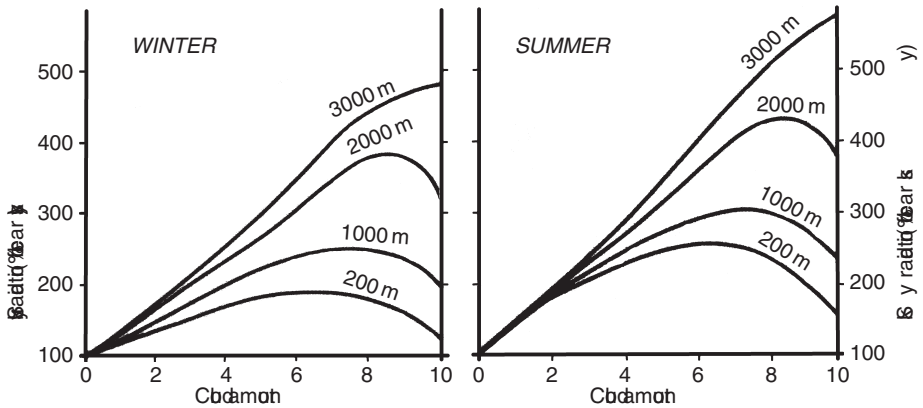
Fig. 2.10 Diffuse (sky) radiation versus cloud amount in winter and summer at different elevations in the Alps (from Sauberer and Dirmhirn, 1958).

nm = nanometers (10^{-9} m). Erythemal radiation, which causes skin reddening, is a spectrally weighted value of UV-B and A, mainly between 280–310 nm, decreasing steeply to 330 nm and with weak representation out to 380 nm. Most UV-C radiation is absorbed by stratospheric ozone. The effects of air density are not constant with wavelength and there is a wide range of estimates of the magnitude of the effects at short wavelengths. Free-air data indicate that the increase in ultraviolet radiation between sea level and 4 km altitude for $\theta = 90°$ decreases with increasing wavelength, although the absolute intensities are of course greater at the longer UV wavelengths (Elterman, 1964). The increases are $\times 2.5$ at 300 nm, $\times 2.0$ at 320 nm and $\times 1.8$ at 340 nm. The respective intensities in these three wavelengths at 4 km altitude are: 0.06 J m^{-2} min^{-1} Å^{-1}, 21.2 J m^{-2} min^{-1} Å^{-1} and 41.6 J m^{-2} min^{-1} Å^{-1} (1 Ångstrøm = 10^{-4} μm). Gates and Janke (1966) estimated that alpine areas (3650 m) at $40°$ N receive 1.5 times more total ultraviolet radiation (< 320 nm) for $m = 1.05$, and 2.2 times more for $m = 2$, than at sea level. Caldwell (1968), however, measured increases from sea level to 3650 m in Colorado (August–September 1966) that were only 4 and 50 percent for $m = 1.05$ and $m = 2$, respectively, for the biologically effective irradiance (UV-B) between 280 and 315 nm (which is weighted towards the shortest wavelength). He also reported an absolute decrease in sky ultraviolet radiation for these wavelengths with increasing elevation above 1500 m due to reduced atmospheric scattering. This corresponds with earlier findings in the Alps (Eckel, 1936).

Limited measurements of global UV-B in Utah (Caldwell, 1980), show total irradiance increasing 27 percent from 2.77 W m^{-2} at Logan (1463 m) to 3.51 W m^{-2} at Snowbird (3352 m) for a solar altitude of $63.5°$ compared with a corresponding total shortwave radiation increase of only 5 percent. Using the action spectrum for DNA-effective irradiance, the increase over the same altitudinal range amounts to 35 percent.

A summary of research carried out in the Alps, particularly by O. Eckel, indicates that direct UV-B radiation increases between 200 m and 3500 m by

Table 2.10 Mean values, 1975–9, of global radiation and ultraviolet radiation in the Bavarian Alps (W m^{-2}).

		Global radiation			Ultraviolet radiation		
Altitude (km)		0.7	1.8	3.0	0.7	1.8	3.0
June	All days	220	214	257	2.9	3.5	4.3
	Clear days	350	368	401	4.3	5.4	6.3
December	All days	28	55	59	0.5	0.5	0.6
	Clear days	44	80	91	0.5	0.8	0.8
Annual	All days	128	142	167	1.8	2.0	2.6
	Clear days	197	224	246	2.4	3.1	3.6

Source: after Reiter *et al.* (1982).

100 percent in summer and 280 percent in winter, whereas the corresponding increases for global UV-B radiation are only 34 and 72 percent, respectively (Sauberer and Dirmhirn, 1958; pp. 99–100). Air mass values for these data are not given, although the increases are generally in line with Caldwell. Using an interference filter and photo-elements in the range 0.32–0.34 μm, Wessely (1969) found that in late April 1964, the relative direct-beam UV radiation was reduced to about 90 percent of that at the Sonnblick (3106 m) at 2700 m and to about 73 percent at 1600 m.

Some of the most detailed continuous measurements of UV-B radiation have been made in the Bavarian Alps (Reiter *et al.*, 1972). Absolute UV for the 0.305–0.335 μm band (centered on 0.314 μm) has a daily mean value for 1975–9 on the Zugspitze (2964 m) of 2.6 W m^{-2}. The corresponding extraterrestrial UV radiation is 28 W m^{-2}. Under cloudless skies, mean daily values in June averaged 6.3 W m^{-2}. The UV/global radiation ratio on clear days is 1.0 percent in winter, 1.3 percent in summer, and on cloudy days is 1.5 and 2.2 percent, respectively. A summary of the annual, mid-winter, and mid-summer daily values is given in Table 2.10. Reiter *et al.* (1982) also provide information on altitudinal gradients based on data for individual days. The mean increases in UV radiation between Garmisch (740 m) and the Zugspitze for these days are 27 percent km^{-1} for cloudless days and 13 percent km^{-1} on all days in summer; corresponding rates in winter are 17 and 14 percent km^{-1}, respectively. These seasonal differences are attributable to variations in cloud amount and cloud vertical structure. Comparing records for a decade at Innsbruck (577 m asl) and Jungfraujoch (3576 m asl), which are widely separated stations, Blumthaler *et al.* (1992, 1993) report that altitudinal gradients range from 9–24 percent km^{-1} for UV-A and 13–36 percent km^{-1} for UV-B. They argue that the gradient is site specific and depends on solar elevation, albedo, and turbidity. For low aerosol loading, the increase in ultraviolet radiation in spring 1999, was 9 percent km^{-1} at 400 nm, 20 percent km^{-1} at 320 nm and 30 percent km^{-1} at 300 nm (Groner *et al.*, 2000).

In a literature survey, Calbo *et al.* (2005) cite a range of altitude increases for cloudless skies of 2–23 percent km^{-1} for UV-B, 7–15 percent km^{-1} for UV-A, and

6–18 percent km^{-1} for erythemal irradiance. Most of the data are from Europe. From photometer measurements on a few cloudless summer days at 23° S from Antofagasta, Chile on the coast to Tumbre (3850 m) and 5500 m on the extinct volcano of Sairecabur, Piazena (1996) reports vertical gradients of direct and diffuse UV-A (313–374 nm) and (mainly) UV-B (308–319 nm). The aerosol optical depth was ≤ 0.15. He found a linear, but solar elevation-dependent, increase (decrease) with altitude of the global and direct (diffuse) components in both the UV-A and UV-B. At solar elevations between 20 and 90° the increase of the irradiance was about 8–10 percent km^{-1} for UV-B and changed from 15 to 7 percent km^{-1} for UV-A. These changes in the comparatively clear, dry atmosphere over the Andes are significantly smaller than are observed in the more humid Alps. The increase of the direct component with altitude changes from 60 to 20 percent km^{-1} for solar elevations between 20 and 90°. In contrast, the diffuse UV-A and UV-B irradiation shows a small decrease of 2–4 percent km^{-1} between solar elevations of about 30–90°. The direct/diffuse ratio was found to increase with solar elevation and altitude, reaching values as high as about 5 (average 3.5–4) for UV-A and up to 4 (average 3) for UV-B. These ratios are $\times 2 - \times 2.5$ those at the comparable elevation of Jungfraujoch (3576 m). Another recent study focuses on erythemally weighted UV (Pfeiffer *et al.*, 2006). For an ideal atmosphere, the modeled increase is 3–7 percent km^{-1}. Data for cloud-free conditions in Germany–Swiss Alps and Bolivia indicate increases of 7–16 percent km^{-1} for Munich (527 m) to the Zugspitze (2964 m), 5–10 percent km^{-1} from the lowlands of Bolivia (600 m) to the Altiplano (3800–4000 m), and 8–23 percent km^{-1} from the Altiplano to the mountain station of Chacaltaya (5240 m). Chacaltaya is above the layer with heavy aerosol concentrations, which can locally exaggerate the altitudinal increase. There is significant effect of solar elevation angle. For Munich–Zugspitze, the gradient is 6.9 ± 3.3 percent km^{-1} for a 50° elevation angle and 16.5 ± 8.0 percent km^{-1} for one of 20°.

Determination of cloud effects on UV radiation is made difficult by the visual nature of most cloud observations, instrument differences, varying ozone column totals, and solar zenith angle effects (Calbo *et al.*, 2005). The net effect of clouds (scattering, absorption) on solar and UV radiation – the ratio of global irradiance for cloudy conditions to the irradiance for cloud-free conditions – is termed a "cloud modification factor" (CMF) by Schwander *et al.* (2002). Cloud cover should in general modify UV radiation to a lesser degree than total shortwave radiation, because a larger proportion (40 to 75 percent for global UV-B irradiance) is in the form of diffuse radiation (Caldwell, 1980). Indeed, Calbo *et al.* (2005) find that the CMF ranges from 0.3–0.7 according to cloud type (low values for cumulonimbus and high values for high cloud). These figures are 15–25 percent less than the corresponding ratios of overcast/cloudless sky values of total solar radiation. This is apparent in Table 2.10, although the differences are generally modest. At 3 km, the mean annual UV radiation for all days is 72 percent of that on clear days, compared with 68 percent for global radiation. Figure 2.11 shows the general form

Fig. 2.11 Curvilinear relationships between the cloud modification factor (CMF) and UV radiation reported by different sources (from Calbo *et al.*, 2005).
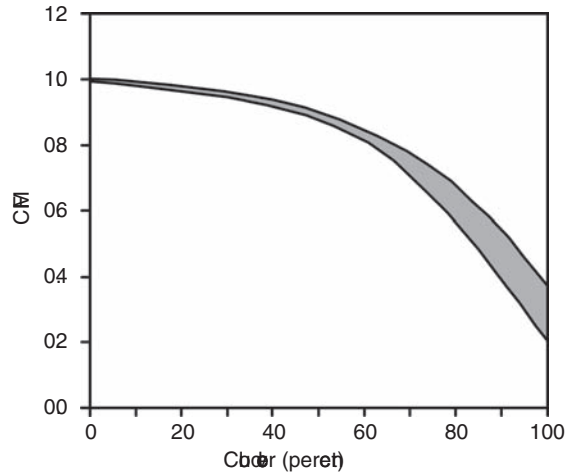
of the relationship between the CMF for UV radiation versus cloud cover amount. Note that for small cloud fractions it can occasionally exceed one. It has been observed that maximum UV intensities are recorded just below the upper boundary of stratiform cloud layers, rather than in cloudless conditions, as a result of the scattering effect.

Snow cover can have an important effect on downward UV flux in spring. The reflected radiation undergoes atmospheric scattering causing an increase in downward diffuse UV irradiance. The effect increases at shorter wavelengths due to increased molecular scattering. Caldwell (1980) cites a 20 to 60 percent increase (depending on solar altitude) of downward global UV flux (0.33 μm) over snow cover at Davos (1560 m), as measured by P. Bener. Lenoble *et al.* (2004) find that UV enhancement by snow cover depends on its spatial distribution around the observing site rather than on the topography itself. The maximum effect for erythemal UV is of the order of 22 percent in early March, assuming an albedo of 0.8 above the snow line, and 0.3 between the snow line and tree line. The enhancement is slightly greater at 0.320 μm than at 0.305 or 0.340 μm.

For the infrared end of the solar radiation spectrum (> 0.65 μm) there is also an altitudinal dependence. For example, Kondratyev (1969; p. 234), based on studies by S. P. Popov in the USSR, shows that the fraction of solar infrared radiation to the total incoming increases from about 64 percent near sea level to 83 percent at the 2000 m level, for a constant optical air mass of 3. There is a corresponding increase in the infrared components in polar latitudes that, like the altitudinal effect, is a result of lower vapor contents and therefore reduced attenuation.

2.3.5   Infrared radiation

While the effect of reduced atmospheric density with altitude is important for solar radiation, the maximum absorptance (one minus reflectance + transmittance) by

Table 2.11 Altitude and cloudiness effects on infrared radiation in the Austrian Alps (for thick, low cloud) (W m^{-2}).

	A Atmospheric back radiation Cloud cover					
	December			June		
Altitude (m)	0/10	5/10	10/10	0/10	5/10	10/10
200	227	255	304	323	345	390
1000	210	237	287	295	308	370
2000	193	225	275	260	292	342
3000	176	206	255	228	255	302

	B Outgoing radiation (mean values)			
	December		June	
Altitude (m)	Bare ground	Snow cover	Bare ground	Snow cover
200	289	301	385	–
1000	270	287	366	–
2000	255	274	355	320
3000	240	255	304	302

January values are slightly lower than those for December and July values are slightly higher than those for June, in response to air temperatures primarily. The same months are used to allow comparison with Tables 2.6–2.8.
Source: after Sauberer and Dirmhirn (1958).

an atmospheric column under clear skies is only about 15 percent of the incoming extra-terrestrial solar radiation. In contrast, infrared radiative fluxes are significantly affected by the increased atmospheric transparency at high elevation and by the lower air temperatures.

In general, both the infrared radiation emitted from the surface and the atmospheric back radiation decrease with altitude (see Table 2.11). This arises due to the lower effective temperature and, in the case of the atmospheric emittance, as a result of the smaller vapor content in the overlying air column. Calculations by Fliri (1971) over the Alps also illustrate these trends. There is a small increase in the (negative) net infrared radiation with altitude according to Fliri, whereas the results of Sauberer and Dirmhirn (1958; p. 78) indicate that, for a bare soil surface under 5/10 cloud cover, the net infrared radiation ($I\downarrow - I\uparrow$) decreases slightly with altitude: They consider that realistic regional values, taking into account surface conditions and sky cover, cannot yet be estimated.

According to Marty et al. (2002), clear-sky down-welling infrared radiation in the Alps decreases on average by 33 W m^{-2} km^{-1}, but the amount ranges from -37 W m^{-2} km^{-1} on summer days to -28 W m^{-2} km^{-1} in winter. This altitude dependence is mainly attributable to the profile of water vapor, which shows

an altitudinal decrease due to the lower temperatures with height (see Figure 2.5). For all-sky values, the gradient ranges from $28\,\mathrm{W\,m^{-2}\,km^{-1}}$ in summer to $31\,\mathrm{W\,m^{-2}\,km^{-1}}$ in winter (Figure 2.8b). The greater cloud cover at mountain stations accounts for the difference from the cloud-free conditions. At low elevations there is a diurnal variation in the down-welling component with a maximum around 1500–1600 hours and a minimum in early morning for cloudless days, whereas above about 2500 m values remain almost constant.

There is no pronounced altitudinal gradient of net infrared radiation in the ASRB data (compare Figures 2.8b and c). For cloud-free annual averages, there are greater losses at the higher stations and a vertical gradient of $-8\,\mathrm{W\,m^{-2}\,km^{-1}}$. Under cloudy skies, gradients are variable depending on cloud amount and type. There is a strong diurnal signal with more negative values, at all elevations, during the daytime when the surface is warmer (Philipona *et al.*, 1996). The observations in the Swiss Alps show good overall agreement with calculated values from the Moderate Resolution Transmittance (MODTRAN) radiative transfer model (see Berk *et al.*, 1998). The code calculates atmospheric transmittance and radiance for frequencies from 0 to $50\,000\,\mathrm{cm^{-1}}$ at moderate spectral resolution, principally at $2\,\mathrm{cm^{-1}}$ ($20\,\mathrm{cm^{-1}}$ in the UV).

There are few measurements of infrared radiation at mountain stations elsewhere, although there have been profile studies by balloons and aircraft which help to provide additional information. LeDrew (1975) demonstrates, from observations and model estimates on Niwot Ridge, Colorado, that estimates of atmospheric emittance under clear skies cannot be made using semi-theoretical models of the Brunt-type (1932) without special adjustments. Such models use screen-level climatological values and are successful because a large contribution to the atmospheric back radiation originates in the lowest 100 m or so. At 3500 m (640 mb), however, the corresponding optical length, in terms of its vapor content, is of the order of 1750 m. The coefficients of the Brunt expression (and other similar ones) lead to overestimates of the downward flux.

2.3.6   *Net radiation*

Net radiation (R_n) is usually most strongly affected by the absorbed solar radiation, $S(1-\alpha)$, since: $R_\mathrm{n} = S(1-\alpha) + (I\!\downarrow - I\!\uparrow)$. On an annual basis, the increased duration of snow cover at higher elevations causes the absorbed shortwave radiation to be reduced and, consequently, net radiation tends to decrease with elevation.

The small increase in net infrared radiation adds to this effect. Budyko (1974; p. 192) notes that, below the snow line, the net radiation changes little with altitude, since an increase in absorbed shortwave radiation (resulting from the higher totals of global solar radiation) is offset to some extent by the increase in net infrared radiation. This altitudinal pattern will occur, at least during the snow-free season.

Table 2.12 Mean net radiation at different altitudes in Austria (W m^{-2}).

Altitude (m)	March	June	December
500	32.0	141.5	6.8
1000	24.2	151.6	15.0
1500	25.2	164.8	15.0

Source: after Sauberer and Dirmhirn (1958).

Fig. 2.12 Altitudinal variation of seasonal and annual mean values of all-sky net radiation (R_n, W m^{-2} km^{-1}) measured at ASRB stations in the Swiss Alps (adapted from Marty et al., 2002).
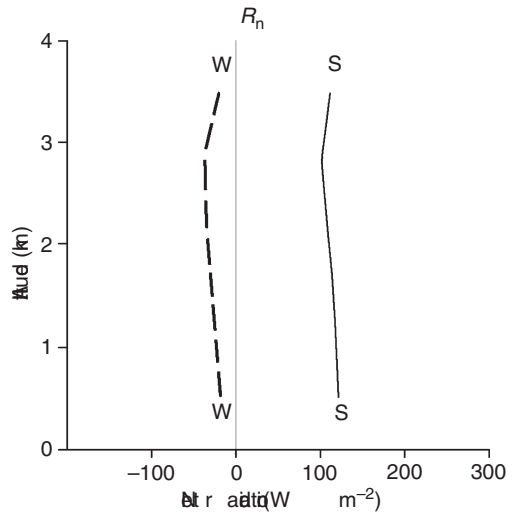
For Austria, mean monthly values of R_n were calculated by Sauberer and Dirmhirn (1958; p. 83) between 500 and 1500 m (Table 2.12). These are based on sunshine duration at 43 stations and the longwave fluxes illustrated in Table 2.11 (p. 48). The figures show an altitudinal decrease of R_n only to about 1000 m in March and December and altitudinal increase in June when there is no snow cover effect up to at least 1500 m elevation.

Measurements confirm that net radiation gradients are mainly determined by the gradient of shortwave radiation since there is only a small altitudinal variation in the net infrared radiation. The gradient in the annual mean at the ASRB stations is 14 W m^{-2} km^{-1} (Figure 2.12). The longer duration of snow cover at the higher stations is a major factor in reducing the absorbed shortwave radiation. In summer, net radiation is almost constant with altitude.

At lower elevations in the Black Forest region of Germany a comparison of three sites is available for 1992–5 (Iziomon et al., 2001). The annual clear-sky global solar irradiance at Feldberg (47.9° N, 8.0° E, 1489 m) was 76 percent of the extra-terrestrial amount compared with only 68.5 percent at nearby Bremgarten (212 m). The all-sky global solar radiation (S) at Bremgarten is 129 W m^{-2} and almost the

Fig. 2.13 The ratio of net radiation (R_n) to solar radiation (S) versus height in the Caucasus in summer (after Voloshina, 1966).
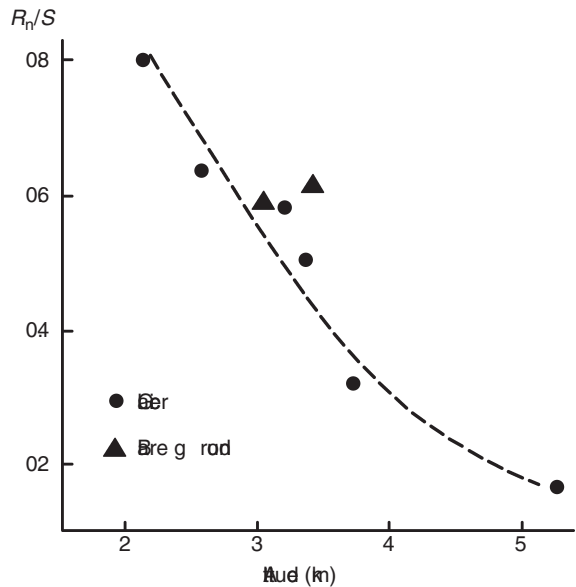
same at Feldberg The annual net radiation at Bremgarten (212 m) is $54.5\,W\,m^{-2}$, whereas at Feldberg (1489 m) it is 73 percent of that value, and at an intermediate elevation at Geiersnest (870 m) it is 84 percent. The annual gradient of R_n is $11.3\,percent\,km^{-1}$. The annual mean ratio of R_n/S decreases from 0.41 at Bremgarten to 0.37 at Geiersnest and 0.32 at Feldberg. R_n is negative due to snow cover effects during December–February at Feldberg, and in December–January at Bremgarten. The monthly mean values reach $128\,W\,m^{-2}$ at Bremgarten and $106\,W\,m^{-2}$ at Feldberg in July, a gradient of $17.2\,percent\,km^{-1}$.

In the humid equatorial Andes, net radiation declines by about 20 percent from 1000 to 3100 m in elevation, and in Peru and Bolivia it decreases by 30 percent from about $105\,W\,m^{-2}$ (for daily values) at 1000 m to $75\,W\,m^{-2}$ around 4000 m in association with increased effective infrared radiation loss (Frère et al., 1975). The first region has a bimodal regime of annual precipitation and of incoming solar radiation, whereas in the southern tropical Andes the annual regimes are unimodal. Net radiation as a percentage of incoming solar radiation decreases from 55–60 percent below 1000 m in the equatorial Andes to 43 percent at 4000 m; corresponding figures for the southern tropical Andes are 50–55 percent and 34 percent, respectively. Where there is snow cover, the sharp increase in albedo causes a large reduction in absorbed shortwave radiation and, therefore, in net radiation. Over glacier surfaces in the Caucasus, there is, in the summer months, a progressive decrease in the ratio of net to solar radiation with height (Figure 2.13), from about 0.8 at 2000 m to below 0.2 at 5000 m (Voloshina, 1966). However, this is primarily related to an albedo gradient with albedos ranging from 0.28 at 2130 m to 0.74 at 5300 m.

2.3.7   Temperature

During the eighteenth century there was still considerable controversy as to the cause of the general temperature decrease with height. De Saussure, working in the Mont Blanc massif, was one of the first physical scientists to approach a realistic explanation of the cause of cold in mountains (see Barry, 1978). Since the atmosphere is relatively transparent to solar radiation, 45 percent of the incoming total is absorbed at the Earth's surface as a global average. The atmosphere is heated primarily through absorption of terrestrial infrared radiation (although the *net* effect is still one of cooling, especially above cloud layers) and by turbulent heat transfers from the ground.

The average temperature decrease with height, or the *environmental lapse rate*, approximates $6\,°C\,km^{-1}$ in the free atmosphere. At night and in winter, the gradient may be temporarily reversed, over limited vertical distances, in a layer of *temperature inversion*. This may occur due to nocturnal radiative cooling at the surface, large-scale subsidence in an anticyclone, or advection of a warm air mass over a colder surface.

There is an upper limit to the absolute rate of temperature decrease with height, due to the hydrostatic stability of the atmosphere. This limit – the dry adiabatic lapse rate (DALR) of $9.8\,°C\,km^{-1}$ – is the rate at which an unsaturated air parcel cools when it is displaced upward. The environmental lapse rate may locally exceed the DALR, especially as a result of surface heating. In this super-adiabatic situation, the density difference between the surface air and that overlying it causes overturning. When air is saturated, the cooling rate of an air parcel displaced upward depends on its initial temperature, but is always less than the DALR due to the release of latent heat by the condensation process. Above $20\,°C$, this saturated adiabatic lapse rate (SALR) is less than $5\,°C\,km^{-1}$, whereas at sub-zero temperatures, the available moisture content of the air is so small that only a very limited amount of latent heat can be released. At $-40\,°C$, the SALR is almost identical with the DALR (see also p. 267).

Average lapse rates show considerable variability in relation to climatic zone, as well as to season (Lautensach and Bogel, 1956; Hastenrath, 1968). The highest values tend to be reached in summer over tropical deserts, whereas the strongest negative rates, due to temperature inversions, occur in eastern Siberia, northwest Canada and the polar regions in winter. Such differences render the practice of adjusting average station temperatures, or pressures, to sea level likely to produce noncomparable and therefore misleading results.

Another factor that affects the altitudinal decrease of temperature is the type of air mass. Yoshino (1966) shows that lapse rates are generally greater for northerly than southerly winds (in the northern hemisphere). For example, continental polar air is frequent in February in Japan, which tends to make lapse rates a maximum in this month. Mean values for 1939–48 between Mt. Fuji and Kofu, with an altitudinal range of 3500 m, are $6.1\,°C\,km^{-1}$ in February compared with $5.4\,°C\,km^{-1}$ in November.

By comparison with the surrounding atmosphere, the slope air over a mountain is affected by radiative and turbulent heat exchanges. These processes modify the temperature structure over the massif so that lapse rates on a mountain slope may differ from those in the free atmosphere according to the time of day. In the Austrian Alps, von Hann (1906; p. 102) found the following temperature decreases between Kolm Saigurn, 1600 m, and Sonnblick, 3106 m.

> Winter 4.9 °C km^{-1} at 0200 h, 6.6 °C km^{-1} at midday;
> Summer 6.0 °C km^{-1} at 0200 h, 8.9 °C km^{-1} at midday.

An analysis by Pepin *et al.* (1999) for stations in the Pennines of northern England, with a vertical separation of 700 m, indicates that lapse rates are determined by atmospheric temperature and moisture level, cloudiness/solar radiation, and wind speed. Hence, changes in lapse rate can result from changes in the frequency of cyclonic/anticyclonic circulation regimes. A shallower (steeper) lapse rate may be expected under warmer, moister atmospheric conditions (increased solar radiation).

An exhaustive analysis of records from 640 stations in the Austrian–Italian Alps by Rolland (2003) suggests that the results of many earlier regional studies are biased by the use of a small number of stations and short records. The stations he uses range from below 100 m to over 2000 m, and valley and slope sites are identified. Lapse rates are calculated using simple linear regression of temperature with altitude in the four station groups. Figure 2.14 shows the annual course of lapse rates for minimum, mean and maximum temperatures, revealing a clear and consistent seasonal variation, with higher lapse rates during April–September. The largest lapse rates in summer, and the least in winter, are for maximum temperatures and valley bottom locations in the Trentino–Adige region. Overall, the mean annual lapse rate ranged from 5.4 to 5.8 °C km^{-1}.

The influence of nocturnal inversions at night and of near-adiabatic conditions by day, together with the effects of föhn winds and katabatic drainage, led von Ficker (1926) to the view that "true" lapse rates cannot be determined in mountain regions. However, a unique approach to direct measurement was performed in the Austrian Alps in a little noted study by Brocks (1940). A goniometer was used to determine density differences in air layers between five locations near Salzburg on two clear autumn days in 1938. Brocks found that the diurnal amplitude of lapse rate decreases with altitude more rapidly in the free air over the plains than over the mountains, and also that the mountain atmosphere extends above mean ridge height.

It is important to distinguish between the effects of local topography which cause diurnal changes in lapse rate, as illustrated above, and large-scale topographic effects that modify the atmospheric structure. Tabony (1985) outlines three idealized topographic situations – an isolated mountain, a plateau of limited extent, and an extensive plateau (Figure 2.15). The temperature curve is representative of a surface inversion on a clear winter night. In the first case, the variations

Fig. 2.14 Lapse rates of minimum, mean and maximum temperatures in the Alps (after Rolland, 2003). VB, valley bottom.
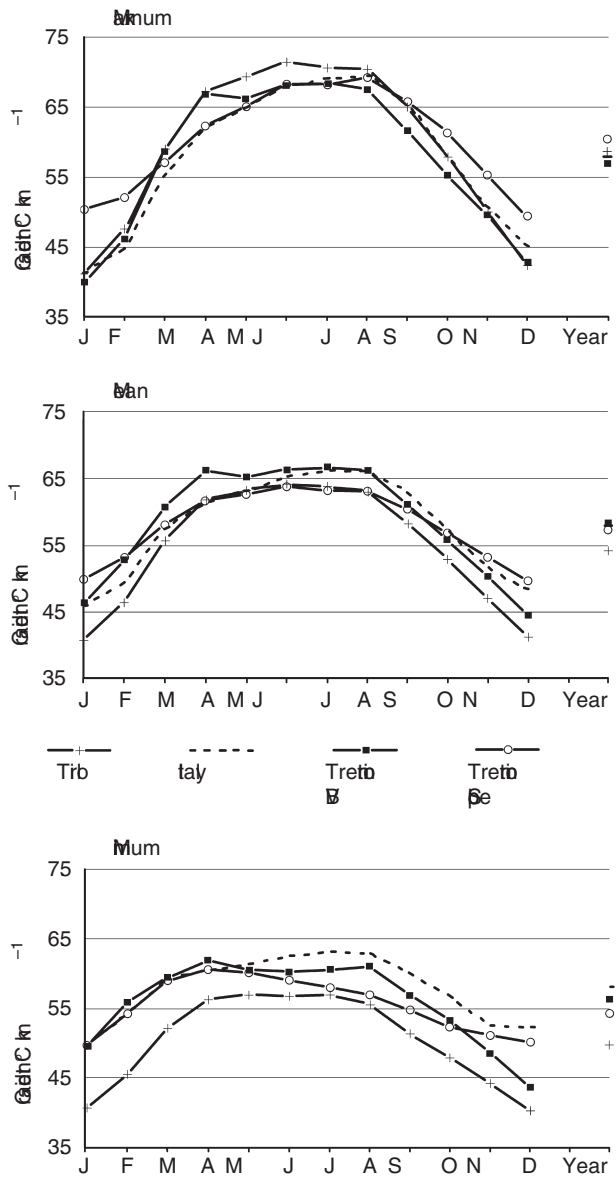
in mountain temperature are similar to those in the free atmosphere, diurnally and seasonally. In the third case, the entire profile is displaced upward creating a seasonally modified atmosphere and lower surface temperatures over an extensive plateau. In the case of the limited plateau, lapse rates are like those in the seasonally modified atmosphere, but the terrain does not displace the profile upward and temperatures are independent of altitude. Tabony notes that, in the Austrian Alps, winter temperature profiles show a $6\,°C\,km^{-1}$ lapse rate near the surface and an
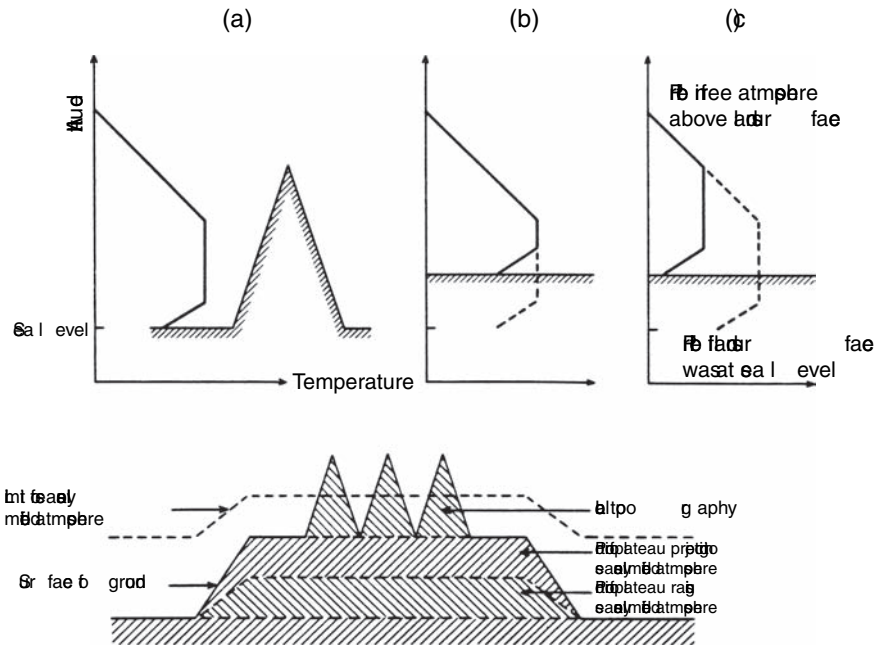
Fig. 2.15 Schematic vertical temperature profiles on a clear winter night for three topographic situations; (a) isolated mountain; (b) limited plateau; (c) extensive plateau; and a generalized model of the effects of local and large-scale mountain topography on the depth of the seasonally-modified atmosphere (after Tabony, 1985).

isothermal layer between 700 and 1400 m. The main valleys enclosed by mountains are at about 700 m; above 1400 m the mountain slopes project into the free atmosphere, while locations between 700 and 1400 m are still enclosed. Radiosonde soundings near the Alps show slightly warmer conditions in the lower layers in winter, with a surface inversion. Thus, mean winter temperatures up to 500–600 m above the surface are modified, comparable to the depth of diurnal variations, and this layer has been displaced upward.

Thermal contrasts between low-level snow-free ground and snow-covered mountain slopes can also modify lapse rates. The timing and duration of snow melt in spring, when air temperatures remain close to $0\,°C$, is especially important. The date of snow melt is retarded considerably at higher altitudes; it occurs in the Austrian Alps in late March at 2000 m, in late April at 2500 m, and in June at 3000 m according to Geiger et al. (2003). Moreover, snow depths are greater at higher altitudes and the altitudinal gradient of snow depth is increased in spring as the snow boundary rises. Thus, a steep lapse rate is to be expected across the zone of the melting snow.

British data show that altitudinal effects are dominant for height gradients of mean maximum temperatures, whereas local topography is at least as important for minimum temperatures (Harding, 1978). The mean gradient of maximum temperatures in Great Britain is about 8–9 $°C\,km^{-1}$ but with a general winter minimum

Fig. 2.16 The annual variation of altitudinal gradients of air temperature and 30 cm soil temperature between two upland stations in the Pennines and the lowland station of Newton Rigg (from Green and Harding, 1979).
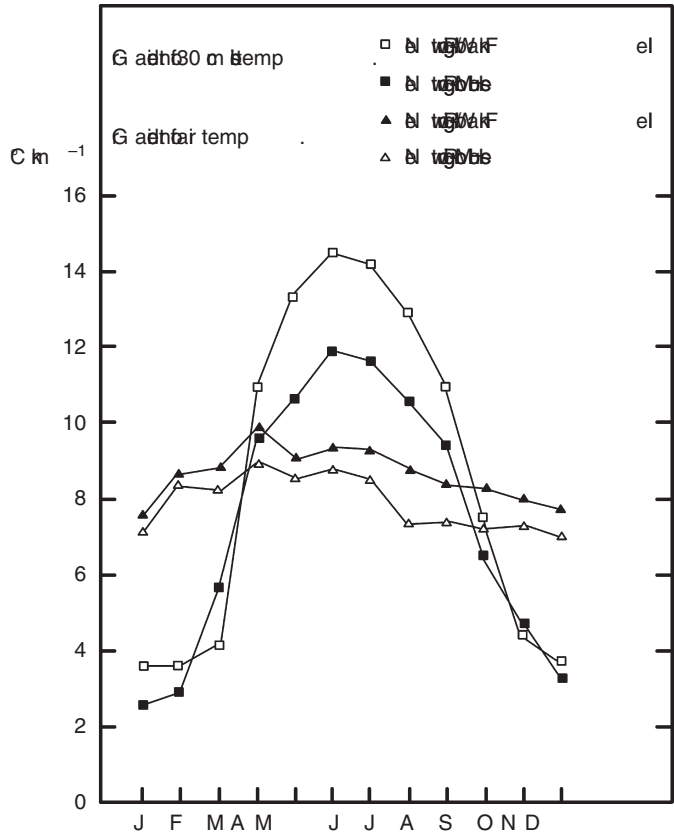
(6–7 °C km^{-1}) and spring maximum (9–10 °C km^{-1}) (see Figure 2.16). The spring maximum is apparently *not* due to airflow direction, but may be related to the seasonal increase of instability; the atmosphere is generally more stable in winter. Both the form and magnitude of this pattern are also present in gradients of mean temperature in southern Norway and central France (Harding, 1978; Figure 3). Using data from the Pennines of northern England, Harding (1979) shows that a linear relationship exists between the gradient of daily *maximum* temperature and the difference in sunshine hours between lowland and upland sites; the upland stations are between 500 and 800 m asl. Where there is a positive excess of 2 hours of sunshine at lowland stations, the altitudinal gradient of maximum temperatures averages about 9.5 °C km^{-1}. The reduction of solar radiation by cloud cover in the uplands will reduce the sensible heat flux into the boundary layer, thereby potentially lowering screen level maximum temperatures. For a 2-hour reduction of the upland sunshine duration, maxima may be lowered about 0.5 °C according to Harding's estimates. The observed gradient of maximum temperature increases approximately 0.45 °C km^{-1} per hour of increase in lowland minus upland sunshine duration.

In the case of altitudinal gradients of soil temperature, studies in Great Britain show clearly that the effects of soil properties are subordinate to meteorological controls (Gloyne, 1971; Green and Harding, 1979). Gloyne found the annual mean altitudinal gradients of air and soil temperature to be similar, based on observations at 0900 UTC, which approximate the daily minimum temperature in the soil. Records of daily maximum and minimum soil temperatures, for two upland stations in Wales at just over 300 m asl, and a lowland station (30 m), show strong seasonal variations in gradient, ranging from $1\,°C\,km^{-1}$ in winter to $6\,°C\,km^{-1}$ in summer for maxima and from 0 to $4\,°C\,km^{-1}$ for minima (Green and Harding, 1979). This matches the earlier finding of Harrison (1975) for maximum soil temperatures in the same locale. Confirmation that this seasonal pattern is not a result of coastal influences or of soil properties, is provided by Green and Harding's analysis of 30 cm soil temperatures between three station pairs in and around the Pennines (with the upland stations at 400–550 m) and ten other station pairs with an altitude difference of 200–300 m in northern England and Scotland. Subsequent work by the same authors for stations in Europe shows it to be a general result, with the seasonal range of soil temperature being of similar magnitude down to at least 1 m depth (Green and Harding, 1980).

Whereas the seasonal amplitude of the altitudinal gradient of air temperature is only $2\,°C\,km^{-1}$ in Britain, that for soil temperatures is $10–11\,°C\,km^{-1}$ (Figure 2.16). Similar amplitudes in these respective gradients are recorded in most other European countries (Green and Harding, 1980). The seasonal amplitude shows little spatial variation in the case of soil temperature gradient (although absolute values vary), but the magnitude of the altitudinal gradient of air temperature decreases with increasing continentality in Europe and the seasonal amplitude of the gradient shows a corresponding increase. Figure 2.17 illustrates *differences* in altitudinal gradients of air and soil temperatures for several locations. The seasonal patterns are remarkably similar, with steeper altitudinal gradients of soil temperature in summer and of air temperature in winter. Absolute values of the gradient differences are somewhat affected by horizontal climatic gradients between the station pairs and also perhaps by latitudinal influences. The excess of soil temperature lapse rates over the dry adiabatic rate in summer implies that the upland soils are relatively cool. This is probably due to the greater use of available energy for evaporation from the moist upland peats (Oliver, 1962; Green and Harding, 1979). The cause of the excess of upland soil temperatures over air temperature in winter is more problematic. A seasonal snow cover will generally keep the ground surface temperature above that of the air temperature by retaining heat gained in the summer and autumn. However, a transient snow cover – such as tends to occur in British uplands – should only diminish the diurnal cycle without raising the mean temperature and it does not appear that the soil could maintain the required upward flux of sensible heat (approximately $25\,W\,m^{-2}$ according to Green and Harding (1979). The intermittent freezing of soil water is a further possible heat source, but again this effect does not match the observed increase of soil maximum
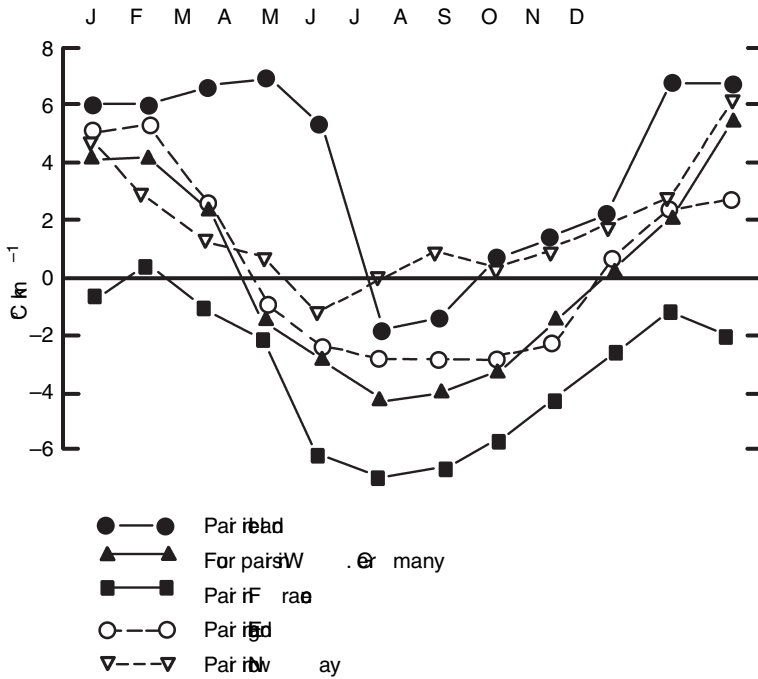
Fig. 2.17 Differences between altitudinal gradients of soil and air temperature at pairs of stations in Europe (from Green and Harding, 1980).

and minimum temperatures in Wales, nor the occurrence of this positive soil–air difference with frozen ground and snow cover in the mountains of East Germany in January–February 1963 (Green and Harding, 1980).

While the altitudinal gradients of soil and air temperatures may be broadly similar, the absolute values differ. In the Colorado Rocky Mountains, the mean annual $0\,°C$ isotherm of air temperature occurs at about 3225 m whereas that for the soil (15–30 cm depth) is almost 400 m higher (Thompson, 1990). Although the insulating effect of snow cover on winter ground temperatures must play a role, a multiple regression analysis of weekly soil temperatures with air temperature, precipitation, wind speed and snow depth shows that only a few percent of the variance in soil temperatures is accounted for by the inclusion of variables additional to air temperatures (Barry, 1972). Absorption of solar radiation by the ground in summer is the likely cause.

In many high mountains and on the Tibetan Plateau, the ground may be permanently frozen. *Permafrost* is said to be present when the ground temperature is below freezing during two consecutive summers. On a global scale, permafrost is generally sporadic or in isolated patches in mountains. In the Rocky Mountains, patches occur around 3750 m in the Colorado Front Range, for example (Ives and Fahey, 1971; Greenstein, 1983). Janke (2005) estimates that permafrost underlies 12 percent of the surface in this region. In Switzerland permafrost occupies around

Fig. 2.18 Mean daily temperature range versus altitude in different mountain and highland areas: I, Alps; II, western USA; III, eastern Africa; IV, Himalaya; V, Ethiopian highlands (after Lauscher, 1966).
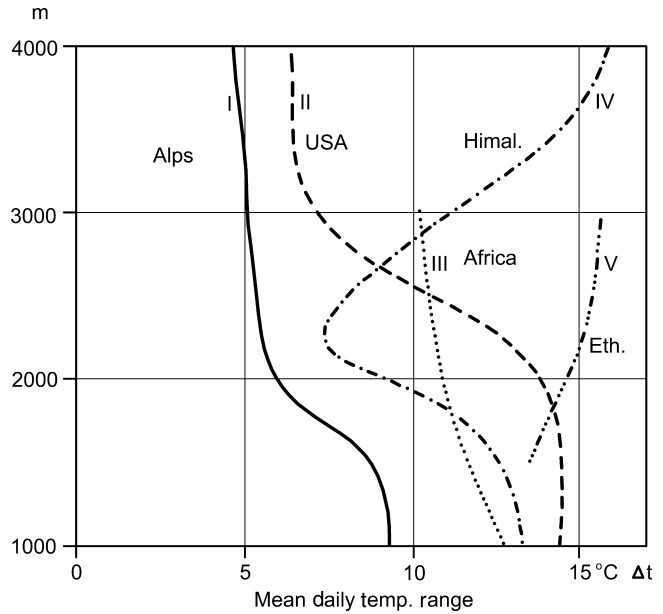
4–6 percent of the surface area, or twice that covered by glaciers (Vonder Mühl *et al.*, 1999). The presence of permafrost is determined by the ground surface temperature, vegetation cover and snow cover depth and duration; hence microclimatic conditions are all important. Discussion of these controls is beyond our scope here but a useful survey is provided by Williams and Smith (1989), for example.

The diurnal range of temperature in the free air decreases with increasing altitude. Typically, in the middle latitudes, it is of the order of 1.5 °C at 850 mb, 1.0 °C at 700 mb and 0.7 °C at 500 mb. There is a phase lag with increasing height; observations in the Alps in summer 1982 showed that the temperature maximum at 850 mb occurs about half an hour later than at the ground. Surprisingly, however, the phase was reversed at higher levels, probably as a result of local advection effects (Richner and Phillips, 1984). Mountain slope and summit data reflect the same decreasing amplitude of diurnal air temperature range with increasing altitude, reflecting the mixing of slope air with the free atmosphere. This is clearly apparent in middle latitudes where the westerlies increase with height. Figure 2.18 illustrates this for the Alps and North America. The greater dryness of the air over western North America may account for the larger range compared with the Alps. Lauscher (1966) suggests that the high moisture content of the air is the cause of the small altitudinal change on the mountains of equatorial Africa. The contrasting curve for the Tibetan–Himalayan region in Figure 2.18 appears to result from cloud and precipitation effects and site location. There is a minimum diurnal range of temperature in the zone of maximum precipitation on the southern slopes and then a substantial increase of the range at stations located in high-lying valleys such as Leh (3496 m) and Lhasa (3685 m). This site factor is probably likewise

Table 2.13 **Components of the daily temperature fluctuation (°C), Austrian Alps.**

	All days (January 1931–June 1934)		Clear days (< 3/10 cloud)	
Periodic	*Winter*	*Summer*	*Winter*	*Summer*
Sonnblick, 3106 m	1.0	2.0	1.6	4.2
Rauris, 943 m	7.6	10.7	12.4	17.3
Aperiodic				
Sonnblick, 3106 m	4.4	4.4	4.0	5.4
Rauris, 943 m	10.2	13.1	14.4	17.9

Source: after Steinhauser (1937).

responsible for the profile of the curve for Ethiopia in Figure 2.18. A further study of worldwide data by Linacre (1982) shows evidence of an increasing daily range between sea level and 200 m, apparently related to coastal sea breezes. Between 750 and 3400 m, the diurnal range generally decreases in response to stronger winds or greater cloudiness, as noted above.

The controls of the daily temperature fluctuation have been demonstrated by Steinhauser (1937) for stations in the Sonnblick area, Austria, by a comparison of their periodic and aperiodic components. The periodic component is determined from the mean daily range of a long record; the aperiodic one from the average of the daily extreme temperatures (Conrad, 1944; p. 202). Thus, in Table 2.13, the periodic component is part of the aperiodic fluctuation. The periodic component was found to be a smaller proportion of the daily fluctuation at the mountain stations in both seasons indicating the role of synoptic variability, whereas at valley stations, such as Rauris, the large amplitude depends primarily on regular local changes, especially in clear weather.

Grant *et al.* (2005) suggest that by examining the times of daily maximum and minimum temperatures on Mt. Washington, NH (1914 m), the summit regime can be characterized as being determined by boundary layer processes when the usual pattern of radiatively forced, early morning temperature minimum and afternoon maximum occurs. This was observed for 37 (24) percent of the time in winter (summer), respectively. In contrast, days when both maxima and minima occur between 2200 and 0200 h, are indicative of advective situations with free air conditions dominant. This was found on 50 percent of days, in agreement with work in the 1930s by V. Conrad.

In 1913, von Hann noted that temperatures observed at summit stations (Sonnblick and Obir, Austria), on average, are lower than those in the free air at the same level. He referred to this as an apparent paradox, in view of the expected effect of the mountain acting as a heat source. Numerous comparisons of mountain temperatures and comparable data from aircraft or balloon soundings have been made (Kleinschmidt, 1913; von Ficker, 1913; Ferguson, 1934; Samson, 1965). The most thorough analyses of this question, however, have been carried out by Peppler

Table 2.14 Mean temperature differences between the Brocken (1134 m) and the free atmosphere at Wernigerode, Germany, April 1957–March 1962.

	J	F	M	A	M	J	J	A	S	O	N	D	Year
00 GMT	−2.2	−1.9	−1.8	−1.4	−1.5	−1.7	−1.9	−1.9	−2.0	−2.3	−1.8	−1.9	−1.8
12 GMT	−1.2	−0.5	−0.6	−0.4	−0.7	−1.0	0.5	0.3	0.7	0.3	−0.8	−0.4	0.0

Local time is one hour ahead of GMT.
Source: after Hänsel (1962).

Table 2.15 Frequency (%) of temperature differences (°C), Zugspitze minus free air, 1910–28.

		≤ −4.3	−4.2 to −1.3	−1.2 to 1.7	≥ 1.8 (°C)	No. of obs.
October–March	a.m.	15.8	35.1	41.8	7.3	876
	p.m.	9.7	27.3	45.1	17.9	421
April–September	a.m.	6.5	32.7	51.5	9.3	1442
	p.m.	2.6	18.9	50.5	28.0	503

Source: after Peppler (1931).

Table 2.16 Average temperature differences (°C), Zugspitze minus free air, according to cloud conditions.

		Cloud amount (tenths)			
		0–1	4–5	8–9	10
October–March	a.m.	−2.8	−2.2	−1.6	−0.3
	p.m.	−2.2	−0.8	0.1	0.5
April–September	a.m.	−2.0	−0.9	−0.5	−0.2
	p.m.	−1.2	−0.4	1.0	0.8

Source: after Peppler (1931).

(1931) in the northern Alps, Eide (1948) in Norway and von Hänsel (1962) for the Harz Mountains, Germany (see Tables 2.14–2.16; Figure 2.19).

Peppler found a strong dependence of the temperature difference on cloud amounts over the mountain. The Zugspitze is always colder on clear mornings in any season (Table 2.15), but the difference is small with overcast skies and in the afternoon, with > 8/10 cover on the mountain, temperatures are on average a little higher than in the free air, particularly in summer.

Overheating of the thermometers in an instrument shelter during temporary calm conditions is unlikely to be a frequent event on most mountain summits and can, therefore, probably be ruled out as the cause of positive departures in summer.
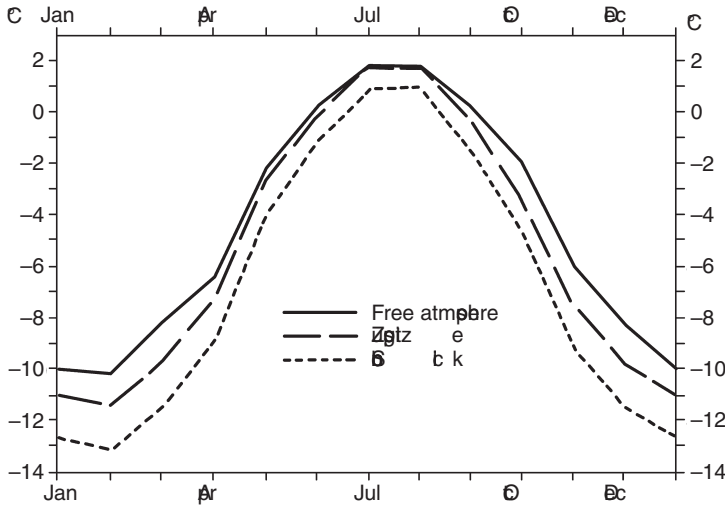
Fig. 2.19 Mean daily temperatures in the free air and at mountain stations in the Alps (after Hauer, 1950).

The negative differences increase with increasing wind speed, up to about $6 \, \mathrm{m \, s^{-1}}$, and then decrease, except on summer afternoons. Maximum negative values occur with northerly winds on the Zugspitze, but in the case of Säntis peak with southerly winds. Variations according to wind direction arise as a result of lee effects, including föhn occurrences (see also Peppler, 1935). In Norway, Eide (1948) also found that the negative temperature difference on mountain summits, which has an annual mean value of $-2.5 \, ^\circ\mathrm{C}$ in the case of Gaustatoppen ($60 \, ^\circ\mathrm{N}$, $9 \, ^\circ\mathrm{E}$; 1792 m) compared with the free air over Kjeller 140 km to the east, increases almost linearly with increasing wind speed. The correlation between summit winds and summit–free air temperature difference is $+0.61$ in the case of Fanaråken ($61.5^\circ \, \mathrm{N}$, $8^\circ \, \mathrm{E}$; 2061 m), and $+0.46$ for Gaustatoppen where the wind data seem subject to local site effects. The negative temperature difference is larger for southeasterly winds than for northwesterly winds at Gaustatoppen, whereas on Fanaråken it is greater with westerly than with easterly winds. In each case, smaller negative departures on the summits occur when the wind direction is such that the station is on the leeward side of the mountains. Eide also points out that some of the temperature difference between northerly and southerly winds at Gaustatoppen could be a result of the thickness relationship with temperatures being lowest in an upper low pressure center. The pressure differences between Gaustatoppen and Kjeller are greatest for isobars oriented north–south and a 4-mb pressure gradient would account for the $0.7 \, ^\circ\mathrm{C}$ difference between northerly and southerly airflows. However, this pressure gradient seems to be too large for the distance involved.

The question has been re-examined in the Alps by Richner and Phillips (1984). Frequent rawinsonde flights were made in summer 1982 and the data compared with mountain-top station values, after corrections for diurnal variations. The mountain stations were slightly cooler, but the twenty-four mean differences,

Fig. 2.20 Mean summit–free air temperature differences (K) in the Alps as a function of time and wind speed (after Richner and Phillips, 1984).
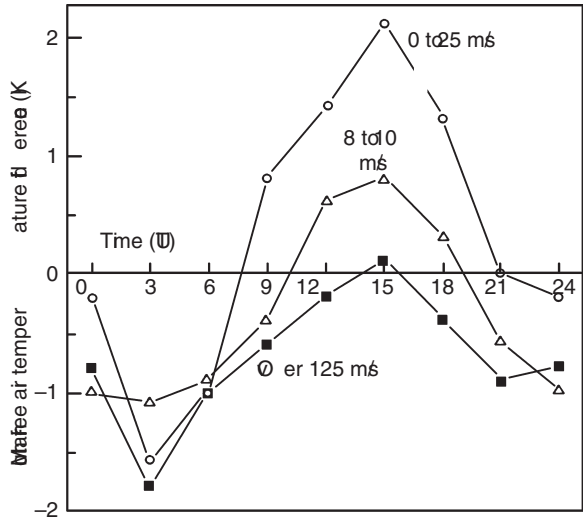
Fig. 2.21 Mean summit–free air temperature differences in the Alps as a function of cloud cover (eighths) for 00 and 12 UT (after Richner and Phillips, 1984).
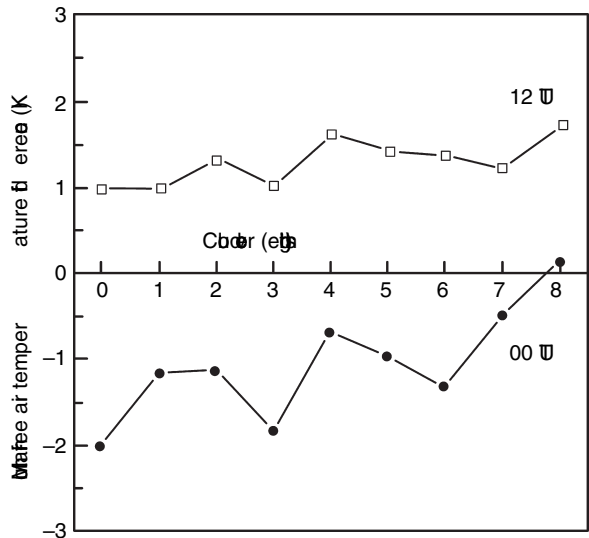
although statistically significant, were less than 1 °C. However, in light winds the difference can reverse with the mountain summits 0.3 °C warmer than the free air (averaged over 24 h) and up to 2 °C warmer at the summit in early afternoon (Figure 2.20). Cloud effects are only apparent for cloud-free and overcast conditions (Figure 2.21), in contrast to the dependence noted by Peppler. Undoubtedly, the pre-1940s measurements in the free air are likely to have been less accurate or reliable. Nevertheless, Richner and Phillip's results are only for a single summer (94 ascents) and for separations of about 100 km between station pairs. Moreover, even modern instruments can show differences of 1 °C between sondes. The conclusion is

that the mountain-top–free air difference is still not conclusively determined. Another recent study (McCutchan, 1983) comparing eight stations on the south-facing slope of the San Bernadino Mountains, California, with radiosonde data collected only 2 km to the west on 19 days in summer–autumn 1975 shows the mountain slope (590–1621 m) to be warmer than the free air at 1000 and 1600 h and colder at 0400 h (PST). The humidity-mixing ratio was higher on the mountain than in the free air at 1000 and 1600 h and lower at 0400 h. The differences were larger than those of Richner and Phillips in the Alps.

Pepin *et al.* (2005) compare mean monthly surface temperatures based on 296 stations of the Global Historical Climate Network/Climatic Research Unit (GHCN/CRU) and 60 snow telemetry (SNOTEL) stations with free-air equivalent temperatures, interpolated from NCEP/NCAR reanalysis data for 1982 to 1999 for the western United States. The SNOTEL sites are between 991 and 3536 m (average 2043 m asl), and the GHCN/CRU sites are between 518 and 2763 m (average 1366 m asl). The surface–free-air temperature difference is calculated for both the SNOTEL data set, which has day and night values, and the daily GHCN/CRU data. Overall, the GHCN/CRU data are 1.1 °C lower than the reanalysis values; the two sets correlate well (> 0.8) except over the Great Basin, due to inversions. The SNOTEL data are also 0.7 °C lower than the reanalysis value, with a seasonal range from -1.8 °C in December to $+0.4$ °C in April. At around 2000 m, the daytime difference is $+4$ °C and the night-time difference -5 °C, in line with the expected effects of elevated surfaces as discussed above. Both differences tend to increase with altitude.

From several studies, the primary control of free air-summit temperature differences seems to be the atmospheric temperature structure. Peppler found that, in the Alps, mountain temperatures are closest to those in the free air when the lapse rate is nearly adiabatic between one and three kilometers whereas, with isothermal or inversion conditions, temperatures in both summer and winter are considerably lower on mountain summits. Eide reported a negative correlation of -0.36 between the summit–free air temperature difference between Gaustatoppen and Kjeller and the lapse rate of Kjeller. This question has been elaborated by Ekhart (1939). Based on data for the period 1930–7 at stations in the northern Alps, and in the free air at the same levels over Munich, he showed that the mean diurnal variation of temperature (between 0700 and 1400 h) was greater at the mountain stations. Following Peppler, he attributed this to adiabatic cooling, due to forced ascent, up to about 1 km, but suggested that above 2 km, the main effect is due to thermal upcurrents. Eide proposes that air mass lifting takes place in proportion to the wind velocity. The average lifting at both Fanaråken and Gaustatoppen is estimated to be of the order of 500 m, assuming dry adiabatic ascent but since the process will be at least partly a saturated-adiabatic one, this figure is probably an underestimate. In addition, where the mountains are isolated peaks, it is clear that "mountain air" is subject to greater mixing with the free air than would be the case over an extensive mountain massif or elevated plateau. This mixing limits the degree of daytime, and

mainly summer-time, heating of the mountain surface. At night radiative cooling from the mountain will probably cause a mean negative temperature departure even in the absence of lifting effects on the air mass. The Brocken data, however, indicate little apparent effect due to the presence or absence of snow cover on the nocturnal cooling rate. The peak is colder than the free air at midnight by an average of 1.4 to 2.2 °C in all months of the year (Table 2.14, p. 54).

The existence of generally negative temperature differences between mountain summits and the free air is important to the question of the so-called mass-elevation (*Massenerhebung*) effect. This concept was introduced by A. de Quervain (1904) to account for the observed tendency for temperature-related parameters such as tree line and snow line to occur at higher elevations in the central Alps than on their outer margins. In studies using this concept, terrain elevation is spatially averaged. The idea has been widely applied in ecological studies and the particular case of the Alps is examined further in Chapter 5 (p. *). Here, we are concerned with general meteorological considerations.

Three components of the mass elevation effect can be distinguished: (i) continentality with a predominance of air mass advection, (ii) mountains where convection is dominant, and (iii) windward blocking with lee-side föhn (Richter, 2000). The first features mild, humid, cloudy windward margins with drier, sunnier conditions in the central region with larger annual and diurnal temperature ranges. It is mainly in the trade wind belt that mountain ranges under a regime of high wind constancy are found, but this pattern is represented to some degree in the European Alps, although north and south foehn effects are also common-pattern (iii). A dominance of convective processes, pattern (ii), referred to by Richter as the Merriam effect, is found in the mountains of the Sahara (see p. 378) and in the mountain ranges of the interior western United States. Type (iii) is dominant in the western Cordilleras of North and South America, and the Southern Alps of New Zealand, but also in the Himalaya and Tien Shan.

Flohn (1953) first proposed that elevated plateau surfaces, such as those of Tibet and the Altiplano in South America, are warmer in summer than the adjacent free air as a result of the altitudinal increase in solar radiation and the relative constancy of the effective infrared radiation with height. The data in the previous sections (pp. 39–49) (see also Table 2.11, p. 48), support this view. Two factors contribute to the heating effect in the mountain atmosphere. One is sensible heat transfer from the surface, the other is the latent heat of condensation due to precipitation from orographically induced cumulus development. Flohn (1968; p. 197) demonstrated that the flux of sensible heat into the atmosphere over the Alai-Pamir Mountains in summer is of the same order of magnitude as that over sea level desert surfaces in the same latitudes. This is indicated by afternoon lapse rates which reach up to $9.0 \,°C \, km^{-1}$ between 4 and 7 km in the Pamir (38° N, 74° E).

Calculations by Yeh (1982) indicated a total daily energy transfer from the plateau to the atmosphere of $230 \, W \, m^{-2}$ in June. Sensible heat flux is important over the drier western part of the Tibetan Plateau, where it reaches $220 \, W \, m^{-2}$.

Fig. 2.22 Components of the mean daily thermal circulation (cm s^{-1}) above Tibet (from Flohn, 1974).
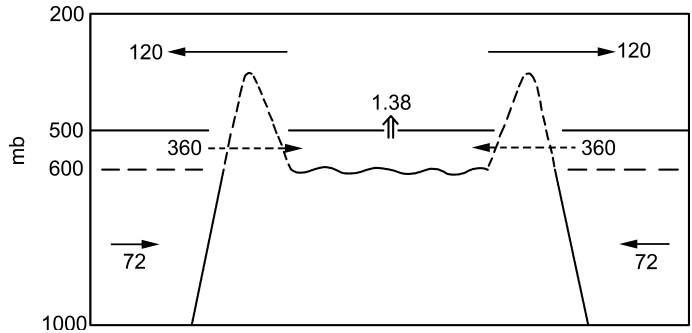
Over southeastern Tibet and the eastern Himalaya–Assam, however, convective activity, due to forced ascent of air against the mountains ("Stau"), provides a major heat input from latent heat of condensation. East of 85° E, the latent and sensible heat terms are almost equal (90 and 100 W m^{-2}, respectively). The maximum heating rates in June for the layer between 600 and 150 mb amount to +1.8 °C day^{-1} from sensible heat, +1.4 °C day^{-1} from latent heat, and radiative cooling of −1.5 °C day^{-1} giving a net heating of +1.7 °C day^{-1} (Yeh, 1982). Various estimates suggest that the heating is about 2 °C day^{-1} over the eastern half of the plateau (Chen *et al.*, 1985). Advective transports export the net heat and there is mean ascent of about 1 cm s^{-1} as illustrated in Figure 2.22.

Luo and Yanai (1984) calculated a heat source over the eastern plateau for the 40-day period 26 May–4 July 1979 of 113 W m^{-2} (vertically-integrated from 150–610 mb). The mean net radiative heating for July is −62 W m^{-2}, the calculated condensational heat of precipitation was 71 W m^{-2} and the sensible heat was 104 W m^{-2}.

Using INSAT geosynchronous visible and infrared satellite data for summer 1988, ECMWF analysis data on pressure, temperature and humidity, and literature estimates of sensible and latent heat, Smith and Shi (1996) determine June–August atmospheric heating sources as follows:

	Western Plateau	Eastern Plateau
Radiative divergence	−79	−90 W m^{-2}
Latent heat of precipitation	29	92
Sensible heat	129	66
Total diabatic heating	(79)	(68)

For the atmosphere between the plateau surface and cloud layers in summer they estimate that infrared radiation gives a warming of 0.5 °C day^{-1} due to water vapor absorption, while shortwave radiation through the cloud albedo effect causes a cooling of 0.2 °C day^{-1}, giving a net lower atmosphere heating of 0.3 °C day^{-1}.

The plateau heating effect is of great importance in the development of an upper tropospheric anticyclone, centered about 30° N, 85° E. Yeh noted that the summertime surface low and upper high vary diurnally, being much stronger in late afternoon than in the early morning hours. Similar atmospheric heating estimates have been made, by Gutman and Schwerdtfeger (1965) and Rao and Erdogan (1989), for the Andes where an upper anticyclone forms in summer over the Altiplano (Kreuels *et al.*, 1975). Rao and Erdogan suggest that the main source of heating in January is latent heat released over the eastern margins of the Bolivian Plateau.

Molnar and Emanuel (1999) point out that the heating effect over a high plateau will be substantially reduced if the atmospheric vapor content is significantly less than that above lowland surfaces, because this will diminish the atmospheric absorption of infrared radiation emitted by the ground surface. They also point out that Flohn (1953) ignores the effects of convective heat transfer. They re-examine the thermal effect of high plateau surfaces on the overlying atmosphere using a radiative–convective model. There is an interactive scheme for water vapor concentration, condensation and precipitation. The model also allows for varying amounts of evaporation by changes in the Bowen ratio, $\beta = H/LE$, set as 1.0, 0.5, 0.25 or 0.0. For sea-level surfaces, calculated atmospheric temperatures are much lower for $\beta = 0$ than the other cases because the absence of latent heat transfer gives low specific humidity and therefore little absorption of infrared radiation. The differences in air temperatures between the atmosphere above a plateau and that above a sea-level surface are shown to increase as the plateau height increases (Figure 2.23). They reach a maximum between about 300–200 mb. The differences

Fig. 2.23 Plots of the temperature structure above plateau surfaces at 900, 700 and 500 mb, plotted as differences between the temperatures calculated above elevated and sea-level surfaces for four values of Bowen ratio, β (from Molnar and Emanuel, 1999).
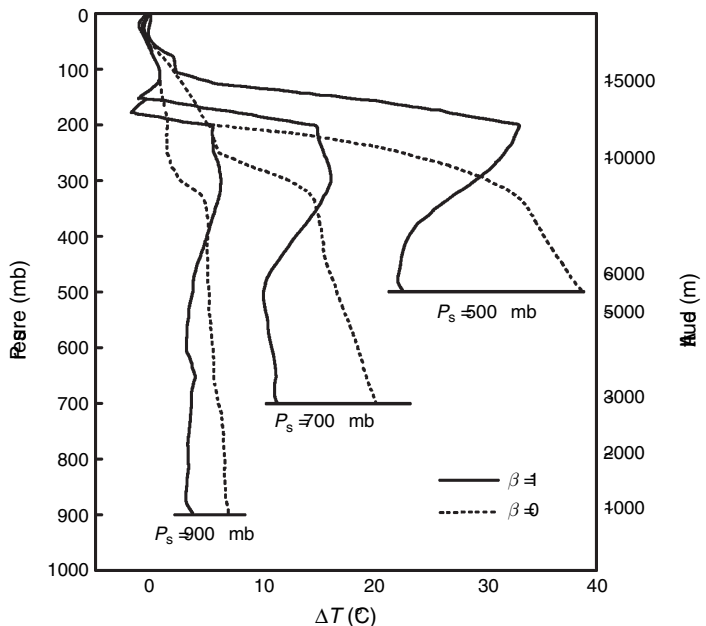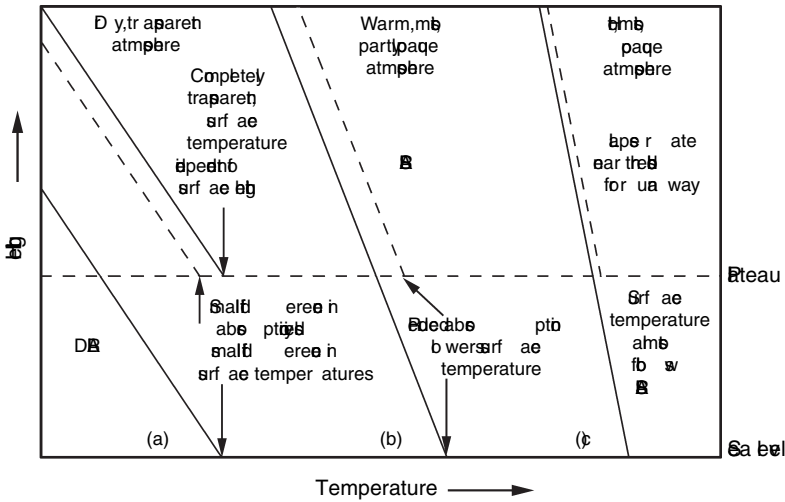
Fig. 2.24 Schematic illustration of the effects on surface and boundary layer temperatures of lowland and high plateau surfaces and three different atmospheric conditions: (a) dry, transparent atmosphere; (b) warm, moist, semi-opaque atmosphere; (c) hot, moist opaque atmosphere (from Molnar and Emanuel, 1999).

are also greatest for $\beta = 1$ (a saturated surface) and decrease as the surface dries out. Figure 2.24 illustrates schematically the possible range of effects on surface temperatures of different surface elevations: (a) for a dry, transparent atmosphere there is weak absorption and emission of infrared radiation, especially where the surface temperature and vapor content are low; hence, surface temperature changes slowly with surface elevation; (b) for a warm, moist, semi-opaque atmosphere, there is increased infrared absorption/emission over lowlands than over elevated surfaces, but convective heat transfer lowers the surface temperature; (c) for a hot, moist opaque atmosphere, the saturated adiabatic lapse rate (SALR) limits the rate at which surface temperature can decrease with height through convective adjustment. For hot, moist air masses, the SALR is around $-4.5\,\mathrm{K\,km^{-1}}$.

The windward "Stau" (blocking) effect is operative over mountain ranges in all latitudes, even low latitude ones, according to Flohn (1953) and adds to the dynamic effect of mountain barriers in the mid-latitude westerlies by causing a ridge of higher pressure over the range (see Chapter 3, p. 126). However, the sensible heat contribution is generally only effective in summer and is absent where the mountains are snow-covered. Hence, the temperatures observed on 15 days in summer 1956, between 4700 and 7000 m on Pobeda Peak in the eastern Tien Shan, averaged 1.8 °C less than free-air temperatures over Almaty according to Borisov *et al.* (1958). It is evident that the *Massenerhebung* concept can only be applied after careful consideration of the region and the meteorological factors that are involved.

Despite the differences between slope conditions and those in the free-air, radiosonde data can sometimes be used as a guide to mountain temperatures. A study in

Fig. 2.25 Schematic isentropes on slopes during surface heating and radiative cooling (after Cramer and Lynott, 1961).
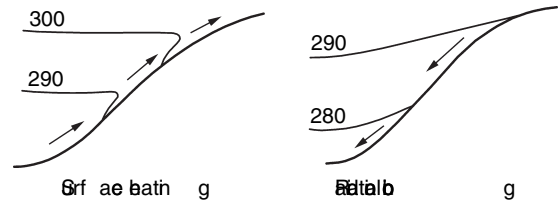
coastal British Columbia (Peterson, 1969) shows that the frequency of below-freezing temperatures in winter can be estimated from 0400 h radiosonde soundings, although periods of temperature inversion were excluded from the analysis.

In general, patterns of mountain temperature distribution can be described conveniently by means of potential temperature analysis. The potential temperature, θ, represents the temperature of an air parcel brought adiabatically to 1000 mb pressure, thus $\theta = T(1000/p) \exp(R/c_p)$, where p = pressure (mb), T = temperature (K), R = gas constant for dry air and c_p = specific heat of dry air at constant pressure; $R/c_p = 0.288$. This conversion is readily carried out graphically on a thermodynamic chart if station elevation is converted to pressure. Little error is generally introduced if standard atmosphere equivalents are used. Surfaces of potential temperature, or *isentropic surfaces* represent the path of air moving adiabatically (unaffected by diabatic processes such as radiative warming or cooling). Cramer (1972) shows that isentropes of surface air temperature generally parallel the terrain contours in the morning hours when the air is stably stratified. As slopes are warmed and a mixed layer forms, the isentropes tend to intersect the topography. This is especially evident on cross-sections (Figure 2.25). Sloping isentropes denote atmospheric discontinuities such as fronts, sea breezes in coastal areas, and slope breezes or mountain/valley winds. Thus, such potential temperature analyses are a useful basis for inferring likely airflow patterns in mountain areas, especially during summer situations with weak pressure gradients.

If the objective of a temperature analysis is to examine air mass characteristics or the location of fronts, in a mountain area, it is preferable to analyze fields of equivalent potential temperature,

$$\theta_E = T_z + \left\{ \frac{L_v r}{c_p} \right\} + \left\{ \frac{g\Delta z}{c_p} \right\}$$

where L_v is the latent heat of condensation (2.5×10^6 J kg^{-1}); r is the humidity mixing ratio (g kg^{-1}); T_z is the temperature (K) at level z; Δz is the height difference (km) between z and the reference height (msl or 1000 mb); g is 9.81 m s^{-2}; and c_p is the specific heat of dry air (1004 J kg^{-1} K^{-1}).
For reduction to sea level,

$$\theta_E = T + 2.5r + 9.81z,$$

where θ_E represents the temperature attained by an air parcel following adiabatic condensation of all water vapor in the air at constant pressure. It is conservative for unsaturated and saturated adiabatic processes.

2.3.8   Wind

The most important characteristics of wind velocity over mountains are related to their topographic, rather than their altitudinal, effects. Nevertheless, it is appropriate to make brief note of the latter here. In middle and high latitudes it is normal to expect that, on average, there will be an increase of wind speed with height, due to the characteristics of the global westerly wind belts (e.g. Reiter, 1963). Isolated peaks and exposed ridges experience high average and extreme speeds as a result of the limited frictional effect of the terrain on the motion of the free air. In some locations, terrain configuration may even increase wind speeds near the surface above those in the adjacent free air. Thus, Mt. Washington, NH (1915 m) has a mean speed of 23 m s^{-1} in winter and 12 m s^{-1} in summer (Eustis, 1942) and has recorded a peak gust of 103 m s^{-1} in April 1934 (Pagliuca, 1934). On this occasion, the wind was from the southeast, associated with a deepening low moving northeastward and a high pressure cell off New England. The southeasterly flow appears to have been channeled up the mountain by Tuckerman's Ravine (D. Brown, pers. comm., 2005).

   More typical of mid-latitude summits is the Sonnblick, Austria (3106 m) with a mean speed of 7 m s^{-1} (Steinhauser, 1938). In contrast, winds on equatorial high mountains appear to be much lighter. In New Guinea at 4250 m on Mt. Jaya (Mt. Carstenz), a mean value of only 2 m s^{-1} is reported during December–February (Allison and Bennett, 1976) and on El Misti, Peru (4760 m) there is an estimated mean speed of about 5 m s^{-1} with a recorded maximum of 16 m s^{-1} (Bailey, 1908). Generally, in the tropics, the easterly trade winds weaken with height. In the winter season, on their poleward margins, they may give way to westerly winds associated with the extra-tropical westerly air circulation. Synoptically, this is most likely when polar troughs in the upper air penetrate into tropical latitudes. In southern Asia there is a marked seasonal change-over, from strong westerly flow over the Himalaya between about October and May, on average, to moderate easterly winds from late June through September. This topic is dealt with more fully in Chapter 5.

   The effect of mountains on the wind flow over them aroused early interest, especially through the manned-balloon flights of von Ficker (1913). On the basis of these observations, pilot balloons and kite surroundings, Georgii (1922, 1923) argued that wind speeds generally increase above mountain summits up to a level corresponding to about 30 percent of their absolute altitude, which he termed the "influence height." Most of his observations were from the 820 m Feldberg (Taunus), however, and A. Wagner questioned the generality of the results, also pointing out that the *relative* relief would more likely determine an influence height. This topic is discussed more fully on p. 81.

The two basic factors that affect wind speeds on mountain summits operate in opposition to each other. The vertical compression of airflow over a mountain causes acceleration of the air, while frictional effects cause retardation. Frictional drag in the lower layers of the atmosphere is caused partly by "skin friction" (shear stress), due to small-scale roughness elements (< 10 m dimension) and partly by "form drag" caused by topographic features 0.1–1 km in size that set up dynamic pressure perturbations. In mountain areas, the latter contributes the largest proportion of the total friction. As we shall see in Chapter 3, the total deceleration (net form drag) is determined also by the formation of gravity waves through the interaction of the atmosphere and the orography. Over simple two-dimensional terrain, drag increases in proportion to (slope)^2, up to the point where flow separation from the surface takes place according to Taylor *et al.* (1989). Balloon measurements in the central Alps indicate that drag influences extend up to about 1 km above the local mean ridge altitude of 3 km (Müller *et al.*, 1980). Special soundings made during ALPEX show that the airflow over the central Swiss Alps is decelerated up to about 4 km (600 mb). Ohmura (1990) suggests that momentum transfer between the atmosphere and the mountains takes place from about 4 km down to 500 m below the ridge tops (3000 m in the study area near the Rhône Glacier, Gletsch). Many of the wind profiles indicated a wind maximum at 1.5 km above the ridges, with speeds greater than over the adjacent lowlands. Such acceleration occurs during warm air advection which sets up an inversion above the valley atmosphere.

Microbarograph measurements along a cross-section from Zurich to Lugano during ALPEX indicate a mean pressure drag of $+0.8$ Pa (± 5 Pa) according to Davies and Phillips (1985). They note that a 5 Pa drag would be sufficient to deplete the momentum of the entire troposphere in traversing the Alps. However, due to its largely east–west orientation, the Alpine region exerts only a slight total mean drag as a result of alternating synoptic regimes with northerly and southerly flows.

By considering friction and compression, Schell (1936) attempted to explain contrasting observations with tethered balloons on three summits in the Caucasus at about 1300 m. He concluded that in the case of an isolated peak, or an exposed ridge, the compressional effect outweighs frictional retardation, giving stronger winds up to about 50–100 m over the summit than in the overlying free air. The acceleration due to "compression" is attributable to a 1–2 mb pressure reduction as a result of the streamline curvature over the crestline – the so-called "Bernoulli effect" (Davidson *et al.*, 1964). The Bernoulli effect may cause mountain-top pressure observations to be unrepresentative of the large-scale flow at that level.

For steady incompressible, frictionless flow along a streamline, Bernoulli's equation states:

$$\frac{V_1^2 - V_2^2}{2} + \frac{P_2 - P_1}{\rho} + g(Z_2 - Z_1) = 0$$

The first term denotes kinetic energy, the second the work done by the pressure force, and the third potential energy. Typically, a 1-mb pressure drop could cause an increase of 4–$5\,\mathrm{m\,s^{-1}}$ in wind speed.

Georgii recognized that mountain effects must depend considerably on wind direction and wind speed, as well as on lapse rate, but there are still few data on mountain and free-air winds to determine the general nature of these relationships. Schumacher (1923) summarized his studies of data for three Alpine stations. For Säntis, Sonnblick and Zugspitze, the mean annual speeds average about 0.8 times those in the free air although the ratio usually exceeds unity for wind speeds below $4\,\mathrm{m\,s^{-1}}$ in the free air. It also depends heavily on the terrain in relation to the general wind direction and on the precise anemometer location on the summit. Thus, on the Sonnblick in the central Alps, southerly winds are stronger than those in the free air, whereas westerly and north-east to easterly winds are weaker. On the Zugspitze, on the northern margin of the Alps, summit speeds exceed the free-air value only for winds from the southerly quadrant.

An extensive survey of wind observations on mountain summits and in the free air was carried out by Wahl (1966). From data for European stations, he found that, in general, speeds on summits average approximately half of the corresponding free-air values. For the median values, a generalized regression equation is:

$$V_\mathrm{m} = 2.1 + 0.5\ V_\mathrm{f}$$

where V_m = summit wind speed ($\mathrm{m\,s^{-1}}$); and V_f = corresponding free-air wind speed.

The relationship for different frequency ranges is shown in Figure 2.26. Where frictional effects are large, the ratio may fall as low as 0.3. Hence, summit speeds are both relatively and absolutely higher in winter when the general increase in atmospheric stability reduces frictional effects. Wahl also notes that the summit–free-air ratio sometimes exceeds 1.01. Such occurrences are determined mainly by the nature of the site and by the wind direction in relation to terrain configuration. The exceptional speeds on Mt. Washington, for example, are recorded there because it is the highest summit in the center of an extensive area of mountain ridges. Eustis (1942) reported summit–free-air ratios of 1.4 in summer and 1.8 in winter for this location.

2.4   TOPOGRAPHY

The interaction between topography and atmospheric circulation systems involves a wide range of scales in the atmosphere and the surface. Atmospheric circulation systems are conventionally defined in terms of their space and time scales in the following categories: planetary, synoptic, meso-scale and micro-scale. The meso-scale range itself is often broken down into subcategories: meso-α = 200–2000 km, meso-β = 20–200 km, and meso-γ = 2–20 km (Orlanski 1975, for example). Particular types of weather system characterize each category, although in practice

Fig. 2.26 Wind speeds observed on mountain summits (V_m) in Europe and at the same level in the free air (V_f) (from Wahl, 1966).
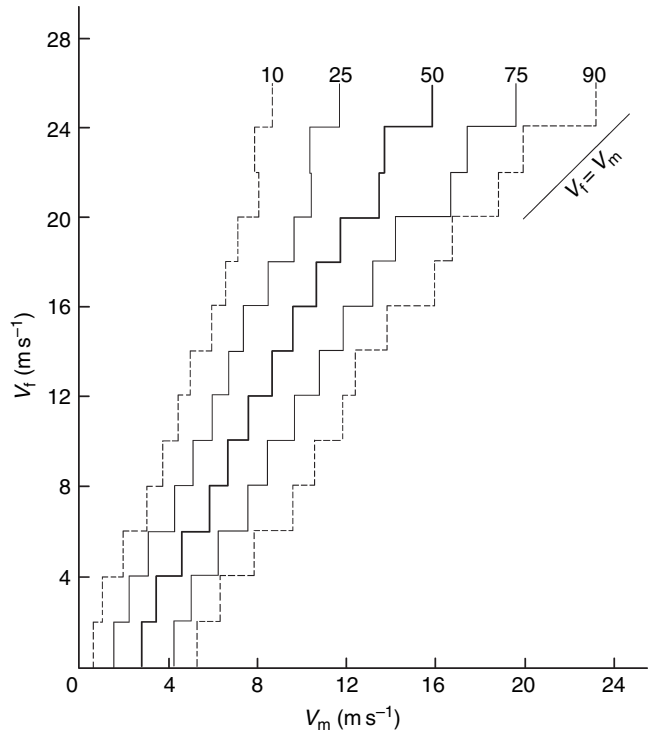
these often overlap in size. Systems with a length scale < 2 km are termed micro-scale. The corresponding elements of orography are: the major plateaus including East Antarctica, Greenland, and Tibet; mountain range systems such as the western cordilleras in North America, or the Pamirs and Tien Shan in central Asia, individual mountain ranges, valley systems, low hills, and individual rock outcrops or boulders. The effects of topography on airflow operate through several basic characteristics of any relief feature. The overall dimensions and the orientation of a mountain range with respect to prevailing winds are important for large-scale processes, relative relief and terrain shape are particularly important on a regional scale, while slope angle and aspect cause striking local differentiation of climate.

2.4.1 Dimensional effects

The effects that a topographic barrier has on air motion depend first on the dimensional characteristics of the barrier – its height, length, width, and the spacing between successive ridges – and, second, on the properties of the airflow itself – the wind direction relative to the barrier, the vertical profiles of wind and of stability. Each of the three dimensions of a mountain barrier interacts with a particular atmospheric scale parameter (Smith, 1979). Hence, the vertical dimension of the mountain should be compared with the atmospheric depth, as measured by the

"density scale height" (~ 8.5 km); this is the thickness of a hypothetical incompressible atmosphere of constant density. Modeling studies indicate that the large-scale flow responds to an "envelope" topography that intersects the mountain peaks, rather than to an average height of the peaks and valleys. The length of the range, in relation to the wind component perpendicular to it, greatly influences the degree of airflow perturbation. An air stream will separate around an isolated mountain whereas a range several hundred kilometers long may cause blocking of the flow, forced uplift, flow deflection, or some combination of these.

Barrier width interacts with five different atmospheric length scales according to Smith (1979). The scales are listed here.

(1)   The thickness of the boundary layer (~ 300 m).
(2)   The distance the air travels downwind during a buoyancy oscillation (~ 1 km).
(3)   The downwind travel during the condensation and precipitation processes (~ 1 h; 10–100 km).
(4)   The downwind travel during one rotation of the Earth ($\sim 10^3$ km).
(5)   The Earth's radius (6000 km), which determines the magnitude of the effect of the Earth's curvature on the large-scale flow.

Scales (1) and (2) are involved in boundary layer turbulence and buoyancy effects such as gravity waves (see pp. 178 and 150), scale (3) involves precipitation processes (section on p. 273), and scales (4) and (5) involve planetary waves and synoptic-scale processes such as orographic cyclogenesis (see pp. 125 and 143). These atmospheric length scales interact with topographic dimensions. For example, average slopes in the Alps are around 1/2 for horizontal scales of 100 m to 10 km, whereas for a horizontal scale of 300 km the relief amplitude is of the order of 4 km giving slope gradients of only 1/40 (Green, 1984). Air will flow more readily over gentle slopes than locally steep ones.

It is useful to consider when and why air crosses a topographic barrier rather than flowing around it. From an energy standpoint, the air arriving at a barrier must have sufficient kinetic energy in order to rise over it against the force of gravity (Stringer, 1972). The level of exhaustion of kinetic energy for an air parcel rising from the surface (and affected by friction) is approximately $0.64U/\sqrt{S}$, where $U =$ surface speed upwind (m s^{-1}) and $S = g(\Gamma - \gamma)/T$ is the static stability, representing the net balance of buoyancy forces and gravity; $\Gamma =$ the adiabatic lapse rate and $\gamma =$ the environmental lapse rate ($-\partial T/\partial z$) (Sheppard, 1956; Wilson, 1974) (see Note 2, p. 108). For an isothermal atmosphere, with a temperature of 270 K, $1/\sqrt{S} = 53$ s and, if $U = 10$ m s^{-1}, the air can surmount a barrier of approximately 320 m. Hence, in an isothermal atmosphere, a surface speed upwind of 19 m s^{-1} is required for the air just to reach the crest of a 1000 m barrier. The magnitude of $1/\sqrt{S}$ increases with decreasing stability. For an inversion with $\Gamma = +6.5$ K km^{-1}, $1/\sqrt{S} = 41$ s, while for lapse conditions with $\Gamma = -6.5$ K km^{-1}, $1/\sqrt{S} = 91$ s. Thus

with $U = 10\,\mathrm{m\,s^{-1}}$, the airflow can just surmount a barrier of 545 m for these lapse conditions, compared with one of only 245 m elevation for the corresponding inversion condition. If the airflow lacks the necessary kinetic energy to rise over the barrier it is deflected across the isobars towards lower pressure, thereby acquiring kinetic energy (Wilson, 1974). After some time this deflection may have extended sufficiently far upwind to provide the air stream with the energy necessary to rise over the barrier. This implies that the isentropic (potential temperature) surfaces rise over the barrier so that the air can flow parallel to them. On the lee side of a ridge, surplus energy may appear as waves in the airflow (kinetic energy), or it goes into potential energy by deflection of the air towards higher pressure. Wilson (1974) also shows that the width of the barrier that will cause blockage of the airflow is given approximately by $0.36U/f$, where f = the Coriolis parameter. For $f = 1.0 \times 10^{-4}\,\mathrm{s^{-1}}$ and $U = 10\,\mathrm{m\,s^{-1}}$ this critical width is 36 km. It is also worth noting here that another appropriate measure of stratification, with respect to blocking effects, is the gradient Richardson number, Ri, a dimensionless number (see Note 3). The flow is statically stable for $Ri > 0$ and statically unstable if $Ri < 0$; and 0 = neutral.

Sheppard's criterion is unrealistic according to Smith (1980; 1990), since it implies that minimum wind speeds should be observed at the top of the barrier, which is not the case. Nevertheless, Smith proposes modifications to it. Snyder *et al.* (1985) suggest that it provides a lower limit for the height of the layer that is decelerated and diverted around a mountain barrier. Trombetti and Tampieri (1987) note that it neglects accelerations due to the pressure field and momentum losses due to viscosity. This argument is extended by Smith (1990), who contends that pressure differences at a constant level, rather than potential energy, are the main control on wind speed. From a Lagrangian form of the hydrostatic equation, Smith develops the following expression for the kinetic energy:

$$U^2 = -2N^2 I_D + U_0^2$$

where $N^2 = -g/\theta\,\{\partial\theta/\partial z\}$

$$\text{and } I_D = \left(\int_{z_0}^{\infty} A\ \mathrm{d}z_0\right) \approx AD$$

where D is the height to which streamlines are displaced (see Figure 2.27); A is the local vertical displacement of a streamline $(z - z_0)$ by the windward slope; z_0 is the initial upstream level of the streamline; and U_0 is the upstream velocity at z_0.

The equation implies that the flow speed is determined by the *integral* of the displacement above a point, not by the local displacement, A, as illustrated in Figure 2.27. It follows that stagnation ($U = 0$) develops where $I_D = U_0^2/2N^2$. Weak winds occur where the integral displacement is large. Smith concludes that increasing pressure along a streamline (due to lifting and positive density anomalies aloft) leads to flow stagnation and, at the lower boundary on the obstacle, to flow splitting.

Fig. 2.27 Schematic illustration of streamlines over a hill showing phase tilt upwind (dashed line) (from Smith, 1990).
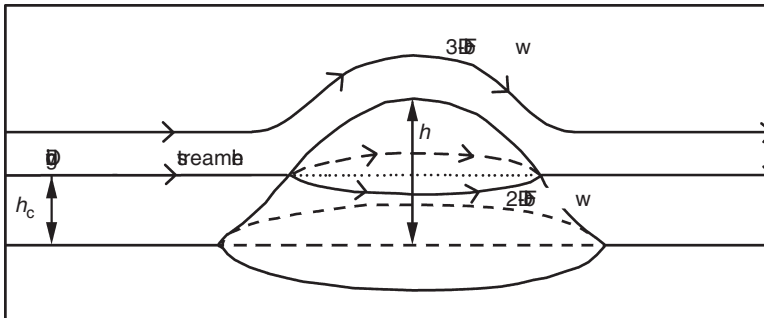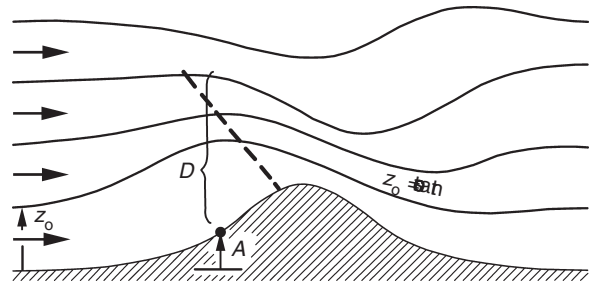
Fig. 2.28 Schematic illustration of a "dividing streamline" in stably-stratified airflow encountering a hill (modified after Etling, 1989).

The general classes of flow for an ideal fluid encountering an obstacle can be described with reference to the Froude number (F), which is the ratio of internal viscous forces to gravitational forces (Nicholls, 1973).

$$F = U/Nh = 2\pi U/hS^{0.5} = 2\pi/lh$$

where U is the undisturbed flow of velocity; h is the mountain height; and S is the static stability and l is the Scorer parameter (discussed below p. 154).

The Froude number can also be interpreted as the ratio of kinetic energy of the air encountering a barrier to the potential energy necessary to surmount the barrier. For flow over a barrier, F describes the ratio of the natural wavelength associated with vertical oscillations in the airflow to the wavelength of the barrier's cross-section (see Note 4).

The effect of three-dimensional hills in deflecting stable or neutrally stratified airflows has been extensively modeled using laboratory towing tanks and wind tunnels. Hunt and Snyder (1980) introduced the concept of a "dividing streamline" to identify the height, H_s, at which a strongly stratified air stream crosses a hill (height, h) rather than being deflected (Figure 2.28). They suggest $H_s = h(1 - F)$ as the criterion for flow impacting a hill or surmounting it, where the Froude number, F, is between 0 and 1. The application of this criterion to wind studies on San Antonia Mountain, an isolated peak in New Mexico, is shown by McCutchan and

Fox (1986) and Wooldridge *et al*. (1987). H_s lowers as F increases; for example, on San Antonia Mountain ($h = 670$ m), $H \sim 400$ m for $F = 0.35$ and ~ 200 m for $F \sim 0.65$–0.70.

The nature of stratified flow over or around an obstacle is determined by the degree of stratification, but also by the obstacle dimensions and the upwind velocity profile (Hunt and Richards, 1984). The degree of stratification can be expressed in terms of both obstacle height (h), $F_h = U_0/Nh$, and obstacle length (L), $F_L = U_0/NL$, where $N = \sqrt{S}/2\pi$ (the Brunt–Väisälä frequency, see p. 75) describes the natural frequency of vertical oscillations in the air stream. In general terms, F_h characterizes the degree of nonlinearity in the flow (the likelihood of stagnation and flow blocking or splitting), while F_L indicates the existence and behavior of any gravity waves.

Generalized flow behavior over a single hill (Hunt and Richards, 1984) is illustrated in Figure 2.29. For a neutral atmosphere, $F_h \geq 1$ and $F_L \geq 1$, the flow has a logarithmic profile of velocity and potential flow is maintained with a largely smooth disturbance over the barrier. The flow depends on the upwind velocity profile and hill shape. There is an extensive "influence zone" and a turbulent wake downstream. The depth of atmosphere perturbed by the terrain is of a scale comparable to half the width of the barrier (L_0). This is because the air tends to move in circular paths with a vertical scale equivalent to the horizontal dimension of the sources and sinks that set up perturbations in the flow (Hunt and Simpson, 1982). At the other extreme, with strong stratification, F_L and $F_h \to 0$ ($U_0/Nh < 1$), the flow is subject to upstream blocking and most of it goes around the hill. For moderate stratification, $F_L < 1$ but $F_h > 1$, the negative buoyancy is sufficient to prevent flow from crossing the barrier and modifies the mean flow above the hill; lee waves and rotors form downstream (see p. 150). The flow is also sensitive to the upwind temperature gradient. Typical flow parameter values are illustrated in Note 5 (see p. 109).

Less attention has been paid to the effects of obstacles on airflow where the slopes are heated. Reisner and Smolarkiewicz (1994) examined the effects of heating over the mountains of the Hawaiian Islands on the location of upwind stagnation in flows where F was small. Building on that analysis, Crook and Tucker (2005) perform linear simulations of flow over heated obstacles, separating the orographic and thermal forcing. They find that, for a symmetrical hill, the orography and heating generate opposite responses: the obstacle sets up downward velocity in the lee of the obstacle whereas heating produces upward velocity downstream of the heat source. The net vertical motion depends on the relative importance of the two forcings. In the case of an elongated ridge, when the flow is parallel to the ridge, an across-stream temperature gradient develops with convergence and ascent over the centerline of the heat source. The effect is a maximum when the flow is along the heat source. The orographic effect over the lee slope is mimimized (maximized) for flow along (across) the ridge. This is summarized schematically in Figure 2.30. Hence, maximum lifting on the lee slope occurs when the flow is orientated along a

Fig. 2.29 **Generalized flow behavior over a hill for various stability conditions (after Stull, 1988). The Froude number is expressed in terms of obstacle height.**

heated ridge. The significance of this for summer convective precipitation over the Colorado Rocky Mountains is discussed in Chapter 5 (p. 405).

It is apparent, therefore, why 4–6 km-high ranges are, in most cases, substantial obstacles to airflow and weather systems encountering them and thus form major climatic divides. This is especially so where they are oriented more or less perpendicular to the flow direction as in the case of the western cordillera and Rocky Mountains of North America, or the Andes, and to a lesser degree in the case of the Southern Alps of New Zealand. The effects on airflow characteristics are much less pronounced if the barrier is more nearly parallel to the predominant airflow direction for at least part of the year, as in the case of the Pyrenees, the Himalaya

Fig. 2.30 Schematic illustration of the forcing and response of airflow along (above) and across (below) a heated barrier (from Crook and Turner, 2005).
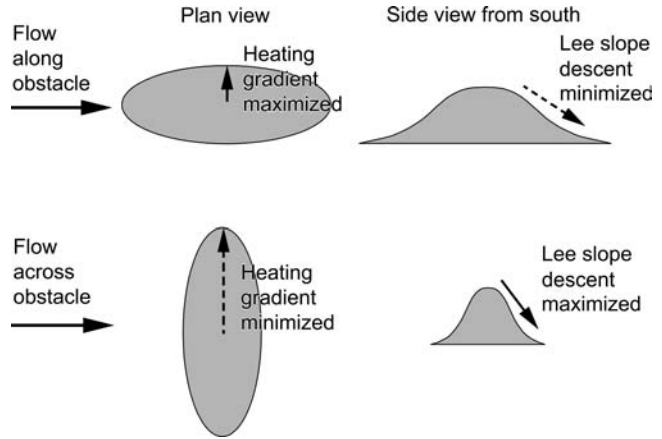
and the ranges of New Guinea. However, while these broad generalizations may be appropriate in a climatic sense, the instantaneous airflow can be directed across any range by dynamic and thermodynamic changes in the pressure field inducing local flow accelerations.

The extent to which deep valleys dissect a mountain range also determines its effectiveness as a climatic barrier. Major through-valleys afford a direct passage for air motion. For example, the 30-km wide Palghat Gap through the Western Ghats at 11° N in India shows no topographic effects on rainfall, although wind speeds at the exit show a two- to three-fold increase over those in the gap (Ramachandran, 1972; Ramachandran et al., 1980). This is similar to the dynamic effect observed when a jet of air passes through a nozzle into a large chamber. Mountain gaps and marine straits flanked by mountains frequently experience *gap winds* that are accelerated by an along-gap pressure gradient (Overland and Walter, 1981), Such occurrences are widespread in major valleys transecting mountain ranges and in narrow straits (Reed, 1931; Dorman et al., 1995; Reid, 1996; Steenburgh et al., 1998). In the cross-gap direction, approximate geostrophic balance develops between the corresponding cross-gap pressure gradient acceleration and the Coriolis acceleration associated with the along-gap flow (Overland, 1984). In the along-gap direction, there is a balance between the pressure gradient and inertial accelerations, although friction and entrainment limit the along-gap wind speed. In the flow exiting a gap (the gap outflow), air parcels follow an inertial path with a radius of curvature, $R_c = -V/f$, where V is the wind speed, and f the Coriolis parameter. Where $R_c < 0$, parcels turn anticyclonically (to the right) in the northern hemisphere. In high latitudes, the small radius of the inertial circle means that the outflow can rapidly become terrain parallel, as shown by Loescher et al. (2006) for gap flows exiting the coastal mountains into the Gulf of Alaska. Similar gap winds are observed in winter over the Gulf of Tehuantepec, and southward, when a pressure gradient from the North Atlantic to the Pacific Ocean accelerates flow through narrow passes in the mountains of the isthmus of Central America.

A low-level jet develops from the north–south gap at 16° N, 95° W, and others from the northeast–southwest gaps at 11° N, 87° W and 8° N, 80° W (Chelton *et al*., 2000; Xie *et al*., 2005). All three jets are present downstream of the passes but the flow is weak in the lee of terrain exceeding 1000 m elevation. Here, the gap outflow appears to spread out over the Gulf of Tehuantepec and to turn anticyclonically due to the inertial effect (Steenburgh *et al*., 1998).

There have been several theoretical studies and numerical simulations of gap winds. Using linear theory for stratified flow, Zängl (2002) shows that in the linear regime, the differences in wind and pressure along a mountain gap are similar to those over a ridge, but have lower amplitude and large horizontal wavelength. This is caused by the radiation of vertically propagating gravity waves from the ridge towards the gap axis and low-level confluence in the gap. In the non-linear regime, these two processes are much less important due to upstream blocking and low-level wave breaking. The gap flow is driven mainly by the pressure difference across the ridge. The gap flow tends to be decoupled from, and is stronger than, that over the ridge. Frictional slowing is greater over the ridge than in the gap. Sprenger and Schär (2001) introduce several parameters for a hydrostatic model of westerly flow, and a valley transecting a two-dimensional barrier: (i) gap depth ($N\,\Delta H/U$), (ii) ratio of ridge height to gap depth ($H/\Delta H$), (iii) a number describing the north–south width of the ridge (R_o), and (iv) a parameter describing gap shape. They show that the gap flow becomes decoupled from that above for intermediate R_o and deep gap flow, and it is driven by the geostrophic pressure gradient. The strength of this gap flow depends on: a deep gap for flow decoupling in the vertical; a ridge width sufficient to allow rotational effects, but narrow enough for gravity wave propagation (see p. 153); and an inversion to the south (of the Alps, for example), increasing the pressure gradient.

If the jet emerging from a gap is tangential to a convex surface it may remain attached to this surface for some distance downstream, despite the increasing deflection of the flow. This is termed the *Coandä*, or *wall attachment effect*, named after a Romanian aircraft engineer who discovered it in 1930. Giles (1976) suggests that the winds observed to the east of the Carpathian Mountains and Transylvanian Alps in Romania appear to reflect this principle since they are deflected southwestward towards the adjacent convex surface of the range. A local low pressure is caused by the entrainment of air into the flow on the south side of the Transylvanian Alps. The deflection of the northerly mistral southeastward over the Rhône delta may indicate a similar effect around the Maritime Alps (see also p. 137, Fig. 3.6).

Apart from its effect on the airflow, the orientation of mountain ranges also modifies the regimes of temperature, evaporation, convection, and thermally induced wind circulations, as a result of the augmentation (reduction) of solar radiation receipts on equatorward- (poleward-) facing slopes. This topic is discussed below. In many cases, the dissection of mountain ranges by valley systems creates a complex pattern of slope facets and therefore of topoclimates. Nevertheless, the

orientation of the major ranges in the European Alps, for example, causes snow lines to be about 200 m higher on southern slopes than northern ones.

2.4.2 Relief effects

The role of relief in modifying the wind velocity over mountains and hills was recognized in the studies of "influence height" in the 1920s (see p. 70), but only recently have more adequate observations and theories become available to describe such effects. The influence zone can be described in terms of the horizontal and vertical deflection of streamlines in the airflow, both upstream and down-stream of the barrier. However, its effects are expressed through many other meteorological variables, including the drag effect on wind velocity (see p. 71) and changes in atmospheric heating forced by the surface (p. 79).

Studies on atmospheric flow modification due to relief have focused largely on low hills of the order of 1 km long and 100 m high. For such hills, stability and geostrophic forces have negligible effects on the air motion, whereas for hills a few kilometers wide, stability becomes important. The effects of such topography on wind velocity are important in terms of understanding the dispersal of pollutants and assessing potential wind energy availability (Hunt and Richards, 1984; Taylor et al., 1987; World Meteorological Organization, Secretariat, 1981).

Local flow perturbations over hills are related to two basic processes that modify the pressure gradient on a local scale (Taylor, 1977). For two-dimensional flow in a neutral atmosphere (ignoring shear stress and Coriolis effects), the dynamic pressure gradient (P_D) on the upwind side of the hill is approximately

$$P_D = -\rho U \Delta L / L, \text{ and if } L\Delta U = hU$$
$$P_D = -\rho U^2 h / L^2$$

where L is the width and $h =$ height of the hill; ρ is the air density; U is the upwind velocity; and $\Delta U =$ the increase over the hill.

The hydrostatic pressure gradient induced by heating (P_H) is approximately

$$P_H = -\rho g \Delta \theta h^* \theta L$$

where θ is the upwind potential temperature and $\Delta \theta =$ increase over the hill; h^* is the smaller of h and h_s, the height of the super-adiabatic layer near the surface; and g is the acceleration due to gravity.

By a dimensional analysis of the ratio of P_D/P_H, for selected values of L, h, and h^*, assuming that $U = 10 \text{ m s}^{-1}$, $g \sim 10 \text{ m s}^{-1}$, and $\Delta \theta/\theta = 0.1$, Taylor shows that dynamic pressure effects are important within the boundary layer ($L \sim 100 \text{ m}$, $h = 10 \text{ m}$, $h^* > h$). For large-scale hills ($L \sim 10 \text{ km}$, $h = h^* = 100 \text{ m}$) thermal effects dominate, while for steeper slopes of 1: 10, the dynamic and thermal effects are of similar magnitude when $h^* \leq h$.

Schematic illustration of the
speed-up of boundary layer
winds (ΔU) over a low hill and
the corresponding pattern of
pressure anomalies (modified
after Taylor et al., 1987; Hunt
and Simpson, 1982).
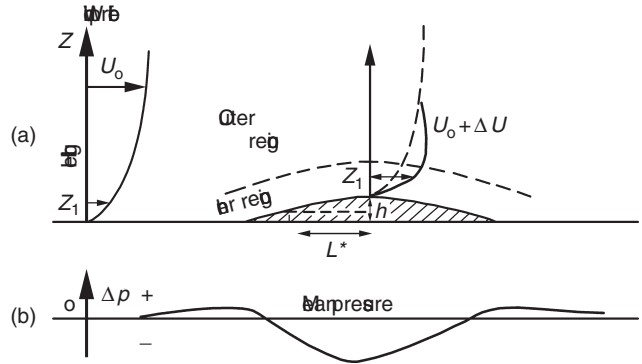
   Most theoretical and observational work has so far concentrated on low hills
with slopes of about 1 in 5. In the work of Jackson and Hunt (1975) and Bradley
(1980) this is expressed by the "aspect ratio" ($L*/h$, where $L*$ the half-width is the
horizontal distance from the summit to the point at which the height is half of its
maximum value, h). The flow is treated in a linear analysis of the equations of
motion in terms of a shallow inner layer, where the dynamics are modified by
turbulent transfers with the surface, and an outer layer of inviscid potential flow,
i.e. viscosity is unimportant for the motion and the flow moves as a set of vertical
columns with relative height above the surface conserved following each fluid
element (Hunt et al., 1988; Carruthers and Hunt, 1990) (see Figure 2.31).
Accelerations and buoyancy effects set up within this outer region extend to heights
equivalent to $L*$, or higher if internal waves are generated (Hunt and Richards,
1984). It can be assumed that at some level above the hill, the horizontal wind
velocity will be the same as in the undisturbed upwind flow (U). Near the surface,
however, the boundary layer is displaced upward by the terrain, setting up a local
pressure gradient which modifies the horizontal velocity. Pressures are reduced
over the hill and increased slightly upwind and downwind, accelerating the flow
over the hilltop. This "fractional speed-up ratio" $\Delta S = (\Delta U/U)_0$ or the excess of
wind speed, ΔU, at height z over the hill top compared with the speed U at the same
absolute elevation upwind (Note 6, see also Figure 2.30), varies according to the
upwind velocity profile, the airflow stratification, the aspect ratio of the hill, and
surface roughness length (Hunt and Richards 1984).
   Taylor and Lee (1984) suggest that $\Delta S = (Bh/L*) \exp(-A(\Delta z/L*))$, where A and
B are constants, $A \sim 3$ to 4 and $B \sim 2.0–1.6$, that vary with hill shape. The speed-up
increases by a factor of about 2 between unstable and stable boundary layers and
ΔS reaches a maximum typically within 3–5 m of the summit surface. Taylor et al.
(1987) consider this to mark the inner layer depth, whereas Jackson and Hunt
(1975) indicate that the boundary corresponds to $\sim 0.05 L*$ (of the order of 25 m).
At Black Mountain, Canberra, for example, a local wind maximum is observed at
$h/5 = 35$ m, for cases of neutral stability (Bradley, 1980). At Brent Knoll, Somerset
($h = 130$ m, $L* \sim 300$ m), the speed at 2 m for cases of neutral westerly flow

increased from $10 \, \text{m s}^{-1}$ upwind to $22–23 \, \text{m s}^{-1}$ over the crest, with a minimum of $4–5 \, \text{m s}^{-1}$ in the lee (Mason and Sykes, 1979).The observed and predicted ΔS are in close agreement.

Field and modeling studies have been combined in the Askervein Hill Project in the Outer Hebrides, Scotland (Salmon *et al.*, 1988; Teunissen *et al.*, 1987). The hill has 116 m relative relief; it is 2 km long perpendicular to the prevailing south-westerly winds and 1 km wide. Fractional speed-up over the summit exceeds 0.7 at 10 m height, with velocities almost constant down to 3 m above the surface, where the largest increases in speed are observed ($\Delta S \geq 1.0$). Effects of the hill in retarding the flow at the surface are detectable 800 m upwind.

The typical maximum speed-up ratios for different types of small-scale topo-graphy can be summarized as follows (Hunt, 1980; Taylor and Lee, 1984):

$\Delta S_{\text{max}} = 2h/L^*$ for two-dimensional ridges (negative for valleys);
$\qquad = 1.6h/L^*$ for three-dimensional axisymmetric hills;
$\qquad = 0.8h/L^*$ for two-dimensional scarps.

These estimates apply for winds $\geq 6 \, \text{m s}^{-1}$, near-neutral stability, horizontal terrain scales of $\leq 1 \, \text{km}$, and $h/L^* \leq 0.5$. Taylor and Lee (1984) and Walmsley *et al.* (1989) provide a convenient step-by-step procedure to estimate wind speed for specific sites. Such information is important for siting wind turbines since the energy is proportional to U^3. In addition to summit speed-up estimates, Taylor and Lee (1984) provide formulae for surface roughness corrections. An application to the terrain of Grindstone Island in the Gulf of St. Lawrence, Canada, indicates a slow-down due to roughness of 20 percent compared with a 30 percent speed-up effect. Average winds are only 10 percent greater than those observed at 10 m over the Gulf (Taylor *et al.*, 1987).

The speed-up ratio of large hills also appears to fit the general Jackson–Hunt model, as extended by Carruthers and Choularton (1982). Gallagher *et al.* (1988) report that flow speed-up over Great Dun Fell (847 m) in northern England is dominated by the elevated air stratification, except when the flow is blocked. Extension of this approach for an inversion-capped boundary layer (Carruthers and Choularton, 1982) shows that the speed-up over a hill depends on the height of the inversion (I_z) relative to the obstacle. When $I_z \geq 2h$ there is increased speed-up as the flow in the inversion layer tends to be subcritical; whereas if $I_z \leq 2h$ the speed-up is reduced. When the stability of the air above the inversion increases, it can lead to asymmetric flow with an upwind lull and a rapid increase in speed at the summit and downwind.

More recent studies of large hills have been performed by Vosper and colleagues. At Black Combe (600 m high, 6 km wide) in northwest England, a simple Bernoulli formulation provides a good approximation along low-level streamlines, implying that turbulence played a limited role (Vosper and Mobbs, 1997). However, for Tighvein hill (458 m, 8 km east–west) on Arran Island, off western Scotland, Vosper

et al. (2002) show that the Bernoulli equation needs to be modified for turbulence – the vertical gradient of the turbulent momentum flux, $\int d_z \overline{u'w'} dx$ where the primed terms are time departures of the motion in the x direction normal to the barrier (u) and vertically (w), and the over-bar denotes the time average of their product. They demonstrate that this term has similar magnitude to both p^*/ρ and $\mathbf{V}^2/2$, where p^* is the flow-induced perturbation of surface pressure; ρ is the density; and $\mathbf{V}$ is the vector wind at 2 m above the surface, and all quantities are averaged so as to account for temporally-fluctuating values (Reynolds averaging, see Note 7).

Linear models of airflow over large hills can give considerable errors in the lee of the obstacle, where the pressure perturbation due to gravity waves can create a turbulent wake and/or flow separation from the surface. Non-linear models are impractical for detailed studies of complex terrain, but new approaches using a Fourier transform of the terrain and velocity field have enabled useful models to be developed for neutral and stratified flows (Carruthers and Hunt, 1990; see also Note 5). To obtain flow variables at a point the transform is inverted numerically. The model is suitable for hill slopes $< 1/4$ and $F_h \gg 1$ (i.e. flow over the hill).

The shape or profile of obstacles is also important. A sharp break of slope sets up more turbulence in the air passing over it than if the slope is gradual. Breaks of slope greatly increase the tendency for the airflow to separate from the ground and form vertical eddies or rotors. This may occur as a lee eddy downwind of a salient edge, or as a "bolster" at the foot of a steep windward-facing slope (Scorer, 1955). Where the general airflow is transverse to a large valley, an eddy may occupy the entire valley without disturbance to the flow above, or there may be downward motion following the valley side. These effects are illustrated in Figure 2.32.

Flow separation is characterized by large reductions in mean wind speed and increased variance in the flow components (Taylor *et al.*, 1987), but recirculating flow is not a necessary accompaniment. Separation of the flow from the surface is favored by thermal instability and inhibited by radiative cooling at the surface. Separation is also more likely when the slopes are forested due to the extra drag they create (Ross and Vosper, 2005).

Separation develops at a critical height above the surface where the surface stress becomes zero and it should depend on the hill width scaled on the surface roughness length, L^*/z_0, where z_0 is the the roughness length, the height where the extrapolated neutral wind profile $= 0$ (Taylor *et al.*, 1987). Assuming that the background flow profile is logarithmic, the critical angle needed for separation is a function of $4 L^*/z_0$ according to Ross and Vosper (2005). They show that the critical angle for forested slopes is in the range 0.05–0.1 for $4 L^*/z_0$ of the order of $10^3 - 10^4$.

Studies on San Antonia Mountain, New Mexico, by Wooldridge *et al.* (1987) indicate that for $F_h \ll 1$ separation is controlled by the pressure distribution relative to the lee wave pattern, whereas for $F_h \gg 1$ it is determined by the boundary-layer flow. A recirculation occurs near the base of the lee slope for $0.4 < F_h < 0.7$ and this develops higher up the lee slope as F increases. Separation may occur at a hill summit for $F \sim 1.7$ according to Hunt and Richards (1984). It may also occur on
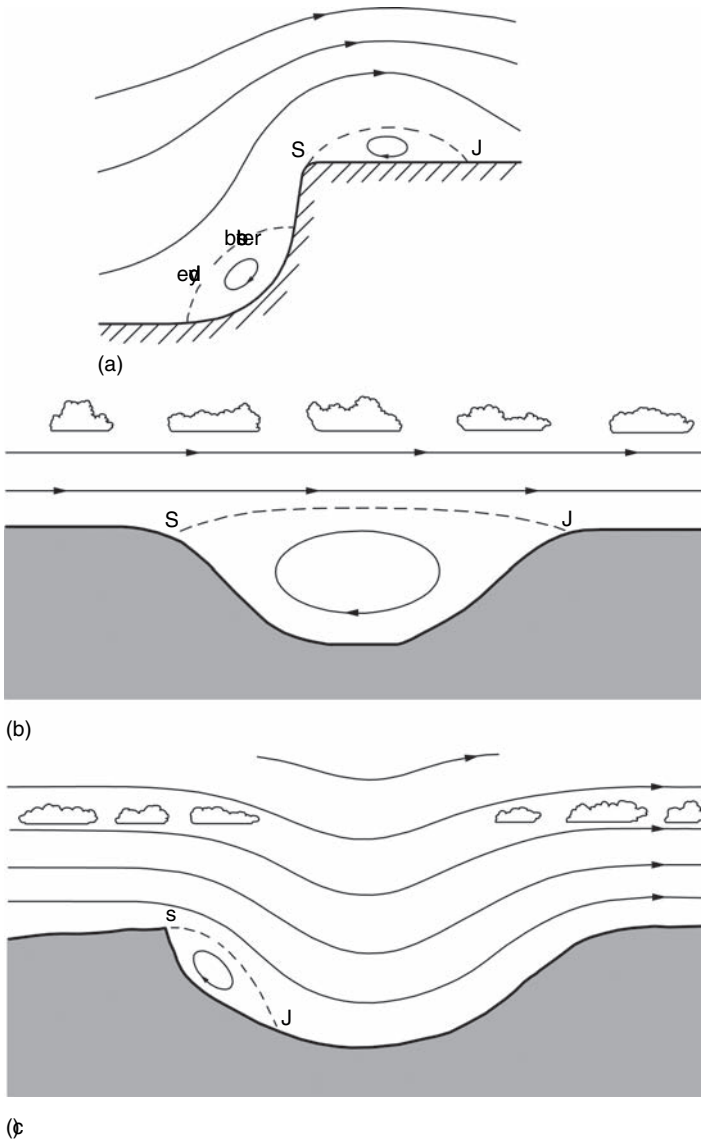
Fig. 2.32 Examples of flow separation: (a) separation at a cliff top (S), joining at J. A "bolster" eddy resulting from flow divergence is shown at the base of the steep windward slope; (b) separation on a lee slope with a valley eddy. The upper flow is unaffected; (c) separation with a small lee slope eddy. A deep valley may cause the air to sink resulting in cloud dissipation above it (from Scorer, 1978).

upwind slopes under stratified flow, when $F_L \geq 1$, while being suppressed on lee slopes. On San Antonia Mountain, upwind separation is reported with neutral flow; the deflected flow may rise to about 2 h (see Figure 2.29, p. 78).

Tampieri (1987) provides estimates of the height and location of the separation point for different stability conditions and valley shapes. In general, it occurs lower

down a valley slope than on a single hill, and is lower for sinusoidal topography than irregularly spaced ridges. It is characteristic on lee slopes $> 20°$ ($h/L^* \geq 0.35$); the separation distance from the hilltop down the lee slope is of the order of $\lambda/2$, where λ is the lee wavelength (Hunt and Snyder, 1980). The region of separation or reversed flow can extend up to $10h$ downwind of a hill, with a vertical extent between a fraction of h and up to $2h$ (Hunt and Simpson, 1982).

The effects of air flowing over a succession of ridges and valleys are also of interest. For neutral static stability airflow over the valleys of southern Wales, UK, with slopes of $32°$, marked separation occurs when the flow is cross-valley (Mason and King, 1984). In a further study, both unstable and neutral flows show separation, whereas around dawn and dusk the flow remains attached (Mason, 1987). This may be of considerable significance for pollution dispersal since it ensures that the valley is well ventilated.

Valley sweeping requires $F \geq 1.5$ according to Kimura and Manins (1988), but depends also on the topography up- and downwind, as well as on terrain shape. They suggest that complete sweeping of periodic valleys occurs for $F \sim 2.8$ and blocked flow with $F \sim 1$. The threshold between ventilation and stagnation in a valley depends on the ratio between the separation distance (D) between the ridges and the lee wavelength (λ), and also on the ratio D/L^* according to Hunt and Richards (1984). With strong periodic waves, beneath an upper inversion layer, the criterion is $D \sim \lambda$. In stable conditions, successive ridges may set up significant flow interactions. Thus, higher speeds in the lee of one ridge may exceed the slowing down caused by the upstream influence of a second ridge downwind. In general, cross-valley flows are associated with stagnation and re-circulation in the valley, except for a narrow range of F_h, F_L and D/L^* conditions (Tampieri and Hunt, 1985; Tampieri, 1987). For example, separation is reduced for $0.5 < F_L < 1$; for $F_L \sim 1$, the ratio D/L^* must be about 4 to 6 for ventilation. Similar results are illustrated by Lee *et al.* (1987) in a towing tank experiment with a pair of ridges. Typically, stagnation begins near the valley bottom and slowly deepens. Meroney (1990) gives a detailed review of the laboratory modeling of flow over hills.

The relative relief of a topographic obstacle need not be great in order for it to influence the airflow or the occurrence of climatic elements such as precipitation. Even "microrelief" of 50 m or less can affect precipitation distributions according to studies by Bergeron (1960) near Uppsala, Sweden. There is little or no effect during convective conditions, but precipitation amounts increase over the hills from stratiform cloud. In these situations the flow pattern is more nearly stationary. Since the process of rain droplet growth cannot be accomplished during the short time interval while the air passes over a small hill, Bergeron suggested that washout of cloud droplets from low-level *scud* (or *pannus*) cloud must occur due to rain from an upper cloud layer falling through it (see Chapter 4, p. 273). The boundary layer must be close to saturation for scud to form over the hills. Frictional influences are probably important in such situations in initiating mechanical turbulence (forced convection). Over small hummocks of about 10 m, differences in precipitation

amounts are attributable to wind effects on gauge catch, rather than orographic factors as such.

In the case of large barriers to airflow, where the mountain height exceeds that of the planetary boundary layer, many other factors need to be taken into account as noted in the preceding section. Mountain-produced effects include: lee waves and flow blockage on the meso-scale; frontal modification and lee cyclogenesis on a regional macro-scale; and planetary wave effects for airflows perpendicular to high, semi-infinite barriers. These features are examined in detail in Chapter 3.

2.4.3   Slope and aspect

Slope angle and aspect (or orientation) have fundamental effects on radiation income and temperature conditions, which have been the subject of many observational and analytical studies. The radiation falling on slopes of given angle and orientation has been calculated for direct or global radiation at various latitudes by many authors. Geiger *et al.* (2003), for example, tabulate a number of these sources, some of which are based on actual measurements. Other studies are cited by Kondratyev (1969; pp. 342 and 485; also Kondratyev and Manolova, 1960; Kondratyev and Federova, 1977) and Hay (1977).

The basic effects of season, slope angle and orientation are demonstrated in Figure 2.33 for two mid-latitude stations at the solstices. Except on north-facing slopes, there is a displacement of the maximum intensity of direct radiation from steeper slopes in winter, to gentler ones in summer when the solar altitude is higher. South-facing slopes at the equinoxes show a symmetrical diurnal pattern; since the Sun rises due east, it cannot shine immediately on a south-facing slope and the delay is greater the steeper the slope. This effect is even more marked on west-facing slopes, whereas on east-facing ones it is the time of apparent sunset that is affected by slope angle. East- (and west-) facing slopes have a maximum intensity that shifts according to both solar declination angle, and therefore, season, and slope angle. Declination angle is the angular distance (latitude) between the Sun and the celestial equator; angles are positive (negative) to the north (south) of the equator. On north-facing slopes in middle latitudes, direct radiation is only received around midday in winter if the solar altitude exceeds the slope angle (see Figure 2.1, p. 25, for example); the maximum is always centered on an inclination of zero.

It is important to recognize that not only the magnitude, but even the sign, of slope effect changes with latitude (Lee, 1978: p. 171). Equatorward of 40° latitude, north-facing slopes in the northern hemisphere at the summer solstice receive *more* direct radiation over the course of the day than south-facing ones, with the difference increasing with slope angle (Figure 2.34). Nevertheless, south-facing slopes receive more in the few hours around noon. This difference in daily totals of direct radiation arises from the day length and the fact that the Sun rises and sets to the north of local east and west. On an annual basis, theoretically possible direct radiation totals show the greater relative differences between north- and
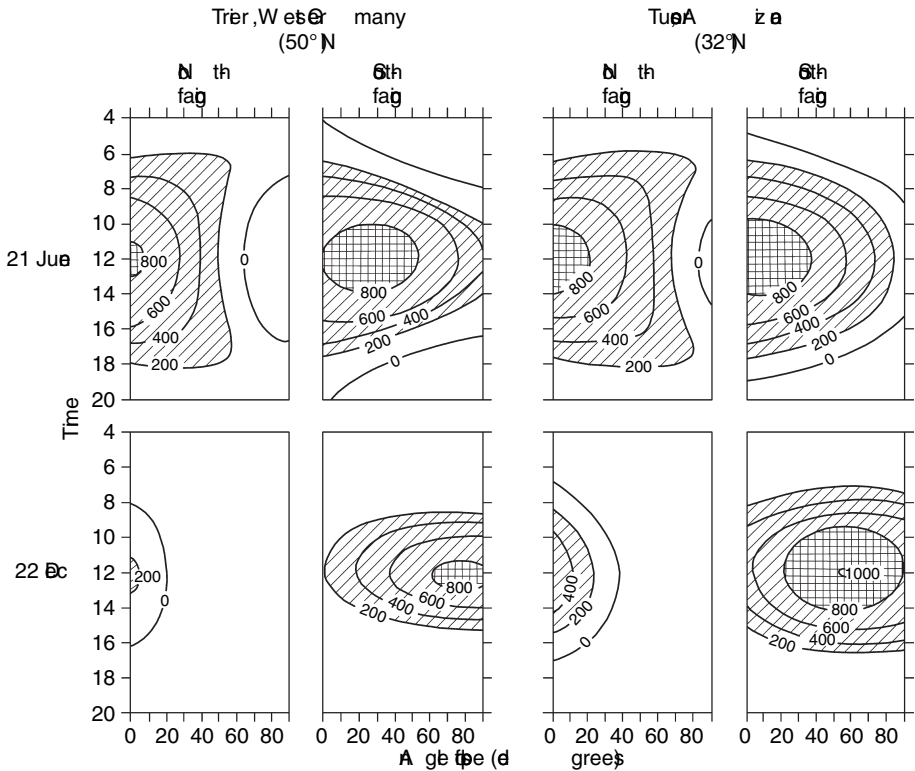
Fig. 2.33 Average direct beam solar radiation (W m^{-2}) incident at the surface under cloudless skies at Trier, West Germany and Tucson, Arizona, as a function of slope, aspect, time of day and season of year (from Barry and Chorley, 1987, after Geiger, 1965 and Sellers, 1965).

Fig. 2.34 Relative radiation on north- and south-facing slopes, at latitude 30° N for daily totals of extra-terrestrial direct beam radiation on 21 June (after Lee, 1978).
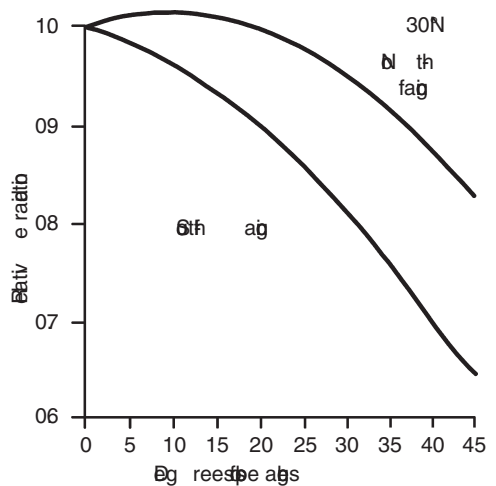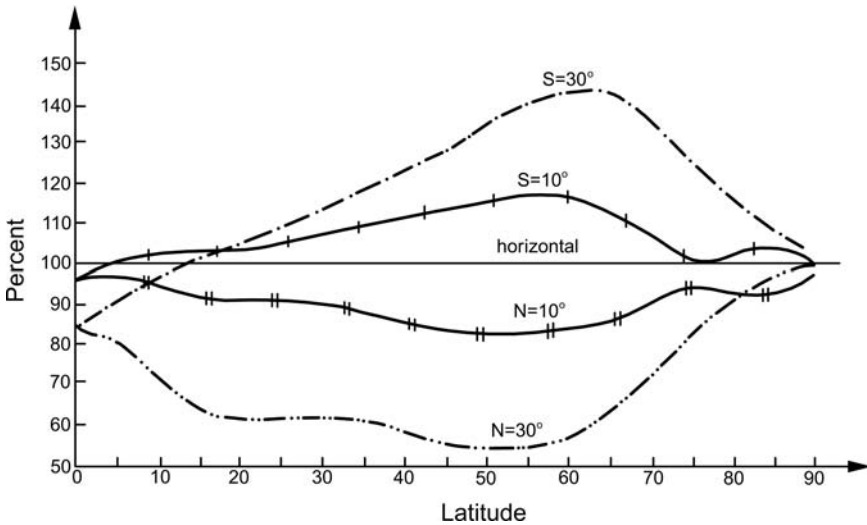
Fig. 2.35 Annual totals of possible direct solar radiation according to latitude for 10° and 30° north- and south-facing slopes, in percentages relative to those for a horizontal surface (from Kondratyev and Federova, 1977).

south-facing slopes in middle latitudes (Figure 2.35) (Kondratyev and Federova, 1977). It is interesting to note that a 30° N slope causes a greater deficit in the tropics than near the pole.

We can now examine some of the geometrical considerations involved in slope radiation. The solar radiation received on a sloping surface comprises three components: the direct beam S'_b, the diffuse radiation S'_d, and that reflected from surrounding surfaces (S_r). The instantaneous direct beam solar radiation incident on a slope can be expressed:

$$S'_b = S_b \cos i$$

where i is the angle between the solar beam and the normal to the slope; and S_b is direct beam radiation on a plane normal to the beam at the Earth's surface.

Various approaches for evaluating this expression in terms of measurable parameters have been devised (see Heywood, 1964; Loudon and Petheridge, 1965; Kondratyev, 1969: p. 344 *et seq*.; Revfeim, 1976; Hay, 1979; Zekser *et al.*, 2005). Duguay (1993) provides a useful review of many of these approaches. The method of determining the geographical coordinates of an "equivalent" horizontal site, proposed by Lee (1962, 1978) has the drawback that it applies only to instantaneous values since the times of sunrise and sunset on slopes differ from those on a horizontal surface. Hence, complex calculations are required to obtain daily or monthly sums.

Direct radiation is determined as follows (Kondratyev and Federova, 1977; Hay, 1979):

$$\cos i = \cos s \cos Z + \sin s \sin Z \cos(A - A_s)$$

where s is the slope angle; Z is the zenith angle ($= 90°$ – solar elevation)

and $\cos Z = \sin \phi \sin S + \cos \phi \cos \delta \cos \omega t$

where ϕ is the latitude; δ is the declination angle of the sun from the apparent noon (clockwise positive); ωt is the time from solar noon; ω is the Earth's angular velocity ($\pi/12$ radians h^{-1}); A is the solar azimuth; A_s is the azimuth of the slope.

$$\cos A = \frac{\sin \phi \cos Z - \sin \delta}{\cos \phi \sin Z}$$

and

$$\sin A = \frac{\cos \delta \sin \omega t}{\sin Z}.$$

Thus,

$$S'_b = S_b[\cos s \cos Z + \sin s \cos(A - A_s)]$$
$$= S_b \Bigg\{ \cos s[\sin \phi \sin \delta + \cos \phi \cos \delta \cos \omega t] + \sin s$$
$$\left[\cos A_s \left(\frac{\sin \phi \cos Z - \sin \delta}{\cos \phi} \right) + \sin A_s(\cos \delta \sin \omega) \right] \Bigg\}$$

The diffuse radiation on a slope, S'_d, differs from that on a horizontal surface, since only part of the sky is visible. Assuming isotropic sky radiation (S_d),

$$S'_d = S_d \cos^2 \left(\frac{s}{2} \right) = 0.5 S_d (1 + \cos s)$$

For gentle slopes up to $20°$, the effect is negligible, especially for daily totals, since $\cos^2 (20°/2) = 0.97$, whereas for a slope of $45°$, $S'_d = 0.85 \, S_d$.

An isotropic model underestimates the clear-sky diffuse radiation on equator-facing slopes since the incident flux is anisotropic. According to Kondratyev and Federova (1977), the diffuse radiation flux from the circumsolar half of the sky (i.e. divided by a plane normal to the solar vertical) is about 75 percent of the total diffuse radiation falling on a horizontal surface. This azimuthal dependence causes differences according to slope orientation for all slope angles. Horizon screening of a point from the side towards the Sun is important for slopes facing either towards or away from the Sun (Kondratyev, 1969: pp. 489–92). Hay (1979) has developed a model for anisotropic diffuse radiation on slopes and shows that it gives lower systematic and random errors than either the isotropic model or one using a 50 : 50 combination of circumsolar and isotropic components. Hay's anisotropic formulation is:

$$S'_d = \left\{ \left(\frac{S_b}{S_0} \right) \cdot \frac{\cos i}{\cos Z} S_d \right\} + \left\{ 0.05 S_d(1.0 + \cos s) \left[1.0 - \left(\frac{S_b}{S_0} \right) \right] \right\}$$

where S_0 is the solar constant; and (S_b/S_0) $\cos i$ is an "anisotropy index" for the slope.

The first term in the right side of the equation is the circumsolar component and the second accounts for the isotropically distributed radiation flux.

In an alternative approach, the diffuse irradiance on slopes has been calculated by integrating the mean radiance distribution under cloudless skies for the sector seen by the slope (Steven, 1977; Steven and Unsworth, 1979). Their tabulations show the pronounced effect of slope azimuth for steep slopes and low solar elevations.

The reflection from adjacent slopes (S_r) is not in general readily estimated. However, if we assume a uniform landscape (in terms of albedo) that is diffusively reflective, then the reflective component on the slope is

$$S_\gamma = (S_b + S_d)\alpha \sin^2(s/2) = 0.5(S_b + S_d)\alpha(1 - \cos s),$$

where α is the albedo of the landscape.

As for the diffuse component, anisotropy gives rise to important discrepancies from the theoretical S_γ calculated as above, especially in the presence of a snow cover. Relative values of $S_\gamma/(S_b + S_d)$ determined from measurements and from isotropic approximation for S_γ have been compared by Kondratyev (1969: p. 492). He shows that the isotropic estimates are too small for slopes facing the Sun. Differences, expressed by the ratio (measured isotropic estimate)/measured, for 30° slopes with a melting snow cover for a solar elevation of 30° were +49 percent for slopes facing toward the Sun and −46 percent for slopes facing away from the Sun.

The net effect of reflected and diffuse radiation is small compared with direct radiation when the Sun is not obscured by cloud and the solar elevation is large ($\geq 60°$). However, the reflected component can provide a larger contribution than the diffuse flux on steep slopes facing away from the Sun in the presence of a winter snow cover. Table 2.17 provides an illustration of calculated mean daily values of S'_b, S'_d and S_γ for Churchill, Manitoba, in December and June from Hay's (1977) analysis (using a slightly different formulation for S'_d from that presented above). Realistic cloud and surface albedo estimates are used and the starting point for the calculations is *measured* global radiation on a horizontal surface.

Beginning with the work of Garnier and Ohmura (1968, 1970), a variety of computer programs have been developed to calculate solar radiation (under cloudless skies) at any location. Map output can be generated directly from such routines using digital terrain data in gridded form (Williams *et al.*, 1972). The steps involved in such computations are: (1) determination of the extra-terrestrial radiation for the required date, time and latitude; (2) calculation of the direct beam radiation for cloudless skies, assuming a specific transmission coefficient for the appropriate atmospheric turbidity conditions; (3) calculation of the direct radiation on a slope of given azimuth and inclination; (4) calculation of the sky radiation according to

Table 2.17 Calculated slope radiation components for Churchill, Manitoba, in December and June (MJ m^{-2} day^{-1}).

Orientation	Slope angle										
	0°		20°			40°			90°		
	S_b	S_d	S_b	S_d	S_r	S_b	S_d	S_r	S_b	S_d	S_r
December: Surface albedo = 0.60, cloud amount = 51%											
North			0.0	0.65	0.03	0.0	0.35	0.11	0.0	0.01	0.47
West[a]	0.63	0.92	0.80	0.89	0.03	1.02	0.81	0.11	1.14	0.42	0.47
South			2.60	1.13	0.03	4.26	1.26	0.11	5.87	1.13	0.47
June: Surface albedo = 0.25, cloud amount = 63%											
North			10.85	8.37	0.17	7.25	7.04	0.65	2.10	2.17	2.78
West	13.14	9.08	12.64	8.72	0.17	11.51	7.70	0.65	7.03	3.38	2.78
South			14.08	9.07	0.17	13.55	8.35	0.65	6.49	4.21	2.78

[a] Values for east-facing slopes differ by only a small amount.
Source: from Hay (1977).

dependence on solar altitude and slope azimuth and inclination; and (5) calculation of the effect of horizon screening by nearby mountains. The details of these calculations are beyond the scope of our discussion here, but they are readily available in the cited references and are discussed in a review by Duguay (1993). Steps (2) and (5) present the major difficulties. In Williams *et al*. (1972), for example, allowance is made for the altitude of the slopes through an optical air mass correction (see Table 2.3).

An example of a map generated by such a procedure is given in Figure 2.36 – for the Mount Wilhelm area, Papua New Guinea. It shows theoretical global solar radiation totals between sunrise and 1000 h illustrating the pronounced effect of the terrain. The slope contrasts are clearly evident in observed daily soil temperatures down to at least 7 cm (Barry, 1978). Cloud cover eliminates these slope contrasts later in the day. The improvements for anisotropic effects, discussed above, and extension of the methods to deal with spatially variable albedo and varying cloud cover are already well advanced (Hay, 1977, 1979; Dozier, 1980). The latter is developed for spectrally distributed irradiance. Modeling slope radiation in high latitudes is treated by Skartveit and Olset (1986).

One of the more recent models, TOPORAD, incorporates a fast solution for the calculation of horizon screening (Dozier and Frew, 1990). It has been applied by Cline *et al*. (1998) to model snow melt for Emerald Lake basin in the Sierra Nevada, California. Compared with solar radiation measurements, they found an RMS error of 70 W m^{-2} for cloud-free skies, but over 300 W m^{-2} for overcast conditions. Dozier (pers. comm., 2005) considers that the major source of error under most
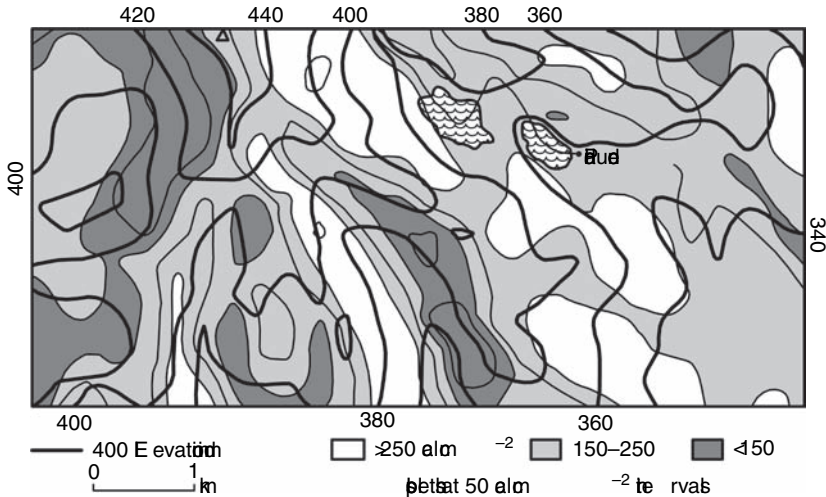
Fig. 2.36 Computed global solar radiation for cloudless skies, assuming a transmission coefficient of 0.75, between 0600 and 1000 h on 23 September for Mt. Wilhelm (Δ = summit) area of Papua New Guinea (from Barry, 1978).

circumstances is the assessment of the atmospheric properties. Any topographic radiation model has to be able to separate the direct and diffuse components. In a clear atmosphere this is not difficult; because most of the irradiance is direct and the diffuse component is only significant on shaded slopes. Varley *et al.* (1996), using the model of Williams *et al.* (1972) with the Dozier and Frew horizon algorithm, show for a catchment in central Scotland with average slopes of 15–20° and maximum slopes up to 35°, that in June (December) the horizon effect reduces the overall basin radiation by only three (14) percent. The corresponding ratios of direct/diffuse radiation are about 3.3 and 0.225.

Essery (2004) notes that for the sub-grid scale effect of mountain shading to be included in a surface energy balance model, a statistical representation is required. Positive and negative slope components (*s*) calculated from digital elevation models (DEMs) in North Wales and the French Alps exhibit double-exponential (Laplace) distributions:

$$P(s) = 1/\sqrt{(2\sigma)} \exp\left\{\frac{-\sqrt{2}s}{\sigma}\right\}$$

Expressions are then developed for the fractions of the areas that will be either self-shaded or shaded by remote topography as functions of solar elevation and time of day. These expressions showed good agreement with results from a terrain-shading model of Corripio (2003).

Molotch *et al.* (2004) run a snowmelt model which uses TOPORAD as part of the input. With "nominal" snow albedo values using a standard decay function for the decline of albedo with age of the snow, the errors in calculated snowmelt are not only large but systematic. However, when running the model with albedo values

derived from remote sensing, and applying an empirical albedo-decay function for each grid cell, based simply on periodic remotely sensed values, the errors are smaller and are centered around zero. TOPORAD has recently been coupled to hourly two-stream satellite solar radiation products from GOES and is run operationally to provide the solar forcing for the CONUS snow model that is used in the US National Snow Analyses prepared by the National Operational Hydrologic Remote Sensing Center (NOHRSC). TOPORAD has been further developed for grid applications as GTOPORAD (see http://cirque.nwrc.ars.usda.gov/~ipw/man1/gtoporad.html) This "global-scale" radiative transfer and terrain processing tool allows solar geometry, atmospheric properties, and sunrise and sunset to vary over the grid. They also correct for Earth curvature when computing horizons, terrain and sky view factors, and illumination angles. It is planned to incorporate it in a future version of ArcGIS (Dozier, pers. comm., 2005).

The effect of slopes in terms of net radiation is especially complex in view of the added role of infrared fluxes. Observations are very limited, although Kondratyev (1969: pp. 680–5), for example, treats the theoretical basis. By analogy with the above discussion for solar radiation we can write an expression for slope net radiation:

$$R'_n = (S'_b + S'_d) + S_r - r' + \varepsilon L'_i + \varepsilon' L_b - \varepsilon' L'_0$$

where $(S'_b + S'_d)$ is the global solar radiation on the slope;

$S_r = (S_b + S_d)\,\alpha\,\sin^2(s/2)$, shortwave reflection onto the slope;
$r' = (S'_b + S'_d + S_r)\,\alpha'$, shortwave radiation reflected by the slope;
$L'_i = L_i \cos^2(s/2)$, atmospheric emission to the slope;
$L_{i,r} = (1 - \varepsilon)\,L_i \sin^2(s/2)$, atmospheric emission to the adjacent surface reflected onto the slope;
$L_b = \varepsilon\sigma T^4 \sin^2(s/2)$, infrared flux from the adjacent surface received by the slope;
$L'_0 = \varepsilon\sigma\, T'^4$, infrared flux from the slope at temperature T';
$\alpha =$ albedo of adjacent surface; $\alpha' =$ slope albedo;
$\varepsilon =$ emissivity (absorptivity) of surface; $\varepsilon' =$ slope value;
$\sigma =$ the Stefan–Boltzmann constant.

The various components are illustrated in Figure 2.37. In general, $L_{i,r}$ and S_r are of minor importance although as already noted S_r becomes important in the presence of a highly reflective snow cover. The surface albedo for infrared radiation is typically 0.05–0.10. The estimation of the hemispheric surface albedo, integrated over the shortwave spectrum, remains a major challenge in mountainous terrain, whether through empirical modeling or satellite measurements (Duguay, 1993). A model for calculating atmospheric radiation (L_i and $L_{i,r}$) in mountain areas is available (Marks and Dozier, 1979). It requires estimates of air temperature and vapor pressure, as well as topographic data in order to calculate the "thermal view

Fig. 2.37 Components of solar and infrared radiation incident on slopes.
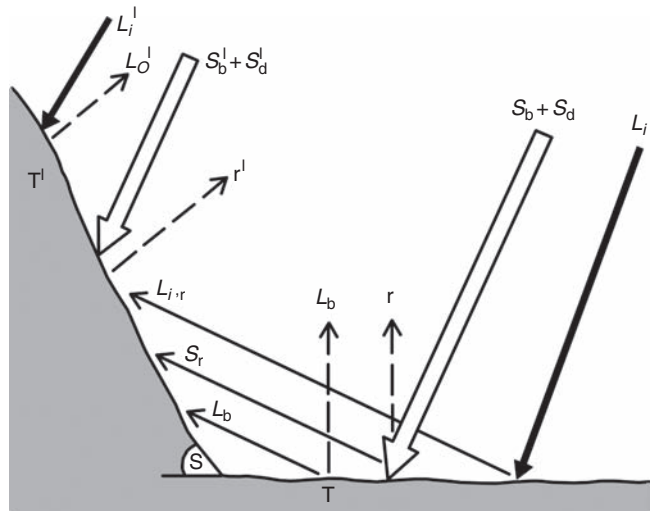
factor," the unobscured sky. This is obtained from $\cos^2 (\overline{Z}_H)$, where $\overline{Z}_H =$ mean horizon angle from the zenith.

For slopes less than $30°$, Kondratyev and Federova (1977) show that the net infrared radiation on a slope (L'_n) is approximated by $L_0 \cos s$.

Likewise, for net radiation, Wilson and Garnier (1975) show that the slope radiation can be approximated within 4 percent for daily totals by:

$$R'_n = (S'_b + S'_d) - r' + L_i - L_0$$

for slopes less than $20°$.

The Riviera project in southern Switzerland near Lake Maggiore examined the problem of the radiation incident on inclined valley surfaces compared with that measured by radiometers that are horizontal rather than slope parallel (Matzinger et al., 2003). A semi-empirical method is used to estimate the net radiation in a slope-parallel frame of reference. The valley runs NNW–SSE, is U-shaped, and rises from 250 to 2500 m asl, with slopes of $30–35°$; it is mainly forest covered to 1200 m, then meadows with patches of rocky rubble. The analysis was performed at seven sites for days with weak synoptic control, when valley winds typically developed, during August–October 1999. By day, downward solar and infrared fluxes show strong site contrasts in total receipts and the phasing of their diurnal cycles. Inter-site differences of incoming global radiation are caused by the different orientations of valley surfaces relative to the direct solar beam component and by the timing of topographic shading. Diurnal cycles of albedo indicate that reflection of the direct beam component from the inclined surfaces is predominantly anisotropic diffuse radiation. Downward infrared radiation decreases with elevation in the valley because the higher sites have an increased sky view. Inter-site variations of the daytime net radiation result from variations in the absorbed direct

beam component of solar radiation. At night, net outgoing radiation increases with elevation, again because of the increasing sky view. Significant contrasts are found in mean diurnal cycles and daily sums of net radiation between southwest and northeast facing slopes on valley wind days, whereas inter-site contrasts are greatly reduced when direct beam short-wave radiation is absent.

Apart from the direct effects of slope angle and orientation on sunshine hours, radiation totals and therefore soil temperature, slope "exposure" also affects precipitation input, snow cover, evaporation rates, and windiness. Since air motion is critical for these other elements, however, that topic is treated first in Chapter 3.

2.4.4   *Topo- and microclimates*

In the high mountains, especially above the tree line, plant and animal life is strongly controlled by the climate at and near the ground surface – the *microclimate*. Additionally, the spatial pattern of microclimate forms a mosaic due to the effects of topography, which cause distinctive *topoclimates*. Topoclimates show spatial differences in standard climatic elements over distances of 100 m to 1–10 km; microclimates are represented within the vegetation canopy and soil layer and show spatial differences over distances of a few cm (plant surfaces) to 100 m (clearings) (Turner, 1980).

Topoclimatic effects are especially important in the case of such physiographic features as glacierized cirques, mountain valleys with lakes, fiords in mountainous terrain, deep mountain gorges, and canyons cut into high plateaus, among others. Some examples of the effects of such features on wind and temperature regimes are presented throughout the book, but each case is so specific that generalization is impossible.

The combination of topo- and microclimatic effects largely determines local variability in plant cover. Small topographic irregularities and differences of slope angle and aspect produce marked contrasts in vegetation due to the combined effects of radiation, evaporation, wind speed and snow accumulation.

Turner (1980) suggests that alpine microclimates can be categorized in terms of: (i) slope irradiation; (ii) wind exposure; (iii) depth of winter snow cover; and (iv) density and height of ground cover. The first two are independent variables, whereas the latter two are partially dependent variables (see below, p. 101). On this basis the following types of microclimate can be differentiated:

(1)   sunny windward slope – irradiation and wind speeds high;
(2)   sunny lee slope – irradiation high, wind speeds low;
(3)   shaded windward slope – irradiation low, wind speeds high;
(4)   shaded lee slope – irradiation and wind speeds low.

Appropriate local threshold values can be set for these, or intermediate, categories. The degree of slope and its shape may also be considered. Turner also notes

that a key variable for characterizing alpine microclimate is soil heat flow, because it is highly conservative. It is governed by the four variables listed above and by the heat capacity and thermal conductivity of the soil, which are greatly affected by soil moisture. The microclimates of alpine and montane plants are strongly determined by the stature and canopy structure of the vegetation. Körner (2003) shows that vegetation of lower stature is increasingly decoupled from the atmospheric conditions, especially plant temperature, in moving from trees → shrubs → tussock grass→ rosette plants → prostrate dwarf shrubs→ cushion plants.

Some basic influences of altitude on microclimates are considered first. These arise from the typical altitudinal profiles of the meteorological elements discussed in the section on p. 31.

2.4.4.1 *Microclimatic gradients*

The great intensity of solar radiation at high altitudes results in high absolute surface temperatures. During July 1957, Turner (1958) reliably measured extreme temperatures of 80 °C on dark humus at 2070 m in the Otztal, Austria, for example. The site had a southwest exposure and 35° slope and the air temperature (at 2 m) was 30 °C. Using a radiation thermometer, which registers infrared emittance from the surface, the author recorded a bare soil temperature of 60 °C on a level site at 3480 m on Mt. Wilhelm, Papua New Guinea, during September 1975 (Barry, 1978). On this occasion the air temperature was only 15 °C. This effect of altitude is apparent from climatic data. Mean annual ground temperatures in the Alps at 1.2 m depth exceed air temperatures by 0.5 °C at 600 m, 2.0 °C at 1800 m and 2.9 °C at 3000 m (Maurer, 1916). Between sites at 2140 m and 2740 m in the central Alps, on a clear summer day, Lüdi (1938) observed a gradient of 10-cm soil temperature of +2.5 °C /100 m compared with an air temperature lapse rate of −0.57 °C/100 m.

Since air temperatures decrease with altitude, surface heating effects usually produce stronger near-surface temperature gradients at higher elevations (Schwind, 1952; Aulitsky, 1962), although the soil–air difference depends on weather conditions. From detailed measurements at the tree line (2072 m) near Obergürgl, Austria, Aulitsky (1962) shows that there is a linear relationship between mean and extreme values of soil and air temperature when the soil is unfrozen (Figure 2.38). Soil temperatures are lower than air temperature in the transition seasons, due to radiative cooling of the surface in autumn and to lag effects of the snow cover in spring. In the Alps, soils generally reach their lowest temperature during autumn through cold penetration, whereas winter snow cover tends to insulate the ground. In shaded lee situations, however, persistently low snow temperatures may enable subzero temperatures to penetrate through even deep snow cover into the soil. Snow cover is important because of its low thermal conductivity. Thus snow cover acts as an insulator and damps temperature variations within the soil compared with those at the ground surface. The amplitude of the diurnal temperature cycle is reduced with depth and its timing is progressively delayed. These effects depend on the date of onset of snow cover, its duration, and

Fig. 2.38 Relations between monthly soil temperatures (0–1 cm) and air temperature (2 m) near the forest limit, Obergürl, Austria (2072 m), June 1954–July 1955 (Aulitsky, 1962, from Yoshino, 1975).
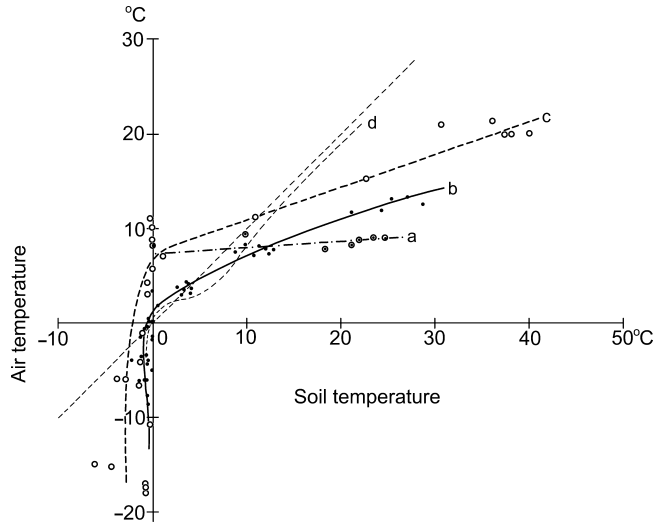
depth according to Bartlett *et al.* (2004). However, Sokratov and Barry (2002) find that the thermo-insulation effect of snow cover at Barrow, Alaska, is only present after the active layer is frozen (about mid-October) until the still-frozen soil begins to gain energy (late April) with the start of snow melt.

Differences in other vertical microclimatic gradients are apparent at high altitude. Summit winds generally maintain high average speeds in middle latitudes due to the vertical increase in wind velocity. Consequently, the accentuated vertical wind profile near the ground enhances the vertical fluxes of heat and moisture. This is significant in the Rocky Mountains, for example, in terms of strong advection of rather dry air causing high rates of evapotranspiration from alpine tundra surfaces in summer (LeDrew, 1975; Isard and Belding, 1986).

Small-scale topography and vegetation cover play a major role in modifying microclimates in mountains, especially near the timberline (Aulitsky, 1984, 1985).

Studies in the subalpine in Switzerland, for example, show that ridges and gullies with a relief of 5–12 m can modify the wind speed by ±60 percent when the direction is perpendicular to the ridges (Nägeli, 1971). More important is the formation of vertical eddies in the form of a rotor, in the lee of obstacles. Gloyne (1955) shows that these extend horizontally downwind 10–15 times the height of the obstacle. For a vegetation barrier of 50 percent density, the wind speed is reduced by 80 percent up to three to five times the height of the vegetation downwind. In association with the wind regime, therefore, trees and shrubs generate distinctive and recurrent patterns of snow accumulation in their lee. Drifts form in the lee of each tree cluster (or "island") and these protect the downwind limbs from winter desiccation, whereas exposed shoots in the crown or on the upwind side gradually go brown and die. The desiccation apparently causes evaporative stress at a time when moisture in the roots and stem, or in the soil, is frozen. Wardle (1974) considers that inadequate pre-winter hardening is also responsible. The desiccation

Fig. 2.39 A "flagged" Engelmann spruce tree in the alpine forest–tundra ecotone, Niwot Ridge, Colorado. Growth occurs only on the downward side of the stem (G. Kiladis).

stresses give rise to anatomical and morphological changes in the trees. The latter are evident in the deformation of the tree crown, which shows "flagging" with most of the growth on the lee side of the trunk (Figure 2.39). In extreme conditions within the upper Krummholz (crooked wood) zone, the tree assumes a prostrate cushion form (Yoshino, 1973; Wardle, 1974; Grace, 1977; Körner, 2003; Holtmeier, 2003).

Since the wind effect on trees is well established although not entirely understood, attempts have been made to use tree deformation as an index of local wind

conditions in areas of extreme data paucity. Thus, small-scale maps of wind direction have been constructed for an area in the Whiteface Mountains, New York, by Holroyd (1970) and in the Indian Peaks, Colorado, by Holtmeier (1978). Such maps can be used to infer local areas of wind convergence/divergence which may be important in siting buildings, power lines, ski-lifts and wind power installations, or in predicting pollutant dispersal. Wade and Hewson (1979) have tried to quantify the relationship between indices of tree deformation and wind speed. They developed regression equations for deformation with mean annual wind speed, although the duration of speeds above a threshold of the order of 3–5 m s^{-1} seems to be a more likely parameter of wind effects on the trees.

In terms of vegetation growth on mountains, ecologists interpret the dominant influence of altitude to be that of *exposure* (Ingram, 1958). This concept seems not to have been defined quantitatively although it obviously involves wind velocity and its effect on snow cover – both in the Cairngorms, where Ingram worked, and in the Colorado Rockies, where Wardle and Holtmeier worked. However, wind velocity also affects transpiration stress, which involves factors other than wind (Gale, 1972). Studies near the tree line in the Alps (Davos) show that relatively high wind speeds and early snow melt favor the survival of tree plantings (larch, spruce and pine) on ridges and warm slopes (Schönenberger, 1975). As in the Rocky Mountains, deep late-lying snow encourages snow-blight fungus. In contrast, vertical tree growth is favored by sunny, but wind-sheltered sites. Figure 2.40 schematically illustrates these results (Turner *et al.*, 1975). For plants in the alpine belts, Larcher (1980) considers that the climatic stresses imposed by low and strongly fluctuating temperatures have induced various adaptation processes to ensure cold resistance in both summer and winter conditions. At present, however, no definitive interpretation of "exposure" seems to be feasible.

The converse of exposure is "shelter." Ecologists have used the concept to examine conifer establishment and mortality at and above the tree line in the northern Rocky Mountains. Resler *et al.* (2005) found that 211 conifer patches in three locations in Glacier National Park, Montana, were associated with the shelter provided by large boulders and small terrace risers on slopes. Means to characterize shelter quantitatively in the case of snow accumulation in complex terrain have been suggested by Lapens and Martz (1992). They analyzed grid cells along vectors in each cardinal direction away from every grid cell in a given domain. They define two topographic variables – *fetch* and *directional relief*. Fetch is the horizontal distance to a terrain obstacle in a specified direction from a given location. For their study area in the Saskatchewan prairies, a location was considered sheltered for fetch > 0 m and < 60 m and exposed if the fetch exceeded 60 m. Directional relief is the elevation of a point above/below the average topography in a given direction. Positive (negative) directional relief indicates that a location is lower (higher) than the average elevation in a specified direction. The fetch identifies local relief features whereas directional relief characterizes the general relief in a given direction. Winstral *et al.* (1998) extend this approach and use high-resolution DEMs to
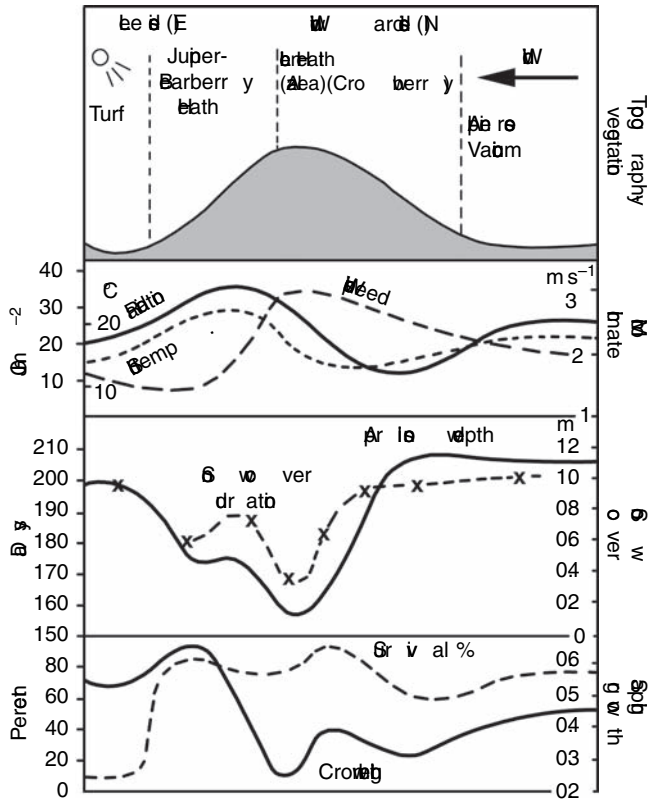
Fig. 2.40 Schematic relationships between terrain, microclimate, snow cover and tree growth at the tree line (2170 m) near Davos, Switzerland (after Turner *et al.*, 1975). The site is a 40–45° northeast-facing slope through an avalanche track and an adjacent spur. Climatic averages are for the growing season, global solar radiation (kcal cm^{-2}), on the slope under cloud-free conditions, surface soil temperature, 1 m wind speed, for 06–18 h, mean April snow depth and duration of snow cover. The bottom graph shows crown growth and percentage survival of 12-year old larch plantings in pots.

derive terrain parameters relevant for modeling alpine snow accumulation. The degree of exposure/shelter is determined from the maximum upwind slope angle. An analysis is performed for a sector bounded by azimuths of 60° on either side of the prevailing wind direction. Cells located along vectors every 5° are searched for the slopes at distances of 50, 100, 300, 500, 1000 and 2000 m from each target cell. This allows upwind breaks of slope that may cause flow separation to be quantified. The method was tested for a 2.25 km^2 area on Niwot Ridge, Colorado. Using the same index for the adjacent Green Lakes Valley watershed, Erickson *et al.* (2005) report a maximum slope of 64° and a minimum of −33°. Positive (negative) values denote increased (decreased) shelter and lower (higher) wind speeds.

2.4.4.2 Topoclimatic effects

Topoclimates are primarily manifestations of slope angle, aspect and horizon effects. These are relatively obvious in the case of radiation and temperature, but

second-order effects may come into play through the influence of terrain on wind velocity and in setting up slope and mountain valley winds.

The most obvious topoclimatic effects are those between: (1) north-facing slopes, on the one hand, and south-facing on the other; and (2) between valley bottoms and ridge tops. Other effects may also arise according to valley orientation with respect to the mountain range, and valley cross-profile. The primary control of conditions relating to slope orientation is solar radiation, whereas effects of airflow and air drainage are important supplementary factors for ridge top and valley bottom locations, especially for night-time and winter conditions.

An extensive series of observations on slope, aspect and elevation effects has been obtained for San Antonia Mountain, in northern New Mexico. It is an isolated conical mountain rising from 2740 to 3325 m. Hourly data have been collected at three elevations and the four cardinal directions for 3–5 years (McCutchan *et al.*, 1982). McCutchan and Fox (1986) show that the effect of aspect (acting to generate slope winds) exceeds that of elevation on wind velocity and, to a lesser degree, on temperature. Furthermore, wind speeds in excess of $5 \, \mathrm{m \, s^{-1}}$ eliminate any differences associated with slope, aspect or elevation.

Minimum temperatures at rural stations in Britain show that topographic influences operate at two scales. Tabony (1985) distinguishes the role of "local shelter" – the height above the valley bottom (represented by the drop in altitude within 3 km of the site), and "large-scale shelter" associated with cold air drainage (represented by the average height of the terrain above the valley over a 10 km radius). Tabony observes that nocturnal radiational cooling rapidly establishes a cooled layer that is deepest where there is significant local shelter. During the night, air drainage causes minima where the large-scale shelter is pronounced. The temperature drop is limited by the infrared back radiation from the atmosphere. The large-scale shelter is more important in the winter months. The effect of local shelter (height above valley) has a maximum effect on daily temperature range in autumn when there are large altitudinal differences in soil moisture deficit (Tabony, 1985).

Slope effects on radiation and ground temperature have been extensively analyzed by Grunow (1952) at Hohenpeissenberg, Bavaria. Figure 2.41 illustrates differences in direct and diffuse radiation receipts on NNW- and SSE-facing slopes of about 30°. Global totals differ most in winter when the solar altitude is low; the north-facing slope receives only 32 percent of that facing south, and almost all of the radiation on the former is diffuse. The associated differences in ground temperatures are shown in Figure 2.42 for daily means and means at 1400 h. The difference in ground temperatures (50–100 cm) shows minima in winter and summer and maxima in the transition seasons. In winter, the snow cover insulates the ground leading to almost no difference between the slopes. The slopes are snow-covered from November through March (April on the north slope) and the north slope also is generally more moist. At 1400 h, the effect of diurnal heating on the upper soil layer is apparent in summer.
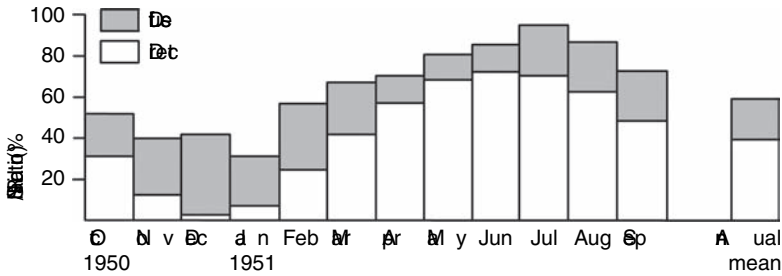
Fig. 2.41 Direct and diffuse solar radiation measured on 30° slopes facing north-northwest and south-southeast at Hohenpeissenberg, Bavaria (after Grunow, 1952). The radiation on the two slopes is expressed as N slope/S slope (percent) for each component.

Fig. 2.42 Differences in monthly mean ground temperatures, south slope minus north slope, May 1950–September 1951 at Hohenpeissenberg, Bavaria. Daily means (a) and means at 1400 h (b) (after Grunow, 1952).
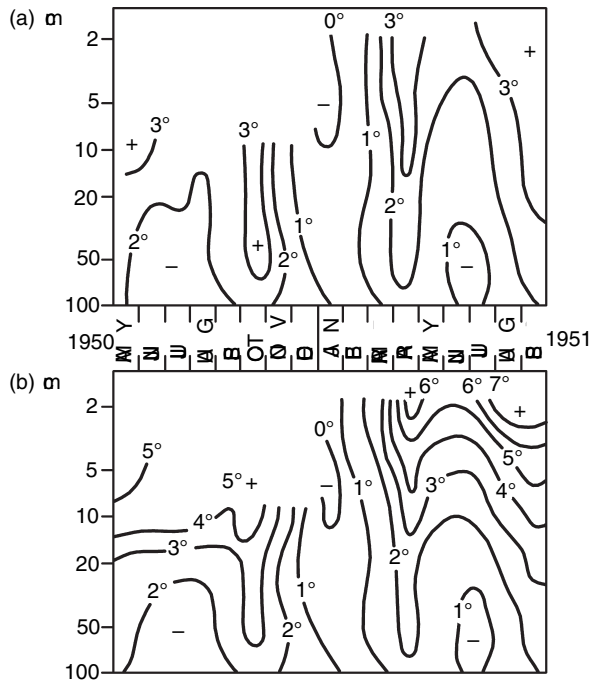
There are three general approaches to topoclimatic differentiation in mountainous terrain. One is by direct measurement of climatic elements at a network of stations; another is from field studies of the distribution of climatic effects, such as frost damage or wind shaping, on vegetation. The third method is based on calculation of radiative fluxes from topographic map analysis. However, observational data are often too sparsely distributed for mapping topoclimatic variability. Deng and Stull (2005) illustrate a method to distribute surface potential temperatures anisotropically in deep valleys between ridges and demonstrate its applicability to the coastal mountains of southwest British Columbia. The problem of mapping topoclimatic data is even greater for variables that are subject to sharp

local gradients or discontinuities (radiation, precipitation, wind velocity, etc.) and generally modeling with a high resolution digital elevation model (DEM) is becoming the preferred approach. Examples of this are noted at various points in the text.

Topoclimatic investigations have been performed in southeastern Alaska, the Polish Carpathians, the European Alps and the Southern Alps. Some general results from these studies are worthy of note. The characterization of topoclimates in Poland by Hess *et al.* (1975), based on temperature and relative humidity indices, relates to three broad terrain categories: (1) valleys, subdivided according to valley bottom, terraces, and valley sides; (2) slopes, including the "thermal belt" (p. 264), and lower ridges; and (3) ridges, summits and slopes in low–moderate sized mountains. Valleys typically have the greatest diurnal temperature range, and the greatest frequency of frosts and radiation fogs, while the slopes have the smallest temperature range and longest frost-free season. The upper zone has lower mean temperatures and small diurnal temperature variability. Within each category, microclimatic differences are identified according to small-scale terrain features and vegetation cover.

For the West Carpathians of Poland, Hess *et al.* (1976) relate various thermal parameters to mean annual temperature via regression equations; mean annual temperature itself is linearly related to elevation. Separate equations are developed for convex and concave landforms and for north/south slopes. The results show that extreme minima are considerably lower on concave slopes, for example. Similar sets of equations are also developed for parameters such as the duration of the frost-free season in relation to mean annual minimum temperatures. These are applicable only to sites above the level of valley inversions. Such equations have to be based on local data since the regression coefficients may vary widely in different regions. Consequently, this type of approach requires extensive measurements over a range of weather conditions.

The spatial coherence of some climatic elements is obviously less than others in heterogeneous terrain. For example, correlations of air temperature between stations in different topoclimatic settings within a small area in the Chitistone Pass (1774 m), southeast Alaska, are much weaker for daily minima than for maximum temperatures (Brazel, 1974). This is evidently due to the effects of glacier winds and cold air ponding on minimum readings at valley stations. Further studies in the same area (Brazel and Outcalt, 1973a) demonstrate that the surface thermal regime is primarily determined by slope angle, aspect, and horizon elevation angle. It is less sensitive to radiative properties of the surface (albedo and emissivity), except where snow or ice is present, and to thermal properties such as volumetric heat capacity, thermal diffusivity and depth to the freezing plane in the soil.

Topographic analysis, involving the calculation of potential radiation on uniform slope facets, was first carried out laboriously by a combination of field or map measurements of slope angle, orientation and horizon screening and field measurements or calculation of direct or global solar radiation for cloudless skies (Turner, 1966; Wendler and Ishikawa, 1974). The effect of valley orientation and slope angle

Table 2.18 Global solar radiation in valley location in Austria as a percentage of that on a horizontal surface for different cloud conditions.

		North–south valley			East–west valley		
Horizon angle		10°	20°	30°	10°	20°	30°
Summer							
Cloud	0	97	92	85	99	98	96
	5/10	98	93.5	88.5	99	97	93.5
	10/10	99	96	93	99	97	93
Winter							
Cloud	0	95	86	74	95	17	17
	5/10	96	88.5	80.5	96.5	47	46
	10/10	99	98	96	99	98	96

Source: from Sauberer and Dirmhirn (1958).

of the valley sides in Austria on global solar radiation is summarized in Table 2.18. The effects of altitude and slope orientation on radiation have been calculated by Borzenkova (1967) based on theoretical methods of Kondratyev and Manolova (1960) and observations of Aizenshtat (1962). Her results are shown in Table 2.19. For cloudless skies, north-facing slopes of 30° receive only 49 percent of the annual direct solar radiation falling on a horizontal surface at 3600 m compared with 57 percent at 400 m. The corresponding figures for 30° south-facing slopes are 122 percent of horizontal at 3600 m and 126 percent at 400 m. At lower elevations there is also a greater tendency for direct radiation to be reflected onto slopes from adjacent mountains than at higher elevations, although this factor is not calculated. With overcast conditions (low cloud), unit surface areas on all 30° slopes receive about 92 percent of the global solar radiation on a horizontal surface. Figure 2.33 illustrates the striking differences between 30° north-facing and south-facing slopes in winter months in middle latitudes (p. 88).

Dubayah (1994) incorporates the TOPORAD approach to construct a monthly solar radiation topoclimatology of the upper Rio Grande River Basin (37.7° N, 107° W) in the San Juan Mountains of Colorado for 1987–90, which takes account of snow cover. Use is made of hourly pyranometer observations taken 50 km away. The map products are at a resolution of 30 × 30 m. An important conclusion is that much of the spatial variability in solar radiation receipts occurs at distances of less than 300 m, and almost all at less than 1 km, due to the variations of slope and aspect in rugged terrain. In general, therefore, it is essential to use a modeling approach, with appropriate in situ data for purposes of calibration and validation. Locations within the 3420-km^2 watershed, ranging in elevation between 2432 and 4215 m, have an eightfold range in annual total solar radiation (36–265 W m^{-2}) about a watershed mean of 191 m^2. The variance for sub-regions of 36 and

Table 2.19 Calculated direct beam solar radiation and net radiation for horizontal and sloping surfaces in the Caucasus.

	Horizontal surface			30° N slope			30° S slope		
	Direct Solar	Net Radiation	R_n/S_b	Direct Solar	Net Radiation	R_n/S_b	Direct Solar	Net Radiation	R_n/S_b
Annual averages (kJ cm^{-2}year^{-1}) and ratios									
Cloudless sky									
400 m	683	347	0.51	389	108	0.28	857	490	0.57
3600 m	917	144	0.16	453	− 5	–	1125	288	0.26
Overcast									
400 m	142	79	0.56	132	79	0.60	132	79	0.60
3600 m	185	40	0.22	170	40	0.24	170	40	0.24
June averages (kJ cm^{-2} month^{-1}) and ratios									
Cloudless sky									
400 m	89	54	0.61	70	41	0.59	85	54	0.64
3600 m	116	42	0.36	85	28	0.33	107	68	0.64
Overcast									
400 m	18	11	0.61	16	11	0.69	16	11	0.69
3600 m	23	13	0.56	21	13	0.62	21	13	0.62

Source: after Borzenkova (1967); personal communication 1979.

100 km^2 is linearly related to the average slope, $\overline{S}$, in the sub-region (sin$^2 \overline{S}$) with almost 40 percent of the variance explained in each case (Dubayah and van Katwijk, 1992).

For net radiation (Table 2.19), the clear-sky values also show an important annual difference between north- and south-facing slopes, especially at lower elevations. At high elevations the difference is most marked in summer months. Aizenshtat (1962) measured net radiation at 3150 m on north and south slopes of the Kumbel Pass (near Shakhristan), on the northern slope of the Turkestan Mountains (40° N; 31–33° slopes). He found that on five clear days in September the daytime total on the south-facing slope (1784 mJ m^{-2}) was 3.4 times greater than on the north-facing one, while the 24-h total (1298 mJ m^{-2}) was respectively 7.5 times greater. (The albedo difference was small; 0.15 on the south-facing and 0.20 on the north-facing slope).

Recent work uses digital elevation models (DEMs) with surface radiation budget model and satellite imagery to obtain information on land surface cover types (Dubayah, 1994). For the Tekapo watershed in the Southern Alps, Oliphant *et al.* (2003) follow this approach to examine the spatial variability of the radiation budget components. They show that, in order of importance, variations in net radiation are sensitive to: slope aspect, slope angle, elevation, albedo, shading, sky view factor, and leaf area index. For a summer case (12 February 1999) spatial

Table 2.20 Latent heat fluxes (W m^{-2}) and Bowen ratio at three sites in Chitistone Pass, Alaska for 11 days in July–August.

Site	Hour	00	03	06	09	12	15	18	21	Daily value	Evaporation (mm)
				Latent heat flux (W m^{-2})							
Horizontal		10.5	7.0	−66.3	−181.4	−233.8	−177.2	−48.8	10.5	−126.9	4.4
SE Slope (34°)		34.9	34.9	−167.5	−361.5	−321.0	−101.2	34.9	34.9	−97.4	3.4
NW Slope (28°)		−20.9	−20.9	−20.9	−41.9	−80.2	−97.7	−80.2	−17.4	−45.5	1.6
Bowen ratio											
Horizontal		2.86	4.70	−0.01	0.33	0.39	0.42	−0.21	2.67		
SE Slope		0.80	0.86	0.35	0.36	0.39	0.48	0.48	0.70		
NW Slope		−0.60	−0.93	−1.10	−0.17	0.53	0.86	1.09	0.36		

Bowen ratio = sensible heat flux/latent heat flux. Both fluxes are positive towards the surface.
Negative values of Bowen ratio occur when the fluxes are of opposite sign.
Source: after Brazel and Outcalt (1973b).

variability is greatest in mid-morning (0815 h local time) and mid-afternoon (1515 h local time), and it is a function of optical depth.

Slope comparisons of turbulent heat fluxes are rare. In southeastern Alaska, data for 11 summer days at a valley floor site, a southeast-facing slope, and a northwest-facing slope show large differences in magnitude and phase of the latent heat flux (Table 2.20) (Brazel and Outcalt, 1973a and b). Daily totals of evaporation on the northeast-facing slope are only a third of those on the valley floor, but vegetation cover is a major determinant here. The valley floor and southeast slope were predominantly moss-lichen tundra, with willow on the slope, whereas the site on the northwest slope was fine scree and rubble.

The large contrasts in radiation on sunny and shaded slopes at the tree line in the Alps are apparent in mean soil temperature values to about 10 cm depth in January and 25 cm or more in July (Figure 2.43). But, in spite of the calculated radiation differences at high altitudes (Table 2.19), several studies show decreasing differences in soil temperatures between slopes of north and south aspect with altitude. This is true in the Colorado Front Range on 7–10° north- and south-facing slopes between 2200 and 3750 m, and in the Santa Catalina Mountains in Arizona between 2150 and 2750 m (Barry and Van Wie, 1974). In the Northwest Himalaya, Mani (1962: p. 7) notes that soil temperatures in summer are almost the same on north- and south-facing slopes above 4500 m. More comparisons of calculated and measured energy fluxes and of observed soil temperatures seem to be required to check these results.

Direct calculation and mapping of incident radiation is now possible from DEM data, as illustrated in Figure 2.36 (p. 93). Olyphant (1984, 1986) uses terrain data and radiance estimates to assess potential ablation on cirques glaciers in the Front Range,
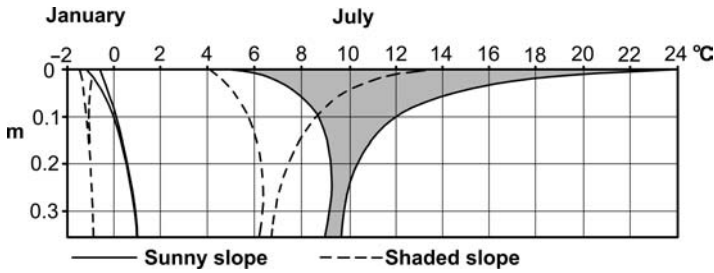
Fig. 2.43 Daily mean maximum and minimum soil temperatures to 35 cm depth on sunny and shaded slopes near the tree line, Davos (2170 m) in January and July 1968–70 (after Turner *et al.*, 1975).

Colorado. He finds that the rock walls enhance net radiation by reducing net long-wave loss compared with a level surface. Diurnal solar radiation receipts are very asymmetric as a result of summer afternoon cloudiness. Thus east-facing basins receive large totals before the typical cloud build up. The computer model of Dozier and Outcalt (1979) is available to simulate energy balance components over mountainous topographic surfaces. Incoming solar and infrared radiation are calculated for every point, taking account of slope, exposure and horizon data. Values of air temperature, humidity and wind speed must be specified over the grid and these are used to determine vertical profiles for the calculation of heat fluxes. Roughness length, albedo and soil thermal properties are also specified. Surface temperature, soil heat flow, sensible and latent heat fluxes, and net radiation are simulated and can be mapped for specific times of day. The underlying basis of the model is the equilibrium temperature theory, which states that a unique surface temperature satisfies the energy flux equations for a given set of boundary conditions. At present the model is applicable only to cloudless sky conditions and has numerous limitations, but it represents a significantly new approach to studies of topoclimate.

2.5   NOTES

(1)   These data need reducing by 2 percent to correct them to the 1956 International Pyrheliometric Scale. Values from early European measurements should likewise be increased by 1.5 percent.

(2)   Wilson (1968) illustrates the derivation of this relationship, neglecting frictional effects:

$$\frac{dw}{dt} = -S(z_1 - z_0)$$

where w is the vertical motion, $(z_1 - z_0)$ is the vertical displacement from the base level. By integration,

$$\Delta\frac{w^2}{2} = \frac{S(z_1 - z_0)^2}{2}$$

If the kinetic energy of the upwind flow ($= U^2/2$) is the source for $\Delta(w^2/2)$, then $(z_1 - z_0) = U/\sqrt{S}$.

(3)   The Richardson number,

$$Ri = \frac{g(\partial\theta/\partial z)}{\theta(\partial U/\partial z)^2}$$

is a dimensionless ratio relating the suppression of turbulence by buoyancy to its generation by shear.

(4)   Froude number (F) is the non-dimensional ratio of the inertial force to the gravitational force for a fluid flow: $F = V^2/Lg$, where $V =$ a characteristic velocity, $L =$ a characteristic length, $g =$ gravitational acceleration (Glickman, 2000). F may also be expressed as the square root of this expression. For airflow over a barrier, a useful form is $F = V/NL$ where $V =$ wind speed component normal to the barrier, $N =$ the Brunt–Väisälä frequency of the upstream flow and $L =$ width of the barrier. This represents the natural wavelength of the airflow to the wavelength of the terrain. In another form of this expression, L is replaced by $(z_1 - z_M)$ where $z_1 =$ depth of the mixed layer and $z_M =$ height of the barrier.

The definition and use of the Froude number (F) is discussed in detail by Baines (1995). He notes that, for flow past an obstacle, typically F is expressed as $U/(gl)^{0.5}$, where $U =$ fluid speed, $g =$ gravity, $l =$ a length (the horizontal length, L, or vertical height, h, of an obstacle). For continuously stratified fluids, the following quantities have been variously designated as "Froude numbers": U/NL, U/ND and U/Nh, where $D =$ fluid depth. The first two relate to wave drag and wave propagation, respectively, but Baines points out that U/Nh involves non-linear factors such as wave steepness and blocking of the lower level flow. He defines the Froude number for unsheared, uniformly stratified flow as $F = U/(Nh/\pi)$; the flow is subcritical for $F < 1$, critical for $F = 1$, and supercritical for $F > 1$ (Baines, 1995, p. 16).

(5)   Typical values of the flow parameters cited by Carruthers and Hunt (1990) are as follows:

Neutral flow $F_L \gg 1$; $F_h \gg 1$.
e.g. $N = 0.005 \, \text{s}^{-1}$, $H = 20 \, \text{m}$, $L = 100 \, \text{m}$.
Moderately stable stratification $F_L \leq 1$, $F_h > 1$.
e.g. $N = 0.01 \, \text{s}^{-1}$, $H = 200 \, \text{m}$, $L = 1000 \, \text{m}$, and $U_0 = 5 \, \text{m s}^{-1}$.
Strongly stable stratification $F_L \leq 1$, $\Delta u \sim U_0$.
e.g. $N = 0.04 \, \text{s}^{-1}$, $H = 200 \, \text{m}$, $U_0 = 5 \, \text{m s}^{-1}$.

(6)   In these papers, and some other sources, normalized wind speeds, expressed as $(1 + \Delta S)$, or $(\Delta U + U)/U$, are reported.

(7)   "Reynolds averaging" refers to averaging of variables such as wind speed or fluxes in a turbulent flow. It involves a decomposition into a mean (over time

or space) and an instantaneous, or local, deviation. The average of the deviations equals zero. The instantaneous, or local value is the difference between the mean and the deviation.

BIBLIOGRAPHY

Abbott, C. G. and Fowle, F. E., Jr. (1911) The value of the solar constant of radiation. *Astrophys. J.*, **33**, 191–6.

Abetti, G. (1957) *The Sun* (transl. J. B. Sidgwick). London: Macmillan.

Aizenshtat, B. A. (1962) Nekotorie cherti radiatsionnogo rezhima teplogo balansa i mikroklimata gornogo perrevala (Some characteristics of the heat balance regime and microclimate of a mountain pass). *Met. i Gidrol.*, **3**, 27–32.

Allison, I. and Bennett, J. (1976) Climate and microclimate: In G. S. Hope, *et al.* (eds), *The Equatorial Glaciers of New Guinea*. Rotterdam: A. A. Balkema, pp. 61–80.

Ångstrøm, A. K. and Drummond, A. J. (1966) Note on solar radiation in mountainous regions at high altitude. *Tellus*, **18**, 801–5.

Ångstrøm, K. (1900) Intensité de la radiation à differentes altitudes. Recherches faites à Tenériffe. 1895 et 1896, *Nova Acta Reg. Soc. Sci. Upsal.*, **20**(3).

Aulitsky, H. (1962) Die Bodentemperaturverhältnisse einer zentralalpinen Hochgebirgs-Hangstation II *Archiv. Met. Geophys. Biokl.*, B, **11**, 301–62.

Aulitsky, H. (1984) Die Windverhältnisse an einer zentralalpinen Hangstation und ihre ökologische Bedeutung. 1 Teil, *Cbl. ges. Forstw.*, **101**, 193–232.

Aulitsky, H. (1985) Die Windverhältnisse an einer zentralalpineu Hangstation und ihre ökologische Bedeutung. 2 Teil, *Cbl. ges. Forst.*, **102**, 55–72.

Aulitsky, H., Turner, H. and Mayer, H. (1982) Bioklimatische Grundlagen einer standorts-gemässen Bewirtschaftung des subalpinen Lärchen-Arvenwaldes, *Eidg. Anst. forstl. Versuchswes., Mitt.*, **58**(4), 325–580.

Bailey, S. I. (1908) Peruvian meteorology: observations made at the auxiliary stations. 1892–1895. *Ann. Astron. Obs. Harvard Coll.*, **49**(2), 104–232.

Baines, P. G. (1995) *Topographic Effects in Stratified Flow*. Cambridge: Cambridge University Press, 482 pp.

Barry, R. G. (1972) *Climatic Environment of the East Slope of the Colorado Front Range*, Occasional, Paper No. 3, Institute of Arctic and Alpine Research. Boulder, CO: University of Colorado, 206 pp.

Barry, R. G. (1973) A climatological transect on the east slope of the Front Range, Colorado. *Arct. Alp. Res.*, **5**, 89–110.

Barry, R. G. (1978a) Diurnal effects on topoclimate on an equatorial mountain. *Arbeiten. Zentralanst. Met. Geodynam.*, **32**, 72, 1–8.

Barry, R. G. (1978b) H.-B. de Saussure: the first mountain meteorologist. *Bull. Am. Met. Soc.*, **59**, 702–5.

Barry, R. G. and Chorley, R. J. (2003) *Atmosphere, Weather and Climate*, 8th edn, London: Methuen, p. 48.

Barry, R. G. and Van Wie, C. C. (1974) Topo- and microclimatology in alpine areas. In J. D. Ives and R. G. Barry (eds), *Arctic and Alpine Environments*. London: Methuen, pp. 73–83.

Bartlett, M. G., Chapman, D. S. and Harris, R. N. (2004) Snow and the ground temperature record of climate change. *J. Geophys. Res.*, **109** (4), F04008, 14.

Becker, C. F. and Boyd, J. S. (1957) Solar variability on surfaces in the United States as affected by season, orientation, latitude, altitude and cloudiness. *J. Solar Energy*, **1**, 13–21.

Bener, P. (1963) Der Einfluss der Bewölkung auf die Himmelstrahlung. *Arch. Met. Geophys. Biokl.*, B, **12**, 442–57.

Bergeron, T. (1960) Preliminary results of Project Pluvius. Helsinki: International Association for Science of Hydrology Publication No. 53, pp. 226–37.

Berk, L. S., *et al.* (1998) MODTRAN cloud and multiple scattering upgrades with application to AVIRIS. *Remote Sens. Environ.*, **65**, 367–375.

Bishop, B. C., *et al.* (1966) Solar radiation measurements in the high Himalayas (Everest region). *J. appl. Met.*, **5**, 94–104.

Blumthaler, M., Ambach, W. and Rehwald, W. (1992) Solar UV-A and UV-B radiative fluxes at two Alpine stations at different altitudes. *Theor. Appl. Climatol.*, **46**, 39–44.

Blumthaler, M., Ambach, W. and Huber, M. (1993) Altitude effects of solar UV radiation dependent on albedo, turbidity and solar elevation. *Met. Zeit.*, **NF 2**, 116–20.

Borisov, A. M., Grudzinski, M. E. and Khrgian, A. Kh. (1958) O meteorologicheskikh usloviakh vysokogornogo Tian-Shanya (Meteorological conditions of the high Tien-Shan). *Trudy Tsentr. Aerol. Obs.*, **21**, 175–99.

Borzenkova, I. (1967) K voprosy o vliyanii mestnykh faktorov na prikhod radiatsii v gornoi mestnosti (Concerning the influence of local factors on the course of radiation in mountain locations). *Trudy Glav. Geofiz. Obs.*, **209**, 70–7.

Bradley, E. F. (1980) An experimental story of the profiles of wind speed, shearing stress and turbulence at the crest of a large hill. *Q. J. R. Met. Soc.*, **106**, 101–24.

Brazel, A. (1974) A note on topoclimatic variation of air temperature, Chitistone Pass region. Alaska. In *Icefield Ranges Research Project, Scientific Results*. New York: American Geographical Society, Vol. 4, pp. 81–7.

Brazel, A. and Outcalt, S. I. (1973a) The observation and simulation of diurnal surface thermal contrast in an Alaskan alpine pass. *Arch. Met. Geophys. Biokl., B*, **21**, 157–74.

Brazel, A. and Outcalt, S. I. (1973b) The observation and simulation of diurnal evaporation contrasts in an Alaskan alpine pass. *J. appl. Met.*, **12**, 1134–43.

Brocks, K. (1940) Lokale Unterschiede und zeitliche Änderungen der Dichteschichtung in der Gebirgsatmosphare. *Met. Zeit.*, **57**, 62–73.

Bruegge, C. J., *et al.* (1992) Aerosol optical depth retrievals over the Konza Prairie. *J. Geophys. Res.*, **97**, 18 743–58.

Brunt, D. (1932) Notes on radiation in the atmosphere. *Q. J. R. Met. Soc.*, **58**, 389–420.

Budyko, M. I. (1974) *Climate and Life*. New York: Academic Press, pp. 189–92.

Calbo, J., Pages, D. and González, J.-A. (2005) Empirical studies of cloud effects on UV radiation. *Rev. Geophys.*, **43**(2), RG 2002, 28 pp.

Caldwell, M. M. (1968) Solar ultraviolet radiation as an ecological factor for alpine plants. *Ecol. Monogr.*, **38**, 243–68.

Caldwell, M. M. (1980) Light quality with special reference to UV at high altitudes. In U. Benecke and M. R. Davis (eds), *Mountain Environments and Subalpine Tree Growth*. Wellington: Technical Paper No. 70, Forest Research Institute, New Zealand Forest Service, pp. 61–79.

Carroll, T., *et al.* (2001) NOHRSC operations and the simulation of snow cover properties for the coterminous U. S. In *Proc., 69ᵗʰ Annual Meeting, Western Snow Conference*, Sun Valley, Idaho: NOAA/NWS, pp. 1–10.

Carruthers, D. J. and Choularton, T. W. (1982) Airflow over hills of moderate slope. *Q. J. R. Met. Soc.*, **108**, 603–24.

Carruthers, D. J. and Hunt, J. C. R. (1990) Fluid mechanisms of airflow over hills: Turbulence, fluxes, and waves in the boundary layer. In W. Blumen (ed.), *Atmospheric Processes over Complex Terrain*, Met. Monogr. 23(45), Boston, MA: American Meteorological Society, pp. 83–103.

Chelton, D. B., Freilich, M. H. and Esbensen, S. K. (2000) Satellite observations of the wind jets off the Pacific Coast of Central America. Part I, Case studies and statistical characteristics. Part II. Regional relationships and dynamical considerations. *Mon. Wea. Rev.*, **1993–2017**, 2019–43.

Chen, L., Reiter, E. R. and Feng, Z. (1985) The atmospheric heat source over the Tibetan Plateau; May–August 1979. *Mon. Wea. Rev*, **113**, 1771–90.

Cline, D., Bales, R. and Dozier, J. (1998) Estimating the spatial distribution of snow in mountain basins using remote sensing and energy balance modeling. *Water Resour. Res.*, **34**(5), 1275–85.

COESA (1962) US Standard Atmosphere, 1962. US Comm., Extension Standard Atmosphere, Washington DC: COESA.

Conrad, V. (1944) *Methods of Climatology*. Cambridge, MA: Harvard University Press.

Corripio, J. (2003) Vectorial algebra algorithms for calculating terrain parameters from DEMs and solar radiation modeling in mountainous terrain. *Int. J. Geogr. Inf. Sci.*, **17**, 1–23.

Cramer, O. P. (1972) Potential temperature analysis for mountainous terrain. *J. appl. Met.*, **11**, 44–50.

Cramer, O. P. and Lynott, R. E. (1961) Cross-section analysis in the study of windflow over mountainous terrain. *Bull. Am. Met. Soc.*, **42**, 693–702.

Crook, N. A. and Tucker, D. F. (2005) Flow over heated terrain. Part I: Linear theory and idealized numerical simulations. *Mon. Wea. Rev.*, **133**(9), 2442–64.

Davidson, B., *et al.* (1964) *Sites for Wind-power Installations*. W. M.O. Tech. Note 63. Geneva: World Meteorological Organization.

Davies, H. C. and Phillips, P. D. (1985) Mountain drag along the Gotthard section during ALPEX. *J. Atmos. Sci.,* **42**, 2093–109.

Deng, X. and Stull, R. (2005) A mesoscale analysis method for surface potential temperature in mountainous and coastal terrain. *Mon. Wea. Rev.*, **133**, 389–408.

de Quervain, A. (1904) Die Hebung der atmosphärischen Isothermen in der Schweizer Alpen und ihre Beziehung zu deren Höhengrenzen. *Gerlands Beitr. Geophys.*, **6**, 481–533.

Ding, L., Calhoun, R. J. and Street, R. L. (2003) Numerical simulation of strongly stratified flow over a three dimensional hill. *Boundary-Layer Met.*, **107**, 81–114.

Dirmhirn, I. (1951) Untersuchungen der Himmelstrahlung in den Ostalpen mit besonder Berücksichtigung ihrer Höhenabhängigkeit. *Arch. Met. Geophys. Biokl.* **B, 2**, 301–46.

Dorman, C. E., Beardsley, R. C. and Limeburner, R. (1995) Winds in the Strait of Gibraltar. *Q. J. R. Met. Soc.*, **121**, 1903–21.

Dorno, C. (1911) *Studie über Licht und Luft des Hochgebirges*. Braunschweig: Vieweg und Sohn.

Dozier, J. (1980) A clear-sky spectral solar radiation model for snow-covered mountainous terrain. *Water Resour. Res.* **16**, 709–18.

Dozier, J. and Frew, J. (1990) Rapid calculation of terrain parameters for radiation modeling from digital elevation data. *IEEE Trans. Geosc. Rem. Sensing*, **28**(5), 963–69.

Dozier, J. and Outcalt, S. I. (1979) An approach toward energy balance simulation over rugged terrain. *Geog. Anal.*, **11**, 65–85.

Drummond, A. J. and Ångstrøm, A. K. (1967) Solar radiation measurements on Mauna Loa (Hawaii) and their bearing on atmospheric transmission. *Solar Energy*, **11**, 133–44.

Dubayah, R. (1994) Modeling a solar radiation topoclimatology for the Rio Grande River Basin. *J. Vegetation Sci.*, **5**, 627–40.

Dubayah, R. and Van Katwijk, V. (1992) The topographic distribution of annual incoming solar radiation in the Rio Grande basin. *Geophys. Res. Lett.*, **19**, 2231–34.

Duguay, C. R. (1993) Radiation modeling in mountainous terrain: Review and status. *Mountain Res. Devel.*, **13**, 339–57.

Eckel, O. (1936) Uber einige Eigenschaften der ultravioletten Himmelstrahlung in verschiedenen Meereshöhen und bei Föhnlage. *Met. Zeit.*, **53**, 90–4.

Eide, O. (1948) On the temperature difference between mountain peak and free atmosphere at the same level. II. Gaustatoppen-Kjeller. *Met. Annal.*, **2**(3), 183–206.

Ekhart, E. (1939a) Mittlere Temperaturverhältnisse der Alpen und der freien Atmosphäre über dem Alpenvorland. Ein Beitrag zur dreidimensionalen Klimatologie. 1. Die Temperaturverhältnisse der Alpen. *Met. Zeit.*, **56**, 12–26.

Ekhart, E. (1939b) Temperaturverhältnisse der freien Atmosphare über München und Vergleich mit den Alpen. *Met. Zeit.*, **56**, 49–57.

Elterman, L. (1964) Atmospheric attenuation model, 1964, in the ultraviolet, visible and infrared regions for altitudes to 50 km. Environment Research Paper No. 46, AFCRL-64-740. Cambridge, MA: US Air Force Cambridge Research Laboratories.

Erickson, T. A., Williams, M. W. and Winstral, A. (2005) Persistence of topographic controls on the spatial distribution of snow in rugged terrain, Colorado, United States. *Water Resour. Res.*, **41**, W04014, 17 pp.

Essery, R. (2004) Statistical representation of mountain shading. *Hydrol. Earth Syst. Sci.*, **8**, 1045–50

Etling, D. (1989) On atmospheric vortex streets in the wake of large islands. *Met. Atmos. Phys.*, **41**, 157–64.

Eustis, R. S. (1942) The winds over New England in relation to topography. *Bull. Am. Met. Soc.*, **28**, 383–7.

Ferguson, S. P. (1934) Aerological studies on Mt. Washington. *Trans. Am. Geophys. Union*, **15**, 114–17.

Ficker, H. von (1913a) Die Wirkung der Berge auf Luftströmungen. *Met. Zeit.*, **30**, 608–10.

Ficker, H. von (1913b) Temperaturdifferenz zwischen freier Atmosphäre und Berggipfeln. *Met. Zeit.*, **30**, 278–304.

Ficker, H. von (1926) Vertikale Temperaturgradienten im Gebirge. *Veroff. Preuss. Met. Inst.*, **335**, 45–62.

Flach, E. (1966) Geographische Verteilung der Globalstrahlung und Himmelstrahlung. *Arch. Met. Geophys. Biokl.*, **B 14**, 161–83.

Fliri, F. (1971) Neue klimatologische Querprofile der Alpen-ein Energiehaushalt. *Ann. Met.*, **N. F. 5**, 93–7.

Flohn, H. (1953) Hochgebirge und allgemeine Zirkulation. ll. Die Gebirge als Wärmequellen. *Arch. Met. Geophys. Biokl.*, **A, 5**, 265–79.

Flohn, H. (1968) Contributions to a meteorology of the Tibetan Highlands. Atmos. Sci. Paper No. 130. Ft. Collins, CO: Colorado State University.

Flohn, H. (1974) Contribution to a comparative meteorology of mountain areas. In J. D. Ives and R. G. Barry (eds), *Arctic and Alpine Environments*. London: Methuen, pp. 55–71.

Frère, M., Rijks, J. Q. and Rea, J. (1975) *Estudios Agroclimatologico de la Zona Andina*, Informe Technico. Rome: Food and Agricultural Organization of the United Nations.

Fujimara, I. (1971) The climate and weather of Mt. Fuji. *Fujisan-sogogakujutsuchosa-hokoku (Mt. Fuji, Scientific Report)*. Tokyo: Fujikyuko Co. Ltd, pp. 215–304.

Gale, J. (1972) Elevation and transpiration: some theoretical considerations with special reference to Mediterranean-type climate. *J. Appl. Ecol.*, **9**, 691–702.

Gallagher, M. W., Choularton, T. W. and Hill, M. K. (1988) Some observations of airflow over a large hill of moderate slope, *Boundary-Layer Met.*, **42**, 22–50.

Gams, H. (1931) Die klimatische Begrenzung von Pflanzenarealen und die Verteilung der hygrischen Kontinentalität in den Alpen. I. Teil, *Zeitschr. Ges. f. Erdkunde, Berlin*, Nr. 9/10, 321–46.

Gao, Y.-X. and Li, C. (1981) Influences of Qinghai-Xizang Plateau on seasonal variation of atmospheric general circulation. In *Geoecological and Ecological Studies of Qinghai-Xizang Plateau*. Beijing: Science Press, Vol. 2, pp. 1477–84.

Garnier, B. J. and Ohmura, A. (1968) A method of calculating the direct short wave radiation income of slopes. *J. Appl. Met.*, **7**, 796–800.

Garnier, B. J. and Ohmura, A. (1970) The evaluation of surface variations in solar radiation income. *Solar Energy*, **13**, 21–34.

Gates, D. M. and Janke, R. (1966) The energy environment of the alpine tundra. *Oecol. Planta*, **1**, 39–62.

Geerts, B. (2002) Empirical estimation of the annual range of monthly-mean temperature. *Theor. Appl. Climatol.*, **73**, 107–32.

Geiger, R., Aron, R. H. and Todhunter, P. (2003) *The Climate near the Ground*. 6th edn. Lanham, MA: Rowman and Littlefield, 584 pp.

Georgii, W. (1922) Die Windbeeinflussung durch Gebirge. *Beitr. Phys. frei Atmos.*, **10**, 178–84.

Georgii, W. (1923) Die Luftströmung über Gebirge. *Met. Zeit.*, **40**, 108–12, 309–11.

Giles, B. D. (1976) Fluidics, the Coanda effect and some orographic winds. *Arch. Met. Geophys. Biokl.*, **A, 25**, 273–80.

Glassy, J. M. and Running, S. W. (1994) Validating diurnal climatology logic of the MT-CLIM model across a climatic gradient in Oregon. *Ecol. Applications*, **4**, 248–57.

Glickman, T. S. (ed.) (2000) *Glossary of Meteorology*. Boston, MA: American Meteorological Society, 855 pp.

Gloyne, R. W. (1955) Some effects of shelter-belts and windbreaks. *Met. Mag.*, **84**, 272–81.

Gloyne, R. W. (1971) A note on the average annual mean of daily earth temperature in the United Kingdom. *Met. Mag.*, **100**, 1–6.

Grace, J. (1977) *Plant Response to Wind*. London: Academic Press.

Grant, A. N., Pszenny, A. A. P. and Fischer, E. V. (2005) The 1935–2003 air temperature record from the summit of Mount Washington, New Hampshire. *J. Climate*, **18**(21):4, 445–53.

Green, F. H. W. and Harding, R. J. (1979) The effect of altitude on soil temperature. *Met. Mag.*, **108**, 81–91.

Green, F. H. W. and Harding, R. J. (1980) Altitudinal gradients of soil temperatures in Europe. *Trans. Inst. Brit. Geog.*, **5**, 243–54.

Green, J. S. A. (1984) Describing the Alps, *Riv. Met. Aeronaut.*, **44**, 23–30.

Greenstein, L. A. (1983) An investigation of midlatitude alpine permafrost on Niwot Ridge, Colorado Rocky Mountains, USA. In T. L. Pewe and J. Brown, (eds), *Permafrost; Fourth International Conference Proceedings*. Washington, DC: National Academy Press, pp. 380–3.

Groner, J., *et al.* (2000) Variability of spectral solar ultraviolet radiation in an Alpine environment. *J. Geophys, Res.*, **105(D22)**, 26 991–27 003.

Grunow, J. (1952) Beiträge zum Hangklima, *Berichte dt. Wetterdienstes in der US-Zone*, **8**(35), 293–8.

Gutman, G. J. and Schwerdtfeger, W. (1965) The role of latent and sensible heat for the development of a high pressure system over the subtropical Andes in the summer. *Met. Rdsch.*, **18**, 69–75.

Hand, I. F., Conover, J. H. and Boland, W. A. (1943) Simultaneous pyrheliometric measurements at different heights on Mount Washington, N. H. *Mon. Weather Rev.*, **71**, 65–9.

Hann, J. von (1906) *Lehrbuch der Meteorologie*. Leipzig: C. H. Tauchinitz.

Hann, J. von (1913) Die Berge kälter als die Atmosphäre, ein meteorologisches Paradoxon. *Met. Zeit.*, **30**, 304–6.

Hänsel, C. von (1962) Die Unterschiede von Temperatur und relativer Feuchtigkeit zwischen Brocken und umgebender freier Atmosphäre. *Zeit. Met.*, **16**, 248–52.

Harding, R. J. (1978) The variation of the altitudinal gradient of temperature within the British Isles. *Geogr. Ann.*, **A 60**, 43–9.

Harding, R. J. (1979) Altitudinal gradients of temperature in the northern Pennines. *Weather*, **34**, 190–201.

Harrison, S. J. (1975) The elevation component of soil temperature variation. *Weather*, **30**, 397–409.

Hastenrath, S. L. (1968) Der regionale und jahrzeitliche Wandel des vertikalen Temperaturgradienten und seine Behandlung als Wärmhaushaltsproblem. *Met. Rdsch.*, **21**, 46–51.

Hastenrath, S. (1997) Measurements of solar radiation and estimation of optical depth in the high Andes of Peru. *Met. Atmos. Phys.*, **64**, 51–9.

Hauer, H. (1950) Klima und Wetter der Zugspitze. *Berichte d. Deutschen Wetterdienstes in der US-Zone*, **16**.

Hay, J. E. (1977) An analysis of solar radiation data for selected locations in Canada. *Climate Studies*, 32. Downsview, Ontario: Atmos. Env. Service.

Hay, J. E. (1979) *Study of shortwave radiation on non-horizontal surfaces*. Downsview, Ontario: Canada Climate Centre, Atmos. Env. Serv. Rep. no. 79–12.

Hay, J. E. (1983) Solar energy system design: the impact of mesoscale variations in solar radiation. *Atmos.-Ocean*, **21**, 138–57.

Hay, J. E. and McKay, D. C. (1985) Estimating solar irradiance on inclined surfaces: A review and assessment of methodologies. *Int. J. Solar Energy*, **3**, 203–40.

Hedberg, O. (1964) Features of afroalpine plant ecology. *Acta phytogeographica suecica*, **49**.

Hess, M. (1968) A method of distinguishing and specifying vertical temperature zones in temperate zone mountains. *Geogr. Polonica*, **14**: 133–40.

Hess, M., Niedzwiedz, T. and Obrebska-Starkel, B. (1975) The methods of constructing climatic maps of various scales for mountains and upland territories exemplified by the maps prepared for southern Poland. *Geogr. Polonica*, **31**, 163–87.

Hess, M., Niedzweidz, T. and Obrebska-Starkel, B. (1976) The method of characterizing the climate of the mountains and uplands in the macro-, meso- and microscale (exemplified by Southern Poland). *Zesz. Nauk. Univ. Jagiellon., Prace Geog.*, **43**, 83–102.

Heywood, H. (1964) Solar radiation on inclined surfaces. *Nature*, **204** (4959), 669–70.

Hnatiuk, R. J., Smith, J. M.B. and McVean, D. N. (1976) *Mt. Wilhelm studies. II. The Climate of Mt. Wilhelm*. Canberra: Australian National University, Biogeography Studies 4.

Holroyd, E. W., III (1970) Prevailing winds on Whiteface Mountain as indicated by flag trees. *For. Sci.*, **16**, 222–9.

Holtmeier, F. K. (1978) Die bodennahen Winde in den Hochlagen der Indian Peaks Section (Colorado Front Range). *Münster Geogr. Arbeit.*, **3**, 3–47.

Holtmeier, F. K. (2003) *Mountain Timberlines: Ecology, Patchiness, and Dynamics*. Kluwer: Dordrecht, 369 pp.

Hunt, J. R. (1980) Winds over hills. In J. C. Wyngaard (ed.), *Workshop on the Planetary Boundary Layer*. Boston, MA: American Meteorological Society, pp. 107–44.

Hunt, J. C. R. and Richards, K. J. (1984) Stratified airflow over one or two hills. *Boundary-Layer Met.*, **30**, 223–59.

Hunt, J. C. R. and Simpson, J. E. (1982) Atmospheric boundary layers over non-homogeneous terrain. In E. J. Plate (ed.), *Engineering Meteorology*. Amsterdam: Elsevier, pp. 269–318

Hunt, J. C. R. and Snyder, W. H. (1980) Experiments on stably and neutrally stratified flow over a model three-dimensional hill. *J. Fluid Mech.*, **96**, 671–704.

Hunt, J. C. R., Richards, K. J. and Brighton, P. W. M. (1988) Stably stratified flow over low hills. *Q. J. R. Met. Soc.*, **114**, 859–86.

Ingram, M. (1958) The ecology of the Cairngorms. IV. The Juncus zone: Juncus trifidis communities. *J. Ecol.*, **46**, 707–37.

Isard, S. A. (1986) Evaluation of models for predicting insolation on slopes within the Colorado alpine tundra. *Solar Energy*, **36**, 559–64.

Isard, S. A. and Belding, M. J. (1986) Evapotranspiration from the alpine tundra of Colorado. USA. *Arct. Alp. Res.*, **21**, 71–82.

Ives, J. D. and Fahey, B. D. (1971) Permafrost occurrence in the Front Range, Colorado Rocky Mountains, USA. *J. Glaciol.*, **10**, 105–111.

Iziomon, M. G., *et al.* (2001) Radiation balance over low-lying and mountainous areas in south-west Germany. *Theoret. Appl. Climatol.*, **68**, 219–31.

Jackson, P. S. and Hunt, J. C. R. (1975) Turbulent wind flow over a low hill. *Q. J. R. Met. Soc.*, **101**, 929–55.

Janke, J. R. (2005) The occurrence of alpine permafrost in the Front Range of Colorado. *Geomorphology*, **67**, 375–89.

Kastrov, V. G. (1956) Solnechnaia radiatsiia v troposfere v sluchae absoliutno chistnogo i sukhogo vozdukha. *Trudy Tsentr. Aerol. Obs.*, **16**, 23–30.

Khrgian, A. Kh. (1965) Atmospheric moisture distribution over mountain country. *Atmos. Ocean. Phys. Izvestiya Acad. Sci. USSR*, **1**(4), 233–6.

Kimball, H. H. (1927) Measurements of solar radiation intensity and determinations of its depletion by the atmosphere with bibliography of pyrheliometric measurements. *Mon. Weather Rev.*, **55**, 155–69.

Kimura, F. and Manins, P. (1988) Blocking in periodic valleys. *Boundary-Layer Met.*, **44**, 137–69.

Klein, W. H. (1948) Calculation of solar radiation and the solar heat load on man. *J. Met.*, **5**, 119–29.

Kleinschmidt, E. (1913) Die Temperaturverhältnisse in der freien Atmosphäre und auf Berggipfeln nach den Massungen der Drachenstation am Bodensee und der Observatorien auf der Säntis und der Zugspitze. *Beitr. Phys. frei. Atmos.*, **6**, 1–18.

Kondratyev, K. Ya. (1969) *Radiation in the Atmosphere*. New York: Academic Press.

Kleissl, J., Honrath, R. E. and Henriques, D. V. (2006) Analysis and application of Sheppard's airflow model to predict mechanical orographic uplifting and the occurrence of mountain clouds. *J. Appl. Met. Climatol.*, **45**, 1376– 87.

Kondratyev, K. Ya. (1969) *Radiation in the Atmosphere*. New York: Academic Press, pp. 485–502.

Kondratyev, K. Ya. and Federova, M. P. (1977) Radiation regime of inclined slopes. Geneva: World Meteorological Organization, W. M.O. Tech. Note no. 152.

Kondratyev, K. Ya. and Manolova, M. P. (1960) The radiation balance of slopes. *Solar Energy*, **4**, 14–19.

Körner, C. (2003) *Alpine Plant Life: Functional Plant Ecology of High Mountain Ecosystems*, 2nd edn. Berlin: Springer, 344 pp.

Kreuels, R., Fraedrich, K. and Ruprecht, E. (1975) An aerological climatology of South America, *Met. Rdsch.*, **28**, 17–26.

Kuz'min, P. P. (1972) *Melting of Snow Cover* (Russian original 1961). Jerusalem: Israel Prog. Sci. Transl.

Langley, S. P. (1884) Researches on solar heat and its absorption by the earth's atmosphere. A report on the Mount Whitney expedition. Washington, DC: US War Dept., Prof. Pap. Signal Service XV.

Lapen, D. R. and Martz, L. W. (1992) The measurement of two simple indices of wind sheltering-exposure from raster digital elevation models. *Comput. Geosci.*, **19**, 769–79.

Larcher, W. (1980) Klimastress im Gebirge-Adaptionstraining und Selektions-filter für Pflanzen, *Rheinisch-Westfalien Akad. Wiss. no.* **291**, 49–80.

Lauscher, F. (1937) Die Zunahme der Intensität der Sonnenstrahlung mit der Hohe. *Gerlands Beitr. Geophys*, **50**, 202–15.

Lauscher, F. (1966) Die Tagesschwankung der Lufttemperatur auf Höhenstation in allen Erdteilen. *60–62 Jahresberichte des Sonnblick-Vereines für die Jahre 1962–64*. Vienna. pp. 3–17.

Lauscher, F. (1976) Methoden zur Weltklimatologie der Hydrometeore. Der Anteil des festen Niederschlags am Gesamtniederschlag. *Arch. Met. Geophys. Biokl.*, **B, 24**, 129–76.

Lautensach, H. and Bogel, R. (1956) Der Jahrsgang des mittleren geographischen Höhengradienten der Lufttemperatur in den verschiedenen Klimagebieten der Erde. *Erdkunde*, **10**, 270–82.

LeDrew, E. F. (1975a) The estimation of clear sky atmospheric emittance at high altitudes. *Arct. Alp. Res.*, **7**, 227–36.

LeDrew, E. F. (1975b) The energy balance of a mid-latitude alpine site during the growing season, 1973. *Arct. Alp. Res.*, **7**, 301–14.

Lee, J. T., Lawson, R. E., Jr., and March, G. L. (1987) Flow visualization experiments on stably stratified flow over ridges and valleys. *Met. Atmos. Phys.*, **37**, 183–94.

Lee, R. (1962) Theory of the "equivalent slope". *Mon. Wea. Rev.*, **90**, 165–6.

Lee, R. (1978) *Forest Microclimatology*. New York: Columbia University Press.

Lenoble, J., Kylling, A. and Smalskaia, I. (2004) Impact of snow cover and topography on ultraviolet irradiance at the Alpine station of Briançon. *J. Geophys. Res.*, **109(D8)**, D08107, 7 pp.

Linacre, E. (1982) The effect of altitude on the daily range of temperature. *J. Climatol.*, **2**, 375–82.

Loescher, K. A., *et al.* (2006) Climatology of barrier jets along the Alaskan coast. Part 1: Spatial and temporal distribution. *Mon. Wea. Rev.*, **134**, 437–53.

Loudon, A. G. and Petheridge, P. (1965) Solar radiation on inclined surfaces. *Nature*, **206** (4984), 603–4.

Lowry, W. P. (1980a) Clear-sky direct-beam solar radiation versus altitude: a proposal for standard soundings. *J. appl. Met.*, **19**, 1323–27.

Lowry, W. P. (1980b) *Direct and Diffuse Solar Radiation: Variations with Atmospheric Turbidity and Altitude*. Urbana-Champaign: Institute for Environmental Studies, University of Illinois. Research Report No. 6.

Luedi, W. (1938) Mikroklimatische Untersuchungen an einem Vegetationsprofil in den Alpen von Davos. *Ber. Geobotan, Inst ETH, Stift Ruebel* **1938**, 29–49.

Luo, H.-B. and Yanai, N. (1984) The large-scale circulation and heat sources over the Tibetan Plateau and surrounding regions during the early summer of 1979: Part II. Heat and moisture budgets. *Mon. Wea. Rev.*, **112**(5), 966–89.

Mani, M. S. (1962) *Introduction to High Altitude Entomology*. London: Methuen, pp. 1–73.

Marks, D. and Dozier, J. (1979) A clear-sky longwave radiation model for remote alpine areas. *Arch. Met. Geophys. Biokl.*, **B.27**, 159–87.

Marty, C., *et al.* (2002) Altitude dependence of surface radiation fluxes and cloud forcing in the Alps: results from the Alpine Surface Radiation Budget network. *Theoret. Appl. Climatol.*, **72**, 137–55.

Mason, P. J. (1987) Diurnal variations in flow over a succession of ridges and valleys. *Q. J. R. Met Soc.*, **113**, 1117–40.

Mason, P. J. and King, J. C. (1984) Atmospheric flow over a succession of nearly two-dimensional ridges and valleys. *Q. J. R. Met. Soc.*, **110**, 821–45.

Mason, P. J. and Sykes, R. I. (1979) Flow over an isolated hill of moderate slope. *Q. J. R. Met. Soc.*, **105**, 383–95.

Matulla, C., *et al.* (2005) *Outstanding Past Decadel-scale Climate events in the Greater Alpine Region Analysed by 250 years Data and Model Runs*. GKSS 2005/4. Geesthacht, Germany: GKSS Forschungszentrum, 114 pp.

Matzinger N., *et al.* (2003) Surface radiation budget in an Alpine valley. *Q. J. R. Met. Soc.*, **129**(588), 877–95.

Maurer, J. (1916) Bodentemperatur und Sonnestrahlung in den Schweizer Alpen. *Met. Zeit.*, **33**, 193–9.

McCutchan, M. H. (1983) Comparing temperature and humidity on a mountain slope and in the free air nearby. *Mon. Wea. Rev.*, **111**, 836–45.

McCutchan, M. H. and Fox, D. G. (1986) Effect of elevation and aspect on wind, temperature and humidity. *J. Clim. Appl. Met.*, **25**, 1996–2013.

McCutchan, M. H., Fox, D. G. and Furman, R. W. (1982) San Antonia Mountain Experiment (SAMEX). *Bull. Amer. Met. Soc.*, **63**, 1123–31.

Meroney, R. N. (1990) Fluid dynamics of flow over hills/mountains – insights through physical modeling. In W. Blumen (ed.), *Atmospheric Processes over Complex Terrain*. Met. Monogr. 23(45). Boston, MA: American Meteorological Society, pp. 145–71.

Minzer, R. A. (1962) *A History of Standard and Model Atmospheres. 1847 to 1962*. Bedford, MA: Geophysics Corp. America, TR 62-6-N.

Molnar, P. and Emanuel, K. A. (1999) Temperature profiles in radiative-convective equilibrium above surfaces at different heights. *J. Geophys. Res.*, **104**(D20), 24, 265–271.

Molotch, N. P., *et al.* (2004) Incorporating remotely sensed snow albedo into spatially distributed snowmelt modeling. *Geophys. Res. Lett.*, **31**, L0350, 4 pp.

Mueller, H. (1984) Zum Strahlungshaushalt im Alpenraum. In *Mitteilungen der Versuchsanstalt fuer Wasserbau, Hydrologie und Glaziologie*. No. 71. Zurich: ETH, 167 pp.

Mueller, H. (1985) Review paper on the radiation budget in the Alps. *J. Climatol.*, **5**, 445–62.

Müller, F., *et al.* (1980) Combined ice, water and energy balances of a glacierized basin of the Swiss Alps – the Rhonegletscher Project. *Geography in Switzerland. Geogr. Helvet.*, **35**(5), 57–69.

Nägeli, W. (1971) Der Wind als Standortsfaktor bei Aufforstungen in der subalpinen Stufe. *Mitt. Schweiz. Anst. Förstl. Versuch*, **47**, 33–147.

Neuwirth, F. (1979) Beziehungen zwischen Globalstrahlung, Himmelstrahlung und extra-terrestrischer Strahlung in Osterreich. *Arch. Met. Geophys. Biokl.*, **B 27**, 1–13.

Nicholls, J. M. (1973) *The Airflow over Mountains. Research, 1958–1972*. Geneva: World Meteorological Organization, WMO Tech. Note no. 127.

Ohmura, A. (1990) On the wind profile over the Alps, *Proc. xxi Internat. Tagung f. Alpine Meteorologie, Veröff, Schweiz. Met. Anstalt* **48**, 102–5.

Oliphant, A. J., *et al.* (2003) Spatial variability of surface radiation fluxes in mountainous terrain. *J. Appl. Met.*, **42**(1), 113–28.

Oliver, J. (1962) The thermal regime of upland peat soils in a maritime temperate climate. *Geogr. Ann.*, **44**, 293–302.

Olyphant, G. A. (1984) Insolation topoclimates and potential ablation in alpine snow accumulation basins: Front Range, Colorado. *Water Resour. Res.*, **20**, 491–8.

Olyphant, G. A. (1986) Longwave radiation in mountainous areas and its influence on the energy balance of alpine snowfields. *Water Resour. Res.*, **22**, 62–6.

Orlanski, I. (1975) A rational subdivision of scales for atmospheric processes. *Bull. Amer. Met. Soc.*, **56**(5), 527–30.

Overland, J. E. (1984) Scale analysis of marine winds in straits along mountainous coasts. *Mon. Wea. Rev.*, **112**, 22530–4.

Overland, J. E. and Walter, B. A., Jr. (1981) Gap winds in the Strait of San Juan de Fuca. *Mon. Wea. Rev.*, **109**, 2221–33.

Pagliuca, S. (1934) Winds of superhurricane force, and a heated anemometer for their measurement during ice-forming conditions. *Mon. Wea. Rev.*, **62**, 186–9.

Pepin, N., Benham, D. and Taylor, K. (1999) Modeling lapse rates in the maritime uplands of northern England: Implications for climate change. *Arct. Antarct. Alp. Res.*, **31**, 151–64.

Pepin, N., *et al.* (2005) A comparison of SNOTEL and GHCN/CRU surface temperatures with free-air temperatures at high elevations in the western United States: Data compatibility and trends. *J Climate*, **18**(12), 1967–85.

Peppler, W. (1931) Zur Frage des Temperaturunterschiedes zwischen den Berggipfeln und der freien Atmosphäre. *Beitr. Phys. frei. Atmos.*, **17**, 247–63.

Peppler, W. (1935) Ergänzung zu meiner Arbeit: "Zur Frage des Temperaturunters-chiedes zwischen den Berggipfeln und der freien Atmosphäre". *Beitr. Phys. frei. Atmos.*, **21**, 172–76.

Peterson, E. B. (1969) Radiosonde data for characterization of a mountain environment in British Columbia. *Ecology*, **50**, 200–5.

Pfeiffer, T., Koepke, P. and Reuder, J. (2006) Effects of altitude and aerosol on UV radiation. *J. Geophys. Res.*, **111(D1)**, D01203, 1–11.

Philipona, R., Marty, C. and Froehlich, C. (1996) Measurement of the longwave radiation budget in the Alps. In W. Smith and K. Stamnes (eds), *Current Problems in Atmospheric Radiation*. Hampton, VA: A. Deepak Publishing, pp. 786–9.

Piazena, H. (1996) The effect of altitude upon the solar UV-B and UV-A irradiance in the tropical Chilean Andes. *Solar Energy*, **57**, 133–40.

Pope, J. H. (1977) Computations of solar insolation at Boulder, Colorado. Washington, DC: NOAA Tech. Mem., NESS 93.

Prohaska, F. (1970) Distinctive bioclimatic parameters of the subtropical-tropical Andes. *Int. J. Biomet.*, **14**, 1–12.

Ramachandran, G. (1972) The role of orography on wind and rainfall distribution in and around a mountain gap: an observational study. *Ind. J. Met. Geophys.*, **23**, 41–4.

Ramachandran, G., Rao, K. V. and Krishna, K. (1980) An observational study of the boundary-layer winds in the exit region of the mountain gap. *J. appl. Met.*, **19**, 881–8.

Rao, G. V. and Erdogan, S. (1989) The atmospheric heat source over the Bolivian Plateau for a mean January. *Boundary-Layer Met.*, **46**, 13–33.

Rathschuler, E. (1949) Über die Änderung des Tagesganges der Luftfeuchtigkeit mit der Höhe. *Arch. Met. Geophys. Biokl.*, **B1**, 17–31.

Reed, T. R, (1931) Gap winds in the Strait of San Juan de Fuca. *Mon. Wea. Rev.*, **59**, 373–6.

Reid, S. (1996) Pressure gradients and winds in Cook Strait. *Wea. Forecasting* **11**, 476–88.

Reisner, J. M. and Smolarkiewicz, P. K. (1994) Thermally forced low Froude number flow past three-dimensional obstacles. *J. Atmos. Sci.*, **51**, 117–33.

Reitan, C. H. (1963) Surface dew point and water vapor aloft. *J. appl. Met.*, **2**, 776–9.

Reiter, E. R. (1963) *Jet-stream Meteorology*. Chicago: University of Chicago Press.

Reiter, E. R. and Tang, M. (1984) Plateau effects on diurnal circulation patterns. *Mon. Wea. Rev.*, **112**, 638–51.

Reiter, R., Carnuth, W. and Sladkovic, R. (1972) Ultraviolettstrahlung in alpinen Höhenlagen. *Wetter u. Leben*, **24**, 231–47.

Reiter, R., Mungert, K. and Sladovic, R. (1982) Results of 5-year concurrent recordings of global, diffuse and UV radiation at three levels (700, 1800, and 3000 m a.s.l.) in the northern Alps. *Arch. Met. Geoph. Biokl.*, **B30**, 1–28.

Resler, L. M., Butler, D. R. and Malanson, G. P. (2005) Topographic shelter and conifer establishment and mortality in an alpine environment, Glacier National Park, Montana. *Phys. Geog.*, **26**, 112–25.

Revfeim, K. J. A. (1976) Solar radiation at a site on known orientation on the earth's surface. *J. appl. Met.*, **15**, 651–6.

Richner, H. and Phillips, P. D. (1984) A comparison of temperature from mountaintops and the free atmosphere – their diurnal variation and mean difference. *Mon. Wea. Rev.*, **112**, 1328–40.

Richter, M. (2000) A hypothetical framework for testing phytodiversity in mountainous regions: the influence of airstreams and hygrothermic conditions. *Phytocoenologia* **30**, 519–42.

Rolland, C. (2003) Spatial and seasonal variations in air temperature lapse rates in Alpine regions. *J, Climate*, **16**(7): 1032–46.

Ross, A. N. and Vosper, S. B. (2005) Neutral turbulent flow over forested hills. *Q. J. R. Met.Soc.*, **131** (609), 1841–62.

Salmon, J. H., *et al.* (1988) The Askervein Hill Project: Mean wind variations at fixed heights above ground. *Boundary-Layer Met.*, **43**, 247–71.

Samson, C. A. (1965) A comparison of mountain slope and radiosonde observations. *Mon. Wea. Rev.*, **95**, 327–30.

Sauberer, F. and Dirmhirn, I. (1958) Das Strahlungsklima. In F. Steinhauser, O. Eckel, and F. Lauscher (eds), *Klimatographie von Osterreich*. Vienna: Springer, pp. 13–102.

Schell, I. I. (1936) On the vertical distribution of wind velocity over mountain summits. *Bul. Am. Met. Soc.*, **17**, 295–300.

Schönenberger, W. (1975) Standortseinflüsse auf Versuchsaufforstungen an des alpinen Waldgrenze. *Mit Schweiz Anst. forstl. Versuch.*, **51**(4), 358–428.

Schüepp, W. (1949) Die Bestimmung der Komponenten der atmosphärischen Trübung aus Aktinometermessungern. *Arch. Met. Geophys. Biokl.*, **B 1**, 257–346.

Schumacher, C. (1923) Der Wind in der freien Atmosphäre und auf Säntis, Zupgspitze und Sonnblick. *Beitr. Phys. frei Atmos.*, **11**, 20–42.

Schwander, H., *et al.* (2002) Modification of spectral UV irradiance by clouds. *J. Geophys. Res.*, **107(D16)**, AAC 7.1–7.12.

Schwind, M. (1952) Mikroklimatische Beobachtungen am Wutaischan. *Erdkunde*, **6**, 44–5.

Scorer, R. S. (1955) Theory of airflow over mountains. IV. Separation of flow from the surface. *Q. J. R. Met. Soc.*, **81**, 340–50.

Scorer, R. S. (1978) *Environmental Aerodynamics*. Chichester: Ellis Horwood.

Sellers, W. D. (1965) *Physical Climatology*. Chicago: University of Chicago Press.

Sheppard, P. A. (1956) Airflow over mountains. *Q. J. R. Met. Soc.*, **82**, 528–9.

Sivkov, S. I. (1971) *Computation of Solar Radiation Characteristics*. Leningrad: Gidromet, Izdat. Jerusalem: Israel Prog. Sci. Translations.

Skartveit, A. and Olseth, J. A. (1986) Modeling slope irradiance at high latitudes. *Solar Energy*, **36**(4), 333–41.

Smith, E. A. and Shi, L. (1996) Reducing discrepancies in atmosphere heat budget of Tibetan Plateau by satellite-based estimates of radiative cooling and cloud-radiation feedback. *Met. Atmos. Phys.*, **56**, 229–60.

Smith, R. B. (1979) The influence of mountains on the atmosphere. *Adv. Geophys.*, **21**, 87–230.

Smith, R. B. (1980) Linear theory of stratified hydrostatic flow past an isolated mountain. *Tellus*, **32**, 348–64.

Smith, R. B. (1990) Why can't stably stratified air rise over high ground? In W. Blumen (ed.), *Atmospheric Processes over Complex Terrain*, Met. Monogr. 23(45). Boston, MA: American Meteorological Society, pp. 105–7.

Snyder, W. H., *et al.* (1985) The structure of strongly stratified flow over hills: Dividing streamline concept. *J. Fluid Mech.*, **52**, 249–88.

Sokratov, S. A. and Barry, R. G. (2002) Intraseasonal variation in the thermoinsulation effect of snow cover on soil temperatures and energy balance. *J. Geophys. Res.*, **107(D10):** ACL 13.1–13.7, (correction, *ibid.*, **107(D19)**, ACL, 3.1).

Sprenger, M. and Schär, C. (2001) Rotational aspects of stratified gap flows and shallow föhn. *Q. J. R. Met. Soc.*, **127**(571), 161–87.

Steenburgh, W. J., Schultz, D. M. and Colle, B. A. (1998) The structure and evolution of gap outflow over the Gulf of Tehuantepec, Mexico. *Mon. Wea. Rev.*, **126**(10), 2673–91.

Steinacker, R., *et al.* (2006) A mesoscale data analysis and downscaling method over complex terrain. *Mon. Wea. Rev.*, **134**(10), 2758–71.

Steinhauser, F. (1936) Uber die Haufigkeitsverteilungen des Dampfdruckes in Gebirge und in der Niederung und ihre Beziehungen zueinander. *Met. Zeit.*, **53**, 415–19.

Steinhauser, F. (1937) Uber die täglichen Temperaturschwankungen im Gebirge. *Gerlands Beitr. Geophys.*, **50**, 360–7.

Steinhauser, F. (1938) *Die Meteorologie des Sonnblicks. I. Beiträge zur Hochgebirgs-meteorologie*, Vienna: J. Springer.

Steinhauser, F. (1939) Die Zunahme der Intensität der direkten Sonnenstrahlung mit der Höhe im Alpengebiet und die Verteilung der "Trubung" in den unterer Luftschichten. *Met. Zeit.*, **56**, 173–81.

Steven, M. D. (1977) Standard distributions of clear sky radiance. *Q. J. R. Met. Soc.*, **103**, 457–65.

Steven, M. D. and Unsworth, M. H. (1979) The diffuse solar irradiance of slopes under cloudless skies. *Q. J. R. Met Soc.*, **105**, 593–602.

Storr, D. (1970) A comparison of vapour pressure at mountain stations with that in the free atmosphere, *Can Met. Res. Rep.*, 1/70, Dept. of Transport, Canada.

Stringer, E. T. (1972) *Foundations of Climatology*. San Francisco: W. H. Freeman and Co., pp. 141–67.

Stull, R. B. (1988) *An Introduction to Boundary Layer Meteorology*. Dordrecht: Kluwer Academic Publishers.

Tabony, R. C. (1985a) Relations between minimum temperature and topography in Great Britain. *J. Climatol.*, **5**, 503–20.

Tabony, R. C. (1985b) The variation of surface temperature with altitude. *Met. Mag.*, **114**, 37–48.

Tampieri, F. (1987) Separation features of boundary-layer flow over valleys. *Boundary-Layer Met.*, **40**, 295–307.

Tampieri, F. and Hunt, J. C. R. (1985) Two-dimensional stratified fluid flow over valleys: linear theory and a laboratory investigation. *Boundary-Layer Met.*, **32**, 257–79.

Tang, M. and Reiter, E. R. (1984) Plateau monsoons of the northern hemisphere: a comparison between North America and Tibet. *Mon. Wea. Rev.*, **112**, 617–37.

Taylor, P. A. (1977) Numerical studies of neutrally stratified planetary boundary-layer flow above gentle topography. I. Two-dimensional cases. *Boundary-Layer Met.*, **12**, 37–60.

Taylor, P. A. and Lee, R. A. (1984) Simple guidelines for estimating wind speed variations due to small-scale topographic features. *Climatol. Bull. Ottawa*, **18**, 3–32.

Taylor, P. A., Mason, P. J. and Bradley, E. F. (1987) Boundary-layer flow over low hills. *Boundary-Layer Met.*, **39**, 107–32.

Taylor, P. A., Sykes, R. I. and Mason, P. J. (1989) On the parameterization of drag over small-scale topography in neutrally-stratified boundary layer flow. *Boundary-Layer Met.*, **48**, 409–22.

Temps., R. C. and Coulson, K. L. (1977) Solar radiation incident upon slopes of different orientation. *Solar Energy*, **19**, 179–84.

Teunissen, H. W., *et al.* (1987) The Askervein Hill Project: Wind-tunnel simulations at three length scales. *Boundary-Layer Met.*, **40**, 1–29.

Thams, J. C. (1961a) The influence of the Alps on the radiation climate. In *Recent Progress in Photobiology, Proc. 3rd Int. Congress*. New York: Elsevier, pp. 76–91.

Thams, J. C. (1961b) Der Einfluss der Bewölkungsmenge und art auf die Grösse der diffusen Himmelstrahlung. *Geof. pura appl.*, **48**, 181–92.

Thompson, W. F. (1990) Climate related landscapes in world mountains: Criteria and map. *Zeit. f. Geomorph., Suppl.* **78**, 92 pp.

Troll, C. (1964) Karte der Jahreszeitenklimate der Erde. *Erdkunde*, **18**, 5–28.

Trombetti, F. and Tampieri, F. (1987) An application of the dividing-streamline concept to the stable airflow over mesoscale mountains. *Mon. Wea. Rev.*, **115**, 1802–6.

Turner, H. (1958) Maximal Temperaturen oberflächennaher Bodenschichten an der alpinen Waldgrenze. *Wetter u. Leben*, **10**, 1–12.

Turner, H. (1966) Die globale Hangbestrahlung als Standortsfaktor bei Aufforstungen in der subalpinen Stufe. *Mitt. Schweiz. Anst. forstl. Versuch.*, **42**(3), 109–68.

Turner, H. (1980) Types of microclimate at high elevations. In U. Benecke and M. R. Davis (eds), *Mountain Environments and Subalpine Tree Growth*. Wellington: Technical Paper No. 70, Forest Research Institute, New Zealand Forest Service, pp. 21–6.

Turner, H., Rochat, P. and Streule, A. (1975) Thermische Charakteristik von Hauptstandortstypen im Bereich der oberen Waldgrenze (Stillberg, Dischmatal bei Davos). *Mitt. Eidgenöss. Anst. forstl. Versuch.*, **51**, 95–119.

Valko, P. (1961) Untersuchung über die vertikal Trübungsschlichtung der Atmosphäre. *Arch. Met. Geophys. Biokl.*, **11**, 148–210.

Valko, P. (1980) Some empirical properties of solar radiation and related parameters. In *An Introduction to Meteorological Measurements and Data Handling for Solar Energy Applications*, Chapter 8, DOE/ER-0084. Washington, DC: US Dept. of Energy.

Varley, M. J., Beven, K. and Oliver, H. R. (1996) Modeling solar radiation in steeply sloping terrain. *Int. J. Climatol.*, **16**, 93–104.

Voloshina, A. P. (1966) *Teplovoi balans poverkhnosti vysokogornykh lednikov v letnii period.* (The energy balance of high mountain glaciers in summer). Moscow: Izdat. Nauka.

Vonder Mühl, D. and Permafrost Coordination Group of the SAS (1999) Permafrost – distribution and particular aspects. In *Hydrologic Atlas of Switzerland*, Plate 3.9. Bern: Bundesamt Wasser u. Geologie.

Vosper, S. B. and Mobbs, S. D. (1997) Measurement of the pressure field on a mountain. *Q. J. R. Met. Soc.*, **123**, 129–44.

Vosper, S. B., Mobbs, S. D. and Gardiner, B. A. (2002) Measurements of the near-surface wind field over a hill. *Q. J. R. Met. Soc.*, **128**, 2257–80.

Wade, J. E. and Hewson, E. W. (1979) Trees as a local climatic wind indicator. *J. appl. Met.*, **18**, 1182–7.

Wahl, E. (1966) *Windspeed on Mountains*. Final Report AFCRL–66–280. Milwaukee, WI: Meteorology Dept., University of Wisconsin.

Walmsley, J. L., Taylor, P. A. and Salmon, J. R. (1989) Simple guidelines for estimating wind speed variations due to small-scale topographic features – an update. *Climatol. Bull.*, **23**, 3–14.

Wardle, P. (1974) Alpine timberlines. In J. D. Ives and R. G. Barry (eds), *Arctic and Alpine Environments*. London: Methuen, pp. 371–402.

Wendler, G. and Ishikawa, N. (1974) The effect of slope exposure and mountain screening on the solar radiation of McCall Glacier, Alaska: a contribution to the International Hydrological Decade. *J. Glaciol.*, **13**(68), 213–26.

Wessely, E. (1969) Messung der UV-Strahlung mit Interferenzfilter und Photoelementen bei.332μm. Ph.D. dissertation, University of Vienna.

Williams, L. D., Barry, R. G. and Andrews, J. T. (1972) Application of computed global radiation for areas of high relief. *J. appl. Met.*, **11**, 526–33.

Williams, P. J. and Smith, M. W. (1989) *The Frozen Earth. Fundamentals of Geocryology*. Cambridge: Cambridge University Press, 306 pp.

Wilson, H. P. (1968) *Stability Waves*. Toronto: Dept. of Transport, Met. Branch, TEC703.

Wilson, H. P. (1974) A note on mesoscale barriers to surface airflow, *Atmosphere*, **12**, 118–20.

Wilson, R. G. and Garnier, B. J. (1975) Calculated and measured net radiation for a slope. *Climat. Bull, Montreal*, **17**, 1–14.

Winstral, A., Elder, K. and Davis, R. E. (2002) Spatial snow modeling of wind-redistributed snow using terrain-based parameters. *J. Hydromet.*, **3**, 524–38.

Wooldridge, G. L., Fox, D. G. and Furman, R. W. (1987) Airflow patterns over and around a large three-dimensional hill. *Met. Atmos. Phys.*, **37**, 259–70.

World Meteorological Organization, Secretariat (1981) *Meteorological Aspects of the Utilization of Wind as an Energy Source*, Technical Note No. 75, WMO no. 575. Geneva: WMO.

Xie, S.-P., *et al.* (2005) Air–sea interaction over the eastern Pacific warm pool: Gap winds, thermocline dome, and atmospheric convection. *J. Climate*, **18**, 5–20.

Yeh, D.-Z. (1982) Some aspects of the thermal influences of Qinghai–Tibetan plateau on the atmospheric circulation. *Arch. Met. Geophys. Biocl.*, **A31**, 205–20.

Yoshino, M. M. (1966) Some aspects of air temperature climate of the high mountains in Japan. *Jap. Progr. Climat.*, **November**, 21–7.

Yoshino, M. M. (1973) Studies on wind-shaped trees: their classification, distribution and significance as a climatic indicator. *Climat. Notes*, **12**, 1–52.

Yoshino, M. M. (1975) *Climate in a Small Area*. Tokyo: University of Tokyo Press, pp. 445–59.

Zaitchik, B. F., Evans, J. P. and Smith, R. B. (2007) Regional impact of an elevated heat source: The Zagros Plateau of Iran. *J. Climate*, **20**(16), 4133–46.

Zängl, G. (2002) Stratified flow over a mountain with a gap: linear theory and numerical simulation. *Q. J. R. Met. Soc.*, **128**(581), 927–49.

Zekser, K., Podobnikar, T. and Ostir, K. (2005) Solar radiation modelling. *Computers and Geoscience*, **31**, 233–40.

3 CIRCULATION SYSTEMS RELATED TO OROGRAPHY

3.1 DYNAMIC MODIFICATION

The effects of topography on air motion operate over a wide range of scales and produce a hierarchy of circulation systems through the mechanism of dynamic and thermal factors. Here, we concentrate on three major types of dynamic process. First, extensive mountain ranges set up planetary-scale wave motion through large-scale rotational effects. Second, mountains give rise to modifications of synoptic-scale weather systems, especially fronts. Third, topography on all scales introduces wave motion through local gravitational effects. While these categories are not always sharply differentiated from one another, they provide a convenient basis for discussion. Detailed accounts of orographic effects on airflow are given in Alaka (1960), Nicholls (1973), Smith (1979a), and Hide and White (1980); Beer (1976) provides a convenient summary.

3.1.1 Planetary-scale effects

The influence of mountain barriers on the planetary-scale atmospheric circulation involves three principal processes: the transfer of angular momentum to the surface through friction and form drag; the blocking and deflection of airflow; and the modification of energy fluxes, particularly as a result of the airflow effects on cloud cover and precipitation. Various attempts have been made to distinguish the relative importance of these factors in generating standing planetary waves, through diagnostic, theoretical and modeling studies (Kasahara, 1980; see Barry and Carleton, 2001, pp. 294–300). Orography and diabatic heating (latent heat release, absorption of solar radiation, infrared cooling and surface sensible heat) each contribute to the forcing of the planetary waves, but their effects are poorly quantified according to Dickinson (1980). As far as the mountain belts are concerned, they tend to be located beneath an upper ridge of high pressure, but this feature is only well developed over high-middle latitudes in western North America. The significance of these planetary waves is that they influence the formation and movement of pressure systems. Mid-latitude depressions commonly tend to develop or intensify beneath the eastern limb of an upper wave trough, over the eastern seaboard of North America and off the east coast of Asia, for example.

The effects of orography on global climate were first discussed by meteorologists in the 1950s in terms of the structure of the planetary standing waves. The high mountains and plateaus of eastern Asia and western North America, for example, exert a strong control on the winter wave pattern, as confirmed by general circulation models (GCM) experiments with and without mountains (Manabe and Terpstra, 1974). This topic has received new attention in light of the suggested rapid uplift of these plateaus and mountain ranges during the Late Cenozoic, particularly the last 10 million years (Ruddiman et al., 1989; Ruddiman and Kutzbach, 1989). Simulations with the NCAR Community Climate Model were performed for January and July with present-day mountains, no mountains, and an intermediate "half-mountain" case (Kutzbach et al., 1989). The three cases show that in January the planetary waves increase in amplitude with terrain uplift and the low-level flow is progressively blocked or diverted around the barriers. In July, monsoon-like circulations form near the Tibetan and Colorado plateaus in response to higher barriers. Patterns of vertical motion and precipitation show corresponding adjustments to increasing elevations. Similar experiments with the Geophysical Fluid Dynamics Laboratory model by Manabe and Broccoli (1990) imply that in the absence of orography, relatively moist climates would be found over central Asia and western interior North America. This could explain the paleo-botanical evidence for reduced aridity in those regions during late Tertiary time.

The large-scale effects of an orographic barrier on an airflow crossing it are usually explained as a consequence of the relationship between divergence and vorticity. This is illustrated by the equation for the conservation of potential vorticity

$$\frac{\zeta + f}{\Delta p} = \text{constant}$$

where ζ is the relative vorticity about a vertical axis (cyclonic = positive in the northern hemisphere); f is the Coriolis parameter (expressing the component of the Earth's rotation in a horizontal plane; $f = 2\omega \sin \phi$, where $\omega =$ the angular velocity of the Earth, $\phi =$ latitude angle); and Δp is the thickness of the air column in pressure units.

It is assumed that the atmosphere is incompressible and that the air motion is adiabatic. This is equivalent to stating that the flow is *isentropic*, i.e. it is along surfaces of constant potential temperature (the temperature of air brought dry-adiabatically to a pressure of 1000 mb).

The equation shows that, if the expression on the left-hand side is to remain constant as an air column approaches a mountain range from the west and Δp decreases, then there must be a corresponding decrease in $(\zeta + f)$. In other words, vertical shrinking of the column must be matched by lateral expansion, implying horizontal divergence. For $(\zeta + f)$ to decrease, either the air stream undergoes anticyclonic curvature or the air must be displaced equatorward, where f is smaller. Conversely, on the downward side of the barrier, Δp increases again with the

opposite effects, producing a mountain ridge and lee trough pattern. For flows approaching a mountain ridge from the east, the vertical shrinking of the column leads to a decrease of absolute vorticity. The flow is deflected to higher latitudes and experiences increased Earth's vorticity, f. This leads ζ to decrease causing greater anticyclonic curvature and looping the flow. No wave pattern is created by easterly flows (Kasahara, 1980; Queney, 1948; Colson, 1949; Bolin, 1950).

The flow patterns observed over major mountain ranges indicate that the effect on the curvature (or relative vorticity) of the airflow is predominant. Over the Rocky Mountains, for example, there tends to be anticyclonic curvature of the upper westerlies, despite the associated slight poleward displacement (f changes very little by comparison with the reversed sign of ζ). However, Smith (1979b) shows the correct explanation does *not* involve vorticity changes due to vertical stretching. Rather, air parcels crossing a range in a quasi-geostrophic flow undergo volumetric expansion as they rise. This creates anticyclonic vorticity and the effect of the expansion does not cancel out, but causes a nonvanishing circulation.

Hoskins and Karoly (1981) show that the response of westerly airflow to an orographic barrier is wavelength dependent (Figure 3.1). In a barotropic atmosphere, for wavelengths less than the stationary wavelength, an anticyclone is generated by column shrinking over the mountains due to zonal advection of vorticity. For long wavelengths (i.e. the Rossby wave number is smaller then the wave number for the corresponding stationary wave, or $k < k_s$), the dominant β term ($= \partial f / \partial y$) sets up a cyclone in the same location. In the upper troposphere, $k_s \sim 7000$ km, so the first case is more likely. In the baroclinic atmosphere, there is adiabatic cooling (warming) on the windward (leeward) slopes. For mountain ranges of 2 km or higher, the upslope cooling is balanced by a poleward flow of warmer air, and vice versa on the lee slopes. This forcing also generates anticyclonic conditions over the mountains. The combined effects of orographic and thermal forcing on planetary waves in winter and summer in the northern hemisphere are shown by Hoskins *et al.* (1989). As

Fig. 3.1 Schematic vertical section illustrating the response of the atmosphere to westerly flow over a mountain range. (a) and (b) are barotropic atmospheres; the clockwise (counterclockwise) arrows indicate the generation of anticyclonic (cyclonic) vorticity for a northern hemisphere case. (c) and (d) are baroclinic atmospheres (from Hoskins and Karoly, 1981).

expected, the longitudinal distribution of thermal effects varies seasonally. However, it must be noted that the effect of orography is not just mechanical but involves latent heat released in orographic clouds.

Laboratory experiments can be used to investigate topographic effects on rotating fluids (Boyer and Davies, 1982; Boyer and Chen, 1987). A tow-tank containing saltwater and freshwater solutions, to establish a vertical density gradient, is rotated on a turntable. When the system reaches solid body rotation, a model mountain is towed steadily through the fluid. This system can generate eddies, but neglects the β-effect of the latitudinal variation of the Coriolis parameter. Boyer and Chen find qualitative agreement between observations of westerly flow over the Rocky Mountains and simulated features in such a system. These include a ridge over the mountains, a lee trough, and the characteristic slope of the ridge and trough lines; maximum relative cyclonic vorticity is located to the southeast of the central part of the mountains.

The amplitude of the wave disturbance depends strongly on the latitudinal extent of the barrier. Mountain ranges such as the Rocky Mountains, the Andes, and the Himalaya affect the large-scale planetary airflow whereas the extent of the European Alps is insufficient for such effects. The Southern Alps of New Zealand, spanning $5°$ of latitude, are also probably below the critical threshold for such effects although data for the South Pacific are sparse. In the southern hemisphere, the effects on the planetary waves of the Andes, which are high but narrow, are mainly confined to latitudes equatorward of $40°$ S (Walsh, 1994). The Antarctic continent is more extensive and higher over eastern than western Antarctica. Consequently this modifies the planetary wave structure in high southern latitudes; the polar vortex in the mid-troposphere has a well-developed wave number one with its trough located about $45°$ E (Epstein, 1988; Watterson and James, 1992; Barry and Carleton, 2001, Chapter 4).

Reiter (1963: pp. 382–3) shows two other interesting results. First, a narrow jet stream flow may be deflected anticyclonically, so as not to cross a mountain range, if the wind speed is below a particular threshold. For zonal flow encountering a 2 km high, 1000 km wide, barrier, the critical speed is $20 \, \text{m s}^{-1}$. If the curvature of the flow is cyclonic (anticyclonic), this critical value will be correspondingly less (greater), respectively. Second, if we consider the cyclonic and anticyclonic sides of a jetstream axis, the vorticity relationships can lead to airstream diffluence. South of the jet axis, where the absolute vorticity $(\zeta + f)$ approaches zero, the mountain barrier effect on the flow leads to a reduction of f, deflecting the current equatorward. On the north side of the jet axis, the current is deflected poleward, assuming conservation of absolute vorticity. Upper wind profiles in winter suggest that such splits occur in the westerly jet streams which encounter the Rocky Mountains and the Tibetan Plateau-Himalaya (Chaudhury, 1950), although in the latter case at least the cause is probably not simply a dynamical one. In winter, the Tibetan Plateau is a high-level cold source, which causes a strong baroclinic zone on its southern edge where the westerly subtropical jet tends to be anchored.

3.1.1.1 Topography in GCMs

The question of how to treat mountain terrain and associated sub-grid scale processes in GCMs merits discussion since knowledge of mountain topography and climates can provide some guide as to what aspects need to be adequately parameterized in order to obtain realistic model results, and to aid in their interpretation. Only a few aspects of atmospheric modeling relevant to mountain meteorology can be addressed here. Detailed information is provided by Mote and O'Neill (2000) and for climate modeling by McGuffie and Henderson-Sellers (2005) and Washington and Parkinson (2005).

Especially critical is the question of the scale of the topography in relation to the horizontal and vertical resolution of the model. In the vertical dimension most GCMs specify multiple levels. In early models these usually had an almost regular height spacing (e.g. 3 km) whereas most models now use sigma coordinates (p/p_0) with greater resolution in the lower layers. GCM results are usually presented in terms of spatial fields at standard geopotential or sigma levels, or as vertical cross-sections. Actual surface conditions in mountain regions are not considered unless special fine-mesh submodels are nested within the GCM to examine specific problems such as orographic precipitation.

A critical factor in model simulations is the horizontal resolution of the grid. The horizontal resolution of current GCMs is typically of the order of 2.5° latitude, with fine-mesh resolution of 1° latitude available for some purposes such as forecasting. Early models used latitude–longitude grids whereas many GCMs now treat the horizontal domain spectrally (Washington and Parkinson, 2005). Atmospheric GCMs in climate experiments are frequently run with a spectral (triangular) truncation at T42 (corresponding to ~ 280 km), but for regional studies even T106 (~ 120 km) will not capture orography such as the Pyrenees (Deque, 2000). The modeled topography is greatly smoothed, so that mean elevations are lower, and adjacent to high mountains and plateaus there may be dips in the modeled surface extending below sea level. Hoskins (1980) provides illustrative data on the depiction of topography at several spectral resolutions (see Figure 3.2). Table 3.1 illustrates the maximum topography represented at three resolutions and spurious minima. Spectral truncation gives rise to the "Gibbs phenomenon"-ripples in the modeled surfaces, including dips in the ocean surface upstream of major mountain ranges. The ripples set up spurious horizontal fluxes of mass and momentum giving rise to convergence/divergence and vertical motions and also affecting energy and moisture transfers (Williamson and Laprise, 2000).

The presence of orographic barriers to airflow gives rise to lee waves (see Chapter 3, p. 150), which are a form of vertically propagating gravity waves. If the flow is sufficiently distorted, large amplitude waves can break down into turbulence thereby transferring momentum from the large-scale, low-level flow to upper levels as the waves dissipate. This results in "gravity wave drag" on the atmosphere (McFarlane, 2000). The representation of mountains in models is therefore critical and this remains a problem in the case of high narrow ranges like the Andes (see Table 3.1).

Table 3.1 **The representation of topography in a 1° input grid and three triangular truncations of a spectral grid. The main topographic maxima and spurious minima are listed (after Hoskins, 1980).**

Location	1° data	T21	T42	T63
Rocky Mts	3100	1530	2120	2360
Greenland	3100	1330	2590	3020
Himalaya	6100	3920	5250	5440
Off Western N. America		−80	−60	−60
Andes	5500	1490	2820	3770
Off Western S. America		−140	−300	−350
Antarctica	4000	3680	3700	3960
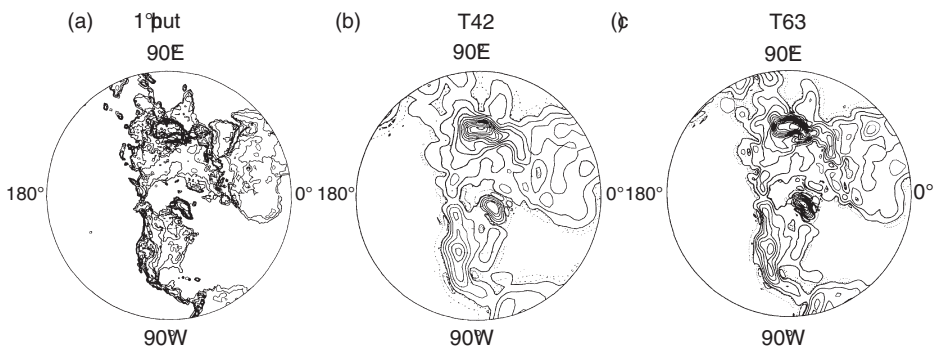
Fig. 3.2   **The representation of northern hemisphere topography in 1° resolution data and in spectral models with triangular truncation at T42 and T63 (from Hoskins, 1980).**

Flow deceleration due to form drag was introduced in Chapter 2 (p. 71). Here we can note that actually it has four contributing mechanisms: (i) boundary-layer drag due to upstream blocking of the flow (discussed below), forming almost-stagnant layers that change the effective mountain height; (ii) vertically-propagating lee waves with gravity wave breaking and dissipation aloft; (iii) dissipation by breaking of large-amplitude gravity waves near the mountain summits; and (iv) dissipation in trapped lee waves (see Welch *et al.*, 2001; Kim and Doyle, 2005). Flow blocking, as modeled by Shutts (1998), predicts the upstream drag force and flow features satisfactorily but overestimates the effect of rotation (Coriolis force) on the drag according to Wells *et al.* (2005).

Two approaches to correct this model deficiency have been tested. The first is to raise the mountains by using an envelope orography to increase surface drag and the second is to incorporate the effects of breaking orographic gravity waves, mainly in the lower stratosphere. The atmosphere responds more to the "envelope" topography through the mountain peaks than to mean elevation because deep valleys and basins act as part of the terrain when they are filled with stagnant air. The truncation levels adopted in spectral models, especially those used for

most climate sensitivity experiments, result in mountains being greatly smoothed. Therefore, adjustments have to be made to the mean surface heights in order to obtain adequate representation of the "envelope" orography (Wallace *et al.*, 1983). One procedure is to add twice the standard deviation of height values, determined over a fine resolution (10-minute spacing) terrain grid, to the mean for each grid box. Slingo and Pearson (1987) provide a comparative evaluation of both alternatives with the UKMO model. The envelope orography approach is not satisfactory because it does not remove the problem of strong zonal flow in mid-latitudes of the northern hemisphere – "the westerly problem" – and introduces other biases in the circulation fields. Wallace *et al.* (1983) showed similar findings with the European Centre for Medium Range Weather Forecasting (ECMWF) model. Envelope orography is also likely to generate spurious elevated heat sources in summer over high mountains and plateaus. The UKMO simulations incorporating gravity-wave drag show substantial improvement in the circulation patterns in both seasons and in the storm track locations. However, the best treatment of orography in models is still an open question (Slingo and Pearson, 1987). The solution may involve the use of mean elevations at high spatial resolution because this should result in better precipitation patterns. Another approach to estimating surface drag considers the silhouette of a mountain barrier as "seen" by an approaching air stream.

Increased resolution generally improves the pressure field and increases the precipitation due to the increased accuracy in the solution of the hydrodynamic equations. Atmospheric GCMs often compensate for the transfers of energy to smaller, unresolved scales by incorporating horizontal diffusion (damping) to prevent energy from accumulating in the smallest resolved scales (Williamson and Laprise, 2000). Hence, horizontal diffusion must decrease as model resolution increases. Models with high spatial resolution may give erroneous airflow and precipitation in complex terrain as a result of the overestimation of horizontal diffusion. Juang *et al.* (2005) show that using a modified diffusion calculation on pressure instead of height surfaces in the NCEP Mesoscale Spectral Model (MSM) can lessen this problem. In conditionally unstable conditions, erroneous warming and moistening over mountains due to diffusion can be reinforced by low-level, condensation-induced convergence leading to excessive precipitation.

For a meso-scale model study of the Pyrenees, Georgelin *et al.* (1994) employ a sub-grid scale parameterization of orography, based upon the use of an effective roughness length (see Note 1, p. 230). The impact of this parameterization is investigated for three different orographic flow simulations and the results are compared with PYREX data. The simulations show that, by accounting for the sub-grid scale orography, the mountain wave amplitude is reduced, blocking is increased, leeside low-level turbulence is intensified, and the regional wind characteristics are modified. The inclusion of sub-grid scale orography significantly improves the model results.

3.1.2 Synoptic-scale effects

While changes of the planetary flow are of major importance to global climate, modifications to synoptic systems are of more immediate consequence for conditions in the mountains themselves. Orography has three major effects on such systems: flow blocking and barrier winds upstream of the barrier; modification of frontal cyclones crossing a mountain range; and enhanced cyclogenesis in the lee of the mountains. The second of these effects is of more direct importance for mountain weather, although the other two help determine conditions on the windward and leeward slopes.

3.1.2.1 Blocking effects and barrier winds

The so-called "barrier effect" of mountain ranges to air motion is most evident when they are high and continuous. The barrier effect of the Himalaya ranges, in limiting northward movement of summer monsoon air, and of the Tibetan plateau on the southward movement of cold air from the shallow Siberian high in winter are well known in terms of average climatic conditions, although hardly investigated in detail. Mountain barriers are especially effective when the movement of stable cold air masses is involved. An analysis of an outbreak of continental polar air from central Canada towards the Pacific coast of the state of Washington in January 1940 illustrates this (Church and Stephens, 1941). The Rocky Mountains, especially, and to a lesser extent the Cascades, only permitted air with higher potential temperatures above the summit levels to move westward. Subsidence occurred over a depth of at least 2000 m as the air moved westward with warming occurring at close to the dry adiabatic lapse rate.

Various model studies of flow blocking by meso-scale topography have been performed. Pierrehumbert and Wyman (1985) identify the Rossby number, expressed as $R_0 = U/fL$, where L is the mountain half-width and U the cross-mountain flow component, and the reciprocal Froude number ($F^{-1} = U/Nh_m$), where h_m is the mountain height) (see p. 109), as the parameters controlling the effect of ridges on the airflow. They show the importance of rotation in limiting the upstream extent of flow blocking to a distance set by the Rossby radius of deformation (Note 2), $L_R = Nh_m/f$, where N is the Brunt–Väisälä frequency. Air parcels that have been deflected to the left (in the northern hemisphere) are at lower pressure and so move faster than air parcels on the right side of the flow, provided F^{-1} is large. The Coriolis force, f, is thus shown to be the major factor limiting the upstream extent of flow blocking and also the degree of deceleration. Air crossing the mountains at summit level is slightly accelerated. Figures 3.3a and b illustrate schematically the flow patterns for a three-dimensional barrier where, for F^{-1} large, the upstream effect is limited by horizontal dispersion to a distance proportional to the ridge length. Using a three-dimensionl nonhydrostatic model, Wells et al. (2005) also found that the upstream location of the horizontal dividing streamline (see p. 76) is linearly related to the across-wind ridge length.

Fig. 3.3 **Flow patterns in plan view showing the effect of a three-dimensional ridge: (a) for F^{-1} large and a ridge length $L_y < S$; (b) the point of flow splitting is close to the ridge ($S \ll L_y$) and a barrier jet forms; (c) cross-section view from the south, corresponding to (a) showing lower flow splitting around the barrier and upper flow passing over it; (d) cross-section view corresponding to (b) showing isentropic surfaces that approximate flow lines. (a) based on Pierrehumbert and Wyman (1985); (c) and (d) on Shutts (1998).**
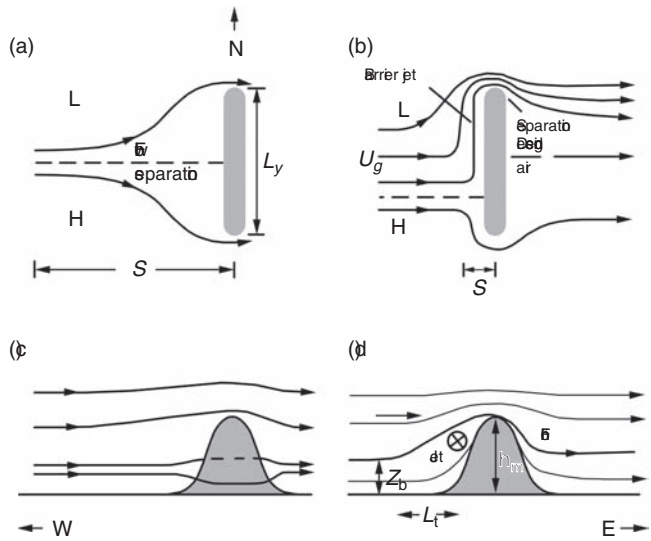
Where the pressure force exerted by the wind on the windward slope (the form drag) causes the flow to become subgeostrophic, the flow moves to the left (in the northern hemisphere) along the mountain, setting up a barrier wind (Figure 3c and d). A relatively simple case of an upwind *barrier jet* can be observed in California along the western slope of the Sierra Nevada, California, in winter, as stable air approaching from the west causes pressure excesses of ~ 5 mb (Parish, 1982). The slowing of the westerly flow upwind decreases the Coriolis force, acting to the right of the geostrophic wind, leading to unbalanced flow which turns northward towards the lower pressure, setting up a southerly low-level jet (LLJ). Air parcels that have been deflected to the left are at lower pressure and so move faster than air parcels on the right side of the flow. Maximum speeds reach 20–$25 \, \mathrm{m \, s^{-1}}$ at around 1 km elevation, and the barrier wind has a width of around 100 km, similar to that reported by Schwerdtfeger (1975b) in the southerly surface winds east of the Antarctic Peninsula in winter. Barrier jets are common off coastal Alaska between $137°$ and $146°$ W, especially south of the east–west, 4–5-km high Valdez-Cordova Mountains. Here, they develop with SSE winds and have an 8–11 percent frequency of occurrence during September–March (Loescher *et al.*, 2006). The large-scale circulation features a deep upper-level trough approaching the Gulf of Alaska and an anomalous ridge over interior Alaska and western Canada (Colle *et al.*, 2006). There is an increasing correlation (reaching ~ 0.7) between the along-coast distribution of the jet and terrain height within about 100 km of the coast. Furthermore, the strength of the barrier wind appears to increase with increasing barrier width (Braun *et al.*, 1999). Along the south coast of Alaska, a distinct category of "hybrid" barrier wind events represents about 45 percent of all cases. These involve a major contribution of cold interior air exiting through gaps in the mountains, particularly the

Copper River delta, Icy Bay, Yakutat Bay and Cross Sound. Flows exiting gaps in high latitudes can rapidly turn parallel to the mountains because the radius of the inertial circle is proportional to f^{-1} (Loescher *et al.*, 2006), in contrast to the situation in the Tropics (Steenburgh *et al.*, 1998).

Shutts (1998) suggests that the maximum barrier wind speed in a steady-state solution is given by:

$$V_b = [(\Delta\theta/\theta) \, gh_0]^{0.5} \, [(h_m/h_0) - 1]$$

where $\Delta\theta$ refers to an interface temperature difference, θ is the mean potential temperature of the two layers, h_m is the barrier height and h_0 is the depth of the airflow. For example, for a barrier of 1500 m, $h_0 = 300$ m, $g = 9.81$ m s^{-2}, $\theta = 280$ K and $\Delta\theta = 3$ K, $V_b = 22$ m s^{-1}. Characteristically, the barrier jet entrance region upwind of the range is closer to the equatorward end of the ridge than to its center in the across-wind direction, as noted by Petersen *et al.* (2005) and earlier in a heuristic model by Shutts (1998) (see Figure 3.3b). Shutts (1998) also shows that the barrier jet will detach from the ridge at its poleward end. This detachment will cause downstream advection of a band of low potential vorticity – an anticyclonic shear line – as reported for the Alps by Thorpe *et al.* (1993). After separation, the air moves downstream as an unbalanced flow for a distance $\sim V_b / f$, where V_b is the speed of the barrier jet; for a 20 m s^{-1} jet, this is about 200 km (Shutts, 1998).

The interaction of the topography of southern Greenland with the circulation associated with passing cyclonic systems plays a major role in the occurrence of high winds off Cape Farewell and off the southeast coast in the Denmark Strait. Using QuickSCAT microwave scatterometry data for 1999–2003, Moore and Renfrew (2005) show that in winter the derived 10-m level winds exceed 25 m s^{-1} in WNW "tip jets," or ENE reversed tip jets, 15 percent of the time south and east of Cape Farewell (at 59.4° N, 42.9° W), and 10 percent of the time as northeasterly barrier winds at 65–67° N in the Denmark Strait. The tip jets develop when air descends over the orography, with velocity conservation according to the Bernoulli principle (see p. 71) and acceleration due to the flow splitting of stable air passing around Cape Farewell. The barrier winds along the Denmark Strait are interpreted as a geostrophic response to stable northeasterly airflow with a low (~ 0.3) Froude number (see p. 109) being forced against the high topography. A reverse tip jet can form when a northeasterly barrier wind reaches the end of the barrier and, in moving from geostrophic to gradient wind balance (see Barry and Chorley, 2003; pp. 114–5) becomes super-geostrophic as a result of the anticyclonic curvature (see Figure 3.3b).

Petersen *et al.* (2005) analyze the combined effect of wind direction and rotation (i.e. Coriolis force) on the flow around a N–S elliptical mountain. The aspect ratio of the mountain varies as the wind direction is changed. They find that, contrary to linear theory without rotational effects (Smith, 1989), for a certain range of non-dimensional mountain height ($= Nh/U$), the flow is blocked for low aspect ratio (see p. 82) while for higher aspect ratio it is not blocked. The upwind barrier wind

is pronounced for southwest flow relative to northwest flow. However, this is not linked to the effects of Coriolis force and mountain-induced flow anomalies. Rather, the drag force and pressure deficit in the wake is greater in the southwest flow case. The interaction of the Coriolis force and low-level flow anomalies leads to a shallower wake and less surface pressure drag in northwest cases than southwest ones.

Barrier effects are observed in winds over the west coast of the South Island of New Zealand, due to the southwest–northeast trending Southern Alps. These mountains average 2000 m in elevation, with peaks rising to 3000 m. During anticyclonic situations with northwesterly airflow, the lower level flow is commonly blocked and deflected by the barrier to give northeasterly winds over the coast and for some distance out to sea (McCauley and Sturman, 1999). For 106 soundings when the winds above 2700 m at Hokitika were from the northwest (270–360°), they found that at 300 m altitude the wind direction was northeasterly (0–90°) on 29 percent of occasions, southeasterly on 10 percent, southwesterly on 38 percent, and northwesterly on 23 percent. The north easterlies also show some flow acceleration and layers of wind maxima.

Mountain barriers exert substantial influence on shallow stable airstreams in high latitudes (Dickey, 1961; Schwerdtfeger, 1975a). In winter, north of the Brooks Range, Alaska, for example, stable cold air approaching the range from the north is deflected to the left, giving westerly *barrier winds* parallel to the mountains. The isobaric temperature gradient perpendicular to the north slope (with cold air against the slope) causes a thermal wind component parallel to the mountain from the east (Figure 3.4a). This is equivalent to a strong south to north pressure gradient, thus giving a *westerly* component of geostrophic wind at the base of

Fig. 3.4 Schematic illustration of barrier winds north of the Brooks Range, Alaska, where northerly upslope flow is deflected to give westerly components at levels near the mountains: (a) vertical cross-section of stable air flowing towards the Brooks Range; (b) plan view of the wind vector (after Schwerdtfeger, 1975a). ∇T, temperature gradient (cold to warm); V_g, geostrophic wind; subscript numeral 0, 1 and 2 denote levels; $V_{o(A)}$ and $V_{o(B)}$ are the surface winds at points A and B, deflected about 30° left of the corresponding V_g.
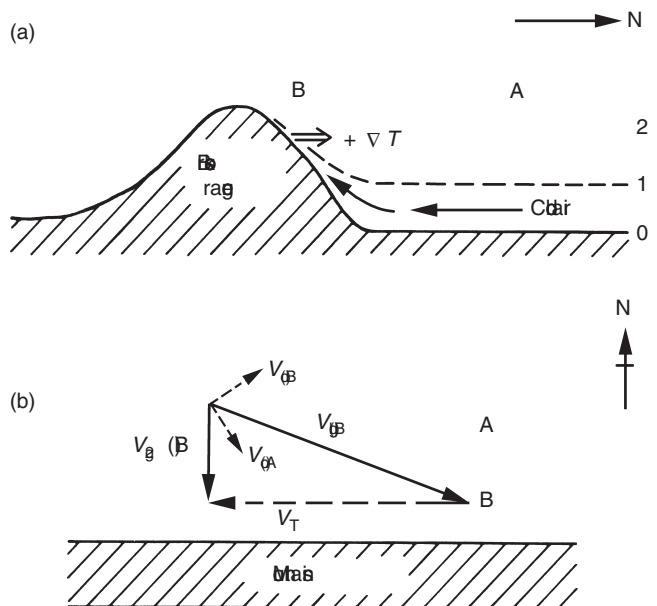
Fig. 3.5   Cold air damming east of the Appalachian Mountain, USA, looking north. There is a sloping inversion above the cold air dome, a cold northeasterly low level jet (LLJ), easterly warm advection over the cold dome, and a southwesterly flow aloft (adapted from Bell and Bosart, 1988).
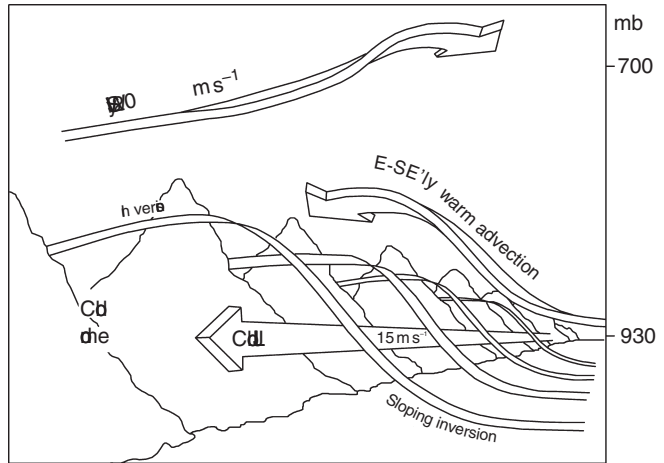
the cold air on the slope. The thermal wind vector between the layers has to be subtracted from the upper layer geostrophic wind in order to obtain the lower layer geostrophic wind (Figure 3.4b). The slope of the terrain (and the cold air boundary), the inversion intensity, and the damming up of the cold air by the barrier, determine the magnitude of the thermal wind effect.

Cold air "damming" against a mountain range is quite widely observed. It is a common occurrence in winter to the east of the Appalachian Mountains in the eastern USA (Bell and Bosart, 1988) when a cold northeasterly airflow is accelerated by a pressure gradient force along the mountain range (Figure 3.5). The Coriolis force (f), acting to the right of the motion in the northern hemisphere, serves to trap the cold air against the eastern slopes of the mountains. Geostrophic balance cannot be established within a Rossby radius of deformation [here $L_R = (g \Delta\theta H/\theta_2)^{0.5}/f$, where H is the depth of the cold air of potential temperature, θ_2, and $\Delta\theta$ is the vertical difference in potential temperature of the mountains], so the cold air is accelerated like a trapped density current (Bluestein, 1993; p. 360). The most frequent, prolonged and intense events are recorded in winter; when three to five events per month can be expected (Bell and Bosart, 1988). Through a synoptic case study (21–23 March, 1985), they show that cold-air damming is critically dependent upon the configuration of the synoptic-scale flow. A U-shaped ridge in the sea level isobars identifies a cold dome. Differential horizontal and vertical thermal advection, as well as adiabatic and evaporative cooling, gives rise to a strongly sloping inversion at the top of the cold dome and a baroclinic zone (a shallow cold front) along its eastern edge. Evaporative cooling accounts for ~ 30 percent of the total cooling in parts of the dome, while adiabatic cooling explains a similar percentage adjacent to the mountain slopes.

The various types of low-level wind maxima discussed above are collectively referred to as low level jets (LLJs). Stensrud (1996) describes their global occurrence and relationship to meso-scale convective complexes and other features. Here,

"Corner effect" on airflow east of the Massif Central (the Mistral), east of the Pyrenees (the Tramontane), and east of the Cantabrian Mountains of Spain (partly after Cruette, 1976). ESL, eastern shear line of the Mistral; WAW, western Alps wake.
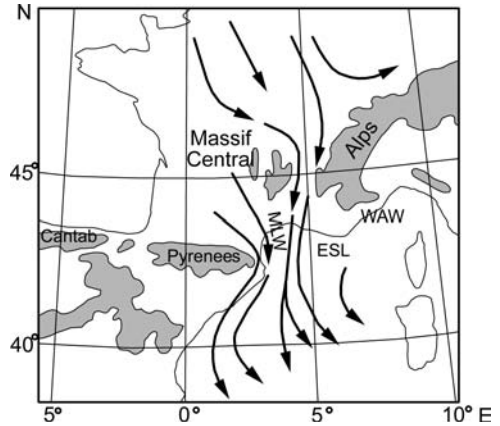
it is only pertinent to note that many recurrent LLJs involve the role of complex terrain (barriers and gaps) but others are forced by inertial oscillations caused by diurnally-varying eddy viscosity in the boundary layer, low-level baroclinicity due to sloping terrain (see p. 135) or cold-air damming, and upper level jet streak forcing, as well as combinations of these processes.

Queney (1963) examined the results of the anticyclonic deformation of streamlines over a ridge. He noted that this sets up an intensified pressure gradient at the left end of the ridge viewed downwind (in the northern hemisphere), referred to as the *corner* effect (Tor Bergeron, in Godske *et al.*, 1957; p. 606). The gradient causes local wind maxima such as that observed during general northwesterly airflow east of the Pyrenees, known as the Tramontane, and the well known Mistral east of the Massif Central in southern France (Cruette, 1976; Pettre, 1982; Jansá, 1987). These patterns are illustrated by the streamlines in Figure 3.6. The Mistral over the Rhone valley and delta has been interpreted as funneling of cold air by the valley, with descent and warming when upper northerly flow overlies the low level flow. The air typically accelerates downstream of Valence and may also strengthen over the Gulf of Lions; winds typically reach 15–$20\,\mathrm{m\,s^{-1}}$ with gusts to $45\,\mathrm{m\,s^{-1}}$. Jiang *et al.* (2003) re-examine the Mistral using the detailed MAP data and find that on different occasions it may have the characteristics of a gap wind or a "fall" wind (see p. 170) The airflow is sometimes deep enough to override the Massif Central and there is cloud clearing in the lee. The Mistral is also wide enough to be affected by the Coriolis force. Under large-scale NNW flow over Western Europe, blocking by the Swiss Alps may form a cold air reservoir, from which cold air leaks in to the upper Rhône valley and accelerates into the Mistral. On its west flank, the Mistral is separated from the Tramontane by a wake formed by a hydraulic jump (see p. 159) in the lee of Mount Lozère in the southern Massif Central. To the east, a shear line separates the Mistral from a wake in the lee of the Western Alps (Jiang *et al.*, 2003; Guenard *et al.*, 2006). (Meso-scale wakes in the lee of island mountains, and other features occurring with the Mistral, are discussed below, p. 164 and p. 183,

respectively), The origin of the wake is not established but may involve kinetic energy dissipation in hydraulic jumps.

The degree of influence of the Alps on airflows depends on the flow direction according to Reuter and Pichler (1964). For 500 mb northerly flow, the latitudinal decrease in the Coriolis term is balanced by orographically induced anticyclonic curvature (see p. 126), resulting in no significant deflection. For southerly flow, the orographic and Coriolis terms have the same sign leading to reduced wave amplitude. Jiang (2006) demonstrates that the concave form of the southern Alps ridge line around $7°$ and $14°$ E modifies the occurrence of flow confluence over the upwind slope and leads to enhanced precipitation.

Mountain barriers also modify the wind field through differential pressure effects. Observations across many mountain ranges show two characteristic types of flow disturbance: first, a pressure differential (of the order of 10 mb at the surface) between windward (high) and leeward (low) slopes of the range; and second, an upstream deflection of airflow to the left in the northern hemisphere, in association with the orographically-disturbed pressure field (Smith, 1982). Some of the pressure differential may be caused by horizontal temperature advection and latent heat effects; the typical "föhn nose" evident on synoptic pressure maps during classical föhn situations in the Alps and Rocky Mountains illustrates such effects (Malmberg, 1967; Brinkmann, 1970). Pressure data from valley stations, however, are commonly biased by daytime heating and nocturnal ponding of cold air (cf. Walker, 1967). The windward-side high pressure "nose" in Smith's (1979a; p. 103; 1982) analyses is primarily attributable to hydrostatic flow over the mountains; lifting causes mid-level adiabatic cooling creating a deeper layer of cool, dense air, which hydrostatically increases the lower level pressure. In the lee of the mountain range, warm air descends to replace that deflected by the barrier. Smith (1982) shows that for steady hydrostatic flow, air approaching a mountain range decelerates as it encounters the high pressure region; the Coriolis force is thereby decreased and the air turns to the left (in the northern hemisphere) because of the background pressure gradient (see barrier winds, p. 133). The essence of this theory is the alteration of the horizontal trajectories of air parcels by the Coriolis force, whereas the pressure field is unaltered. In contrast, idealized geostrophically balanced flow, with isentropic surfaces parallel to the terrain, requires an unrealistic "mountain anticyclone" (Smith, 1979a, 1982).

3.1.2.2 Frontal modifications

Over high mountains and plateaus, weather conditions during the passage of synoptic systems reflect the fact that upper level features become "surface" ones over high ground. Taylor-Barge (1969) notes that *tro*ughs of *w*arm *al*oft ("trowals" in the terminology of the Canadian Atmospheric Environment Service), for example, may affect the weather on the St Elias Mountains above 2500 m. Likewise, studies of weather on the Greenland ice sheet show that 700-mb synoptic analyses best describe frontal systems crossing the area (Hamilton, 1958a, b).

Fig. 3.7 An example of a streamline analysis for the Alps, omitting areas exceeding 750 m altitude, 24 June 1978 (from Steinacker, 1981).
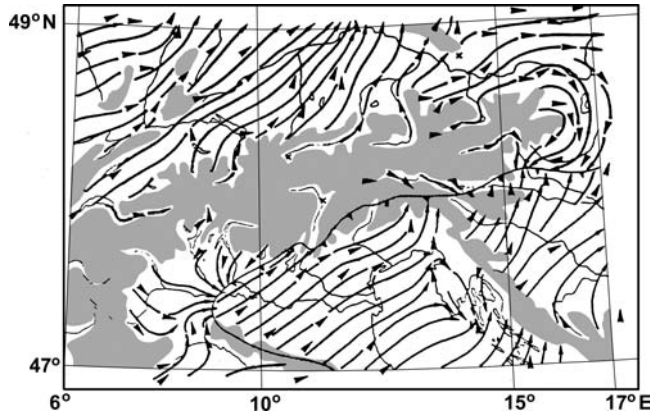
The routine analysis of synoptic phenomena in mountain areas is greatly hindered by the limited availability of data and the pronounced meso-scale effects induced by the orography. Special analyses are necessary in such circumstances; Steinacker (1981) suggests the use of streamline analyses that omit areas lying above 750 m altitude, as illustrated in Figure 3.7, and also the analysis of stream functions on isentropic surfaces. Available mountain station data can be incorporated into 850 and 700 mb analyses, if any systematic errors exist, they are first removed by comparison of their long-term mean values with those at surrounding stations. Rawinsonde data also need adjustment, when pressure tendencies are large, if there is a time difference between the sounding and the standard synoptic observation.

There are several dynamic and thermodynamic mechanisms involved in the orographic modification of frontal characteristics. One category of effect is referred to as "masking" (Godske et al., 1957; pp. 610). Fronts crossing mountain systems with extensive intermontane basins may over-ride shallow cold air. This can diminish the low-level temperature contrast across a cold front and accentuate that across a warm front. In situations where pre-frontal föhn occurs, a warm front can also be masked due to the reduced temperature difference.

Dynamic and thermodynamic effects of orography result from the forced ascent of air over the barrier, which leads to distortion of the temperature structure through adiabatic processes. Since warm fronts have a typical slope of $1:100$, subparallel to the usually steeper ($1:20$) windward slope of the barrier, air ahead of the front can become trapped, thus tending to retard the motion of the lower section of the front (Figure 3.8). This gives rise to prolonged cloud and rain on the windward slopes. The motion of the upper front is unimpeded and lee-slope föhn may cause it to separate from the lower front, with subsequent regeneration taking place downwind of the range. As a result of such retardation of warm fronts approaching the Scandinavian Mountains, or Greenland, from the west, the system may occlude with a new center developing to the south where the warm

Fig. 3.8   **The effects of mountain barriers on frontal passages: (a) warm front advance; (b) windward retardation; (c) separation.**
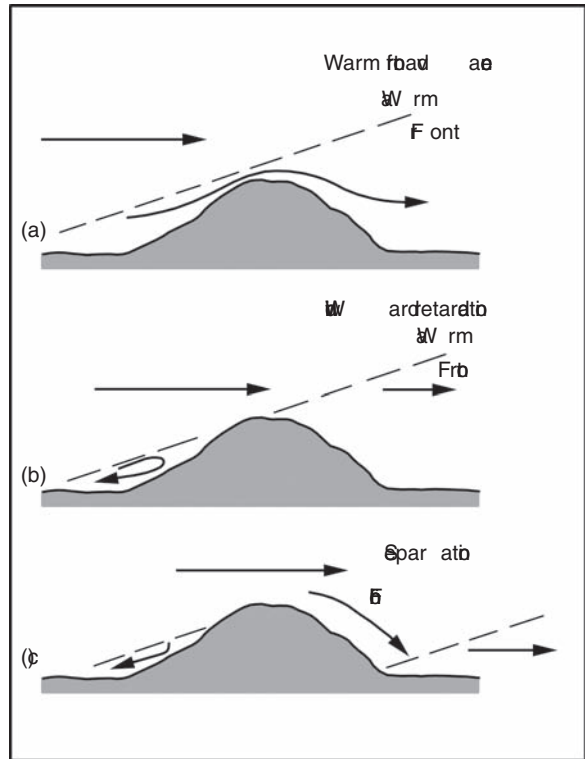
front swings around the barrier (Godske *et al.*, 1957; pp. 613). Cold fronts, with a typical 1:50 backward slope, also tend to be slowed down by mountain barriers, since the wind component normal to the front is slowed first, and to a greater degree, at lower levels. This tends to lift the frontal surface through the accumulation of cold air near ground level (Radinovic, 1965). In these situations, cold air may penetrate through major gaps in the mountain barrier, thus distorting the frontal profile. This is often apparent when cold fronts move southeast across Spain and France, encountering the Pyrenees, Massif Central and Alps. When a cold front crosses a mountain barrier, it undergoes stretching near the southern end of the range according to Smith (1982). This helps to accentuate cross-front gradients, which may serve to promote baroclinic instability.

Mesoscale model simulations of cold front passages over mountain ridges of varying height and width are reported by Dickinson and Knight (1999). They find that for tall/narrow mountains and weak fronts, there is upstream blocking and frontal propagation is discontinuous across the ridge. For low/wide mountains, and strong fronts, there is only weak retardation on the windward slope and the front moves continuously across the mountain. Regardless of mountain size and shape, the front reaches the base of the lee slope stronger, sooner, and with a decreased cross-front scale compared to a "no-mountain" simulation.

Fig. 3.9 Schematic picture of a cold front propagating across a mountain ridge. The isolines depict potential vorticity (after Dickinson and Knight, 2004).

Figure 3.9 illustrates how a mountain retards and blocks an approaching cold front at the surface while the upper-level anomaly of potential vorticity (PV) associated with the front moves eastward unaffected. Warm advection ahead of the lee trough forces convergence and cyclonic vorticity growth near the base of the lee slope creating a secondary trough. The approaching upper-level PV anomaly then couples with this new surface vorticity center and propagates downstream. The original surface front remains trapped on the windward slope and slowly erodes.

Figure 3.10 illustrates a detailed analysis of isochrones of a cold front moving over the Alps (Steinacker, 1981); note the lee side acceleration of the front. Lydolph (1977; pp. 160–9) describes other examples. In the lee of a range, and in intermontane basins, the presence of residual pools of cold air can weaken the lower section of a cold front.

Retardation and distortion of fronts also cause modifications of the vertical motion field and therefore of cloud and precipitation patterns. For example, when uplift on the windward slope results in precipitation, fronts that cross the range resemble those in a dry atmosphere. This implies an absence of condensational heating and weakening of the frontogenetic tendencies (Palmén and Newton 1969;

Fig. 3.10   Isochrones showing the
passage of a cold front over
the Alps, 0000 GMT 23 June
to 1200 GMT 25 June 1978
(from Steinacker, 1981).

pp. 265 and 344). In general, frontolysis (frontogenesis) is favored on the windward (leeward) slopes of mountain barriers in the westerlies due to forced ascent (descent) and adiabatic cooling (warming) of the air ahead of the front. Airborne Doppler radar observations of a cold front approaching the Cascade Mountains, 200 km inland from the North Pacific Ocean in Oregon, on 8–9 December 2001, show that the associated wide frontal rain band rapidly weakened due to upstream blocking of low-level flow, reducing the flow towards the front from behind, and the presence of a mountain wave-induced perturbation that increased the westerlies over and upstream of the crest of the range, thereby weakening the (relative) flow towards the front from ahead of it (Bond *et al.*, 2005).

Mountain effects are most pronounced when fronts move in a direction perpendicular to the barrier, although, even then, the system may undergo some deflection towards one end of the range. The effects also depend on the intensity and speed of the system. The modification of strong, rapidly moving systems crossing the St Elias Mountains, Alaska–Yukon, for example, is limited, while fronts moving parallel to the range are scarcely affected (Taylor-Barge, 1969). Studies during ALPEX illustrate considerable complexity (Smith, 1986). As a cold front approaches the Alps from the northwest, the cross-front winds that advect the front at low levels like a density current are blocked or deflected by the barrier. A shallow pre-frontal south föhn is often experienced in the northern Alpine valleys associated with higher pressure to the south. This conjunction promotes the formation of an orographic low-level jet (Egger, 1989). The cold air is accelerated eastward along the mountain front as a trapped density current since the mountains block the Coriolis acceleration to the right. This flow favors propagation of the front along the north side of the Alps producing a lateral "nose"; cold air may penetrate around the mountains into Slovenia–Croatia. This is similar to the features associated with cold air damming east of the Appalachians (Figure 3.5) and for flows east of the Great Dividing Range in Australia where the cold outbreak is termed the "Southerly Buster." In each case, the cold air commonly forms a wedge banked up against the eastern slopes of the mountains.

3.1.2.3 *Lee cyclogenesis*

Lee cyclogenesis is of major importance downwind of mountain barriers to the mid-latitude westerlies. The distribution of cyclogenesis in the northern hemisphere in winter is shown in Figure 3.11. It is immediately apparent that all major centers are in the lee of mountain ranges – the Rocky Mountains (in Colorado and Alberta), the European Alps (in the Gulf of Lions) and the Tibetan Plateau (over northwestern China). The topic merits discussion here in terms of the processes involved and also because the lee cyclone may affect weather conditions at least on the lee slopes.

The effect of the Rocky Mountains in causing cyclogenesis, especially in eastern Alberta and Colorado, is well known (Hess and Wagner, 1948; McClain, 1960; Hage, 1961; Chung *et al.*, 1976; Palmén and Newton, 1969, Chapter 11). Buzzi *et al.* (1987) state that cyclogenesis in the lee of the Rocky Mountains involves the following events.

(1)   A precursor low-pressure system over the Pacific Ocean that slows, moves northward and fills as it approaches the west coast.
(2)   The parent low disappears above the Rocky Mountains while a pre-existing lee trough, associated with low-level adiabatic warming in the westerly downslope flow component, strengthens.
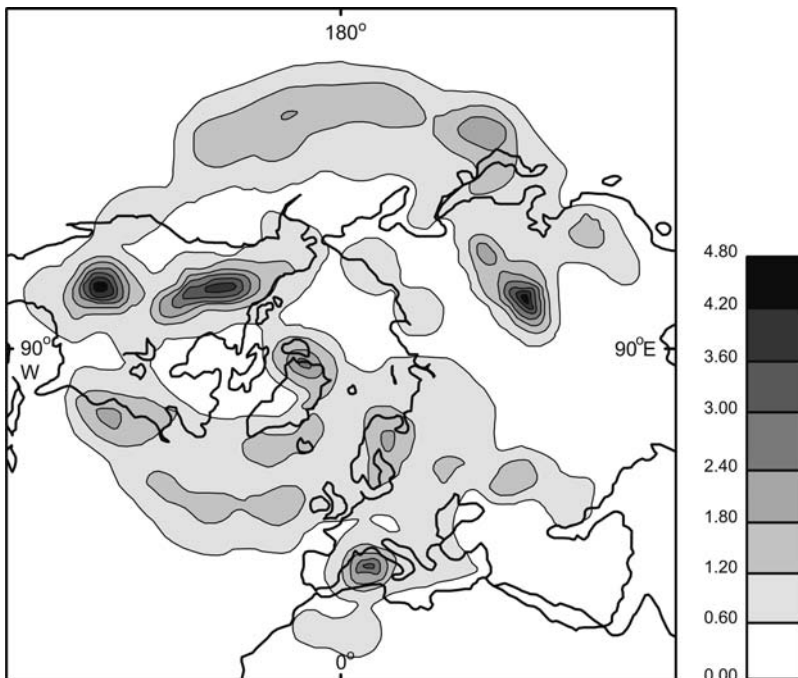
Fig. 3.11 The density of cyclogenesis (per 10^6 km^2 per month) in the northern hemisphere analyzed from ECMWF ERA-15 reanalysis data, updated with operational analyses, for December–February, 1979–2000 (from Hoskins and Hodges, 2002).

(3)   Cyclonic vorticity generation takes place east of the mountains and a lee cyclone develops to the south of the latitude of the parent system (typically over either Alberta or Colorado).

(4)   In the subsequent stage of development, cold air advection offsets any warming due to adiabatic descent. The cyclogenetic tendencies continue, however, as a result of upper level advection of positive (cyclonic) vorticity with upper level divergence encouraging low-level convergence and rising air.

(5)   The surface cold front of the Pacific system may move into the lee trough and orographic effects cease as the downslope component of flow disappears with a shift of the surface wind direction to the northwest.

(6)   The cyclone drifts southeastward whilst it remains close to the mountains and then accelerates northeastward and may re-intensify.

Karyampudi *et al.* (1995a, b) provide a case study of cyclogenesis in the lee of the Rocky Mountains in April 1986 using wind profiler and hourly meso-meteorological observations. A Pacific cyclone and cold front moved eastward towards the Rocky Mountains, accompanied by an upper-level jet streak, and this generated a meso-scale lee cyclone and a trailing wind-shift line. Lee cyclo-genesis occurred due to the conjunction of upper-level frontogenesis with the low-level mesocyclone. A meso-scale tropopause fold extruded downwards to the middle troposphere in association with the descending secondary upper-level jet streak. A stable region was present in the mid-troposphere, as a result of low-level adiabatic warming and mid-level cooling east of the Rocky Mountains. Propagation of the jet stream into this stable region gave rise to unbalanced flow conditions at scales less than the Rossby radius of deformation (Note 2).

Cyclones forming in the lee of the Alps may occur in any season, but are most frequent in autumn and the cold half-year generally. Two patterns leading to lee cyclogenesis have been identified from the ALPEX studies (Pichler and Steinacker, 1987). They are listed here.

(1)   Blocking of cold northwesterly airflow by the Alps. A Mistral in the Rhône valley accompanies this pattern as cold air flows around the Alps. In this type, a cyclone is present upstream of the Alps; this weakens on the windward side and intensifies downwind of the mountains. The system develops and moves rapidly southeast causing limited effects within the Alps.

(2)   Southwesterly upper-level flow ahead of an eastward-moving trough. Here, blocking and flow splitting may generate a warm front over northern Italy and a cold front in the Gulf of Genoa.

Laboratory model studies simulating the orography of the Pyrenees and Alps by Boyer *et al.* (1987) indicate that, with westerly to northwesterly flows, flow splitting is generated west of the Alps with lee vortex development. This is illustrated in Figure 3.12.

The processes involved in the case of the Alps are complex (Speranza, 1975; Buzzi and Tibaldi, 1978; McGinley, 1982; Radinovic, 1965, 1986). An analysis of eight
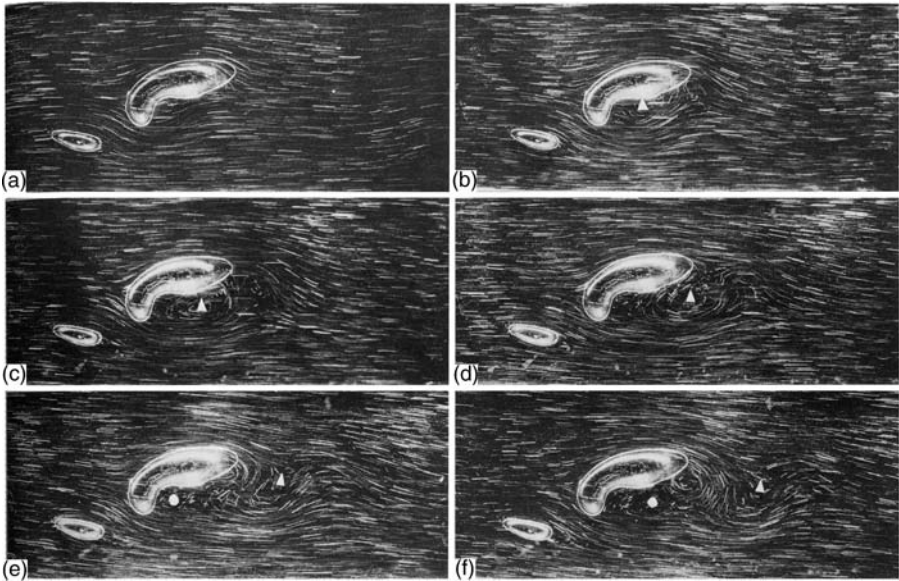
Fig. 3.12 Cyclonic eddies forming in westerly flow over a model Alpine/Pyrenean topography. The laboratory experiment uses a towed obstacle in a linearly stratified rotating water channel 2.4 m long, 0.4 m wide and 0.3 m deep. The flow evolves from (a) 13 h equivalent atmospheric time through (b) 26 h (c) 39 h (d) 52 h (e) 65 h and (f) 78 h, respectively. The triangle marks the center of the first cyclone and the circle the second; flow splitting occurs at the western end of the Alps (D. J. Boyer and *Met. Atmos. Physics* 1987, Springer).

cases of Alpine lee cyclogenesis during ALPEX (March–April 1982) shows that over a 27-h period they develop from the surface upward to 300 mb (Radinovic, 1986). Half of these were most intense at the surface, the other half in the upper troposphere. The eight cases show that lee cyclogenesis is preceded by diffluent upper level flow over the Alps and western Mediterranean. Cyclogenesis is triggered by the orographic blocking of a meridional flow of cold air and an increase of baroclinicity in the lower troposphere (McGinley, 1982). Development begins when an upper trough approaches the Alps and undergoes deformation.

A case study by Buzzi and Tibaldi (1978) illustrates the interaction between topography and a cold front advancing from the northwest, operating in conjunction with an intensifying upper-level baroclinic field over northern Italy (Figure 3.13 a–d). They show that it is important to distinguish between the low-level effects of the Alps on the pressure field and on frontal structures, on the one hand, and upper tropospheric adjustments on the other. Below 2 km, where the Alps form a 450 km barrier to westerly airflow (Egger, 1972), interaction between the barrier and the airflow initiates a low-level pressure perturbation with anti-cyclonic vorticity, produced by vortex tube compression, over the mountains and cyclonic vorticity set up in the lee. The arcuate, convex shape of the western Alps causes distortion of the thermal field at low levels due to blockage of the cold air, and this, accentuated by cold air advection west of the Alps along the Rhône valley, modifies the upper tropospheric flow structure, as implied by the thermal wind
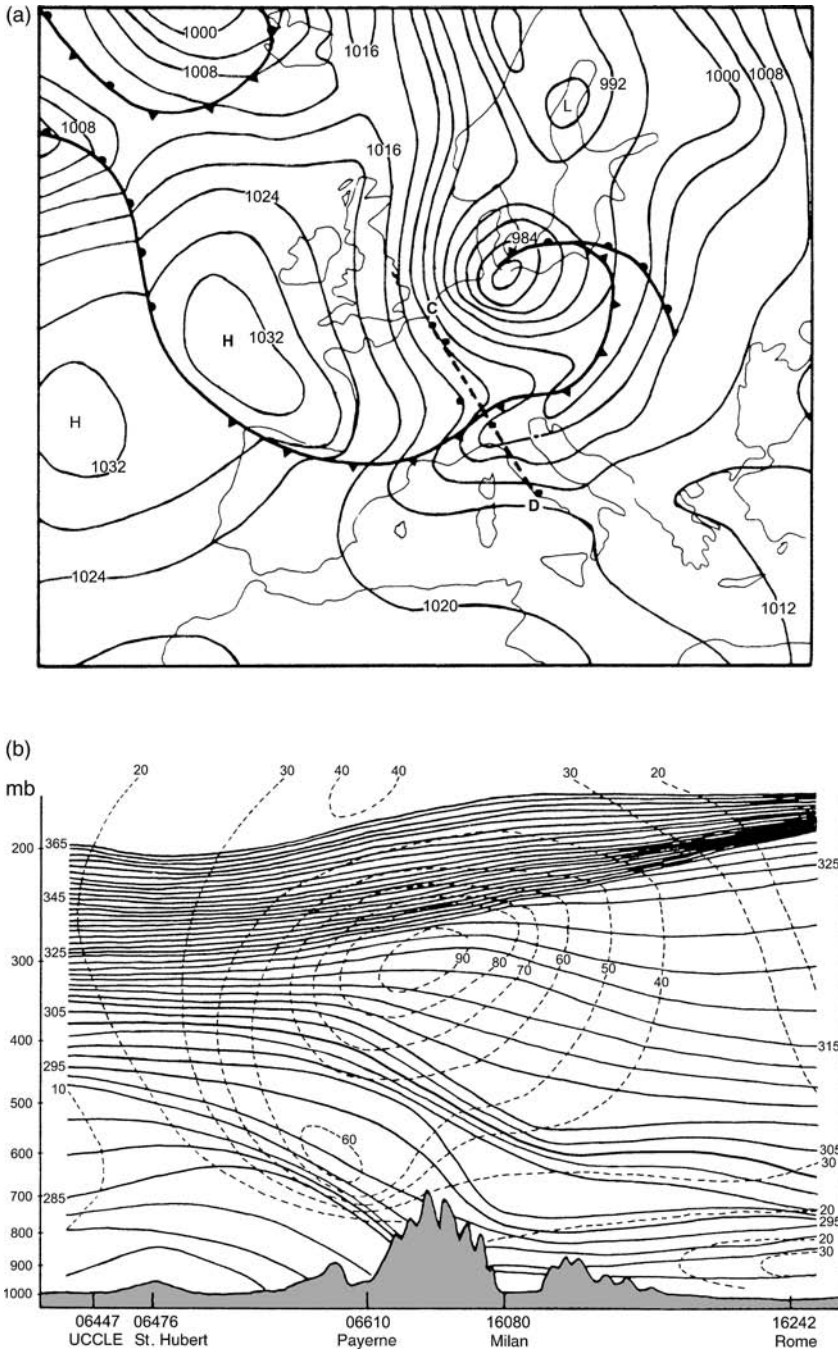
Fig. 3.13 Lee cyclogenesis associated with a frontal passage over the Alps. (a) Surface pressure map, 3 April 1973, 0000 GMT; (b) Cross-section along the line C–D of (a). Isentropes (K) and isotachs (knots); (c) As (a) for 1200 GMT; (d) As (b) for 1200 GMT along the line E–F (from Buzzi and Tibaldi, 1978).
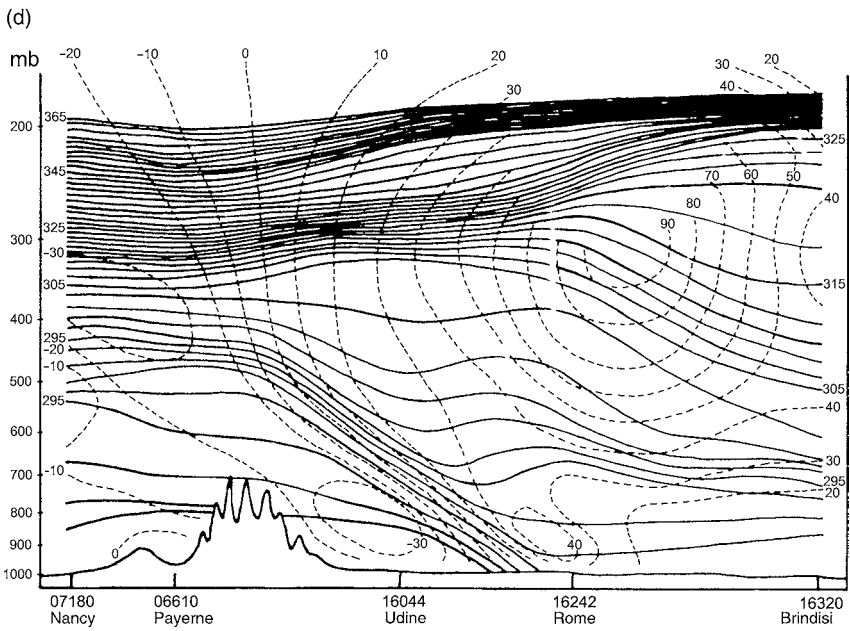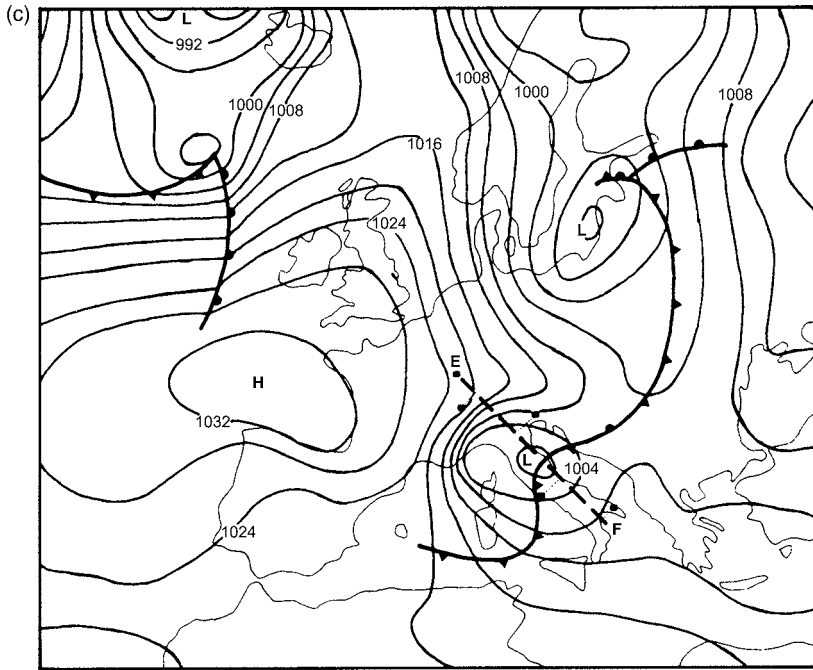
Fig. 3.13   (cont.)

relationship (Radinovic, 1965). Thus, strong northwesterly jet streams across France tend to split with one branch curving cyclonically eastward, north of the Alps, and the other penetrating southward toward the Gulf of Lions (Buzzi and Rizzi, 1975). According to Radinovic, the effects of nonadiabatic heating (such as condensation release) on the thickness field changes are much less than those caused by the blockage or retardation of advection in the lower layers. The 1000–500 mb thickness pattern typically shows a trough west of the Alps, that is deformed as it approaches the mountains, and a ridge in the concave lee area of the Alps related to cyclonic development at the surface. Cyclogenesis takes place on the eastern limb of a confluent thermal trough, associated with the southward penetration of cold air to the west of the Alps and the ridge south of the mountains. Illustrations of thickness patterns and cyclogenesis/anticyclogenesis are given by Sutcliffe and Forsdyke (1950); and also by Stringer (1972; p. 407).

Several studies indicate that in many cases an eddy forms in the lee of the Alps *prior* to the arrival of post-frontal cold air. This is related to low-level blocking of the cold air mass accompanied by flow splitting and frontal deformation. The maximum height of the barrier seems to control the blocking, not an "average" height of the mountain surface. The criteria for determining the likelihood of blocking and flow splitting by a mountain barrier are rather arbitrary and are not always reliable. Chen and Smith (1987) examined low-level trajectories of northerly and northwesterly flows of post-cold frontal air approaching the Alps. They defined a splitting parameter S as the length of the Alps (800 km) divided by the distance between the starting positions of two flow trajectories that just pass round the west and east ends of the barrier (near Lyon and Vienna, respectively). Blocking occurs for $S \sim 2$, whereas for $S \sim 1$ there is no blocking. They note, however, that in all eight cases analyzed, the surface winds north of the Alps are steered parallel to the mountains. A second key element is the advection of upper-level vorticity across the mountains in propagating jet streaks (Mattocks and Bleck, 1986). Such high velocity wind zones are associated with intense cyclones moving directly over the Alps, rather than passing to the north.

In the example shown in Figure 3.13 there is strong cold air advection on the windward side of the Alps in the northern and western sectors of the cyclone and above mountaintop level over the developing surface cyclone. The orographically induced pressure perturbation (Figure 3.13a, b) is initially sub-synoptic scale (250 km). When cold air begins to flow over the mountains, and around them (via the Rhône valley) into the western Mediterranean, the upper trough moves over the low level cyclone. This causes positive vorticity advection aloft that triggers baroclinic instability. Rapid pressure falls associated with this readjustment are then followed by more moderate deepening and enlargement of the system as a synoptic-scale upper level trough deepens with the intensification of the thermal gradient parallel to the convex front of the Alps and the deflection of the upper jet system (see Figure 3.13d). Vertical coupling between the low-level pressure perturbation and the upper trough then allows for normal development by baroclinic instability forming a cut-off low.

In an attempt to provide a comprehensive theory of lee cyclogenesis, Buzzi *et al.* (1987) stress the direct interaction between orography and pre-existing baroclinic waves. The large-scale slopes of the mountains modify the spatial structure of the waves, so that the wave amplitude intensifies downwind on the warmer side of the mountain and weakens on the colder upstream side. Radinovic (1986) noted that sea level pressure tendencies (based on eight cases of cyclogenesis during ALPEX) were positive (rising) north of the Alps and negative (falling) over Italy. The modifications occur on a scale comparable with the Rossby radius of deformation (i.e., the horizontal distance beyond which rotational effects exceed buoyancy effects). A case study for the Alaskan Coast Ranges (cyclogenesis in the Gulf of Alaska during northwesterly air flow parallel to the mountains) and model simulations for cyclogenesis in the lee of the Alaska ranges, the Rocky Mountains, and the Tibetan Plateau, support the theoretical concepts. For cyclogenesis west of the mountains bordering the Gulf of Alaska, cyclogenetic tendencies are enhanced because the thermal wind is parallel to the mountains. However, the approach of an upper trough from the northwest sets off the development. Similar pre-existing lows are found in the other two areas. Lee cyclogenesis occurs as lows approach the Rocky Mountains from the Pacific, or the Tibetan Plateau from the west.

In the lee of the Alps, some 10 to 20 cases of moderate to strong lee cyclones occur annually (Tibaldi *et al.*, 1990). Critical factors in their initiation are:

(i)   the blocking of cold air on the windward side of the Alps as a cold front, associated with a parent cyclone to the north, approaches from the northwest; and

(ii) the distortion of the front by the orography, with a delay in the advection of cold air to the lee side. A positive thermal anomaly develops at low levels in the lee, and frontogenesis occurs over the mountains. The initial growth stage involves strong orographic influence operating on the meso-scale deepening of a trough aloft, with a jet maximum directed towards the western Mediterranean. The upper flow splits around the Alps and this tends to fill the upper trough north of the Alps and deepen it to the south.

Lee cyclogenesis is thought to be attributable mainly to a wave-scattering process rather than vortex generation by an obstacle in the flow. Following the initial stages, baroclinic instability leads to a synoptic scale cyclone. The end result is often a cut-off low extending through the troposphere. Most of the cyclones forming in the lee of the Alps move out over the eastern Mediterranean and have a life-time of about 4 days.

Flow deflection and lee side effects are observed over mountains in the Sahara. In summer, the Hoggar massif (25° N, 7.5° E) augments an anticyclonic circulation above and to the north of it, leading to stronger easterlies upstream of the barrier and a rotation of wind direction from southeasterly to northeasterly. This flow pattern contributes to a leeward pressure trough that enhances the Saharan heat

low around 15–20° N, 25° E–10° W (Dobrinski *et al.*, 2005). The amplification of the heat low is also associated with the abrupt onset of the West African monsoon in late June. The pressure difference across the Hoggar increases from 2.4 mb before the onset to 3.6 mb after onset. In contrast, the Tibesti mountains and Ennedi plateau do not show any significant effects on the airflow or pressure field.

3.1.3   Local airflow modification

3.1.3.1   Wave phenomena

Airflow over mountains involves motions with a horizontal scale of 1–100 km, apart from the major long wave features discussed earlier (p. 125), and these perturbations to the flow are of great importance to weather in the immediate area.

The behavior of airflow over an obstacle depends principally on: (1) the vertical wind profile; (2) the stability structure; and (3) the shape of the obstacle. First, we can examine the effects of a simple long ridge perpendicular to the airflow for the case of a stable atmosphere, where the potential temperature increases with height. For these conditions, Förchgott (1949) distinguished three basic types of flow, according to the vertical profile of wind speed (Figure 3.14). With light winds that remain essentially constant with height, the air flows smoothly over the ridge in a shallow wave (a) and there are only weak vertical currents. This is known as *laminar streaming*. When the wind speeds are somewhat stronger and show a moderate increase with height, the air overturns on the lee side of the barrier forming a *standing eddy* (b). With a more intense vertical gradient of wind speed, the oscillation caused by the mountains sets up a train of *lee waves* (c) and wave clouds for 25 km or more downwind (Figures 3.15 and 3.16). These are stationary gravity waves, provided that the flow conditions do not change. Lee waves usually form only when there is a deep airflow directed within about 30° of perpendicular to the ridgeline, with little change in wind direction with height. These are known as transverse waves. The wind speed must increase upward, with a minimum horizontal velocity of about 7 m s^{-1} at the crest for low ridges (1 km) and 15 m s^{-1} for ranges 4 km high (Nicholls, 1973). In b, c and d of Figure 3.14, the streamlines show separation of the airflow from the surface.

When separation occurs, rotor motion develops forming individual vortices below the wave crests (Scorer, 1955). Rotors are highly turbulent zones that present a severe hazard to aircraft. Sometimes, the vortex may attain mountain-sized dimensions as illustrated for Mt. Fuji, Japan (Soma, 1969) and the Little Carpathian Ridge, Czechoslovakia (Förchgott, 1969). In katabatic drainage (see p. 187), separation is suppressed since the flow follows the slope, whereas under convective conditions especially on the lee slope, the likelihood of separation is enhanced. Generally, separation occurs when the air in the overlying layers cannot maintain the necessary steady motion (see p. 187). However, its occurrence reduces the effect of the mountains on the upper-level airflow, by lessening the lee wave amplitude (Scorer, 1955).

Förchgott's scheme is supported by the conclusions of an observational program carried out in the French Alps by Gerbier and Bérenger (1961). They distinguish
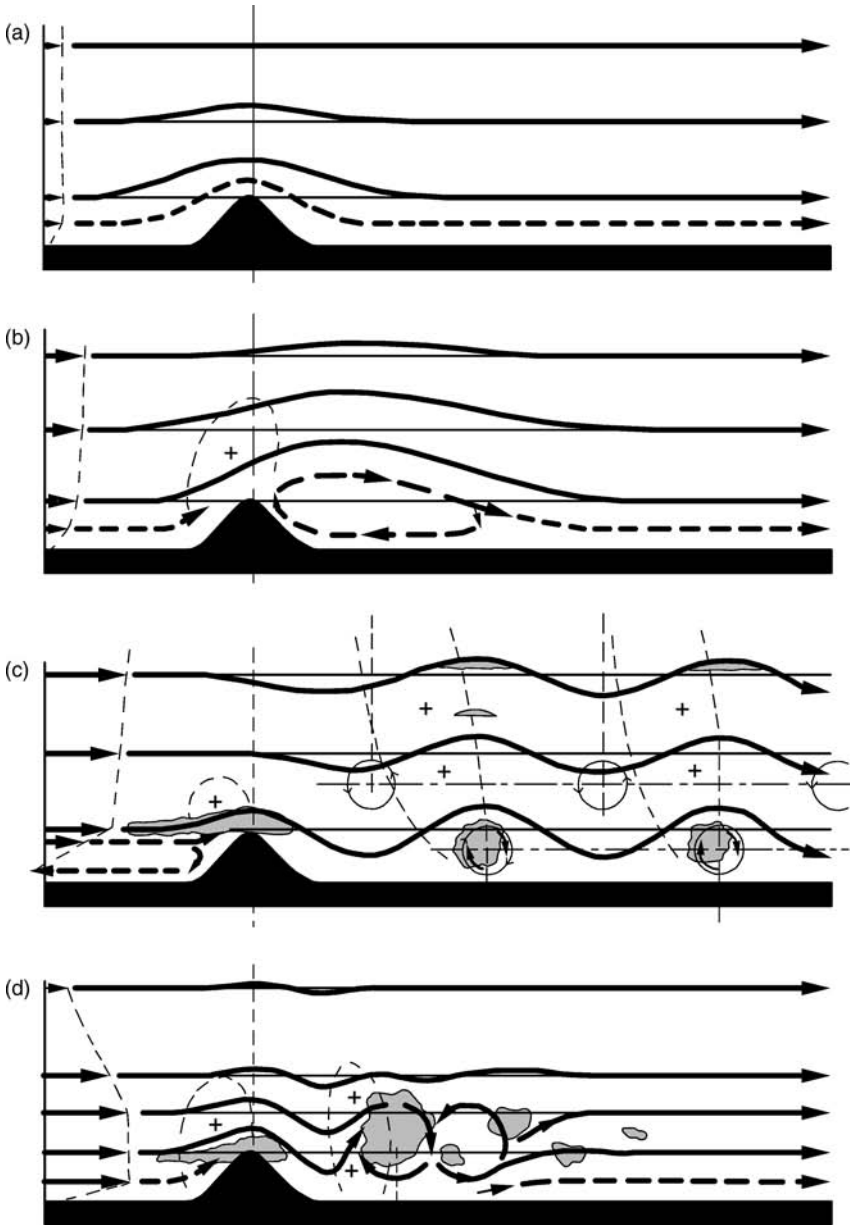
Fig. 3.14 **Types of airflow over a mountain barrier in relation to the vertical profile of wind speed. (a) Laminar streaming; (b) Standing eddy streaming; (c) Wave streaming, with a crest cloud and downwind rotor clouds; (d) Rotor streaming (from Corby, 1954).**

Fig. 3.15 Lee wave clouds – a pile of plates, Sangre da Cristo, Colorado (E. McKim).

Fig. 3.16 Lee wave clouds in the San Luis valley, Colorado (G. Kiladis).

three general cases according to the strength of the wind component normal to the ridge.

(1)   For winds $< 8\,\text{m s}^{-1}$, any waves are weak and shallow. Turbulent flow predominates with one lee rotor. The mountain effect is limited to the layer of speed discontinuity 100–200 m above the ridge crest.

(2)   For winds of 8–$15\,\text{m s}^{-1}$, the flow is more turbulent with a succession of low-level rotors in phase with the ridges. Waveforms increase in amplitude with height if the speed is constant, and are stronger if the atmosphere is stable.

(3)   For winds $> 15\,\text{m s}^{-1}$ the features are similar to case (2). The lee wavelength and their vertical amplitude and the occurrence of rotors depend on the stability and vertical gradient of wind speed. Rotors tend to be weak if the stratification is stable and the wind speed increases regularly with height.

Theories of airflow over mountains are mathematically complex and only the essential points can be given here. A topographic barrier initiates a vertical displacement in air crossing it and, on the lee side, this is counteracted by the

restoring force of gravity. The air commonly "overshoots" the equilibrium position and thereby develops vertical oscillations as it flows downwind. If the atmosphere is stable and winds are light, the oscillation period is short (i.e. high frequency) whereas, in situations with low stability and strong winds, slow oscillations of long wavelength are formed. A stable atmosphere favors the formation of short-wavelength, large-amplitude waves by facilitating the restoring action of the force of gravity on the air motion; the occurrence of a shallow inversion near the ridge crest is especially effective (Corby and Wallington, 1956). The natural air stream oscillations are disturbed over mountains, with *resonance* occurring if a topographically forced wave amplifies the "free" waves (Beer, 1976).

The natural frequency of vertical oscillation for a compressible medium, in the absence of frictional and pressure effects, is referred to as the Brunt–Väisälä frequency; it has a magnitude of the order of $10^{-2}\,\mathrm{s}^{-1}$, and is given by

$$N = \frac{1}{2\pi}\left[\frac{g(\Gamma - \gamma)}{T}\right]^{1/2} = \sqrt{S/2\pi}$$

where S is the static stability parameter; Γ is the adiabatic lapse rate (defined as positive for a decrease of temperature with height); γ is the environmental lapse rate ($= \partial T/\partial z$).

Wilson (1968) shows that the maximum vertical displacement of an air parcel from a given reference level is $w/\sqrt{S}$, where $w =$ vertical velocity. For an isothermal atmosphere ($\partial T/\partial z = 0$), where $T = 270\,\mathrm{K}$, $1/\sqrt{S}$ is 53 s; in this case, the displacement ranges from 0.5 m for $w = 1\,\mathrm{cm\,s}^{-1}$ to 160 m for $w = 3\,\mathrm{m\,s}^{-1}$. Greater (smaller) displacements occur in more unstable (stable) conditions.

In the presence of pressure gradients a vertically-displaced air parcel can oscillate along a path tilted from the vertical by an angle θ; in this case the oscillations have a reduced frequency $N\cos\theta$ (Durran, 1990).

In a stratified atmosphere, flowing over sinusoidal ridges, gravity waves occur when the intrinsic frequency ($n_i = \overline{U}k$) of the motion is less than the Brunt–Väisälä frequency; here $k = 2\pi$/wavelength of the terrain ridges. This type of gravity wave is *vertically propagating*, implying that the disturbance does not decay with height. The phase lines for such waves tilt upstream with height, associated with the propagation of energy vertically upward (the group velocity) (Figure 3.17). It is assumed that no components of the flow can radiate energy downward (the "radiation condition"). The energy flux is parallel to the parcel trajectories in the gravity wave. The pressure and velocity perturbations are zero where the buoyancy perturbations have extreme (maximum and minimum) values, as shown in Figure 3.17. Wave fronts, or lines of constant phase, propagate perpendicular to the energy flux and air parcel trajectories. It should be noted that a steady airflow crossing sinusoidal ridges can set up waves that are aligned vertically with the ridges, and decay exponentially with height (evanescent waves), if $\overline{U}k > N$. This is because buoyancy forces cannot be supported at frequencies in excess of the Brunt–Väisälä frequency (Durran, 1990).
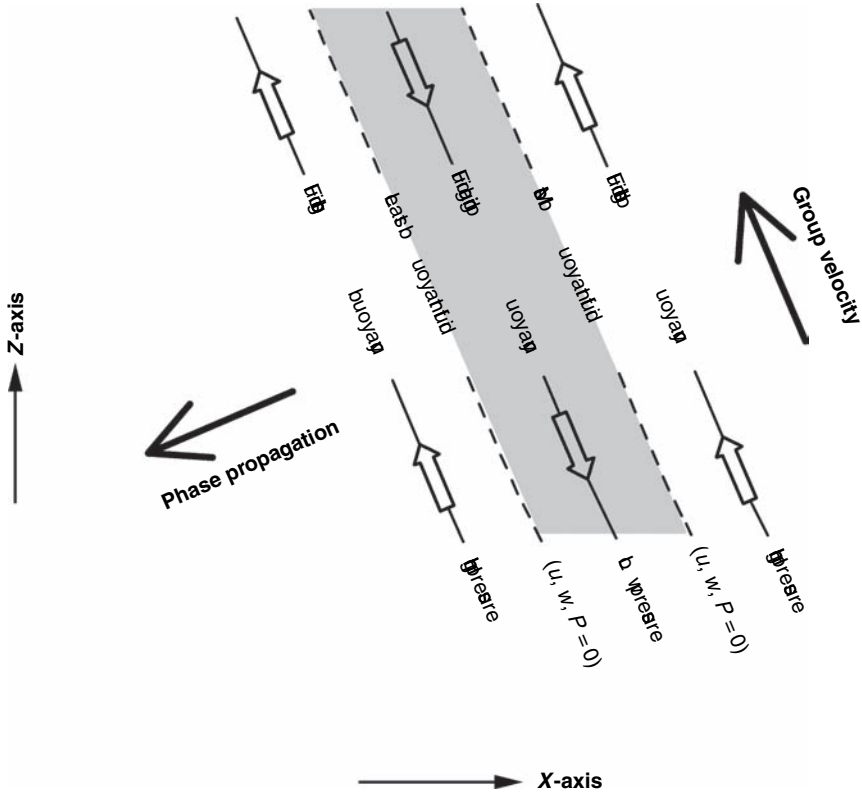
Fig. 3.17   The distribution of velocity, pressure and buoyancy perturbations in an internal gravity wave in the $x - z$
plane (from Durran, 1990). The phase of the wave is constant along the slanting lines; along the solid lines
buoyancy perturbations are zero, while velocity (u, w) and pressure (p) perturbations have extrema; along
the dashed lines, buoyancy perturbations have extrema while velocity and pressure perturbations are zero.
Small arrows indicate perturbation velocities.

A second basic type of wave is the *trapped lee wave* which occurs downstream of
the barrier. The development of lee waves is favored when there is a vertical
decrease of stability, and/or an increase in wind speed. This implies a decrease
with height of l^2; l is a stability factor known as Scorer's parameter (Scorer, 1949).
Neglecting effects due to large shear the vertical wind profile (measured by the
quantity $\partial^2 U/\partial z^2 \sim 0$), l^2 can be expressed in terms of the Brunt–Väisälä frequency:

$$l^2 \cong \frac{1}{U^2}\left\{\frac{g}{T}(\Gamma - \gamma)\right\} = \frac{S}{U^2} = \frac{4\pi^2 N^2}{U^2}$$

where U is the horizontal wind speed perpendicular to the barrier, and the other
terms are defined above.

A threshold condition exists for the formation of waves; if l_1^2 is specified for a
lower layer of thickness z_1 and in a higher layer l_2^2 is determined, then this condition
is $l_1^2 - l_2^2 > (\pi/2z_1)^2$.

Synoptic situations favorable for wave formation include those with a jet stream aloft (increasing wind speed with height) and near fronts with middle level stability and a large change of density (Corby, 1957). Seasonally, waves are more common in winter due to increased low-level stability and stronger circulation.

Typical values of l ($\times 10^6$) may range in the vertical from ~ 1 to $< 0.05\,\mathrm{km}^{-1}$. A scale for determining values of l from a tephigram plot of an appropriate upper-air surrounding has been developed by Scorer (1953) and Wallington (1970). Corby (1957) provides numerous examples of atmospheric soundings and profiles of l^2, while Casswell (1966) gives graphs for computing wave dimensions and velocities from l.

The wavelength (λ) of the dominant lee waves is related to the mean horizontal component perpendicular to the barrier (U) and is inversely proportional to stability. If vertical accelerations are neglected, (Lyra, 1943; Scorer, 1949):

$$\lambda \sim 2\pi \overline{U} \left\{ \frac{T}{g(\Gamma - \gamma)} \right\}^{1/2} = 2\pi/l$$

For $U = 10\,\mathrm{m\,s}^{-1}$, $\partial T/\partial z = 6.5\,\mathrm{K\,km}^{-1}$ and $T = 260\,\mathrm{K}$, $l = 1.116\,\mathrm{m}^{-1}$ and $\lambda = 5.6\,\mathrm{km}$, for example.

The wavelengths tend to increase with a daytime reduction in stability in the lower layers, because l decreases. In the evening hours, conversely, the wavelength may gradually decrease (Scorer, 1953).

Examples of vertical temperature and wind profiles and the calculated wave development are illustrated in Figure 3.18. In (a) the streamlines are tilted upstream near the ridge crest and there is strong downward flow over the lee slope. In the vertical, the pattern repeats with a wavelength of $2\pi/l$; the descending flow is displaced some 2–3 km eastward at 10 km. In Figure 3.18b there are low-level lee waves as well as vertically propagating waves aloft with tilted phase lines. When l changes rapidly with height, wave energy may be partially or totally reflected. Computations by Sawyer (1960) for soundings from various actual airstreams show general agreement with observations made at the time. The lee flow shown in Figure 3.18a is quite characteristic, but the relationships between wave amplitude over the ridge, or in its lee, and the profiles of wind, temperature, and l^2, are complex and variable (see Cox, 1986).

It is worth noting that the wind profile in Figure 3.18 implies l^2 increases with height; hence smooth waves cannot form, as shown by Förchgott's observations. Severe turbulence occurs in such cases up to two to three times the height of the barrier (Corby, 1957). For airflow normal to a long ridge, Smith (1989) shows theoretically that flow stagnation begins aloft, leading to wave breaking and turbulence. For flow parallel to the ridge, the waves weaken dispersively aloft and stagnation begins at the surface.

A useful approximate relationship for the wavelength (λ, in km) of lee waves in the lower troposphere is:

$$\lambda = 0.5\overline{U}$$
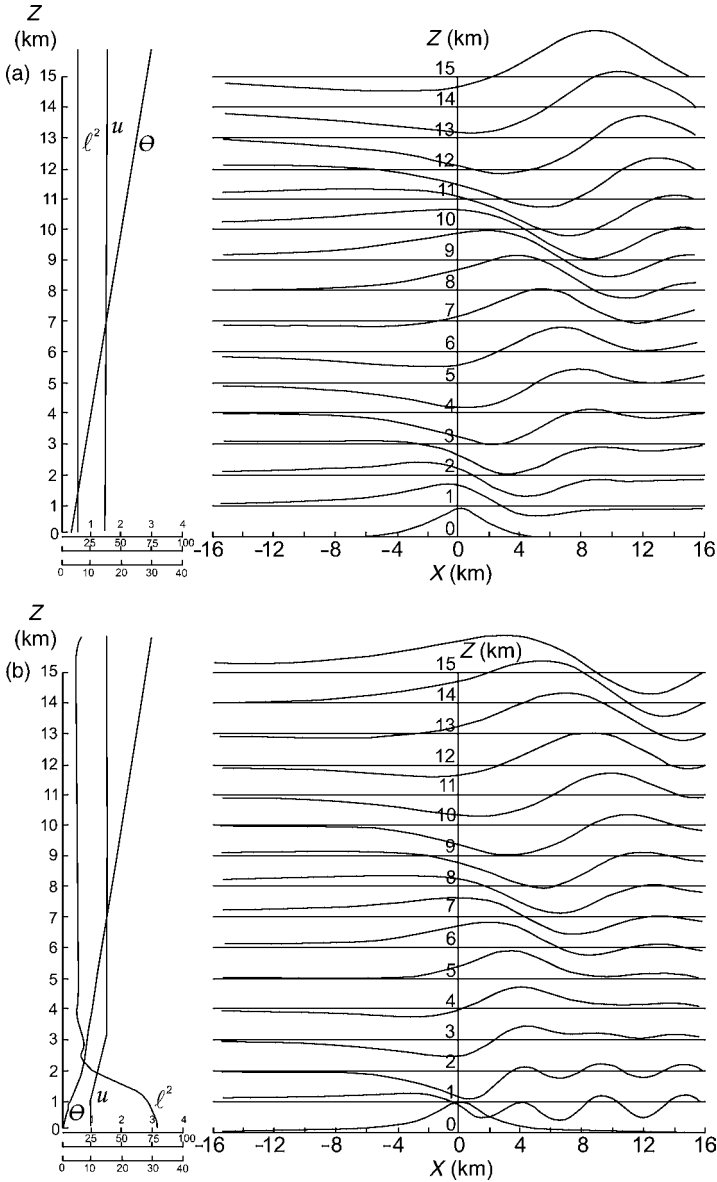
Fig. 3.18 Calculated streamlines showing wave development over a ridge for two idealized profiles of wind speed (*u*) and potential temperature (*θ*) (from Sawyer, 1960). Values of l^2 are also shown (see text) In (a) *u* and l^2 are constant with height; in (b) l^2 is large in the lowest layer and then decreases rapidly to low values.

where $\overline{U}$ is the mean tropospheric wind speed (m s^{-1}), assuming an average temperature lapse rate of 5 °C km^{-1} (see Corby, 1954). The relationship between λ and U is closely linear. However, the *first* lee wave crest downstream of a mountain range is approximately 0.75λ downwind. Observations of lee waves

indicate a wavelength range of 5–30 km with a modal value of about 10 km. The horizontal extent of the lee waves downwind of topographic barriers is inversely proportional to the thickness of the stable layer according to Cruette (1976). Her results are based on 226 cases over western Europe and North Africa in 1966–8 examined via satellite photography and aircraft measurements. The stable layer traps the energy of the mountain perturbation acting as a "wave guide."

It is interesting to note why waves form only *downstream* of a mountain barrier. Smith (1979; pp. 113) provides an explanation based on the fact that in fluid flow the speed of motion of wave crests (phase velocity) exceeds the rate of energy propagation (group velocity). The phase velocity in a standing wave has to be equal and opposite in direction to the mean wind speed, $\overline{U}$. Thus, $\overline{U}$ exceeds the group velocity, and advection by the mean wind dominates the transport of wave energy downstream away from its source at the obstacle. The wave energy is reflected up and down between the ground and an upper region where l^2 is small (see Figure 3.18b).

The lee wave amplitude depends on the decrease with height of l^2, the mountain height, and width. Analysis shows that the largest amplitude waves occur when the air stream characteristics meet the condition for waves by only a small margin (Corby and Wallington, 1956). Moreover, maximum amplitudes tend to occur when there is a shallow inversion layer in the lower troposphere. For a given height of barrier, the amplitude is largest when the width of the range is adjusted to the natural wavelengths in a particular air stream; this occurs where λ/π is equal to the half-width of the barrier. Thus, the largest waves occurring in an air stream are *not* necessarily associated with the largest mountain ranges. The height of the maximum wave amplitude generally corresponds to the top of the wave clouds (if present) and this is also usually an inversion layer (Scorer, 1967).

Most studies of mountain lee waves have dealt with the effects of isolated ridges or peaks on the airflow while few address more complex terrain. When the topography consists of a succession of ridges perpendicular to the airflow there may be superposition of several "wave trains" that are set up independently by the different obstacles (Scorer, 1967). This can lead to amplification or damping of the waves, depending on the spacing (the phase relationship) of the individual wave trains. An obstacle located one-half wavelength downstream can eliminate the lee waves set up by an upstream ridge. For this reason, air may sometimes descend while crossing some sections of a broad mountain range; Wallington (1961) has observed this during aircraft profiles across the Welsh mountains. Even over simple symmetrical ridges, however, there are commonly two or more different wave modes, with maximum amplitudes at different heights in the lower troposphere, as a result of the complexities of air stream characteristics. The effects of a series of ridges was examined for the Blue Ridge by Smith (1976) and periodic meso-scale topography was modeled by Welch *et al.* (2001). They found that as ridges are spaced further apart (from one mountain width up to 15), the form drag gradually increases,

because there is a greater distance available for shooting flow. The layer of airflow blocked by the mountains becomes shallower as they are increasingly separated, implying a higher effective mountain height. This permits larger amplitudes of the gravity waves creating greater pressure differences across the summits and there-fore larger form drag. Teixeira *et al.* (2005) analyze high-drag states in a linear model of stratified flow over ridges and asymmetric mountains lower than 1000 m and with the necessary conditions for lee waves absent. The wind speed is assumed constant at low levels and then, above a height z_1, decreases linearly with height. They show that the drag depends on a nondimensional height parameter (Nz_1/U_0) of the discontinuity in $\partial U/\partial z$ and on the Richardson number *(Ri*, see Note 3) in the shear layer above; N is the Brunt–Väisälä frequency and U_0 is the surface wind speed. The drag oscillates as z_1 is increased, with a periodicity of half the hydro-static vertical wavelength of the gravity. waves $(\pi U_0/N)$, in accord with the reso-nance model of Clark and Peltier (1984). For flow over a two-dimensional ridge, the locations of maximum drag occur at $Nz_1/\pi U_0 = 0.25 + n$, where $n = 1, 2, 3, \ldots$. Drag maxima (minima) occur where there is constructive (destructive) interference of upward- and downward-propagating gravity waves in the region, where $z < z_1$. Wave reflection increases at the interface of z and z_1 as *Ri* decreases. However, the proposal of Clark and Peltier (1984) that there exists a *critical level* (Note 4) for wave reflection leading to resonance is not found to play a role in the drag amplification in this model.

The synoptic conditions that favor lee wave development are, of course, quite variable according to location. In the Sierras, lee waves may occur with westerly flow associated with an upper trough, or with the passage of a cold front or occluded front from the northwest (Alaka, 1960; pp. 38). The jet stream associated with the frontal zone is usually north of the area, and its occurrence is not a requirement for lee wave development. As implied by the earlier mathematical discussion, the characteristics of waves occurring in a specific situation depend critically on the particular air stream characteristics. Since these may change rapidly, and cannot always be specified by appropriate upper-air soundings, it has been suggested that radar observations may be the most feasible means of providing short-term aviation forecasts (Starr and Browning, 1972). Distortions of the air motion are detected by variable backscatter from layers of different density and humidity and, therefore, different refractive index.

The basic theories of wave motion are strictly applicable to disturbances of small amplitude, and they do not provide the necessary mechanisms for upstream block-ing of airflow, rotor development, or "hydraulic jump" type phenomena. Theories of large-amplitude disturbances were developed more slowly since in these circum-stances the equations of motions become non-linear, except in special cases. As discussed in the section on pp. 139–40 the flow of air (or water) over an obstacle may be supercritical ($F > 1$) or subcritical ($F < 1$). In the former case, the flow thickens and slows down as it crosses the barrier. Potential energy goes into creating kinetic energy. In the subcritical case, the opposite occurs; the flow thins and accelerates

Fig. 3.19   **Schematic illustrations of water flow over an obstacle in a channel. (a) Absolutely subcritical flow; (b) partially blocked flow with a bore progressing upstream at velocity *c* and a hydraulic jump in the lee; (c) totally blocked flow; (d) absolutely supercritical flow (from Long, 1969).**
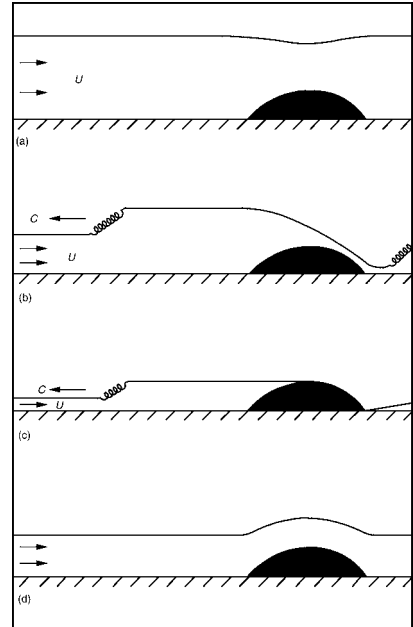
over the obstacle (Figure 3.19a). If the flow is partially blocked, with an increase in velocity as air ascends the obstacle and a decrease in thickness, a transition from sub- to supercritical flow may occur over the crest. The flow accelerates down the slope (shooting flow) and then jumps to a higher level (Figure 3.19b). The *hydraulic jump* is a well-known feature of water flow in channels in the wake of large boulders, where there is a region of depressed flow, which breaks down into turbulence downstream.

In the atmosphere, hydraulic jumps are common occurrences in the strong katabatic flows in coastal Antarctica (p. 184). They may also be initiated when the airflow across a ridge is partially blocked (Long, 1970). A wave disturbance (a "bore") formed by the barrier propagates *upstream*; the deeper flow is drawn down over the obstacle, becoming shallow on the lee side before jumping back to a higher level (Figure 3.19b). Houghton and Isaacson (1970) show that hydraulic jumps may occur with high mountain ranges and a low upstream Froude number. Grace and Holton (1990) describe possible jump features during downslope winds in the lee of 600 m Mt. Lofty, near Adelaide, Australia. Smith (1985) developed a model for downslope windstorms (see below, p. 181), based on a hydraulic analogy, which produces a hydraulic jump-like feature that may account for the high-drag states, discussed above. This model predicts that the critical-level heights producing high-drag states have a periodicity of one hydrostatic vertical wavelength of the gravity waves ($\pi U_0/N$).

For multi-layer fluids, an internal Froude number (F_L) is defined (Long, 1954) (see Chapter 2, Note 4):

$$F_L = \frac{U}{\left(g\frac{\Delta\rho}{\rho}H\right)^{1/2}}$$

where $\Delta\rho$ is the density difference between the top and bottom layers, and H is the total fluid depth.

Assuming an incompressible fluid

$$F_L = \frac{U}{\left(g\frac{\Delta\theta}{\theta}H\right)^{1/2}}$$

where θ is the potential temperature.

For a laboratory model resembling the atmospheric situation with a tropopause and a lower tropospheric inversion, lee jumps occur for $F_L \geq 0.2$, approximately. This corresponds to a mean wind of $20\,\mathrm{m\,s^{-1}}$ and $(g(\Delta\theta/\theta)H)^{0.5} \approx 10^4$ (Long, 1954). In models with stratified flow over three-dimensional hills, jumps occur for $F_L \geq 0.4$, but the types of flow are essentially those inferred for two-dimensional flow (see Figure 3.20) (Hunt and Snyder, 1980).

Klemp and Lilly (1975) argue that the hydraulic jump mechanism is too restrictive in its assumption to account for many observed aspects of strong wave amplification and downslope windstorms. They propose instead that partial
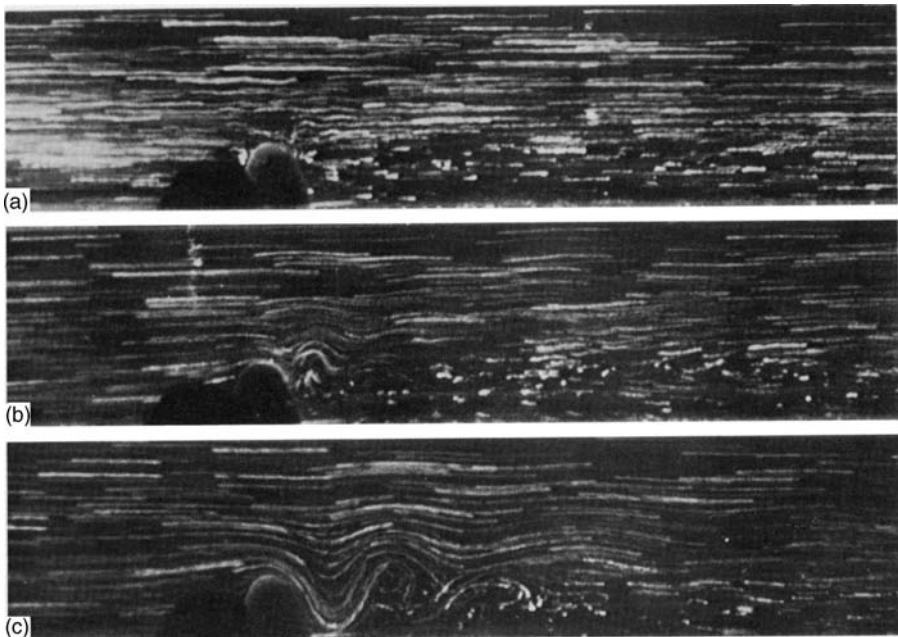
Fig. 3.20   **Lee waves developed in simulated northwesterly flow over a model Alpine/Pyrenean topography. This laboratory experiment is similar to that of Figure 3.12. The sequence shows (a) no lee waves (b) upper level lee waves and (c) lee waves at all levels in response to increasing Froude number, F_0. The transitions between (a) → (b) and (b) → (c) occur for $F_0 = 0.25$ and 0.37, respectively; the equivalent atmospheric free stream winds are $8.6\,\mathrm{m\,s^{-1}}$ and $12.8\,\mathrm{m\,s^{-1}}$ (D. J. Boyer and *Met. Atmos. Physics* 1987, Springer).**

reflection of upward-propagating wave energy by a mid-tropospheric stable layer leads to wave amplification of the kind that is observed.

Numerical solutions of the equations of motion have been used to examine non-linear flow behavior over mountains. Peltier and Clark (1979) show that, for homogeneous stable flows over a two-dimensional barrier, non-linearities are related to the aspect ratio of the barrier. When the mountain height is comparable to the height of any inversion present or, in a continuously stratified atmosphere, to the vertical wavelength of hydrostatic waves $(= 2\pi U/N)$, linear theory ceases to be applicable. This is typically the case for mountains exceeding 0.5–1 km. For inhomogeneous flows, Peltier and Clark find resonant lee waves and trapping and amplification of internal wave disturbances by reflection from a region of wave breaking and turbulence in the lower stratosphere. Klemp and Lilly (1978) incorporate an upper dissipative boundary region to remove upward propagating wave energy before reflection. They also analyze a non-linear large amplitude case, simulating a downslope windstorm at Boulder, Colorado, on 11 January 1972. In this study, they find upstream influence with a stable layer upwind of the mountains being raised. However, in a subsequent study (Lilly and Klemp, 1979) they demonstrate an *absence* of upstream effects and show that terrain shape has a significant effect on wave amplitude and mountain form drag. This is discussed further below. Long's results suggesting upstream influence (Figure 3.19) appear to be determined by the assumptions of two-dimensional flow and of a rigid-lid upper boundary condition (Smith, 1979a, b).

The occurrence of rotors, as illustrated in Figure 3.14d (p. 151) is one of the most important aspects of mountain waves. The idea that they are related to hydraulic jumps has been proposed (Kuettner, 1958), and Yoshino (1975; pp. 403–6) outlines laboratory wind-tunnel experiments to examine such effects. However, Scorer (1967) shows that the important terms in the equation for the vertical displacement of air, w in standing waves in the xz plane are:

$$\frac{\delta^2 w}{\delta z^2} = (K^2 - l^2)w,$$

where l is the Scorer parameter, and K is the streamline curvature (or wave number in the U direction); $2\pi/K =$ wavelength.

The criterion for rotors to occur is

$$\frac{dw}{dz} > 1 \text{ or} < -1,$$

which implies backward sloping streamlines such that the air has been overturned and has become statically unstable. Rotors therefore tend to develop when the wave amplitude increases where the slope of the w profile is largest. They are most common near the ground, but may occur elsewhere in lee wave troughs and crests depending on the profile of l^2 (Figure 3.14). Figure 3.21 illustrates a classic rotor in the Owens' Valley, California during the Sierra Nevada wave project in February 1952.

When a barrier has steep slopes or bluffs, especially on the lee side, the flow may become highly turbulent. Smith (1977) shows analytically that steep lee slopes
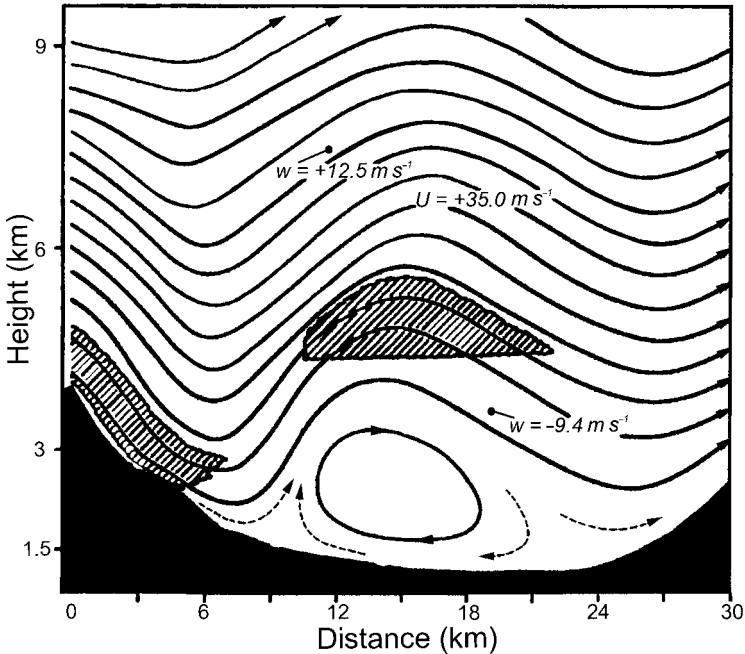
Fig. 3.21 Streamlines for 16 February 1952 in the lee of the Sierra Nevada, based on glider measurements, showing a large rotor and lenticular wave cloud (adapted from Holmboe and Klieforth, 1957).

accentuate the forward steepening of mountain waves, causing earlier breakdown of the waves and increased downslope wind velocity. Gust speeds during the downslope windstorms on the lee slopes of the Rocky Mountains appear to be intensified by this factor at locations such as Boulder, Colorado (Lilly and Zipser, 1972; Brinkmann, 1974a). In their numerical study of the effect of mountain cross-profile on wave motion, Lilly and Klemp (1979) find that the ratio of maximum/mean surface wind speed over a symmetrical mountain is 1.72, whereas over one with a steep lee slope and a gentle windward one it is 2.36. Steep slopes, especially on the lee sides of a barrier, also accentuate separation of the flow from the ground. For stratified flow over low to moderate slopes ($< 45°$), the boundary layer flow regime is determined primarily by the ratio of the wavelength of the lee waves ($2\pi U/N$) to the total width of the barrier (W), not by its height (Hunt and Snyder, 1980). When this ratio is close to unity, separation is unlikely, but when $W \ll 2\pi U/N$ (i.e. $F \gg 1$), lee separation is induced by the boundary layer flow. In this case, separation tends to occur near the hillcrest (or other location of maximum slope curvature) (see Figure 2.32, p. 85, for example).

Most theoretical analyses of mountain effects on airflow treat the problem as a two-dimensional one, but it is evident that in many cases there will be passage of air through mountain valleys and gaps, or around the ends of the barrier as illustrated for the French Alps in Figure 3.22. As might be anticipated, isolated peaks cause the least vertical perturbation, although air tends to flow around any mountain

Fig. 3.22 Lee wave locations in relation to wind direction in the French Alps (after Gerbier and Bérenger, 1961).
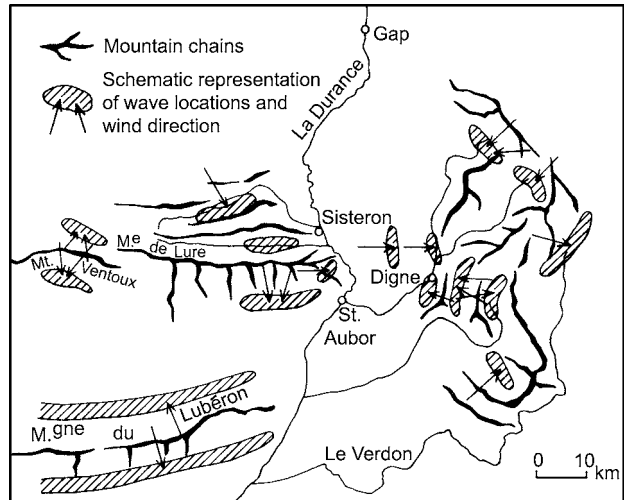
range of limited length rather than rise over it. This effect is augmented when the crestline is convex upwind, whereas a crestline that is concave upwind accentuates any tendency to wave development.

The effects of isolated obstacles on airflow are seen in satellite photography depicting lee wave clouds behind mountain ranges or peaks. Gjevik and Marthinsen (1978), for example, report trapped waves during inversion conditions in the lee of Jan Mayen, Bear Island and Hopen. The waves occur in a wedge-shaped wake behind the island, frequently in a diverging pattern with the crests orientated outward from the wave center.

A valuable case study of the effect of the Mont Blanc massif in the French Alps was made possible by the Mesoscale Alpine Program (MAP), which provided extensive aircraft and remote sensing data including airborne differential absorption lidar (DIAL) and dropsondes (Smith *et al.*, 2002). On 2 November 1999, the region was affected by strong southwesterly flow with vertical gradients of temperature and wind speed satisfying the conditions for trapped lee waves. There was a stagnant layer below 2500 m, due to blocking by the Alps, and an upper tropospheric jet stream. In the northwestern Alps, peaks rise to 3500–4500 m, with Mont Blanc reaching 4807 m. Aircraft data showed a large mountain wave in the lee of Mont Blanc that was stationary for at least 4 h. The peak-to-trough amplitude in the vertical displacement data was 800 m at 5.5 km, and 500 m at 7.6 km, diminishing slowly to above 11 km. There were two downstream wave crests, the first attributed to Mont Blanc and the second related to the eastern lee slope of the massif. The lowest cloud layer, located at 5.5 km altitude, descended sharply by some 1500 m just downstream of the Mont Blanc summit and a lenticular cloud was intermittently observed at 7.5 km, 26 km downstream of the summit. Linear lee wave theory predicts a train of trapped lee waves, which was not observed. Smith *et al.* (2002) propose that the wave energy from the two vertically

Fig. 3.23 **Vortex street downstream of the Cape Verde Islands, 5 January 2005, as seen in MODIS bands 1, 3 and 4 (NASA-GSFC).**

propagating waves was reflected downward from the jet stream level (where the Scorer parameter is decreasing and the waves become evanescent), but underwent absorption at the top of the stagnant layer, rather than being reflected to create a wave train. In the absence of an absorbing lower layer, lee wave clouds may extend up to 200 km downstream. A further feature of this case is that the waves were not the usual transverse kind, but dispersive-forming a V-shaped pattern opening out away from the point of origin.

Another meso-scale circulation pattern that may occur in the lee of isolated topography is the *vortex street*. This is common in marine stratocumulus in the lee of steep islands in the trade wind zone and other areas with low-level inversions (Figure 3.23). By analogy with von Karman's vortex street theory, airflow drag over high, steep-sided islands leads to eddies with a vertical axis being shed alternately on each side with a period of about 5–10 h (Zimmerman, 1969; Chopra, 1973). In the case of the Canary Islands, which project above the trade wind inversion to 2–3 km elevation, the eddies are typically 10–30 km in size, and the downstream wakes are of the order of 50 km wide and 500 km long. Clouds below the inversion serve as tracers of the vortices, which in the easterly airflow are cyclonic from the northern sides and anticyclonic from the southern sides of the islands (Figures 3.23 and 3.24). Analysis of 30 Moderate Resolution Imaging Spectroradiometer (MODIS) satellite images shows that the aspect ratio between the cross-street and along-street spacing of the vortices (h/a) is larger than predicted by von Karman – 0.42 versus 0.28 – and the ratio of cross-street spacing to the crosswind width of the island (h/d) is larger than theoretically – 1.6 versus 1.2 (Young and Zawislak, 2006). This is consistent with turbulent diffusion of the vortices in the lee of the island and vortex expansion a few vortex diameters downwind.

Schär and Durran (1997) show that at a certain height an isentropic surface is pierced by the mountain. The "hole" is deformed as potentially warm surface air is

Fig. 3.24 Schematic illustration of a von Karman vortex in the lee of a cylindrical obstacle (after Chopra, 1973). d = obstacle diameter; h = lateral street width; a = longitudinal spacing between successive vortices in each row. Empirically, $0.3 < h/a < 0.5$.
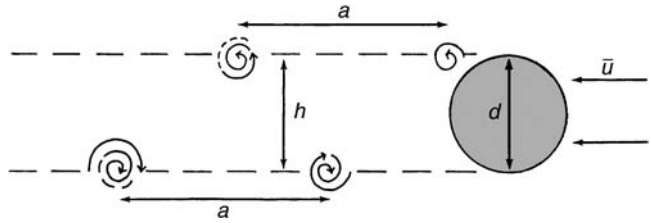
advected off the mountain top and it extends downstream in two tentacles that develop some roll-up, are advected farther downstream, and detach from the part of the hole that remains over the mountain. The tentacles detach due to the reversed flow in the wake. It was formerly assumed that the vorticity is generated by boundary-later friction and boundary layer separation, but this was found not to be the case. Epifanio and Durran (2002) show that over the island the isentropic surfaces in the wave field slope steeply downward forming a zone of weak stability above the lee slope. Below this is a region of accelerated flow, which decelerates abruptly downstream as the isentropes return almost to their upstream height forming a jump-like feature. Downstream of the jump a wake of nearly stagnant air develops and narrow bands of vertical vorticity extend downstream from the sides of the jump. Flow reversal occurs behind the jump and recirculating vortices form. The vorticity originates in the baroclinic generation and tilting in the wave upstream of the jump and is amplified by vortex stretching as the air passes through the jump.

The Windward Islands in the southeastern Caribbean Sea are fully exposed to the easterly trade winds and frequently display long, straight mountain wakes that extend more than 300 km downwind with a width of only 20 km as illustrated in Figure 3.25 (Smith *et al.*, 1997). Boat and aircraft studies around St. Vincent show several interesting features: near the islands wake structures reflect the island topography and there is a sharp wake boundary with the ambient airflow. There is descent over the islands and the wake air is relatively warm and dry. The length of the wake (L) can be expressed as $L = H/2C_d$ (where H is the wake depth and C_d is the surface drag coefficient). This relationship implies that reacceleration of the wake air is caused by the ambient downstream pressure gradient rather than by lateral entrainment of momentum, or geostrophic adjustment. These so-called "weak" wakes form when the potential vorticity generated by a mountain is not strong enough to advect itself into eddies and it is simply transported downstream by the ambient flow. Model analyses indicate that the long straight wake is attributable to descent of air over the island together with acceleration, wave breaking, and weak potential vorticity generation.

Laboratory simulations of flows on a β-plane (i.e. the Coriolis parameter increases with latitude) show that downstream of obstacles flow separation is suppressed (enhanced) for westerly (easterly) flows (Boyer and Davies, 1982). Westerly flows have downstream acceleration and a stationary Rossby wave,

Fig. 3.25   **Wakes in the lee of the Windward Islands of the Lesser Antilles (NASA Visible Earth).**

whereas easterly flows exhibit eddy shedding resembling Figure 3.24, with stronger cyclonic than anticyclonic eddies (see Figure 3.26). Laboratory experiments are typically performed with hemispheric or conical obstacles whereas slopes of islands, where downstream eddies are observed, are seldom steeper than 1:10 to 1:15. The additional factor contributing to vortex street formation in many cases is the presence of a stably stratified flow. Etling (1989) notes that this is present in the trade wind zones and during wintertime outbreaks of cold air off East Asia, for example. In such situations, there is an elevated inversion below the island summit. The air below the level of the "dividing streamline" (see Figures 2.28 and 3.3) goes around the obstacle and a train of vertical eddies forms downwind.

Experimental analysis of strongly stratified flow past a bluff obstacle by Brighton (1978) supports the idea of the key role of a strong low-level inversion in vortex shedding. His results demonstrate that flow around the obstacle remains nearly horizontal at low levels, but with intermittent vortices forming in the lee. Near the summit level, however, lee waves are present downstream and occasionally a "cowhorn" eddy may develop, initially below the first lee wave crest, with the horns of this eddy pointing downstream.

Small vertical vortices ("mountainadoes") have occasionally been reported at Boulder during windstorms, as well as during more moderate westerly flow conditions (Bergen, 1976). These may well represent vortex shedding in the lee of the locally sharp and irregular mountain front. Similar vortices, made visible as "cloud
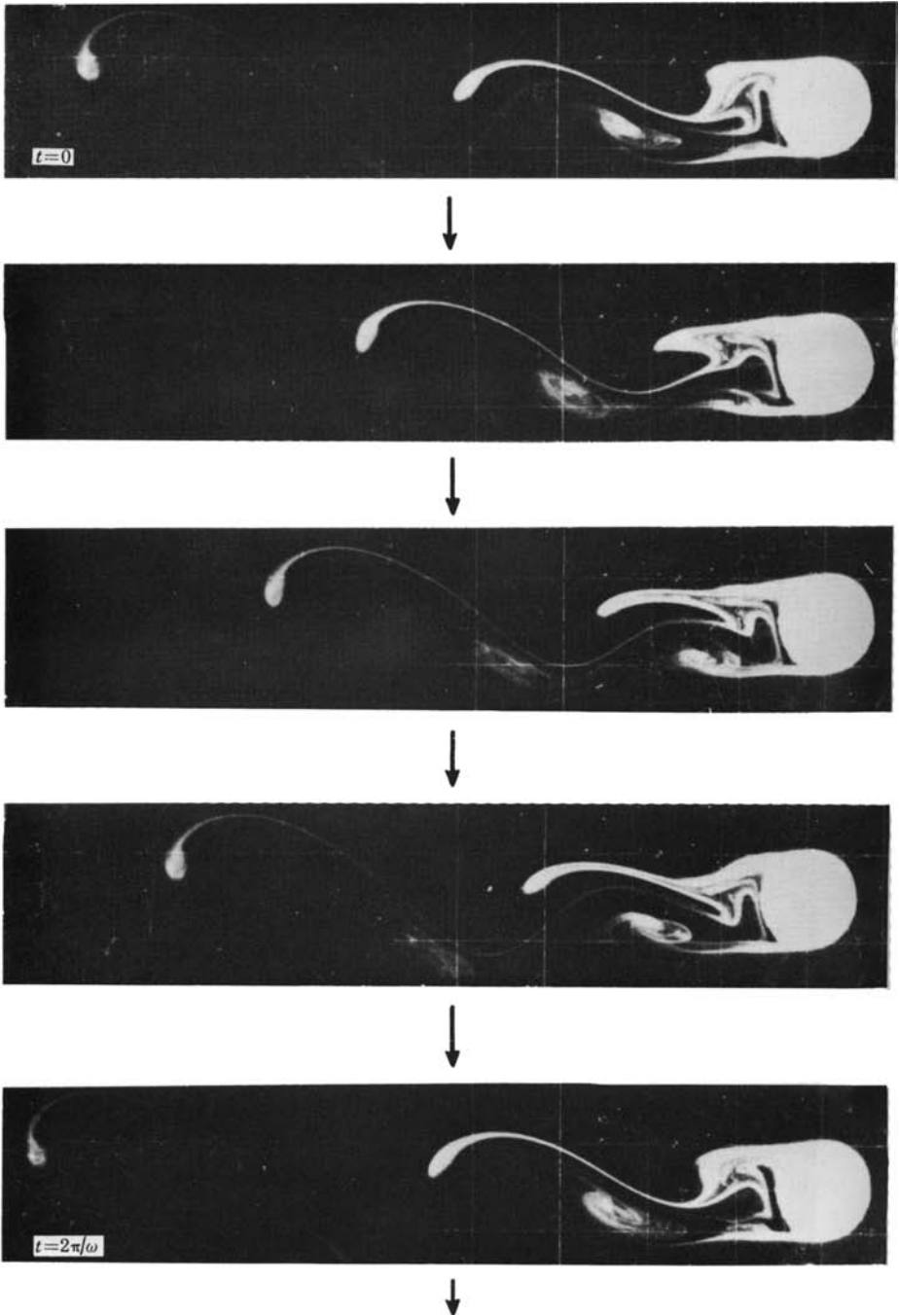
Fig. 3.26 **Laboratory model of vortex shedding (D. J. Boyer and the Royal Society, London *Phil. Trans.* 1982, plate 6, pp. 542). Laboratory model of double eddy formation in the lee of a cylindrical obstacle for easterly flow in a rotating water tank. Motion in the larger eddy at the right-hand edge of the obstacle, viewed downstream, circulates cyclonically, while motion in the smaller detached eddy at the left side is anticyclonic.**

spouts" extending 300 m below the cloud base, have been observed in the lee of Mt. Washington, New Hampshire (Brooks, 1949).

3.1.3.2 *Associated cloud forms*

Abe (1941) proposed a detailed classification of orographic clouds from cine-photography of Mt. Fuji, Japan, and studies of laboratory models, but it is unnecessarily elaborate. Nevertheless, he notes that cumuliform cloud, stratocumulus, and turbulent fracto-forms, may all occur over or near mountains.

Several distinctive cloud forms characterize the mountain wave system. All of them are *stationary* clouds that continually dissipate on the lee edge and reform on the upwind edge. The three principal categories are the cap cloud, lenticular cloud and rotor cloud, which may or may not occur together.

3.1.3.2.1 The cap (or crest) cloud   This forms over a ridge or isolated peak when forced ascent of air raises it to saturation level (see Figure 3.27). The cloud base is usually near or below the summit level for the term, "cap cloud," to be applied. It has a smooth upper outline, but the lee side often appears as a wall (föhn wall, or chinook arch in the Rocky Mountains) with fibrous elements dissipating from it downward.

A further type of cap cloud form is the *banner cloud*. This forms in the lee of sharp isolated peaks, such as the Matterhorn (Douglas, 1928). The pressure reduction resulting from the flow of air around the mountain causes air to rise on the lee side. This form is sometimes hard to distinguish from streamers of snow blowing

Fig. 3.27 **Cirriform clouds at 8.5 km over the Himalaya. Lhotse Peak (8500 m, 29.6° N, 86.6° E) is visible in the center. The cloud forms indicate winds probably in excess of 30 m s^{-1} over the summits (K. Steffen).**

off the summit area. Banner clouds up to 100 km long are reported in the lee of Mt. Lozère in the Massif Central, France during northerly mistral events (Jiang *et al.*, 2003) (see p. 137). Jiang and Doyle (2006) report cirrus plumes extending 400–500 km downwind of the Sierra Nevada, 70 km wide, and 400 km wide downwind of the southern Rocky Mountains. These were attributed to a relatively deep, upper moist layer, strong updrafts over the mountains, and slow downstream descent associated with terrain-induced, inertia–gravity waves.

3.1.3.2.2 Lenticular clouds   These are lens-shaped clouds forming in regularly spaced bands parallel to the mountain barrier on the lee side (Figure 3.16). The first descriptions of lee waves (Moazagotl), to the north of the Karkonosze (Sudeten) Mountains on the Czech–Polish border, were derived from study of such cloud forms (Küttner, 1939a). The Moazagotl cloud occurs with southerly flow and typically extends 50–60 km from its windward edge just north of the 1200–1500 m mountain range. Within this zone, Küttner (1939b) has identified up to six lee waves extending 250 km cross-wind with cloud 1–4 km thick. Ludlam (1980) proposed the term "great hill-wave cloud" for such features related to major escarpments. In complex terrain, the wave pattern may not be clearly related to the underlying surface. Indeed, the "hohe Föhnwelle" identified over the eastern Alps is an example of upper cloud related to the overall mountain effect, rather than a particular range (Krug-Pielsticker, 1942). Due to a variable humidity stratification, these clouds sometimes occur in layers, one above another, forming a "pile of plates," so that stratocumulus, altocumulus and cirriform cloud may be involved (Figure 3.15). Affronti (1963) describes such forms in the lee of Mt. Etna where they are termed Contessa del Vento. On rare occasions, particularly in winter, the wave motion extends into the stratosphere and forms nacreous (mother-of-pearl) clouds at a height of 25–30 km. The cloud top in the wave tends to be sharply defined when a stable layer, which causes a marked upward decrease in humidity, is present.

The lee cloud forms at Mt. Fuji are termed "turusi" (suspended). However, they include vertical rotary forms that cannot be explained solely on the basis of wave motion (Abe, 1941; p. 108). In the case of an isolated conical mountain, turusi commonly assume a V-shaped form, with the wings pointing downstream. Abe's photographs and laboratory model results show a clear resemblance between this form and the "cowhorn eddy" described by Brighton (1978).

3.1.3.2.3 Rotor clouds   A rotor cloud band commonly occupies the first wave crest downwind of the mountains (see Figure 3.21 in the lee of the Sierra Nevada). At Cross Fell in the Pennines of northern England, such a rotor forms the well-known "helm bar," which develops during strong easterly winds (Manley, 1945). The rotation in these clouds is readily visible in time-lapse camera photography. Turbulence connected with the rotor usually causes the cloud outline to be ragged, such that the "fracto-" designation is appropriate.

Superimposed on the forms of these three clouds, especially lenticular and rotor clouds, may be bands or striations known as *billows* (Ludlam, 1967). These are caused by small-scale instabilities induced by the vertical shear of the wind which move through the larger-scale wave cloud. They may form in existing shallow layer clouds in the lower troposphere when radiative fluxes set up an unstable stratification. The overturning occurs transverse to the shear vector with a typical wavelength of about 1 km. Less commonly, irregular cirriform billows may occur near fronts or jet streams. A relationship with orographic features is apparent in the case of the lower tropospheric forms and even high-level cirrus billows can develop 20–30 km downward of particular hills and ridges.

3.1.4   *"Fall" winds*

When the synoptic situation is favorable, the mechanical and thermodynamic effects of topography on airflow can give rise to distinctive winds blowing down the lee slopes of a mountain range. These so-called "fall" winds include the föhn (or chinook), the bora, and (meso-scale) katabatic winds. In the simplest terms, the föhn wind is defined with reference to a downslope wind that causes temperature to rise and relative humidity to fall on the lee side of a mountain range, whereas the corresponding bora causes temperatures to fall. Both may be gusty. The föhn also has important desiccating effects on vegetation and soil moisture extending up to 50 km from the foothills of the Rocky Mountains in Colorado (Ives, 1950; Riehl, 1974). A katabatic wind is a gravity wind down any incline, but, in the present context, the reference is to wind systems on a scale affecting more than individual slopes (see p. 183). The generic term "drainage wind" is also used, particularly to denote a downslope flow on a scale larger than on a single simple slope. It may apply to broad flows, not confined to valleys, over large uniform slopes (Sturman, 1987).

3.1.4.1   *Föhn*

The recognition and study of föhn winds has a history of over 100 years in the European Alps, where Hann (1866) gave the first broadly correct account of their origin. The generic name derives therefore from the Alps, although the term *chinook* is used along the high plains east of the Rocky Mountains and there are many other local names throughout the world (Brinkmann, 1971). The classical mechanism used to account for the föhn phenomenon begins with the forced ascent of moist air against a mountain range, causing cloud build-up and precipitation on the windward slope. The rising air cools at the saturated adiabatic lapse rate (ca. 5–6 °C km^{-1}) due to latent heat release by condensation above the cloud base. On the lee slope, following the evaporation of any cloud droplets, the descending, cloud-free air warms at the dry adiabatic lapse rate of 9.8 °C km^{-1}. It is the removal of some cloud water through precipitation that is responsible for a net gain of energy. Thus, potential temperatures are higher on the lee side
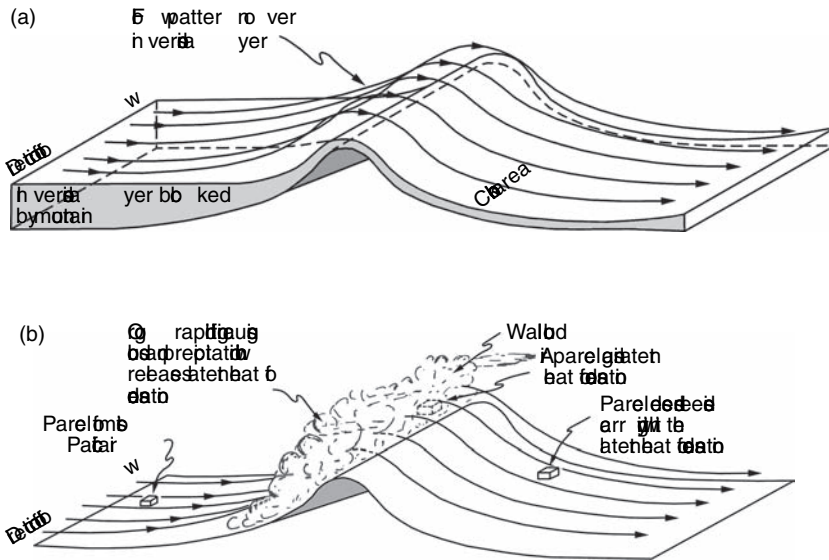
Fig. 3.28 Adiabatic temperature changes associated with different mechanisms of föhn descent. **(a) Blocking of low-level air to windward slope, with adiabatic heating on the lee (from Beran, 1967). (b) Ascent partially in cloud on windward slope, giving cooling at SALR with descending air on lee slope warming at the DALR.**

(Figure 3.28b). In an extreme case of south föhn on 8 November 1982, surface potential temperatures were 20–30 °C higher in the Alpine Foreland of southern Germany, including the Black Forest, than in the valleys on the south side of the eastern Alps (Seibert, 1990). In many instances, however, föhn may occur without moisture removal on the windward slope. This was first noted by Hann (1885) and has subsequently been widely demonstrated (Cook and Topil, 1952; Lockwood, 1962; Brinkmann, 1973). Hence, it is sufficient for air to descend from the summit level to the surrounding lowland and undergo adiabatic compression, due to blocking of air at low levels by an inversion (Figure 3.28a). Seibert (1990) suggests that at least half of the south föhn occurrences at Innsbruck, Austria are not associated with precipitation on the windward, southern slopes of the Alps. Typical effects during north- and south-föhn in the Alps are discussed in Chapter 5 (see Tables 5.6 and 5.7). It is also worth noting that the large-scale conditions differ for chinooks east of the Rocky Mountains and föhn north of the Alps (Hoinka, 1985b). In North America the westerly flow has lower humidity, after traversing the western cordilleras, than does the south föhn from northern Italy and the latter often occurs in a pre-frontal pattern in contrast with the post-frontal situations east of the Rocky Mountains.

Beran (1967) identified two further mechanisms producing föhn-type temperature fluctuations on the east slope of the Rocky Mountains. One is a nocturnal feature that occurs when advection of (warm) air from the west sets up turbulence and prevents, or greatly reduces, the normal radiational cooling trend. The second involves the displacement of a pool of shallow, cold polar air covering the lower east slopes by

air of Pacific origin that crosses the mountains. The interface between these two air masses may develop minor waves roughly parallel to the mountain front causing pronounced temperature fluctuations to be recorded at locations near the interface. Both situations are effectively special cases of the basic downslope föhn wind.

Cadez (1967) proposed a classification of föhn winds, based on the temperature and pressure differences across the mountain barrier. His three types are illustrated schematically in Figure 3.29. Types (a) and (b) both occur in a cyclonic pressure field; the atmosphere is less stable in (b) and the leeward temperature rise is correspondingly greater. The pressure gradient across the Alps may be up to 10 mb/100 km during föhn situations, compared with a mean value of only 2 mb/ 100 km (Hoinka, 1985b). In type (c) there is damming of cold air on the windward side due to an anticyclonic inversion. In this connection it may be mentioned that Bilwiller (1899) first introduced the term "anticyclonic föhn" to refer to dynamic warming by large-scale anticyclonic subsidence over the Alpine area. Other meteorologists have subsequently used the term "free föhn" in the same sense (e.g. Flohn, 1942). Such cases are not in the category of fall winds.

Circulation systems related to orography
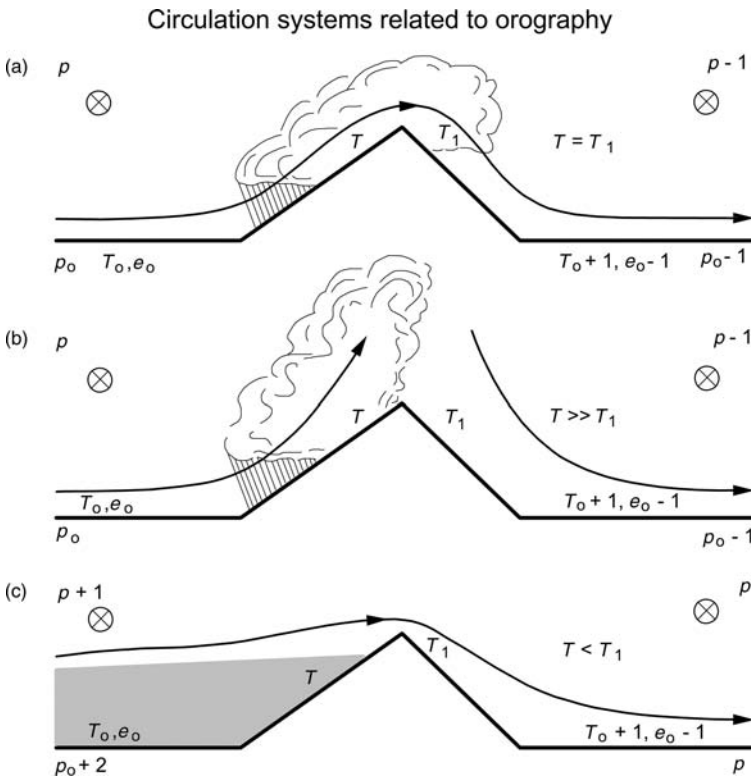
Fig. 3.29 **Three types of föhn. (a) Cyclonic föhn in a stable atmosphere with strong winds; (b) cyclonic föhn in a less stable atmosphere; and (c) anticyclonic föhn with a damming up of cold air (after Cadez, 1967; from Yoshino, 1975).**

The problem of definition is one of some importance since the criteria adopted determine the frequency of föhn conditions calculated for particular locations (Brinkmann, 1970; 1971). For a study in Alberta, for example, Longley (1967) used an arbitrary maximum temperature of $\geq 4.4\,°C$ in winter months. He showed that over a wide area of southern Alberta chinooks occur on 15 percent or more of winter days. Commonly, three criteria are used at lee stations. They are: surface winds blowing from the direction of the mountains, an abrupt temperature rise, and simultaneous drop in relative humidity (Osmond, 1941; Frey, 1957). Ives (1950) used a definition in accord with the original thermodynamic theory of föhn requiring precipitation occurrence on the windward slope and higher potential temperatures on the lee side. Ives noted that about a third of these cases were not recognized as chinooks by the plains dwellers of Colorado because there was no temperature rise. Conversely, about half of the warm wind events recognized as chinooks by the plainsmen did not satisfy the meteorological criteria! A further possible criterion is the existence of isentropic conditions (dry adiabatic lapse rate) between mountain summit and leeward valley stations. In this connection, Schütz and Steinhauser (1955) assumed a lower limit of $7\,°C\,km^{-1}$ since a pair of stations may not be exactly on the same streamline. Brinkmann (1970) also attempted to use synoptic criteria. For chinooks, the upper flow should be perpendicular to the mountains and the surface pressure field should show a "föhn nose," or ridging, over the mountains. These cases were compared with "non-chinook" periods of westerly surface winds, defined by upper airflow parallel to the mountains and no föhn nose in the surface isobars over the Canadian Rockies. Analysis based on the three most common climatic criteria (surface wind speed, temperature and relative humidity) used to identify chinooks indicated that nearly 50 percent of the cases were misclassified by discriminant analysis. The föhn nose pattern is not usually well marked over the western United States, probably due to the occurrence of stable cold air pools in the Great Basin, according to Brinkmann (1971).

The Santa Ana winds of coastal southern California occur in the winter months. Easterly–northeasterly winds blow from east of the Sierra Nevada (the Mojave Desert) to the California coast, in contrast to the normal northwesterly alongshore flow. From an analysis of daily weather maps for 1968–2000, Raphael (2003) identifies an average of 20 events annually, with three in each of the months NDJ. The Santa Ana develops when there is a Great Basin high to the northeast, and a surface low off the California coast. At upper levels, Sommers (1978) identified situations involving northerly flow, associated with an upper trough to the east and a ridge in the eastern North Pacific. The presence of large-scale subsidence on the windward side of the mountains, which gives strong stability and, together with an inversion near summit level, act as important controls. Sommers agrees with Brinkmann's findings for Colorado, that temperatures on the lee slopes with these föhn situations may increase or decrease. Air temperatures in winter are low over the Great Basin, but the Santa Ana winds are often hot and

dry due to adiabatic descent over the mountains (San Gabriel, San Bernadino, Santa Ana) with average dewpoint temperatures of around $4\,°C$ and, in a mesoscale model simulation, relative humidity 15–20 percent below the seasonal mean (Conil and Hall, 2006). Relative humidity may fall below 10 percent, creating major forest fire risks, and wind gusts of $10–50\,m\,s^{-1}$ are observed.

A different approach has been developed from the theory of lee waves. According to Scorer and Klieforth (1959), upstream blocking of the airflow by a mountain barrier occurs if the ridge height $h > \pi/l$, where $l =$ Scorer's parameter (see p. 154). This criterion is equivalent to $F < \pi^{-1}$. Lockwood (1962) found that in four out of five cases of föhn winds in the British Isles, π/l slightly exceeded the mountain height. In Colorado, Beran (1967) found it to be a necessary but not a sufficient criterion for predicting chinook occurrence in the lee of the Rocky Mountains. Shutts (1998) argues that cold air blocking by a mountain range causes air of high potential temperature at the summit level to descend in the lee of the mountains providing a mechanism for föhn occurrence that does not require gravity wave or latent heat processes. A small-scale three-dimensional numerical model has been used by Vergeiner (1978) to analyze föhn winds in the vicinity of Innsbruck, Austria. The equations are linearized, but they are used in time-dependent form with several arbitrary airstreams. The topography is idealized with a 2.5 km horizontal and 250 m vertical grid. The model results show: (1) forced orographic waves at low levels, with wavelengths of 10–15 km, tilting backward with height; and (2) "free" resonant lee waves of shorter wavelength generally at higher levels. These latter are trapped and propagate wave energy downstream (cf. the discussion on p. 154). The wind fields are similar to those observed during northerly and southerly föhn with strong föhn recurring in preferred locations, according to the assumed airflow characteristics, and "blocking" effects due to the slopes facing the wind direction, causing flow reversal. Vergeiner also finds evidence of strong ascent over the crest of the northern (Karwendel) Alps (termed hohe Föhnwelle – high föhn wave), which is related to the orographic effect of the Alps as a whole, rather than that of individual ranges. While such models are useful diagnostically, input data are in most cases lacking for predictive use.

Occurrences of south föhn at Innsbruck are affected by the large-scale wind direction above the ridgeline to the south (Zaengl, 2003). Flow down-valley from the Brenner Pass (between Italy and Austria) accelerates in the lower section of the valley towards Innsbruck due to gravity wave propagation over the nearby mountains. The wave amplitude is sensitive to the wind direction, becoming larger as the angle between the winds and the ridgeline increases. With southwesterly flow aloft (700 mb), wave amplitudes are larger to the east of Innsbruck than to the west. Shallow föhn, occurring when the flow at 700 mb is westerly, has rather weak wave activity along the valley. Seibert (1990) shows that air in the south föhn crossing the Eastern Alps originates around 2000–2500 m over the Po valley and not at ground level as originally proposed. The terrain blocks the northward movement of low-level air, which is stably stratified due to an inversion layer between 2 and 3 km

elevation. There are 8 days with föhn at Innsbruck in each month of March–May and 6 days each in October–November (1958–80) (Schrott and Verant, 2002).

Intensive airborne measurement programs were carried out across the Alps during the Mesoscale Alpine Programme. Analysis of a north föhn event on 6–8 November 1999 by Jiang *et al.* (2005), finds a cloud-free föhn window zone and also a hydraulic jump to the south of the Alps. There was a stable layer at 3–5 km with a deep layer of weak flow beneath it. A further MAP study of south föhn conditions in the upper Rhine valley, between Chur and Lake Constance in northeastern Switzerland, on 10 November 1999 shows that a cold pool in the valley can prevent the föhn flow from reaching the valley floor (Jaubert *et al.*, 2005). The cold air pool can be removed in several ways: (i) diurnal surface heating; (ii) turbulent entrainment at the top of the cold pool; or (iii) intensification of upper level mountain waves, with wave breaking, forcing the föhn flow to descend and flush out the cold air. Jaubert *et al.* show that the main term in the heat budget of the cold pool is advective since there is only weak radiative forcing. The large-scale circulation during this event was west-southwesterly with the flow splitting along the western edge of the Alps. Air passing over the Alps descended via mountain waves and was then channeled into the valley of the upper Rhine.

McGowan and Sturman (1996) describe case studies of föhn onset in the lee of the Southern Alps, New Zealand. They investigate the headwaters of north–south valleys of the Lake Tekapo catchment, on the eastern side of the Southern Alps. Here, the deeply incised glacial valleys channel northwesterly gradient winds, and speeds of up to 40–50 m s^{-1} are regularly observed. They find that föhn onset can occur when surface pressure gradients suggest no cross-barrier flow and upstream winds at the crest line level (2500 m) are only 5–10 m s^{-1}. Daytime heating over extensive dry gravel streambeds leads to convective turbulence that brings the föhn to the surface by downward momentum transfer. Hence, föhn onset and cessation tends to show a diurnal regime. The presence of Lake Tekapo (87 km^2) introduces further complications by setting up lake breezes (McGowan and Sturman 1996) that locally decouple the föhn flow from the ground. The föhn flow decelerates where the valley widens and the lake breeze–valley wind circulation undercuts it.

In summary, there are various approaches to defining and predicting föhn occurrence, none of them wholly satisfactory. In part, this reflects the different situations that may give rise to "föhn conditions." Föhn and chinook winds can be expected to exhibit some differences because the Alps form a lower barrier than the Rocky Mountains and, especially during southerly föhns, the air is considerably more humid; this is likely to modify the wave dynamics (Hoinka, 1985b). Additionally, a south föhn in the Alps is usually pre-frontal.

3.1.4.2 *Bora*

The cold, dry and gusty winds that blow in winter over the Dinaric Alps of Slovenia–Croatia towards the Adriatic Sea give their name to this type of fall

Table 3.2 Mean conditions during bora in January at Senj, Slovenia.

	Air temperature (°C)	Relative humidity (%)	Wind speed (m s^{-1})
Cyclonic bora	−0.1	61	15.6
Anticyclonic bora A[a]	1.5	49	13.4
Anticyclonic bora B[b]	−0.2	55	18.8
Non-bora	7.4	64	5.3

[a] High pressure over western Europe.
[b] High pressure over the eastern Atlantic.
Source: from a study by the Hydrometeorological Institute, Zagreb, after Yoshino (1976).

wind. Subsequently, it has been widely used for similar downslope winds on the Black Sea coast of the Crimea (Arndt, 1913) and elsewhere in the former USSR (see Yoshino, 1972), in the Apennines of Italy (Georgii, 1967), the fjords of northern Norway (Köppen, 1923; Mook, 1962) and along the east slope of the Colorado Front Range (Brinkmann, 1974b). Analogous winds with local names also occur at Cross Fell, in the northern Pennines of England – the northeasterly helm wind (Manley, 1945), and in the Kanto Plain, inland of Tokyo, Japan – the *oroshi* (Yoshino 1975; pp. 368–72).

Bora winds commonly affect the eastern shore of the northern Adriatic Sea in the vicinity of Trieste, Italy, and southward for nearly 500 km between Rijeka and Dubrovnik, in winter. They are also stronger at this season; with gusts in excess of 40 m s^{-1} frequently recorded at Trieste and inland in the Ajdovscina basin. Strong northeasterly gusts may be encountered up to 50–60 km offshore (Yoshino *et al.*, 1976). Velocities show a nocturnal maximum, peaking between about 0500 and 0800 h, due to the stable stratification. There can also be a land–sea breeze during the night hours that enhances the cross-mountain flow.

Each event lasts 12–20 h, on average, but spells of 6–7 days or more with bora usually occur at least once each winter. Temperatures are around freezing on the coast (Table 3.2) and the relative humidity may fall below 40 percent during anticyclonic situations.

Boras develop when there is a well-developed anticyclone over central or eastern Europe and there are cyclonic conditions over the central Mediterranean. Cold air from the Pannonian Plain is blocked by the Dinaric Alps, which rise to 1100–1500 m, but it can cross a narrow section of the mountains over the low 700 m-high Vratnik Pass east of Senj, and a similar area east of Trieste. Jurcec (1980) identifies Senj (45° N, 15° E) as the location of the strongest and most frequent boras along the Adriatic coast (Table 3.2). She cites a study by I. Luksic documenting a persistent event from 11–25 January 1972 when the mean wind speed was almost 15 m s^{-1}. On 12 December 1967 a maximum speed of 46 m s^{-1} was recorded at Senj. The airflow conditions associated with most bora events involve

Table 3.3 Climatological characteristics for winter bora days expressed as differences (Split–Zagreb).

Level (mb)	Air temperature (°C)	Relative humidity (%)	Wind speed (m s^{-1})
500	−0.1	+2.4	−1.5
700	+1.8	−0.8	−2.7
850	+5.4	−10.2	−2.0
Surface	+7.4	−26.7	+3.9

Positive values indicate Split (leeward) > Zagreb (windward).
Source: from Yoshino (1976).

northeasterly winds up to 2–3 km and a gradual transition to southwesterly–westerly flow aloft that often creates an inversion structure (Jurcec, 1980). A case study of an anticyclonic bora on 28 March 2002, showed deep northeasterly, cross-mountain flow with amplified gravity waves and trapped lee waves throughout the troposphere (Gohm and Mayr, 2005). Boundary-layer separation over the steep lee slope prevented the bora from descending at the coast, although it reached the sea surface downwind. Gaps in the mountains, particularly upstream of Senj, allowed 10–20 km-wide bora jets to reach the surface while downwind of higher terrain there were broad wakes of weaker flow.

The vertical structure of bora conditions 130 km to windward (Zagreb) and leeward (Split) of the Dinaric Alps is illustrated in Table 3.3 showing differences between these stations for 142 winter cases. The wind is only stronger at Split near the surface, but temperature and humidity effects extend to about 3 km.

Although the "type" bora is thought to be a cold dry wind, Jurcec (1980) emphasizes that temperature and humidity changes are quite variable. Table 3.3 shows that adiabatic warming can be pronounced in the lower troposphere. Cyclonic conditions tend to have low temperatures and relatively high humidity. With the anticyclonic pattern, the bora occurs mainly along the northeastern Adriatic coast while under cyclonic conditions it may occur more widely along the coast of Croatia, south to Split with winds from east to north-northeast and varying wind speed.

Aerial observations over the Dinaric Alps (Smith, 1987) do not support the idea of a "pure" fall wind model for the bora. Internal hydraulic mechanisms are shown to be important, since the initial cross-mountain flow is often weak. The mountains modify the upstream flow conditions and the development of a turbulent layer in the middle troposphere helps to decouple the descending air from the upper flow. Numerical modelling of mountain waves shows several important factors in the dynamics of bora events (Klemp and Durran, 1987). "Shooting flow" resembling that described by hydraulic concepts can be produced during bora conditions. Strong lee slope flow can arise in several ways. Vertical energy propagation may be restricted by a "critical layer" (located near the top of the inversion) where the cross-mountain wind reverses direction. Alternatively, wave overturning may

occur in the continuously stratified cold air beneath the inversion. In several respects there appears to be considerable similarity between bora events and other severe downslope winds (discussed on p. 179).

Aircraft and sounding data collected during ALPEX confirm that the bora is a cold air flow trapped beneath an inversion. Pettre (1984) applies hydraulic theory through the equations of motion for shallow water (used earlier for study of katabatic winds in Antarctica by F. K. Ball; see p. 184). Pettre shows that the flow becomes supercritical in the lee of the Dinaric Alps; over the sea, where the flow is strong, the cold air is only about 500 m deep.

Yoshino (1971) distinguished four synoptic pressure patterns giving rise to bora conditions. In winter these mainly involve a cyclone over the Mediterranean or an anticyclone over Europe. In summer, cyclonic patterns are less common and the anticyclone may be located further west. With each pattern the gradient wind is easterly to northeasterly. Yoshimura (1976) identifies a wider range of synoptic conditions associated with bora and shows that cyclonic cases have shallow bora winds (approximately 1 km) whereas in the anticyclonic patterns they may extend to 3 km. However, these distinctions may be of limited value. Development and maintenance of the bora requires the combination of suitable pressure gradient and the damming up of cold air east of the mountains with its overflow transforming geopotential into kinetic energy (Petkovsék and Paradiz, 1976). The bora is best developed where the Dinaric Alps are narrow and close to the coast as at Split. This accentuates the coastal–inland temperature gradient and the fall wind effect. The Alps rise to 1000 m or more and lower passes, such as that inland of Senj, also favor locally strong bora. On days with bora, an inversion layer is typically present between 1500–2000 m windward of the mountains and at lower levels to leeward (Yoshimura, 1976; Hoinka, 1985b).

On a hemispheric scale, Januaries with frequent bora days on the Adriatic Coast also have frequent oroshi winds in the Kanto Plain of Japan (Tamiya, 1975). The mean 500 mb pattern features a dominant two-wave mode which favors outbreaks of cold polar air in these two sectors.

Yoshino (1976) notes that bora and oroshi winds may show either bora or föhn characteristics in terms of temperature change. The possible difficulties of distinguishing bora and föhn can be illustrated with reference to Figure 3.29c. If the cold air dammed up on the windward side of the mountain range deepens sufficiently to flow across the mountains, then bora conditions will replace föhn. Adiabatic warming through descent and disruption of surface inversions may cause other complexities. As noted by Suzuki and Yabuki (1956), local heating or cooling effects may mask the temperature characteristics on the lower slopes.

In a detailed study of 20 downslope windstorm events at Boulder, Colorado, Brinkmann (1974b) found that almost half were genetically cold, i.e. cold advection lowered the potential temperature on the mountains slopes (at approximately 650–750 mb). Only four out of 20 cases showed warm air advection and the remaining eight cases were indifferent. However, at the foot of the mountains

only four cases showed bora characteristics with temperature decreases of up to 15° C, while 15 appeared as föhn winds; five of these would be considered "cold air föhn," six as indifferent, and only four as true föhn.

3.1.4.3 Windstorms

Considerable insight into causal mechanisms has been derived through study of violent downslope windstorms on lee slopes (Lilly and Zipser, 1972; Brinkmann, 1974a). Theoretical and laboratory model analyses demonstrate the critical role of an inversion (or stable) layer just above the mountain top level in triggering such conditions (Suzuki and Yabuki, 1956; Arakawa, 1968; Long, 1970; Klemp and Lilly, 1975; Durran, 1990). Figure 3.30 illustrates a composite up-wind sounding, using data at Grand Junction, Colorado, Salt Lake, Utah, and Lander, Wyoming according to the upper airflow trajectory and a composite Denver sounding, about the time of onset of wind storms in Boulder and on the slopes. A modal stable layer is indicated with a base at 575 mb; this served as a reference point for averaging the other sounding data (Brinkmann, 1974a). Surface gusts during the analyzed windstorms at Boulder averaged $36 \, m \, s^{-1}$, which is well above the mean wind speeds up to 450 mb. The high speeds at low levels are generated by a small-scale lee trough which is located, hydrostatically, beneath a region of high potential temperature set up by a large-scale lee wave (Figure 3.31). This local trough, which may be superimposed upon a synoptic-scale pressure minimum, accelerates the low-level airflow towards it. Consequently, a narrow zone of very high winds is usually observed parallel to the mountain front (Aanensen, 1965; Whiteman and Whiteman, 1974); on rare occasions this may extend to tens of kilometers from the mountain foot (Lester, 1978).

A numerical simulation of the 11 January 1972 windstorm using a hydrostatic model with a parameterization of turbulent kinetic energy suggests that surface friction plays a significant role in delaying the onset of strong surface wind and in preventing the zone of maximum winds from propagating downstream (Richard et al., 1989). Their results are consistent with the hydraulic theory that a transition from subcritical flow upstream to supercritical flow takes place over the mountain.

The fine structure of a moderate windstorm event at Boulder, Colorado, has been determined by Doppler lidar observations (Neiman et al., 1988). A low-level wind maximum exceeding $42 \, m \, s^{-1}$ was observed near 700 mb. As a result of surface drag, the surface winds averaged $25 \, m \, s^{-1}$, with gusts over $30 \, m \, s^{-1}$. The observed pressure fall of 4.7 mb during the windstorm corresponds to a wind speed of $32 \, m \, s^{-1}$ according to the Bernoulli equation. The lidar also indicated a hydraulic jump-like reversal of the flow along the eastern edge of the mountain wave some 5 km east of Boulder. Propagating discrete wind gusts, advected by the mean wind, were identified with periods of 4–5 and 14 min.

In the Falkland Islands (52.7° S, 58.6° W), flow from 330–360° with a strong temperature inversion near the summit level (640 m) of the Wickham mountain range leads to downstream flow acceleration (Mobbs et al., 2005). Such airflows with inversions represent 9 percent of all winds. The fractional speed up is shown

Fig. 3.30 **Composite soundings for times of windstorms in Boulder, Colorado. (a) Upwind sounding (west of the Continental Divide). (b) Downwind soundings (Denver) for storms in Boulder or on the slopes just to the west (from Brinkmann, 1974a).**
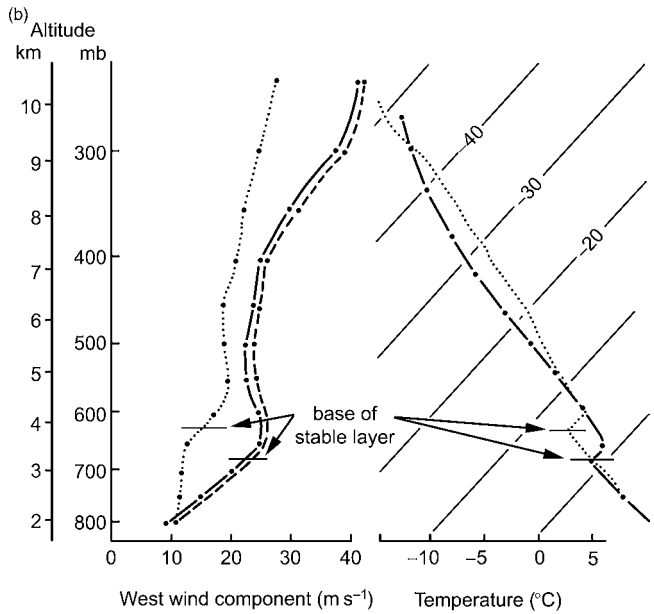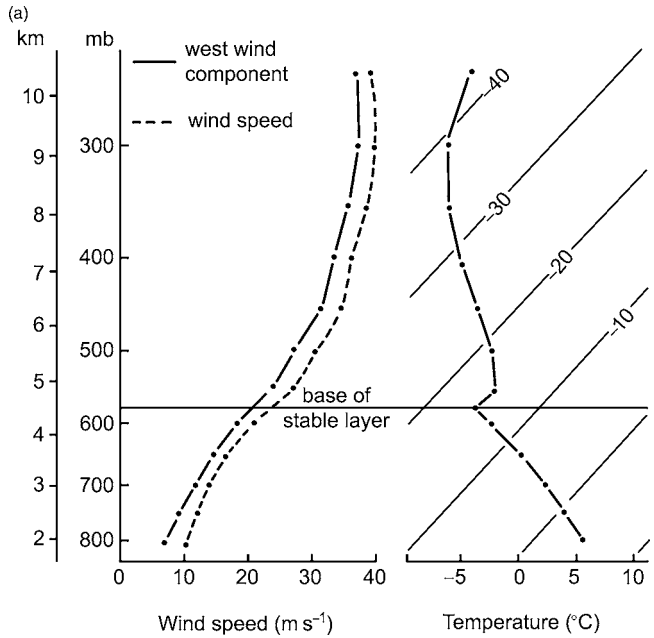
to be proportional to the non-dimensional barrier height and the Brunt–Väisälä frequency. Periodically, unsteady flow may occur for ~ 1 h with separation and rotor formation. Maximum wind gusts are about $22 \, \text{m s}^{-1}$.

In the lee of the Alps, for south föhn events at Innsbruck and Munich, Hoinka (1985b) found that peak gust speeds are related to the lee wave amplitude and momentum flux. Extreme slope winds occurred with mountain waves below 6 km altitude that were convectively overturned. Durran (1990) attributes exceptional downslope winds to the reflection of propagating mountain waves off critical layers (where there is zero wind speed or a flow reversal).

The theoretical basis available for predicting severe downslope winds is still incomplete (Smith, 1985). A key feature of such events appears to be the existence of a zone of weak winds with strong turbulence in the middle troposphere, over-lying the strong low-level wind maximum, with weaker waves at higher levels (cf. Figure 3.31). Strong mountain wave development may be a response to partial resonance produced by upstream conditions and tropopause reflection, or to wave reflection from the turbulent region. Smith notes that no severe winds occur if the mountain amplitude exceeds 0.985 U/N. Higher mountains act to block the upstream flow, thereby modifying the "effective" height of the terrain.

Alternatively, the severe wind mode may be triggered by the mountain-top level inversion causing hydraulic acceleration and a jump feature, as observed in the lidar case study. Similarities between hydraulic-like shooting flows during windstorms along the eastern slope of the Rocky Mountains and during bora events on the western slopes of the Dinaric Alps are apparent (Klemp and Durran, 1987). However, the chinook windstorms involve high speed and deep cross-mountain airflow.
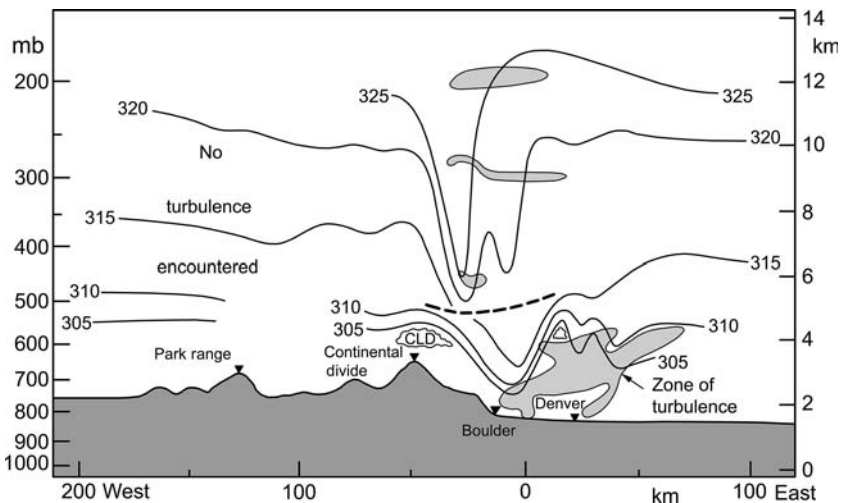
Fig. 3.31 **A cross-section of potential temperature K based on aircraft data during a windstorm in Boulder on 11 January 1972. The dashed line separates data collected at different times. The three bands of turbulence above Boulder were recorded along horizontal flight paths and are probably continuous vertically (after Lilly, 1978).**

A laboratory model study by Rothman and Smith (1989) examined flow over three different ridge cross-sections, with maximum slopes of 13, 27 and 40°. The range of Froude number for which a well-mixed turbulent layer formed over these ridges was $0.2 < F < F_{crit}$, where $F_{crit} = 1.0$, 0.9, and 0.8, respectively, for the three slopes. They also showed that a strong downslope wind can develop without a layered atmosphere if the wind speed and stability are uniform with height, as long as wave breaking occurs.

The following list shows the general conditions necessary for violent, gusty flow according to Yabuki and Suzuki (1967).

(1)   Ascending air on the windward slope subject to the Bernoulli effect enhanced by an inversion just above the ridge line.
(2)   Strong winds forced to descend from the summit level by the wave structure. The evidence from Brinkmann's (1974a) study for Boulder, and analysis of damaging winds at Sheffield, England, by Aanensen (1965), strongly suggests the importance of long wavelength (20–30 km) lee waves in such situations.
(3)   Topography with a steep lee slope.

The last point is supported by model calculations of Smith (1977), Lilly and Klemp (1979) and Hoinka (1985a) (see p. 138). Arakawa (1968) notes that strong winds are also more likely at the surface if the inversion level downstream of the range is lower than over the summit. In fact, Brinkmann's data support this argument (Figure 3.30).

The criteria for a windstorm are quite subtle. An analysis of wind profiler and stability data from Grand Junction, Colorado, and Lander, Wyoming (both upstream) during windstorms in Boulder shows that windstorm/no windstorm conditions are not separable based on wind direction, upper tropospheric wind shear or the vertical phase shift (Bower and Durran, 1986). They suggest that information on the location and strength of inversions is particularly necessary for prediction purposes.

East of the Rocky Mountains, where there have been numerous studies of downslope windstorms, the zone of occurrence extends from about Colorado Springs to Cheyenne. Based on newspaper reports since the 1860s in Boulder, Colorado, as well as more recent scientific analysis, about 85 percent of cases occur between November and March, with a strong January maximum, a preference for the night hours, and lasting an average of 8 h (Julian and Julian, 1969; Whiteman and Whiteman, 1974). The 100-year record suggests a frequency of about 1.5 storms per year, but more complete reporting since 1945 indicates that three or four damaging storms per year cause property losses in Boulder associated with peak wind speeds of about 30 m s^{-1}.

Severe windstorms may differ in important ways. During an event on 24 January 1982, isolated damaging gusts from an easterly direction occurred during otherwise light easterly flow in Boulder, while 45–50 m s^{-1} westerly winds affected the foothills to the west (Zipser and Bedard, 1982). Evidently, a large rotor was present over

Boulder. A week earlier, a closely similar large-scale synoptic situation produced a 9 h downslope windstorm, with west winds that gusted to $61 \, \mathrm{m \, s^{-1}}$ on the roof of the National Center for Atmospheric Research, and caused US$10 million damage in Boulder. Prediction of such severe storms is still unreliable despite improved theoretical understanding.

In reviewing the available evidence and model simulations, Durran (1990) finds strong support for the hydraulic jump mechanism in supercritical flow. Several simulations are inconsistent with the linear resonance mechanism of wave amplification proposed by Peltier and Clark (1979). However, there is an important linkage between the "breaking" of vertically propagating waves set up by high mountain barriers and hydraulic wave amplification. Non-linear effects of the partial reflection of vertically propagating waves by a layer interface become significant with large values of pressure drag. Durran notes that three rather different conditions may favor a transition from sub-critical to super-critical flow.

(1)   Wave breaking forced by a high mountain barrier.
(2)   A two-layer atmosphere in terms of the Scorer parameter, for mountains too small to force wave breaking,
(3)   An atmosphere capped by a mean-state critical layer (see Note 4, p. 231) above mountain top level, as in the bora of the Dinaric Alps, forcing wave breaking.

Windstorms in Boulder, Colorado, and Owens Valley, California, lack condition (3). They occur in deep cross-mountain flow when the wind is nearly perpendicular to the mountains with summit speeds exceeding some terrain-dependent threshold, and a stable layer or inversion located near the summit level (Durran, 1990). The gustiness may be a result of competition between wave build-up by gravity wave forcing and wave breakdown through convective instability (Clark and Farley, 1984; Scinocco and Pettier, 1989).

Recent research in the lower Rhône Valley, between the Massif Central and the Alps (Figure 3.6, p. 137), shows that some *mistral* events have several similarities to other "fall" winds. The valley has a maximum depth of about 500 m; its slope is only 2.5 percent, but the valley width decreases rapidly near Valence (Pettre, 1982). During cold northerly flows, a sharp transition is observed between tranquil flow in the northern part of the valley and the presence of wave motions downstream. If the inversion height is much lower at the exit from the narrows than at their entrance, a hydraulic jump may be present downwind. Violent winds can occur in the lower valley, even as far south as the Mediterranean coast depending on the specific conditions.

3.1.4.4 *Katabatic winds*
This class of fall wind is distinguished from the nocturnal downslope drainage of cold air slopes (see p. 187) by its scale and consequent involvement of additional forces, including Coriolis accelerations. On the polar ice sheets of Antarctica and

Greenland, air drainage may originate on remote ice domes and the extensive high cold plateaus (Chapter 5, p. 418). This motion is modified by the occurrence of a sloping low-level inversion which sets up thermal wind components, such that the winds in the interior of the ice sheets are not properly katabatic flows (Schwerdtfeger, 1970, 1972). They involve a balance between gravitational acceleration, Coriolis acceleration, friction, and inversion strength. The flow adjusts more rapidly to gravitational forcing than to Coriolis effects (Gosink, 1982); the continuity of flow cannot be maintained under equilibrium conditions when the trajectory is > 10–100 km in length.

However, the main interest here is with the coastal zones, where the "katabatic winds" are fall winds that may display föhn or bora characteristics and irregular fluctuations in velocity (Streten, 1963). Reports of extreme wind conditions at Cape Dennison (67° S, 143° E) during Douglas Mawson's 1912–13 expedition were not at first generally accepted. During a 12-month period, the 24-h average wind was $\geq 18\,\mathrm{m\,s}^{-1}$ on 64 percent of the days, and a high constancy of speed and direction was reported throughout the area. Subsequently, similar extremes have been reported at other coastal locations in eastern Antarctica. The katabatic zone is at least 150 km wide and extends inland 300 km from Cape Dennison. The coastal topography does not cause these localized winds, but diagnostic analysis of the flow regime demonstrates that large-scale topography inland determines their strength and persistence through a channeling of radiatively-cooled air from the interior (Mather and Miller, 1967; Parish, 1980).

While the interior slopes of Antarctica are extremely gradual (1 in 500), there are steeper drops (1 in 100) from the Transantarctic Mountains to the Ross Sea and Ross Ice Shelf and here "fall type" katabatic drainage flows are observed. Breckenridge et al. (1993) use AWS data and thermal infrared imagery to analyze their characteristics. While the source air is very cold, it seems that the flows disrupt the strong surface-based temperature inversions and can lead to "warm" signatures (gray streaks in the thermal imagery and Bromwich et al. (1992) show that these can extend hundreds of kilometers out across the Ross Ice Shelf. Breckenridge et al. show that during an intense katabatic event, 28–30 June 1982, air temperatures (potential temperatures) on the East Antarctic plateau were 45 °C (15 °C) lower than on the Ross Ice Shelf. The cold air tends to be funneled towards the Byrd, Beardsmore and other glaciers. By contrast, during non-katabatic conditions, 17–19 July 1982, the corresponding temperatures on the plateau were 15 °C (45 °C) higher than those on the ice shelf. Down-glacier katabatic winds are observed in the Transantarctic Mountains (230–240° at the Byrd Glacier AWS) and these turn to the left (210°) with speeds of up to $10–12\,\mathrm{m\,s}^{-1}$ as they reach the ice shelf. Katabatic outbreaks are also favored when a low-pressure system is present over the ice shelf or southern Ross Sea.

At Mawson (67° S, 63° E), where cyclone activity may be responsible for the frequent strong winds (Streten, 1968), the katabatic is only one component and three types of wind profile can be identified. Streten (1963) distinguishes a "normal" katabatic regime when synoptic control is weak. Here the mean wind is about

$10 \, \mathrm{m \, s^{-1}}$ in the lowest 300 m. Sometimes katabatic flow over-rides the lower layers, with mean speeds of $10 \, \mathrm{m \, s^{-1}}$ at 1200–1500 m. Finally, blizzard winds occur with mean speeds of about $30 \, \mathrm{m \, s^{-1}}$ between 300 and 1000 m when synoptic controls augment any katabatic effect.

Katabatic winds in Greenland are less extreme than those in Adelie Land, although gusts in excess of $50 \, \mathrm{m \, s^{-1}}$ have been recorded on the coast. Fjord gales in East Greenland, which are primarily katabatic in origin, occur on about 20 percent of days (Manley, 1938; Putnins, 1970). Several studies indicate that in East Greenland, near Angmagssalik, and in the southeast, there can be violent katabatic windstorms (known locally as "piteraqs") that are strengthened by transient synoptic cyclones. Heinemann and Klein (2002) examine katabatic flow dynamics for various sectors of the Greenland ice sheet using a hydrostatic limited area model validated with ground and aircraft data over southwestern Greenland in spring 1997. From model analysis of circulation conditions for the month of January 1990, they find that the synoptic pressure gradients are frequently counter to the katabatic flows in southwest and northeast Greenland, in contrast to northwest Greenland. Most slopes of the Greenland ice sheet show a katabatic signal. The strongest katabatic winds were observed north of $70°$ N in the northwest and north of $75°$ N in the northeast, where synoptic influences are weaker.

Using the formulation developed by Ball (1956), the primary driving forces are shown to be the slope and inversion strength. Ball determines the horizontal momentum budget integrated from the surface to the top of the surface boundary layer (SBL):

$$\frac{\mathrm{d} V_{\mathrm{m}}}{\mathrm{d} t} = F_{\mathrm{P}} + F_{\mathrm{C}} + F_{\mathrm{R}}$$

where F_{P} is the two-dimensional pressure gradient force, F_{C} is the Coriolis force, and F_{R} is the friction. For southern Greenland, in the cases examined by Heinemann and Klein (2002), the SBL height was around 100–200 m. Observations showed a mean Froude number for the SBL in excess of 1.0 implying "shooting flow" (see p. 159). In one dimension, x (down slope), the pressure gradient force (PGF) is:

$$\mathrm{PGF} = F_{\mathrm{S},x} + F_{\alpha} + F_{\mathrm{L},x} + F_{\mathrm{DL},x}$$

where $F_{\mathrm{S},x}$ is the synoptic gradient force, F_{α} is the slope gradient katabatic force, $F_{\mathrm{L},x}$ are forces due to spatial variations in the katabatic layer height and $F_{\mathrm{DL},x}$ are forces due to spatial variations in inversion strength. Over most of the ice sheet surface the slope is only 1–2°, but acceleration due to the slope term dominates towards the ice edge. The last two terms in the equation are generally minor contributors.

The onset and cessation of strong coastal winds tends to be very abrupt at Cape Dennison, and Ball (1957) interprets this as a standing jump phenomenon. Between Cape Dennison on the coast and Charcot Station (69° S, 2400 m asl) a strong

temperature gradient enhances the basic gravity flow of cold air from the Antarctic Plateau. At the 2400 m altitude, there is a 17 °C difference in annual mean temperature between these two locations which creates (assuming it is an isobaric temperature gradient) a density difference of about 7 percent (Loewe, 1972). A thermal wind component related to the surface-based temperature inversion is also probably involved since the winds are usually a few hundred metres deep. The jump feature is usually just out to sea, but if it shifts inland the regime of strong winds (shooting flow) upstream of the jump gives way to near calm conditions in a deepened layer of cold air (cf Figure 3.19b). Ball shows that the typical conditions in this area are conducive to a jump since the Froude number is far in excess of unity. Near Davis (68° S, 78° E), standing jumps are commonly marked by a 30–100 m high wall of drifting snow (Lied, 1964). Between 30 May and 14 November 1961, 31 standing jumps were seen or heard (from the roar of the wind) at the Davis station. Lied reports their typical occurrence several hours after the development of a katabatic regime.

Lopéz and Howell (1967) report jump features in a wholly different environment from the Cauca Valley in equatorial Colombia. Here cool, moist Pacific air crosses the Western Cordillera and, as a result of a potential temperature difference of 2–4 °C with the air to the east, descends as a katabatic wind. Speeds of $16\,\mathrm{m\,s}^{-1}$ are observed at Cali in late afternoon, compared with about $5\,\mathrm{m\,s}^{-1}$ at the pass at 700 m asl. Hydraulic jump type phenomena are observed in the longitudinal valleys as the katabatic flow descends and is heated. Lopéz and Howell show that the speed of the katabatic wind is much more sensitive to the difference in potential temperature than to the depth of the overflow.

3.2   THERMALLY INDUCED WINDS

The topographically induced modifications to airflow discussed in the last section are basically due to mechanical effects of mountain barriers. In addition to these influences, the thermal patterns of the topography also give rise to characteristic systems of air motion, especially when the regional pressure gradients are weak. The primary forcing agents are elevation differences in potential temperature, causing vertical motion, and differential heating/cooling along slopes that may set up air circulations with horizontal and vertical components. In some locations, such systems are sufficiently frequent and pronounced in their effects as to create distinctive and semi-permanent topoclimatic patterns. Such is the case, for example, in the deep valleys of the Himalayan ranges.

Thermally driven wind systems include land–sea breezes, which are not discussed here, as well as the more complex mountain–valley winds. The basic dynamic processes that are involved are: (i) an *antitriptic wind* component directed towards low pressure, when the Coriolis effect is small; and (ii) *a gravity wind* component directed downslope, in the absence of any general pressure gradient (Flohn, 1969). It is appropriate to begin by considering the nature and mechanisms of slope winds.
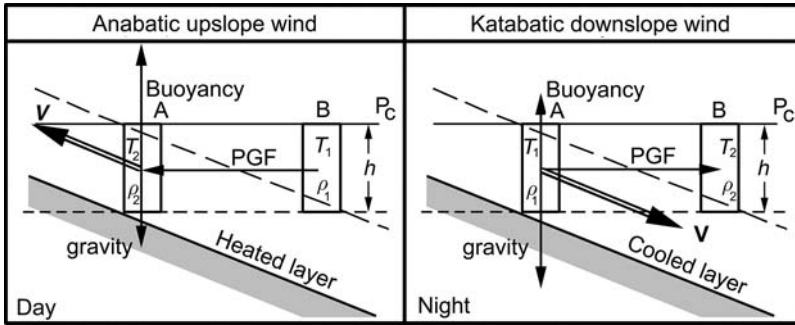
Fig. 3.32   Sketch of the forces involved in anabatic (left) and katabatic (right) slope winds (V). The temperature of the air in columns A and B determines their density (ρ). PGF, pressure gradient force.

3.2.1   Slope winds

In general, downslope movement of cold air at night is referred to as *katabatic* flow and upslope movement during the day is termed *anabatic* flow. Figure 3.32 shows schematically the forces involved.

Katabatic winds in the strict sense are *local* downslope gravity flows caused by nocturnal radiative cooling near the surface under calm clear-sky conditions. The extra weight of the stable layer, relative to the ambient air at the same altitude, provides the mechanism for the flow. Conversely, upslope flow is associated with daytime slope heating and buoyancy induced by this. The basic patterns of slope flow associated with potential temperature gradients are illustrated schematically in Figure 2.25 (p. 69). The cold air thickness over mountain slopes and alpine glaciers is typically 20–50 m with maximum speeds of 2–3 m s^{-1} at 20–40 m (Defant, 1949). The large-scale katabatic-type flows over Antarctica, which may be an order of magnitude deeper and stronger, were discussed above (p. 184). Figure 3.33 shows pilot balloon observations of wind profiles on the Nordkette, near Innsbruck, on a 42° slope. The maximum speed for both upslope and downslope winds occurred at a height of 27 m. As shown, upslope systems are generally stronger than their nocturnal counterparts since, in fine weather, the large daytime radiative exchanges encourage strong buoyancy effects. The entrainment of air from over the valley into the slope circulation also makes the upslope system somewhat deeper. In general, upslope winds are best developed on south-facing slopes, although even there they tend to be concentrated in gullies.

There are some important differences between katabatic slope winds and the weak (~ 1 m s^{-1}) small-scale drainage of air which causes cold air pockets and "frost hollows." While both arise from radiative cooling and density differences, a minimum slope of about 1:150 to 1:100 seems to be necessary for katabatic airflow (Lawrence, 1954), whereas small-scale air drainage does not set up any significant compensating currents, primarily as a result of the limited horizontal scale of surface irregularities. From observations on the Niagara Peninsula,

Fig. 3.33 Pilot balloon observations (B) and theoretical (T) slope winds on the Nordkette, Innsbruck: (a) upslope; (b) downslope (from defant 1949). The dashed lines show the differences between theory and observation.
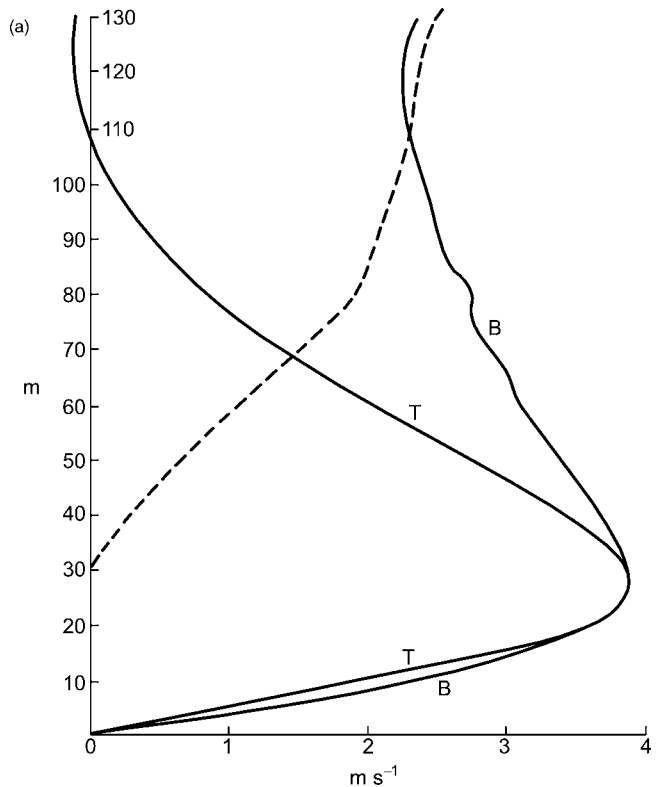
Ontario, Thompson (1986) suggests that cold hollows are a result of the early cessation, or decrease of turbulent heat transfer in sheltered locations rather than a result of cold down-slope airflow. Iijama and Shinoda (2000a, b) describe nocturnal cooling processes in a 150-m-deep basin in the mountains of central Japan (36.1° N, 138.2° E). Cold pools were observed on over half of the days studied in summer–autumn 1995–7 and about 30 percent of days had inversions exceeding 5 °C. Potential nocturnal cooling (PNC) is estimated from the temperature around sunset (T_s) and the night-time downward longwave radiation ($L\downarrow$):

$$PNC = T_s - (L\downarrow/\sigma)^{-4}$$

where T_s is approximated from $(L\downarrow - R_n/\sigma)^{0.25}$; where $\sigma =$ Stefan–Boltzman constant. During clear nights, the PNC reached 10 °C in late July and 20 °C in late September.

The controls of temperature inversions in frost hollows have been re-examined by Whiteman et al. (2004b) for five limestone sinkholes (or dolines) at 1270–1393 m altitude near Lunz, Austria. The dimensions of the depressions range from 45 to 600 m diameter and 7 to 54 m outflow depth, with the largest dimensions referring to the celebrated sinkhole at Gstettneralm (or Gruenloch), investigated by W. Schmidt

Fig. 3.33 (cont.)

(b)
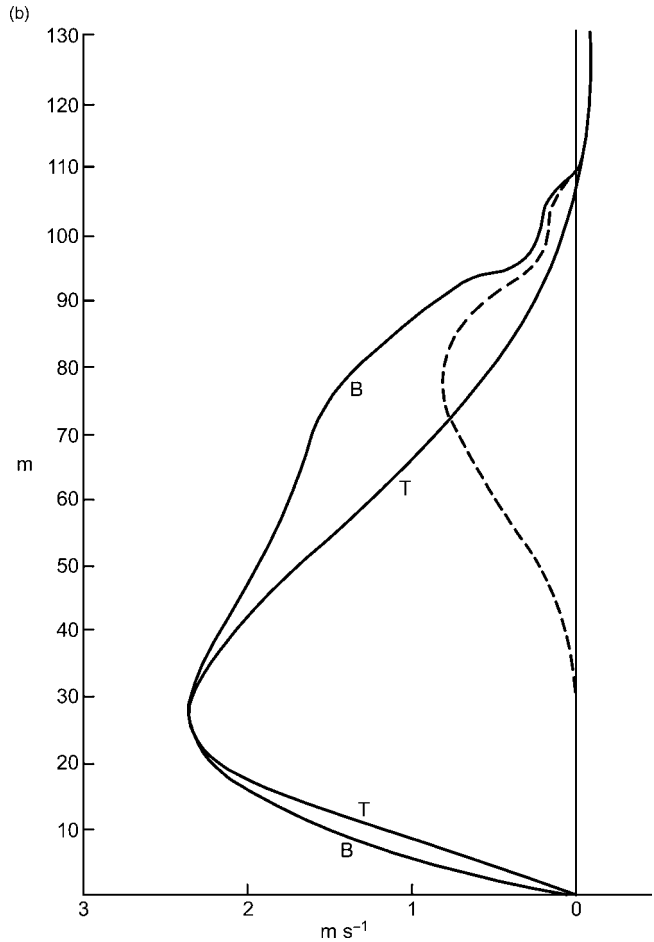
in the 1930s, that has recorded many minimum temperature readings below −40 °C (see Geiger *et al.*, 2003). Detailed measurements are available for two clear, undisturbed periods in mid-October and the beginning of December 2001; during the latter there was 0.4 m of snow cover. Table 3.4 shows representative temperature data for three depressions. Despite the large size difference between S0 and S1, the minimum temperatures are similar. Model analyses find that the sky view is the primary topographic factor controlling the cooling (Whiteman *et al.*, 2004b). Necessary preconditions are: undisturbed clear weather, a low ground heat conductivity, and a mechanism to dry out the low-level air during cooling. Zängl (2005a, b, c) shows that the formation of an ice cloud and subsequent sedimentation of ice particles, together with vapor deposition on the ground surface, can provide effective drying and prevent fog formation. Temperatures fall until the ground heat flux can balance the net longwave radiation loss. A fresh snow cover enhances the likelihood of extreme cooling. The concave basin shape plays an important role in excluding

Table 3.4 Minimum temperatures (°C) on the basin floor (T_f) and at the lowest saddle (T_s) and the vertical temperature gradient (°C m^{-1}) for sinkholes near Lunz, Austria (from Whiteman *et al.*, 2004b; p. 1229).

Sinkhole	Depth (m)	Area drained (m^2)	T_f Oct	T_s Oct	Gradient	T_f Dec	T_s Dec	Gradient
S0	54	295 000	−9.4	−1.6	0.15	−28.5	−13.3	0.29
S1	26	51 000	−9.0	4.0	0.51	−27.8	−10.4	0.73
S2	7	1600	−1.0	1.9	0.43	−16.5	−9.4	0.99

S0, Gstettneralm (Gruenloch); floor elevation 1270 m asl; S1, Seekopfalm, 1368 m asl; S2, Unnamed, 1393 m asl.

mixing of air near the basin floor with the ambient air. Any katabatic drainage that does occur moves into the basin at levels well above its floor.

The diurnal temperature range (DTR) in the sinkholes near Lunz in the October case was 22–28 °C compared with only 6–10 °C on the nearby plateau. In December, with snow cover, the DTR is much reduced although the minima are lower. A cold pool may persist for several days in undisturbed anticyclonic weather conditions. Extreme minimum temperatures have been reported in several high-elevation sinkholes. Both Gstettneralm and Peter Sink at 2500 m asl in the Bear River Range, Utah (Clements *et al.*, 2003) have registered minima below −50 °C! Inversion breakup in the Gstettneralm and Peter Sink occurs some 2.5–3 h after sunrise. Whiteman *et al.*, (2004a) report that air from below the inversion is removed by upslope flows as the sidewalls are heated and that subsidence, causing adiabatic warming, takes place over the basin. Whiteman (1982) described this same process for inversion breakup in valleys in the western United States (see p. 214).

Several expressions have been developed for estimating the wind speed associated with slope drainage. For small-scale movements, the equation of Reiher (1936) seems appropriate. This relates the speed (*v*) to the temperature difference between the cold slope air (*T*) and the surrounding air (*T*′):

$$v = \left(\frac{2gh(T' - T)}{T'} \right)^{1/2}$$

where *g* is the acceleration due to gravity (9.81 m s^{-1}); and *h* is the height above the surface of *v*.

For $h = 500$ cm, $T = 273.2$ K and $T' = 275.8$ K, Reiher calculated a speed of 1 m s^{-1} compared with an observed value of 1.2 m s^{-1}. In an experimental study on artificial slopes, Voights (1951) obtained results that also agreed with this expression.

The basic processes at work on slopes involve density gradients caused by heating/cooling that produce buoyancy differences, downslope advection of momentum, and frictional drag. For example, heating of air over a slope sets up a horizontal density gradient with the ambient air and this generates a horizontal

pressure gradient directed towards the slope. The presence of the valley side prevents an opposite gradient force acting on the parcel, thus the air moves upward along the slope. For slope cooling, the air moves downslope through the component of gravitational acceleration (g) parallel to the slope, while the pressure gradient force balances the component of g perpendicular to the ground (Mahrt, 1982). From the thermodynamics viewpoint, slope flows are determined by very localized, almost instantaneous equilibria (Vergeiner and Dreiseitl, 1987). Thus, upslope flows may cease abruptly when clouds obscure the Sun, cutting off the direct beam radiation on a slope. Vergeiner and Dreiseitl propose that the mass flux is proportional to the thermal forcing by the available sensible heat and inversely proportional to the static stability:

$$V\delta = \frac{(H/\tan s)(1-Q)}{c_p p d\theta/dz}$$

where $V\delta$ is the mass flux per unit width of slope; H is the sensible heat to the slope layer; δ is the slope layer thickness; and Q is the sensible heat transferred into the valley atmosphere.

They also suggest that anabatic slope flows comprise two separate cells on the upper and lower segments of the slope, separated by an inversion layer.

Three theoretical approaches to the analysis of katabatic flows can be distinguished (Manins and Sawford, 1979a). The earliest is based on hydraulic considerations of the downslope flow of a cooled air layer (Defant, 1933). This first approach has been followed subsequently by Fleagle (1950) and by Petkovsek and Hocevar (1971). Internal (vertical) structure of the flow is ignored, but time variations are considered. In the second approach, Prandtl (1952), Defant (1949, 1951) and Holmgren (1971) analyze the vertical structure of the temperature and wind velocity above the slope by regarding the flow as steady and invariant down the slope. This approach ignores effects of advection and assumes small slopes and constant exchange coefficients. The third approach allows inclusion of advection through numerical solution of the primitive equations of motion (Thyer, 1966). The mixing processes are parameterized.

Defant (1933) attempted to formulate a general expression for katabatic flow on slopes incorporating slope angle (s), friction effects, and the depth of the cold air involved (ΔZ):

$$V = \left(g \frac{\Delta Z}{C_d} \frac{\theta_2 - \theta_1}{\theta_2} \sin s \right)^{1/2},$$

where θ is the potential temperature of an upper layer (θ_2) and a lower layer (θ_1) and $C_d = 0.0025$, a dimensionless friction coefficient.

However, the direct relationship between wind speed and slope angle is not in accord with many observations of katabatic airflow. Concave slope profiles lead to

a rapid acceleration of flow on the steep upper slope, with a gradual transition to a structure that evolves more slowly on the lower slopes, with an elevated jet at 10 m or so (Smith and Skyllingstad, 2005). On uniform slopes, by comparison, there is a more regular flow profile with stronger winds at the base of the slope. Lawrence (1954) suggests that slope *length* is probably important, since short slopes can supply little cold air. He proposes that the expression:

$$V = \left(\frac{(2gl \sin s)(T' - T)}{T''} \right)^{1/2}$$

may be representative of the wind speed during the developmental stage of katabatic flow.

Subsequently, Petkovsek and Hocevar (1971) developed an expression for the downslope wind by assuming that, in the steady-state case, downslope acceleration of the cooled slope air due to gravity is balanced by friction. Adiabatic warming due to this motion is also taken into account. The speed is given by:

$$V = \left(\frac{C}{(\Gamma - \gamma') \sin s} \right) \left[1 - \exp\left(-\frac{g}{KT'} (\Gamma - \gamma') \sin^2 S \; t \right) \right],$$

where $C = \dfrac{1}{c_p} \dfrac{dL_n}{dt}$, is the mean radiational cooling of the layer; c_p is the specific heat of dry air at constant pressure; L_n is the effective longwave radiation loss; γ' is the original lapse rate of the surroundings; K is a friction coefficient; T' is the temperature of the ambient warmer air; s is the slope angle; and t is the time.

The maximum speed theoretically occurs as

$$\lim_{t \to \infty} V_{max} = C/[(\Gamma - \gamma') \sin s]$$

and it is proportional to the net radiational cooling and inversely proportional to slope angle and the lapse rate. Calculations illustrating the wind speeds for different lapse rates and friction coefficients with a slope angle of 11.5° are shown in Figure 3.34. Winds on the McCall Glacier, Alaska, are in general accord with calculations based on this model according to Streten *et al.* (1974). Before the steady state is reached, *v* is proportional to the lapse rate in the surrounding air and inversely proportional to the friction coefficient as well as to the slope angle. It must be noted that the model takes no account of possible effects due to a limited extent of slope.

The theoretical treatment of Fleagle (1950) expresses *mean* downslope flow in terms of slope angle, frictional effects and the non-adiabatic cooling rate of the slope air. The solution for equilibrium velocity is again proportional to the net outgoing radiation and inversely proportional to slope angle and to the thickness of the layer that is cooling. In addition, the model indicates that the flow is initially periodic and that during this time the speed is proportional to the cotangent of the
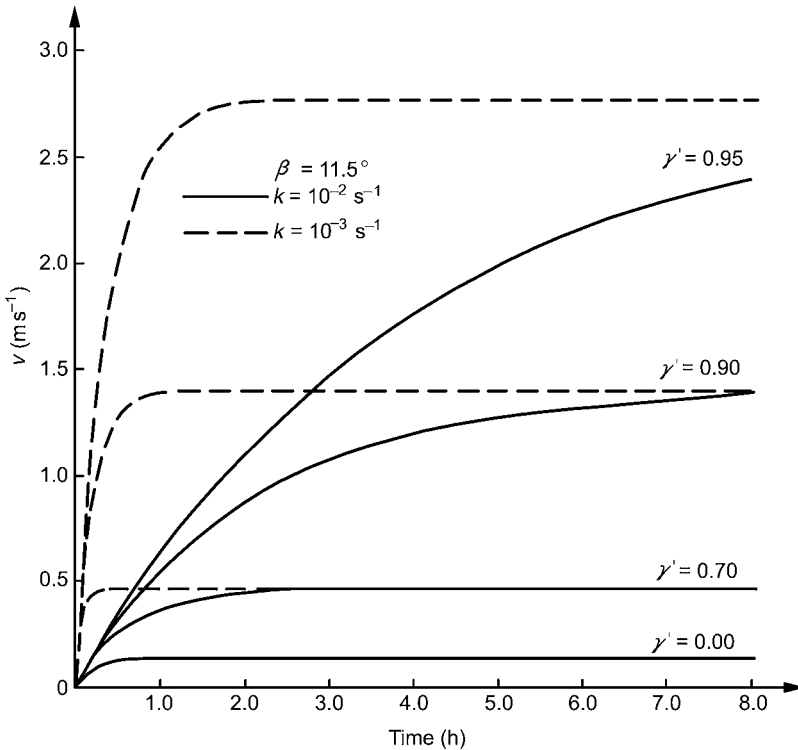
Fig. 3.34 Drainage wind velocity (v) on an 11.5° slope as a function of time, for different values of lapse rate (γ) and friction coefficient (k) (from Petkovšek and Hočevar, 1971).

slope angle. This fluctuating flow is attributed to the accelerating and divergent downslope flow of air weakening the initial pressure gradient. The adiabatic heating then exceeds the radiational cooling and causes an upslope pressure gradient, which slows the airflow. The cycle is repeated when the radiational cooling rebuilds the downslope pressure gradient. McNider (1982) proposes that the fluctuations in downslope flow depend on the temperature difference between the katabatic layer and the valley atmosphere. The oscillation period becomes determined by slope angle, ambient vertical temperature structure and a friction coefficient; the period is shorter as stability increases. Doran and Horst (1981) found temperature and wind speed fluctuations with a period of about 1.5 h in a valley in the Geysers area of northern California.

Surges of air are commonly observed on slopes greater than 10°. Küttner (1949) referred to these as "air avalanches." He noted a regular 5-min interval between gusts throughout two successive nights at a point 100 m below the 2800 m Höllenthal summit in the Wetterstein Mountains.

The final steady velocity, indicated by the model of Fleagle, is that which compensates for the cooling rate, maintaining equilibrium between the pressure gradient and frictional forces. He notes that, since the time required to reach the

final velocity on gentle slopes is so long, changes are likely to occur in the regional pressure field or in the diurnal regime, modifying the katabatic system and thereby removing the apparent paradox of v increasing without limit as $s \to 0$.

The Prandtl–Defant approach relating to the vertical structure of the flow, will not be detailed here since later work appears to invalidate their assumptions, at least for the katabatic case.

Manins and Sawford (1979a) have extended the hydraulic approach to include time dependence, downslope modification due to turbulent entrainment of the ambient air into the katabatic flow, surface stress, and radiational cooling of the katabatic flow. A key conclusion, which contradicts most previous theoretical studies, is that katabatic flows with strong stratification near the ground are dynamically isolated from the surface so that *surface drag is negligible*. The dominant retardation of the flow is by turbulent mixing across the interface with the ambient air. Manins and Sawford parameterize the entrainment of air from the environment into the katabatic flow by making the velocity of inflow proportional to the velocity scale (u) of the layer,

$$W_H = -EU$$

where W_H is the velocity normal to the slope at height H; the volume flux $Uh = \int_0^H u \, \mathrm{d}n$; h is the thickness; n is the direction normal to the slope; and $E = A/S_1 Ri$, where $S_1 = 0.5$ (a constant), $Ri = \Delta h \cos s/U^2$, a layer Richardson number which is a function of the slope. $S_1 Ri$ is an inverse internal Froude number of the flow and for katabatic flows is of order unity, $A \sim 2 \times 10^{-1}$ (a constant). E represents the change in potential energy of the katabatic flow by incorporation of ambient air. It is proportional to the turbulent kinetic energy produced by shear at the interface between the layer and the environment.

The model of Manins and Sawford shows that a katabatic flow grows in thickness linearly with distance downslope and increases in speed at a decreasing rate. The buoyancy of the flow decreases gradually through entrainment of ambient air. For a stably stratified environment with a buoyancy frequency $N = 10^{-2} \, \mathrm{s}^{-1}$, the flow properties at 4, 8 and 12 km downslope from the crest are as follows:

Downslope distance	4 km	8 km	12 km
Speed (m s^{-1})	3.0	3.3	3.0
Thickness (m)	45.0	95.0	186.0
Deficit of potential virtual temperature (°C)	1.6	0.71	0.19

As the cooled air moves downslope it meets denser ambient air and a greater proportion of the cooling is needed to maintain a buoyancy deficit in the layer. A balance between layer cooling and the flux of entrained cool ambient air is

established. The initial cooling involves surface heat fluxes, but as thermal stratification develops radiative divergence in the layer probably dominates. In Veracruz, Mexico, reduced nocturnal cooling and opposing trade winds can delay katabatic onset by 4–8 h (Fitzjarrald, 1984).

A field study by Manins and Sawford (1979b) in southern Australia confirms the inapplicability of previous one-dimensional models. Their observations show that surface friction effects are restricted to a "skin" only a few meters thick. The katabatic flow reaches a maximum in a layer 40 m thick and there is a deep "interface" to the ambient air above 160 m. The onset of the katabatic flow on a 4.5° slope about 0400 h. was related to increasing thermal stability with a gradient of 130 K km^{-1} in the lowest 40 m. The inversion extended to 120 m above the surface. Other studies on a simple slope (Rattlesnake Mountain, Washington) confirm that inversion depth increases with distance downslope and the elevation of the wind maximum rises as the flow strengthens and deepens (Horst and Doran, 1986); however, the inversion strength did not diminish downslope.

By way of summary, the various theories of downslope flow can be categorized according to the terms of the momentum equation that are included (Mahrt, 1982). The principal ones, following Mahrt are listed here.

(1) *Advective-gravity flows* where the downslope advection of weaker momentum balances the buoyancy acceleration. The equation for a gravity flow on a snow surface developed by Businger and Rao (1965) states that

$$V = \left[g \frac{\theta_0 - \theta}{\theta_0} (\sin s) x \right]^{1/2}$$

i.e. the velocity increases as the square root of the distance down the slope (x) and as the square root of the temperature deficit ($\theta_0 - \theta$).

(2) *Equilibrium flows* where buoyancy acceleration is balanced by turbulent-stress divergence. Defant (1949) adopts an eddy diffusivity and heat diffusion balanced by temperature advection. Here the velocity is linearly proportional to the temperature deficit; for constant temperature deficit and flow depth, the speed is constant. In the work of Petkovsek and Hocevar (1971) the flow is linearly proportional to buoyancy deficit and the slope angle.

(3) *Shooting flows* where downslope momentum advection and turbulent transport balance the buoyancy deficit. These flows have a Froude number > 1 and are commonly characterized by the occurrence of a hydraulic jump. Such flows were first noted in coastal Antarctica (see p. 418). The flow adjusts to the equilibrium case at a rate proportional to the stress divergence; i.e. more rapidly for greater drag. Drag can arise through entrainment of momentum at the upper boundary of the downslope flow (Manins and Sawford, 1979a).

(4)   *Ekman-gravity flows* involve the additional effect of Corolis acceleration because of large slope length and long time scales. On large ice sheets the terrain shape also introduces a thermal wind term when the flow is deep.

With regard to upslope circulations, it is worth pointing out that slope winds as such may not develop if the lapse rate is unstable or even neutral. Model calculations by Orville (1964) for a 1000-m-high mountain with 45° slopes indicate that, in a neutral environment, convection bubbles move up and away from the slope. With a stable environment, however, upslope motion occurs with columnar convection over the mountain crest.

For the nocturnal downslope regime, several studies show the existence of a return flow from the valley or adjacent lowland towards the middle slope. This has consequences for the thermal structure, discussed on p. *. Return flows are also an integral part of the circulation in mountain–valley wind systems that we consider next.

3.2.2   *Mountain and valley winds*

Fournet (1840) provided one of the first descriptions of mountain–valley wind systems. He noted that, in the alpine valleys of Savoie, southeastern France, there are daytime up-valley winds, especially in summer, whereas at night the wind is down-valley (a *mountain wind*), especially in winter. Mountain–valley wind systems are widespread phenomena even in cloudy maritime climates. For example, they have been investigated in Norway (Sterten and Knudsen, 1961) as illustrated in Figure 3.35, and in New Zealand (Sturman *et al.*, 1985). In two north–south valleys in the south-central Scottish Highlands, they occur on 20 percent of days during May–September (Price, 2005). These valleys are 4–5 km long, 2.5 km wide, with a longitudinal slope of 2–3° and a depth of about 550 m. Up-valley winds average 2.5–3 m s^{-1} compared with only 1–1.5 m s^{-1} down-valley.

Theoretical explanations began with Julius von Hann (1879) and were greatly elaborated by Wagner (1938), Ekhart (1934, 1944) and Defant (1951), based on aerological studies in the Alps, and later modified by Buettner and Thyer (1966), McNider and Pielke (1984) and Vergeiner and Dreiseitl (1987). Defant argued that upslope winds develop prior to the daytime up-valley wind and, at night, katabatic drainage currents feed the mountain wind. His familiar diagram of the successive stages is widely reproduced, although several other investigations have demonstrated that the various component winds develop almost concurrently. In an alpine valley near Davos, Urfer-Henneberger (1967) found that in over 90 percent of cases the downslope breeze ends at sunrise ± 20 min and the mountain wind about 25 min after sunrise. The upslope breeze begins between sunrise and 40 min later and the valley wind about 1 h after sunrise. Thus, the transitions occupy less than an hour in each case. In a later study (Urfer-Henneberger, 1970), she stresses that the valley wind sets in synchronously along the length of the valley, although in
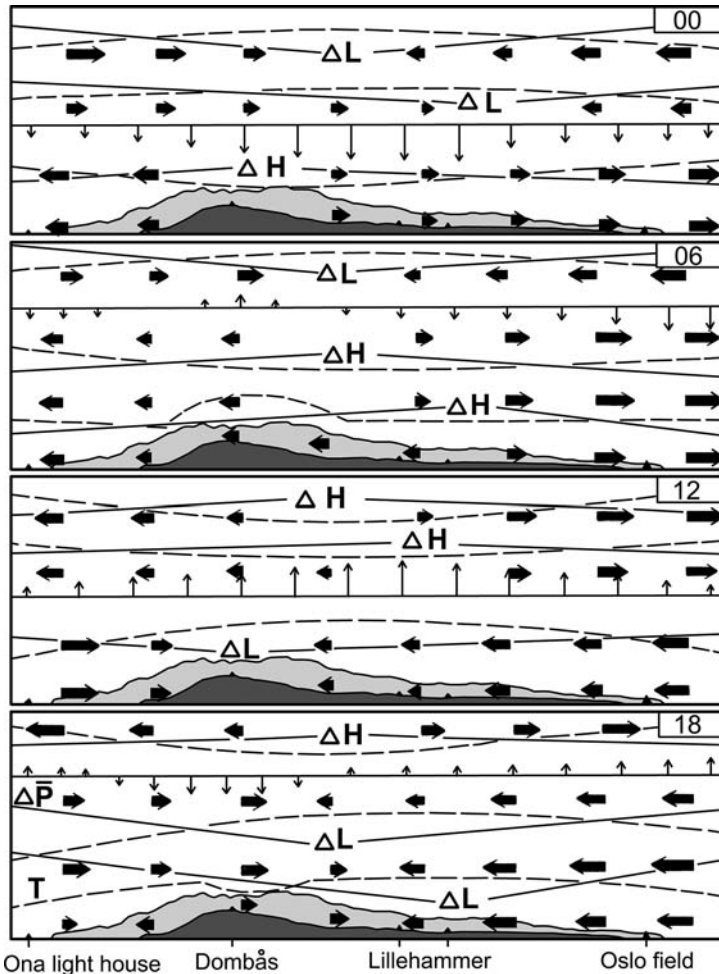
Fig. 3.35 Pressure anomalies (schematic) in relation to the mountain and valley wind system at 6-h intervals along the Gudbrandsdalen, Norway (after Sterten and Knudsen, 1961). Farder (59° N) is at the mouth of Osto Fjord, Ona (63° N) is on the west coast. The land rises to 650 m at Dombas.

the foothills of the Drakensberg, South Africa, the onset of the mountain wind occurs as a local front of cold air moving down valley (Tyson, 1968b).

These diurnal regimes appear to be most regular in narrow mountain valleys. Work by F. Steinhauser in the Rauris Valley north of the Sonnblick (cited by Flohn, 1969), shows the nocturnal mountain wind to have a frequency exceeding 70 percent in all months except May, whereas the valley wind has similar high frequencies only from about 1000–1400 h from May through September. However, even in broad valleys such as the Salzach, at Salzburg, Austria, up- and down-valley circulations are apparent (Ekhart, 1953). The flows along the valley axis are often stronger than the slope winds, despite the gentler topographic gradient, in line with the theories discussed above. For example, in the Inn Valley, maximum speeds average 3–4 m s^{-1} in the mountain wind and occur about 400 m above the valley floor (Defant, 1951).

In addition to these low-level diurnal systems, continuity requirements necessitate the occurrence of "anti-winds" (compensation currents) above the ridge crests. These are also more difficult to detect due to the interaction with the general upper airflow.

The daytime up-valley wind is primarily a feature of fine summer weather. The rising air over the valley slopes is replaced mainly by longitudinal flow from the plains, supplemented in *large* valleys by cross-valley flow with subsidence along the valley axis, as reported by Wagner (1938) (see also Urfer-Henneberger, 1970; p. 38). The primary controlling factor is the pressure gradient between the plains and valley, which extends up to about the mean ridge height (the "effective ridge altitude," Wagner, 1938).

The theoretical basis of the valley–mountain wind system is the circulation theorem of V. Bjerknes that relates to the thermally driven circulation set up by a horizontal temperature gradient. At its simplest, one can envisage two vertical air columns, one in the upper valley, the other on the plain. The former is heated more by radiation on the adjacent slopes and the air expands vertically, aided by the upslope winds. Consequently, airflow develops near the surface from the plain towards the valley head and an upper outward return flow forms. This type of mechanism was proposed by Wenger (1923) and evaluated for a simple case. Steinacker (1984) and Vergeiner and Dreiseitl (1987) show that the valley geometry, specifically the area–height distribution in the valley as a percentage of the total area, determines the difference in diurnal temperature amplitude between the air in the valley and that over the adjacent plains. The valley area is calculated from the valley length × width at the ridge height. The Inn Valley near Innsbruck has a valley : plains volume ratio of 1 : 2.1, corresponding closely to the 2.2 : 1 ratio of diurnal amplitude of virtual mean temperature between Innsbruck and Munich. For individual valley cross-sections, the ratio of valley width at ridge height to area of the vertical cross-section is compared to corresponding measures for the plain (McKee and O'Neal, 1989). For example, a valley with convex sides has a smaller ratio of air volume unit area than one of the same depth with concave sides. For the ideal forms in Figure 3.36, where width is twice the depth the so-called "topographic amplification factor" is 1.27 for a concave U-shaped valley, 2.0 for the V-shaped valley, and 4.66 for the convex shape compared to unity over the plain.

The driving force behind the geometric effect of the valley arises from the volume of air being heated and the associated diurnal temperature range and pressure fluctuations in the air column between the plain (or valley floor) and ridge height. Vergeiner and Dreiseitl note that valley temperatures (as an average of 0700 and 1600 h, local time) are slightly higher than on the plains, but the diurnal range is two to three times greater in the valleys. Correspondingly, there is a plains–valley pressure difference in fair-weather afternoons of approximately 5 mb, which disappears above the mean crest height. Interestingly, the valley wind is found to adjust rapidly to changes in pressure gradient attaining a local balance with frictional effects. Vergeiner and Dreiseitl also find that on days with weak pressure gradients, less than half of them show a well-developed valley wind regime.

Fig. 3.36 Depth–width and shape relationships in idealized valley cross-sections for a valley without and with a horizontal floor. See text (Müller and Whiteman, 1988).
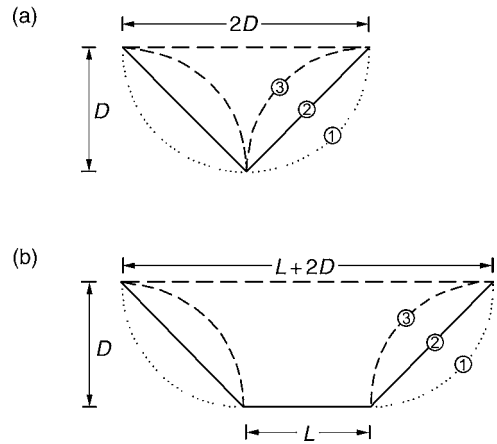
While the role of the "topographic amplification factor" is not in question, simulations by Rampanelli *et al.* (2004) show that the valley atmosphere tends only to be ~ 1–$2\,°C$ warmer than that over the plains. Kuwagata and Kimura (1995) show that in the 2500-m-deep Ina valley in central Japan, cross-valley circulations and the structure of the daytime boundary layer in the bottom of the valley play important roles in the daytime valley wind. By day, there is a turbulent mixed layer below 1000 m, with stably stratified air above, which they attribute to subsidence in a thermally-induced cross-valley circulation. Model simulations by Rampanelli *et al.* (2004) examine idealized two-dimensional valley flows and three-dimensional valley–plains flows. For a straight valley with a horizontal floor they find that the heated valley walls give upslope flows that require compensating cross-valley circulations and subsidence over the valley, as originally proposed by Wagner (1938) and restated by Vergeiner and Dreiseitl (1987). A new finding is that in the three-dimensional case, where the valley widens towards the plains, the subsiding air brings down potentially warmer air from above (see Figure 3.37) and this subsidence heating becomes the main contributor to the valley–plain temperature difference that drives the valley wind via the horizontal hydrostatic pressure gradient.

A second factor that interacts with valley geometry is the stability structure of the valley air (Steinacker, 1984). If energy is input mainly to the narrow, lower parts of a valley, where air volumes are small, the temperature change will be large and conversely if the energy is confined to the larger volume in the upper parts the change is small. Less attention has so far been paid to this effect.

The topographic amplification effect, augmented when there is stratification associated with an inversion, gives a reaction time of about 30 min for the valley wind system to reach equilibrium between pressure gradient and frictional forces (Nickus and Vergeiner, 1984). The pressure differences, typically 1–2 mb/100 km (Whiteman, 1990) have been studied along the Gudbrandsdalen, which transects the mountains of southern Norway, by Sterten and Knudsen (1961). Using pressure anomalies at 6-h intervals from a centered 24-h mean, they show typical
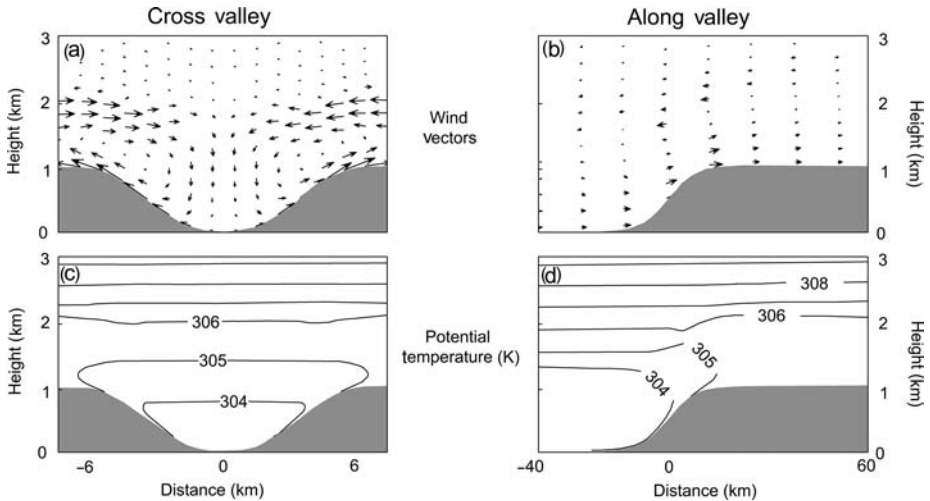
Fig. 3.37 **Sections of wind vectors and potential temperature, respectively, (a) and (c) cross-valley and (b) and (d) along-valley, for a WRF model simulation with three-dimensional plains–valley topography. The cross-sections are 20 km upvalley (from Rampanelli *et al.*, 2004).**

fluctuations of ± 1.5 mb on days with at least three stations recording mountain valley winds in summer, and ± 0.7 mb in winter (see Figure 3.35).

Buettner and Thyer (1966) carried out intensive field measurements, including balloon and aircraft observations, in the Carbon River Valley on the northwest side of Mt. Rainier, Washington State, during the summers of 1957–60. They interpreted the data by plotting time–height and longitudinal sections of wind structure at several valley stations. Figure 3.38a shows a longitudinal section in the upper Carbon River Valley for 8–10 August 1960 and Figure 3.38b a cross-section of the same valley on 9 July 1959. The maximum speeds are located at about a quarter to a third of the valley–ridge height difference above the valley floor, due to friction near the surface and the smaller amplitude of the temperature perturbation with increasing elevation. The anti-winds above have a similar vertical extent to the main system below. Thyer (1966) developed a numerical model incorporating the valley–plains gradient effect and also the slope winds. The mathematical formulation involves the three-dimensional equation of motion and of heat transfer, the equation of continuity of mass, the equation of state and Poisson's thermodynamic equation. These were applied to a symmetrical V-shaped valley 400 m long and 1000 m high with $45°$ slopes. Separate experiments successfully simulated both the shallow slope winds and the longitudinal circulations with their compensation currents. A reduction of slope angle to $26.5°$ and ridge height to 200 m reduced the wind speeds considerably by comparison with the standard run. The experiments represent only the earlier phases of these circulations, since the computer runs were short, although Thyer points out that a steady state does not occur in the valley wind system in nature. An earlier theoretical analysis by Gleeson (1953)
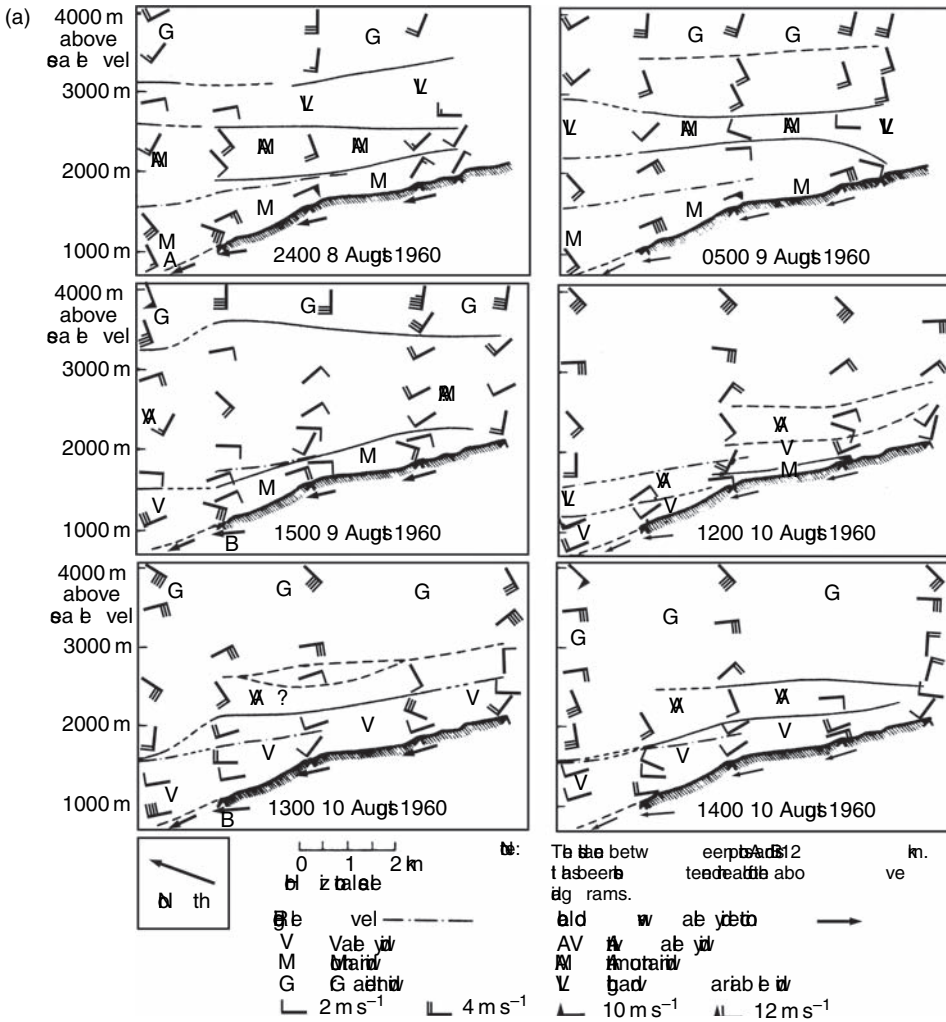
Fig. 3.38 Mountain and valley winds in the vicinity of Mt. Rainier, Washington. (a) Longitudal section in the upper Carbon River Valley, 8–10 August 1960; (b) cross-section in the same valley, 9 July 1959 (from Buettner and Thyer, 1966).

suggests that the Coriolis effect is of some importance, at least in determining the vertical phase of the wind changes, although Thyer's model did not take this into account.

Observations on four nights in September 1984 in the 25-km-long Brush Creek Valley, Colorado, with tethered balloons and Doppler lidar (Clements, *et al.*, 1989) indicate a nocturnal mountain wind maximum of 5–6 m s^{-1} at a height of 0.2 valley depth (80–100 m above the floor). There is a surface-based inversion averaging 3.2 °C/100 m in the lowest 200 m, above which the air is isothermal to above ridge-top height. The depth of the drainage flow and volume flux are inversely related to

Fig. 3.38   (cont.)

(b)
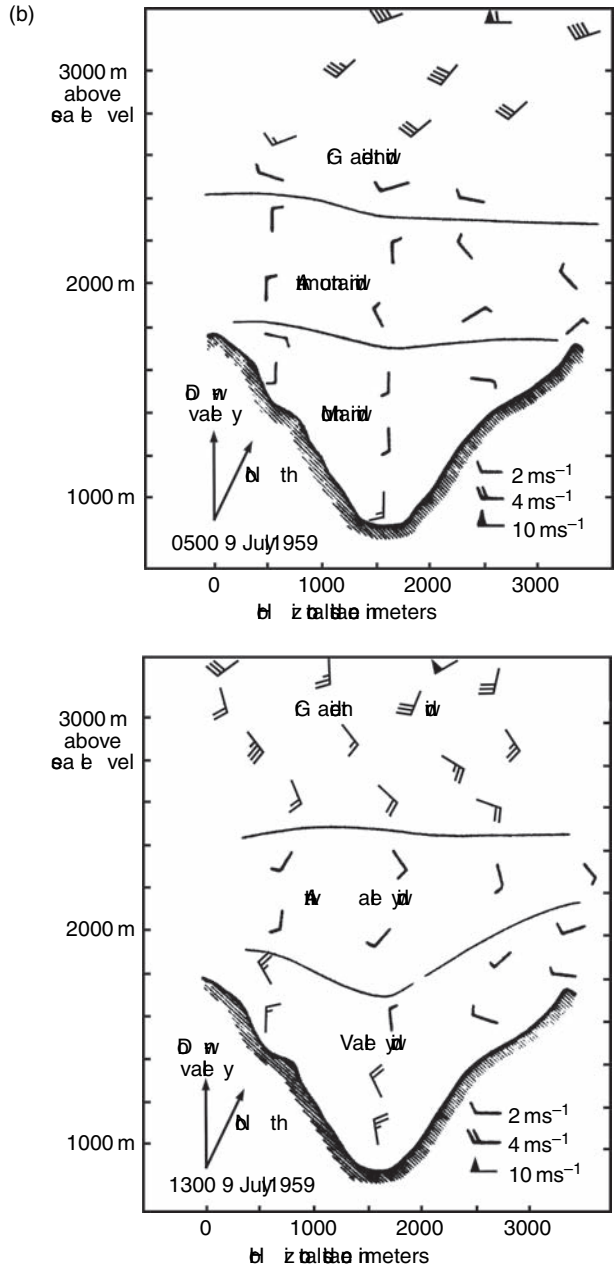
the strength of external geostrophic winds. For Brush Creek, an up-valley wind at ridge level $> 8\,\mathrm{m\,s^{-1}}$ will totally override drainage flow (Barr and Orgill, 1989). Barr and Orgill were able to characterize changes in the depth of cold air drainage and volume flux in terms of the influence of external wind and radiative effects on the collection of cool air in a valley air shed. Under ideal conditions of radiative

cooling and light ambient winds the drainage depth can fill the valley to the ridge
crest level (cf. Figure 3.38b), but when low cloud suppresses radiative cooling, the
drainage may occupy less than 25 percent of the valley depth. Cold air drainage can
also be eroded by turbulent entrainment of ambient air under conditions of
moderate to strong ridge top winds. Barr and Orgill (1989) showed that the top
of the drainage flow is bounded by a transition layer that is variable in time and
space and depends on the thermal stability and also on the wind speed and direction
at ridge level. Standing internal buoyancy waves are thought to determine the
encroachment of ambient air into the valley regime. Other studies in the same
valley show complex interactions between the main valley drainage and that of
small tributaries. These may cause 8–16 min wind oscillations and also changes
during the course of the night due to changes in cooling rates of the tributary
sidewalls and upper ridge slopes (Porch *et al.*, 1989). The large *sky view factor* (solid
angle of visible sky/2π) of upper slopes permits greater radiation and cooling than
lower slopes, which also receive downward infrared radiation from valley walls
(Whiteman, 1990).

The typical diurnal evolution of valley flows in western Colorado is illustrated in
Figure 3.39. At night, a temperature inversion occupies the depth of the valley and
decouples the down-slope and down-valley winds from the flow in the free atmo-
sphere. After sunrise, a convective boundary layer (CBL) forms over heated valley
surfaces, while over ridges there is a neutral layer. The top of the inversion sinks
over the valley and eventually this, combined with the CBL growth, eliminates the
"stable core" and allows the valley air to become well mixed. In the afternoon,
convection is widespread over the valley surfaces and there are up-slope and
up-valley flows. The valley flows can become turbulent and upper level winds can
be channeled into the valley, thereby enhancing or counteracting the valley regime.
In the late afternoon–evening, down-slope flows develop on shaded sidewalls and
a temperature inversion builds in the valley with down-valley flow.

Fig. 3.39 **An idealized view of the typical diurnal evolution of temperature (bold) and wind structure in a 500-m-deep valley in western Colorado (from Whiteman, 1990).**
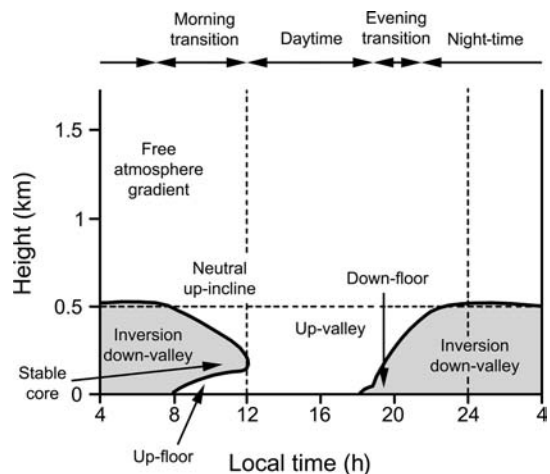
A modeling study by Sato (1989) indicates that when the vertical slope drop δz exceeds a critical value θ/γ, where θ is the potential temperature of the ambient atmosphere and γ is the ambient gradient of θ, the drainage flow establishes an equilibrium velocity and depth independent of topographic parameters. Where δz is below the critical value, the ambient stability does not modify the slope flow. Numerical simulations for drainage flows on the east slope of the Front Range, Colorado show that for a given mountain slope, a decrease in slope gradient in the foothills decelerates the mountain drainage and leads to its lifting (Bossert and Poulos, 1995). They also demonstrate the control of flow strength by the area of the drainage basin. Hence, the speed of the drainage jet from Coal Creek Canyon (between Boulder and Golden, Colorado) is less than half of those emanating from nearby Ralston Canyon and Eldorado Canyon, which have larger basin areas.

McNider and Pielke (1984) use a three-dimensional numerical meso-scale model, forced by a surface energy budget, to simulate mountain and slope winds for an idealized valley and an actual Colorado valley. Realistic downslope flows and cold air pooling were obtained. The model shows that the deep cooling of valley air is not directly due to downslope flow, but is determined by upward motion over the valley axis. The convergence and turbulent mixing of the downslope flows also redistribute radiatively cooled air in the valley bottom.

Valley orientation and therefore slope exposure may considerably modify these theoretical systems as demonstrated by Urfer-Henneberger's (1970) study of the Dischma Valley near Davos; this 15 km long, 4 km wide, 800–100 m deep valley runs south-southeast–north-northwest. Temperature data collected on both slopes display the anticipated time asymmetry of slope heating during fine weather. As a result, the circulations are complicated by lags between the onset of the slope winds and by cross-valley components. The eight diurnal phases that she identified are shown schematically in Figure 3.40 and differ markedly from the original scheme of Defant (1951). Urfer-Henneberger also questions some of the mechanisms inferred by Defant (1949). In particular, air temperatures at the slope stations in the Dischma Valley do not show a nocturnal temperature inversion, although she acknowledges the possibility of stronger ground level cooling. Three-dimensional observations in the Dischma Valley using ground stations, balloons and motor gliders during project DISKUS amplify the earlier investigations. Hennemuth and Schmidt (1985) show that deviations of the slope winds from the downslope gradients are produced by the superimposed valley/mountain winds and the cross-valley components induced by differential slope heating.

In the absence of external forcing, it is observed that winds on valley sides show diurnal turning clockwise (counter-clockwise) on the right (left) bank, facing down-valley (Whiteman, 1990; Whiteman et al., 1999b, Stewart et al., 2002), as originally described by Hawkes (1947). There is daytime turning towards nearby heated terrain features so that flows are upslope in the morning, up-valley in the afternoon, downslope in the evening and down-valley at night. A possible
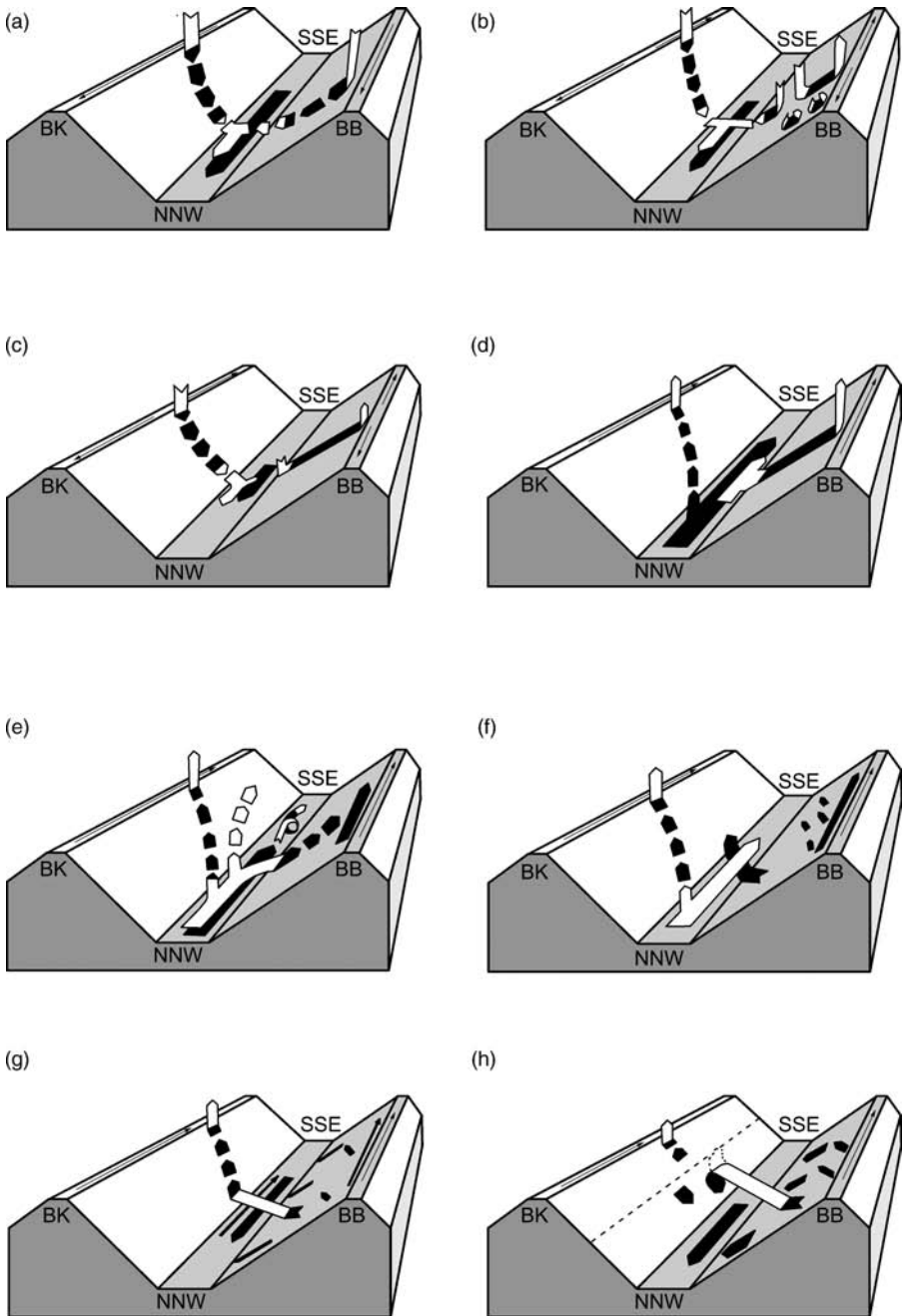
Fig. 3.40 Model of mountain and valley wind system in the Dischma Valley, Switzerland. **(a)** Midnight to sunrise on the east-facing slope; **(b)** sunrise on the upper east-facing slope; **(c)** whole facing slope in sunlight; **(d)** whole valley in sunlight; onset of valley wind; **(e)** west-facing slope receiving more solar radiation than east-facing slope; **(f)** solar radiation only tangential to east-facing slope; **(g)** sunset on east-facing slope and valley floor; **(h)** after sunset on the lower west-facing slope (from Urfer-Henneberger, 1970).

contribution from the expected anticyclonic (cyclonic) lateral wind shear induced by friction along the sidewalls does not appear to have been analyzed.

The effect of cross-valley wind components due to differential slope heating has been analyzed theoretically by Gleeson (1951). He demonstrates that inertia effects, which arise through the cumulative role of solar radiation differences between slopes, have considerable importance for wind dynamics. Such effects are ignored, for example, in Fleagle's equilibrium approach to slope drainage. Changes in friction and in the Coriolis parameter are also shown to be important. As slope angles increase, the maximum speed of the cross-valley winds increases due to the enhanced contrast in slope heating. Likewise, cross-valley winds tend to be stronger in summer than winter. Changes in slope angle and valley orientation also affect the phase of maximum cross-valley winds speeds. For example, if the angle of west-facing slopes is increased, the sunrise occurs later on the slope, giving a maximum speed later in the morning. If the valley orientation is shifted from north–south to northeast–southwest, the wind speed maxima in both morning and afternoon occur later, as illustrated by Urfer-Henneberger's results.

The concept of accounting for the geometry of a drainage basin to explain mountain–valley winds, developed by Steinacker (1984, 1987) and Vergeiner and Dreiseitl (1987) for the Inn Valley, has been evaluated by a program of field measurements. During spring 1982, the Mesoscale Experiment in the Region Kufstein-Rosenheim (MERKUR) took place in a 37-km-long, 8-km-wide section of the Inn Valley that contains major side valleys and terraces. Freytag (1987) estimates the heating rate for the total valley air volume to that of the adjacent foreland is about $2.3:1$. Mean mass fluxes up to 1000 m above the surface of the valley have been calculated for the 2.2-day observational period (Table 3.5). The mean mass budget equation can be expressed:

$$\Delta M_x + M_s + M_y + M_r = 0,$$

where ΔM_x is the horizontal mass flux difference; M_s is the flux into/out of the slope layer; M_y is the flux in/out of the side valley; M_r is the residual ascent/subsidence.

Table 3.5 can be used to distinguish four major phases. Following Freytag (1987), these are listed here.

(1)   Upslope winds and continuation of the mountain wind (0500–1100 GMT). Upslope transport (M_s) accounts for most of the residual flux associated with air subsiding at about $2\,\mathrm{cm\,s^{-1}}$ at ridge height. There is a positive horizontal mass flux down-valley (ΔM_x) as a result of mountain winds converging from the side valleys ($-M_y$), implying that there is a "local" compensation of the upslope flow within any particular valley cross-section.

(2)   Upslope winds and valley wind (1100–1500 GMT). The data show that the valley wind increases up-valley ($\Delta M_x > 0$). This results from greater heating of air in the side valleys, leading to lateral components of valley wind. These

Table 3.5 Mean mass budgets[a] of mountain and valley winds during MERKUR.

Time (UTC) 25–26 March 1982	0500–1100	1100–1500	1500–2100	2100–0100	0100–0500
Phase	Heating			Cooling	
Wind	Mountain	Valley		Mountain	
Horizontal mass flux difference, ΔM_x	7.9	9.5	11.3	12.4	10.1
Flux into the slope layer, M_s	6.3	5.8	−8.5	−7.0	−4.4
Flux into side valleys, M_y	−5.0	7.6	8.6	0.3	−7.3
Residual ascent/subsidence, M_r	−9.2	−22.9	−11.4	−5.7	+1.6
Mean vertical wind, 0–1 km	−1.8	−4.0	−0.8	−1.0	0.1

[a] Mass budget of the valley segment is $\Delta M_x + M_s + M_y + M_r = 0$.
Main budget components for 0500–1100 UTC: $M_s = -M_r$; $\Delta M_x = -M_y$; for 1100–1500 UTC: $M_s + M_y + \Delta M_x = -M_r$; for 1500–2100 UTC: $-M_s = \Delta M_x$; $M_y = -M_r$; for 0100–0500 UTC: $\Delta M_x - (M_y + M_s)$. Fluxes: 10^6 kg s^{-1}; vertical wind: cm s^{-1}.
Source: from Freytag (1987).

must be compensated by subsidence into the foreland end of the main valley ($-M_r$). The main valley narrows up-valley and the side valleys are smaller and less numerous. Hence, the merging upslope and valley winds here produce a mass accumulation and rising air. This phase comprises three superimposed scales of circulation: slope winds with local compensation by subsidence; valley wind components entering the side valleys with subsidence over the main valley; and the longitudinal valley wind with compensating descent over the adjacent foreland;

(3) Continuing valley wind, with downslope winds (1500–2100 GMT). Downslope winds ($-M_s$) now contribute to the valley wind. Less subsidence is required to offset the flow into the side valleys;

(4) Downslope winds and mountain wind (0100–0500 GMT). There is an increasing mountain wind along the Inn Valley ($\Delta M_x > 0$) due to the combined side valley and downslope flows. There may be weak ascent in the center of the valley when the mountain winds are weak. This is the only phase when there is a single overall direction of circulation.

For the Inn Valley, Austria, Zängl (2004) finds that the along-valley mass fluxes in the up-valley wind are increased (decreased) where there are tributary valleys from the northern (southern) sides. The north side is in the direction of the Alpine Foreland. On the south side some of the up-valley flow is deflected into these tributary valleys. For down-valley winds the pattern is reversed and the effects are greater than for up-valley flow. The narrowing of the Inn valley at its exit into the Alpine Foreland reduces the down-valley mass flux at low levels raising the level of maximum wind. Northward of this constriction a transition from subcritical

to supercritical hydraulic flow causes the flow to accelerate, forming a low-level jet, and this band structure is maintained for tens of kilometers into the Foreland.

A related field and modeling study in the Dischma Valley provides an energy balance for the valley atmosphere. Hennemuth and Köhler (1984) show that observed mid-day heating rates of $0.9\,K\,h^{-1}$ agree well with the rate calculated from the convergence of sensible heat flux from the surface. This energy is advected upward during the afternoon and appears to be transported via subsidence into the main Davos valley, which the secondary Dischma Valley joins (Hennemuth, 1985). However, associated studies of the specific humidity suggest that only a small fraction of the daytime surface evaporation leaves the valley by vertical transport. Rather, upslope winds export moisture from the Dischma Valley in the morning while the valley winds import moisture in the afternoon (Hennemuth and Neureither, 1986). These findings emphasize the importance of scale transfers from side valleys into main valleys.

In alpine terrain, it is not uncommon to find small plateaus, often on valley terraces, with high mountains above and deep valleys below. Gantner *et al.* (2004) describe the interacting valley–plateau circulations of Zugspitzplatt in the Wetterstein massif near Garmisch-Partenkirchen, southern Germany. The plateau extends 3 km east–west and 2 km north–south, rising 600 m westward towards the Zugspitze, with a mean slope angle of about $11°$. To the south there is a steep drop of some 700–800 m into the Rein valley, with a less steep descent from the plateau to the east, where the Rein river curves northward. Observations, including balloon soundings, during 5 weeks in July–early August 2002 show that during fine weather there is a well developed diurnal circulation. Nocturnal outflow and daytime inflow a few hundred meters deep at the eastern edge of the plateau are observed, involving descent into and ascent from the valley, respectively. The inflow, which is rather humid coming from the lower valleys, extends westward across the plateau by late afternoon. On 10 out of 36 nights, a nocturnal descent of dry air was observed on the plateau. In one case the dew point temperature dropped 18 K in 5 h, suggesting descent from well above the summit level. Another case of the influence of local plateaus is reported by Hornsteiner (2005). On clear nights in autumn and winter in the Bavarian Alps, nocturnal flows are observed to drain from an elevated plateau south of Mittenwald into the upper Isar Valley forced by the thermal gradient between the plateau surface and the ambient free air. The upper flow crosses a ridge and descends into the valley leading to strong warming and decreased relative humidity that is characterized as a mini-föhn.

The valley geometry concept of Steinacker (1984, 1987) assumes that mountain valleys have immediately adjacent lowlands. In much of the interior of the western United States, however, many valleys are cut into plateaus remote from plains. McKee and O'Neal (1989) extend the topographic analysis by considering variations in valley cross-section geometry along its length. They compare plots of valley width/area against distance down valley for Brush Creek and Gore Greek, Colorado (Figure 3.41) and show that in the former, a "draining" valley for

Fig. 3.41 **Plots of valley width/area (W/A) ratios (m^{-1}) along Brush Creek, Colorado (draining) and Gore Creek, Colorado (pooling) (from Whiteman 1990, after McKee and O'Neal 1989).**
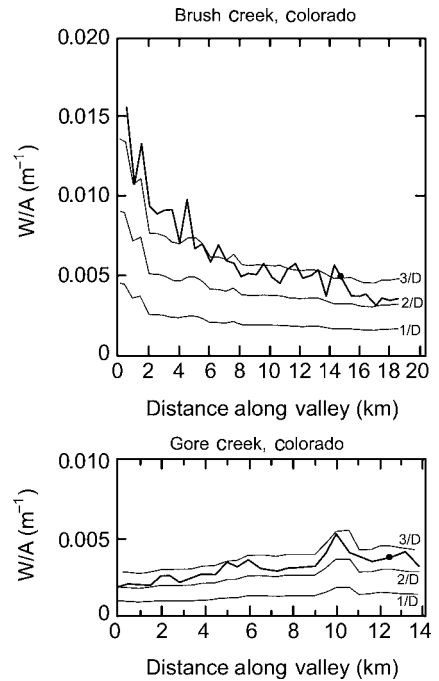
nocturnal airflow, the width/area ratio decreases down valley. Theoretical nocturnal cooling rates decrease from 1.0–1.5 °C h^{-1} at the head of Brush Creek to 0.4 °C h^{-1} 18 km down valley. In contrast, Gore Creek is a "pooling" valley because the cooling rates increase in response to an increasing width–area ratio. Tethersonde profiles of temperature and wind speed and sodar echoes of boundary-layer structure in Brush Creek (see Figure 3.42) and its eventual outlet into the Colorado River east of Grand Junction, Colorado, illustrate the pooling effect of basins (Neff and King, 1989; see Note 5, p. 231). Nocturnal air drainage from Brush Creek, and others joining the southeastward flowing Roan Creek, is blocked 50 km to the south by a 300 m escarpment. The De Beque basin fills with drainage flows over several hours, despite air exiting through De Beque Canyon on the Colorado River. The depth of this cold pool (in excess of 300 m) can modify the tributary drainage in Brush Creek and causes drainage flows from tributary valleys to enter the basin as elevated "jets." Geometric characteristics of basins described by Petkovsek (1978, 1980) can be related to the accumulation and outflow of such cold air pools, but more work on this is needed.

Egger *et al.* (2000, 2002) describe a situation in the Himalaya where the influence of along-valley changes in the valley cross-section is over-ridden by other effects. The NNE–SSW-oriented Kali Gandaki valley in the Mustang Himalaya is 180 km in length, extending up to the Tibetan Plateau, and 5 km deep. During September–October 1998, weak nocturnal mountain winds occurred between 2300 and 0600 LST, averaging 3–4 m s^{-1}. In contrast, up-valley winds that began around
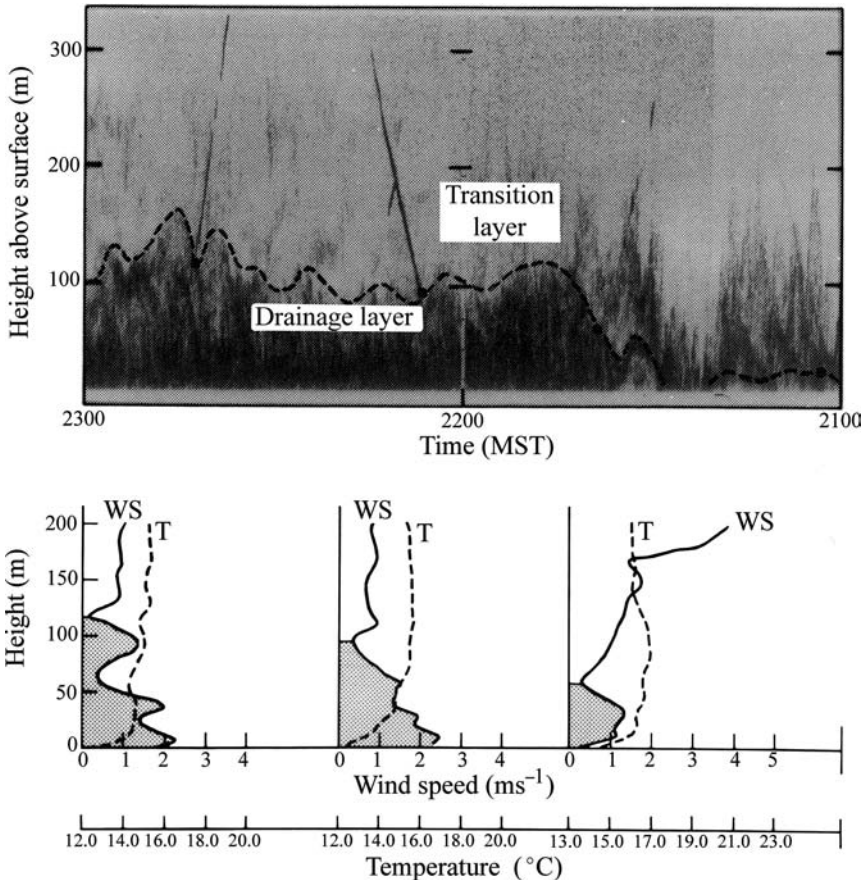
Fig. 3.42 Sodar returns (above) and tethersonde observations (below) during drainage initiation in Willy's Gulch, Colorado, 16 September 1986. The arrows denote the transit direction of the tethersonde balloons; the point at 2140 MST marks the start of northerly drainage flow, with a decrease of southerly ridge top winds from about 7 m s^{-1} to 3–4 m s^{-1}. The drainage layer thickens to ≥ 100 m (dashed line). Wind speed (WS) and temperature (T) profiles correspond to the three soundings on the sodar record; the drainage layer is stippled. Time runs from right to left (Neff and King, 1989, *J. appl. Met.*, **28**, p. 522, Fig.5).

0800–1000 LST reached 15–20 m s^{-1} by 1400 h. Fully developed up-valley flow was confined to a 1–2 km deep, neutrally stratified, turbulent layer above which the air was stable. Hydraulic theories for the strong winds that rely on the presence of strong inversions can be ruled out since these were not generally observed. Simultaneous soundings taken 5–10 km apart along the valley reveal a remarkable variability induced by the topography and, perhaps, by flow instability. The valley cross-profile changes upstream from a narrow V-shape to an open U-shape yet, in spite of this, acceleration was observed in the daytime inflow. Egger *et al.* consider that the daytime wind velocity is related to the overall topography. A strong pressure gradient is set up between the free atmosphere to the south, which has little daytime heating, and the mountains and Tibetan Plateau to the north. The up-valley flow is

essentially an inertial jet; Zängl *et al.* (2001) propose that the flow pattern near the entrance to the Mustang Basin has a supercritical structure to which gravity waves that are set up by the ridges contribute by protruding into the valley. Relatively stable air advected from the foreland into the basin assists the formation of the gravity waves and also explains part of the day–night asymmetry in wind velocity. Mesoscale modeling with MM5 shows that humidity, especially due to the evaporation of rain, is essential for correctly simulating the strength of this asymmetry because of its impact on the boundary layer structure above the Himalayan foothills.

Heavy rainfall in Alpine valleys has been shown to cause down-valley airflows through subsidence resulting from the melt and evaporation of precipitation particles (Steiner *et al.*, 2003). During MAP Intensive Observation Period (IOP) 8 on 21 October 1999, the down-valley flow developed in opposition to moist southerly flow aloft.

Several studies report periodic fluctuations in the mountain wind. Buettner and Thyer (1966) found a 25-min periodicity in the Carbon River Valley with speed fluctuations of 1.5 to $6.5 \, \mathrm{m \, s^{-1}}$. In valleys of 300–350 m depth in the Drakensberg foothills near Pietermaritzburg, South Africa, Tyson (1968a) reports surges in the mountain wind at about 90–150 m above ground level varying between 45 and 75 min with the maximum speed ranging between 1.6 and $3.8 \, \mathrm{m \, s^{-1}}$. He shows that the profile can be approximated by the Prandtl model where maximum speeds occur at 0.75 of the depth of the down-valley air. In another study in Bushmans valley in the Drakensberg, periodicities ranged between 2 and 4 h (Tyson, 1968b).

Two special cases of mountain wind systems merit note. One is the persistent down-valley, *glacier wind*, which occurs in alpine valleys where there is a glacier or snowfield. It is generally strongest and deepest (50–300 m) in early afternoon when the temperature difference between the cold surface and the air is at a maximum (Tollner, 1931; Hoinkes, 1954; see p. 165). The glacier wind is not restricted to fine weather conditions although by day it does not reach far down valley and may be overlain by a valley wind. It is commonly gusty and turbulent, like nocturnal slope winds. Hoinkes reported double maxima (before sunrise and before sunset) and minima (before noon and before midnight) in the Alps. Streten and Wendler (1968) found the same pattern in central and southern Alaska, but in northern Alaska there is a single nocturnal maximum and late afternoon minimum (Streten *et al.*, 1974). They suggest that this is due to the strong "nocturnal" inversion and the weak temperature gradient between the ice and its surroundings during the day.

The second special regime is known as the *Maloja wind*, from its type location between the Engadine and Bergell valleys, Switzerland (Defant, 1951). This is a "mountain wind" blowing from the southwest down the upper Engadine valley during the day. The valley wind in the Bergell valley to the southwest climbs 300 m over the Maloja Pass between the two valleys to flow northeastward along the Engadine towards St Moritz. Frequently associated with the Maloja wind, especially on summer afternoons, is an unusual "snake"-like tube of stratocumulus cloud 100–500 m wide and 30–300 m above the surface. Sometimes it fills most of

Fig. 3.43 Tubular stratocumulus cloud observed late morning in early September in a pass near Kremmling, Colorado. The motion is from the northwest (left) where the valley drops steeply about 200 m. The cloud form and topography are analogous to the Maloja 'snake' (see text) (G Kiladis).

the pass (Holtmeier, 1966; Gross, 1984). It occurs during dry anticyclonic weather with a northeasterly gradient wind, but the phenomenon requires a moist low-level counter-current from the southwest – the valley wind in the Bergell valley. Cloud forms as this flow rises 300 m to the pass and extends northeastward into the Engadine (Gross, 1984) (cf. Figure 3.43). Valley channeling with anti-winds is also reported by Wippermann (1984) in the middle Rhine in Germany.

An interesting approach to classifying valley wind systems caused by channeling or by thermal forcing in areas of complex terrain, is illustrated by Kaufman and Weber (1998). They use directional correlation coefficients, based on the occurrence of two preferred along-valley wind directions, and a hierarchical clustering routine with a distance measure between station-pair correlations. Analysis of data for 50 wind stations operated in the upper Rhine valley during the MISTRAL experiment identified a few major groups. Cluster 1 stations, located near Basel and in hilly terrain, were open to the west enabling synoptic westerly winds to suppress valley influences. Cluster 2 stations were at higher elevations and dominated by large-scale influences. Cluster 3 stations had local, thermally controlled valley regimes while channeling by the mountains of the Vosges and Black Forest affected winds at Cluster 4 stations.

The characteristics of flows in complex alpine valleys that bifurcate downstream at T- or Y-shaped valley junctions has recently been studied by Dobrinski *et al.* (2006). They employ a two-dimensional single layer, shallow water flow model with different valley configurations and widths. Major findings are: (1) that the flow pattern below the junction depends on (i) the Reynolds number (Note 6), $Re = UL/K$, where U is the flow speed at the entrance of the upstream valley (or at the exits of the two downstream valleys), L is the corresponding valley width, and K is the eddy viscosity, or turbulent exchange coefficient, of the order of $\sim 1\,\mathrm{m^2\,s^{-1}}$; (ii) the valley geometry; and (iii) the difference between the hydrostatic pressure upstream and downstream; and (2) the location of the point of flow splitting and the relative fractions of airflow

diverted into one or other of the downstream valleys, with respect to the total mass flux upstream, also depends on factors (ii) and (iii). The T- and Y-shape valley junctions affect the blocking/splitting mechanism and the degree of flow deflection by the sidewalls. At a T-shaped junction, where there is a 90° turn to the right downstream, there is sharp streamline curvature and separation from the right (upstream) sidewall of the right downstream valley, if the valley width is sufficient. As the width of the right downstream valley is increased, the fraction of flow deflected into it also increases and the flow weakens down valley. The separation zone size and structure are more pronounced for large Re. If the angle of the left downwind valley is increased (making more of a Y-shape), the tendency for a recirculation in the separation zone of the right downstream valley is reduced. For a Y-shaped junction, near the entrance to the downstream valleys there is flow deflection by the external sidewalls and the flow speed decreases. As the flow nears the bifurcation point in the Y, there is blocking and flow splitting, with a sharp velocity decrease. The model results are compared with conditions observed where the Wipp valley, south of Innsbruck, enters the broad west–east Inn valley (47.2° N, 11.4° E) and the upper Rhine valley north of Chur, Switzerland, divides to the northwest in the Seez valley or continues northward to Lake Constance (47.0° N, 9.4° E). Better agreement is found in the case of the Rhine with a Y-shaped junction than in the Wipp–Inn valleys, where southerly föhn flow and downslope winds associated with gravity waves, complicate the situation. Nevertheless, Dobrinski *et al.* emphasize that numerical simulations and field data correspond well when the normalized valley depth ($N\Delta H /U_u$, where N is the Brunt–Väisälä frequency, ΔH is the valley depth and U_u is the upstream valley wind speed) $\gg 1$; this implies "flow around" an obstacle with upstream flow deflection and splitting and it indicates that valley stratification is an important factor. $N\Delta H /U_u \approx 1$ indicates a "flow over" regime.

Despite the numerous studies of mountain–valley circulations, several aspects of these systems remain to be clarified. These include the characteristics of the atmospheric structure at the times of wind reversal and the role of cross-valley gradient winds. These questions are considered next.

New instrument systems can now be used to investigate the atmospheric structure in valleys. Whiteman and McKee (1977) used a tethered balloon profiler in the 600 m deep Gore River Valley, western Colorado, to examine the development and decay of the nocturnal inversion in December. In their case study, a 100 m deep ground-based inversion developed by 1600 h decoupling the surface air flow from the continuing up-valley winds. By 2145 h the inversion (of 3 °C) had deepened to 225 m and winds became down-valley throughout the 400 m sounding. The inversion had intensified to 11 °C over 444 m by 0830 h next morning with continuing light mountain winds, but strong up-valley winds developed shortly afterwards just above the inversion. Subsequently, the inversion level descended at 120 m h^{-1} with both adiabatic and sensible heating occurring above the inversion. Shallow up-valley winds also developed at the surface in a superadiabatic layer caused by radiative heating of the ground. They suggest that solar heating of the slopes sets
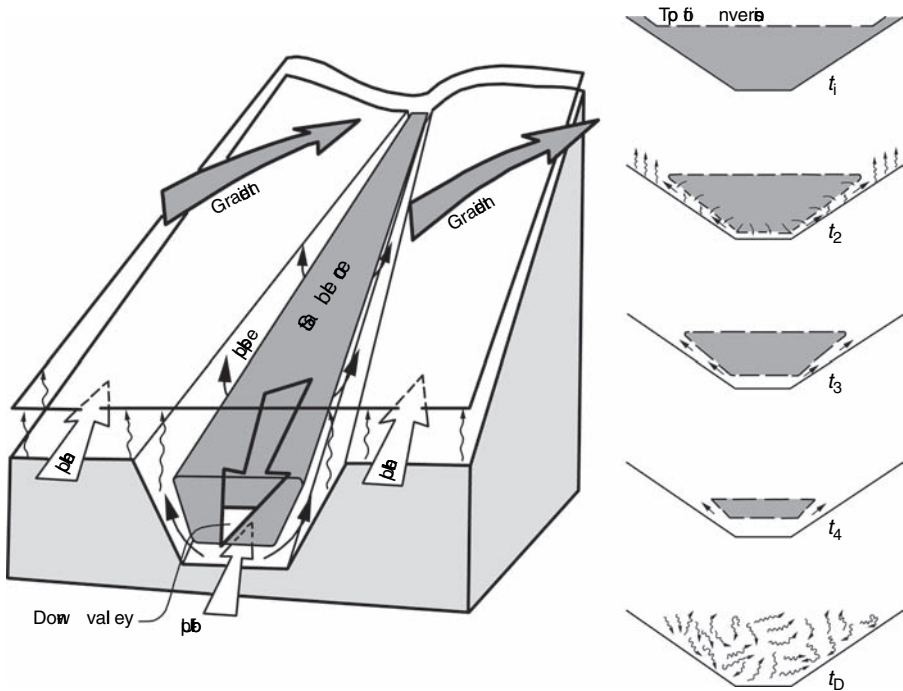
Fig. 3.44 Schematic model of the interacting winds during valley inversion break-up (from Whiteman, 1982). The time sequence (right) shows the air in the valley core becoming entrained in the upslope flows leading to compensation currents over the valley center; t_1 = sunrise, t_2 = sunlight on the floor and slopes; t_3, t_4 = core sinking as convective boundary layers grow over the slopes, t_5 = turbulent well-mixed valley atmosphere.

up convective plumes that penetrate the stable layer of cold air. This entrains cold air from the base of the stable layer, removing it upslope, thereby causing the inversion top to descend through mass continuity (Figure 3.44). The wind data show that the cold stable air did not drain down the valley and that the stable structure above the inversion rules out erosion by turbulent mixing from above.

The time scale of nocturnal boundary layer cooling is investigated by DeWekker and Whiteman (2006), based on tethersonde soundings for clear skies. The cumulative 63.2 percent of the cooling of the nocturnal boundary layer is attained in 3.1 h in a basin atmosphere, compared with 5–6 h in level terrain. The normalized total accumulated night-time cooling is an exponential function of the elapsed time. The time constants are altitude dependent: shortest on the basin floor and upper side-walls of a basin, related to radiative transfer and air drainage.

The idealized model of a valley inversion developed from observations in western Colorado by Whiteman (1982) has been successfully reproduced in a numerical model by Bader and McKee (1983). However, studies in the Inn Valley, Austria, indicate that erosion of the stable core can be more complex. Brehm and Freytag

(1982) attribute the erosion to up-valley flows developing above and below the decaying mountain wind. Warming of the valley atmosphere (calculated for two days in October 1978) occurred through the combined effects of subsidence (45 percent), basal convection (40 percent), and horizontal advection and warming of the slope wind layer (15 percent).

The role of cross-valley winds on the circulation within a valley has been examined both theoretically (Tang, 1976; Wippermann, 1984) and observationally (MacHattie, 1968; Yoshino, 1957). MacHattie, for example, found that winds in the main Kananaskis Valley, Alberta, are more subject to modification by the synoptic-scale gradient winds than is the case in adjoining sub-valleys. Furthermore, daytime valley winds are more affected in this way than the nocturnal system due to the more effective decoupling of the circulations at night. Even a broad and shallow valley, such as the upper Rhine in Germany, causes winds crossing it to be channeled so as to flow almost along the valley direction. Such channeling occurs for winds crossing at any angle (Wippermann, 1984). Moreover, a counter-current often develops; in the south–north Rhine Valley, geostrophic winds from 115° to 170° give rise to northerly valley winds while geostrophic winds from 295° to 350° produce southerly valley winds. These counter-currents exist, according to Wippermann, when the topographically-influenced part of the v component of wind (V_t) is contrary to and greater than the undisturbed part (V_r). The pressure gradient along the valley has the direction of V_r, but since it cannot be balanced by the Coriolis acceleration in the valley, V_t has the opposite direction. Thus, with a westerly geostrophic wind and lower pressure to the north, a southerly flow develops in the Rhine Valley; with a south-southeasterly geostrophic wind and lower pressure to the southwest, northerly valley flow develops.

An analytical treatment by Tang (1976) specifically considers the interaction between a prevailing cross-valley wind and the slope winds; Coriolis terms are neglected. Calculations for a daytime case show that a separated circulation cell develops over the lee slope due to friction, reinforced by upslope winds associated with the typical differential heating on the slope. Downward motion occurs over the valley center (cf. Figure 2.32c, p. 85) and high above the lee slope due to a standing wave tilted upstream from the windward slope. Conversely, at night a separated cell is formed above the windward slope. Tang provides observational evidence from Vermont and near Innsbruck, Austria, showing similar features. Observations by Yoshino (1957) in a small V-shaped valley in Japan also show lee slope eddies in cross-valley wind conditions.

3.2.2.1 Winds in the Grand Canyon

The unique characteristics of winds in the massive Grand Canyon of the Colorado River in northern Arizona (450 km long, 5–29 km wide and over 1600 m deep) merit special attention because of the numerous visitors to the canyon and concerns over visibility and air quality. Studies of flow patterns have been made possible by

mounting a scanning Doppler lidar on South Rim in winter (Banta *et al.*, 1999). The canyon bottom is at about 750 m asl and the V-shaped inner gorge widens out above 1100 m asl rising on the north side at an average 6° angle and on the south side at a 22° angle. The North Rim rises to 2450 m and the South Rim 2150 m asl The canyon trends roughly east–west.

Three flow patterns are identified.

(i) Flow in the canyon is opposite in direction to the flow above the canyon rim. This reversal of flow is best developed on days with northwesterly flow and a strong inversion at the canyon rim.

(ii) The direction of flow inside and above the canyon is similar and coupled under strong, gusty southwest flow.

(iii) Local thermally forced, up- and down-canyon winds develop in the bottom of the canyon under light large-scale ambient flow; there is poor vertical mixing even inside the canyon.

The boundary layer structure and wind regime in the Grand Canyon in winter has been the subject of several field campaigns concerned with visibility and air quality. Wind and temperature data were collected between 12 January and 3 March 1990 (Whiteman *et al.*, 1999a). Most mountain valleys and small basins develop a stable nocturnal boundary layer above the valley floor through the down-slope drainage of air forming a "cold air lake." Likewise, a daytime CBL grows as heating erodes, and eventually destroys, the nocturnal valley inversion. Grand Canyon, in contrast, exhibits neither feature. Soundings show that the stability is generally weak over a deep layer.

Whiteman *et al.* (1999a) define a morning heat deficit (D) as the heat needed to destroy the nocturnal inversion.

$$D = 0.5 \; \rho c_p \; H . \Delta\theta (\mathrm{J\,m^{-2}}),$$

where H is the inversion depth; $\Delta\theta$ is the inversion strength; ρ is the air density; and c_p is the specific heat of the air at constant pressure.

For locations in valleys, basins, canyons and plains of the central-southern Rocky Mountains, D values range from less than $1\,\mathrm{MJ\,m^{-2}}$ at Grand Junction, Colorado to $13\,\mathrm{MJ\,m^{-2}}$ at Bullfrog Basin, Utah. For Phantom Ranch on the valley floor of the Grand Canyon, $D = 7.3\,\mathrm{MJ\,m^{-2}}$ which is comparable with many mid-sized Colorado valleys. It appears that the weak stability is a result of the distribution of nocturnal cooling through a deep layer. Cold plumes sink from the plateaus to north and south of the canyon, especially when there is snow cover, and mix the air vertically. Visual evidence of this is provided by a report of smoke plumes from a controlled fire in September 1980 descending into the canyon in the late afternoon and evening (cited by Whiteman *et al.*, 1999a), and evidence of cold morning fog draining over the southern rim (Barry and Chorley, 2003; plate 5).

Upstream from the Grand Canyon, a series of sub-basins along the Colorado River valley produce a regional circulation system characterized by convergence of low-level air into the sub-basins at night and divergence of air from them by day Whiteman *et al.* (1999b). Contrary to valley wind theory, locations down valley from the sub-basins experience nocturnal up-valley winds due to convergence of cold air from higher ground into the sub-basins at night, and down-valley winds by day through divergence of warmed air from the centers of the basins.

3.2.2.2 Mountain basins

There have been several studies of flows in mountain basins. In central Colorado, Banta and Cotton (1981) identify three wind regimes in a broad mountain basin. There is nocturnal drainage downslope, a shallow upslope flow in the daytime convective boundary layer, and transitional flows related to strong turbulent mixing, in the late morning or afternoon; the transitional flows resemble the general westerly flows above the ridge tops. Over the broad South Park Basin, upslope flows develop in a shallow convective boundary layer on the lee (eastern) side of a heated mountain slope. The presence of a nocturnal inversion layer seems to be a requirement for their development (Banta, 1986) and their duration is inversely related to the westerly winds above the ridge tops. By late morning/early afternoon the slope winds come to resemble the ridge top winds through strong turbulent mixing in the convective boundary layer (Banta and Cotton, 1981). During this transition, a local lee convergence zone may form at the upwind edge of a pool of cold air in the basin. This convergence generates cumulus cloud that later may grow into cumulonimbus (Banta, 1984). The regional aspects of these features are examined more fully below.

3.2.3 Regional-scale interactions

The final element in thermally induced topographic wind systems is large-scale interactions. These involve both regional circulations set up by extensive mountainous areas in relation to surrounding lowlands, as well as synoptic-scale wind systems.

Model studies for a circular plateau with radial valleys show that regional circulations are driven by the heating distribution and its diurnal variations (Egger, 1987). Valley winds make a significant contribution to the plateau circulation. Over the Alps, Burger and Ekhart (1937) identified a regional compensation flow moving radially away from the mountains by day and subsiding over the plains. In the Alpine Foreland, the regional flow from the plains to the mountains in summer 2000 was shown to extend from the vicinity of Munich (about 80 km north of the Alps) by late morning (Weissmann *et al.*, 2005). The northerly flow deepened from 800 m in the north to 1200 m at the edge of the Alps. The boundary layer flow then rose into the free atmosphere over the Alps. Regional circulations were measured over the Inn Valley during the MERKUR project (see p. 207). Freytag (1987) reports nocturnal

mountain winds reaching 30 km into the foreland and estimates that they force a general ascent of about 6 cm s^{-1}. For a 1500 m-deep layer over a drainage area 40 km in width, the anti-mountain wind would have a mean velocity of 40 cm s^{-1}. Yet as Urfer-Henneberger (1970) points out, the level of this flow (approximately 4000 m or more) is such that it is invariably a component of the gradient winds.

As noted above, Banta and Cotton (1981) first documented diurnal circulations in the inter-montane basins of the Colorado Rocky Mountains. Later investigations identified regional-scale diurnal flows from summit wind observations in the Rocky Mountains, using a network of mountain top sites during four summers (Bossert et al., 1989). Two regional-scale diurnal wind regimes are identified. During weak synoptic situations on clear summer days with strong solar radiation, the radiatively-forced wind regime exhibits a simple daytime inflow and nocturnal outflow pattern (Figure 3.45). There are slow transitions lasting 6–7 h in the evening and 4–5 h in the morning. The nocturnal outflow occurs in a shallow layer at mountain level above a deep stable valley air layer caused by radiative cooling. In contrast, during periods with convective thunderstorm activity and latent heat forcing, the gradual morning transition from outflow to inflow is disrupted in mid-afternoon by a shift from inflow to outflow, and by a further reversal in late afternoon–early evening. Data over 4 years indicate that these shifts occur on 27 percent of days. Over lower ranges or single mountains, the return flows occur much lower and can be considered as strictly anti-valley or anti-mountain winds.

This problem has been highlighted by the investigations of Tyson (1968b; Tyson and Preston-Whyte, 1972) on the southeast side of the Drakensberg escarpment, South Africa, spanning a 180 km transect to the Indian Ocean at 30 °S. The escarpment edge is at 3000 m, falling sharply to a sloping plateau at 950 m, which is dissected by valleys 250–550 m deep. While the major valleys trend northwest–southeast, others are at right angles to the general southeastward slope of the plateau. Tyson and Preston-Whyte propose schematic models of the nocturnal wind systems in relation to this topography (Figure 3.46). The mountain–valley winds are overlain by a regional air movement away from the Lesotho Massif and the Drakensberg at night (the "mountain–plain" wind) and its daytime converse.

A specific case is illustrated for the Bushmans Valley (Figure 3.47). The valley– and plain–mountain winds are best developed in summer when the combined mountainward flow may be 1000–1250 m deep. They are seldom related to the general pressure gradients whereas the northwesterly mountain–plain winds may be an integral part of the large-scale circulation.

In Namibia, southwest Africa (23° S), seasonally persistent circulations develop between the mountains and plains. A large-scale, northwesterly plains–mountain wind exceeding 1500 m depth dominates the summer circulation both day and night, in contrast to the diurnally oscillating regime in Natal (Lindsay and Tyson, 1990). In winter, however, there is a nocturnal southeasterly mountain–plains wind.

Fig. 3.45 **Regional-scale diurnal wind reversals over the Rocky Mountains, Colorado, based on mountain-top observations of average resultant wind from (a) 1200 to 1500 MST for 26 August 1985 and (b) 0001 to 0300 MST for 27 August 1985 (from Bossert et al., 1989).**
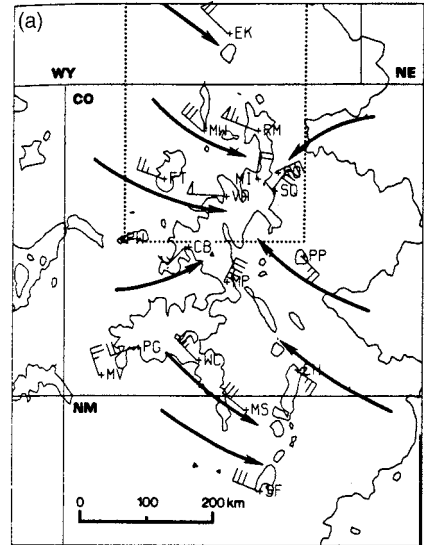
Daytime wind data for 8/26/85
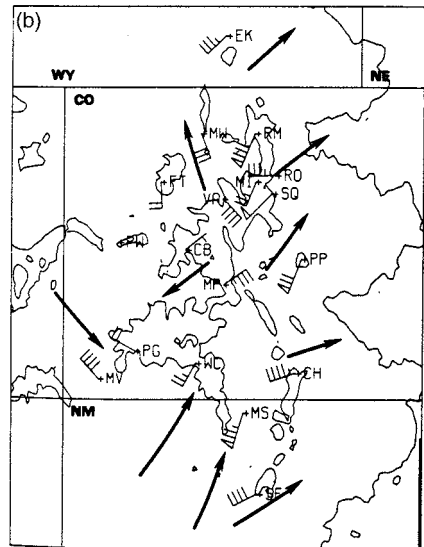
Nocturnal wind data for 8/27/85

Further investigations in Colorado show a diurnal regime with at least three phases: daytime inflow, an evening transition, and nocturnal outflow. Bossert and Cotton (1994) use wind observations collected on mountain peaks during the Rocky Mountain Peaks Experiment (ROMPEX), 1984–7 to examine the circulation over the elevated basins of North Park, Middle Park, and South Park, and the surrounding Rocky Mountains in Colorado. Their conceptual model (Figure 3.48) shows daytime inflows, and nocturnal outflows, with a late afternoon–evening

Fig. 3.46 A model of nocturnal airflow over the Drakensberg foothills in winter (from Tyson and Preston-Whyte, 1972). (a) Valleys normal to mountains and coastline (b) valleys parallel to the slope.
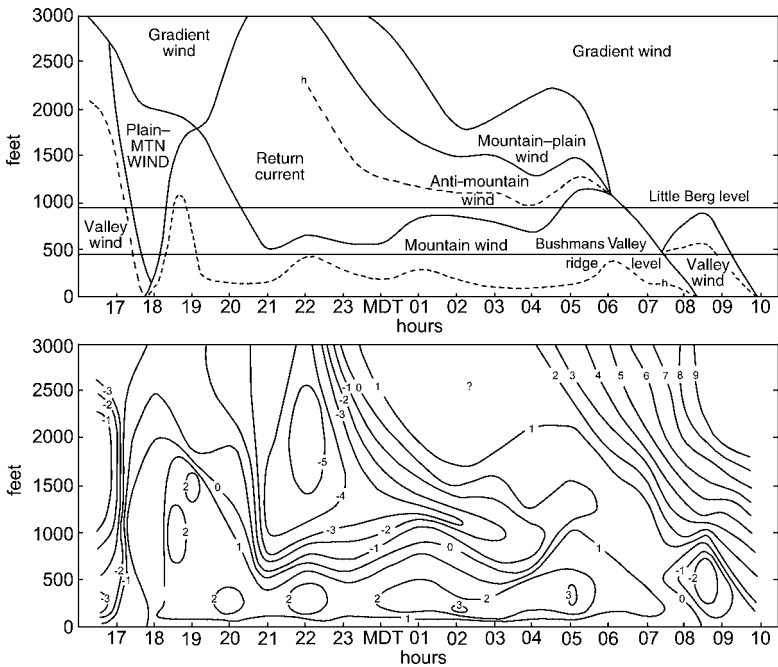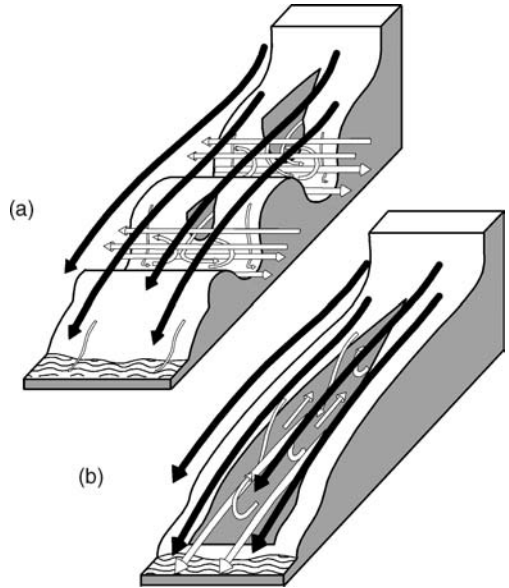
Fig. 3.47 Time section of local winds (m s^{-1}) in and above Bushmans Valley, Drakensberg Mountains, 12–13 March 1965 (from Tyson, 1968b).

Fig. 3.48 Conceptual model of the regional-scale circulation system over the inter-montane basins of the Colorado Rocky Mountains. (a) Daytime inflow; (b) transition phase; (c) nocturnal outflow (from Bossert and Cotton, 1994).
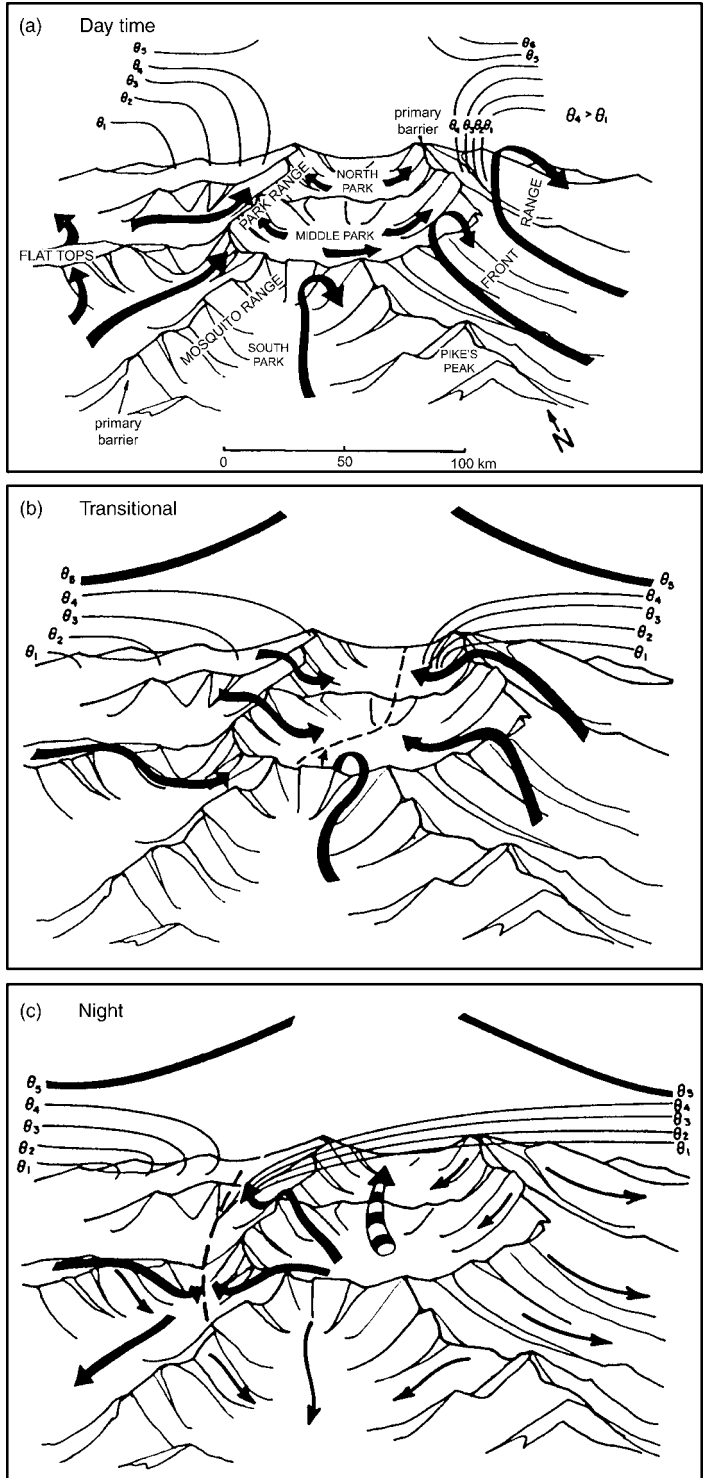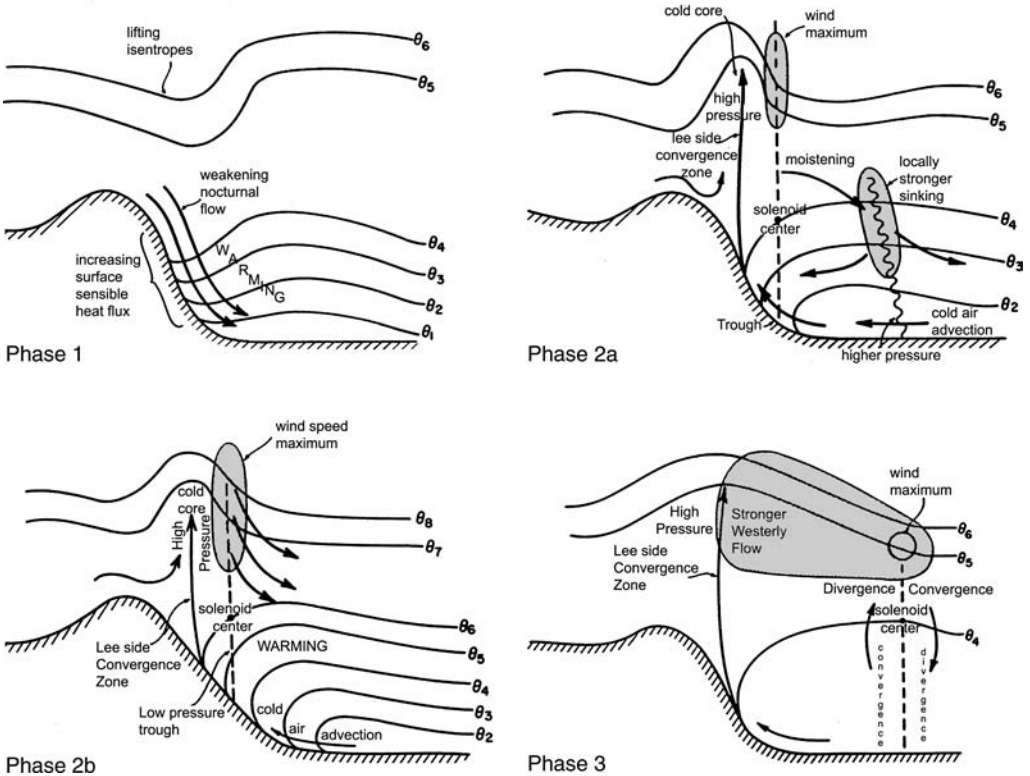
Fig 3.49 Conceptual model of a mountain–plains circulation east of the Front Range, Colorado (from Wolyn and McKee, 1994).

transition period. At 700 mb there are strong nocturnal easterlies along the western slopes counter to the ambient westerly airflow. A westward propagating density current (WPDC) marks the transition from the daytime pattern with a deep mountain–plains solenoid (Figure 3.48c), formed by the intersection of isobaric and isopycnic (equal density) surfaces. The WPDC dissipates around midnight along the western edge of the Park Range and a steady southeasterly to southerly jet develops 1–2 km above the basin surface as a result of the influence of Coriolis effects on the solenoidal circulation and on the WPDC.

Mountain ranges to the east of the same area, comprising a 60-km north–south barrier rising 2000 m above the adjacent high plains, exhibit a well developed mountain–plains circulation, described by Wolyn and McKee (1994). The different phases that evolve during the day are illustrated conceptually in a west–east cross-section (Figure 3.49). At sunrise (not shown), a nocturnal "jet" (*u*-component $\sim 9\,\mathrm{m\,s^{-1}}$) descends at about 300 m above the east slope, leading to convergence over the plains and lifting a stable core of cold air that is between about 1.3 and 2 km deep (the barrier height). In the early morning (Phase 1), the downslope flow weakens as it interacts with surface heating; there is also subsidence warming aloft

so that the isentropic surface bulge upward. During the morning, up to 7 h after sunrise (Phase 2a), cold air advection suppresses the convective boundary layer (CBL) over the plains and the cold air begins to move upslope forming a lee-side convergence zone and a solenoid. Lifting in the convergence zone forms a cold upper core. To the east of this core, sinking air generates a pressure trough. In the afternoon (Phase 2b), the low-pressure trough strengthens on the lee slopes with an associated upper level wind maximum. A westerly return flow forms over the plains and it may transport some moisture eastward. When there is sufficient daytime heating, the solenoid can migrate eastwards in the afternoon–evening. When it passes a given location, there is explosive growth of the convective boundary layer (CBL) and the upslope flow deepens.

Studies of thermally-driven wind systems in several areas of the intermontane region of the western United States show that in the absence of synoptic gradients large-scale thermal circulations regularly overwhelm local flows (Stewart *et al.*, 2002). For example, over southern Nevada and central Arizona, plains–mountain flows have a high daytime consistency and override local thermal flows except where the latter are in deep valleys and canyons. The same is observed with the daytime lake breeze towards the Great Salt Lake, Utah overwhelming an afternoon upslope flow in the Rush Valley.

A nocturnal southerly low-level jet (LLJ) is also observed over the Great Salt Lake Basin in association with formation of a cold pool. Banta *et al.* (2004) show that the jet is already fully formed and apparently is related to the topographic control of a sequence of basins, including Utah Lake basin, to the south. The timing of the wind reversal from daytime, northerly, up-basin flow is sensitive to the north–south pressure gradient. With a weak gradient, katabatic slope and canyon outflows originate from the Wasatch Range to the east, These interact with the LLJ forming localized zones of convergence and divergence. In such convergence areas, updrafts of up to $5 \, \mathrm{cm \, s^{-1}}$ were recorded with Doppler lidar in October 2000.

The evolution of regional-scale diurnal circulations over the Mexican Plateau and Basin, described by Whiteman *et al.* (2000), involves no strong nocturnal inversion or diurnal reversals of valley winds. Regional circulations develop diurnally between the air over the Mexican Plateau and the generally cooler coastal areas. A CBL rapidly builds over the plateau to 2250 m above the surface and strong baroclinic zones form at the plateau edges.

A large-scale diurnal circulation is observed over the Altiplano of Bolivia–Peru. In the austral winter, July–August 2003, soundings and unmanned aircraft were used in a field campaign to investigate this circulation (Egger *et al.*, 2005). Inflow towards the Altiplano begins 3–5 h after sunrise when the stable nocturnal boundary layer is transformed into a neutrally stratified convective boundary layer (CBL). The depth of the inflow is slightly less than this CBL (see Figure 3.50). Up-valley flow along the Rio de La Paz transports moisture into the Altiplano from the east. Egger *et al.* suggest that there is no large heat low over the plateau
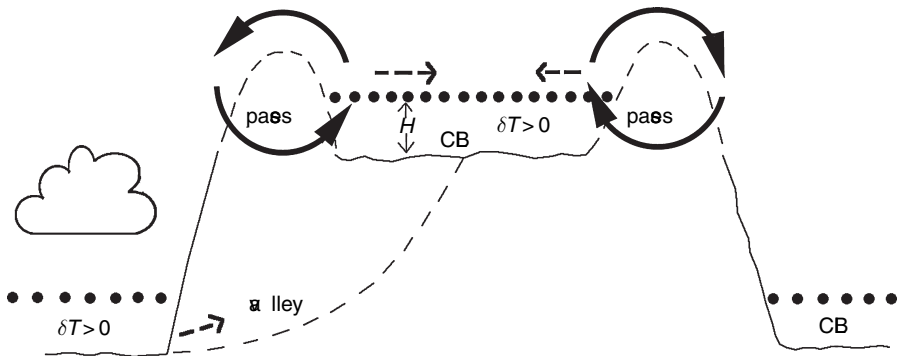
Fig. 3.50   Schematic diagram of the diurnal circulation over the Bolivian Altiplano (from Egger *et al.*, 2005; Fig. 1).

since daytime inflow through the passes is determined by local conditions (snow cover, low cloud).

Further studies of the wind regimes, during August 2003–February 2004, have been made using two stations installed in the Rio de La Paz, near La Paz, and at Tambo Quemado on the western margin of the Altiplano. The latter station was just east of, and a few hundred meters below, a 4600 m pass leading downward to the Chilean Desert, although there is a massif ~ 4500 m high to the west. The pass itself is about 500 m above the Altiplano. Gaps and passes in the mountain ridges favor gravity currents draining to the plateau. At night, winds were typically downslope from the west, with weak upslope easterlies occurring on most days in the morning until around midday. In the afternoon the easterlies weaken and are replaced by inflow from the west, signifying the diurnal circulation of the Altiplano (Figure 3.50), which diminishes after sunset. The Rio de La Paz descends from about 4000 m to the eastern lowlands at ~ 1000 m altitude. The records show a weak westerly, nocturnal down-valley flow that switches regularly and quite abruptly to a diurnal up-valley easterly wind of 8–10 m s^{-1}. However, it is unclear at present whether the return flow is limited to the river valley or whether it forms a part of a larger-scale Altiplano circulation. Model simulations by Zängl and Egger (2005) suggest that the diurnal circulation over the plateau resembles a sea breeze, especially during the initial inflow. This flow propagates at about 4 m s^{-1} so that the opposing inflows do not converge until around sunset. Over narrower plateaus this could occur earlier in the day. They also find that the winds on the lateral slopes of the Altiplano play little role in determining the strength and structure of the circulation, although they do transport some low-level air onto the plateau.

In the context of extensive plateau slopes it is appropriate to mention the thermo-tidal wind theory of Lettau (1978). He shows that large-scale mountain slopes can produce a thermal wind parallel to the terrain contours due to heating effects. For example, if high ground is relatively warm compared to its surroundings (by day/summer), an anticyclonic circulation develops provided the normal

Fig. 3.51 Thermal winds developed in the steady-state boundary layer over sloping terrain in the northern hemisphere. The (a) nocturnal and (b) daytime phases of temperature stratification and associated geostrophic wind shear are shown (from Lettau, 1967).
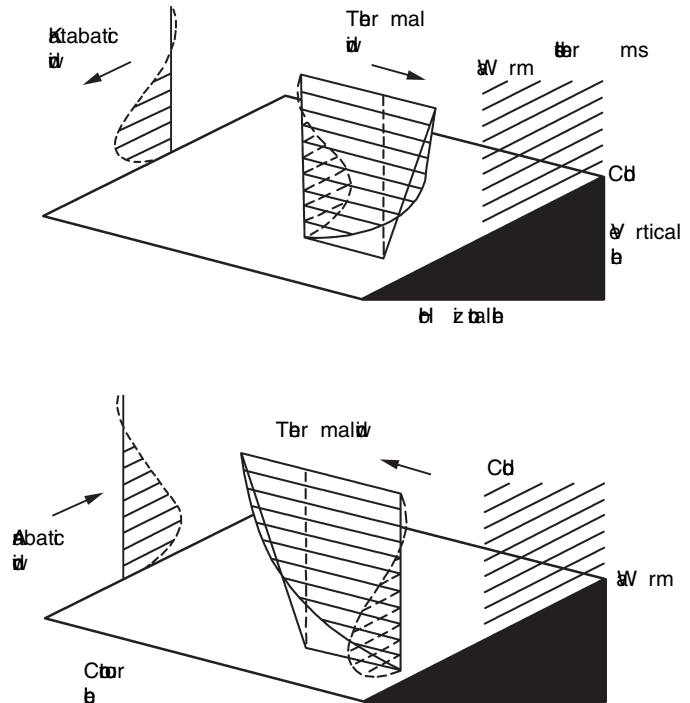
lapse situation prevails. Conversely, over cold highlands, given inversion conditions, a cyclonic circulation will occur. The former is well illustrated over the Tibetan Plateau (see p. 412). In addition, the diurnal heating cycle generates a harmonic forcing function in the boundary layer, giving rise to a "thermo-tidal" wind. Schematic patterns of steady-state solutions are indicated in Figure 3.51. Lettau discusses the apparent contribution of such systems to the nocturnal low-level jet east of the Rocky Mountains and to the shore-parallel winds over the western foothills of the Andes in Peru. The nocturnal boundary layer jet east of the Rocky Mountains and in similar locations elsewhere has been identified in both observational (Paegle, 1984) and modeling studies (McNider and Pielke, 1981; Garratt, 1985). The nocturnal stratification enhances the momentum coupling according to Mason and Sykes (1978), helping to establish a supergeostrophic wind maximum in the lowest kilometer or so. Paegle suggests that the time-averaged jet can be accounted for by western boundary dynamics related to the meridional variation of the Coriolis parameter, while its diurnal velocity fluctuations involve buoyancy oscillations above a sloping surface as proposed by Lettau (1967) and Holton (1967). Lettau's theory shows that the low-level wind speed maximum occurs at different times of day according to latitude. This results from the appearance in the equation for boundary-layer tidal flow of the term $f/(f^2 - \omega^2)$, where f = Coriolis parameter ($= 2\omega \sin \phi$); ϕ = latitude angle; ω = frequency of the tidal force (which here corresponds to Earth's angular velocity), and

$(f^2 - \omega^2) = \omega^2 (4\sin^2\phi - 1)$. The critical latitude is where $f = \pm\omega$, which is latitude $30°$. Lettau (1967) shows that the signs of the two parameters involved are:

	$30° - 90°$ N	$0° - 30°$ N	$0° - 30°$ S	$30° - 90°$ S
f	+	+	−	−
$f^2 - \omega^2$	+	−	−	+

As a result of the implied phase differences, the low-level jet occurs about midnight in middle and high latitudes, whereas equatorward of latitude $30°$ it occurs about midday. This accords with the observed nocturnal maximum east of the Rocky Mountains and the daytime one over the Peruvian Andean foothills. Further general support for this theory is presented by Lettau (1978) for South America, although Tyson (1968b) notes an absence of such winds parallel to the general terrain contours in Natal.

3.2.3.1 Models of the orographic wind field

The dynamic modifications to airflow due to topography, superimposed thermal effects setting up local circulations, and basic altitudinal effects on wind velocity, must obviously combine to make the observed wind field highly complex and variable in mountainous terrain. The individual roles of these factors have already been detailed, but it will be useful to close this chapter by some consideration of interactions in the total wind field. In complex terrain, with several topographic scales represented, the airflow may show different effects at different levels in the atmosphere. Nappo (1977) illustrates this in the 50–60 km wide Tennessee River Valley between the Cumberland Plateau (1000 m) to the northwest and the Great Smoky Mountains (2000 m) to the southeast. Three distinct layers can be identified. Below about 200 m in the valley the flow shows no large-scale terrain effects although there is channeling by minor ridges (100–150 m) with variations in speed and direction occurring virtually independently of stability. Above this layer, up to about 800 m above the valley floor (which is approximately half the height of the major terrain features), the wind speed profile still resembles that for a rough plain surface, whereas wind direction is affected by local topography and stability. At higher levels, speeds increase but the directions tend to remain constant into the free air.

For modeling purposes, the wind field can be regarded as a result of the combined effects of three major factors: synoptic-scale forcing; topographic blocking or channeling; and thermal effects. The synoptic-scale pressure field itself can also be greatly modified by the dynamic and thermodynamic effects of large-scale topography as shown earlier (section on pp. 131–50).

If the gradient winds are strong, mountain winds essentially show only kinematic adjustments to the terrain. For southern California, Ryan (1977) developed

an empirical model where this situation is represented during Santa Ana conditions. Wind direction is expressed by a diversion factor (F_D), which is a function of the downwind slope (s_d, in percent), and the angle between the slope azimuth (A) and the wind direction (V_0):

$$F_D = -0.255 \, s_d \sin[2(A - V_0)]$$

F_D is a maximum of $22.5°$ for $s_d = 100$ percent ($45°$ slope) and $(A - V_0) = 45°$. $F_D < 0$ denotes that the wind is backed (turned counterclockwise) if A is less than $90°$ clockwise from V_0. Ryan also estimates "sheltering effects" due to topography based on the upwind slope between the site and the horizon. The sheltering factor is:

$$F_s = k \arctan(0.17 s_u)/100,$$

where s_u is the upwind slope (percent) (limited arbitrarily to 100 percent); k is unity, except under Santa Ana conditions where it is subjectively adjusted to unity at 600 m and zero at 1250 m and above.

At the other extreme, when the synoptic control is weak, the surface winds in deep mountain valleys are decoupled from the gradient flow and are determined by the thermal forcing (Schwabl, 1934). In southern California this involves the additional complication of sea breeze effects (Sommers, 1976). The airflow at ridge levels under these conditions remains closely related to the gradient pattern. Thermal influences obviously change diurnally and seasonally, with changes in the effects of diurnal season heating on slopes and on lapse rate structure in the lower atmosphere.

Many efforts are now under way to develop meso-scale dynamical models of boundary layer flow over complex terrain, especially in view of its importance to such problems as air pollution dispersal in mountain valleys and the spread of forest fires in mountainous terrain. The low-level airflow over complex terrain can be modeled in a variety of ways. Relatively simple models suitable for diagnostic analyses or forecasting applications can be grouped into three types according to the approach adopted: mass conservation; one-layer vertically-integrated primitive equations of motion; or one-level primitive equations (Mass and Dempsey, 1985).

Mass conservation models (e.g. Dickerson, 1978) assume a well-mixed (constant density) layer beneath a low-level inversion where mass is conserved by applying the continuity equation:

$$\frac{\partial h}{\partial t} + \frac{\partial (hu)}{\partial x} + \frac{\partial (hv)}{\partial y} + w = 0,$$

where h is the height of the inversion base above the ground surface; w is the vertical outflow through the inversion base (upper boundary); u,v are the horizontal components of mean velocity in the mixed layer.

The same approach can be extended for three-dimensional wind fields (Sherman, 1978; Ross et al., 1988). The variational analysis procedure is used whereby a solution

is obtained to an integral function that minimizes the variance of the difference between observed and analyzed variable values, subject to imposed constraints; for example, observed horizontal fluxes must satisfy the continuity equation, and a non-divergent three-dimensional analyzed wind field (Sherman, 1978). Tesche and Yocke (1978) used a mass continuity model to examine wind flow patterns in the Lake Tahoe basin and the Donner Pass area of the Sierra Nevada, California.

Examination of the effect of diurnal heating cycles on airflow over a mountain has been performed numerically using hydrostatic meso-scale models incorporating a detailed boundary layer formulation (Mahrer and Pielke, 1975, 1977). Surface heat and momentum fluxes are parameterized. Analysis with the two-dimensional version shows that, over the windward slope, diurnal heating leads to a decrease in daytime horizontal wind components and an increase at night, while the opposite is found over the lee slope. With respect to vertical motion, the mountain acts as an elevated heat source by day, with stronger ascent over the windward slope, but weaker descent over the lee slope. At night, the descent on the lee side is increased, aided by the accelerating effect of a nocturnal pressure maximum due to cooling at the crest. The planetary boundary layer is predicted to be 600–900 m lower on the downwind side of the mountain than on the windward side. Further simulations with the three-dimensional version (Mahrer and Pielke, 1977) for the area of the Sacramento Mountains and White Sands, New Mexico, illustrate effects of deflection around the mountains, stronger downslope winds on the lee side, augmented winds upwind of ridges, and valley and slope wind effects.

Fosberg et al. (1976) have developed a numerical model based on a combination of their earlier work on thermally induced winds and work by Anderson (1971) on terrain-induced airflow. The procedure is based on a one-layer model of boundary layer flow applied to areas of about 2500 km^2 with a grid spacing of the order of 1–6 km (finer grids with increasing relative relief). The gradient wind pattern is first transferred into the terrain-modified through flow, determined from a steady-state mass continuity equation (Anderson, 1971). A rigid lid, about 1.5–2 km above the spatially smoothed terrain, is applied. Modification of the wind field by thermal and frictional effects are then taken into account based on the divergence and vorticity equations, neglecting advection. The approach is to transform the computed divergence and vorticity into stream functions and velocity potentials (see Barry and Carleton, 2001; p. 49) and then determine horizontal wind components from these. After the calculation of background values, representing the influence of large-scale terrain features on the flow, divergence is calculated for the actual terrain and frictional effects are taken into account. The data requirements of the model are: temperature, pressure, elevation and surface roughness, length at each grid point and values for the area specifying static stability, geostrophic wind velocity, eddy viscosity, latitude, and large-scale vorticity. Tests of the model for summer situations in Oregon and California showed good agreement with observed meso-scale flow patterns. Fosberg et al. comment that flow perturbations due to divergence effects are about 2.5–4 times as large as those due to rotational

effects. They also note that thermal control on the flow vanishes and terrain influences become weak when the background wind speed reaches $10\,\mathrm{m\,s^{-1}}$.

The second simplified model approach uses the primitive equations of motion, vertically integrated for a well-mixed boundary layer (Lavoie, 1974; Overland et al., 1979). These models consider a surface, constant stress, layer, a well-mixed boundary layer, an inversion layer, and the overlying free atmosphere. Mass is conserved in the mixed layer, but not the layers above. The simulated flow may be blocked and deflected when the mixed layer is forced upward by convergence on a hill slope and cooler air in the mixed layer replaces warmer air above the subsidence inversion (Mass and Dempsey, 1985).

The third type of model uses the primitive equations for one level without a continuity equation. For example, Danard's (1977) model requires the geostrophic wind at the surface and 850 mb, the lower tropospheric lapse rate and surface air temperature. It integrates to a steady state the tendency equations at the surface only for wind, pressure and potential temperature. Mass and Dempsey (1985) extend that approach to calculate surface wind and temperature using equations for horizontal momentum and temperature tendency in sigma coordinates. The mass field is determined by the vertical temperature structure. Thermally-induced circulations due to diabatic forcing can also be included. The results of model runs for the coastal mountain area of southern British Columbia, western Washington state and northwestern Oregon with different synoptic-scale forcings indicate that stably stratified air is deflected around high terrain and converges on the lee sides over a zone several times the diameter of the obstacle. Such channeling and deflection is shown to be due to the effects of adiabatic cooling (as air rises) and warming (as it descends), which results in redistributions in the mass field. In view of the modest requirements of such models for initial data and for computing resources, they are useful for analysis and forecasting of wind, temperature, and pollutant transport in areas of mountainous terrain.

Limited area, fine resolution prognostic models that resolve meso-scale features are also available (see, for example, Pielke, 2002). Typically, the output of a GCM provides the necessary boundary conditions for the meso-scale model, which can have a spatial resolution of 10–30 km over areas of 0.25–$25 \times 10^6\,\mathrm{km^2}$. It is not possible to detail such models here; Deque (2000) gives a useful review. However, it is worth noting that a current trend is to embed meso-scale models capable of resolving regional detail in general circulation models. An illustration for the western United States is presented by Giorgi and Bates (1989). The Pennsylvania State University/National Center for Atmospheric Research (NCAR) meso-scale model is embedded in the NCAR Community Climate Model (CCM) and is driven by initial conditions and lateral boundary conditions for January 1979. The meso-scale model has a 60 km grid for a $3000 \times 3000\,\mathrm{km^2}$ area; there are five levels in the lowest 1.5 km and a detailed surface biosphere parameterization. A CCM multi-year simulation provides a set of representative weather patterns for analysis; statistical relations are developed between the climatic patterns given by the

regional model and predictions from the global model. These relationships are then applied to the long-term global simulations to obtain regional climate descriptions. The simulated regional climate patterns for the western United States in January, including precipitation and snow depth, are reasonably realistic in relation to major topographic features although certain model biases in the different variables are noted (Giorgi and Bates, 1989). In a further study using the meso-scale model nested in the NCAR CCM, Giorgi (1990) shows that with forcing from a spectral triangular expansion truncated at wave number 42 (corresponding to $2.89° \times 2.89°$ resolution), the 60 km resolution of the meso-scale model provides regional detail of temperature, precipitation and snow cover distribution that agree well with observations. Giorgi *et al.* (1993) illustrate further meso-scale simulations for the western United States. This type of approach will clearly be useful for climate assessments and scenarios of changed forcings. Ghan *et al.* (2005) extend this approach using the NCAR Community Climate System Model (CCSM) 3 with physically based downscaling for subgrid-scale orography for ten regions with major mountain systems, including the western United States, the Alps, Scandinavia, Himalaya–Tibet, Greenland and the New Zealand Alps. They find too little (much) precipitation on windward (lee) slopes and excessive snow cover in summer. Katzfey (1995) used a meso-scale model nested within ECMWF analyses to study three extreme storm events in the Southern Alps, New Zealand. He shows that the simulated orographic precipitation is greatly improved as the horizontal grid resolution is increased from 30 to 15 km with 10-km sampling of elevation data.

Recent regional-scale modeling of flow over complex terrain has made use of large-eddy simulations, based on the Advanced Regional Prediction System (ARPS) developed for severe weather forecasting (Xue *et al.*, 2001). This is a three-dimensional, nonhydrostatic compressible model formulated in generalized terrain-following coordinates. Chow *et al.* (2006) note that schemes based on the Reynolds Averaged Navier Stokes (RANS) approach, that treat turbulent motions statistically, do not represent many important flow features accurately, particularly if the flow exhibits unsteady or transient behavior. In Large-Eddy Simulation (LES), large-scale motions are treated directly, while for eddies below a threshold size (typically about one mesh interval), a Sub-Grid-Scale (SGS) model is used. Chow *et al.* use horizontal resolutions of 350 and 150 m in their study of the Riviera valley north of Bellinzona in southern Switzerland. They find that higher resolution representation of the topography outside of the fine-resolution domain is needed, because coarse grids are unable to provide accurate lateral boundary condition forcing for the fine grids.

3.3   NOTES

(1)   Roughness length (z_o) is estimated from $0.5 h A/S$, where $A =$ silhouette area of obstacle, $S =$ surface area, $h =$ relief; A/S is typically ≤ 0.1 (Mason, 1985).

(2)   The Rossby radius of deformation, $L_R = NH/f$, where $N =$ average Brunt–Väisälä frequency through the tropospheric depth H, and $f =$ Coriolis parameter); it is the characteristic length scale of mid-latitude disturbances (James, 1994) and corresponds to the scale at which buoyancy and rotational forces are equal (Carlson, 1991). A different form is used by Shutts (1998) in studying ridge effects on cold-air damming. $L_R = (gh_0)^{0.5}/f$, where h_0 is a depth scale of the cold air through which the mountain ridge protrudes.

(3)   The Richardson number (Ri) is a dimensionless ratio of the buoyant suppression of turbulence to the shear generation of turbulence, and can be thought of as a measure of stability. It is defined:

$$Ri = \frac{g\beta}{(\partial u/\partial z)^2}$$

where $g =$ acceleration due to gravity, $\beta =$ vertical stability, and $\partial u / \partial z$ is the vertical wind shear (Glickman, 2000).

(4)   A critical layer occurs where the phase speed of a wave $=$ the mean flow velocity.

(5)   Neff (1988) describes acoustic sounder observations and the full suite of boundary-layer remote sensing techniques (lidar, sodar, radar) is detailed in Lenschow (1986).

(6)   The Reynolds number (Re) is the dimensionless ratio of the inertial force, U^2/L, to the viscous forces, $\nu U/L^2$, where ν is the kinematic viscosity ($\sim 1.46 \times 10^{-5}\,\mathrm{m^2\,s^{-1}}$ for dry air at 0 °C). It is a measure of airflow instability.

BIBLIOGRAPHY

Aanensen, C. J. M. (1965) Gales in Yorkshire in February 1962. *Geophys. Mem.*, **14**(3), No. 108.

Abe (1941) Mountain clouds, their forms and connected air currents, Part II. *Bull. Cent. Met. Observ., Japan*, **7**, 93–145.

Affronti, di F. (1963) Le nubi d'onda sull'Etna con flusso occidentale. *Geofis. Met.* (7 Congr. Int. Met., Alpina), **11**, 75–80.

Alaka, M. A. (ed.) (1960) *The Airflow over Mountains*, Tech. Note no. 34. Geneva: World Meteorological Organization.

Anderson, G. E. (1971) Meso-scale influences on wind fields. *J. appl. Met.*, **10**, 377–86.

Arakawa, S. (1968) A proposed mechanism of fall winds and Dashikaze. *Pap. Met. Geophys.*, **19**, 69–99.

Armi, L. and Mayr, G. J. (2007) Continuously stratified flow across an Alpine crest with a pass: Shallow and deep foehn. *Q. J. Roy. Met. Soc.*, **133**(623), 459–77.

Arndt, A. (1913) Uber die Bora in Noworossisk. *Met. Zeit.*, **30**, 295–302.

Arndt, R. W. and Pielke, R. A. (1986) Interactions of nocturnal slope flows with ambient winds. *Boundary-Layer Met.*, **37**, 83–95.

Bader, D. C. and McKee, T. B. (1983) Dynamical model simulation of morning boundary layer development in deep mountain valleys. *J. Clim. Appl. Met.*, **22**, 341–51.

Ball, F. K. (1956) The theory of strong katabatic winds. *Austral. J. Phys.*, **9**, 373–80.

Ball, F. K. (1957) The katabatic winds of Adelie Land and King George V Land. *Tellus*, **9**, 201–8.

Banta, R. M. (1984) Daytime boundary-layer evolution over mountainous terrain. Part 1. Observations of the dry circulations. *Mon. Wea. Rev.*, **112**, 340–56.

Banta, R. M. (1986) Daytime boundary-layer evolution over mountainous terrain. Part 2. Numerical studies of upslope flow duration. *Mon. Wea. Rev.*, **114**, 112–30.

Banta, R. and Cotton, W. R. (1981) An analysis of the structure of local wind systems in a broad mountain basin. *J. appl. Met.*, **20**, 1255–66.

Banta, R. M., *et al.* (1999) Wind-flow patterns in the Grand Canyon as revealed by Doppler lidar. *J. appl. Met.*, **38**(8), 1069–83.

Banta, R. M., *et al.* (2004) Nocturnal low-level jet in a mountain basin complex. Part 1: Evolution and effects on local flows. *J. appl. Met.*, **43**(10), 1348–65.

Barr, S. and Orgill, M. M. (1989) Influence of external meteorology on nocturnal valley drainage winds. *J. appl. Met.*, **28**, 497–517.

Barry, R. G. and Carleton, A. M. (2001) *Synoptic and Dynamic Climatology*. London: Routledge, pp. 278–82.

Barry, R. G. and Chorley, R. J. (2003) *Atmosphere, Weather and Climate*, 8th edn. London: Routledge, 421 pp.

Barry, R. G. and Perry, A. H. (1973) *Synoptic Climatology: Methods and Applications*. London: Methuen, 555 pp.

Beer, T. (1976) Mountain waves. *Sci. Prog.*, **63**, 1–25.

Bell, G. D. and Bosart, L. F. (1988) Appalachian cold-air damming. *Mon. Wea. Rev.*, **115**, 137–61.

Beran, D. W. (1967) Large amplitude lee waves and chinook winds. *J. appl. Met.*, **6**, 865–77.

Bergen, W. R. (1976) Mountainadoes: a significant contribution to mountain windstorm damage? *Weatherwise*, **29**, 64–9.

Bica, B., *et al.* (2007) Thermally and dynamically induced pressure features over complex terrain from high-resolution analyses. *J. Appl. Met. Climatol.*, **46**, 50–65.

Bilwiller, R. (1899) Uber verschiedene Entstehungsarten und Erscheinungsformen des Föhns. *Met. Zeit.*, **16**, 204–15.

Bluestein, H. (1993) *Observations and Theory of Weather System*. New York: Oxford University Press, 594 pp.

Bolin, B. (1950) On the influence of the earth's orography on the character of the westerlies. *Tellus*, **2**, 184–95.

Bond, N. A., *et al.* (2005) Evolution of a cold front encountering steep quasi-2D terrain: Coordinated aircraft observations on 8–9 December 2001 during IMPROVE-2. *J. Atmos. Sci.*, **62**, 3559–79.

Bossert, J. E. and Cotton, W. R. (1994) Regional-scale flows in mountainous terrain. Part I: A numerical and observational comparison. Part II. Simplified numerical experiments. *Mon. Wea. Rev.*, **122**(7), 1449–71; 1472–89.

Bossert, J. E. and Poulos, G. S. (1995) A numerical investigation of mechanisms affecting drainage flows in highly complex terrain. *Theoret. Appl. Climatol.*, **52**, 119–34.

Bossert, J. E., Sheaffer, J. D. and Reiter, E. R. (1989) Aspects of regional-scale flows in mountainous terrain. *J. appl. Met.*, **28**, 590–601.

Bower, J. B. and Durran, D. R. (1986) A study of wind profiler data collected upstream during windstorms in Boulder, Colorado. *Mon. Wea. Rev.*, **114**, 1491–500.

Boyer, D. L. and Chen, R. R. (1987) Laboratory simulation of mountain effects on large-scale atmospheric motion systems: the Rocky Mountains. *J. Atmos. Sci.*, **44**, 100–23.

Boyer, D. L. and Davies, P. A. (1982) Flow past a circular cylinder on a β-plane. *Phil. Trans. R. Soc. Lond.*, **A306**, 533–66.

Boyer, D. L., Chen, R. and Davies, P. A. (1987) Some laboratory models of flow past the Alpine/Pyrenees mountain complex. *Met. Atmos. Phys.*, **36**, 187–200.

Braun, S. A, Rotunno, R. and Klemp, J. R. (1999) Effects of coastal orography on land-falling cold fronts. Part I: Dry, inviscid dynamics. *J. Atmos. Sci.*, **56**, 517–33.

Breckenridge, C. J., *et al.* (1993) Katabatic winds along the Transantarctic Mountains. In *Antarctic Meteorology Studies Based on Automatic Weather Stations*. Washington, DC: American Geophysical Union, pp. 69–92.

Brehm, M. and Freytag, C. (1982) Erosion of the night-time thermal circulation in an alpine valley. *Arch. Met. Geophys. Biokl.*, **B31**, 331–52.

Brighton, P. W. M. (1978) Strong stratified flow past three-dimensional obstacles. *Q. J. R. Met. Soc.*, **104**, 289–307.

Brinkmann, W. A. R. (1970) The chinook at Calgary (Canada). *Arch. Met. Geophys. Biokl.*, **B 18**, 269–86.

Brinkmann, W. A. R. (1971) What is a foehn? *Weather*, **26**, 230–9.

Brinkmann, W. A. R. (1973) *A Climatological Study of Strong Downslope Winds in the Boulder Area*, Inst. Arctic and Alpine Research, Occasional Paper No. 7. Boulder, CO: University of Colorado.

Brinkmann, W. A. R. (1974a) Strong downslope winds at Boulder, Colorado. *Mon. Wea. Rev.*, **102**, 596–602.

Brinkmann, W. A. R. (1974b) Temperature characteristics of severe downslope winds in Boulder, Colorado. *Zbornik Met. Hidrol. Radova*, **5**, 143–7.

Bromwich, D. H., Carrasco, J. F. and Stearns, C. R. (1992) Satellite observations of katabatic-wind propagation for great distances across the Ross Ice Shelf. *Mon. Wea. Rev.*, **120**, 1940–9.

Brooks, F. A. (1949) Mountain-top vortices as causes of large errors in altimeter heights. *Bull. Am. Met. Soc.*, **30**, 39–44.

Buettner, K. J. K. and Thyer, N. (1966) Valley winds in the Mount Rainier area. *Arch. Met. Geophys Biokl., B*, **14**, 125–47.

Burger, A. and Ekhart, E. (1937) Uber die tägiche Zirkulation der Atmosphäre im Bereiche der Alpen. *Gerlands Beitr. Geophys.*, **49**, 341–67.

Businger, J. A. and Rao, K. R. (1965) The formation of drainage wind on a snow-dome. *J. Glaciol.* **4**, 833–41.

Buzzi, A. and Rizzi, R. (1975) Isentropic analysis of cyclogenesis in the lee of the Alps. *Rivista Ital. Geofis.* (XIII Cong. Int. Met. Alpina), **1**, 7–14.

Buzzi, A. and Tibaldi, S. (1978) Cyclogenesis in the lee of the Alps: A case study. *Q. J. R. Met. Soc.*, **104**, 271–87.

Buzzi, A., Speranza, A., Tibaldi, S. and Tosi, E. (1987) A unified theory of orographic influences upon cyclogenesis. *Met. Atmos. Phys.*, **36**, 91–107.

Cadez, M. (1967) Uber synoptische Probleme in Südostalpinen Raum. *Veröff. Schweiz. Met. Zentralanstalt*, **4**, 155–75.

Carlson, T. N. (1991) *Mid-latitude Weather Systems*. London: Harper Collins Academic, 507 pp.

Casswell, S. A. (1966) A simplified calculation of maximum vertical velocities in mountain lee waves. *Met. Mag.*, **95**, 68–80.

Chaudhury, A. M. (1950) On the vertical distribution of wind and temperature over Indo-Pakistan along the meridian 76° E in winter. *Tellus*, **2**, 56–62.

Chen, W. D. and Smith, R. B. (1987) Blocking and deflection of airflow by the Alps. *Mon. Wea. Rev.*, **115**, 2578–97.

Chopra, K. P. (1973) Atmospheric and oceanic flow patterns introduced by islands. *Adv. Geophys.*, **16**, 297–421.

Chow, F. K., *et al.* (2006) High-resolution large-eddy simulations of flow in a steep alpine valley. Part I: methodology, verification and sensitivity studies. *J. Appl. Met. Climatol.* **45**, 63–86.

Chung, Y. S., Hage, K. D. and Reinelt, E. R. (1976) On lee cyclogenesis and airflow in the Canadian Rockies and the east Asian mountains. *Mon. Wea. Rev.*, **104**, 879–91.

Church, P. E. and Stephens, T. E. (1941) Influence of the Cascade and Rocky Mountains on the temperature during the westward spread of polar air. *Bull. Am. Met. Soc.*, **22**, 25–30.

Clark, T. L. and Farley, R. D. (1984) Severe downslope windstorm calculations in two and three spatial dimensions using an elastic interactive grid nesting: A possible mechanism for gustiness. *J. Atmos. Sci.*, **41**, 329–50.

Clark, T. L. and Peltier, W. R. (1984) Critical level reflection and resonant growth of non-linear mountain waves. *J. Atmos. Sci.*, **41**, 3122–34.

Clemens, C. B., Whiteman, C. D. and Horel, J. D. (2003) Cold-air pool structure and evolution in a mountain basin: Peter Sinks, Utah. *J. appl. Met.*, **42**, 752–68.

Clements, W. E., Archuleta, J. A. and Hoard, D. E. (1989) Mean structure of the nocturnal drainage flow in a deep valley. *J. appl. Met.*, **28**, 457–62.

Colle, B. A., *et al.* (2006) Climatology of barrier jets along the Alaskan Coast. Part II: Large-scale and sounding composites. *Mon. Wea. Rev.*, **134**, 454–77.

Colson, D. (1949) Airflow over a mountain barrier. *Trans. Am. Geophys. Union.*, **30**, 818–30.

Conil, S. and Hall, A. (2006) Local modes of atmospheric variability: A case study of southern California. *J. Climate*, **19L**, 4308–25.

Cook, A. W. and Topil, A. G. (1952) Some examples of chinooks east of the mountains in Colorado. *Bull. Am. Met. Soc.*, **33**, 42–7.

Corby, G. A. (1954) The airflow over mountains: a review of the state of current knowledge. *Q. J. R. Met. Soc.*, **80**, 491–521.

Corby, G. A. (1957) *Air Flow Over Mountains*, Met. Rep. no. 18 (Vol. 3, no. 2). London: Meteorological Office, HMSO.

Corby, G. A. and Wallington, C. E. (1956) Airflow over mountains: the lee-wave amplitude. *Q. J. R. Met. Soc.*, **82**, 266–74.

Cox, K. W. (1986) Analysis of the Pyrenees lee-wave event of 23 March 1982. *Mon. Wea. Rev.*, **114**, 1146–66.

Cruette, D. (1976) Experimental study of mountain lee-waves by means of satellite photographs and aircraft measurements. *Tellus*, **28**, 499–523.

Danard, M. (1977) A simple model for mesoscale effect of topography on surface winds. *Mon. Wea. Rev.*, **105**, 572–81.

Defant, A. (1933) Der Abfluss schwerer Luftmassen auf geneigten Boden, nebst einigen Bemerkungen zur Theorie stationärer Luftstrome. *Sitz. Berichte Preuss. Akad. Wiss.* (Phys. Math. Klasse), **18**, 624–35.

Defant, F. (1949) Zur Theorie der Hangwinde, nebst Bemerkungen zur Theorie der Berg und Talwinde, *Arch. Met. Geophys. Biokl.*, *A*, 1, 421–50. (translated as, A theory of slope winds, along with remarks on the theory of mountain winds and valley winds. In C. D. Whiteman and E. Dreiseitl (eds), (1984) *Alpine Meteorology*, PNL-5141, ASCOT-84-3. Richland, WA: Baltelle, Pacific Northwest Laboratory, pp. 95–120.

Defant, F. (1951) Local winds. In Malone, T. F. (ed.), *Compendium of Meteorology*. Boston MA: American Meteorological Society, pp. 655–72.

Deque, M. (2000) Regional models. In P. Mote and A. O'Neill (eds), *Numerical Modeling of the Global Atmosphere in the Climate System*. Dordrecht: Kluwer, pp. 403–18.

DeWekker, S. F. J. and Whiteman, C. D. (2006) On the time scale of nocturnal boundary layer cooling in valleys and basins and over plains. *J. Appl. Met. Climatol.* **45**, 813–20.

Dickerson, M. H. (1978) MASCON – A mass consistent atmospheric flow model for regions with complex terrain. *J. appl. Met.*, **17**, 241–53.

Dickey, W. W. (1961) A study of topographic effect on wind in the Arctic. *J. Met.*, **18**, 790–803.

Dickinson, M. J. and Knight, D. J. (1999) Frontal interaction with mesoscale topography. *J. Atmos. Sci.*, **56**, 3544–59.

Dickinson, R. E. (1980) Planetary waves: theory and observation. In R. Hide and P. W. White (eds), *Orographic Effects in Planetary Flows*, GARP Publ. Series no. 23, pp. 1–49. Geneva: WMO-ICSU Joint Scientific Committee, World Meteorological Organization.

Dobrinski, P. *et al.*, (2007) Foehn in the Rhone valley during MAP: A review of its multiscale dynamics in complex valley geometry. *Q. J. Roy. Met. Soc.*, **133**(625), 897–916.

Dobrinski, P., Sultan, B. and Janicot, S. (2005) Role of the Hoggar massif in the West African monsoon onset. *Geophys. Res. Lett.*, **32**, L01705 5 pp.

Dobrinski, P., *et al.* (2006) Flow splitting at the bifurcation between two valleys: idealized simulations in comparison with Mesoscale Alpine Programme observations. *Met. Atmos. Phys.*, **92**, 285–306.

Doran, J. C. and Horst, T. W. (1981) Velocity and temperature oscillations in drainage winds. *J. appl. Met.*, **20**, 361–4.

Douglas, C. K. M. (1928) Some alpine cloud forms. *Q. J. R. Met. Soc.*, **54**, 175–7.

Doyle, J. D. and Durran, D. R. (2002) The dynamics of mountain-wave-induced rotors. *J. Atmos. Sci.*, **59**(2), 186–201.

Doyle, J. D. and Shapiro, M. A. (1999) Flow response to large-scale topography: the Greenland tip jet. *Tellus A*, **51**(5), 728–48.

Durran, D. R. (1990) Mountain waves and downslope winds. In W. Blumen (ed.) *Atmospheric Processes Over Complex Terrain*, Meteorological Monograph, 23(45). Boston, MA: American Meteorological Society. pp. 59–81.

Egger, J. (1972) Incorporation of steep mountains into numerical forecasting models. *Tellus*, **24**, 324–35.

Egger, J. (1987) Valley winds and the diurnal circulation over plateaus. *Mon. Wea. Rev.*, **115**, 2177–86.

Egger, J. (1989) Föhn and quasi-stationary fronts. *Beitr. Phys. Atmos.*, **62**, 20–9.

Egger, J., *et al.* (2000) Diurnal winds in the Himalayan Kali Gandaki valley. Part I: Observations. *Mon. Wea. Rev.*, **128**(4), 1106–22.

Egger, J., *et al.* (2002) Diurnal winds in the Himalayan Kali Gandaki valley. Part III: Remotely piloted aircraft soundings. *Mon. Wea. Rev.*, **130**(8), 2042–58.

Egger, J., *et al.* (2005) Diurnal circulation of the Bolivian Altiplano. Part 1. Observations. *Mon. Wea. Rev.*, **133**(4), 911–24.

Ekhart, E. (1934) Neuere Untersuchungen zur Aerologie der Talwinde: Die periodischen Tageswinde in einem Quertale der Alpen, *Beitr. Phys. fr. Atmos.*, **21**, 245–68.

Ekhart, E. (1944) Beiträge zur alpinen Meteorologie. *Met. Zeit.*, **61**, 217–31 (translated as Contributions to alpine meteorology. In C. D. Whiteman and E. Dreiseitl (eds), (1984) *Alpine Meteorology*, PNL-5141, ASCOT-84-3. Richland, WA: Baltelle, Pacific Northwest Laboratory, pp. 45–72.

Ekhart, E. (1953) Uber den täglichen Gang des Windes im Gebirge. *Arch Met. Geophys. Biokl.*, B, **4**, 431–50.

Epifanio, C. C. and Durran, D. R. (2002) Lee vortex formation in free-slip stratified flow over ridges. Part I: Comparison of weakly nonlinear inviscid theory and fully non-linear viscous simulations. *J. Atmos. Sci.*, **59**, 1153–65.

Epstein, E. S. (1988) A spectral climatology. *J. Climate*, **1**, 88–107.

Etling, D. (1989) On atmospheric vortex streets in the wake of large islands. *Met. Atmos. Phys.*, **41**, 157–64.

Fitzjarrald, D. R. (1984) Katabatic winds in opposing flow. *J. Atmos. Sci.*, **41**, 1143–58.

Fleagle, R. G. (1950) A theory of air drainage. *J. Met.*, **7**, 227–32.

Flohn, H. (1942) Häufigkeit, Andauer and Eigenschaften des "freien Föhns" auf deutschen Bergstationen. *Beitr. Phys. frei, Atmos.*, **27**, 110–24.

Flohn, H. (1969) Local wind systems. In H. Flohn (ed.), *General Climatology, World Survey of Climatology*, Vol. 2. Amsterdam: Elsevier, pp. 139–71.

Förchgott, J. (1949) Wave streaming in the lee of mountain ridges, (in Czech). *Met. Zpravy*, **3**, 49–51.

Förchgott, J. (1969) Evidence for mountain-sized, lee eddies. *Weather*, **24**, 255–60.

Fosberg, M. A., Marlatt, W. E. and Krupnak, L. (1976) *Estimating Airflow Patterns over Complex Terrain*. Fort Collins: US Dept. of Agriculture, Forest Service, Research Paper RM-162.

Fournet, M. J. (1840) Des brises de jour et de nuit autour de montagnes. *Ann. Chim. Phys.*, **74**, 337–401.

Frey, K. K. (1957) Zur Diagnose des Föhns. *Met. Rdsch.*, **2**, 276–80.

Freytag, C. (1987) Results from the MERKUR Experiment: Mass budget and vertical motions in a large valley during mountain valley wind. *Meteorol. Atmos. Phys.*, **37**, 129–40.

Gaffin, D. (2007) Foehn winds that produced large temperature differences near the southern Appalachian Mountains. *Wea. Forecasting*, **22**, 145–59.

Gantner, L., *et al.* (2004) The diurnal circulation of Zugspitzplatt: Observations and modeling. *Meteorol. Zeit.*, **12**, 95–102.

GARP-ALPEX (1987) The alpine experiment. *Met. Atmos. Phys.*, **36**, 1–296.

Garratt, J. R. (1985) The inland boundary layer at low latitudes: Part I. The nocturnal jet. *Boundary-Layer Met.*, **31**, 307–27.

Geiger, R. (1965) *The Climate near the Ground*, Cambridge, MA: Harvard University Press. pp. 393–417.

Geiger, R., Aron, R. H. and Todhunter, P. (2003) *Climate near the Ground*, 6th edition. Lanham, MD: Rowman and Littlefield, 584 pp.

Gerbier, N. and Bérenger, M. (1961) Experimental studies of lee waves in the French Alps. *Q. J. R. Met. Soc.*, **87**, 13–23.

Georgelin, M., *et al.* (1994) Impact of subgrid-scale orography on the parameterization of orographic flows. *Mon. Wea. Rev.*, **122**(7), 1509–22.

Georgii, W. (1967) Thermodynamik und Kinematik des Kaltluftföhns. *Arch. Met. Geophys. Biokl.* A, **16**, 137–52.

Giorgi, F. (1990) Stimulation of regional climate using a limited area model nested in a general circulation. *J. Climate*, **3**, 941–63.

Giorgi, F. and Bates G. T. (1989) On the climatological skill of a regional model over complex terrain. *Mon. Wea. Rev.*, **117**, 2325–47.

Giorgi, F., Bates, G. T. and Nieman, S. J. (1993) The multiyear surface climatology of a regional atmospheric model over the western United States. *J. Climate*, **6**, 75–85.

Gjevik, B. and Marthinsen, T. (1978) Three-dimensional lee-wave pattern. *Q. J. R. Met. Soc.*, **104**, 947–58.

Gleeson, T. A. (1951) On the theory of cross-valley winds arising from differential heating of the slopes. *J. Met.*, **8**, 398–405.

Gleeson, T. A. (1953) Effects of various factors on valley winds. *J. Met.*, **10**, 262–9.

Glickman, T. S. (ed.) (2000) *Glossary of Meteorology*. Boston, MA: American Meteorological Society, 855 pp.

Godske, C. L., *et al.* (1957) *Dynamic Meteorology and Weather Forecasting*. Boston, MA: American Meteorological Society.

Gohm, A. and Mayr, C. J. (2005) Numerical and observational case-study of a deep Adriatic bora. *Q. J. R. Met. Soc.*, **131**(608), 1363–92.

Gosink, J. (1982) Measurements of katabatic winds between Dome C and Dumont d'Urville. *Pure Appl. Geophys.*, **120**, 503–26.

Grace, W. and Holton, I. (1990) Hydraulic jump signatures associated with Adelaide downslope winds. *Austral. Met. Mag.*, **38**, 43–52.

Gross, G. (1984) Eine Erklärung des Phänomens Maloja-Schlange mittels numerische Simulation. Dissertation, Fachbereich Mechanik. Darmstadt: Technische Hochschule.

Guenard, V., *et al.* (2006) Dynamics of the MAP IOP 15 severe Mistral event: Observations and high-resolution numerical simulations. *Q. J. R. Met. Soc.* **132**, 757–78.

Hage, K. D. (1961) On summer cyclogenesis in the lee of the Rocky Mountains. *Bull. Am. Met. Soc.*, **42**, 20–33.

Haiden, T. and Whiterman, C. D. (2005) Katabatic flow on a low-angle slope. *J. Appl. Met.* **44**, 113–26.

Hamilton, R. A. (1958a) The meteorology of northern Greenland during the midsummer period. *Q. J. R. Met. Soc.*, **84**, 142–58.

Hamilton, R. A. (1958b) The meteorology of north Greenland during the midwinter period. *Q. J. R. Met. Soc.*, **84**, 355–74.

Hann, J. (1866) Zur Frage über den Ursprung des Föhns. *Zeit. Osterreich Ges. Met.*, **1**(17), 257–63.

Hann, J. von (1879) Zur Meteorologie der Alpengifel. *Wien Akad. Wiss. Sitzungsberichte* (Math.-Naturwiss. Klass.). **78**(2), 829–66.

Hann, J. (1885) Einige Bermerkungen zur Entwicklungs-Geschichte der Ansichten über den Ursprung des Föhns. *Met. Zeit.*, **2**, 393–9.

Hawkes, H. B. (1947) Mountain and valley winds – with special reference to the diurnal mountain winds of the Great Salt Lake region. Ph.D. dissertation. Columbus, OH: Ohio State University, 312 pp.

Heineman, G. and Klein, T. (2002) Modelling and observations of the katabatic flow dynamics over Greenland, *Tellus*, **A54**, 542–54.

Hennemuth, B. (1985) Temperature field and energy budget of a small alpine valley. *Contrib. Atmos. Phys.*, **58**, 545–59.

Hennemuth, B. and Köhler, U. (1984) Estimation of the energy balance of the Dischma Valley. *Arch. Met. Geophys. Biokl.*, **B34**, 97–119.

Hennemuth, B. and Neureither, I. (1986) Das Feuchtefeld in einem alpinen Endtal. *Met. Rdsch.*, **39**, 233–9.

Hennemuth, B. and Schmidt, H. (1985) Wind phenomena in the Dischma Valley during DISKUS. *Arch. Met. Geophys. Biokl.*, **B35**, 361–87.

Hess, S. L. and Wagner, H. (1948) Atmospheric waves in the northwestern United States. *J. Met.*, **5**, 1–19.

Hide, R. and White, P. W. (1980) Orographic effects in planetary forographic effects. In R. Hide and P. W. White (eds), *Planetary Flows*, GARP Publication Series, No. 23. Geneva: World Meteorological Organization, pp. 85–114.

Hoinka, K. P. (1985a) A comparison of numerical simulations of hydrostatic flow over mountains with observations. *Mon. Wea. Rev.*, **113**, 719–35.

Hoinka, K. P. (1985b) Observation of the airflow over the Alps during a foehn event. *Q. J. R. Met. Soc.*, **111**, 199–224.

Hoinka, K. P. and Davies, H. C. (2007) Upper-tropospheric flow features and the Alps: An overview. *Q. J. Roy. Met. Soc.*, **133**(625), 847–65.

Hoinkes, H. (1954) Beiträge zur Kenntnis des Gletscherwindes. *Arch. Met. Geophys. Biokl.* **B, 6**, 36–53.

Holmgren, H. (1971) Climate and energy exchange on a sub-polar ice cap in summer. Part C. On the katabatic winds on the northwest slope of the ice cap. Variations of the surface roughness. *Uppsala Univ. Met. Inst.* Meddel. 109.

Holtmeier, F. K. (1966) Die "Malojaschlange" und die Vorbreitung der Fichte. *Wetter u. Leben*, **18**, 105–8.

Holton, J. R. (1967) The diurnal boundary layer oscillation over sloping terrain. *Tellus*, **19**, 199–205.

Hornsteiner, M. (2005) Local foehn effects in the upper Isar valley, part 1: Observations. *Meteorol. Atmos. Phys.*, **88**(3–4), 175–92.

Horst, T. W. and Doran, J. C. (1986) Nocturnal drainage flow on simple slopes. *Boundary-Layer Met.*, **34**, 263–86.

Hoskins, B. J. (1980) Representation of the earth's topography using spherical harmonics. *Mon. Wea. Rev.*, **108**, 111–15.

Hoskins, B. J. and Hodges, K. T. (2002) New perspectives on the Northern Hemisphere winter storm tracks. *J. Atmos. Sci.*, **59**(6), 1041–61.

Hoskins, B. J. and Karoly, D. J. (1981) The steady linear response of a spherical atmosphere to thermal and orographic forcing. *J. Atmos. Sci.*, **38**(6), 1179–96.

Hoskins, B. J., *et al.* (1989) Diagnostics of the global atmospheric circulation based on ECMWF analyses 1979–1989, Technical Report WRCP-27. Geneva: World Meteorological Organization.

Houghton, D. D. and Isaacson, E. (1970) Mountain winds. *Studies in Num. Anal.*, **2**, 21–52.

Hunt, J. C. R. and Snyder, W. H. (1980) Experiments on stably and neutrally stratified flow over a model three-dimensional hill. *J. Fluid Mech.*, **96**, 671–704.

Iijima, Y. and Shinoda, M. (2000a) Seasonal characteristics of nocturnal cooling in relation to the downward longwave radiation in a mountainous area, central Japan. *Preprint Volume, Ninth Conference on Mountain Meteorology*. P1.36. Boston, MA: American Meteorological Society, pp. 221–4.

Iijima, Y. and Shinoda, M. (2000b) Seasonal change in the cold air pool formation in a subalpine hollow, central Japan. *Int. J. Climatol.*, **20**, 1471–83.

Ives, R. L. (1950) Frequency and physical effects of chinook winds in the Colorado high plains region. *Ann. Ass. Am. Geog.*, **40**, 293–327.

James, I. N. (1994) *Introduction to Circulating Atmospheres*. Cambridge: Cambridge University Press.

Jansá, A. (1987) Distribution of the mistral: a satellite observation. *Met. Atmos. Phys.*, **36**, 201–14.

Jaubert, G., *et al.* (2005) Numerical simulation of meso-gamma scale features of foehn at ground level in the Rhine valley. *Q. J. R. Met. Soc.*, **131**(608), 1339–61.

Jiang, Q.-F. (2006) Precipitation over concave terrain. *J. Atmos. Sci.*, **63**, 2269–2288.

Jiang, Q.-F. and Doyle, J. D. (2006) Topographically generated cloud plumes. *Mon. Wea. Rev.*, **134**(8), 2108–27.

Jiang, Q.-F., Smith, R. B. and Doyle, J. (2003) The nature of the mistral: Observations and modelling of two MAP events. *Q. J. R. Met. Soc.*, **129**(588), 857–75.

Jiang, Q., Doyle, J. D. and Smith, R. B. (2005) Blocking, descent and gravity waves: Observations and modeling of a MAP northerly foehn evet. *Q. J. R. Met. Soc*, **131**, 675–701.

Juang, H.-M., *et al.* (2005) Applying horizontal diffusion on pressure surface to mesoscale models on terrain-following coordinates [sic]. *Mon. Wea. Rev.*, **133**(5), 1384–402.

Julian, L. T. and Julian, P. R. (1969) Boulder's winds. *Weatherwise*, **22**, 108–12, 126.

Jurcec, V. (1980) On mesoscale characteristics of bora conditions in Yugoslavia. *Pure Appl. Geophys.*, **119**, 640–57.

Karyampudi, V. M., *et al.* (1995a) The influence of the Rocky Mountain on the 13–14 April 1986 severe weather outbreak. Part I: Mesoscale lee cyclogenesis and its relationship to severe weather and dust storms. *Mon. Wea. Rev.* **123**, 1394–422.

Karyampudi, V. M., *et al.* (1995b). The influence of the Rocky Mountain on the 13–14 April 1986 severe weather outbreak. Part 2: Evolution of a pre-frontal bore and its role in triggering a squall line. *Mon. Wea. Rev.*, **123**, 1423–46.

Kasahara, A. (1980) Effect of zonal flows on the free oscillations of a barotropic atmosphere. *J. Atmos. Sci.*, **37**, 917–29.

Kasahara, A., Sasamori, T. and Washington, W. M. (1973) Simulation experiments with a 12-layer stratospheric global circulation model. I. Dynamical effects of the earth's orography and thermal influence of continentality. *J. Atmos. Sci.*, **30**, 229–50.

Katzfey, J. J. (1995) Simulation of extreme New Zealand precipitation events. Part 1. Sensitivity to orography and resolution. *Mon. Wea. Rev.*, **123**, 737–54.

Kaufman, P. and Weber, R. O. (1998) Directional correlation coefficients for channeled flow and application to wind data over complex terrain. *J. Atmos. Ocean Technol.*, **15**, 89–97.

Kim, Y.-J. and Doyle, J. D. (2005) Extension of an orographic drag parameterization scheme to incorporate orographic anisotropy and flow blocking. *Q. J. R. Met. Soc.*, **131**(609), 1893–921.

Kleissl, J., Honrath, R. E. and Henriques, D. V. (2006) Analysis and application of Sheppard's airflow model to predict mechanical orographic lifting and the occurrence of mountain clouds. *J. Appl. Met. Clim.*, **45**, 13 767–87.

Klemp, J. B. and Durran, D. R. (1987) Numerical modelling of bora winds. *Met. Atmos. Phys.*, **36**, 215.

Klemp, J. B. and Lilly, D. K. (1975) The dynamics of wave-induced downslope winds. *J. Atmos. Sci.*, **32**, 320–39.

Klemp, J. B. and Lilly, D. K. (1978) Numerical simulation of hydrostatic mountain waves. *J. Atmos. Sci.*, **35**, 78–107.

Köppen, W. (1923) Die Bora in nordlichen Skandinavien. *Ann. Hydrogr. Marit. Met.*, **51**, 97–9.

Krug-Pielsticker, U. (1942) Beobachtungen der hohen Föhnwelle an den Ostalpen. *Beitr. Phys. frei. Atmos.*, **27**, 140–64.

Kuettner, J. P. (1958) The rotor flow in the lee of mountains. *Schweiz. Aero Revue*, **33**, 208–15. Also: (1959) *Geophys. Res. Dir. Res. Notes, no. 6*, Cambridge, MA: US Air Force, Cambridge Research Center.

Küttner, J. (1939a) Moazagotl und Föhnwelle. *Beitr. Phys. frei Atmos.*, **25**, 79–114.

Küttner, J. (1939b) Zur Entstehung der Föhnwelle. *Beitr. Phys. frei Atmos.*, **25**, 251–99.

Küttner, J. (1949) Periodische Luftlawinen. *Met. Rdsch*, **2**, 183–4.

Kutzbach, J. E. (1989) Sensitivity of climate to Late Cenozoic uplift in southern Asia and the American West: numerical experiments. *J. Geophys. Res.*, **94(D15)**, 18, 393–407.

Kuwagata, T. and Kimura, F. (1995) Daytime boundary layer evolution in a deep valley. Part I: Observations in the Ina valley. *J. appl. Met.*, **34**, 1082–91.

Lavoie, R. L. (1974) A numerical model of the trade-wind weather on Oahu. *Mon. Wea. Rev.*, **102**, 630–7.

Lawrence, E. N. (1954) Nocturnal winds. *Prof. Notes. Met. Office* (London), **7**(111), 1–13.

Lee, T. J., *et al.* (1989) Influence of cold pools downstream of mountain barriers on downslope winds and flushing. *Mon. Wea. Rev.*, **117**, 2041–58.

Lenschow, D. (ed.) (1986) *Probing the Atmospheric Boundary Layer*. Boston, MA: American Meteorological Society.

Lester, P. F. (1978) A severe chinook windstorm. *Conference on Sierra Nevada Meteorology, Preprints*. Boston, MA: American Meteorological Society, pp. 104–8.

Lettau, H. H. (1967) Small to large-scale features of boundary layer structure over mountain slopes. In E. R. Reiter and J. L. Rasmussen (eds), *Proceedings of the Symposium on Mountain Meteorology*, Atmospheric Science Paper No. 122. Fort Collins, CO: Colorado State University, pp. 1–74.

Lettau, H. H. (1978) Explaining the world's driest climate. In H. H. Lettau and K. Lettau (eds), *Exploring the World's Driest Climate*, Rep. 101. Madison, WI: Institute of Environmental Studies, University of Wisconsin, pp. 182–248.

Lied, N. J. (1964) Stationary hydraulic jumps in a katabatic flow near Davis, Antarctica, 1961. *Aust. Met. Mag.*, **47**, 40–51.

Lilly, D. K. (1978) A severe downslope windstorm and aircraft turbulence induced by a mountain wave. *J. Atmos. Sci.*, **35**, 59–77.

Lilly, D. K. and Klemp, J. B. (1979) The effect of terrain shape on non-linear hydrostatic mountain waves. *J. Fluid Mech.*, **95**, 241–61.

Lilly, D. K. and Zipser, E. J. (1972) The Front Range windstorm of 11 January 1972 – a meteorological narrative. *Weatherwise*, **25**, 56–63.

Lindsay, J. A. and Tyson, P. D. (1990) Thermo-topographically induced boundary layer oscillations over the central Namib, southern Africa. *Int. J. Climatol.*, **10**, 63–77.

Lockwood, J. G. (1962) Occurrence of föhn winds in the British Isles. *Met. Mag.*, **91**, 57–65.

Loescher, K. A., *et al.* (2006) Climatology of barrier jets along the Alaskan Coast. Part I: Spatial and temporal distributions. *Mon. Wea. Rev.* 437–53.

Loewe, F. (1972) The land of storms. *Weather*, **27**, 110–21.

Long, R. R. (1954) Some aspects of the flow of stratified fluids. II. Experiments with a two-fluid system. *Tellus*, **6**, 97–115.

Long, R. R. (1969) *Blocking Effects in Flow over Obstacles*. Tech. Rep. 32, WB-ESSA. Baltimore, MD: Johns Hopkins University.

Long, R. R. (1970) Blocking effects in flow over obstacles. *Tellus*, **22**, 471–80.

Longley, R. W. (1967) The frequency of winter chinooks in Alberta. *Atmosphere*, **5**, 4–16.

Lopéz, M. E. and Howell, W. E. (1967) Katabatic winds in the equatorial Andes. *J. Atmos. Sci.*, **24**, 29–35.

Ludlam, F. H. (1967) Characteristics of billow clouds and their relation to clear-air turbulence. *Q. J. R. Met. Soc.*, **93**, 419–35.

Ludlam, F. H. (1980) *Clouds and Storms*. University Park, PA: Pennsylvania State University Press, pp. 369–80.

Lydolph, P. E. (1977) *Climates of the Soviet Union*. Amsterdam: Elsevier, pp. 160–9, 193–5.

Lyra, G. (1943) Theorie der stationären Leewellenströmung in freier Atmosphäre. *Zeit. angew. Math. Mechan.*, **23**, 1–28.

MacHattie, L. B. (1968) Kananaskis Valley winds in summer. *J. appl. Met.*, **7**, 348–52.

Mahrer, Y. and Pielke, R. A. (1975) A numerical model of the airflow over mountains using the two-dimensional version of the University of Virginia meso-scale model. *J. Atmos. Sci.*, **32**, 2144–55.

Mahrer, Y. and Pielke, R. A. (1977) A numerical study of the airflow over irregular terrain. *Beitr. Phys. Atmos.*, **50**, 98–113.

Mahrt, L. (1982) Momentum balance of gravity flows. *J. Atmos. Sci.*, **39**, 2701–11.

Malmberg, H. (1967) Der Einfluss der Gebirge auf die Luftdruckverteilung am Erdboden. *Met. Abhand.*, **71**(2).

Manabe, S. and Broccoli, A. J. (1990) Mountains and arid climates of middle latitudes. *Science*, **247**, 192–5.

Manabe, S. and Terpstra, T. B. (1974) The effects of mountains on the general circulation of the atmosphere as identified by numerical experiments. *J. Atmos. Sci.*, **31**, 3–42.

Manins, P. C. and Sawford, B. L. (1979a) A model of katabatic winds. *J. Atmos. Sci.*, **36**, 619–30.

Manins, P. C. and Sawford, B. L. (1979b) Katabatic winds: a field case study. *Q. J. R. Met. Soc.*, **105**, 1011–25.

Manley, G. (1938) Meteorological observations of the British East Greenland Expedition, 1935–1936, at Kangerdlugssuak, 68°10′ N, 31°44′ W. *Q. J. R. Met. Soc.*, **64**, 253–76.

Manley, G. (1945) The Helm wind of Crossfield, 1937–9. *Q. J. R. Met. Soc.*, **71**, 197–219.

Mano, H. (1956) A study on the sudden nocturnal temperature rise in the valley and the basin. *Geophys. Mag.*, **27**, 169–204.

Mason, P. J. (1985) On the estimation of orographic drag, in *Physical Parameterization for Numerical Models of the Atmosphere*, 2. Reading, UK: ECMWF, pp. 139–65.

Mason, P. J. and Sykes, R. I. (1978) On the interaction of topography and Ekman boundary layer pumping in a stratified atmosphere. *Q. J. R. Met. Soc.*, **104**, 475–90.

Mass, C. F. and Dempsey, D. P. (1985) A one-level, mesoscale model for diagnosing surface winds in mountainous and coastal regions. *Mon. Wea. Rev.*, **113**, 1211–27.

Mather, K. B. and Miller, G. S. (1967) The problem of katabatic winds on the coast of Terre Adelie. *Polar Record*, **13**, 415–32.

Mattocks, C. and Bleck, R. (1986) Jet streak dynamics and geostrophic adjustment processes during the initial stages of lee cyclogenesis. *Mon. Wea. Rev.*, **114**, 2033–56.

Mayr, G. J., *et al.* (2007) Gap flows: Results from the Mesoscale Alpine Programme. *Q. J. Roy. Met. Soc.*, **133**(625), 881–96.

McCauley, M. P. and Sturman, A. P. (1999) A study of orographic blocking and barrier wind development upstream of the Southern Alps, New Zealand. *Meteorol. Atmos. Phys.*, **70**, 121–31.

McClain, E. P. (1960) Some effects of the Western Cordillera of North America on cyclonic activity. *J. Met.*, **17**, 104–15.

McFarlane, N. (2000) Gravity-wave drag. In P. Mote and A. O'Neill (eds), *Numerical Modeling of the Global Atmosphere in the Climate System*. Dordrecht: Kluwer, pp. 297–320.

McGinley, J. (1982) A diagnosis of Alpine lee cyclogenesis. *Mon. Wea. Rev.*, **110**, 1271–87.

McGowan, H. A. and Sturman, A. P. (1996) Regional and local scale characteristics of foehn wind events over the South Island of New Zealand. *Met. Atmos. Phys.*, **58**, 151–64.

McGowan, H. A. and Sturman, A. P. (2002) Regional and local scale characteristics of foehn wind events over the South Island of New Zealand. *Meteorol. Atmos. Phys.*, **58**, 151–64.

McGowan, H. A., Owens, I. F. and Sturman, A. P. (1995) Thermal and dynamic characteristics of alpine lake breezes, Lake Tekapo, New Zealand. *Boundary-Layer Met.*, **76**, 3–24.

McGowan, H. A., *et al.* (2002) Observations of foehn onset in the Southern Alps, New Zealand. *Meteorol. Atmos. Phys.*, **79**, 215–30.

McGuffie, K. and Henderson-Sellers, A. (2005) *A Climate Modelling Primer*. 3rd edn. Chichester, UK: J. Wiley and Sons, 280 pp.

McKee, T. B. and O'Neal, R. D. (1989) The role of valley geometry and energy budget in the formation of nocturnal valley winds. *J. appl. Met.*, **28**, 445–56.

McNider, R. T. (1982) A note on velocity fluctuations in drainage flows. *J. Atmos. Sci.*, **39**, 1658–60.

McNider, R. T. and Pielke, R. A. (1981) Diurnal boundary-layer development over sloping terrain. *J. Atmos. Sci.*, **38**, 2198–212.

McNider, R. T. and Pielke, R. A. (1984) Numerical simulation of slope and mountain flows. *J. Clim. Appl. Met.*, **23**, 1441–53.

Mobbs, S. D., *et al.* (2005) Observations of downslope winds and rotors in the Falkland Islands. *Q. J. R. Met. Soc.*, **131**(605), 329–51.

Mook, R. H. G. (1962) Zur Bora an einem nordnorwegischen Fjord. *Met. Rdsch.*, **15**, 130–3.

Moore, G. W. K. and Renfrew, I. A. (2005) Tip jets and barrier winds: A QuickSCAT climatology of high wind speed events around Greenland. *J. Climate*, **18**(18), 3713–25.

Mote, P. and O'Neill, A. (eds) (2000) *Numerical Modeling of the Global Atmosphere in the Climate System*. Dordrecht: Kluwer, 517 pp.

Müller, H. and Whiteman, C. D. (1988) Breakup of a nocturnal temperature inversion in Dischma Valley during DISKUS. *J. Appl. Met.*, **27**, 188–94.

Nappo, C. J., Jr. (1977) Meso-scale flow over complex terrain during the eastern Tennessee trajectory experiment-(ETTEX). *J. appl. Met.*, **16**, 1186–96.

Neff, W. D. (1988) Observations of complex terrain flows using acoustic sounders: Echo interpretation. *Boundary-Layer Met.*, **42**, 207–28.

Neff, W. D. and King, C. W. (1989) The accumulation and pooling of drainage flows in a large basin. *J. appl. Met.*, **28**, 518–29.

Neiman, P. J., *et al.* (1988) Doppler lidar observations of a downslope windstorm. *Mon. Wea. Rev.*, **116**, 2265–75.

Nicholls, J. M. (1973) *The Airflow over Mountains. Research, 1958–1972*. WMO Technical Note No. 127. Geneva: World Meteorological Organization.

Nickus, U. and Vergeiner, I. (1984) The thermal structure of the Inn valley atmosphere. *Arch. Met. Geophys. Biokl.*, A, **33**, 199–215.

Orville, H. D. (1964) On mountain upslope winds. *J. Atmos. Sci.*, **6**, 622–33.

Osmond, H. W. (1941) The chinook wind east of the Canadian Rockies. *Can. J. Res.*, A, **19**, 57–66.

Overland, J. E., Hitchman, M. H. and Han, Y.-J. (1979) A regional surface wind model for mountainous coastal areas, NOAA-TR-ERL 407, Pacific Marine Environmental Lab. 32. Seattle: NOAA.

Paegle, J. (1984) Topographically bound low-level circulations. *Riv. Met. Aeronaut.*, **44**, 113–25.

Palmén, E. and Newton, C. W. (1969) *Atmospheric Circulation Systems*, New York: Academic Press, pp. 344–50.

Parish, T. R. (1980) *Surface Winds in East Antarctica*, Madison, WI: Department of Meteorology, University of Wisconsin.

Parish, T. R. (1982) Barrier winds along the Sierra Nevada mountains. *J. appl. Met.*, **21**, 925–30.

Peltier, W. R. and Clark, T. L. (1979) The evolution of finite-amplitude mountain waves. Part II. Surface wave drag and severe downslope windstorms. *J. Atmos. Sci.*, **36**, 1498–529.

Petersen, G. N., Kristjansson, J. E. and Olafsson, H. (2005) The effect of upstream wind on airflow in the vicinity of a large mountain. *Q. J. R. Met. Soc.*, **131**, 1113–28.

Petkovsék, Z. (1978) Relief meteorologically relevant characteristics of basins. *Met. Zeit.*, **28**, 333–40.

Petkovsék, Z. (1980) Additional relief meteorologically relevant characteristics of basins. *Met. Zeit.*, **28**, 333–40.

Petkovsěk, Z. and Hočevar, A. (1971) Night drainage winds. *Arch. Met. Geophys. Biokl.*, A, **20**, 353–60.

Petkovsék, Z. and Paradiz, B. (1976) Bora in the Slovenian coastal region. In M. M. Yoshino (ed.) *Local Wind Bora*. Tokyo: University of Tokyo Press, pp. 135–44.

Pettre, P. (1982) On the problem of violent valley winds. *J. Atmos. Sci.*, **39**, 542–65.

Pettre, P. (1984) Contribution to the hydraulic theory of bora wind using ALPEX data. *Beitr. Phys. Atmos.*, **57**, 536–45.

Pichler, H. and Steinacker, R. (1987) On the synoptics and dynamics of orographically induced cyclones in the Mediterranean. *Met. Atmos. Phys.*, **36**, 108–17.

Pielke, R. (2002) *Mesoscale Meteorological Modeling*, 2nd edn. Orlando, FL: Academic Press, 676 pp.

Pierrehumbert, R. T. and Wyman, B. (1985) Upstream effects of mesoscale mountain ridges. *J. Atmos. Sci.*, **42**, 977–1003.

Porch, W. H., *et al.* (1989) Tributary, valley, and sidewall air flow interactions in deep valley. *J. Appl. Met.*, **28**, 578–89.

Poulos, G. S., *et al.* (2000) The interaction of katabatic flow and mountain waves. Part I: Observations and idealized simulations. *J. Atmos. Sci.*, **57**, 1919–36.

Prandtl, L. (1952) *Essentials of Fluid Dynamics* (transl. of 1949 edn of Führer durch die Strömungslehre. New York: Hafner Publishing Co., pp. 422–5.

Price, D. (2005) Mountain and valley winds in Scotland: a case study at Balquhidder in the southern central Highlands. *Weather*, **60**(4), 88–91.

Putnins, P. (1970) The climate of Greenland. In S. Orvig (ed.), *Climates of the Polar Regions*. Amsterdam: Elsevier, pp. 3–128.

Queney, P. (1948) The problem of airflow over mountains: a summary of theoretical studies. *Bull. Am. Met. Soc.*, **29**, 16–26.

Queney, P. (1963) Etat actuel de la dynamique des courants aériens près des montagnes. *Geofis. Met.* (7 Cong. Int. Met. Alpina), **11**, 1–11.

Radinovic, D. (1965) Forecasting of cyclogenesis in the West Mediterrenean and other areas bounded by mountain ranges by a baroclinic mode. *Arch. Met. Geophys. Biokl.* A, **14**, 279–99.

Radinovic, D. (1986) On the development of orographic cyclones. *Q. J. R. Met. Soc.*, **112**, 927–51.

Rampanelli, G., Zardi, D. and Rotunno, R. (2004) Mechanisms of up-valley winds. *J. Atmos. Sci.*, **61**, 3097–111.

Raphael, M. N. (2003) The Santa Ana winds of California. *Earth Interactions*. **7**, 1–13.

Reiher, M. (1936) Nächtlicher Kaltluftfluss an Hindernissen. *Bioklim. Beiblätter* (Braunschweig), **3**, 152–63.

Reiter, E. R. (1963) *Jet Stream Meteorology*. Chicago, IL: University of Chicago Press.

Reuder, J. and Egger, J. (2006) Diurnal circulation of the South American Altiplano: Observations in a valley and at a pass. *Tellus*, **58A**, 254–62.

Reuter, H. and Pichler, H. (1964) On the orographic influences of the Alps. *Tellus*, **16**, 40–2.

Richard, E., Mascart, P. and Nickerson, E. C. (1989) On the role of surface friction in downslope windstorms. *J. appl. Met.*, **28**, 241–51.

Riehl, H. (1974) On the climatology and mechanisms of Colorado chinook winds. *Bonn. Met. Abhandl.*, **17**, 493–504.

Ross, D. G., *et al.* (1988) Diagnostic wind field modeling for complex terrain: Model development and testing. *J. Clim. Appl. Met.*, **27**, 785–96.

Rotach, M. W. and Zardi, D. (2007) On the boundary-layer structure over complex terrain: Key findings from MAP. *Q. J. Roy. Met. Soc.* **133**, 937–48.

Rothman, W. and Smith, R. B. (1989) A laboratory model of severe downslope winds. *Tellus*, **41A**, 401–15.

Ruddiman, W. F. and Kutzbach, J. E. (1989) Forcing of late Cenozoic northern hemisphere climate by plateau uplift in southern Asia and the American West. *J. Geophys. Res.*, **94(D15)**, 18, 409–27.

Ruddiman, W. F., Prell, W. L. and Raymo, W. E. (1989) Late Cenozoic uplift in southern Asia and the American West: Rationale for general circulation modeling experiments. *J. Geophys. Res.*, **94(D15)**, 18, 379–91.

Ryan, B. C. (1977) A mathematical model for diagnosis and prediction of surface winds in mountainous terrain. *J. appl. Met.*, **16**, 571–84.

Sato, T. (1989) The sensitivity of nocturnal cooling and drainage flow over an inclined topography to meteorological ground surface and topographic conditions. *J. Met. Soc., Japan*, **67**, 335–50.

Sawyer, J. S. (1960) Numerical calculation of the displacements of a stratified airstream crossing a ridge of small height. *Q. J. R. Met. Soc.*, **86**, 326–45.

Schär, C. and Durran, D. R. (1997) Vortex formation and vortex shedding in continuously stratified flows past isolated topography. *J. Atmos. Sci.*, **54**, 534–54.

Schrott, D. and Verant, W. (2002) Il foehn sulle Alpa. *Nimbus* **31–32**, 13–39.

Schütz, J. and Steinhauser, F. (1955) Neue Föhnuntersuchungen aus dem Sonnblick. *Arch. Met. Geophys. Bioklim.*, **B 6**, 207–24.

Schwabl, W. (1934) Zur Kenntnis der Beeinflussung der Allgemeinströmung durch ein Gebirgstal. *Met. Zeit*, **51**, 342–5.

Schwerdtfeger, W. (1970) The climate of the Antarctic. In S. Orvig (ed.), *Climates of the Polar Regions*. Amsterdam: Elsevier, pp. 253–355.

Schwerdtfeger, W. (1972) The vertical variation of the wind through the friction-layer over the Greenland ice cap. *Tellus*, **24**, 13–16.

Schwerdtfeger, W. (1975a) Mountain barrier effects on the flow of stable air north of the Brooks Range. In G. Weller and S. A. Bowling (eds), *Climate of the Arctic*. Fairbanks, AL: Geophysics Institute University of Alaska, pp. 204–8.

Schwerdtfeger, W. (1975b) The effect of the Antarctic Peninsula on the temperature regime of the Weddell Sea. *Mon. Wea. Rev.*, **103**, 45–51.

Scinocco, J. F. and Peltier, W. R. (1989) Pulsating downslope windstorms. *J. Atmos. Sci.*, **46**, 2885–914.

Scorer, R. S. (1949) Theory of waves in the lee of mountains. *Q. J. R. Met. Soc.* **74**, 41–56.

Scorer, R. S. (1953) Forecasting mountain and lee waves. *Met. Mag.*, **82**, 232–4.

Scorer, R. S. (1955) Theory of airflow over mountains. IV. Separation of airflow from the surface. *Q. J. R. Met. Soc.*, **81**, 340–50.

Scorer, R. S. (1967) Causes and consequences of standing waves. In E. Reiter and J. L. Rasmussen (eds), *Symposium on Mountain Meteorology*, Atmospheric Science Paper No. 122. Fort Collins, CO: Colorado State University, pp. 75–101.

Scorer, R. S. (1978) *Environmental Aerodynamics*. Chichester: Ellis Horwood.

Scorer, R. S. and Klieforth, H. (1959) Theory of mountain waves of large amplitude. *Q. J. R. Met. Soc.*, **85**, 131–43.

Seibert, P. (1990) South foehn studies since the ALPEX experiment. *Meteorol. Atmos. Phys.*, **43**, 91–103.

Seibert, P. (1993) Der Foehn in den Alpen. *Geogr. Rundschau*, **45**, 116–23.

Sherman, C. A. (1978) A mass-consistent model for wind fields over complex terrain. *J. appl. Met.*, **17**, 312–19.

Shutts, G. J. (1998) Idealized models of the pressure drag force on mesoscale mountain ridges. *Contrib. Atmos. Phys.*, **71**, 303–15.

Slingo, A. and Pearson, D. W. (1987) A comparison of the impact of an envelope orography and of a parameterization of orographic gravity-wave drag on model simulations. *Q. J. R. Met. Soc.*, **113**, 847–70.

Smith, C. M. and Skyllingstad, K. D. (2005) Numerical simulation of katabatic flow with changing slope angle. *Mon.Wea. Rev.*, **133**(11): 3065–80.

Smith, R. B. (1976) Generation of lee waves by the Blue Ridge. *J. Atmos. Sci.*, **33**, 587–609.

Smith, R. B. (1977) The steepening of hydrostatic mountain waves. *J. Atmos. Sci.*, **34**, 1634–54.

Smith, R. B. (1979a) The influence of mountains on the atmosphere. *Adv. Geophys.*, **21**, 87–230.

Smith, R. B. (1979b) Some aspects of the quasi-geostrophic flow over mountains. *J. Atmos. Sci.*, **36**, 2385–93.

Smith, R. B. (1982) Synoptic observations and theory of orographically disturbed wind and pressure. *J. Atmos. Sci.*, **39**, 60–70.

Smith, R. B. (1985) On severe downslope windstorms. *J. Atmos. Sci.*, **42**, 2597–603.

Smith, R. B. (1986) Mesoscale mountain meteorology in the Alps. *Scientific Results of the Alpine Experiment (ALPEX), Vol. II.* WMO/TD No. 108, GARP Publ. Series no. 27. Geneva: World Meteorological Organization, pp. 407–23.

Smith, R. B. (1987) Aerial observations of the Yugoslavian bora. *J. Atmos. Sci.*, **44**, 269–97.

Smith, R. B. (1989) Mountain-induced stagnation points in hydrostatic flow. *Tellus*, **41A**, 270–4.

Smith, R. B., *et al.* (1997) The Wake of St. Vincent. *J. Atmos, Sci.*, **54**, 606–23.

Smith, R. B., *et al.* (2002) Mountain waves over Mont Blanc: Influence of a stagnant boundary layer. *J. Atmos. Sci.*, **59**(13), 2073–92.

Smith, R. B., *et al.* (2007) Alpine gravity waves: Lessons from MAP regarding mountain wave generation and breaking. *Q. J. Roy. Met. Soc.*, **133**(625), 917–36.

Soma, S. (1969) Dissolution of separation in the turbulent boundary layer and its application to natural winds. *Pap. Met. Geophys*, **20**, 111–74.

Sommers, W. T. (1976) MASCON – A mass-consistent atmospheric flux model for regions with complex terrain. *J. appl. Met.*, **17**, 241–53.

Sommers, W. T. (1978) LFM forecast variables related to Santa Ana wind occurrences. *Mon. Wea. Rev.*, **106**, 1307–16.

Song, Y., *et al.* (2007) Glacier winds in the Rongbuk valley, north of Mount Everest: I. Meteorological modeling with remote sensing data. *J. Geophys. Res.* **112(D11)** D11101, 1–10.

Speranza, A. (1975) The formation of basic depressions near the Alps. *Ann. Geofis.*, **28**, 177–217.

Starr, J. R. and Browning, K. A. (1972) Observations of lee waves by high-power radar. *Q. J. R. Met. Soc.*, **98**, 73–85.

Steenburgh, W. J., Schultz, D. M. and Colle, B. A. (1998) The structure and evolution of gap outflow over the Gulf of Tehuantepec, Mexico. *Mon. Wea. Rev.*, **126**, 1273–91.

Steinacker, R. (1981) Analysis of the temperature and wind field in the Alpine region. *Geophys. Astrophys. Fluid Dynamics*, **17**, 51–62.

Steinacker, R. (1984) Area-height distribution of a valley in its relation to the valley wind. *Contr. Atmos. Phys.*, **57**, 64–71.

Steinacker, R. (1987) Zur Ursache der Talwindzirkulation. *Wetter u. Leben*, **39**, 61–4.

Steinacker, R., *et al.* (2007) A sinkhole field experiment in the eastern Alps. *Bull. Amer. Met. Soc.*, **88**(5), 7–02–26.

Steiner, M., *et al.* (2003) Airflow within major Alpine valleys under heavy rainfall. *Q. J. R. Met. Soc.*, **123**(558), 411–31.

Stensrud, D. J. (1996) Importance of low-level jets to climate: a review. *J. Climate*, **9**, 1698–1711.

Sterten, A. K. (1965) Alte und Berg- und Talwindstudien. *Carinthia II, Sonderheft*, Vol. 24. Vienna: pp. 186–94.

Sterten, A. K. and Knudsen, J. (1961) *Local and Synoptic Meteorological Investigations of the Mountain and Valley Wind System*. Kjeller-Liuestrom: Forsvarets Forskingsinstitutt, Norwegian Defence Research Establishment Internal Report K-242.

Stewart, J. Q., *et al.* (2002) A climatological study of thermally driven wind systems of the U. S. Intermountain West. *Bull. Amer. Met. Soc.*, **83**(5), 699–708.

Streten, N. A. (1963) Some observations of Antarctic katabatic winds. *Aust. Met. Mag.*, **42**, 1–23.

Streten, N. A. (1968) Some characteristics of strong wind periods in coastal East Antarctica. *J. Appl. Met.*, **7**, 46–52.

Streten, N. A. and Wendler, G. (1968) Some observations of Alaskan glacier winds. *Arctic*, **21**, 98–102.

Streten, N. A., Ishikawa, N. and Wendler, G. (1974) The local wind regime on an Alaskan glacier. *Arch. Met. Geophys. Biokl.*, B, **22**, 337–50.

Stringer, E. T. (1972) *Foundations of Climatology*. San Francisco: W.H. Freeman, p. 407.

Sturman, A. P. (1987) Thermal influences on airflow in mountainous terrain. *Prog. Phys. Geog.*, **11**, 183–206.

Sturman, A. P., Fitzsimmons,. S. J. and Holland, L. M. (1985) Local winds in the Southern Alps, New Zealand. *J. Climate*, **5**, 145–60.

Sutcliffe, R. C. and Forsdyke, A. G. (1950) The theory and use of upper air thickness patterns in forecasting. *Q. J. R. Met. Soc.*, **76**, 189–217.

Suzuki, S. and Yakubi, K. (1956) The air-flow crossing over the mountain range. *Geophys. Mag.*, **27**, 273–91.

Tamiya, H. (1972) Chronology of pressure patterns with bora on the Adriatic coast. *Climat. Notes* (Tokyo), **10**, 52–63.

Tamiya, H. (1975) Bora and oroshi: their synoptic climatological situation in the global scale. *Jap. Progr. Climatol.*, 29–34.

Tang, W. (1976) Theoretical study of cross-valley wind circulation. *Arch. Met. Geophys. Biokl.*, A, **25**, 1–18.

Taylor-Barge, B. (1969) *The Summer Climate of the St. Elias Mountain Region*, Arctic Institute of North America Res. Pap. No. 53, Montreal.

Teixeira, M. A. C., *et al.* (2005) Resonant gravity-wave drag enhancement in linear stratified flow over mountains. *Q. J. R. Met. Soc.*, **131**(609), 1795–814.

Tesche, T. W. and Yocke, M. A. (1978) Numerical modeling of wind fields over mountain regions in California. *Conference on Sierra Nevada Meteorology* (Preprint Volume). Boston, MA: American Meteorological Society, pp. 83–90.

Thompson, B. W. (1986) Small-scale katabatics and cold hollows. *Weather*, **41**, 146–53.

Thorpe, A. J., Volkert, H. and Heimann, D. (1993) Potential vorticity of flow along the Alps. *J. Atmos. Sci.*, **50**, 1573–90.

Thyer, N. H. (1966) A theoretical explanation of mountain and valley winds by a numerical method. *Arch. Met. Geophys. Biokl.* A, **15**, 318–47.

Tibaldi, S., Buzzi, A. and Speranza, A. (1990) Orographic cyclogenesis. In C. W. Newton and E. O. Holapainen (eds), *Extratropical Cyclones: The Erik Palmen Memorial Volume*. Boston, MA: American Meteorological Society, pp. 107–27.

Tollner, H. (1931) Gletscherwinde in den Ostalpen. *Met. Zeit.*, **48**, 414–21.

Tyson, P. D. (1968a) Velocity fluctuations in the mountain wind. *J. Atmos. Sci.*, **25**, 381–4.

Tyson, P. D. (1968b) Nocturnal local winds in a Drakensberg valley. *S. Afr. Geog. J.*, **50**, 15–32.

Tyson, P. D. and Preston-Whyte, R. A. (1972) Observations of regional topographically-induced wind systems in Natal. *J. appl. Met.*, **11**, 643–50.

Urfer-Henneberger, C. (1967) Zeitliche Gesetzmässigkeiten des Berg und Talwindes. *Veröff. Schweiz. Met. Zentralanstalt*, **4**, 245–52.

Urfer-Henneberger, C. (1970) Neurere Beobachtungen über die Entwicklung des Schönwetterwindsystems in einem V-förmigen Alpental (Dischma bei Davos). *Arch. Met. Geophys. Biokl.* B, **18**, 21–42.

Vergeiner, I. (1978) Foehn flow in the Alps – three-dimensional numerical simulations on the small- and meso-scale. *Arbeiten, Zentralanstalt Met. Geodynam.*, **32** (63), 1–37.

Vergeiner, I. and Dreiseitl, E. (1987) Valley winds and slope winds – observations and elementary thoughts. *Met. Atmos. Phys.*, **36**, 264–86.

Voights, H. (1951) Experimentalle Untersuchungen über den Kaltluftfluss in Bodennähe bei verschiedenen Neigungen und verschiedenen Hindernissen. *Met. Rdsch.*, **4**, 185–8.

Vorontsov, P. A. (1958) Nekotorie voprosi aerologicheskikh issledovanii po granichnogo sloia atmosferi (Some questions on aerological observations of the atmospheric boundary layer). *Sovremenie Problemy Meteorologii Prizemnogo Sloia Vozdukha: Sbornik Statei.* Leningrad: Glav. Geofiz Observatory, pp. 157–79.

Vosper, S. B. (2005) Inversion effects on lee waves. *Q. J. R. Met. Soc.*, **130**(600), 1733–48.

Wagner, A. (1938) Theorie und Beobachtungen der periodischen Gebirgswinde. *Gerlands Beitr. Geophys.*, 52, 408–49 (translated as, Theory and observation of periodic mountain winds. In C. D. Whiteman and E. Dreiseitl (eds), (1984) *Alpine Meteorology*, PNL-5141, ASCOT-84-3. Richland, WA: Baltelle, Pacific Northwest Laboratory). pp. 11–43.

Walker, J. M. (1967) Subterranean isobars. *Weather*, **22**, 296–7.

Wallace, J. M., Tibaldi, S. and Simmons, A. J. (1983) Reduction of systematic forecast errors in the ECMWF model through the introduction of an envelope orography. *Q. J. R. Met. Soc.*, **109**, 683–717.

Wallington, C. E. (1961) Airflow over broad mountain ranges: a study of five flights across the Welsh mountains, *Met. Mag.*, **90**, 213–22.

Wallington, C. E. (1970) A computing aid to studies of airflows over mountains. *Met Mag.*, **99**, 157–65.

Walsh, K. (1994) On the influence of the Andes on the general circulation of the southern hemisphere. *J. Climate*, **7**(6), 1019–25

Washington, W. M. and Parkinson, C. L. (2005) *An Introduction to Three-Dimensional Climate Modeling*, 2nd edition. Sausalito, CA: University Science Books, 353 pp.

Watterson, I. G. and James, I. N. (1992) Baroclinic waves propagating from a high-latitude source. *Q. J. R. Met. Soc.*, **118**, 23–50.

Weissmann, M., *et al.* (2005) The Alpine mountain-plain circulation: Airborne Doppler measurements and numerical simulation. *Mon. Wea. Rev.*, **133**(11), 3095–109.

Welch, W. P., *et al.* (2001) The large-scale effects of flow over periodic mesoscale topography. *J. Atmos. Sci.*, **58**, 1477–92.

Wells, H., Webster, S. and Brown, A. (2005) The effect of rotation on the pressure drag force produced by flow around a long ridge. *Q. J. R. Met. Soc.*, **131**(608), 1321–38.

Wenger, R. (1923) Zur Theorie der Berg-und Thalwinde. *Zeit Met.*, **40**, 193–204.

Whiteman, C. D. (1982) Breakup of temperature inversions in deep mountain valleys. Part I. Observations, *J. Appl. Met.*, **21**, 270–89.

Whiteman, C. D. (1990) Observations of thermally developed wind systems in mountainous terrain. In W. Blumen (ed.), *Atmospheric Processes over Complex Terrain*, Meteorological Monograph 23(45). Boston, MA: American Meteorological Society. pp. 5–42.

Whiteman, C. D. and McKee, T. B. (1977) Observations of vertical atmospheric structure in a deep mountain valley. *Arch. Met. Geophys. Biokl.*, A, **26**, 39–50.

Whiteman, C. D. and Whiteman, J. G. (1974) *A Historical Climatology of Damaging Downslope Windstorms at Boulder, Colorado*, Technical Report ERL-336-APCL 35. Boulder, CO: NOAA.

Whiteman, C. D., Bian, X.-D. and Sutherland, J. L. (1999a) Wintertime surface wind patterns in the Colorado River valley. *J. Appl. Met.*, **38**(8), 1118–30.

Whiteman, C. D., Bian, X. and Zhong, S. (1999b) Wintertime evolution of the temperature inversion in the Colorado Plateau Basin. *J. Appl. Met. Climatol.*, **38**, 1103–17.

Whiteman, C. D., *et al.* (2000) Boundary layer evolution and regional-scale diurnal circulations over the Mexico Basin and Mexican Plateau. *J. Geophys. Res.*, **105(D8)**, 10, 81–102.

Whiteman, C. D., *et al.* (2004a) Inversion breakup in small Rocky Mountain and Alpine basins. *J. appl. Met.*, **43**(8), 1069–82.

Whiteman, C. D., *et al.* (2004b) Minimum temperatures, diurnal temperature ranges, and temperature inversions in limestone sinkholes of different sizes and shapes. *J. Appl. Met.*, **43**(9), 1224–36.

Whiteman, C. D., *et al.* (2004c) Comparison of vertical sounding and sidewall air temperature measurements in a small alpine basin. *J. appl. Met.*, **43**(11), 1635–47.

Whiteman, C. D., De Wekker, S. F. J. and Haiden, T. (2007) Effect of dewfall and frostfall on nighttime cooling in a small, closed basin. *J. Appl. Met. Climatol.*, **46**, 3–13.

Williamson, D. L. and Laprise, R. (2000) Numerical approximations for global atmospheric general circulation models. In P. Mote and A. O'Neill (eds), *Numerical Modeling of the Global Atmosphere in the Climate System*. Dordrecht: Kluwer, pp. 127–219.

Wilson, H. P. (1968) Stability waves, Meteorological Branch Technical Memorandum 703. Toronto, Canada: Department of Transport.

Wilson, H. P. (1974) A note on meso-scale barrier to surface airflow. *Atmosphere*, **12**, 118–20.

Wippermann, F. (1984) Airflow over and in broad valleys: channelling and counter-current. *Contrib. Atmos. Phys.*, **57**, 92–105.

Wolyn, P. G. and McKee, T. B. (1994) The mountain-plains circulation east of a 2-km high north-south barrier. *Mon. Wea. Rev.*, **122**, 1490–508.

Xue, M., *et al.* (2001) The Advanced Regional Prediction System (ARPS) - A multi-scale nonhydrostatic atmospheric simulation and prediction tool. Part II: Model physics and applications. *Met. Atmos. Phys.*, **71**, 143–65.

Yabuki, K. and Suzuki, S. (1967) A study on the airflow over mountain. *Bull. Univ. Osaka Prefecture*, **B**, 19.

Ye, J. S., *et al.* (1990) On the impact of atmospheric thermal stability on the characteristics of nocturnal downslope flow. *Boundary-Layer Met.*, **51**, 77–97.

Yoshimura, M. (1976) Synoptic and aerological climatology of the bora day. In M. M. Yoshino (ed.), *Local Wind Bora*. Tokyo: University of Tokyo Press, pp. 99–111.

Yoshino, M. M. (1957) The structure of surface winds over a small valley. *J. Met. Soc. Japan*, **35**, 184–95.

Yoshino, M. M. (1971) Die Bora in Yugoslawien. Eine synoptisch-klimatologische Betrachtung. *Ann. Met.*, N.F., **5**, 117–21.

Yoshino, M. M. (1972) An annotated bibliography on bora. *Climat. Notes*, **10**, 1–22.

Yoshino, M. M. (1975) *Climate in a Small Area. An Introduction to Local Meteorology*. Tokyo: University of Tokyo Press, 549 pp.

Yoshino, M. M. (ed.) (1976) *Local Wind Bora*. Tokyo: University of Tokyo Press.

Yoshino, M. M., *et al.* (1976) Bora regions as revealed by wind-shaped trees on the Adriatic Coast. In M. M. Yoshino (ed.), *Local Wind Bora*. Tokyo: University of Tokyo Press, pp. 59–71.

Young, G. R. and Zawislak, J. (2006) An observational study of vortex spacing in island wake vortex streets. *Mon. Wea. Rev.* **134**, 2285–94.

Zaengl, G. (2003) Deep and shallow south foehn in the region of Innsbruck. *Meteorol. Atmos. Phys.*, **83** (3–4), 237–61.

Zängl, G. (2004) A reexamination of the valley wind system in the alpine Inn valley with numerical simulations. *Meteorol. Atmos. Phys.*, **87** (4), 241–56.

Zängl, G. (2005a) Formation of extreme cold air pools in elevated sinkholes: An idealized numerical process study. *Mon. Wea, Rev.*, **133**(4), 925–41.

Zängl, G. (2005b) Dynamical aspects of winter-time cold pools in an Alpine valley system. *Mon. Wea. Rev.*, **133**(9), 2721–40.

Zängl, G. (2005c) Wintertime cold air pools in the Bavarian Danube valley basin: Data analysis and idealized numerical simulations. *J. Appl. Met.*, **44**(12), 1950–71.

Zängl, G. and Egger, J. (2005) Diurnal circulation of the Bolivian Altiplano. Part II. Theoretical aspects. *Mon. Wea. Rev.*, **133**(12), 3624–43.

Zängl, G., Egger, J. and Wirth, V. (2001) Diurnal winds in the Himalayan Kali Gandaki valley. Part II. Modeling. *Mon. Wea. Rev.*, **129**(5), 1062–80.

Zimmerman, L. I. (1969) Atmospheric wake phenomena near the Canary Islands. *J. Appl. Met.*, **8**, 896–907.

Zipser, E. J. and Bedard, A. J. (1982) Front Range windstorms revisited. *Weatherwise*, **35**, 32–5.

4 CLIMATIC CHARACTERISTICS OF MOUNTAINS

The basic factors and processes affecting mountain climate have been discussed in Chapters 2 and 3. When climatic elements such as temperature or precipitation are considered, their temporal and spatial characteristics in mountain areas are inevitably determined by the total complex of these factors – latitude, continentality, altitude and topography – operating together. In this chapter, therefore, some general climatic characteristics of mountain areas are examined for individual climatic elements. We begin by considering energy budgets and slope temperature profiles. This is followed by a discussion of cloudiness, precipitation, other hydrometeors, and evaporation. The ways in which altitudinal and topographic effects, in particular, interact to create orographic patterns in the spatial and temporal distribution of each climatic element are illustrated.

4.1 ENERGY BUDGETS

It was noted in Chapter 2 that mountain sites were of special importance to early research on solar radiation, but there has been a general lack of modern radiation and energy budget studies in the mountains. An adequate level of information on the spatial and temporal distribution of radiation exists only for the European Alps. This material provided the basis for the generalizations on altitudinal effects presented in Chapter 2 (pp. 34–51) and all that can be usefully added here is to illustrate the types of work carried out in a few other mountain areas and some of the findings.

Radiation studies in the Alps show that, up to about 3 km, global solar radiation increases by about 7–10 percent km^{-1} under clear skies and 9–11 percent km^{-1} under overcast, with the most rapid increase occurring in the lower levels, due to the vertical distribution of water vapor (p. 32). Data in the Valais of the southwestern Alps for global solar radiation, show a small increase of only 2.6 percent km^{-1} between 2 and 3.5 km in summer, whereas downward infrared radiation decreases by 10 percent km^{-1} (Müller, 1985).

Cloud conditions significantly affect the theoretical rates of altitudinal increase, particularly since cloud cover may be more frequent on mountain slopes. This is the case on the east slope of the Front Range, Colorado, where there is no altitudinal increase on an annual basis (Barry, 1973). However, in individual months there may be an increase or decrease with height, depending on the frequency of cloud cover. This is apparent in Table 4.1. Concurrent cloud observations are not

Table 4.1 **Daily averages of global solar radiation on the east slope of the Front Range, Colorado (W m^{-2}).**

	Altitude (m)				
	1590	2591	3022	3480	3743
	Station				
	Boulder	Sugarloaf	Como	Niwot Ridge (tree line)	Niwot Ridge
	Distance east of Divide (km)[a]				
Period	37	22.5	9.7	4.5	2.6
1965[b]					
January–February	–	98	117	–	112
March–May	–	184	210	–	221
June–September	–	229	185	–	199
October–December	–	119	111	–	103
1977[c]					
January–February	96	–	–	98	–
March–May	220	–	–	222	–
June	262	–	–	248	–

[a] The Continental Divide in this area is approximately 4000 m.
[b] Bimetallic actinographs, calibrated against a 50 junction Eppley pyranometer.
[c] Eppley pyranometers.
Source: after Greenland (1978).

available to evaluate the specific cloud–radiation relationships, but Greenland (1978) illustrates the magnitude of probable differences due to cloud cover by comparison of two synoptic regimes. During 16 days of upslope flow in 1977, a daily average of 142 W m^{-2} was recorded at 3480 m, compared with 105 W m^{-2} in Boulder, whereas for the same number of days of downslope flow the averages were 165 W m^{-2} and 188 W m^{-2}, respectively. Upslope weather, with more cloud at low elevations on the east slope of the Front Range, is common in spring, while downslope weather, which brings cloud mainly to the high elevations, is characteristic of winter months. In summer, cumuliform clouds predominate, with greater development occurring earlier in the day over the mountains. The radiation data in Table 4.1 illustrate some of these seasonal differences.

At high elevation stations, 5000 m and above, cloud layers are frequently thin and have high transmissivity. Thus, for Mt. Logan (5365 m), Yukon, the difference between clear and cloudy conditions (which averaged about 7/10 cover) was only 18 percent in July 1970 (Brazel and Marcus, 1979). Data for July 1968–70 show that, whereas solar radiation at Kluane Lake (787 m) averaged only 43 percent of possible, the figure was 83 percent for Mt. Logan (Marcus and LaBelle, 1970; Marcus and Brazel, 1974). The difference implies an average altitudinal increase of

8.7 percent km^{-1}; the rate is greatest at low levels decreasing to about 6 percent km^{-1} above 2650 m.

Complete energy budget studies in mountain areas are rare and there are very few measurements in the absence of snow cover. In the equatorial Andes, Korff (1971) showed that net radiation for 12 days in July on Cotapaxi at 3570 m, with a surface albedo of 0.22, averaged 60 percent (53 percent on clear days) of the incoming shortwave. These figures are in line with data given by Voloshina (1966) for the Caucasus at 3000–3500 m (see Figure 2.13). At 4750 m on Mt. Everest (28° N) the net radiation on 9 days in April 1963 represented 55 percent of the incoming shortwave with a surface albedo of 0.16 (Kraus, 1971). In Colorado, data were collected in summers 1984–5 during the ROMPEX Program (Bossert and Cotton, 1994). Figure 4.1 compares data for a week of fine weather at three high elevation sites west of the Continental Divide. Mt. Werner is about 100 km northeast of Flat Tops and Crested Butte is about 135 km to the south-southeast of Flat Tops. The sites show a high degree of consistency in net radiation values and the partitioning of the three heat flux terms. The sensible heat flux (H) tracks the net radiation curve while the latent heat (LE) has an early morning maximum.

Energy budget measurements have been made in summer over a number of surface types in the Saddle area of Niwot Ridge (40.1° N, 105.6° W, 3506–3568 m) by Greenland (1991, 1993). The albedo of alpine tundra surfaces shows considerable temporal and spatial variability – of the order of 25 percent of the mean values for densely vegetated meadow and shrub tundra (0.17–0.18), sparsely vegetated fellfield (0.27) and krummholz (0.15) (Goodin and Isard, 1989). Temporal variations are caused particularly by varying moisture conditions; and spatial variations by the heterogeneous surfaces. Spatial variability can be modeled in terms of canopy structure (foliage inclination, canopy strata and plant area), as illustrated for light extinction in alpine plant communities by Tappenier and Cernusca (1989). However, albedo differences in Greenland's study were minor. He points out that surface heat budgets can vary as much between different tundra surfaces (dry fell field, dry meadow, wet meadow, shrub tundra and snow bed) at a given time as between similar surfaces in different years with different moisture budgets. Spatial variations in vegetation seem to be largely controlled by topoclimate, particularly soil moisture and the distribution of snow beds as determined by the interaction of surface winds and small-scale topography (Komarkova and Webber, 1978). Estimated Bowen ratios ($\beta = H/LE$) for mid-summer ranged from 0.84 for moist shrub tundra to 0.51 for moist meadow (Greenland, 1991; corrected Table 5) The corresponding values of sensible and latent heat ranged between -5.1 and -3.8 MJ m^{-2} day^{-1}, and -6.1 and -7.3 MJ m^{-2} day^{-1}, respectively.

A major component of the energy budget in snow-covered areas is the summer snowmelt. Snowmelt rates are of particular significance for forecasting runoff from alpine basins. In the early melt phase, melt water is retained in the snow until the free (liquid) water content of the pack (about 2 percent by volume) is attained. Nocturnal refreezing may also take place at this stage (Martinec, 1989).

Fig. 4.1   **The diurnal variation of surface energy fluxes averaged for 23–31 August 1985 at Mt. Werner (40.5° N, 106.7° W, 3250 m), Flat Tops (40.0° N, 107.3° W, 3441 m) and Crested Butte (38.9° N, 107.9° W, 3354 m), Colorado (adapted from Bossert and Cotton, 1994).**
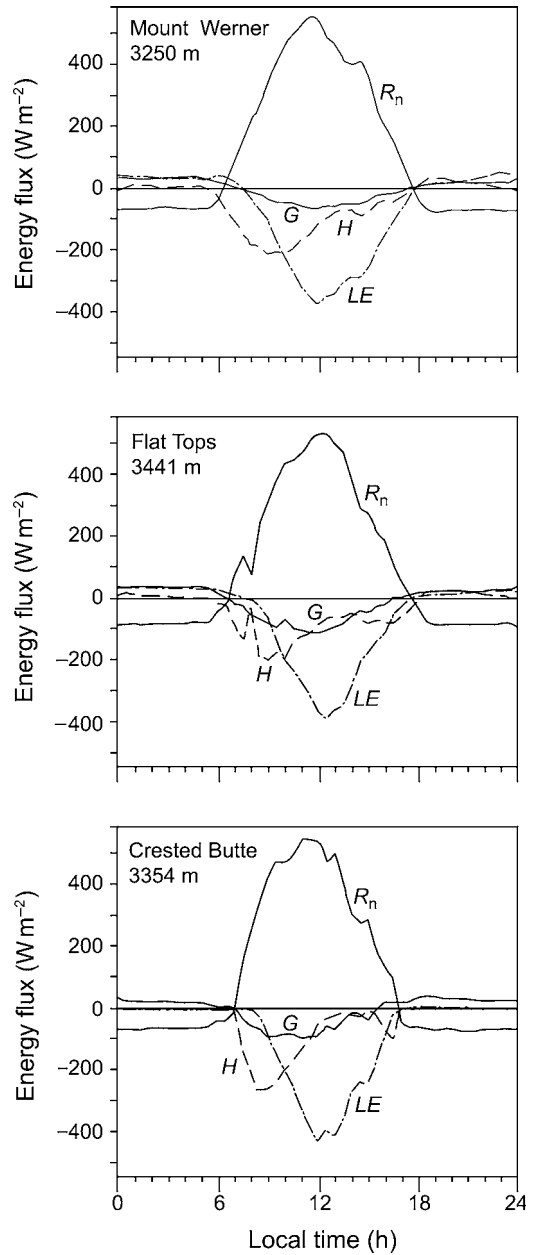
Measurements for a complete melt season (9 May–15 July 1985) made at the Weissflujoch, Switzerland (2540 m), indicate snowmelt of about 30 cm water in both May and June and 40 cm in July. Martinec shows that net radiation accounts for 60 percent of melt, sensible and latent heat for 40 percent. Evaporation losses from the snow cover were estimated at 4 percent. Energy budgets on Niwot Ridge

during snowmelt have been determined by Cline (1997). For the period 25 April–6 June 1994, the net energy gain was 185 MJ m^{-2}, with net radiation accounting for 75 percent and sensible heat 25 percent of the snowmelt energy requirement.

Most work has been performed on glacier surfaces during the summer ablation season. Table 4.2 summarizes some of the available literature results, but these are insufficient to form a reliable basis for general conclusions. Data for glacier surfaces in the Caucasus show a distinct decrease in the ratio of net radiation to incoming solar radiation with altitude (Figure 2.13, p. 51). In fact, as the Quelccaya and Mt. Logan data in Table 4.2 show, over snow surfaces at high altitudes net radiation is frequently negative. Voloshina (1966) discusses the difference in net radiation over snow/ice and snow-free surfaces. For 20 days at 3250 m on Karachaul Glacier (Mt. Elbrus), the net radiation is 119 W m^{-2} on bare ground (albedo of 0.10) compared with 111 W m^{-2} on ice (albedo of 0.37) only 200 m away. While the absorbed solar radiation is much greater on the bare ground, the effective back-radiation is at least two times greater than over the ice, leading to the near equality.

One of the most extensive series of alpine measurements is that of LeDrew (1975; LeDrew and Weller 1978). Averages for the growing season at 3650 m on Niwot Ridge, Colorado, show large sensible heat fluxes due to the generally strong advection of cool westerly airstreams. The Bowen ratio ranges between 4 and 6 during daylight hours, indicating much higher moisture stresses than implied by the mean value in Table 4.2. Surface canopy temperatures on 41 days around solar noon averaged 28 °C compared with 14 °C at screen level (1.5 m). Measurements at Mt. Werner, Colorado, during August 1984 show a similar range to those of LeDrew for Niwot Ridge (Sheaffer and Reiter, 1987) although the ground heat flux is much smaller and the Bowen ratio at that site averaged only 0.6.

In the Austrian Alps, Rott (1979) provides comparative data at two elevations. Figure 4.2 illustrates his results on a clear day in July. The solar incoming and net radiation values are, respectively, about 10 percent and 15 percent greater at Hohe Mut (2560 m) than at Obergürgl (1960 m) for cloudless conditions (Table 4.2). This is attributed to greater horizon screening at Obergürgl, as well as to the larger atmospheric extinction effect. Latent heat accounts for a larger fraction of the available energy at the lower station, over a meadow, than over alpine grass heath at the higher station. During night-time hours, under cloudless skies, the negative radiation balance averaging about 70–75 W m^{-2} is largely offset by sensible heat flux from the air at Obergürgl, but by both ground heat flux and sensible heat flux at Hohe Mut (Rott, 1979). For the Dischma Valley, near Davos, the energy balance has been determined using observations at three stations, measurements of surface temperature from an airborne infrared thermometer, a map of the vegetation and a digital elevation model (Hennemuth and Köhler, 1984). Net radiation is shown to be determined mainly by topographic exposure and latent heat flux by vegetation cover.

In view of the paucity of observational data for mountain regions, several sources have provided calculations of net radiation and energy fluxes. Figure 4.3 illustrates calculated clear-sky net radiation on north- and south-facing slopes at

Table 4.2 Selected energy budget data.

Location	Altitude (m)	Month	S (W m^{-2})	α	R_n (W m^{-2})	H (% of R_n)	LE (% of R_n)	G (% of R_n)	References
Mt. Everest (28° N)	4750	April	291	0.16	161	60	36	4	Kraus (1971)
Niwot Ridge (39° N)	3650	July	252	0.17	144	50	38	12	LeDrew and Weller (1978)
Turkestan Mts (41° N)	3150	September	–	0.14	169	71	14	14	Aizenshtat (1962)
Turkestan Mts (31° south slope)	3150	September	–	0.20	70	59	28	13	Aizenshtat (1962)
Turkestan Mts (31° south slope)	3150	September	–	0.15	206	71	18	11	Aizenshtat (1962)
Austrian Alps (47° N)									
Hohe Mut	2560	July	367	0.23	183	28	64	8	Rott (1979)
Obergurgl	1960	July	331	0.20	157	9	89	2	Rott (1979)
Quelccaya Ice Cap (14° S)	5645	July	244	0.80	−2	–	–	–	Hastenrath (1978)
Mount Logan (61° N) (snow surface)	5365	July	373	0.84	−57[a]	10	90[b]	~0	Brazel and Marcus (1979)
Mount Kilimanjaro (3° S)	5794	12-mo	327	0.74	13	92	−54[d]	46	Mölg and Hardy (2004)
McCall Glacier (69° N)									
ice surface	1730	July	226	0.33	72	(78)[c]	7	13	Wendler and Ishikawa (1973)
moraine	1740	July	226	0.19	71	49	43	8	Wendler and Ishikawa (1973)
snow surface	2140	July	226	0.59	43	(59)[c]	63	1	Wendler and Ishikawa (1973)

[a] H and LE here are towards the surface.
[b] Includes sublimation.
[c] H here is towards the surface.
[d] LE is here towards the surface.
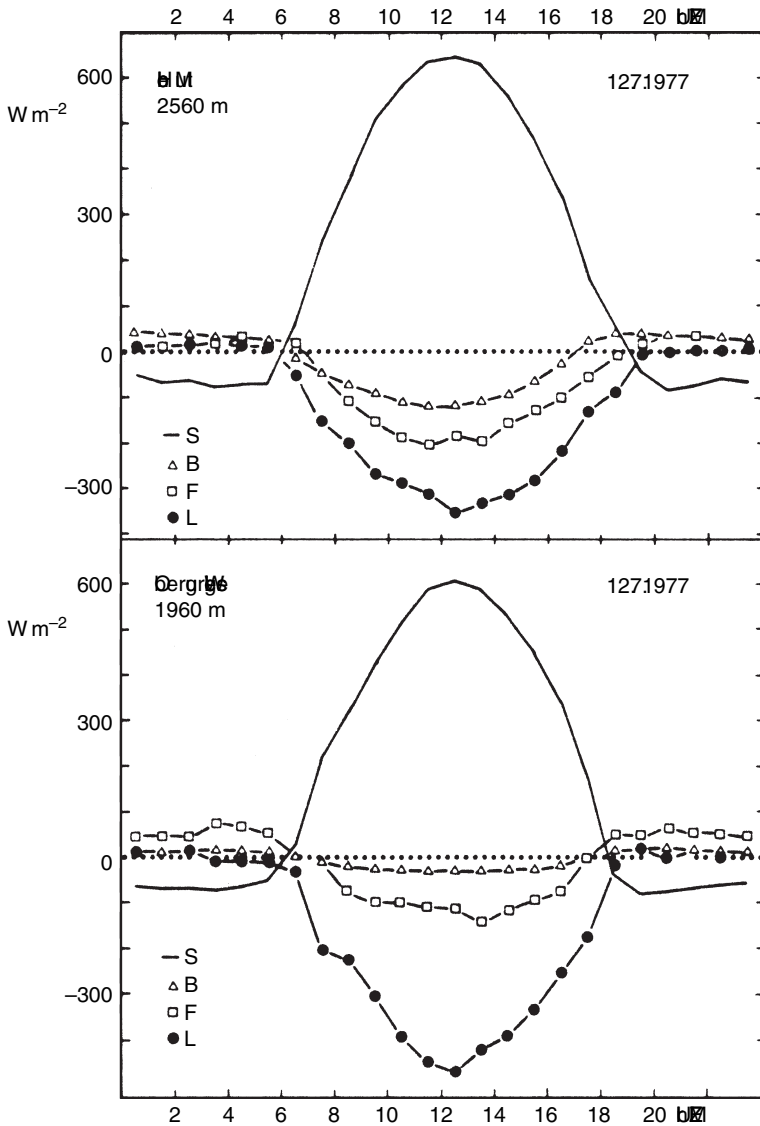
Fig. 4.2   **Hourly values of energy budget components in the Austrian Tyrol, 12 July 1977, at Obergürgl-Wiese (1960 m) and Hohe Mut (2560 m) (from Rott, 1979).**

400 and 3600 m in the Caucasus, based on temperature and albedo data at Tbilisi and Kasbegi, respectively, and equations of Kondratyev and Manolova (Borzenkova, 1967). Mean albedos are 17–21 percent at Tbilisi and range from 75 percent in March–April to 20 percent in August at Kasbegi, due to snow cover (Borzenkova, 1965). On an annual basis, net radiation decreases 15–16 percent km^{-1} for both cloudless and overcast skies. In June, however, there is a decrease of 7 percent km^{-1} for cloudless skies, but an increase of almost 4 percent km^{-1} with overcast

Fig. 4.3   **Calculated net radiation on north- and south-facing slopes of 30° in the Caucasus at 400 m and 3600 m (based on Borzenkova, 1967).**
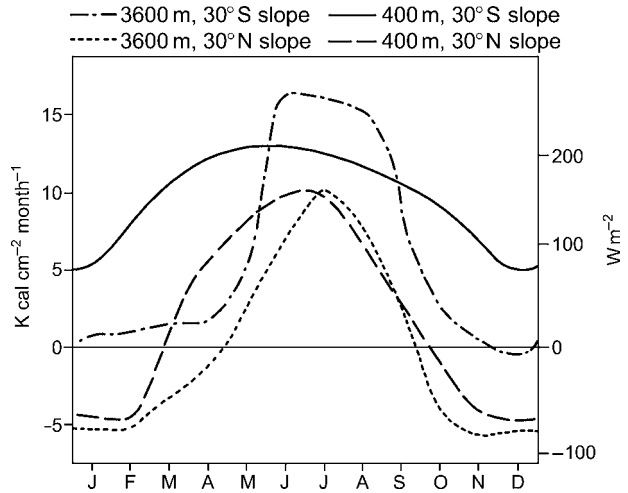
conditions. This may not be wholly real since the calculations assume low cloud layers whereas the cloud at 3600 m is certainly less opaque than at low levels. The ASRB observations for the Alps show a small decrease of net radiation with height in summer and winter up to 3 km and a slight increase above (Figure 2.8).

For the Caucasus, Borzenkova (1965) also provides calculated annual values of turbulent heat fluxes based on the methods of M. Budyko (Table 4.3). In both the Greater Caucasus and the Armyanski Mountains, the sensible heat flux decreases steadily with elevation, whereas the latent heat flux reaches a maximum at 2500–3000 m. The sensible heat loss is slightly greater in the drier, more southerly range.

Similar estimates on a monthly basis have been prepared for Croatia (Plesko and Sinik, 1978) also using equations of M. Budyko. The stations range from 120–1594 m, at approximately 45°–46° N. Figure 4.4 shows the seasonal variation with height of R_n, H and LE. There is virtually no height variation for any of the components in winter. In summer, on the other hand, R_n is more or less constant to about 700 m and then decreases slightly above that height. LE increases likewise, perhaps due to higher rainfall, and then decreases above about 800 m possibly as a result of increased infrared radiative cooling and lower surface temperatures, according to Plesko and Sinik. The sensible heat flux is slightly negative in winter, in association with winter temperature inversions. In summer, H increases with height, apparently in response to increased advection effects and a greater air–surface temperature gradient. This pattern is the opposite of that calculated by Borzenkova for the Caucasus area. The results for Croatia seem consistent, although over snow cover, of course, H will be zero or negative.

Recent studies in the Alps have addressed the issue of energy budget closure (Rotach et al., 2004). In a study for the Riviera valley, near Lake Maggiore they show that there is a consistent gap between measured net radiation and the heat flux

Table 4.3 Annual turbulent fluxes in the Caucasus (W m^{-2}).

	Greater Caucasus			Armyanski Mts		
	Sensible heat	Latent heat	Bowen ratio	Sensible heat	Latent heat	Bowen ratio
Surface	44	27	1.65	–	–	–
1 km	29	44	0.67	32	24	1.33
2	19	55	0.34	23	28	0.81
3	9	44	0.21	13	35	0.38
3.5	4	28	0.14	–	–	–

Source: after Borzenkova (1965).
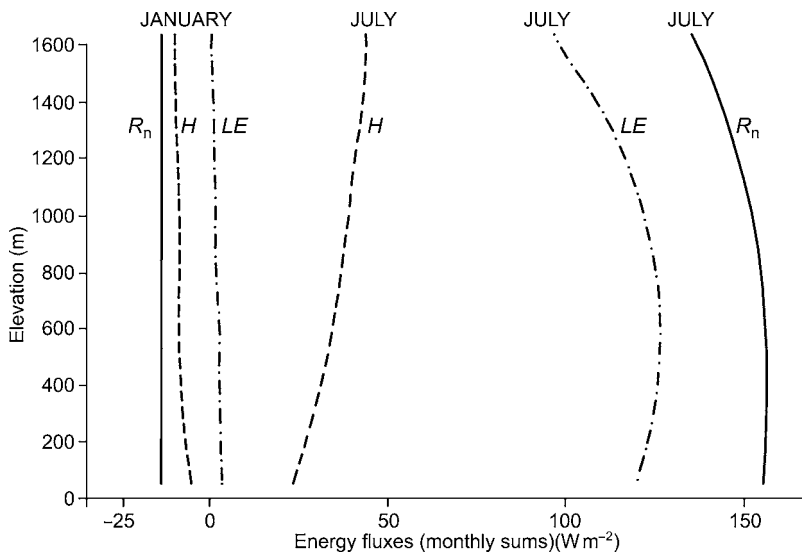
Fig. 4.4 Seasonal variations of net radiation and turbulent heat fluxes with altitude in Croatia (after Pleško and Šinik, 1978).

terms. This implies that divergence of the turbulent fluxes and vertical advection between the surface and the measurement height need to be taken into account. On a diurnal basis both soil heat storage and especially vertical advection of sensible and latent heat, need to be incorporated in the calculations, otherwise closure of the energy budget is not achieved.

4.2 TEMPERATURE

4.2.1 Slope profile

Temperature is undoubtedly the single most important aspect of mountain climates. It has been widely observed in most mountain areas of the world and there are many

statistical studies dealing with its altitudinal variation. This variation is a particular problem for climatic atlases, due to the sharp temperature gradients over short distances and their seasonal variability (Steinhauser, 1967). Several investigations of mountain temperatures use regression analysis to relate temperatures to altitude and to separate the effects of slope-aspect and inversions, for example, Douguédroit and de Saintignon (1970) and de Saintignon (1976). Pielke and Mehring (1977) use linear regression analysis of mean monthly temperatures as a function of elevation in an attempt to improve the spatial representation of temperature for an area in north-western Virginia. They show that the correlations are greatest ($r = -0.95$) in summer, as is commonly the case in middle latitudes. Inversions at low levels in winter introduce greater variability and better estimates may be obtained by fitting polynomial functions, or alternatively by the use of potential temperatures (Hennessy, 1979). Numerous regression equations have been worked out in a similar fashion for the West Carpathian Mountains (Hess et al., 1975) in order to produce topoclimatic maps. For this purpose, separate regressions are used according to the slope profile, as described in Chapter 2, pp. 104. Remarkably, there have been few attempts to describe mountain temperature variations with any more general statistical model.

Seasonal lapse rates determined from high resolution terrain-interpolated station data in the Canadian Rockies by Shea et al. (2004) are as follows:

MAM	JJA	SO	NDJFM
-6.0	-5.3	-4.6	$-4.9 \, °C \, km^{-1}$

It is not uncommon for lapse rates to be steepest in spring when there are more frequent unstable air masses. An autumn minimum, rather than a winter one when valley inversions are common, is perhaps unusual.

Although altitudinal and aspect effects determine the *mean* seasonal values of temperature (and other variables) in a mountainous area, there is some indication that short-term deviations, associated with synoptic weather events, are not so influenced. Furman (1978) shows that daily maximum temperatures (T_1) in summer at stations on a forested ridge in Idaho can be described by a second-order autoregressive model $T_i = a_1 \, T_{i-1} + a_2 \, T_{i-2}$. For seven sites over a 1000 m height range, with north and south aspects, a_1 was between 0.795 and 0.980, indicating a strong dependence on the previous day's value (T_{i-1}), whereas a_2 was between -0.004 and -0.176. The differences in coefficients between sites were shown to be a result of sampling variations, and the probability distribution of the residuals also showed no effects of location. It remains to be determined how widely these results are applicable in situations where the mountain scale has a greater range. Also, whereas daily maxima bear a close relationship to global radiation totals, minimum temperatures are much more site-dependent, especially with respect to cold air drainage.

The vertical lapse rate on a mountain slope may bear a close relationship to that in the free air or may be almost independent. Free air conditions dominate those

at the surface when winds are strong and the flow is more or less perpendicular to the barrier. However, in slack pressure gradients allowing cold air drainage and under high-pressure situations with large-scale subsidence, the local topography becomes important and often temperature inversions develop that can be more persistent than those over adjacent lowlands.

Observed screen temperatures on slopes can be adjusted to estimate "free air" temperature in a valley atmosphere if supplementary information is available. Dreiseitl (1988) uses a 4-year record of hourly readings at six stations on the north side of the Inn Valley, Austria, to develop correction functions for each station, between 580 and 2260 m altitude, that take account of day length, weather type, and cloudiness. The lower slopes are several degrees warmer than the valley air in the afternoon and slightly cooler in the morning. The seasonal values of corrected daily temperature range agree well with those derived from diurnal pressure fluctuations at Innsbruck and the summit station. In the case of small alpine basins (frost hollows), Whiteman *et al.* (2004) show that vertical soundings and sidewall air temperature measurements are in close agreement.

Most studies of slope lapse rates rely on data from a summit and a base station, although in a few cases attempts have been made to provide detailed transects. C. L. Wragge and assistants, for example, made daily ascents of Ben Nevis in the summers of 1882 and 1883, taking observations at eight slope stations (Buchan, 1890). However, such transects suffer from the problem of time differences between the observations, requiring averages to be taken over the ascent and descent.

Wagner (1930) provided a specimen continuous transect on the Nordkette, north of Innsbruck, by use of the cable car. Temperatures were determined every five seconds with an aspirated thermometer suspended from the car. Figure 4.5
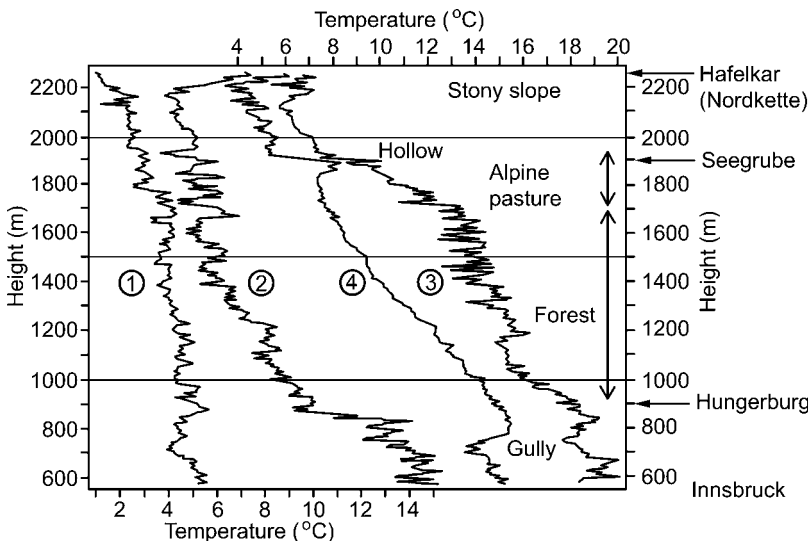
Fig. 4.5   **Slope temperatures on the Nordkette, Innsbruck, 2 April 1930 (after Wagner, 1930).**

shows four profiles: the first and third upward, between 0800 and 0850 h and between 1500 and 1550 h, the second and fourth downward, between 1015 and 1100 h and between 1805 and 1835 h. The morning was mainly overcast, clearing completely before noon, with cumulus development in the afternoon and a clear sky again by evening. The morning profile shows only a 4 °C change over the 1700 m interval, but by mid-morning there is a marked warming on the steeper south-facing slopes below the Hafelkar, and at lower levels below the Hungerburg (although here the thermometer was only about 1 m above the track). There is also a considerable increase in micro-scale irregularity between 0830 and 1030 h and this feature is even more pronounced in the afternoon, when it is concentrated in the forested section (1300–1700 m). Wagner suggests that this irregular pattern is due to the canopy acting as a primary heating surface. The sharp cooling just above Seegrube, evident in plots 3 and 4, identifies a hollow where the cable car is up to 70 m above ground. The effect of a shady gully is also evident just below 750 m (except at mid-morning). The final transect, when the whole slope was in shadow, shows a markedly smooth profile. The relative warmth of the upper forest section has now gone and the mean temperature gradient between 900 and 2200 m is 0.85 °C/100 m, almost adiabatic. Another transect by Wagner on 23 November 1929 illustrated the descent of a föhn layer over a surface-based inversion. The latter persisted through a layer only some 60 m deep for 8 h during the day before the föhn reached the valley floor.

In work on the Zugspitze, Reiter and Sladkovic (1970) adopted a similar approach. Lapse rates determined from the cable car are compared with the exchange coefficient for eddy diffusivity based on radon (RaB) measurements. For days without fog or precipitation and ≤ 5/10 high cloud, they find correlations of about –0.7 under all conditions in the layer between 1800 and 3000 m. Similar values were also obtained under unstable conditions between 700 and 1800 m, but there is no correlation between lapse rate and exchange coefficient in this layer during stable conditions. Their analysis provides information that is of value in assessing the potential for aerosol dispersion in mountain environments (see Chapter 6, pp. 460–8).

Such case studies provide useful insight into small-scale spatial and temporal variability and illustrate the need for care in siting stations and in interpreting slope lapse rates based on data at only a few stations at fixed times. Aerial surveys using a radiation thermometer (Fujita *et al.*, 1968) offer another means of determining "apparent" (radiative) temperatures over mountain slopes, but such data are expensive to acquire and are not readily converted to absolute values. Furthermore, the spot size viewed by the instrument is likely to be of the order of several hundred meters across and vary irregularly as the aircraft crosses the terrain. Nevertheless, the work of Fujita *et al.* over Mt. Fuji provided the interesting observation that solar heating of rocky slopes can cause nearly identical temperatures at the ground surface with negligible altitudinal differences (Figure 4.6). Independent slope measurements under similar conditions showed that, in contrast to the rapid surface heating, the rise in screen temperatures was very gradual.
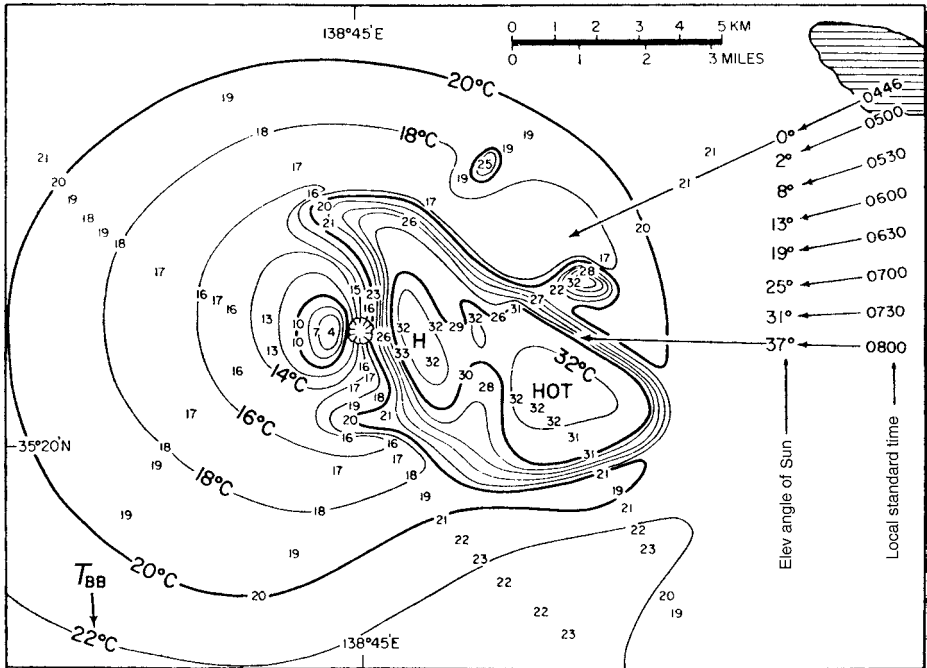
Fig. 4.6 Equivalent black-body temperatures (T_{BB}) measured by radiation thermometer from an aircraft over Mt. Fuji, 0743–0756 JGT, 28 July 1967. Solar altitude and azimuth is shown since sunrise (from Fujita *et al.*, 1968).

A technique for predicting surface temperature in mountainous terrain using 12 and 24-h regional forecast data from the US National Weather Service Limited-Area Fine Mesh (LFM) model has been developed by McCutchan (1976). Diurnal temperature variation (T) is represented by the first two harmonic terms:

$$T_t = A\left[\left(a_0 + a_1\cos\frac{\pi t}{12} + b_1\sin\frac{\pi t}{12} + a_2\cos\frac{\pi t}{6} + b_2\sin\frac{\pi t}{6}\right) - B_t\right]$$

where A is an aspect pararameter relating to solar radiation; a_0 is the mean temperature; a_1, b_1 are coefficients of the first harmonic; a_2, b_2 are coefficients of the second harmonic; and B_t is a bias condition function which depends on time, synoptic weather category, and elevation.

Five synoptic weather categories relating to temperature and moisture conditions were determined separately by discriminant analysis. The model first calculates each of the Fourier coefficients independently using stepwise regression analysis based on observed temperature, dew point and wind speed at the surface, 850 mb chart data, weather class, the sine and cosine of the Julian day, and 12-h and 24-h predictions from the LFM. On this basis, McCutchan developed surface temperature predictions up to 36 h in advance for the San Bernardino Mountains, southern California. In areas where there are less detailed forecasts, other techniques

would have to be evolved, but, in any case, a key factor would be the siting of suitable reference stations.

4.2.2   Thermal belts and cold air lakes

The effect of nocturnal radiation on downslope air drainage has been examined earlier (p. 187). The result of such drainage, in clear calm weather, is the formation of a pond of cold air in valley bottoms (Mori and Kobayashi, 1996), with high temperatures on the slope; the latter zone is referred to as the *thermal belt* (Figure 4.7). The first description of such zones is attributed to Silas McDowell, a farmer in the southern Appalachian Mountains of North Carolina in 1861 (Chickering, 1884; Dunbar, 1966). In this area the thermal belt is centered, on average, about 350 m above the valley floors (Cox, 1923). The reduced risk of spring frosts in this zone makes it of importance to agriculture and horticulture.

Extensive studies of thermal belts and inversion heights on valley slopes have subsequently been performed in many parts of the world. Observations between 515 and 830 m on the southeastern slope of Mt. Bandai, Japan (37° 36′ N, 140° 04′ E) illustrate the circulations and the thermal belt with higher nocturnal temperatures on the slope, where air ascends over the inversion layer towards the mountain (Figure 4.7). Vorontsov (1958) reports a similar pattern of down-slope winds and return circulations over a shallow slope near Aryk-Balyk (53° N, 68° E), Kazakhstan. There, the depth of the *cold air lake* at the foot of the slope is approximately 0.20–0.25 of the relative relief. Such cold air pools are common in winter in Alpine valleys of northern Switzerland. Zängl (2005b) shows that the cold air readily drains into the Alpine Foreland during the eastward passage of a warm front to the north of the Alps. However, the cold air can persist in inner Alpine valleys where constrictions in the cross-valley profile reduce the drainage. The primary dynamical control of the drainage of these cold air pools depends on the
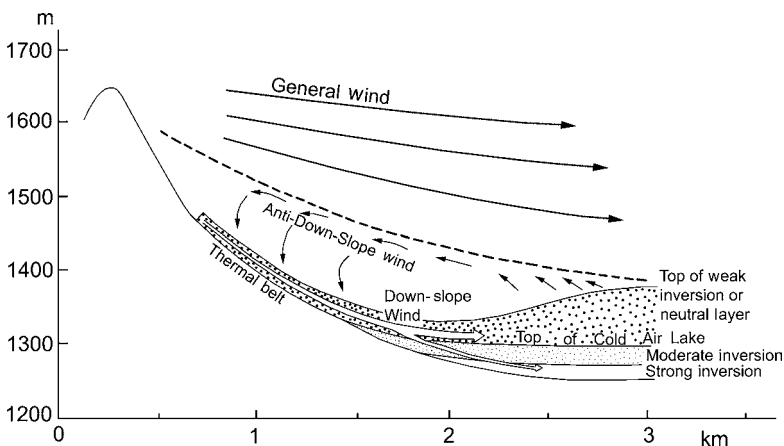
Fig. 4.7   **Model of the thermal belt and cold air drainage on a mountain slope in central Japan (from Yoshino, 1984).**
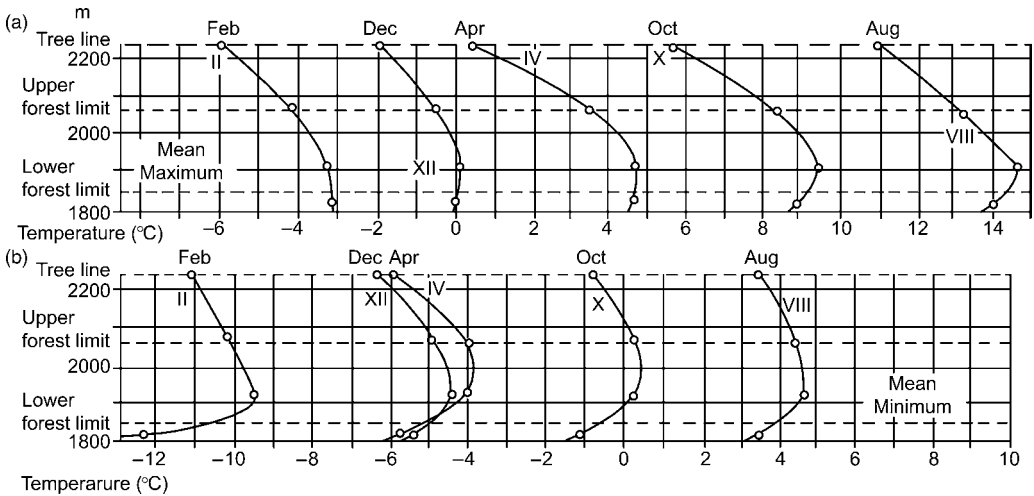
Fig. 4.8   Mean monthly maxima (a) and minima (b) of air temperature (1954–5) near the forest limits on a west-northwest slope near Obergurgl (after Aulitsky, 1967).

pressure gradient set up by the geostrophically balanced ambient flow. Hence, the interactions of the flow direction, speed, and valley geometry are together important factors. Zängl (2005b) points out that vertical turbulent mixing can assist in the erosion of a cold pool, but it is mainly effective in the case of shallow cold air lakes, or in basins where the topography restricts outflow.

In Bavaria, R. Geiger and colleagues investigated the vertical temperature structure on Grosse Arber (1447 m) and demonstrated the more moderate diurnal temperature range on the slope, particularly during clear weather in spring. Slope and summit locations also have a corresponding lower range of relative humidity than the valley floor (Geiger et al., 2003). In the same area, Baumgartner (1960–2) performed detailed climatological and phenological studies on Grosse Falkenstein (1312 m). The "growing season" (defined phenologically) is shown to be 1–2 weeks longer in the thermal belt than on the valley floor 200 m below, or 100 m or so higher up the slope. An effect is also apparent in earlier snow melt (Waldemann, 1959). Hence, this mainly clear weather phenomenon is of sufficient magnitude to be manifested in a climatological sense. Observations in the Ötztal near Obergürgl, Austria, by Aulitsky (1967) from June 1954 to May 1955 show that the inversion intensity averages 3 °C in winter and 1.5 °C in summer for mean monthly minimum temperatures but only 1 and 0.2 °C, respectively, for monthly mean temperatures (Figure 4.8).

There has been considerable discussion as to the elevation of the thermal belt with respect to the valley floor. Obrebska-Starkel (1970) summarizes data from valleys in Europe on the mean *upper* limit of the inversion layer, capping the thermal belt, which approximates the center of the belt (see also Yoshino, 1975; p. 434). These figures indicate that in hilly terrain (the Mittelgebirge) with a relative relief of 500 m or less, the center of the thermal belt is typically 100–400 m above the

valley floor. In high mountains, Aulitsky's work in the Ötztal suggests that it is centered about 350 m above the valley floor in summer and 700 m above in winter. This difference is attributable to the deeper cold air in winter with the possibility of more stable inversion conditions. However, investigations by Koch (1961) show that terrain *profile* is more important than relative relief or absolute elevation in determining the height of the thermal belt. It is usually located at the steepest section of the valley side since the slope exercises a controlling effect on air drainage.

4.3 CLOUDS

Cloud cover is more frequent and thicker, in general, over mountains than over the surrounding lowlands. The ability of mountains to generate clouds at any given time depends on: (i) the atmospheric conditions – moisture content and stability; and (ii) the lifting caused by mountains. There are three main processes that cause air to be lifted – direct forced ascent; aerodynamic effects when airflow is deflected around an obstacle; and thermal forcing over mountain slopes (Banta, 1990) (see Figure 4.9). Forced ascent (mechanical uplift) of stable moist air results in the formation of orographic stratus when the air reaches its lifting condensation level (LCL). If the rising air reaches its level of free convection (LFC), where it can rise due to instability without further orographic forcing, then convective (cumulus) cloud will form. Heating over mountain slopes gives rise to anabatic currents and valley winds (see Chapter 3), that lead to thermally forced cumulus clouds when the air reaches the LFC. If the air flows around a mountain, clouds may form in the downstream convergence zone. When cloud is already present, slowing down of the air by the mountain barrier also leads to an increase in cloud water content (Pedgley, 1971).

If an air parcel is forced to rise it expands due to the lower ambient air pressure, and therefore cools. This assumes no exchange of heat between the parcel and its surroundings, i.e. an *adiabatic process*. The rate of cooling, for unsaturated air, can be determined as follows. The First Law of Thermodynamics states that the heat (dQ) supplied to a unit mass of gas must be balanced by an increase in the internal energy of the gas and the work done externally by the gas. For an adiabatic process $dQ = 0$, and the changes in internal energy and work done by a parcel of gas also sum to zero. This can be expressed:

$$c_p dT - V dp = 0$$

where c_p is the specific heat of air at constant pressure ($\sim 1.0 \times 10^3 \, \text{J kg}^{-1} \text{K}^{-1}$); and V is the specific volume of gas.

By substitution for dp from the hydrostatic equation,

$$\frac{dp}{dz} = -g\rho,$$

Fig. 4.9 Schematic illustration of the effects of a mountain barrier on cloud formation (modified after Banta, 1990).

(a) LCL→ Orographic forcing (stable)

(b) LFC→ Orographic lifting (unstable)

(c) Obstacle effects

(d) CCL → Thermal forcing
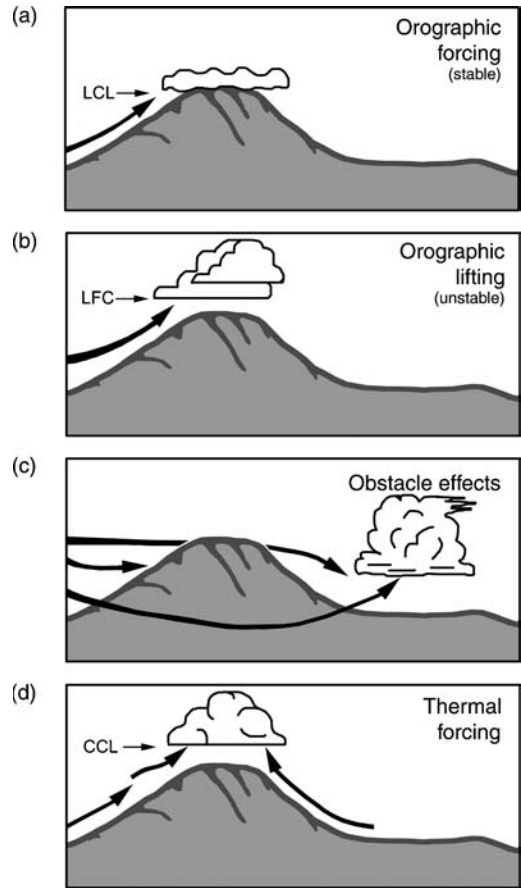
where $g = 9.81$ m s^{-2} and $\rho =$ air density, and since $V\rho = 1$, the changes in the rising air parcel can also be expressed as

$$c_p dT + g dz = 0$$

Hence, the lapse rate is

$$\frac{dT}{dz} = -\frac{g}{c_p}$$

This *dry adiabatic lapse rate* ($\Gamma = dT/dz$) has a value of 9.8 K km^{-1}, and is negative for increasing height. If the air rises above its condensation level, cloud begins to form. Further ascent now causes cooling at some lesser rate, known as the saturated adiabatic lapse rate, due to the release of latent heat, which partially offsets the cooling.

A hypothetical path curve for a rising air parcel plotted on a tephigram chart (Note 1) is illustrated in Figure 4.10a. This chart has coordinates of temperature
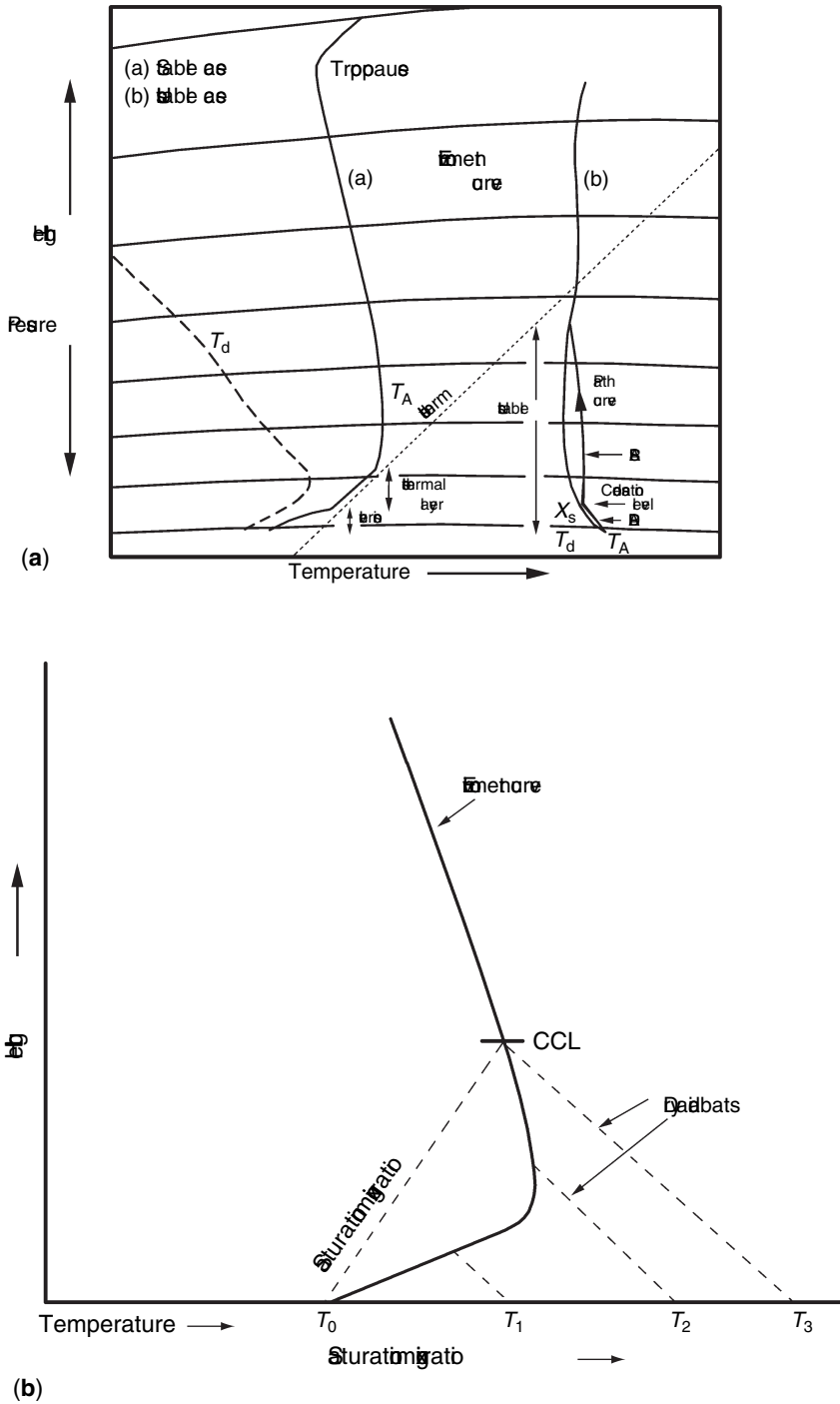
Fig. 4.10 Tephigram charts showing; (a) typical environment curves and atmospheric stability; (b) cloud formation following surface heating (from Barry and Chorley, 1987).
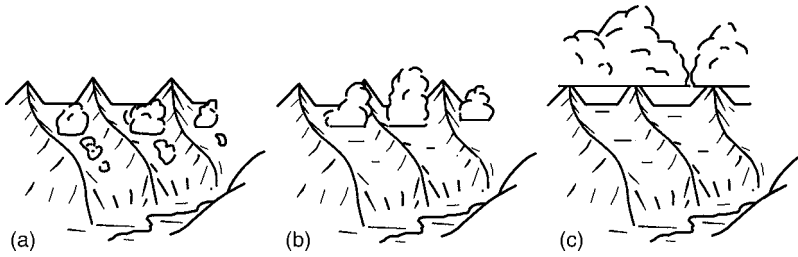
Fig. 4.11 **Observation of the daytime growth of cumulus over south-facing slopes in alpine terrain: (a) 0700 UTC; (b) 0900 UTC; (c) 1300 UTC (from Tucker, 1954).**

and $p^{0.288}$. It may be noted that $T/p^{0.288}$ is a constant value and the potential temperature, θ, is determined from $T (1000/p)^{0.288}$. Figure 4.10b also shows the *lifting condensation level* – the intersection of a dry-adiabat (or θ line) through the air temperature (T_A) with a saturation mixing ratio line through the dew-point temperature (T_d); T_A and T_d are both at screen level. If we assume a daytime increase in T_A from T_0 to T_3, the *convective condensation level*, similarly determined, indicates a higher cloud base. This is characteristically observed in the course of diurnal heating. A useful empirical relationship states that the base of cumulus cloud (in meters) triggered by surface heating is approximately 120 $(T_A - T_d)$, where the screen temperatures are in degrees Centigrade. Fliri (1967) has expressed the same relationship in terms of temperatures and relative humidity.

The effect of diurnal heating on the build-up of mountain cumulus in the Tyrol is described by Tucker (1954). In the morning, small fractocumulus develop over south-facing slopes in side valleys adjacent to the major valley troughs (Figure 4.11). Later, as diurnal heating raises the general condensation level, the main cumulus growth occurs over the ridge crests between the major valley systems. This lifting of the general condensation level is dramatically evidenced in the central highlands of Papua New Guinea where the nocturnal stratiform cloud in the valleys at about 1800–2000 m usually dissipates within an hour of sunrise and is replaced by fractocumulus on valley slopes. Within 2–3 h, cumulus may extend up the higher slopes above 3500 m towards the valley heads.

Although the parcel method is a useful approximation, when an air stream crosses a mountain barrier it is, in practice, lifted as a slab. In the process of such uplift the lapse rate (γ) of the entire layer is modified: if $\gamma > \Gamma$ (a superadiabatic lapse rate), ascent decreases γ, stabilizing the layer; if $\gamma < \Gamma$ (a subadiabatic lapse rate), ascent increases γ, leading to destabilization of the layer.

Furthermore, if the layer has higher moisture content at lower levels, it reaches saturation more quickly for a given amount of uplift than the top of the layer. Consequently, with further lifting the lapse rate in the layer becomes greater. This is referred to as *potential* (or *convective*) *instability*.

Cloud droplet growth can occur via two processes: (1) droplet coalescence by collision and the sweeping effect of falling drops entraining smaller droplets in their

wake; (2) the Bergeron–Findeisen mechanism that arises in a mixed phase cloud comprising ice particles and super-cooled droplets. The droplets tend to evaporate and the crystals grow by vapor deposition because the saturation vapor pressure is lower over ice than over a water surface (see Barry and Chorley, 2003; pp. 100–2). Subsequently, snow flakes form and snow or rain may reach the surface, depending on the height of the freezing level (see p. 293). Droplet collision–coalescence processes, forming "warm cloud," require about 30–40 min in maritime air and up to 2 h in continental air masses according to Braham (1968). Nevertheless, the major mountain ranges in the western United States, for example, are extensive enough to provide upwind lifting for 1–2 h. In winter, in middle and higher latitudes, the Bergeron–Findeisen process is more rapid and is the principal mechanism of raindrop formation in the cloud systems of synoptic weather disturbances.

Cloud type in mountain areas is primarily determined by air mass characteristics and is therefore related to the regional climate conditions. Special mountain cloud forms due to meso-scale air motion have been discussed already in Chapter 3 (p. 169). On west coasts in middle latitudes, stratiform cloud is common, particularly in winter, and often occurs as hill fog, enveloping high ground. The mountains of northwestern Europe and western North America experience such conditions frequently (see p. 398). If stratus cloud is already present in an air mass, due to turbulent mixing, orographic uplift tends to lower the cloud base. It is not always easy to distinguish orographically produced cloud from that occurring in a cyclonic system. Rawinsonde data from studies over the San Juan Mountains of southwestern Colorado (Hjermstad, 1975) indicate that, in winter orographic cloud systems, there is usually a moist layer extending some 1500–2000 m above the general summit level (3500–3800 m) and capped at around 500 mb by a stable dry layer. In contrast, deep cyclonic storm clouds may extend up to the 300 mb level.

In mid-latitudes in summer, and generally in continental and subtropical–tropical areas, the predominant cloud form is convective. The spatial distribution of convective upcurrents (*thermals*) in mountain regions shows some pronounced effects of topography. For example, there may be strong contrasts between shaded and sunny slopes. Fujita *et al.* (1968) reported rapid cumulus build-up on the slope of Mt. Fuji between 0845–0915 h in July as the solar altitude increased from 47° to 53° and surface temperatures on the rocky slopes exceeded 30 °C (see Figure 4.6). Surface temperatures on mid-latitude mountains during summer afternoons tend not to differ much from those in adjacent valleys since the change of net radiation with height is small (Scorer, 1955; MacCready, 1955). Consequently, potential temperatures are higher in the mountains. In Idaho, for example, MacCready found an average potential temperature gradient on summer afternoons of 2.9 K km^{-1} between 700 and 1700 m, with maximum rates of 5.5 K km^{-1}. Therefore, thermals start more readily over high ground, although because of the higher potential temperatures, cloud bases over these locations also tend to be higher. In such terrain, the height difference between the bases of cumuli over valleys and over hilltops is about half of the valley–summit relative relief (assuming cumulus actually forms at the lower level).

This pattern of stronger convective motion over high ground is confirmed by observations of Silverman (1960) in the Santa Catalina Mountains, Arizona, which rise 2000 m above the surrounding terrain. However, the wind field determines the cloud locations with respect to the ridge line and, in most cases, it is difficult to separate the effects on convection of barrier heating on the one hand and lifting, on the other (Hosler *et al.*, 1963; Orville, 1965a, b, 1968; Kuo and Orville, 1973). The role of lee convergence in thunderstorm initiation in relation to ridge top wind direction in the Colorado Rocky Mountains is discussed in Chapter 5, (p. 405). Fujita (1967) also demonstrated that a mountain mass, such as the San Francisco Peaks of Arizona, can cause a convective shower system to split due to downwind wake effects with cyclonic vorticity on the right and anticyclonic vorticity on the left, viewed downwind. Aircraft measurements during fair weather conditions over the San Mateo Mountains, west-central New Mexico, suggest a scale interaction between 3 and 4 km wide convective eddies and a 20-km diameter toroidal "heat island" type of circulation (Raymond and Wilkening 1980). Turbulent heat is transferred upward by the eddies to 200–1400 m above the summit levels creating a positive temperature anomaly. Mean sensible heat fluxes of 400 W m^{-2} or more are common at mountain-top level. This buoyancy generated by the meso-scale eddies supports lower-level inflow and higher level outflow. Given moisture availability, conditional instability in such situations would favor the initiation of cumulonimbus growth and thunderstorm activity.

There are few data available on cloudiness variations with altitude in mountain regions. Müller (1984; pp. 112–13) shows altitudinal variations in both cloudiness in the Alps in summer months. Data from Schüepp (1963), based on seven stations in southwest Switzerland, indicate that mean cloudiness in JJA increases by about 5 percent km^{-1} between 2000 m and 3500 m (from 50–55 percent to 56–63 percent).

A special problem relating to cloud data from mountain stations is the frequent obscuration of view by cloud at station level (i.e. hill fog). Moreover, cloud tops, especially in winter, may be below the station (Figure 4.12). Observations for 1939–48 from the Zugspitze show that the tops of stratiform cloud limited by an inversion layer have a maximum frequency about 1500–1800 m altitude, day and night in winter (Figure 4.13), for a total of 5650 cases. For April–September, the tops of stratiform cloud are most frequently about 2600 m with a secondary nocturnal maximum at 1500–1800 m for 1865 cases. Hauer (1950) notes that the explanation of the nocturnal distribution, with cloud tops frequent above 2700 m, probably lies in the persistence of a stratocumulus layer derived from the spreading out of daytime convection cloud in the proximity of the mountain.

Some practical problems with cloud reporting at high mountain stations result from the fact that the low cloud category, which includes stratocumulus and cumulus, has a height range of 0–2 km for the cloud base (World Meteorological Organization, 1975), whereas over extensive mountain areas the base may lie at an altitude typical of that for medium cloud according to the

Fig. 4.12 **Low-level stratus filling the Swiss lowlands and valleys – a typical autumn phenomenon when surface inversions form during anticyclonic weather. The mountain in the center is the Rigi, near Lucerne (K. Steffen).**

Fig. 4.13 **The diurnal frequency distributions with altitude of the tops of stratiform cloud observed from the Zugspitze in summer and winter, 1939–48 (after Hauer, 1950).**
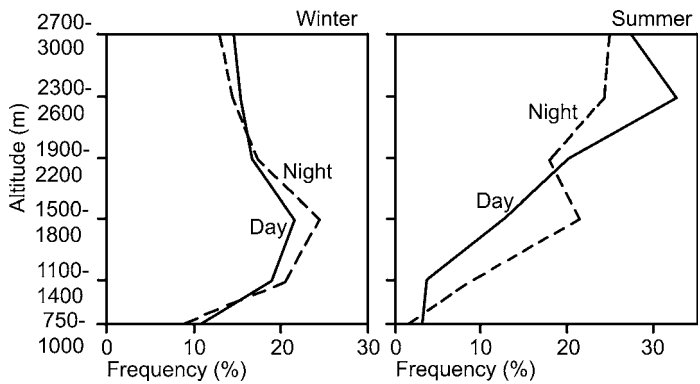
synoptic reporting code. Also, various cloud forms occur in mountain areas, such as a chaotic "föhn sky," and fracto-types of cloud, which are not adequately covered by the code categories (Küttner and Model, 1948; World Meteorological Organization, 1987).

4.4 PRECIPITATION

4.4.1 Precipitation processes

The influence of mountain barriers on precipitation distribution and amount has been a subject of long-standing debate and controversy (e.g. Henry, 1919; Bonacina, 1945). It is a problem that is compounded by the paucity of high-altitude stations and the additional difficulties of determining snowfall contributions to total precipitation, especially at windy sites. As recognized by Salter (1918) from analysis of British data, the effect of altitude on the vertical distribution of precipitation in mountain areas is highly variable in different geographical locations. To gain adequate understanding of these variations we must consider the basic condensation processes and the ways in which mountains can affect the cloud and precipitation regimes.

During the 1950s–1970s, Tor Bergeron devoted considerable attention to studies of precipitation mechanisms and orographic effects on precipitation amounts and their spatial distribution (Andersson, 1981). In particular, Bergeron investigated maxima in winter: (i) close to coastlines; and (ii) over low hills. In low-lying coastal areas and over small hills, forced ascent is absent. In the first case, it was found that the wind direction was parallel to the coast with higher pressure over the land (in the northern hemisphere). The greater friction over land sets up horizontal wind shear and stress-differential-induced convergence, with low-level flow up the pressure gradient (Bryson and Kuhn, 1961). The resultant lifting causes precipitation when the low-level air is moist, the condensation level is low and the airflow is basically stable. In the second case, Bergeron invoked terrain-induced lee waves and the seeder–feeder cloud mechanism (see Figure 4.14) to explain patterns of locally enhanced precipitation, which he demonstrated during intensive field campaigns in central Sweden. He designated such purely orographic precipitation as
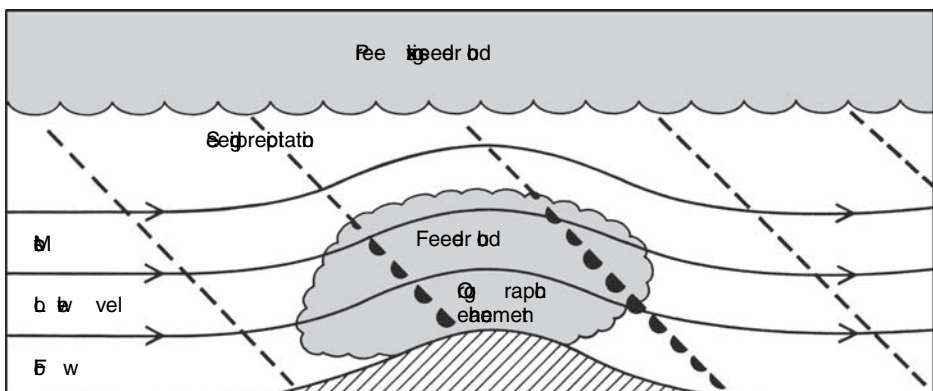
Fig. 4.14 Schematic illustration of seeder–feeder clouds and enhancement of precipitation over a hill (from Browning and Hill, 1981).

"oreigenic" (Bergeron, 1961), although the term has not been widely adopted, and such cases are very infrequent according to Smith (1979; Smith *et al.*, 1998). Orographic **enhancement** of precipitation that is occurring due to synoptic scale uplift or convective instability is most common. The processes involved in orographic precipitation are discussed below.

As pointed out by Fliri (1967), the primary distinction is between convective and air mass situations. Basically, mountain effects on precipitation in mid-latitudes involve the modification of extratropical cyclones in the winter half-year (Browning, 1985) and convective systems in summer (Cotton *et al.*, 1983). The physical variables concerned are the vertical profiles of moisture content and wind speed. The atmospheric water vapor content decreases quite rapidly with height in the lower troposphere (see p. 35), so that, at 3 km, the figure is typically about one-third of that at sea level. From this standpoint, precipitation amounts might be expected likewise to decrease upward, but the vapor flux convergence, cloud-water content and vertical wind profile are the dominant influences.

In a simple convective cloud system (with only vertical motions), the precipitation maximum should be located close to the cloud base, where the maximum size and number of falling drops occur before beginning to evaporate. In cumulonimbus clouds with strong vertical updrafts the drops tend to be transported upwards so that the zone of maximum precipitation may even be somewhat above the cloud base. A convective pattern of vertical precipitation distribution is widely found in the tropics where the cloud base is typically about 500–700 m in coastal areas and 600–1000 m inland. As noted by Weischet (1969), these areas characteristically have a rainfall maximum between 1000 and 1500 m. This pattern is especially pronounced in the trade-wind inversion belt where the air is very dry above the inversion. On Hawaii, for example, more than 550 cm falls at 700 m on the eastern slopes of Mauna Loa, whereas the summit (3298 m) receives only 44 cm; similar trends are apparent on windward slopes of the coastal mountains of Central America (Hastenrath, 1967). Flohn (1974) states that, in the area of the intertropical convergence, precipitation amounts on mountains above 3000 m are only 10–30 percent of those in the maximum zone (e.g. Mt. Kenya and Mt. Cameroon).

In the middle latitudes, precipitation in the winter half-year at least is predominantly derived from advective situations. The large-scale forced ascent of air over a mountain barrier leads to a lifting condensation level (p. 269). This ascent may intensify the general vertical motion in a cyclonic system or it may release conditional instability and shower activity, especially in polar maritime airstreams (Smithson, 1970).

In the tropical easterlies wind speeds typically decrease with height, whereas the westerlies in middle latitudes generally increase. This increase more than compensates for the vertical decrease in moisture content up to at least 700 mb, according to evaluations for stations in the Alps by Havlik (1968). He shows that the totals increase up to the highest stations around 3500 m. Only a small fraction of this

increase can be attributed to an increased frequency of days with precipitation. Instead, days with 30 mm day^{-1} at mountain stations account for almost half of the excess. These are commonly warm-sector situations with southwesterly airflow at 500 mb. Days with large vertical increases in precipitation amounts are shown to have three to four times the mean annual vapor flux between 850 and 500 mb. Nevertheless, an analysis of sounding data on the windward side of the Park Range, Colorado, suggests that only 2–5 percent of the moisture flux is precipitated. Hindman (1986) estimates a vapor inflow of 3.20×10^6 (± 0.74) g h^{-1} for several orographic storms, an outflow of 2.96×10^6 (± 0.68) g h^{-1} of vapor, 0.14×10^6 g h^{-1} of liquid water and 0.01×10^6 g h^{-1} of ice particles. The precipitation averaged only 0.1×10^6 g h^{-1}.

The amount of orographic precipitation depends on three factors operating on quite different scales (Sawyer, 1956). They are: (1) air mass characteristics and the synoptic-scale pressure pattern; (2) local vertical motion due to the terrain; and (3) microphysical processes in the cloud and the evaporation of falling drops. These are examined in turn.

Air mass characteristics of major importance are the stability and moisture content of the air; the pressure field determines the wind speed and direction. Heavy orographic precipitation is most likely in Britain when winds are strong and perpendicular to an extensive mountain range, the air is already moist and cloudy, and the lapse rate is near neutral, facilitating the release of conditional instability through uplift (Douglas and Glasspoole, 1947). Such conditions are common in the warm sectors of frontal cyclones. Poulter (1936) noted that the orographic increase at warm fronts was about two-fold over windward slopes of similar inclination to the front (1 : 100), whereas cold fronts (slope 1 : 50) resulted in smaller increases of about 50 percent. Radar studies (Browning et al., 1974, 1975) show that, over Britain, orographic effects are negligible at surface cold fronts, where precipitation is heavy in any case. Ahead of the front, in the warm sector, orographic effects vary according to the existence, first, of a low-level jet maintaining high liquid water contents in the low-level "feeder clouds" and, second, of seeding particles falling from higher-level "seeder" clouds as illustrated in Figure 4.14 (Bergeron, 1949; Storebö, 1968; Andersson, 1980; Browning and Hill, 1981). Such seeding augments rainfall rates through the washout of droplets, or by enhancing snow crystal growth, in orographic cloud over low hills. Convective meso-scale precipitation areas (MPAs) within cyclone warm sectors (Hobbs, 1978; Smith, 1979) may also be accentuated by orography (see Figure 4.15). They can persist for 6 h or more and contribute much of the heavy precipitation. Radar analyses show that most of the augmentation occurs in the lowest 1500 m associated with pre-existing rain areas, high humidity and winds ≥ 20 m s^{-1} (Hill et al., 1981; Figure 4.16). These newer studies appear to confirm earlier ideas of Bonacina (1945) on the role of convective instability and the need for "pre-conditioning" of the upstream airflow, but the relative roles of: (1) existing stratiform-derived precipitation giving an orographic seeder–feeder effect; (2) existing convective instability

Climatic characteristics of mountains
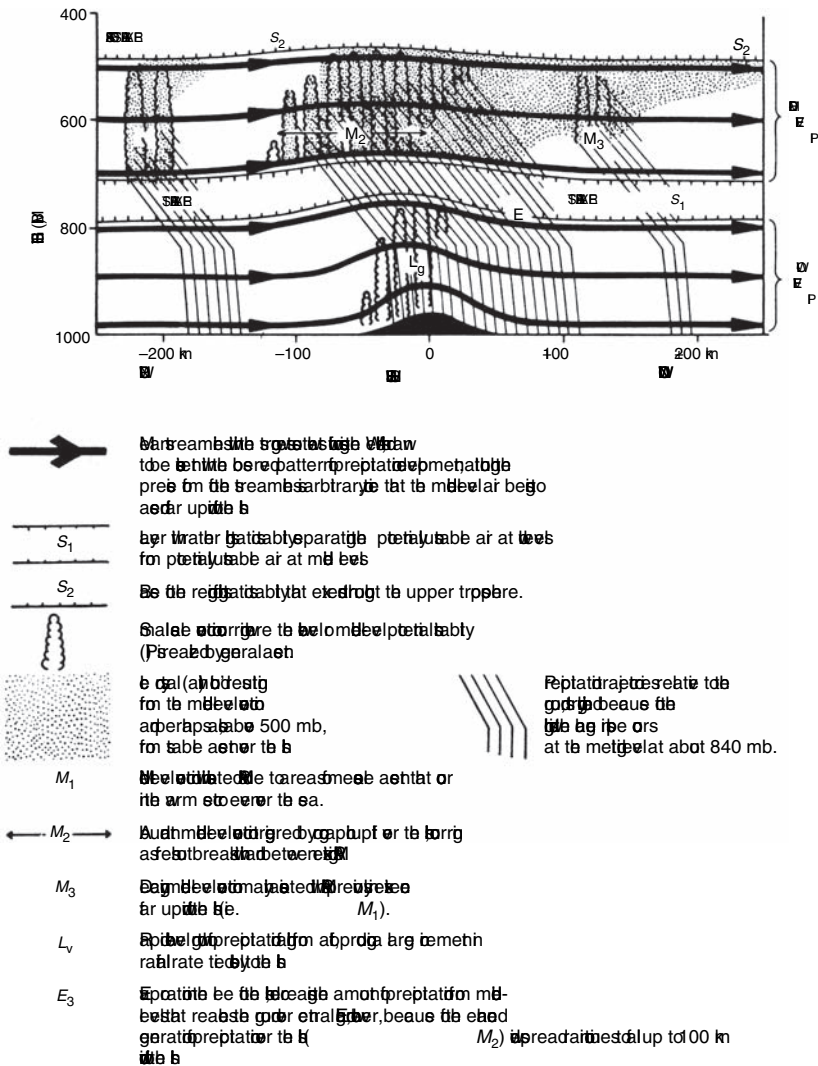
Fig. 4.15 Model of warm sector rainfall based on radar studies over the Welsh hills showing the role of potential instability in meso-scale precipitation areas (MPAs) and orography (from Browning *et al.*, 1974).

released by forced ascent; and (3) existing baroclinicity releasing instability through orographic blocking or frontal deformation, remains uncertain (Smith, 1982). According to Carruthers and Choularton (1983), for wide hills with half-width ≥ 20 km the precipitation maximum occurs not on the upwind side, but at the summit or in the lee side of narrow hills due to wind drift.

The vertical motion induced by the terrain is determined by the relief and shape as well as by air mass stability, wind speed and direction (see Chapter 3, pp. 132–42).
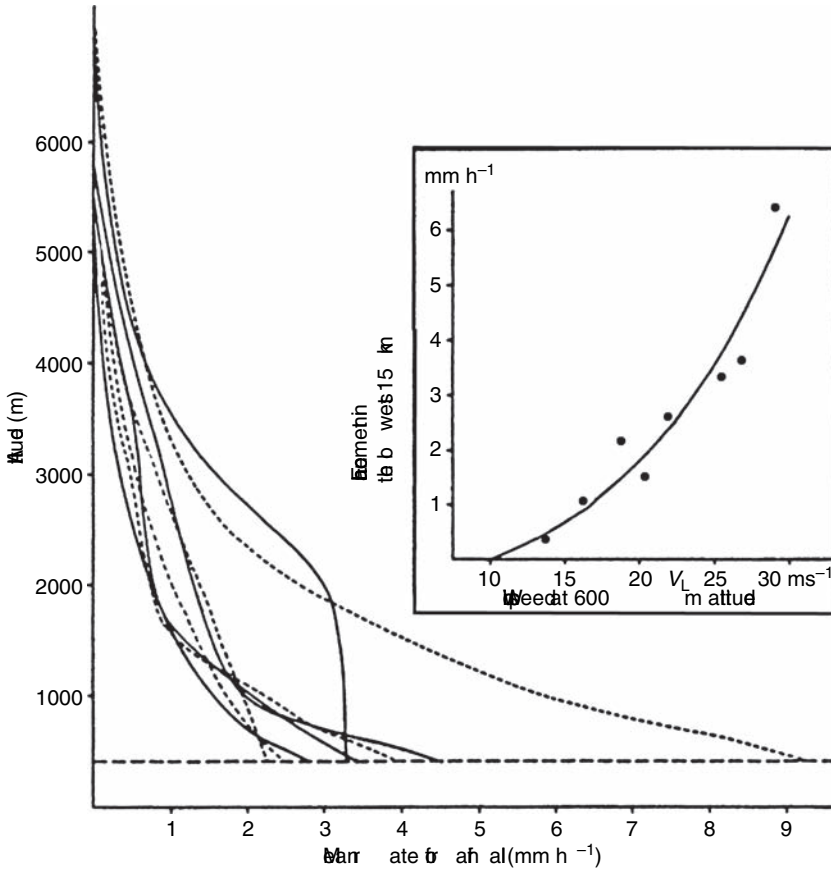
Fig. 4.16 The relationship between altitude and orographic enhancement for eight cases of cyclonic precipitation in south Wales. The inset shows the effect of wind speed at 600 m on the enhancement of rainfall rates in the lowest 1500 m for the same cases (modified from Hill *et al.*, 1981).

For the apparently simple case of southwesterly monsoon airstreams approaching the Western Ghats, India, the evidence suggests that smooth orographic uplift is an insufficient explanation (Smith and Lin, 1983). The rainfall occurs in wet spells of 5–10 days' duration. Localized meso-scale lifting that is driven by latent heating apparently triggers deep cumulus convection. Smith and Lin argue that the Ghats merely anchor the rainfall system. However, low-level flow interactions with the mountains and the extent of upstream influence are still debated (Smith, 1985). For low hills, assuming no deflection or blockage of the flow, the vertical velocity (w_s) of the low-level air can be obtained from:

$$w_s = u \tan s,$$

where u is the component of the wind normal to the barrier; and s is the corresponding slope angle.

Orographic precipitation models are discussed below.

The causes of the sharp increase of precipitation on windward slopes, and its drop-off above some limiting elevation have been re-examined with the aid of airborne and surface vertically-pointing and dual polarized scanning radar during the Mesoscale Alpine Program (MAP), September–November 1999, and the Improvement of Microphysical Parameterization through Observational Verification Experiment -2 (IMPROVE-02) over the Cascade Mountains in Oregon in November–December 2001. Houze and Medina (2005) suggest that turbulence is a mechanism for orographic enhancement of precipitation. A layer of strong shear is observed to develop between low-level blocked flow and overlying cross-barrier flow. Shallow, vertically overturning cells form in the shear layer (when the shear is $\geq 10\,\mathrm{m\,s^{-1}\,km^{-1}}$) promoting rapid growth of condensate which falls out over the lower windward slopes. Snow particles falling from overlying frontal cloud grow rapidly by riming and aggregation. Medina *et al.* (2005) further show that the layer of strong vertical shear slopes upward towards the mountain crest. The structure is identified in both the Alps and coastal mountains of Oregon and seems to be characteristic of situations where a baroclinic wave approaches a mountain range with stable stratification upstream.

The amount of condensation depends on the lifting depth, the amount of air lifted, and the moisture content of the air. In a stable air mass, the lifting depth may be only a few kilometers, whereas, in a cloudy air mass with strong winds the lifting may be up to 6 km. The condensation rate (c) for saturated air subject to orographic lifting can be expressed:

$$c = -\int_z pw\,\frac{\mathrm{d}r_\mathrm{s}}{\mathrm{d}z}\,\mathrm{d}z$$

where r_s is the saturation mixing ratio; and w is the vertical velocity. This implies that c decreases with a decrease in temperature (which determines r_s) and with increasing altitude. For given amounts of uplift calculated along specific mountain cross-sections, an equation of this form can be solved by assuming appropriate profiles of w and r_s (Fulks, 1935). Pedgley (1970) indicates that, for each kilometer of uplift, the condensation from saturated air is about $1.5\,\mathrm{g\,kg^{-1}gm^{-3}}$ of liquid water.

The fallout of raindrops (or snow flakes) depends on the growth rate of cloud droplets, their coalescence efficiency, and their fall speed in relation to wind velocity. About 1 h is required for droplet growth to raindrop size by coalescence, compared with about half as long for snow flakes by the Bergeron–Findeisen process in clouds with both ice crystals and supercooled droplets present. The ice crystals grow by accretion while the supercooled droplets evaporate due to the lower saturation vapor pressure over an ice surface compared with a water surface.

An analysis (Pedgley, 1970) of six cases of heavy precipitation associated with strong southwesterly airflows over Snowdonia, north Wales, in summer 1966, suggests that there would be insufficient time for raindrops to grow in the air

stream across these mountains. Pedgley calculates that if droplets of 2×10^{-1} cm radius were already present, and if the winds were $< 11\,\mathrm{m\,s^{-1}}$, small drizzle drops (10^{-2} cm radius) could grow within half an hour. The center of Snowdonia (averaging 600 m) is about 20 km from the margins of the elevated dome. Heavy rainfalls apparently require a scouring process by droplets of 0.1–0.5 mm radius falling from upper cloud layers. Large drops have a high fall speed and so gain little by accretion. However, a droplet of 0.5 mm may grow to 1.0 mm radius (a volume increase of 8) in about 10 min while falling through 3 km of cloud with a liquid water content of $0.5\,\mathrm{g\,m^{-3}}$. Such raindrop growth is therefore feasible for winds $< 33\,\mathrm{m\,s^{-1}}$. Observations indicate that wind speeds are typically $22\,\mathrm{m\,s^{-1}}$. Furthermore, the heavy rains are commonly of the prolonged "fine rain" type with intensities of about $6\,\mathrm{mm\,h^{-1}}$. Half of the liquid water in a cloud column is removed in about 6 min by which time the cloud has been displaced 5–10 km. Sawyer (1956) suggests that, in favorable conditions, most of the available water is precipitated, but as little as 30–50 percent of the available water may fall out if only shallow moist layers are present. This example illustrates the importance of taking account of the microphysical processes in the clouds.

Soundings and aircraft data for wintertime storms over the Colorado Rocky Mountains indicate some findings that contrast with conditions over the lower and less extensive British mountains. Marwitz (1980) identifies four stages that occur in most cyclonic storms over the San Juan Mountains. First, moist westerly flow does not extend above mountain top level (3.5–4 km) and so is blocked and diverted. This stable atmosphere situation changes to a neutral one as a deep storm extends throughout the troposphere. However, a baroclinic zone is usually only present in the upper half of the troposphere. In stage three, a convective cloud line develops above a low-level horizontal convergence zone at the base of the mountains and upwind. Finally, in stage four, dissipation begins with subsidence occurring at mountain top level. Microwave and radar measurements of storms in the northern Colorado Rocky Mountains show that liquid water content is related to cloud top temperature (i.e. higher, colder clouds), but there is an inverse relation between liquid water content and precipitation rate (Rauber et al., 1986).

The influence of the extensive barrier of the Sierra Nevada in California on wintertime Pacific storm systems has also received much attention. Marwitz (1987) examined two deep orographic storms that caused heavy snowfalls using aircraft and Doppler radar data. Precipitation rates averaged $4\,\mathrm{mm\,h^{-1}}$ with forced ascent rates of $0.4\,\mathrm{m\,s^{-1}}$ in the very stable storm case. This blocking reduced the wind component normal to the barrier. The stable orographic clouds were found to have concentrations of cloud droplets that are typically marine above the freezing level, i.e., mean diameters of 20–30 μm. The ice crystals concentrated near the $-5\,°\mathrm{C}$ level were predominantly needles indicating rime-splintering. The cloud droplets are efficiently accreted by ice crystals, depleting the condensate and producing ice multiplication. Marwitz notes that little supercooled water will pass over the crest line of the Sierras. A further analysis of orographic enhancement on the windward

slopes of the central Sierra Nevada has been made for DJF 1953–99 (Dettinger *et al.*, 2004). They compare the average precipitation on wet days (> 0.2 mm) at three stations near sea level in the Central Valley to that at three stations between 1300 and 2200 m on the western slope. These storm situations account for 25 percent of winter days. On average, precipitation at the high altitude sites is 3.3 times that at the low altitude ones but daily indices may range from 8 to 30, and the interannual variation of the ratio is from one to five. They find that storms with strong orographic enhancement have winds from near due west, they transport more water vapor across the range, and the atmosphere is less convectively stable. Storm totals are largest with moisture transport from the southwest, but the larger orographic enhancements occur with more westerly flows. The latter cases typically feature the warm sector of a mid-latitude cyclone over the central Sierra Nevada. James and Houze (2005) examined heavy precipitation events in northern California using radar reflectivity and Doppler velocity data. When one quarter of 73 recording gauges received ≥ 25 mm rainfall, the storms were characterized by southwesterly flow with a $20 \, \text{m s}^{-1}$ low-level jet and a high moisture influx. The low level flow, which was blocked below 1000 m, showed an increase 60 km upstream of the coast (150 km upstream of the crest of the coast range) and over the mountains. The precipitation was mainly stratiform and the radar showed an embedded core of maximum reflectivity over the first mountains encountered by the unblocked flow. The second series of mountains showed less intense radar echoes. When the flow was strong, these echoes were displaced slightly downwind of the first mountain crest.

A case study for a winter rainfall event in north Wales indicates a five- to ten-fold enhancement in the mountains of Snowdonia (Capel Curig, 215 m), compared with the coastal lowlands and valleys (Sibley, 2005). Winds above 900 mb were uniformly 35–$40 \, \text{m s}^{-1}$ throughout the troposphere. Lee effects are highly variable for individual storms. Pedgley (1971) demonstrates for Snowdonia that "rain-shadow" patterns are weak when the air stream already has substantial cloud cover, with precipitation falling upwind of a range and strong winds. The same is true also when there is little orographic lifting due to light winds and the airstream has only shallow moist layers. A model analysis by Zaengl (2005) suggests that the fractional enhancement of lee slope precipitation is × 10 in convectively unstable situations and × 100 in moist neutral cases. The presence of a lee side cold pool increases spillover by suppressing down-slope motion and evaporation of drops. There is also a smaller effect on upwind precipitation through the effect of a cold pool on the pattern of gravity wave motion.

In general, precipitation maxima over mid-latitude mountain ranges are closely related to the "smoothed" topography (Pedgley, 1970). Thus, gauges in small valleys within a mountain complex may record totals more characteristic of the surrounding ranges. Large, deep valleys, however, set up their own wind systems that can cause very different precipitation distributions (see p. 223). Convective activity may also cause erratic patterns of precipitation distribution.

Orographic precipitation involves airflow dynamics and physical processes in clouds. Key factors in the former are the depth of air affected by orographically forced ascent and the strength of the uplift. Low hills have limited effect on deep moist air crossing the terrain. However, if there is upstream tilt of the streamlines ahead of a mountain range (see Figure 2.27, p. 76) then condensation may occur upstream of the barrier (Smith *et al.*, 2005). With regard to cloud physics, critical processes concern the condensation rate, snow generation efficiency, carry-over of condensate, precipitation efficiency, and spillover of precipitation to the lee of the mountain due to the wind. There seems to be no characteristic time scale for hydrometeor formation according to Jiang and Smith (2003) because the microphysical cloud processes are non-linear. Precipitation efficiency is the ratio of total precipitation rate to the total condensation rate over a given area. It is highly variable as a result of differences in the moisture content of the low-level flow, wind velocity and stability, the height and width of the mountains encountered by the air stream, and the mountain location (coastal/inland). Precipitation efficiency depends on three time scales (Jiang and Smith, 2003): that for advection of air across a mountain barrier (τ_A); that for fallout of hydrometeors (τ_F); and that for snow generation (τ_S).

Snow generation can occur by several means. In general order of importance, in the meso-scale storm prediction model used by Jiang and Smith (2003), these are: (1) condensation $\rightarrow$ supercooled cloud droplets by accretion $\rightarrow$ snow crystals; (2) vapor deposition $\rightarrow$ rimed cloud particles $\rightarrow$ snow; (3) vapor deposition directly on snow particles. Snow generation is itself controlled by the ratio $(\tau_S)\,/\,(\tau_A)$ while the fraction of snow that reaches the ground is controlled by the ratio $(\tau_F)\,/\,(\tau_A)$. Their model analysis suggests that increasing mountain width allows more time for hydrometeor formation, thus increasing precipitation. However, as the barrier width increases (for a fixed height), the mountain slope is decreased and this decreases the condensation rate thereby weakening the efficiency of snow generation. Precipitation efficiency in this case is increased by increased fallout and less carry-over. Jiang and Smith's analysis does not take account of convection, that will tend to augment precipitation efficiency, nor of flow blocking which will change the effective mountain width, the uplift and the cloud development.

Barstad and Smith (2005) use rain gauge data from several field campaigns in complex terrain to test their physical model of orographic precipitation, based on a new linear theory that includes airflow dynamics, condensed water advection, and leeside evaporation. The model predictions show that the wind direction, stability, and especially the cloud time delay (τ), are the sensitive parameters for point precipitation. The cloud time delay (in the range 0–1000 s) is the primary control of point precipitation amplitude, while the stability tends to shift the precipitation pattern. They conclude that the observational networks are inadequate to determine representative values of cloud time delay.

Most studies of orographic enhancement have been carried out for mid-latitude cyclonic systems in winter. However, Miniscloux *et al.* (2001) describe orographic

precipitation in the Cévennes of southern France during shallow, warm convection events moving from the southeast. Doppler radar shows rain cells moving northward with the low level winds (Cosma *et al.*, 2002). The cells are activated on the southeastern flanks of ridges that are spaced about 15 km apart. Winds of $25 \, \mathrm{m \, s^{-1}}$ give rise to mean daily totals of 50 mm and locally up to two to three times the mean values. Studies of shallow convective precipitation events over the Coastal Range in Oregon also report two cases with quasi-stationary banded structures giving strong precipitation enhancement in favored locations (Hirshbaum and Durran, 2005). The rain bands resemble convective roll circulations, formed parallel to the vertical shear that occurs within an unstable orographic cap cloud. Mountains with small-scale roughness, as well as random low-amplitude ($\sim 30 \, \mathrm{m \, rms}$) topographic features, seem to be equally effective in organizing and locating orographic rain bands of the kind observed in western Oregon and also reported four decades ago over low hills by Bergeron (1960, 1961). Whether rain bands form, rather than cellular structures, seems to depend on atmospheric characteristics, not the terrain. Kirshbaum and Durran (2005) propose that the atmosphere's susceptibility to convection upstream and the environment in the unstable mountain cap cloud are important factors. Convective cells that form upstream tend to disrupt any topographically determined rain bands as they are advected through the orographically formed cloud. If the cap cloud is potentially unstable, longitudinal bands of convection develop aligned with the vertical shear and mean wind vector, as is observed in trade wind cloud streets and in boundary layer roll vortices (Weckwerth *et al.*, 1997).

Larger, regional-scale influences appear in the diurnal cycle of convection over and near mountain ranges. Sato and Kimura (2005), for example, observe a late afternoon increase in water vapor over the Central Alps of Japan through low-level moisture convergence forced by a plains–mountains circulation enhanced by a sea breeze from the east. This moisture propagates towards the plains in the evening accompanied, in their case, by the simultaneous eastward propagation of a region of convection in the ambient flow. Convective instability gives rise to nocturnal precipitation over the plains east of the Central Alps, as is also observed east of the Rocky Mountains. Towering cumulus generated by thermal convection and valley wind effects over the Rocky Mountains, for example, is typically carried eastward by the general airflow and may cause afternoon–evening thunder showers if continued convection over the adjacent high plains permits cumulonimbus to form in the lee of the mountains (Henz, 1972). Riley *et al.* (1987) report a diurnal maximum in summer around 1600–1800 LST in the mountains of Colorado–Wyoming that becomes a nocturnal maximum eastward over the Great Plains.

4.4.2   *Altitudinal characteristics*

Following these general considerations of precipitation processes let us now examine the empirical evidence of altitudinal effects. During the late nineteenth century,

several studies were made of the vertical distribution of precipitation in the Himalaya (Hill, 1881) and the Alps. Subsequently, many computations have been made of the rate of precipitation change with height and its geographical variation. For example, Salter (1918) found increases of 8–15 cm per 100 m in southern England and about 12–30 cm per 100 m on windward slopes in western England. However, he noted that the rate of increase was much lower where there are high ranges to windward. On lee slopes the increase with height was found to be larger, especially on the lower slopes, due to the frequent occurrence of descending air motion and the removal of moisture upwind. Salter (1918; p. 54) also noted that stations in narrow valleys in mountain areas typically record much larger annual totals than would be expected from their relatively low elevation. For the eastern Pennines, mean elevation over an 8 km radius from a gauge site appears to be a better predictor of annual precipitation than station height (Chuan and Lockwood, 1974).

Several studies demonstrate that the altitudinal increase is due to the combined effect of higher intensities and greater duration of precipitation (Atkinson and Smithson, 1976). In north Wales, for example, average daily rainfall rates in Snowdonia are nearly twice those on the Irish Sea coast but, in addition, there are almost twice as many hours with rain falling in the mountains. This reflects the complex make-up of orographic precipitation discussed above.

The most complete global survey of vertical precipitation profiles has been carried out by Lauscher (1976a) using data for 1300 long-term stations grouped into three major categories: below 1 km (1029 stations), 1–2 km (222) and 2–3 km (43), for 10° latitude–20° longitude sectors between 35° S and 55° N, from 130° E westward to 110° W. He distinguishes four general types as shown in Figure 4.17. These are: "tropical" with a clear maximum at about 1.0–1.5 km; "equatorial" where there is a general decrease with height above a maximum close to sea level; a "transition" type in the subtropics, where there is either little height dependence, or conditions vary considerably locally; and a "mid-latitude" type which shows a strong increase with height. These four altitudinal patterns reflect the processes discussed above. Lauscher also showed a "polar" type where higher totals tend to occur near sea level, at least in the vicinity of open water. However, more recent work revises that picture.

Despite these useful generalities, many local or regional complications occur. For example, Lauer (1975) shows that the southern slopes of Mt. Cameroon, West Africa, have a maximum at their foot due to the monsoon regime but on the northeast side, where trade wind influences are dominant, it occurs at 1500 m. On the Caribbean slopes of the Mexican meseta, the typical tropical maximum occurs between 600 and 1400 m but there is a weak secondary maximum around 3000 m. This results from convective heating over the high basins. Lauer reports a similar phenomenon in Ethiopia. The low-level, warm-level moist monsoon air reaches the plateau along the valleys where it enhances convective activity causing maximum precipitation to occur between 2000 and 2500 m. Similar intense heating occurs over the subtropical deserts so that in the Sahara, for example, convection is set off
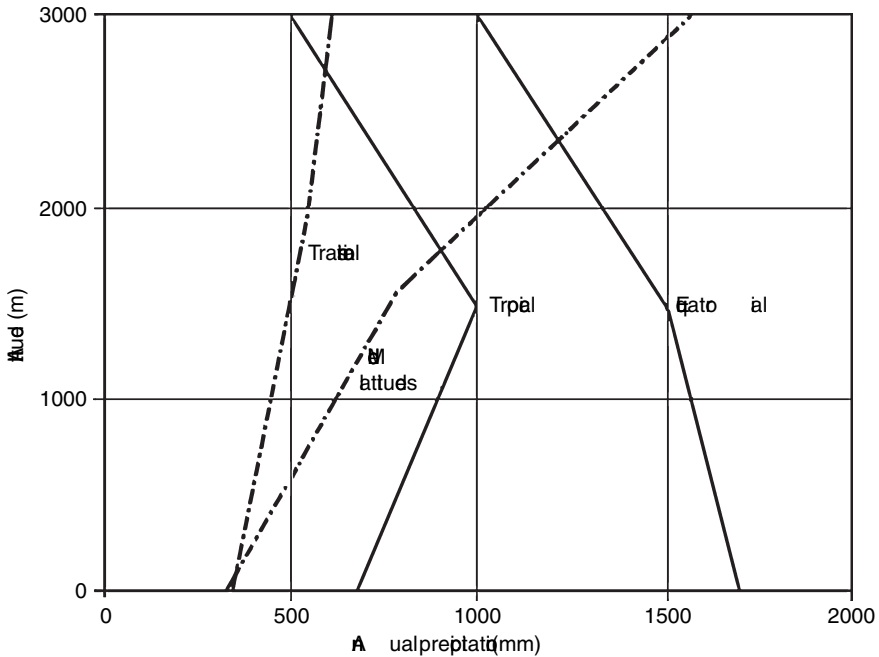
Fig. 4.17 Schematic profiles of mean annual precipitation (cm) versus altitude in equatorial climates, tropical climates, middle latitudes, and transitional regions (after Lauscher, 1976a).

within disturbances in the tropical easterlies and gives rise to a precipitation maximum at 2500 m altitude in the Hoggar (see p. 379). Lauer summarizes this variety of equatorial and tropical patterns of precipitation profile (see Figure 4.18), showing that the maximum zone in these regions tends to rise with decreasing annual total. Locally, of course, altitudinal gradients may be the reverse of those anticipated due to the presence of regional gradients caused by atmospheric circulation effects or moisture sources. An illustration for New Guinea is provided in Figure 5.1 (p. 365).

In the equatorial Andes of Peru (1° S), annual totals on the western slopes show a tropical pattern with maximum values around 1500 m, corresponding to a greater number of rain days, whereas on the eastern slopes values decline from 600 m to about 2500 m, with a secondary maximum about 3250 m, again corresponding to the frequency of rain days (Frère *et al.*, 1975). The annual regime is bimodal on the eastern slopes, but unimodal with precipitation during November–May on the western slope. At 16°–18° S in Bolivia, where there are no trade winds, amounts decline almost linearly with elevation from about 900 mm at 500 m to around 200–250 mm at 3500–4000 m altitude. There is little change in the numbers of rain days, but the amount per rain day decreases. Amounts per rain day in Bolivia and western Ecuador decrease from around 13 mm/rain day at 500–800 m to 4–5 mm/rain day at 3500 m; in eastern Ecuador, amounts fall off rapidly to about 5 mm/rain day at 2000 m.
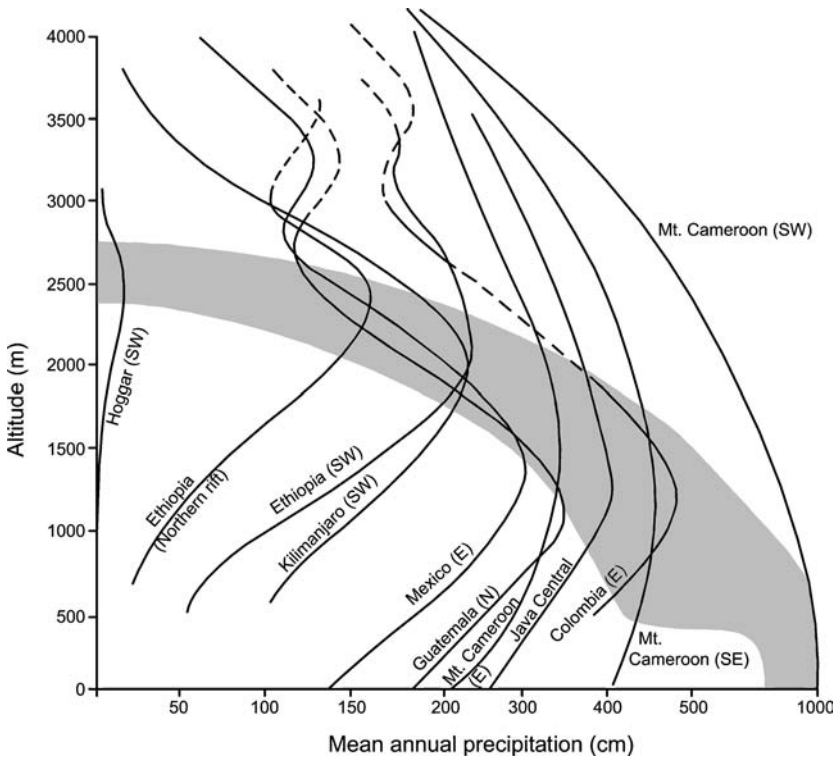
Fig. 4.18 **Generalized profiles of mean annual precipitation (cm) versus altitude in the tropics (from Lauer, 1975). The shading denotes the zone of maximum precipitation.**

Fig. 4.19 **The altitudinal profile of mean annual precipitation (cm) for Austria as a whole, for the Otzal in a lee situation and the Bregenz area in a windward situation (from Lauscher, 1976a).**
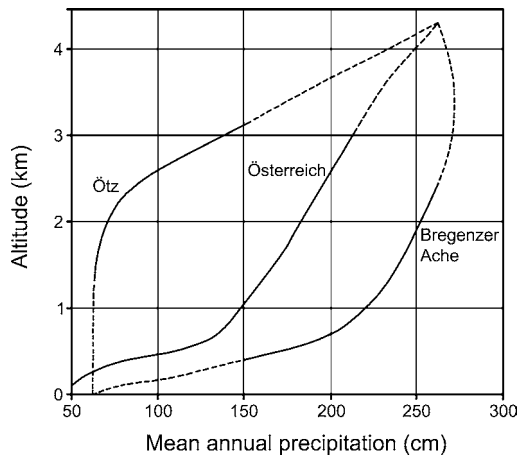
In middle latitudes, the general tendency for increased precipitation with height, often to the highest levels of observations, is modified considerably by a leeward or windward slope location. Lauscher (1976a) illustrates this for the eastern Alps in Austria, The profile for the lee situation of the Ötz valley contrasts strongly with that for the windward exposure of the Bregenz district (Figure 4.19). Similar

differences are observed in the Swiss Alps. In the sheltered Valais (Wallis), the rate of increase averages 27 mm per 100 m from 470 to 1700 m altitude and 99 mm per 100 m from 1700 to 3810 m, whereas in the northeastern Alps the opposite is found: 85 mm per 100 m from 380 to 1700 m and 57 mm per 100 m from 1700 to 3810 m. In both areas, however, the overall average from 400 to 3800 m altitude is close to 75 mm per 100 m (Lang, 1985).

In the coast ranges of western North America there is an increase usually up to the summit level, (as in the Olympic Range, Washington, around 2200 m; Schermerhorn, 1967), whereas the maximum appears to occur on the western slopes around 1600 m in the Sierra Nevada further inland (Armstrong and Stidd, 1967). In the Rocky Mountains, patterns are complicated by the Pacific origin of winter precipitation and the Gulf of Mexico origin of precipitation in the summer half-year (see Chapter 5, pp. 402–6). On the western slopes of the central Colorado Rockies, winter precipitation at 3200 m is almost six times that at the base of the slopes (1750 m) according to an analysis by Hjermstad (1970) (see Table 5.8, p. 404). Hanson (1982) showed strong linear relations exist between annual amounts and elevation in southwest Idaho both on upwind (southwestern) slopes and lee (northern) slopes for elevations between 1200 and 2100 m. However, lee sites received more precipitation than upwind ones at equivalent elevations. The annual pattern is determined by the winter season altitudinal gradient associated with cyclonic storms whereas summer thunderstorm rainfall shows only a small altitudinal effect.

For polar regions, data on altitudinal effects on precipitation relate primarily to snow accumulation records on the Greenland and Antarctic ice sheets. Using precipitation and accumulation data for Greenland, Ohmura (1991) shows the existence in western Greenland of a zone of maximum occurring around 2400 m at 69° N and descending northward to about 1500 m at 76° N. In eastern Greenland, the highest values are along the coast, while in southeast Greenland the maximum occurs about 750 m (Sugden, 1977). In eastern Antarctica the maximum also occurs about 750 m, although in Antarctica latitudinal effects introduce complications.

The altitude of maximum precipitation (P_{max}) for an ideal bell-shaped mountain is determined primarily by the lapse rate (γ) and the height of the mountain according to an analytical expression developed by Alpert (1986). This altitude and the amount of precipitation, decrease as γ increases. For a saturated atmosphere with $\gamma = 6.5\,°C\,km^{-1}$, the limiting altitude of P_{max} is shown to be about 3.8 km. Large-scale synoptic uplift is a less important variable than lapse rate, according to Alpert's model. In contrast to these results for high mountains, however, microphysical processes and meso-scale flow characteristics in the boundary layer play a much more significant role for precipitation over low hills, as shown above.

Studies of elevation effects in complex terrain frequently find that precipitation is weakly correlated with elevation alone. In a bivariate regression analysis of the statistical relationships between topography and precipitation for ten different
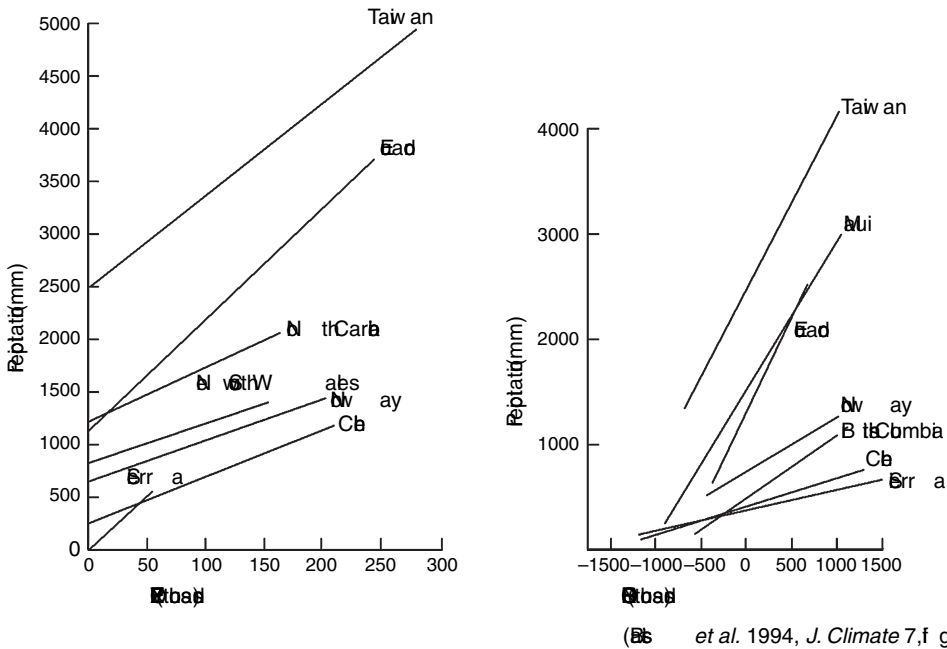
Fig. 4.20 **The relationship between annual precipitation and topographic parameters: (a) an elevation–exposure index; (b) a slope–orientation index for mountain ranges in middle and low latitudes (from Basist *et al.*, 1994).**

mountain regions, Basist *et al.* (1994) use six topographic predictors of annual precipitation. These are: the elevation; the greater of the up/down slope for 10 km from the station; "exposure" – the distance to an upwind barrier within 100 km that is at least 500 m higher than the station; and the orientation – the angle between the prevailing 700 mb wind and the major axis of the watershed upwind of the station, as well as two "interaction" parameters – elevation × exposure and slope × orientation. Elevation and slope were found to be the weakest individual predictors, while orientation and exposure were the best. Overall, the interaction parameters were the most useful predictors of precipitation. Figure 4.20 illustrates these findings for annual precipitation in a number of mountain ranges in middle and low latitudes.

In addition to geographical patterns, there are also distinctive patterns on seasonal and shorter time scales. For example, Erk (1887) noted a winter maximum at 700 m in the Bavarian Alps, but a summertime increase up to 1600 m. This shift reflects the predominance of cyclonic or convective precipitation types. Using monthly data for 1956–75 to construct profiles on the northern and southern sides of the Sonnblick Observatory in Austria, Lauscher (1978) shows that the typical mid-latitude pattern, with a summit maximum, occurs in 73 percent of months on the south side, and 66 percent on the north side. This pattern also characterizes the average profiles for the 12 wettest months and the 12 driest months. Nevertheless, there is a maximum around 2300 m on the north side in

26 percent of months and in 15 percent on the south side. This "tropical" pattern obviously reflects the predominance of particular storm types.

Storm "types" and synoptic flow patterns can also introduce major differences in orographic effects. For example, Peck (1964, 1972b) shows that in the Wasatch Mountains, Utah cold lows have a lower ratio (2.7 : 1) of summit/base precipitation than non-cold low storms (4 : 1 ratio). In the San Juan Mountains, Colorado, winter storms from the southeast and northwest are generally associated with light precipitation, due to high upper air temperatures, whereas storms from the west or southwest generally give rise to more precipitation over the mountains. Such differences are of great significance for winter cloud-seeding operations (Rangno, 1979).

High-resolution fields of precipitation in mountain areas are almost impossible to obtain from gauge data, given typical network densities, even with sophisticated interpolation procedures. Nevertheless, some topographic indexes (*TI*) may prove more effective. In a local area in southern Italy, for example, Diodato (2005) finds that an index expressed in terms of a fractional vegetation cover fraction (*VC*) and elevation (*E*), $TI = VC(E)^{0.5}$ accounts for 54 percent of the variance of precipitation. A novel approach suggested by Smith *et al.* (2005) for Oregon is to use satellite maps of vegetation characteristics as a surrogate. In semi-arid regions, the normalized difference vegetation index (NDVI) from reflected red light and near-infrared radiation indicates vegetation density that is mainly a function of moisture at low elevations. A second indicator is the infrared brightness temperature in the "window" region (9–11 μm). Moist areas where evaporation is occurring have lower brightness temperatures than dry areas. These indices, derived from 1-km MODIS data, show a sharp moisture discontinuity in Oregon about 121–122° W in good agreement with values estimated from the statistical Parameter-elevation Regression on Independent Slopes Model (PRISM) (see below).

4.4.3   *Evaluating the orographic component*

The precipitation falling on a mountainous area consists of an amount that would occur in the absence of the mountains as a result of convection and cyclonic convergence, and an orographic component due to the intensification of these processes over the mountains, as well as to the forced uplift of air by the terrain. Usually the total precipitation only is discussed, especially when statistical prediction is attempted by regression methods, but there have also been some attempts to distinguish the specific contribution of orographic effects.

For the Rocky Mountains in Alberta, Reinelt (1970) uses a statistical approach. The mean monthly precipitation is first calculated for each of five zones located parallel to and east of the mountains. Each zone is 100–150 km wide. These averages show that, between October and April, precipitation decreases eastward since most of it is caused by the upslope flow of shallow arctic air, which generates widespread stratiform cloud. There is also a strong orographic effect in May–June

when deep unstable air in cold lows sets off large-scale precipitation. Between July and October, thermal convection largely outweighs orographic influences so that the plains receive larger totals. A harmonic analysis is performed on the monthly zone-averages and the seasonal regime, as expressed by the phase angle and the amplitude of the first three harmonic components, is shown to differ markedly between the mountains and the other four zones. Precipitation in zone 5, 500–600 km east of the mountains, is assumed to be free of orographic influences and its monthly averages are therefore used as a reference datum. By subtracting the amounts in zone 5 from the corresponding averages for each of the other four zones, Reinelt shows that the orographic component for the Rocky Mountains in Alberta averages 37 percent of the total annual precipitation and exceeds 50 percent during September through to April. In the foothills zone around Calgary and Lethbridge, the annual orographic component is still 18 percent.

The orographic enhancement over Britain has been estimated for different air-flow directions by stratifying daily data according to the ratio of the contribution of falls with rates $\geq 0.05\,\mathrm{mm\,h^{-1}}$ to the mean annual precipitation (Hill, 1983). For hills exposed to maritime winds, enhancement factors are 1.5 to 3.5. Similar enhancements are estimated for the Hawaiian Islands, and it is suggested that mountain shape is more important than its size (Nullet and McGranaghan, 1988).

A specific case study of precipitation during the passage of an occluded front over the Cascade Mountains, Washington, shows a similar magnitude of orographic augmentation (Hobbs *et al.*, 1975). There is also evidence of a 20-h period of light precipitation on the windward slopes, after the frontal passage, attributable to orographic effects. In contrast, the only significant falls on the lee side are associated with the front. Aircraft measurements of liquid water content, ice particle concentrations, and riming of ice particles showed maximum values in the clouds leeward of the crest and closest to the frontal location. The concentration of the frontal precipitation in an 80 km-wide meso-scale convective cloud band is another noteworthy feature of this situation. Such band structures are now widely recognized to be a general feature of frontal zones (Browning and Harrold, 1969; see also Figure 4.15).

Statistical analyses of total precipitation in mountain areas have traditionally used regression techniques incorporating topographic parameters (Spreen, 1947; Linsley, 1958; Peck and Brown, 1962; Sporns, 1964). Formerly, precipitation maps for mountain areas were obtained by extrapolation from existing station data, empirical altitude–precipitation relationships, and adjustments for windward/leeward location (Steinhauser, 1967). There may be serious errors with this approach, especially where the mountains do not form a simple range. For western Colorado, Spreen showed by a graphical analysis that mean winter precipitation amounts are highly correlated ($R = 0.94$) with the combined influence of station elevation, the maximum relative relief within an 8 km radius, "exposure" (the fractional circumference of a circle 32 km in radius not containing a barrier more than 300 m higher than the station) and "orientation" (the direction to the sector of greatest exposure).

By comparison, correlation of precipitation with elevation alone gave a value of only 0.55. The use of modern multiple regression techniques allows spatial patterns of residuals from the regression to be analyzed and this may enable additional parameters to be incorporated in the equations in order to improve the statistical explanation (Hutchinson, 1968; Bleasdale and Chan, 1972). This type of procedure has been used to construct precipitation frequency maps for mountain areas of the United States by Miller (1972) and to analyze elevation, orientation and inland distance effects on precipitation in West Africa (Gregory, 1968) and in the Great Basin of the western United States (Houghton, 1979).

A similar regression approach can also be used to estimate snow depth. Rhea and Grant (1974) find that 80 percent of the variance of water content on snow courses in Colorado and Utah can be accounted for in terms of two parameters: the directionally adjusted slope which potential precipitation-bearing air currents must cross for a distance of 200 km upwind; and the number of upwind barriers to the airflow.

A regression model developed by Daly et al. (1994), described as the Parameter-elevation Regression on Independent Slopes Model (PRISM), has been widely adopted in North America to provide statistical maps of mean monthly and annual precipitation from digital elevation model (DEM) information and point precipitation data distributed to regular grid cells. The model assumes that precipitation on a given slope increases up to the mountain crest (unless local station data show otherwise); hence it is primarily valid for mid-latitude mountains. They point out that the "best" DEM resolution for analysis depends primarily on the density of available precipitation data rather than on the scale of orographic effects on rainfall processes. However, for monthly precipitation in three regions in southeastern Australia, Sharples et al. (2005) found that the optimal DEM resolution for the topography-dependent interpolation of point data is around 6–8 km. Even low hills are known to produce precipitation enhancement (Bergeron, 1960) while deep narrow valleys may cause deficits (Longley, 1975) or the precipitation may be influenced by uplift over adjacent mountains. Nevertheless, topographic features of the order of 2–15 km in dimension are better correlated with precipitation amounts than smaller scale topography (Spreen, 1947; Schemmerhorn, 1967 and others). Daly et al. (1994) suggest that, because of this, a 5-min latitude–longitude ($\sim 6 \times 9$ km) DEM can often provide a better indication of the effective elevation of a precipitation station than its actual altitude. Each DEM grid cell is first assigned to a topographic facet based on slope orientation (north, south, east or west, if it is not flat) calculated from south–north and west–east elevation gradients across the cell. Precipitation for each DEM cell is estimated from a precipitation-DEM elevation regression function based on nearby precipitation stations. Where there are few data points for a facet, its spatial extent can be augmented using spatial filtering to retain only large-scale topography. Testing of PRISM compared with three geostatistical methods (kriging, detrended kriging and co-kriging) used by Phillips et al. (1992) for the Willamette River basin of

Oregon showed that PRISM results had lower bias and mean absolute error of predicted to observed values (from a detailed isohyetal map) than the other three methods. It should be noted that PRISM is less satisfactory for precipitation over local high-relief features and with summer convective precipitation. Nevertheless, it has been used by the Oregon Climate Service to produce mean precipitation maps for 1961–90 for each state in the contiguous United States, as well as for regions of the United States, the Hawaiian islands and Canada (http://www.wrcc.dri.edu/ precip.html). The US Natural Resources Conservation Service has also used PRISM for mapping temperature and other variables.

Modern studies mapping precipitation often seek to exploit the relationship between precipitation and secondary variables, such as elevation, slope orientation, exposure, etc. There have been a number of comparisons of these various techniques. Lloyd (2005) assesses whether such methods provide more accurate estimates than those that do not use secondary elevation data for mapping monthly precipitation in Great Britain. The techniques he applied were: (i) moving window regression (MWR); (ii) inverse distance weighting (IDW); (iii) ordinary kriging (OK); (iv) simple kriging with a locally varying mean (SKlm); and (v) kriging with an external drift (KED). For MWR, SKlm and KED, elevation data were used to determine their effect on precipitation estimates. The relationship between precipitation and local elevation, and its effect on the accuracy of estimates, were examined for each month of 1999. The performance of each method was assessed by examining mapped estimates of precipitation and cross-validation. Lloyd found that KED provides the most accurate estimates of precipitation for all months from March to December, while OK was most accurate for January–February. There was also a geographical pattern to the difference between the two methods. For locations in southeastern Britain, however, the difference between the methods was small.

Goovaerts (2000) examines various algorithms for incorporating a digital elevation model into the spatial prediction of rainfall for monthly and annual rainfall data for 36 climatic stations in a 5000 km region of Portugal. The performance of three geostatistical algorithms – kriging with varying local means; kriging with an external drift (KED); and collocated co-kriging – is compared with the linear regression of rainfall against elevation, and three univariate techniques – the Thiessen polygon (fitted to a network of stations that represent a watershed, for example); inverse square distance weighting; and ordinary kriging (OK). Larger prediction errors are obtained for the inverse square distance and Thiessen polygon methods that ignore both the elevation and rainfall records at surrounding stations. The three multivariate algorithms outperform other interpolators, in particular the linear regression, which takes account of spatially dependent rainfall observations and the collocated elevation. However, OK yields more accurate predictions than linear regression when the correlation between rainfall and elevation is moderate (below 0.75 in the case study).

Recently, a knowledge-based geostatistical approach to mapping precipitation has been evaluated for a region of the Sangre de Cristo Mountains, New Mexico by

Guan *et al.* (2005). They find it gives better maps of winter precipitation than PRISM and outperforms kriging and co-kriging with precipitation and elevation. They also show that, for winter, elevation is the primary factor and aspect a secondary one, while during the monsoon season the two factors have similar weight in the precipitation distribution. In September–October, only elevation is important whereas in May–June only aspect is important. The approach appears to be useful in identifying the meteorological processes, such as moisture transport, that are involved.

Estimation of *probable maximum precipitation* (PMP) – the maximum that can fall over a particular drainage basin during a specified time interval and season – is a particular problem in mountainous areas (Miller, 1982). In general, PMP estimates are based on an assessment of major storms over the basin, or closely similar regions, and the transportation of such storms to the area in question. The moisture in the storm is maximized based, for example, on the surface dew point value attained for 12 h or more. For the storm model it is generally assumed that the atmosphere is saturated with a pseudo-adiabatic lapse rate. Moisture inflow is determined from maximized wind speeds from representative directions. PMP estimates are made for areas of different size, up to that of the basin, and different duration, and the largest value for each duration and area is determined. In mountainous regions, various terrain influences will modify the precipitation characteristics. Miller describes two different approaches to estimating PMP in such situations. One possibility is to estimate PMP for lowlands adjacent to the mountains and then to make adjustments for orography. Large biases can be introduced by this approach, however, as shown for the Front Range in Colorado (see p. 403). The second method is termed "orographic separation;" it involves estimating precipitation generated by convergence using the above-described procedures for the non-mountainous portions of the basin. The orographic precipitation is then calculated using a multilayer flow model similar to Myers (1962) (see below p. 298) for several adjacent cross-mountain profiles. Values are then mapped for different time intervals. The two components – due to convergence and orographic uplift – are then combined. Other, purely statistical, approaches based on precipitation frequency data and probabilities of extreme values are also used if long records are available.

4.4.4   Snowfall and snow cover

Several studies show that, at lowland stations in middle latitudes, a threshold temperature can be used to discriminate type of precipitation on a statistical basis. For lowland Britain, there is an equal probability of precipitation occurring as rain or snow when the screen temperature is 1.5 °C; this implies a freezing level about 250 m above the surface (Murray, 1952; Lamb, 1955). In the mountains of central Asia, however, Glazyrin (1970) finds that this threshold temperature increases from about 1 °C at 500 m elevation to 4 °C at 3500–4000 m. Correspondingly, the range

about the threshold value, delimiting the temperatures below (above) which snow (rain) always occurs, increase from $\pm 2.5\,°C$ at 500 m, to $\pm 5\,°C$ at 3500–4000 m. This apparently reflects a higher frequency of snow occurring in shower form and perhaps also a locally steeper lapse rate. When rain is falling at near-freezing temperatures, the removal of latent heat of fusion from the air by melting snow-flakes is sufficient to cool a layer of 200–300 m deep (Stewart, 1985). Thus, if the wet-bulb temperature is $0\,°C$ at 300–400 m altitude when precipitation begins, snow may fall at altitudes of only 150–200 m within an hour according to Lumb (1983). Wet-bulb temperature is often better correlated with precipitation type than dry-bulb temperature, because snowfalls at positive temperatures are commonly associated with low relative humidity. In central Europe, snowfalls are rare when wet-bulb temperatures exceed $2\,°C$ (Steinacker, 1983). Moreover, the intensity of such falls is usually low (Rohrer, 1989).

The fraction of annual precipitation falling as snow obviously increases with altitude. Even in July–August, 65 percent falls in solid form (excluding hail) at 3000 m in the eastern Alps, whereas the figure drops to only 12–15 percent at 2000 m (Lauscher, 1976b). For European mountain stations, Lauscher has developed a general relationship between solid precipitation, altitude and mean monthly temperature (Figure 4.21). The annual solid fraction, for a mean temperature of $0\,°C$, increases from about 40 percent near sea level to 75 percent at 3000 m, with the most rapid increase taking place in the lowest thousand meters. Thus, for the Sonnblick Observatory (3106 m), the relationship between solid precipitation (S) as a percentage of total, and mean monthly temperature (°C) is:

$$S = 75 - 8T$$

Fig. 4.21 **Empirical relationship between monthly mean temperature (°C) and annual percentage frequency of solid precipitation in the northern hemisphere compared with the regression (50–5T) (from Lauscher, 1976b).**
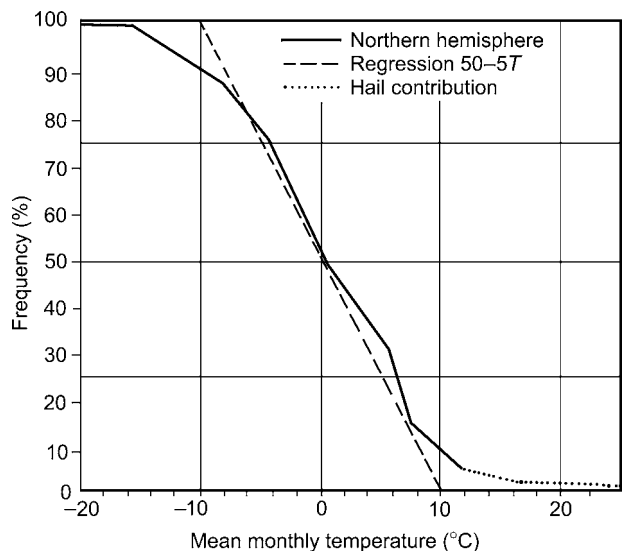
whereas the global relationship for stations near sea level is:

$$S = 50 - 5T$$

A study using data from 32 Swiss stations located between 300 and 1800 m (mean station altitude 716 m) by Sevruk (1985) indicates

$$S = 61 - 5T$$

between 1000 and 1800 m altitude, and

$$S = 41 - 3.5T$$

between 500 and 700 m altitude. Sevruk illustrates graphically the variation of these relationships over the cold season. The mean monthly temperature for which half of the monthly precipitation falls as snow varies between $-1.9\,°C$ in January and $3.9\,°C$ in April; it is $0\,°C$ in November and February.

When the snowfall fraction is expressed directly in terms of altitude, there is a general linear relationship (Conrad, 1935). The same is true for days with snowfall (Yoshino, 1975; p. 218). In the eastern Alps, the number of days with snowfall increases linearly from about 30 days at 300 m to 50 days at 1000 m and then slightly more rapidly to around 100 days at 1800 m and about 185 days at 3000 m (Geiger et al., 2003; p. 408). Linear relations are also found for snow cover duration in the Tatra (Koncek, 1959) and in the French Alps, although the relationship of snow cover duration to altitude in the inner Savoy Alps may become curvilinear with an upward increase (Poggi, 1959). Slatyer et al. (1984) cite linear relationships for snow cover duration in the Australian Alps ($38°$ S), the Swiss Alps ($47°$ N), and Britain ($53°$ N), which differ only in the constants relating to the latitudinal variation of mean temperature. A snow cover duration ≥ 90 days is found above 930 m in Switzerland, but only above 1700 m in Australia.

Many regional studies of snowfall and snow cover have been performed and it is now beginning to be possible to compare empirical relations developed in different areas. Jackson (1978) has re-evaluated British data using median rather than mean duration since the latter is strongly biased by abnormal values. Given the sea level median duration of snow cover (D_0) (defined as a day with more than half of the ground covered at 0900 GMT), the duration at any altitude (D_H) is given by:

$$D_H = D_0 \exp(H/300) \text{ for } H < 400 \text{ m}$$
$$\text{and } D_H = 3.75\, D_0[1 + (H - 400)/310] \text{ for } H > 400 \text{ m}.$$

Hence, the relationship is linear above 400 m. Jackson notes that data for Vancouver, British Columbia, fit a similar profile. In both areas, the steep lapse rates associated with maritime air masses cause substantial increases in snow cover with altitude. The rate of increase varies with latitude from 5 days per 100 m in southwest England to 15 days per 100 m in the Scottish Highlands where there are
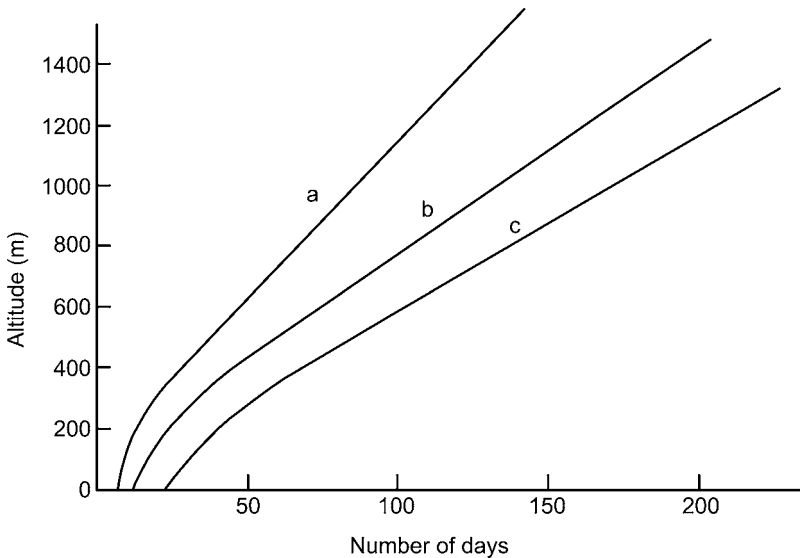
Fig. 4.22 **The average number of days with snow lying versus altitude on various mountains in Great Britain: (a) an average mountain in the west of Great Britain; (b) an average mountain in the whole of Great Britain; (c) an average mountain in central Scotland (from Jackson, 1978).**

typically 220 days with snow cover at 1200 m (Manley, 1971). Mountains in central and eastern Scotland have considerably greater durations of snow cover than mountains in western Britain (Figure 4.22).

In the Tyrol of Austria, snow cover duration increases quite rapidly with elevation up to about 2000 m and then amounts increase substantially above about 2400 m (see Figure 4.23).

Snow depth in a small area varies at horizontal scales of 1–100 m due to the interactions of precipitation amounts, wind transport, and melting/sublimation with the local terrain and vegetation cover. Deems *et al.* (2006) show that depth characteristics differ with horizontal scale. Below 15–40 m, a fractal dimension $(D) \sim 2.5$ indicates large spatial variability ("roughness") while at greater distances $D \sim 2.9$ indicating nearly random variability. The variation of snow depth with altitude is generally complex, even when local differences due to relief effects and small-scale terrain features are ignored. For example, in Austria the average maximum depth of snow increases (although not linearly) up to about 1000 m, where there is a pronounced decrease, followed by a further increase above this level (Steinhauser, 1948). This pattern is attributed to the frequent winter occurrence of an inversion between about 900 and 1100 m, with cold foggy conditions in the valley and clearer skies with more radiation falling on the slopes above. In the Swiss Alps, snow depths (water equivalent) appear to be maximal around 2700 m altitude, and may decrease slightly above, according to Martinec (1987). His estimates

Fig. 4.23 Snow cover depth and duration at different elevations in Austria (F. Steinhauser, 1974).
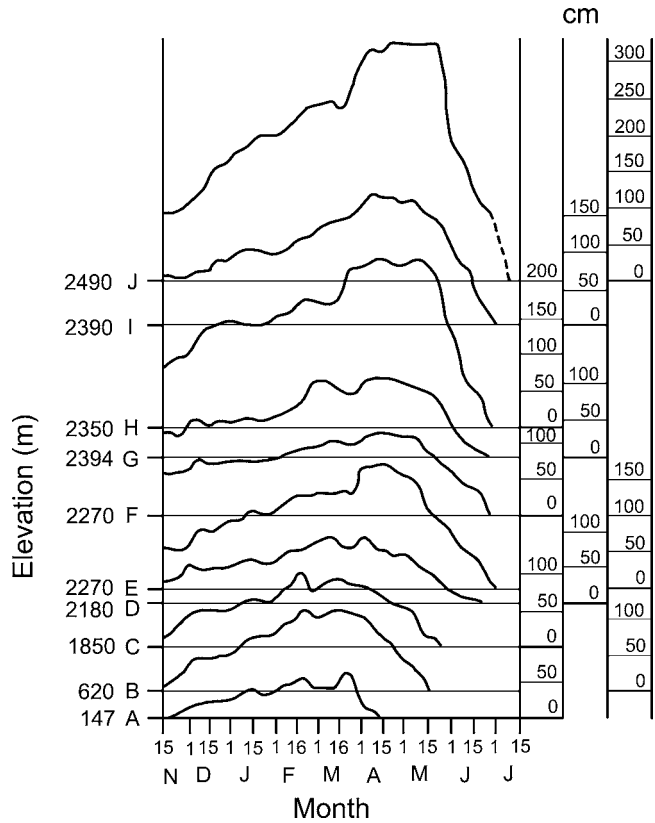
are based on depletion curves of basin snow cover, where the usual time axis is replaced by the cumulative snow-melt derived from calculated daily values for several years. From satellite observations of the seasonal reduction in basin snow-covered area, an estimate of snow water equivalent at the beginning of the melt season can be obtained.

In the San Juan Mountains, Colorado, Caine (1975) finds an elevation influence in the relative variability of maximum snow pack as well as on the accumulation. The latter increases linearly at a rate of 65.5 cm km^{-1} (with a correlation coefficient of 0.66 for 24 snow courses) from a zero-accumulation level at 2400 m. Variability, on the other hand, decreases with increasing elevation. Caine notes that this may in part reflect the longer season of snow accumulation, which at 3500 m is about twice that at 2600 m, with consequently a greater number of storms helping to even out the year-to-year differences. However, since this inverse relationship is concentrated in years with above-normal snowfall, whereas below-normal years show a direct relationship, Caine suggests that there is an interaction between topography and atmospheric factors. In snowy winters, there is a high frequency of cold lows, which cause widespread precipitation with relatively more falling at low elevation, whereas in winters with light accumulation there is a higher frequency of local

Fig. 4.24 The altitudinal gradient of winter precipitation (solid dots) determined from snow-course data and accumulation measured on glaciers in the Front Range, Colorado in 1970 expressed as snow water equivalent (from Alford, 1985).
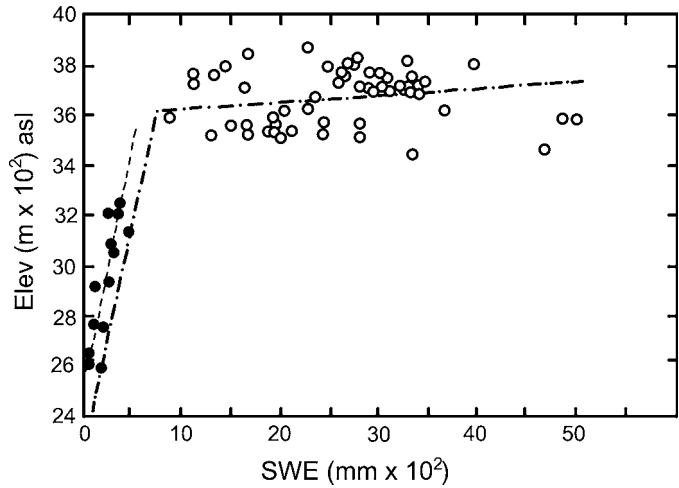
storms, which nevertheless provide sufficient snowfall to keep the pack on snow courses at high elevations closer to average depth.

In high mountain areas, snow accumulation is sometimes recorded only in glacier basins. Figure 4.24 illustrates the contrast between measurements from snow courses below tree line and accumulation on cirque glaciers in the Front Range, Colorado (Alford, 1985). The high accumulation on the glaciers is apparently caused by large-scale rotors on the lee side of the Front Range summits that transport snow back into the cirque basins.

4.4.5 Theoretical models of orographic precipitation

There are two basic approaches to modeling orographic precipitation on windward slopes in terms of water vapor flux: the upslope and the parcel models (Smith *et al.*, 2005). The upslope model determines the point precipitation from the terrain gradient and the horizontal water vapor flux at the surface. Theoretical analysis of precipitation rates over mountains has a long history. Pockels (1901) used the hydrodynamic equations for frictionless two-dimensional flow to calculate vertical velocities and condensation due to adiabatic ascent over an idealized slope, specified by Fourier functions. He concluded that slope angle was more important than absolute height for the precipitation rate on a windward slope. Wagner (1937) noted that Pockels' model ignored the effect of air motion on fallout. Thus snowflakes, in the presence of strong winds, may not show any altitudinal maximum, whereas large drops are little affected by wind. He cited winter and summer observations from the vicinity of the Sonnblick to support this argument. Another similar theoretical analysis to that of Pockels was carried out by Ono (1925) and tested with Japanese data. This type of formulation tends to over-estimate regional precipitation unless the terrain is sufficiently smoothed.

The parcel method assumes saturated adiabatic ascent with instantaneous condensation, raindrop formation and fallout. Precipitation is calculated from the vertically integrated condensation above each point. The decay of forced ascent aloft has to be prescribed, together with a history of upstream lifting and drying. The drying ratio is given by the water vapor removed / initial amount of water (Smith *et al.*, 2005).

Modeling of orographic precipitation has subsequently followed two broad lines of approach. Some analytical studies have used a combination of the Bernoulli equation, the continuity equation and hydrostatic flow for mountains of arbitrary shape. Other analyses have been based on the perturbation method (see below) and idealized barriers. Most models at present are two-dimensional, for a mountain cross-section, although a few numerical models are now three-dimensional. The treatment of water substance is quite variable, it has received considerable attention since many studies of orographic precipitation are related to cloud seeding assessments. In some models, all of the condensed moisture is precipitated, others use various "precipitation efficiency" factors; for "warm" clouds (with temperatures above about $-10\,°C$), such as occur over the low coastal ranges of California, the ratio of precipitation to condensate is about 0.3, increasing to about 0.6 for "cold" clouds in winter cyclones over Colorado mountains (Marwitz, 1974). In models such as those of Young (1974) and Nickerson *et al.* (1978), cloud microphysics is also incorporated.

The essential components of an orographic precipitation model include measures of the vertical displacement of air over the barrier, adiabatic ascent (descent), condensation (evaporation), and precipitation of some fraction of the condensate. It may also be important to include "blocking" of the low-level airflow by the barrier and lee-wave effects.

For simple barriers, several models use a calculation of the vertical transport of water vapor due to the mean terrain slope. The horizontal wind may be adjusted directly to the mean flow perpendicular to the barrier (Elliot and Shaffer, 1962; Myers, 1962), or for actual topography the vertical wind component (w_s) relative to the slopes can be determined by:

$$w_s = \frac{u\,dh}{dx} + \frac{v\,dh}{dy}$$

This is used by Danard (1971), for example. Illustrative maps of terrain-induced vertical motion have been prepared for the Appalachian Mountains (Jarvis and Leonard, 1969) and the Canadian Arctic (Fogarasi, 1972), indicating values of $\pm\,2–10\,\mathrm{cm\,s^{-1}}$ for winds of $10\,\mathrm{m\,s^{-1}}$. The theoretical decrease with height of terrain-induced vertical motion has an approximately parabolic profile (Berkovsky, 1964). The magnitude is less than half of the surface value at 700 mb.

A simple orographic precipitation model is proposed by Roe *et al.* (2000; Anders *et al.*, 2004). Precipitation rate (p) is expressed as a function of the slope aligned

with the wind (S), saturation vapor pressure (e_s) as a measure of precipitable water content and surface air temperature (T)

$$p = (a + bS)e_s T$$

where a and b are constants for the region modeled.

In an application evaluating Tropical Rainfall Measuring Mission (TRMM) radar-derived precipitation estimates for the region 25–36° N, 64–106° E and a sub-region 29–31° N, 94–96° E. Anders *et al.* (2004) conclude that the model captures features at the 10 km scale but not the large east–west precipitation gradient (see Chapter 5, p. 414), nor maxima < 200 km in scale. The TRMM patterns for 1998–2001 display repeatable features caused by topographic effects, including a tongue of high values northward along the Tsangpo–Brahmaputra River valley and also recurring small scale features in the sub-region.

Myers (1962) uses an airflow model based on the work of Scorer (see p. 155) for the mechanical lifting of stable air. The orographic precipitation in t hours is expressed:

$$P_t(10^{-3}\text{cm}) = \frac{\Delta p}{g}\left(\frac{\bar{V}t}{\Delta x}\right)(\bar{q}_1 - \bar{q}_2)$$

where Δp is the depth of the air current to windward of the barrier (mb); $\bar{V}$ is the mean wind speed in layer Δp, perpendicular to the barrier (km h^{-1}); Δx is the downwind distance (km) over which precipitation falls; $g = 9.81$ m s^{-2}; and $\bar{q}_1$ and $\bar{q}_2 = $ mean specific humidity (g kg^{-1}) of the air to windward and leeward.

The calculated precipitation with this model is about one-third too large, due to the saturation assumption.

An elaboration of this type of approach by Elliott (1977) expresses the orographic component (P_s), defined as the mountain precipitation minus the upwind lowland amount, by:

$$P_s = \bar{V} \tan s \, (-\partial q/\partial z)\Delta C$$

where $\bar{V}$ is the mean wind perpendicular to the slope (assumed uniform); s is the slope angle; and ΔC is the cloud depth.

Again, the model assumes cloudy air with all of the moisture being condensed. Rhea (1978) has adapted this scheme to develop an operational model for winter precipitation in the Rocky Mountains of Colorado. It is a steady-state, multi-layer model incorporating upstream barrier effects, but not allowing for horizontal streamline displacement. After calibration of model parameters against two seasons of snow course and precipitation data, an analysis of 13 winters was performed using twice-daily upper-air soundings as input. Calculated seasonal totals correlate well with observed spring runoff, and a derived map of mean precipitation for the 13 winters compares favorably with one based on point observations and

altitudinal–topographic regressions. The model gives the best results for ridges and high plateaus, but overestimates amounts in narrow mountain valleys and under-estimates for broad intermontane basins. It has been verified for southwest Colorado by Hay and McCabe (1998).

More complex models have been developed based on the perturbation approach. The motion in an x,z plane (where x here is along the wind direction), can be expressed as a perturbation superimposed on a steady basic current of velocity, V. The linearized equations for the perturbation vertical velocity were originally developed by Queney (1948) and Holmboe and Klieforth (1957). The following abbreviated presentation is based on Walker (1961) and Wilson (1978). The approximate vertical velocity equation is:

$$\frac{d^2\omega(z,k)}{dz^2} + [f(z) - k^2]\omega(z,k) = 0$$

where ω is the amplitude of the vertical velocity (sinusoidal with wave number k); k is the wave number of the ground profile (assumed sinusoidal) in the x direction; and

$$f(z) = \frac{\partial(\ln\theta)}{\partial z}\frac{g}{V^2} - \frac{1}{V}\frac{\partial^2 V}{\partial z^2}$$

$\partial(\ln\theta)/\partial z$ is the static stability expressed in terms of potential temperature, θ. This expression for $f(z)$ is used extensively in meso-scale studies (see p. 154). For rainfall situations in British Columbia, $f(z) = 0.09\,\text{km}^{-2}$, in unstable situations $f(z) \to 0$.

The lower boundary condition, assumed to be sinusoidal, has an amplitude:

$$\begin{aligned}\zeta_0 &= f(k)\cos kx \\ &= ah\exp(-ak)\cos kx\end{aligned}$$

where h is the maximum height of the perturbation in the surface profile; a is the "half width" (the distance along x from the mountain crest to the point where $\zeta_0 = h/2$); and ζ is the streamline displacement.

The idealized surface profile is shown in Figure 4.25 for $h = 1\,\text{km}$ and $a = 10\,\text{km}$. Two airflow cases are illustrated from Walker (1961).

Case 1. Static stability $\partial(\ln\theta)/\partial z = 0$, and $\partial V/\partial z = 0$. Thus $f(z) = 0$. This leads to the perturbation vertical velocity:

$$W = -\frac{2axhV(a+z)}{[(a+z)^2 + x^2]}$$

and

$$\zeta_z = \frac{ah(a+z)}{[(a+z)^2 + x^2]}$$
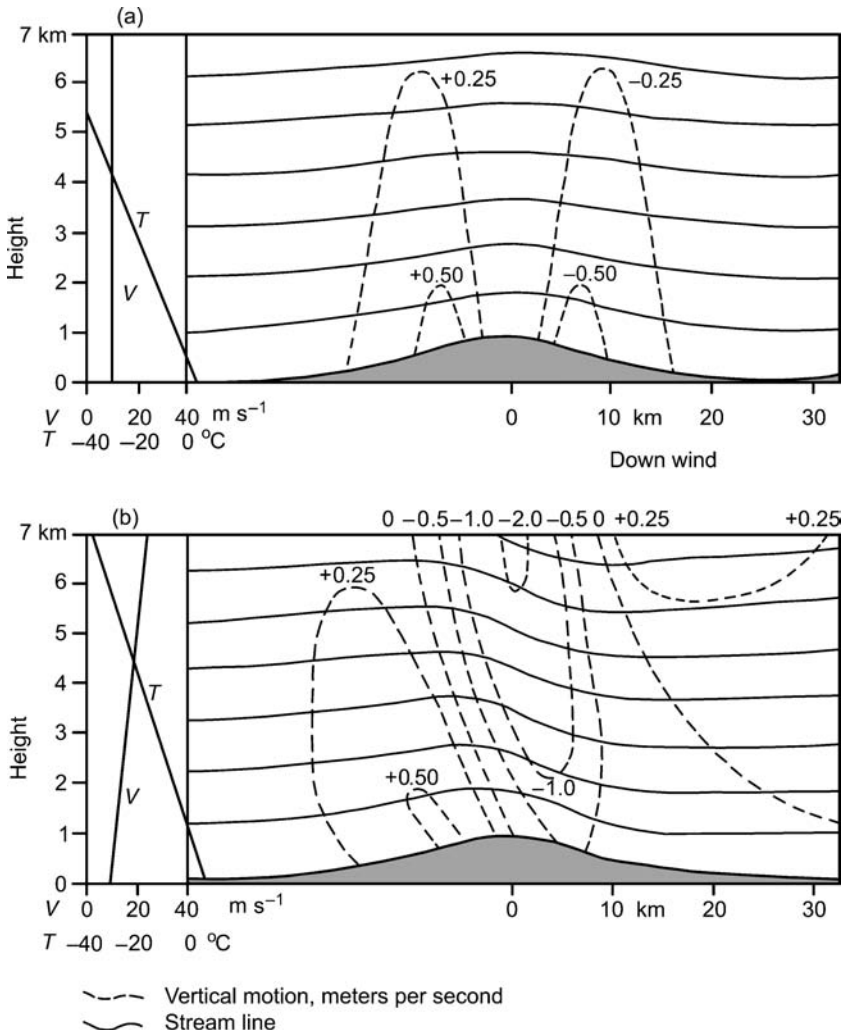
Fig. 4.25 **Orographically induced vertical motion for a simple barrier with westerly flow: (a) $f(z) = 0$; (b) $k = 0$ (from Walker, 1961). The solid lines are streamlines; the dashed lines are vertical motion (m s^{-1}). The assumed gradients of wind speed and temperature are shown.**

for the streamline perturbation at some upper level, z. The example shown in Figure 4.26a is fairly representative of mid-latitude west coast mountains in summer.

Case 2. $k = 0$. This represents the general mountain perturbation, excluding possible lee waves. Here,

$$W = -\frac{2axhV}{(a^2 + x^2)}\left\{ a\cos\sqrt{f(z)}Z - x\sin\sqrt{f(z)}Z \right\}$$
$$-\frac{ahV}{a^2 + x^2}\sin\sqrt{f(z)}Z$$
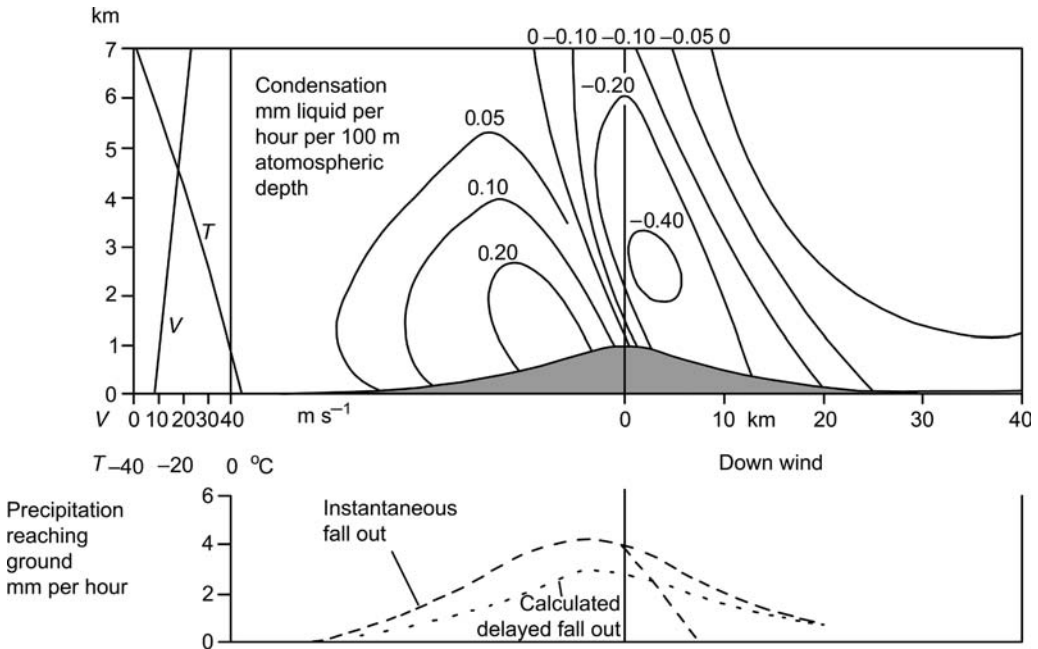
Fig. 4.26   Calculated condensation and precipitation (mm h^{-1}) for the airflow case shown in Figure 4.25 (b) (from Walker, 1961).

and

$$\zeta_z = \frac{ah}{a^2 + x^2}\left\{a\cos\sqrt{f(z)}Z - x\sin\sqrt{f(z)}Z\right\}$$

The solution for ζ_z is periodic in the vertical with wavelength $= 2\pi/\sqrt{[f(z)]}$. In Figure 4.26b, $\sqrt{[f(z)]}$ is approximately 0.3 km^{-1}.

There is a good agreement between Walker's (1961) version of this model and climatological profiles across British Columbia, where most of the precipitation falls with westerly or southwesterly tropospheric flow during the cold season. Precipitation amounts are calculated from the estimated condensation rate for saturated airflow (Fulks, 1935) crossing an idealized mountain range. The assumed air temperature and wind speed profiles are shown in Figure 4.26b. Two alternative precipitation rates are determined: one assumes instantaneous fallout, with terminal velocities of 5 m s^{-1} for raindrops and 1 m s^{-1} for snowflakes; the other assumes delayed fallout with appropriate droplet coalescence (50 percent of the droplets fall out in 10 min for a rainfall rate of 2.5 mm h^{-1}). Precipitation is assumed to fall through the evaporation zone both with and without loss. The frequency of airflow directions at 700 mb in 1956 was used to compute mean seasonal profiles. An annual profile, combined with observations of precipitation frequency and amounts, also allowed Walker to construct improved mean precipitation maps over southern British Columbia.

Fig. 4.27 Model simulations for a storm with a westerly airflow over northern California, 21–23 December 1964: (a) computed steady-state vertical motion field (cm s^{-1}); (b) computed precipitation rate (solid line) and observed values (dots) (from Colton, 1976).
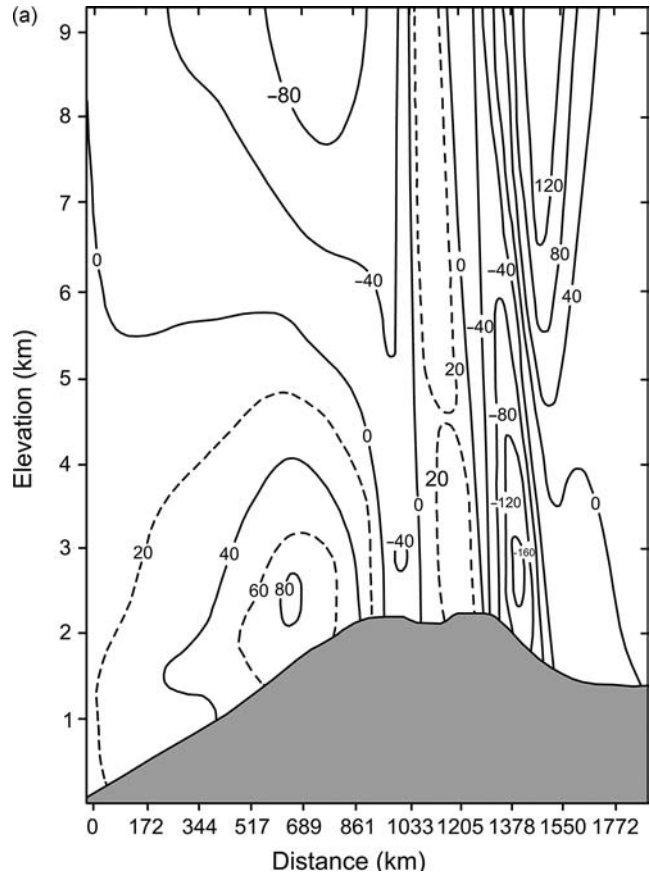
Sarker (1966, 1967) independently used the same basic model for the Western Ghats of India. The results correctly position the maximum falls near the crestline on days of strong monsoon flow, and on average the model accounts for about 65 percent of the coastal precipitation. It also suggests that "spill-over" on the leeward slope, due to the winds, extends less than 10–15 km beyond the crest. This result may not be general, however. Walker suggests that most of the leeside evaporation of cloud droplets and precipitation due to streamline descent takes place from the smaller particles, based on calculated and observed precipitation profiles (Figure 4.27). Studies of westerly airstreams crossing the Cascade Mountains in California indicate that solid precipitation can be transported up to 50–70 km downwind (Hobbs et al., 1973; Hobbs, 1975). This is most likely when crystal aggregation is unimportant, if ice particle concentrations are about 100 l^{-1} and growth is mainly by deposition rather than riming. All of these effects favor particles of low density and small fall speed.

More recent modeling studies use the primitive equations of motion. A meso-scale numerical model developed by Colton (1976), originally in two-dimensional
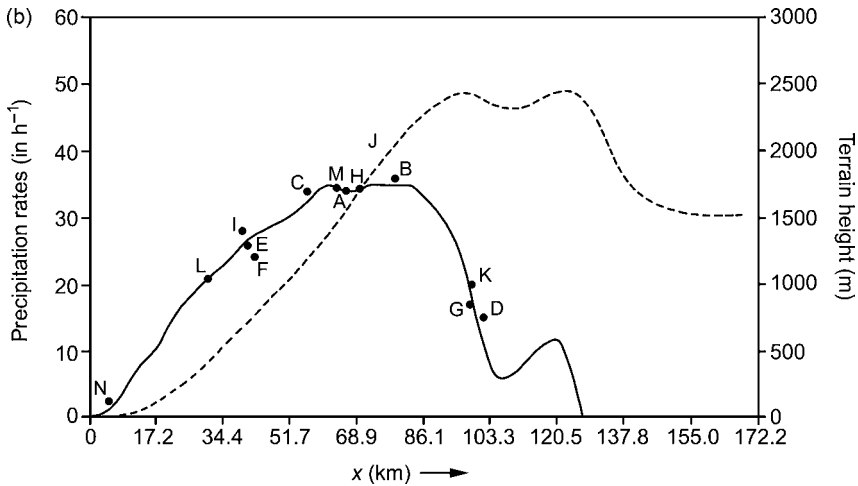
Fig. 4.27 (cont.)

form, has seven equations as follows: the horizontal momentum equations (to predict the horizontal components of motion), the diagnostic mass continuity equation (to determine vertical motion), the thermodynamic equation (to obtain potential temperature), the continuity equations for water vapor and for liquid water, and the hydrostatic equation. Computations for cases of westerly airflow over the Sierra Nevada Mountains used geostrophic winds and sounding data as input at 13 levels (0 to 11 km) with a fine mesh (4.3 km) resolution, except towards the lateral boundaries. Results for a situation on 21–23 December, 1964, which caused severe flooding in northern California (Figure 4.27) indicate a realistic vertical motion field, correct positioning of maximum precipitation rates, and an appropriate degree of spillover. A different meso-scale boundary-layer model has been used to study the effect of arctic outbreaks over the foothills of the Rocky Mountains in Alberta (Raddatz and Khandekar, 1977). They demonstrate the sensitivity of "upslope" weather to surface heating through its triggering of convective precipitation.

Smith and Barstad (2004) developed a model of orographic precipitation that includes airflow dynamics, condensed water advection, and leeside evaporation. The model adopts linear treatments of mountain waves and cloud physics. It uses the product of a double Fourier transform of the terrain ($\mathbf{h_{k,l}}$) and a transfer function to obtain the double Fourier transform of the precipitation field, $\mathbf{P_{k,l}}$. An inverse Fourier transform is used to determine the spatial pattern of precipitation. The transfer function incorporates a condensation coefficient, C, the moist layer depth, H_Q, time scales for droplet conversion, τ_C, and fallout, τ_F. The general form of the equation is:

$$\mathbf{P_{k,l}} = \frac{C \iota\sigma \, \mathbf{h_{k,l}}}{(1 - \iota\, m H_Q)(1 + \iota\sigma\, \tau_C)(1 + \iota\sigma\, \tau_F)}.$$
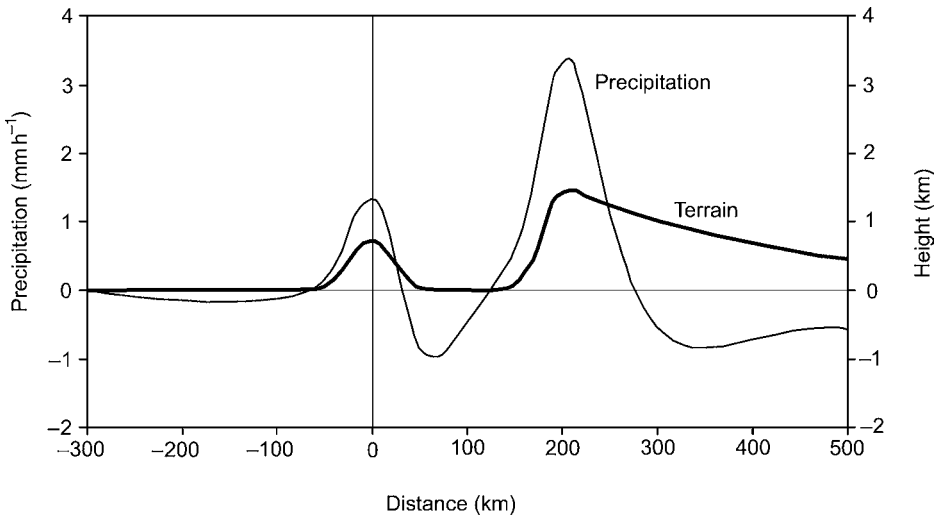
Fig. 4.28 Precipitation rate (mm h^{-1}) for idealized terrain heights (km) in western Oregon according to the linear theory of Smith and Barstad (2004) (from Smith *et al.*, 2005).

where $\iota = \sqrt{(-1)}$; the intrinsic frequency $\sigma = Uk + Vl$; and $m_{k,l}$ is the vertical wave number. The terms in the denominator of the equation represent: the airflow dynamics; advection during the conversion of cloud droplets to hydrometeors; and the advection of hydrometeors during fallout, respectively.

The model predictions show that the wind direction, stability, and especially the cloud time delay (τ), are the sensitive parameters for point precipitation. The cloud time delay (in the range 0–1000 s) is the primary control of the amount of point precipitation, while the stability tends to shift the precipitation pattern. Figure 4.28 illustrates the precipitation rates calculated by this linear theory for idealized terrain in western Oregon. Smith *et al.* (2005) estimate that the cloud delay time in Oregon is of the order of 20–40 min and the drying ratio is about 43 percent. They also determine that the effective terrain width is 23 km implying that relatively small-scale terrain elements are important in the distribution of orographic precipitation. A similar conclusion was reached in studies in the Alps (Smith *et al.*, 2003). Barstad and Smith (2005) examine the use of rain gauge data from several field campaigns in complex terrain to test their linear model. They conclude that the observational networks are inadequate to determine representative values of cloud delay time.

The advent of numerical modeling techniques and aircraft observation of orographic clouds has greatly augmented our understanding of orographic precipitation. Up to now, however, most of the attention has focused on synoptic investigations with an emphasis on possibilities for precipitation augmentation via cloud seeding. The interpretation and generalization of many of these findings in a climatological context is still largely unexplored.

The prediction of orographic precipitation presents special problems because the spatial resolution, even of fine mesh models, is inadequate to account for most

orographic features. One procedure is to use the output of a prognostic model as input to a fine resolution diagnostic model. Tucker and Reiter (1988) use a six-layer primitive equation model over the United States, within which is nested a 1000×1000 km domain over the southern Rocky Mountains. Terrain influences on the lowest two levels cause modifications to the wind fields and, therefore, affect mass and moisture divergence and precipitation. Realistic simulations of two terrain-related heavy rainstorm and flood events are obtained. Another approach is to use satellite and radar data for short-term forecasts and flood warnings ("nowcasting") (Browning, 1980). Both model predictions and "nowcasting" information can be refined by empirical data on the local-scale precipitation climatology, categorized according to synoptic types. Using a dense local gauge network in north Wales, UK, Nicholass and Harrold (1975) analyzed the precipitation over sub-catchments of about 60 km^2 (R_c) versus the average amount over the entire 1000 km^2 area (R). The mean ratio $\overline{R}_c/\overline{R}$ varied from about 0.5 to 2.0 according to sub-catchment, synoptic type and surface wind. Such statistics can be incorporated into forecasts.

4.4.6   Observational problems

It has been assumed up to now that precipitation amounts can be reliably measured. In fact this is far from the case. This section examines rainfall and snowfall observations; other moisture inputs are discussed in the following section.

The errors involved in the measurement of liquid and solid precipitation are illustrated in Figure 4.29. They involve the wind field determined by the topography in the general area, the immediate site characteristics affecting air motion over the gauge top, the gauge height and design, especially its rim, specific measurement difficulties, and observer error. Errors can be characterized as non-systematic (e.g. site-specific factors, instrument malfunction, observer error) and systematic biases related to gauge design, type of precipitation and wind speed over the gauge, for example. The latter can be assessed and appropriate adjustments made to the reported raw data. Some of these factors have been investigated minutely in lowland situations. Rodda (1967) shows, for example, that rain catch in a standard gauge mounted on the ground with a rim at 25 cm height is systematically 6–8 percent less than that caught by a ground level (sunken) gauge. This error increases as the gauge top is raised above the ground; a problem first noted over a century ago by Jevons (1861). The source and magnitude of systematic errors in precipitation measurement are estimated to be the following (Sevruk, 1986a): wind-field deformation above the gauge, 2–10 percent for rainfall and 10–50 percent for snowfall; losses from wetting of the internal walls of the collector and measuring container, 2–10 percent; evaporation losses, 0–4 percent; splash-out/in, 1–2 percent. The overall systematic error is about 5–15 percent for rainfall and 20–50 percent for snowfall. However, "correction" factors are valid only for particular gauge types and site exposure. Mountain terrain creates severe problems of data inhomogeneity in time

Fig. 4.29 Schematic summary of processes and problems involved in the determination of rain gauge catch (after Rodda, 1967).
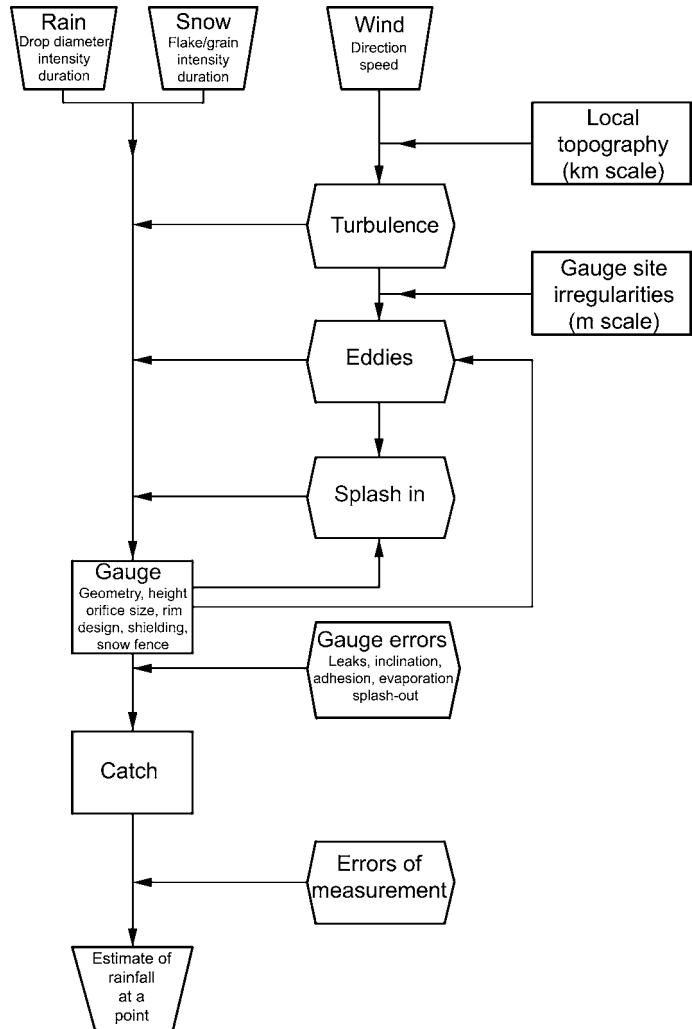
and space (Sevruk, 1989). Storage gauges, which are often used in remote areas are also affected by evaporation losses when the gauge is read infrequently. A film, at least 5 mm thick, of a "suppressant" such as a glycol can be used to prevent this (Sevruk, 1972b).

It is well recognized that snowfall is seriously underestimated with standard precipitation gauges due to wind effects (Sevruk, 1989). The gauge catch is a function of wind speed over the gauge, and snowflake fall velocity. The latter, of the order of 0.5–1.5 m s^{-1}, depends on crystal shape, which is also temperature dependent. Snowfall catch is also affected by the gauge dimensions and by the geometry of the orifice rim, which modify airflow, and by the effects of gauge wetting and losses due to evaporation. Currently, some 50 different types of standard gauge are in use by national meteorological services worldwide (Sevruk and Klemm, 1989).

Considerable attention has been given to the problem of gauge shielding to minimize wind eddies around a gauge. However, neither the solid shield, invented by F. E. Nipher (1878), nor the flexible Alter (1937) type is adequate by itself in windy mountain locations where a significant fraction (>20 percent) of the precipitation falls as snow. Shields of the Alter type commonly blow apart in strong winds and the rigid shield often causes a larger underestimate due to "bridging" of snow over the orifice. While no absolute reference standard exists, Larson (1971) demonstrated that the catch of a gauge with an Alter shield in Wyoming was only 66–75 percent of a similarly shielded gauge surrounded by snow fencing. The purpose of the snow fence is to minimize local site eddies. Further experiments of this type have been conducted in the same locale (Rechard, 1972), using various configurations of 1.2 m vertical-lath fences of 50 percent density with a gap at the base of between 15 and 30 cm.

During the 1980s and 1990s, the World Meteorological Organization (WMO) carried out an intercomparison of rain and snowfall data obtained with different gauges and windshields, known as the Solid Precipitation Intercomparison Project (Goodison *et al.*, 1989; Yang *et al.*, 2001). Measurements were made at 23 stations in several climatic zones, employing selected standard national gauge types – the Hellmann (Europe), the Nipher (Canada), the Tretyakov (Russia) and the US National Weather Service 8-inch standard gauge. The differences were <5 percent for rainfall, but up to 110 percent for snowfall totals. To reduce these differences a double wind fence can be mounted around a gauge equipped with a windshield. One design, the "blow fence," has the shielded gauge within two concentric circles of fence; the inner one has a 1.5 m radius and slopes at $60°$, with the base of the fence positioned 0.6 m above the base of the gauge, which is itself 1.5 m above the ground. The object is to keep the area beneath the gauge free of snow accumulation by directing airflow downward. Analyses suggest that while this installation catches less than reference gauges in forest clearings, the degree of protection seems to be relatively constant for wind speeds of 4–$9\,\mathrm{m\,s}^{-1}$.

A further WMO investigation – the Double Fenced Intercomparison Reference (DFIR) gauge project – has enabled bias corrections to be developed for the gauges referred to above, which are in common use around the world. An octagonal vertical double-fence shield, surrounding a Russian Tretyakov (shielded) precipitation gauge mounted at 3 m, is the adopted Intercomparison Reference (see Figure 4.30). The vertical 50 percent density fences form 12 m and 4 m diameter circles; the outer one is 3.5 m and the inner one 3 m high, with gaps between the base of the fences and the ground of 2 and 1.5 m, respectively. Goodison *et al.* (1998) report that the catch of both the Canadian AES–Nipher shielded gauge and the Universal Belfort gauge with a Nipher shield were almost identical to that of the DFIR in a 1-month field test in January 1987. Golubev (1986) reported the results of a long-term study of the Tretyakov gauge in an open plot surrounded by double fence structures of different dimensions (installed both vertically and inclined outward $15°$), with a control gauge in a plot sheltered by bushes. The

Fig. 4.30 WMO DFIR and
Wyoming shield gauges
(AGU, 2000).

results (Table 4.4) show the necessity for the double fence installation, especially for solid precipitation. Moreover, at wind speeds $> 5\,\mathrm{m\,s^{-1}}$, some correction for wind speed is required even for fenced gauges.

Since the late 1970s, the Wyoming double-fence gauge (Figure 4.30) has been used to measure snowfall at more than 25 locations in Alaska (Yang *et al.*, 2000). At Rabbit Ears Pass, Colorado (2925 m), the Wyoming double fence gauge, recorded 94 percent of the snowfall registered by a Tretyakov gauge equipped with the DFIR for a mean wind speed of $3\,\mathrm{m\,s^{-1}}$ at 3 m height, the same height as the gauges. Comparisons of Alter-shielded gauges (widely used in the western United States) and the DFIR gauge show that gauge under catch of the former is 30 percent for average wind speeds of 2.4–$4.3\,\mathrm{m\,s^{-1}}$, increasing to 54 percent for winds averaging 5–$6\,\mathrm{m\,s^{-1}}$ (Fassnacht, 2004).

As indicated in Figure 4.29, gauge catch is strongly affected by local and microscale wind effects. The effect of slope aspect on precipitation has been the subject of various investigations with rather differing conclusions. In Yorkshire, England,

Table 4.4 Ratios of precipitation measured at Valdai, Russia, by Tretyakov gauges with various fence configurations compared with a control gauge surrounded by bushes.

Fence type[a]	Fence heights (m) Outer (inner)	Gauge orifice height (m)	December	April	July	Year
1V	2.5 (2.0)	2.0	0.96	0.96	0.99	0.95
1I	2.5 (2.0)	2.0	0.92	0.98	0.99	0.96
DFIR	3.5 (3.0)	3.0	0.91	0.95	0.90	0.93
1V	2.5 (2.0) circle diameters 4 m, 2 m	2.0	0.88	0.89	0.95	0.91
Wyoming (I)		2.0	0.82	0.87	0.93	0.88
–	Unfenced	2.0	0.66	0.87	0.98	0.84

[a] See text for further description of DFIR and Wyoming type. Type 1 differs in having shorter fences with basal gaps of 1 m and 0.5 m. V denotes vertical fences, I = inclined outward 15°.
Source: after Golubev (1986).

Reid (1973) maintained two grids, each of six gauges, across the 12°–15° slopes of a west–east valley about 60 m in depth. For a 50-week period, the north-facing slope received 8 percent less than the south-facing one. The latter was a windward slope for 49 percent of the time with precipitation and leeward 28 percent of the time. In contrast, Hovkind (1965) recorded the maximum on the lee of the crest of a conical hill near Santa Barbara, but he considered that these gauges may have over-recorded relative to ones on the windward side. Indeed, such a pattern of over- and under-representation has been found on a larger scale. Grunow (1960) shows that at Hohenpeissenberg Observatory (975 m) in Bavaria, the catch on the windward slope may be under-estimated 14 percent and that on the lee.

Correction factors for monthly totals are typically about × 1.06 for shielded gauges in summer, but are of the order of × 2 for winter precipitation, with light winds (3 m s^{-1} at 2 m) (Goodison *et al.*, 1989). Sevruk (1986b) gives a general equation for estimating corrected monthly precipitation:

$$P_{k\kappa} = k(P_m + W)$$

where P_m is the precipitation total from daily gauges; k is the conversion factor for wind speed over the gauge orifice; and W is the correction for wetting losses.

He provides detailed tables of these coefficients for Switzerland. The value of k varies with gauge type, the wind speed during precipitation, and a precipitation parameter which depends on the number of days with rainfall in a month and the fraction falling with an intensity ≤ 1.8 mm h^{-1} (or, in winter, the snowfall fraction). For the Hellman gauge in Switzerland, k is between 1.015 and 1.72 for wind speeds at 2 m of 0.5–4.0 m s^{-1}. The average annual correction for stations below 2000 m with daily gauges is about × 1.07 in summer and × 1.11 in winter. Above 2000 m, where storage gauges are used, the corresponding figures are × 1.15 and × 1.35.

A simpler and reasonably accurate approach for snowfall determination in mountain areas is to use snow boards, which are reset on the snow surface daily (or whenever practicable) (Föhn, 1977). Flat shoulders are the most suitable sites for such installations. The depth is read against a vertical scale and water equivalent is obtained by concurrent density measurements. Over a 30-year winter record, near the Weissfluhjoch station, a Nipher-shielded gauge averaged only 502 mm compared with 794 mm on snow boards. By determining the water equivalent of new snowfall measured on snow boards, corrections can be determined for individual gauge measurements (Sevruk, 1983). Martinec (1985) shows that the ratio may vary considerably from year-to-year. For example, corrections to a Hellman recording gauge ranged from $\times$ 1.13 to $\times$ 1.45 during 1951–80, with a mean of $\times$ 1.26.

Net snow accumulation in alpine watersheds can be investigated more thoroughly using accumulation data collected at snow pits located in a stratified random sampling arrangement. For a study in the Sierra Nevada (Elder *et al.*, 1989), the survey points were carefully located using orthographically corrected aerial photographs, topographic maps and compass survey. The topographic data were available in a 5 m resolution digital elevation model (DEM) grid. Zones of similar snow properties were identified based on elevation, slope and net radiation values calculated using the DEM. In North America, at sites below timberline, considerable use has been made of snow courses to determine net accumulation (as water equivalent) from depth–density surveys on a monthly basis. At some sites, comparable data are now gathered by telemetry from a snow pressure-pillow, which weighs the snow pack (Warnick and Penton, 1971) and, therefore, gives the water content directly.

An extensive network of more than 700 snow reporting stations is now operated by the National Resources Conservation Service in the western United States and Alaska; the first sites were instaled in the early 1980s. The stations (snow "pillows," accumulation gauges, and air temperature sensors), many in remote mountain locations, report with high frequency to data collection stations in Boise, Idaho, and Ogden, Utah, using meteor-burst relay (Rallison, 1981). This SNOTEL (Snow Telemetry) network transmits VHF signals that are reflected by the trails of numerous small meteorites in the ionosphere to activate the remote station. Near real-time data are available online (http://www.wcc.nrcs.usda.gov/snotel/).

In steeply sloping terrain the gauge orifice is sometimes constructed to be parallel to the ground and presumably the air flow. Such "stereo" or "tailored" gauges have been tested in various locations. Sevruk (1972a, 1974) argues from long-term experiments in Switzerland that they give more representative measurements on steep, open slopes exposed to rain-bearing winds, although on other slopes they may give a smaller catch than a horizontal gauge (Grunow, 1960). The subject is reviewed in detail by Peck (1972a). He notes that if the aim is to measure the precipitation on a horizontal plane at or near the surface (the "meteorological precipitation" which is mapped) then a normal gauge is appropriate. Moreover, he emphasizes that the angle of inclination of falling precipitation particles has no direct effect on the catch of a horizontal orifice (see Figure 4.31). The stereo-top gauge (or a tilted gauge) may
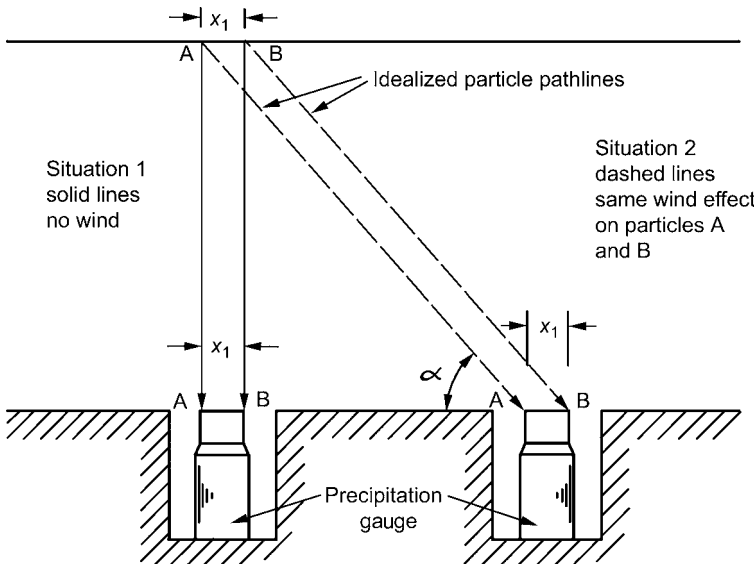
Fig. 4.31 The absence of any direct effect of the inclination angle of falling precipitation on gauge catch (from Peck, 1972a).

be appropriate, however, if the precipitation falling on unit area parallel to a slope (the "hydrological precipitation") is of interest. Peck also indicates that, in sites protected from strong winds, there is little difference between gauges with horizontal or stereo orifices.

Even when the catch at a given site is adequately registered, the question of site representativeness remains. Below the timberline, gauges may be set in forest clearings. These must be large enough to ensure a 30° horizon from gauge to the tree crowns to avoid over-sheltering. However, Soviet research shows that in moderately sheltered locations the catch of snow exceeds that in open terrain by considerable amounts, particularly at moderate wind speeds (Struzer *et al.*, 1965); see Table 4.5.

Comparisons of winter (October–March) precipitation and water equivalent of the snow pack on 1 April have been made over four to six seasons at 30 sites above 2400 m in Utah (Brown and Peck, 1962). The sites were subjectively classified as to their exposure, with the following results:

Site exposure	Sets of measurements	Winter precipitation minus 1 April w.e.(mm)	Percentage excess/deficit
Well-protected	77	63	+17
Fairly well-protected	9	0.0	0
Moderately windy	6	−63	−10
Windy	26	−65	−15
Very windy	13	−90	−16
Overprotected	11	−8	−2

Table 4.5 Excess catch of snow in a sheltered location versus open terrain (percent).

		2 m wind speed (m s^{-1})	
		2.5	5.0
	≥ 0	32	57
Air temperature (°C)	-20 to -5	53	120
	< -20	80	200

Source: after Struzer *et al.* (1965).

The excess (or deficit) of measured precipitation over the snow pack water equivalent shows good general agreement with the subjective exposure categories in terms of anticipated wind effects. The figures also indicate the magnitude of average seasonal differences that might result from such site differences. The elevation of these stations avoided possible effects of snowmelt on the ground during the winter months.

Well protected sites in Brown and Peck's study are those with sheltering on all sides given by objects subtending angles of 20–30° from the gauge orifice. The objects must be broad enough to exclude eddy effects and the general terrain should afford some wind protection. Overprotected sites, on the other hand, have some objects extending above the 45° angle from the gauge. The other categories denote subjective rankings of shelter provided by nearby objects and the general terrain.

An expression for sheltering of individual gauge sites has been developed by Catterall (1972). Protection (*P*), on a scale of zero (exposure in all directions) to one (complete protection), is given by:

$$P = \sum_{a=1}^{8} \left(\frac{H_{A\,\max} - H}{D_{A\,\max}} \right)^2 / W_a$$

where H is the elevation of the gauge sites; $(H_{A\,\max} - H)$ is relative relief; $D_{A\,\max}$ is the distance (m) between the gauge and the height maximum along direction A; W_a is the time when sheltering is effective in terms of the percentage annual frequency of wind direction a. In practice P rarely exceeds 0.5. The distance considered in determining $D_{A\,\max}$ and $H_{A\,\max}$ is based (subjectively) on the size of the catchment and the scale of local relief.

The areal representativeness of a gauge is obviously less in complex terrain than in lowlands. Thus, the recommended densities of gauge networks for hydrometeorological applications are considerably larger in mountain regions. The minimum network densities suggested by the World Meteorological Organization (1984: 3.13) are as follows:

(1)   flat terrain in temperate, subtropical and tropical zones, 1 station per 600 to 900 km^2;
(2)   mountainous regions in these zones, 1 station per 100–250 km^2;
(3)   arid and polar regions, 1 station per 1500 to 10 000 km^2;
(4)   mountainous islands with irregular precipitation, 1 station per 25 km^2.

The error in areal estimates of precipitation increases not only in relation to network density, but also the time interval (day, month) for which the estimates are made. However, the gauge locations within a sub-area, such as a mountain basin, also affect the accuracy of basin averages. Sevruk (1989) suggests that the most representative gauges are centrally located and close to the mean basin altitude.

In view of the many problems associated with point measurements, experiments have been conducted to test the use of radar determinations of precipitation volume over extensive mountain watersheds (Harrold, 1966). Anderl *et al.* (1976) found, for two small basins near Hohenpeissenberg, Bavaria, that results were as good as could be obtained with a gauge network density of 1 per 25 km^2, and much better than with the regular network at 1 per 500 km^2. More recently, over the Dee catchment in north Wales, Collier and Larke (1978) showed that even for snowfall, accuracy similar to that for areal rainfall is feasible. Their mean accuracy was within 13 percent. Calibrations based on snow depth at an upland site and a lowland site can be used to allow for the effect of snowmelt at lower elevations.

A quite different approach is to reconstruct solid precipitation using measurements of snow depth and a Land Surface Model (LSM). Cherry *et al.* (2005) illustrate this for the Reynolds Creek Experimental Watershed in southwestern Idaho (43.2° N, 116.75° E), where there is a station at 2200 m. Measurements include an unshielded and an Alter-shielded Universal Recording Gauge, a snow course and a snow pillow. The LSM (Koster *et al.*, 2000) incorporates a topographic index and three snow layers; it is forced by data on air temperature, relative humidity, atmospheric pressure, wind speed, solar radiation, snow depth and SWE. An analysis of 11 snowfall seasons shows that the method gives better results than gauge-adjusted measurements. The RMS error of reconstructed solid precipitation is 30 percent less than that based on gauge-adjusted data.

The availability of reliable automatic instrumentation and transmission capabilities that provide frequent sampling of mountain weather, in contrast to the higher costs and practical difficulties associated with remote stations that need to be visited at weekly/monthly intervals, has led many countries to implement such new systems. In Switzerland, for example, 72 automatic stations (ANETZ) installed in 1980 provide observations via telephone lines every 10 min, that are averaged into hourly values. Nevertheless, the question of designing an appropriate network of precipitation gauges remains. For the Auvergne region of France, Benizou (1989) has used an optimization technique to propose an expanded network that takes account of topographic parameters (west–east slope, north–south slope, mean altitude, and relative relief, over a scale of 10–50 km). The

procedure analyzes the spatial pattern of errors in monthly rainfall predicted by a linear regression of precipitation and relief, weighted by the topographic parameters at an individual station. Results using the existing network and alternative expanded networks are compared over a grid of interpolated precipitation amounts.

A more practical approach in remote mountain areas is to estimate a hydrological budget for entire drainage basins. Flohn (1969, 1970) shows that in subtropical mountain ranges, snowfall accumulation on glaciers and runoff may be a more reliable guide to basin precipitation than precipitation data from valley stations, since mountain and valley wind systems cause the valleys to be much drier than the surrounding ridges. Examples of this source of information are presented in Chapter 5 for Central Asia. Furthermore, in mapping mountain precipitation, estimates of seasonal altitudinal relationships using data from storage gauges or snow courses can usefully supplement the regular gauge network (Peck and Brown, 1962).

The issue of orographic effects on precipitation data on a regional scale has recently been addressed by Adams et al. (2006). They develop consistent corrections applicable for mountain river basins, using a combined water balance approach applied to 357 mountain basins and the relationship proposed by Budyko (1974) between evaporation/precipitation (E/P) and his semi-empirical aridity index (mean potential evapotranspiration/precipitation). From global 0.5° resolution topographic data, they determine the dominant wind direction for precipitation from NCEP/NCAR reanalysis data and whether the slope is up- or downslope, or cross-wind. The corrections are used to scale monthly precipitation data for 1979–99. Adams et al. have found a 20.2 percent increase in precipitation in orographic regions and a 6.2 percent global increase.

A modern focus of attention for watershed studies is the development of appropriate methods to estimate basin-wide snow cover characteristics from limited point measurements. Various techniques of distributing point values spatially have been reported; involving statistical relationships between terrain (slope, elevation, slope curvature and wind sheltering) and precipitation or snow accumulation. Spatial functions include trend surfaces, regression trees, and kriging. Erickson et al. (2005) note that most of these methods treat the parameter of interest as the sum of a deterministic and a stochastic component. The former may be represented by a linear model or by providing a mean value for discrete sub-regions of a basin; the stochastic component represents residual differences between the model and actual values. The residuals can be treated as independent (termed in geostatistics a "nugget effect" model), or as spatially correlated and involving a co-variance model. The details of such geostatistical procedures cannot be treated here but may be found in texts such as Cressie (1993) and Webster and Oliver (2001). Applications of basin discretization based on geomorphological criteria derived from a DEM and land cover data in a GIS are presented by de Jong et al. (2005) for the Dischma valley and a small mountain basin in Styria, Austria. Basin snow

water equivalent in mountain areas is also being estimated experimentally using a combination of visible band and passive microwave satellite data (Rango *et al.*, 1989). However, the present low spatial resolution of the microwave data (10–25 km) permits the use of this method only for large basins.

4.5   OTHER HYDROMETEORS

Hydrometeors include not only the common precipitation forms, discussed above, but also liquid or solid water particles suspended in the atmosphere (clouds, fog), wind-raised particles (blowing snow), and liquid or solid water particles deposited on the surface (dew, fog deposition, hoar frost, rime ice and glaze) (World Meteorological Organization, 1975). While the information on most of these phenomena is limited, all are important components of mountain weather and climate.

4.5.1   *Fog*

The visible suspension of water droplets in the air as fog, or cloud, is a prominent feature of most mountain areas. It occurs in valleys and basins, as well as over summits and slope, according to the particular physical processes in different weather regimes. Nocturnal radiation and cold air drainage, associated with low-level inversions, cause rather persistent *ground fog* in mountain valleys (see Figure 4.12). Fog on the summits, in contrast, may simply be a result of the height of the mean condensation level, and therefore cloud base, in a particular air stream. Orographically induced adiabatic cooling also occurs in upslope flow, especially with large-scale advection in the warm sector of mid-latitude cyclones. In both cases, such summit and slope cloud is simply termed *hill fog* in the British Isles. *High fog*, which may affect slopes, also forms by radiative and mixing processes associated with high-level inversions.

For mountains in Japan, Yoshino (1975; pp. 205) shows a pronounced altitudinal maximum of fog occurrence at about 1500 m where fog frequency (visibility < 1 km) exceeds 300 days year^{-1}. The single altitudinal-maximum pattern observed in Japan is apparently determined by the dominance of the summer monsoon cloud regime. On Mauna Loa, Hawaii, there is a well defined fog belt on the windward slope between 1500 and 2500 m (Juvik and Ekern, 1978). Here it is related to the level of summer orographic clouds below the trade-wind inversion, which is typically located at about 2000 m over Hilo, on the east coast, but occurs somewhat higher over the mountain slopes (Mendonca and Iwaoka, 1969). The summit zone (3400 m) of the mountain, in contrast, has a weak winter maximum of fog frequency associated with high-level cloud in synoptic disturbances in the upper westerlies.

In contrast, in the European Alps, the frequency is greatest at the highest stations, such as Sonnblick (275 days year^{-1}), while there are zones of minimal frequency

around 600 and 1000 m along the valley slopes (Fliri, 1975; Wanner, 1979). This
distribution is related to the occurrence of both ground-based radiation fog and
high fogs associated with upper inversions in winter, as well as orographic cloud
in all seasons. In maritime climates in middle latitudes high frequencies may occur
at much lower elevations. For example, thick fog (with visibility below 200 m)
occurs at 60 percent of observations at Dun Fell (848 m) in northern England. In
western Poland, the Karkonozse (Sudety) experience a high frequency of moist
maritime air. On Mt. Szrenica (1362 m), fog was observed 45% of the time, and
there were 250–300 days with fog per year during 1961–90 (Marek *et al.*, 2002).
Based on data from 51 meteorological stations and fog deposition measurements,
it is shown that altitude is not the only factor controlling fog frequency. Slope
aspect and site location in relation to local and regional topography are also
important.

4.5.2   *Fog precipitation*

On many mountain slopes, especially in the tropics and subtropics, frequent oro-
graphic cloud augments the total moisture budget through the interception of fog
droplets by the vegetation. This effect is noticeable at the edge of forest stands
(Geiger *et al.*, 2003), but it occurs generally on forested slopes.

   Normal rain gauges miss this moisture deposition and special traps have been
devised, using wire mesh or louvres above the gauge, to simulate the filtering effect
of vegetation. Studies at Hohenpeissenberg show that, whereas a rain gauge caught
682 mm during May–September 1950, one with a wire mesh fog-trap caught
853 mm (25 percent more) (Grunow, 1952a). On days when only fog precipitation
occurred, however, the fog-trap caught only 4.6 mm more. Using the same device
on Table Mountain, Cape Town, Nagel (1956) estimated that fog-drip may con-
tribute an additional 70 percent to the measured rainfall, while at Thodung
(3100 m) in eastern Nepal, an additional 22 percent (582 mm) was recorded during
the monsoon months, June–September 1963, (Kraus, 1967). Similar findings are
reported from many forested coastal mountain ranges (Parsons, 1960; Vogelman,
1973) and other foggy environments. Fog-traps recorded 100–150 percent of pre-
cipitation gauge totals during winters November–May 1959–65 on the Sonnblick,
Austria (Grunow and Tollner, 1969). Deposition rates as high as 6.9 mm h^{-1} were
observed during warm air incursions from the Mediterranean. The fog contri-
bution in the Alps appears to increase with height above the mean cloud base level.
Grunow-type collectors used along a traverse in the Dischma valley, near Davos,
Switzerland, for summer 1961–5, showed no additional increment in the valley,
5–10 percent more than in the regular gauge at 2100 m (the forest limit), and
20 percent more catch on hill crests at 2550 m (Turner, 1985).

   Uncertainties exist as to the absolute amounts. Juvik and Ekern (1978) made a
careful study on Mauna Loa, Hawaii, using louvred-screen fog gauges and calcula-
tions based on drop-size distributions, to separate the rain and fog ($< 100\,\mu m$
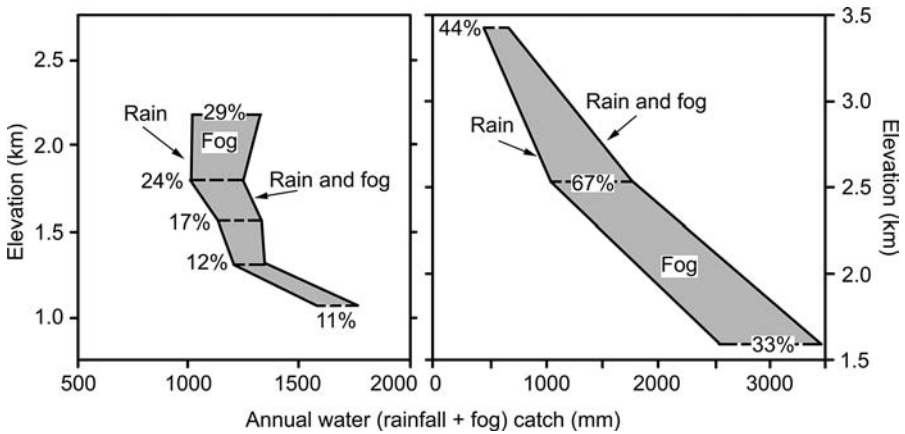
Fig. 4.32   **Annual rainfall and fog catch versus elevation on Mauna Loa, Hawaii. Left: lee slope. Right: windward slope. The percentage increase in annual total due to fog catch is shown at the elevations of measurements (after Juvik and Ekern, 1978).**

diameter) components during precipitation episodes. On the windward slope there is a well-defined fog belt between 1500 and 2500 m, where fog-drip amounts to about 750 mm, augmenting the annual precipitation by 50 percent or more. Above 2000 m, the relative contribution of the fog-drip adds 65–70 percent to the rainfall, although amounts are small. On the leeward slope of Mauna Loa, fog-drip contributes about 250 mm (a 25 percent increase in annual total). Vertical profiles of the moisture, components illustrated in Figure 4.32, are controlled to a large measure by the trade-wind inversion and its seasonal variations. There is a clear maximum of fog moisture on the windward slope in summer, related to the development below the inversion of shallow orographic clouds that bank against the slopes. On the lee slope, fog-drip increases in both relative and absolute amounts above 1300 m elevation. Here upslope flow is associated with the sea breezes, supplemented by a valley–mountain wind on the higher slopes. There is a nocturnal maximum of fog precipitation on the windward slopes and an afternoon maximum on the lee slopes, in both cases closely corresponding to the diurnal occurrence of rainfall.

In the tropics, fog interception has long been regarded as an important determinant of the occurrence of montane *cloud forest*, which is characterized by an abundance of mosses and liverworts. The role of fog interception has been investigated in northern South America where a stunted tree canopy (elfin cloud forest) is often present (Cavelier and Goldstein, 1989). The water intercepted by a cylindrical plastic screen (40 mesh cm^{-2}) was scaled to measured forest through-fall per unit horizontal surface area. In northern Colombia (Serrania de Macuira) fog interception occurs almost daily, but rainfall is much less frequent. Fog interception increased linearly with altitude from 600 to 750 m and in one 9-day period in July 1984 it was 2.5 times greater on a windward slope than a leeward one. In the

coastal Caribbean mountains of Colombia and Venezuela, rainfall increases eastward, whereas fog interception decreases. Thus, in 1985 rainfall was 853 mm at Macuira, Colombia (865 m) and fog interception 796 mm, while on Cerro Sta. Anna, Peninsula de Paraguana, Venezuela (815 m), the corresponding figures were 1630 and 518 mm, and on Cerro Copey, Margarita Island, Venezuela (987 m), 4461 and 480 mm, respectively. In the driest month at each site, fog interception accounted for over 60 percent of the water income at Macuira and Sta. Anna, but only 9 percent at Cerro Copey. Even in the wettest month at Macuira it represented 33 percent of the water income (Cavelier and Goldstein, 1989).

4.5.3 Rime

Rime ice is deposited when supercooled fog droplets encounter standing objects such as trees or buildings and also wires (Figure 4.33a and b). Three types of rime are distinguished (Table 4.6). However, rime deposits are frequently heterogeneous

Fig. 4.33 (a) soft rime needles on a twig; the air temperature was –4° C with 96 percent relative humidity in a light wind, 1030 , 20 January 1953. (b) hard rime feathers on an anemometer support cable in a light, at –3° C, 100 percent relative humidity, with occasional light drizzle and fog, 0900 , 28 November 1953 (Hohenpeissenberg Observatory).
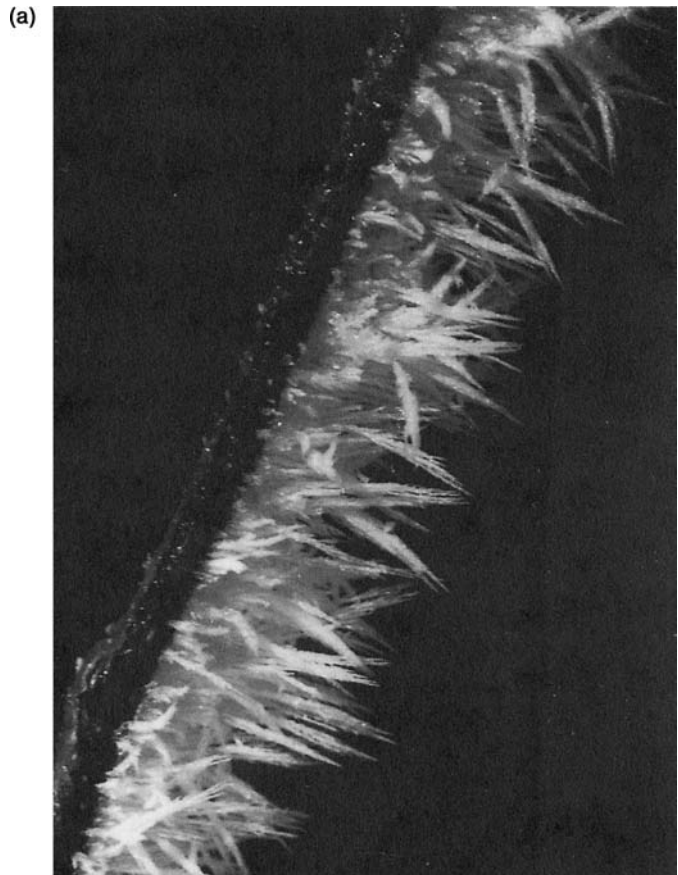
Fig. 4.33 (cont.)   **(b)**
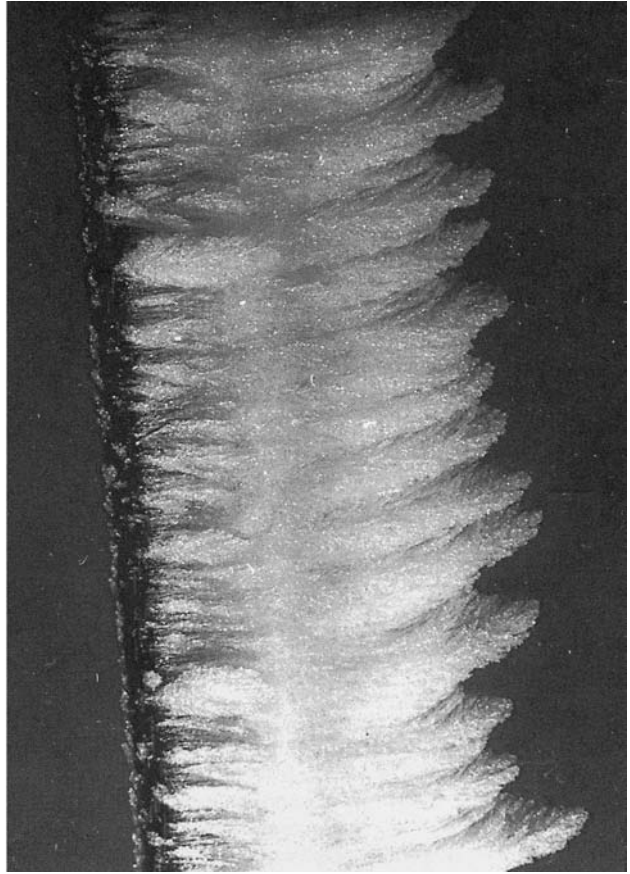
due to the more or less simultaneous, or consecutive, development of several forms with slightly varying conditions.

Studies in Czechoslovakia (Hrudicka, 1937), Poland (Baranowski and Liebersbach, 1977), Romania (Tepes, 1978) and eastern Germany (Kolbig and Beckert, 1968) indicate that the frequency of rime (all forms) increases from about 20 days year^{-1} at lowland stations to 80–100 days year^{-1} at 1000–1500 m, and up to 180 days year^{-1} above 2500 m. Hrudicka suggests an *S*-form curvilinear trend with the major increase between about 750 and 1250 m related to wintertime cloud levels. Frontal situations with altostratus or nimbostratus cloud gave rise to most of the rime events recorded in the Tatra during 1952–3 (Koncek, 1960), but in the West Carpathians they occur with cold maritime arctic air advection or due to radiative cooling of polar maritime air (Tepes, 1978). In winter, rime deposition from fog is common. On Mt. Szrenica (1362 m) in the Karkonozse, Poland, there were 149 days year^{-1} when rime deposition occurred during 1961–90. Mean daily rime accumulation is 0.56 kg per 200 cm^2 of surface area, but locally it can be three to four times higher (Migala *et al.*, 2002).

Table 4.6 Characteristics of rime deposits.

Type[a]	Characteristics	Mode of formation	Surface adhesion	Temperature Criteria (°C)
SOFT RIME (Rauhreif)	Fine needles/dendrites, clear crystalline structure, mean density $\sim 0.2\,\mathrm{g\,cm^{-3}}$	Deposition of vapor in solid form from super-cooled fog, or air super-saturated with respect to ice. Fog *not* essential	Easily detached	< -8
HARD RIME (Rauhfrost)	White granular structure with crystalline branches more or less separated by entrapped air. The deposit grows triangularly upwind, mean density $\sim 0.5\,\mathrm{g\,cm^{-3}}$	Fog essential. Rapid freezing of super-cooled fog droplets leaving interstices	Brittle, easily detached at low temperatures	-2 to -10
CLEAR ICE (Rauheis)	Amorphous compact ice with alternate transparent and opaque (bubbles of air) layers, mean density $0.8\,\mathrm{g\,cm^{-3}}$	Slow *freezing* of fog drops with released heat hindering crystallization	Firmly adheres to surface	0 to -3
GLAZE (Glatteis)	Clear ice layer, density of pure ice	Freezing of super-cooled raindrops on impact with surface; or of rain/fog drops contacting a super-cooled surface	Firmly adheres on surface	0 ± 3

[a] This terminology follows WMO (1975) and Grunow (1952b). Kuroiwa (1965) uses soft rime for what is here listed as hard rime, and hard rime for what is here clear ice.
Source: after Grunow (1952b); Waibel (1955); Kuroiwa (1965); and World Meteorological Organization (1975).

Heavy rime accumulations during strong winds can pose a serious problem for structures (see Figure 4.34) and power lines (Phillips, 1956) by increasing the dead-weight load and increasing the wind resistance. Ice growth on power lines may also lead to galloping excitation, due to wind forces (Sachs, 1972). Mountain observatories in cloudy "maritime" climates, such as Mt. Washington, New Hampshire, and the former Ben Nevis Observatory in Scotland, have experienced severe difficulties in maintaining reliable weather records due to rime accretion on instrument shelters and anemometers (Alexeiev *et al.*, 1974). Half of the icing events on Mt. Washington lead to thicknesses in excess of 2.7 cm (18 kg m^{-2} loading), but

Fig. 4.34 **A weather screen on Mt. Coburg, Arctic Canada (76° N, 79.3° W) heavily coated with rime ice. Open water in the North Water, Baffin Bay (visible in background) provides a moisture source in spring. The air temperature was −15° C (K. Steffen).**

the frequency of events and accretion rates are much less on nearby Mt. Mansfield (1339 m) (Ryerson, 1988). Icing events lasting 3–20 h with rates of 7 mm h^{-1} are typical in the Colorado Rockies (Hindman, 1986). Riming is less severe in the western Cordillera around Tahoe, but it occurs frequently and the water equivalent may amount to 14–66 percent of the precipitation during comparable periods (Berg, 1988).

A 17-year study of rime accretion on Mt. Vitosha (2286 m), Bulgaria, indicates a mean duration of events in winter of about 36 h (Stanev, 1968). Almost half the cases occur with temperatures between −2 and −6 °C with winds of 10–12 m s^{-1}. On the Feldberg (1490 m) in the Black Forest, Germany, the accretion of ice on power lines (measured over two winters) averaged 50 g m^{-1} h^{-1}, with a maximum daily load of 3.2 kg m^{-1} (Waibel, 1955). The loading is directly related to wind speed and water content according to Diem (1955), although Sachs (1972) states that the accretion depends on drop size, with the wind effect being debatable, and it is also inversely related to cable diameter. According to observations on Mt. Fuji and Mt. Neseko (1300 m) in Japan, wires are more often cut by the dynamic wind pressure than by ice load; a 10–15 m s^{-1} wind produced a tension of 30 kg on 20 m length wires (Kuroiwa, 1965). Clear ice build-up with winds of 20 m s^{-1} and temperatures of −5 to −10 °C was 2–5 kg m^{-1} over 20 h. However, Kuroiwa also noted that snow accretion with temperatures near 0 °C and winds of only 1–2 m s^{-1} can give loads of up to 5 kg m^{-1} for a 20 cm diameter ribbon of snow. On 19 March, 1969, a 260 m television transmitter mast on Emley Moor (400 m elevation), in the Pennines of northern England, collapsed following several days with glaze conditions (Page, 1969). Fog and cloud shrouded the area for the preceding week with temperatures between −3 and +2.5 °C. Apparently, the build-up of ice on the support stays, to a radial thickness of 10 cm or more, was a major contributor to the structure's collapse.

There are few quantitative measurements of the moisture contributions from this source. Studies of the weight of rime accretions on branches of lodgepole pine in the Cascade Range, Washington (about 1900 m elevation), indicate that daily amounts average 0.014 cm w.e. (Berndt and Fowler, 1969). The total contribution

during periods without snowfall in the winter of 1966–7 amounted to 3.8 to 5 cm compared with a mean annual precipitation of 90 cm of which 85 percent falls as snow. This contribution is similar to the estimate of 5–12.5 cm for the mountains of southeastern Australia (Costin and Wimbush, 1961). In northern Norway, data on rime provided by H. Köhler from the vicinity of the Haldde Observatory, indicate an order of magnitude increase on summits only 100–200 m above the observatory, due to stronger winds and more frequent hill fog (Landsberg, 1962; 186).

4.5.4 Deposition on horizontal surfaces

The deposition of dew (or its frozen form hoarfrost) on the ground or vegetation surfaces has received little attention in mountain areas. In part, this may reflect the predominance of fog droplet or rime deposition in cloudy mountain environments. However, there are also observational problems. In a survey of records for the Austrian Alps, Lauscher (1977) concluded that many inhomogeneities were present in the data on hoarfrost, apparently due to failure to report such occurrences. He suggested that calculations may be preferable. In the presence of a snow cover, incursions of warm humid air commonly cause condensation on the surface. The saturation vapor pressure over melting snow is 6.1 mb and with an air temperature of 5 °C, for example, the *maximum* relative humidity of the air corresponding to this limiting vapor pressure is only 70 percent. (The snow surface temperature in the morning is about 1 °C below the screen wet-bulb psychrometer reading according to Lauscher.) Based on more or less reliable observations of hoarfrost for four stations during 1946–75, and calculated condensation on snow, Lauscher estimated that average annual frequencies in the Austrian Alps vary with elevation approximately as follows:

Elevation (km)	Days with snow cover	Hoarfrost on bare ground	Hoarfrost on snow	Condensation on snow	Total days
3	365	7	81	49	137
2	200–250	16	55	33	104
1	110–145	25	29	17	71
(0)	30–45	35	3	1	39

Apart from making a contribution to the total moisture budget, such ice crystal deposits must also have an effect on the physical properties of the snow surface. These may be worthy of investigation in terms of their possible significance for spectral radiation signatures.

4.5.4.1 Blowing and drifting snow

Redistribution of snow by the wind is a major feature of the winter environments of the northern continents, as well as polar and alpine regions. Windblown snow is a strikingly visible element of the climatic environment of many mountain areas, yet
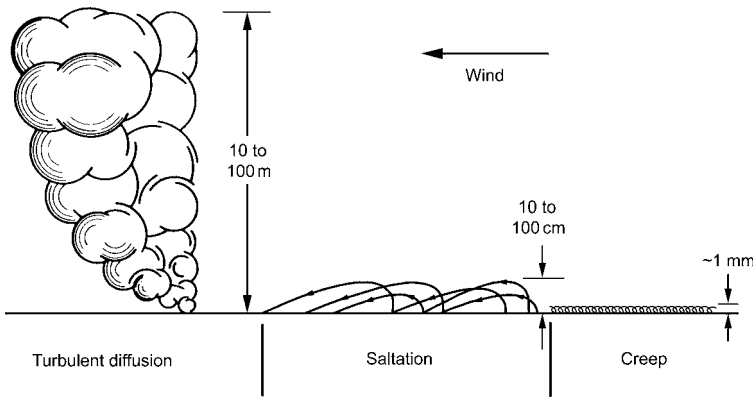
Fig. 4.35   **Modes of snow transport by the wind (from Mellor, 1965).**

the literature specifically addressing the problem is sparse. It has been investigated in Antarctica and Greenland, primarily from the standpoint of ice sheet mass balance, and in middle latitudes mainly in light of practical engineering concerns, such as snow control on highways and water resources for agriculture.

Meteorological observations make a distinction between blowing snow, which is raised to a height of 1.8 m or more so as to obscure visibility, and drifting snow near the surface. Blowing snow will occur with modest winds whenever snow is falling but snow particles are also lifted by turbulence in the boundary layer. The critical wind speed ("threshold" velocity) at which snow is picked up from the surface by turbulent eddies obviously depends on the state of the snow cover, including the temperature, size, shape and density of the snow particles and the degree of intergranular bonding (Pugh and Price, 1954; Tabler, 1975a). For loose, unbonded snow, the typical threshold wind speed (at 10 m) is $5 \, \mathrm{m \, s^{-1}}$, whereas for a dense and bonded snow cover winds $> 25 \, \mathrm{m \, s^{-1}}$ are necessary to cause blowing. Gauer (2005) noted that new snow is picked up in regions of wind acceleration, near hill crests and over small humps and brows.

Three modes of snow transport are illustrated in Figure 4.35. *Creep* involves the rolling of dry snow particles along the surface. *Saltation* – where particles bounce along the surface in a layer about 10 cm deep, dislodging other particles as they return to the surface – occurs with winds of 5–$10 \, \mathrm{m \, s^{-1}}$ over cold loose snow. Creep accounts for perhaps 10 percent of the saltation load (Berg and Caine, 1975). *Suspension* is caused by turbulent diffusion lifting particles tens of meters above the surface, and this is considered to be the major mechanism for snow redistribution in windy environments (Radok, 1977; Takeuchi, 1980), although Russian scientists regard saltation as the most significant factor for snow drifting (Mikhel *et al*., 1971; Dyunin and Kotlyakov, 1980). Measurements at Weissflujoch (2690 m) in the Alps show that saltation flux in the lowest 1 m is enhanced by stronger winds in this layer over crests, and on slopes that lie across wind direction (Meister, 1987). Radok (1968) shows that for dry snow the transition from saltation to suspension

occurs with winds of about $15\,\mathrm{m\,s^{-1}}$, when 60 percent of the up currents in the surface boundary layer exceed the fall velocity of the snow particles.

Schmidt (1984) provides a relationship between the threshold wind speed for snow drift in the lower suspension layer (U_t) and mean particle diameter (d) based on measurements at 0.25 m above the surface:

$$U_t(\mathrm{m\,s^{-1}}) = U - (d/100)^4 - 4,$$

where U is the mean wind speed at 0.25 m.

Using hourly data during six winters for 16 stations in the western Prairies of Canada, Li and Pomeroy (1997) obtained U_t values for 10-m winds of 4–$11\,\mathrm{m\,s^{-1}}$ (mean $7.7\,\mathrm{m\,s^{-1}}$) for dry snow and 7–$14\,\mathrm{m\,s^{-1}}$ (mean $9.9\,\mathrm{m\,s^{-1}}$) for wet snow transport.

Snow particles rapidly become rounded by mechanical abrasion on the surface, since natural concentrations in blowing snow are too low for particle interaction according to Schmidt (1972). Particles have a typical size of 0.1 mm and a terminal velocity of $0.5\,\mathrm{m\,s^{-1}}$. The mass transport above the 50 cm surface layer is in the range 0.05–$0.40\,\mathrm{kg\,m^{-2}\,s^{-1}}$ for winds of 20–$30\,\mathrm{m\,s^{-1}}$ in Antarctica (Mellor, 1965), but is an order of magnitude smaller over an Alpine crest (Föhn, 1980). Meister (1987) reports that for 75 runs averaging 3 h in length, with an overall mean wind speed of $11\,\mathrm{m\,s^{-1}}$ at 4.3 m height, the average flux in the lowest 5 m at Weissflujoch was $48\,\mathrm{g\,m^{-1}\,s^{-1}}$. Direct measurement of the volume of snow transported is possible by means of an aerodynamically shaped trap coupled to a precipitation gauge (Jairell, 1975) or by photoelectric devices which determine the attenuation of a light beam (Schmidt, 1977).

On Niwot Ridge, Colorado (3750 m), blowing snow occurred more than 50 percent of the time in winters 1973/4 and 1974/5 and on over 75 percent of the hours in January (Berg, 1986). There are about 30 events per winter with an average duration of 35 h. In the mountain environment, snow distribution as well as drift profiles (Pedgley, 1967) are strongly affected by meso- and micro-scale topography, including the vegetation structure. Deposition occurs where the airflow decelerates as in the lee of a ridge, where a cornice may form, and in gullies and hollows. Hollows 10–100 m across are filled in during the course of each winter season until an equilibrium level of the snow surface is reached where erosion balances deposition. This is illustrated in Figure 4.36 for an alpine site in Colorado. The minimum change of ground slope angle necessary to cause streamline separation and the initiation of drift development is about $10°$ (Berg and Caine, 1975). For 17 high elevation sites in Colorado and Wyoming, with fetches of 600–6000 m, Tabler (1975a) shows that the major controls of the slope of the drift surface, D, are the mean exhaust slope angle of the ground downwind of the break of slope, E, and the mean approach slope angle for 45 m upwind, A:

$$D(\%) = 0.25A + 0.55E_1 + 0.15E_2 + 0.05E_3$$

where E_1 is the mean ground slope 0–15 m downwind (as a percentage), E_2 is for 15–30 m and E_3 for 30–45 m downwind. This equation accounted for 87 percent
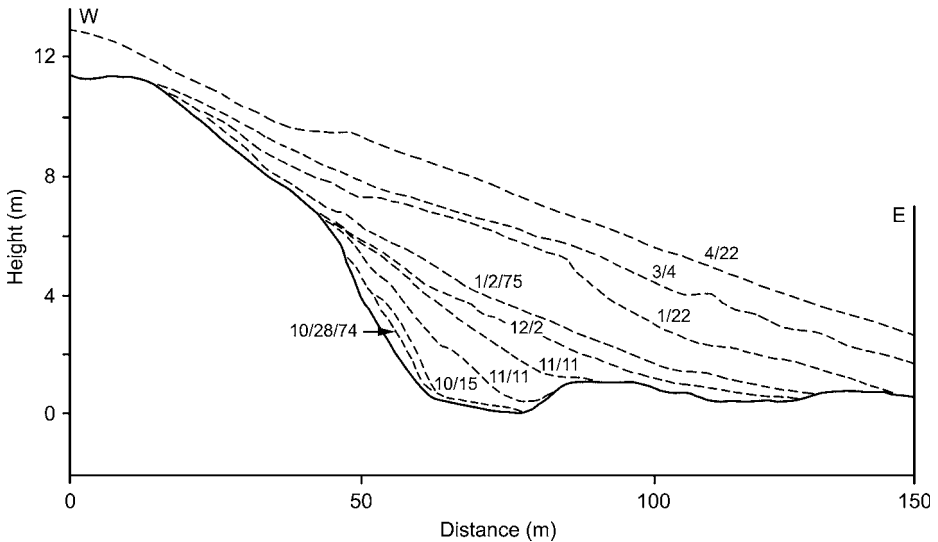
Fig. 4.36 Snow drift accumulation, 1974–5 at a site on Niwot ridge, Colorado (3450 m) (after Berg and Caine, 1975). Winds are predominantly downslope from the west.

of the variance in Tabler's data. On the lee side of hill tops and other locations where there is a sharp surface discontinuity, cornices may form due to the flow separation. The angle of the approach slope seems to be critical in determining whether a cornice or snowdrift forms (Santeford, 1972). Föhn (1980) measured snow deposition on 30° ridge slopes at 2700 m near the Jungfraujoch following three storm periods with winds of 5–13 m s^{-1}. Totals were 61 kg m^{-2} on the windward slope and 236 kg m^{-2} on the lee slope, within $\pm$ 200 m of the crest, compared with 125 kg m^{-2} on a level surface. Snow transport contributed 87.5 kg m^{-2} on to the lee slope, primarily through the recurrence of a rotor in the lee of the crest. More extensive measurements during four winters show that the topography simply redistributes the snow. Amounts within 20–50 m of an elongated crest line average 1.6 times more on the lee than on the windward slope, but the entire ridge accumulates only the same amount as level terrain (Föhn and Meister, 1983). The across-ridge profile of snow depth resembles a damped sine wave whose amplitude depends on the size of the ridge and the crest angle. On steep lee slopes ($> 25°$), the first depth maximum is an attached cornice.

In topographic traps, such as Figure 4.36, the rate of infill and shape of the drift are determined by the amount of snow transported into the trap, which in turn is dependent upon its size, the amount of precipitation and the wind velocity. The "blow past" increases during the winter as the trap size decreases through infilling.

Deposition in drifts is clearly an important component of alpine water storage. For the Colorado Front Range, water contents of 400 m^{3} per linear meter width

of the drift are estimated (Martinelli, 1973); figures of up to 1000–1200 m^2 per meter are cited for mountain areas such as the Altai in Central Asia (Mikhel and Rudneva, 1971).

The wind transport of snow is now thought to be a major factor in snow sublimation in windy environments. Schmidt (1972) indicates that the sublimation rate at any given time is proportional to the 3/2 power of the diameter of the grains. A 100-μm diameter ice particle ventilated at 1 m s^{-1} loses 20 percent of its weight in 1 min at an air temperature of −20 °C, 90 percent relative humidity and sea level pressure. For the same temperature, humidity, and ventilation velocity, this rate may be increased 50 percent at 4 km altitude, considering the increased diffusivity due to decreased air pressure (which more than offsets the decreased ventilation due to lower air density) and the increased solar radiation.

In a column of blowing snow, the situation is complicated by the vertical temperature and moisture profiles. Schmidt suggests that, in order to exhaust the vapor created by sublimation, an upward-directed gradient of moisture must exist, but estimates of probable sublimation rates are not provided. Tabler (1975b) expresses the ratio of the residual mass, M, of a snow particle to its original value, M_0, in terms of the distance traveled, D:

$$\frac{M}{M_0} = e^{-2(D/\overline{D})}$$

where $\overline{D}$ is the mean transport distance of the average size particle. Measurements of $\overline{D}$ in Wyoming, based on snow accumulation behind fences and in natural traps compared with precipitation data, indicate a value of about 3000 m in rolling terrain and 850 m at a mountain site. The residual mass decreases to 39 percent of the initial value for $D/\overline{D} = 0.5$, 11 percent for $D/\overline{D} = 1$, and 0.4 percent for $D/\overline{D} = 2$. The percentage of relocated precipitation lost to evaporation/sublimation, in relation to distance between natural traps, increases from about 60 percent for $D/\overline{D} = 1$, to 80 percent for $D/\overline{D} = 3$.

The rate of transport of mass by blowing snow across a unit length normal to the wind direction is given by Essery et al. (1999) as:

$$Q_{\text{Total}} = Q_{\text{salt}} + \int_{h^*}^{Z_h} S_z U_z dz$$

where Q_{salt} is the rate of saltation transport in a layer of depth h, S_z is the mass concentration of suspended snow, and U_z is the wind speed at height z.

The upper boundary of suspended snow (Z_b) increases with wind speed, surface roughness, and distance downwind. In agreement with Schmidt (1984), snow transport scales approximately with U^4.

Estimates of the return of seasonal snowfall to the atmosphere by sublimation of blowing snow range from 10–50 percent in prairie and tundra environments of

North America (Pomeroy and Essery, 1999). This topic is discussed below in the context of the water balance (p. 336).

Theoretical aspects of blowing snow transport are summarized by Mellor (1965), Radok (1968) and Dyunin and Kotlyakov (1980). Meso-scale models of snow transport and accumulation are now beginning to be developed, incorporating sub-models of the terrain-modified wind field, of snow transport and diffusion, and of cloud microphysics for the solid, liquid and vapor phases. Tesche (1988) describes a three-dimensional hydrometeorological model for cold orographic storms that features these three components. Snow accumulation is treated in three steps – transport by advection and diffusion just above the surface, transport to the surface as modified by terrain shape, and the incorporation of deposited snow into the ice crystal matrix. Furthermore, snow erosion is computed in relation to the critical shear stress for re-suspension. The complete model and its individual sub-models were validated using various data sets for the Lake Tahoe basin area.

Pomeroy and Essery (1999) have developed a two-phase particle model of blowing snow, which allows for phase change to calculate turbulent fluxes during blowing snow conditions. Gauer (2005) formulates a numerical model using one layer for the driving wind field and blowing snow in suspension, and a second layer to describe snow erosion, saltation, and deposition. Changes in the snow surface topography due to these processes are incorporated. Mass and momentum conservation are applied for an air–snow mixture. Particle trajectories are calculated to parameterize the characteristics of the saltation layer.

4.6   EVAPORATION

4.6.1   *Processes and methods of calculation*

The transfer of water vapor from a water surface or from bare soil (*evaporation*) depends on both the properties of the ambient air and the energy supply to the surface. A number of meteorological factors are involved: the surface–air difference in vapor pressure; the temperatures of the air and of the evaporating surface (since temperature determines the saturation vapor pressure); the rate of air movement over the evaporating surface; and the energy supply via absorbed radiation, warm air advection, and heat storage beneath the air–surface interface. Lower atmospheric pressure, which leads to a higher evaporation rate, is also a factor but the pressure reduction due to high altitude is more than compensated by the decrease in air temperature.

In the case of bare soil, the availability of soil moisture is an additional factor and the transpiration of water from vegetation also involves consideration of plant physiological characteristics, particularly the stomatal characteristics of the leaves, the root structure, and any special drought-resistant adaptations. The total moisture loss from a vegetated surface is commonly referred to as *evapotranspiration*; where moisture is non-limiting, the term *potential evapotranspiration* is used. This

value is more readily estimated from energy balance considerations (Henning and Henning, 1981).

Where the surface is snow covered, there may be a direct crystal to vapor exchange, or *sublimation*. This phase change requires more energy than evaporation: the latent heat of vaporization for a water surface is $2.50 \, \text{MJ} \, \text{kg}^{-1}$, to which must be added the latent heat of fusion. For snow at $0 \, ^\circ\text{C}$, the energy requirement is $2.83 \, \text{MJ} \, \text{kg}^{-1}$.

A brief summary of theoretical approaches to evaporation estimation must suffice in view of the complexity of the problem and the limited number of studies relating specifically to conditions at high altitude. Four main approaches can be distinguished.

4.6.1.1 *Hydrological balance calculations*

This is primarily of use for estimating evaporation from water bodies. The water budget equation is written:

$$E = P - \Delta F - \Delta S,$$

where E is the evaporation volume from the water body; P is the precipitation on the water body; ΔF is the net volume of outflow (above and below ground); and ΔS is the net storage change in the water body.

Methods for estimating water budgets from monthly climatic data, extensively developed by C. W. Thornthwaite, are described in standard climatological texts; Willmott (1977) gives algorithms for the Thornthwaite formulation. The same principle can be applied to a snow pack (Krestoviskiy, 1962). Here the precipitation component includes condensation, runoff which involves surface and groundwater; and the storage changes include both the snow pack and the soil.

4.6.1.2 *Energy balance method*

The basic formulation is as follows:

$$LE = R_\text{n} - H - G - \Delta S + LP,$$

where L is the latent heat of vaporization (or sublimation); R_n is the net radiation; H is the sensible heat flux to the atmosphere; G is the sensible heat flux to the soil interface; ΔS is the change of heat storage in the snow pack; P is the precipitation and condensation.

Since the sensible heat flux to the atmosphere is not readily determined with any reliability, it is usual to employ the ratio of sensible to latent heat (the Bowen ratio, β)

$$\beta = H/E = \frac{0.61(T_\text{s} - T_\text{a})}{(e_\text{s} - e_\text{a})} \cdot \frac{p}{1000},$$

where T is the temperature (°C); e_a is the vapor pressure in the air (mb); e_s is the saturation vapor pressure for the temperature of the water; and p is the air pressure (mb).

β is close to unity for moist vegetated surfaces and increases to 5–10 for dry surfaces.

Substituting β in the equation above (ignoring the ΔS and LP terms),

$$LE = (R_n - G)/(1 + \beta).$$

However, it is more common to use this approach in some combination method (described below).

Evaporation estimates based on this procedure, in the case of snow covers in the Valdai and at Omsk, gave random errors of 0.44 mm day^{-1} according to Kuz'min (1972; p. 151).

4.6.1.3 The aerodynamic method

This method considers the role of turbulent diffusion in the vertical flux of water vapor. The basic expression, for the so-called "bulk method," is known as Dalton's equation.

$$E = K_w(e_w - e_a),$$

where K_w is the turbulent exchange coefficient for water vapor.

K_w is expressed as a function of the wind speed. For a water surface, evaporation (mm) can be determined from the empirical equation:

$$E = 0.13u_2(e_s - e_2),$$

where u_2 is the wind speed (m s^{-1}) at 2 m; e_2 is the vapor pressure at 2 m (Gangopadhyaya et al., 1966).

For snow, Kuz'min (1970) gives the following expression.

$$E = (0.18 + 0.098u_{10})(e_s - e_2),$$

where u_{10} is the wind speed (m s^{-1}) at 10 m; and e_2 is the saturation vapor pressure (mb) at snow surface temperature.

The rate of snowdrift sublimation (kg m^{-2} s^{-1}) is given as the sum of the sublimation rates over the entire particle size spectrum and integrated from 1 cm to the top of the suspension layer (Bintanja, 2001):

$$S_z = \int_{1cm}^{H} \left\{ M_r(\partial/\partial r)\left[n_r/4\pi r^2 \rho_p\right] dz \right\}$$

where M_r is the mass of a particle with radius r, n_r is the number of particles of size r in a unit volume of air, and ρ_p is the density of the particles. The change in mass term $(\partial m \,/\, \partial t)_r$ involves the relative humidity of the air with respect to ice.

More generally, equations for vertical vapor flux take account of the profiles of wind and vapor pressure. Assuming *neutral* stability and therefore a logarithmic wind profile, and assuming that the coefficient of vapor exchange is equivalent to that for momentum exchange, then

$$E \,(\text{cm s}^{-1}) = \frac{k^2 \rho (q_2 - q_1)(u_2 - u_1)}{\ln(z_2/z_1)},$$

where k is the von Karman constant (~ 0.37); ρ is the air density (g cm^{-2}); q is the specific humidity; u is the wind speed (cm s^{-1}); and z is the height.

This is essentially Sverdrup's equation (see Light, 1941).

4.6.1.4 *Combination methods*

The most widely used methods combine the aerodynamic and energy budget equations. Penman's (1963) equation for evapotranspiration from a vegetated surface (E_T, mm day^{-1}) is:

$$E_T = \left(\frac{\Delta}{\gamma}\frac{R_n}{L} + E\right) \bigg/ \left(\frac{\Delta}{\gamma} + 1\right),$$

where γ is the psychrometric coefficient (0.66 mb K^{-1} at sea level); Δ is the slope of the saturation vapor pressure curve at mean air temperature ($\Delta/\gamma = 1.3$ at 10 °C, 2.3 at 20 °C, and 3.9 at 30 °C at sea level); R_n is the net radiation over the natural surface; L is the latent heat of vaporization (2.5×10^6 J at 0 °C);

E_a (mm day^{-1}) is an aerodynamic term depending on wind speed and saturation vapor pressure deficit:

$$E_a = (0.263 + 0.138\,u)(e_s - e),$$

where u is the wind at 2 m (m s^{-1}); $(e_s - e)$ is the saturation deficit of the air at screen level (mb).

A computer solution for the equations is described by Chidley and Pike (1970). At elevated stations, corrections must be made to the psychrometric coefficient (Storr and den Hartog, 1975; Stigter, 1976, 1978) since:

$$\gamma = c_p\,p/\varepsilon L,$$

where p is the atmospheric pressure (mb); c_p is the specific heat of dry air constant pressure (J kg^{-1} K^{-1}); and ε is the ratio of the molar mass of water vapor to that of dry air ($= 0.622$).

Tables for calculating Penman's estimate incorporating this altitude pressure effect have been published by McCulloch (1965). Stigter (1978) demonstrated that

it is unnecessary to modify the aerodynamic term for pressure dependence, except in high-altitude (and therefore cold) windy environments, where the ratio of the net radiation/aerodynamic terms in the Penman equation is less than one; in such environments evaporation tends to be low anyway. Altitudinal corrections for γ are appropriate, however, since use of the "standard" value may cause underestimates of evaporation at mountain stations (Storr and den Hartog, 1975; Stigter, 1976, 1978). More important, however, are the demonstrated effects of the type of vegetation cover. Various field programs confirm that evaporation losses from forested basins exceed those from other surfaces due to the changes in surface albedo, interception and roughness (Bosch and Hewlett, 1982; Calder, 1990). It is inappropriate to attempt a detailed discussion of this topic here, especially since the theory is still being examined (Thom and Oliver, 1977).

The term γE_a in the Penman equation can under certain conditions be estimated as a constant fraction of the energy term. Priestley and Taylor (1972) define a proportionality factor

$$\alpha = LE \Big/ \left(\frac{\Delta}{\Delta + \gamma}\right)(R_n - G)$$

and show that over large areas potential evapotranspiration is given by

$$E_T = 1.26\left(\frac{\Delta}{\Delta + \gamma}\right)(R_n - G)$$

The proportionality factor, α decreases linearly as LE/R_n decreases; $\alpha = 0.8$ for $LE/R_n = 0.5$ (Thompson, 1975).

4.6.1.5 *Measurements*

There are several approaches to direct measurement of evaporation and evapotranspiration. An overview of the instrumentation used is given by Strangeways (2000). The "eddy correlation" method provides accurate instantaneous measurements of the vertical wind component (with an ultrasonic wind sensor) and vertical differences in vapor content (with an infrared humidity sensor). By determining the instantaneous vertical transports of moisture in each direction the net vertical flux can be calculated. In practice, instantaneous departures of vertical wind, temperature and humidity from their mean values are measured and the cross-correlation of these is determined computationally;. Fast-response, accurate measurements are essential and, therefore, this technique is only suitable as a research procedure (Oke, 1987). More widely applicable is the use of a weighing lysimeter. A block of soil with its plant cover is weighed and the change due to evaporation losses is determined from knowledge of the amounts of precipitation and drainage. Simple systems have been designed for field use (LeDrew and Emerick, 1974). Lake evaporation is commonly estimated on the basis of water losses from evaporation

pans (Gangopadhyaya *et al.*, 1966). Appropriate pan coefficients must be determined for each location but, unless additional corrections are made for seasonal climatic factors, only annual totals of lake evaporation can be estimated by this means. In the case of a snow cover, the weighing of plexiglass monoliths sunk in the snow is reported to give relatively good results with daily errors of about 0.1 mm (Kuz'min, 1972; p. 151). Snow pans should be deep enough (30 cm) to eliminate radiation absorption by the bottom; "false bottoms" are desirable to drain melt water in spring; and it should be large enough to avoid disturbance to the normal air and vapor circulation in the pack (mesh walls are recommended) (Sabo, 1956). Most of these criteria are usually ignored, however. As a result of the large horizontal variability in snow pack properties, both size of lysimeter used ($2 \, \text{m}^2$, $5 \, \text{m}^2$ or larger), and the spatial arrangement of the lysimeter installation (usually an array of many trays), can have a significant effect on the results. Careful sampling is required.

Little consideration has been given to the applicability of theoretical formulations in mountain environments, and few special observational programs have been carried out. Clearly, the altitudinal effect may increase the solar radiation theoretically available for evaporation, although cloud cover may reverse this tendency. The atmospheric vapor content and air pressure both decrease with height. However, the most important factor on mid-latitude mountains at least is probably wind velocity. Many mountain locations are exposed to the wind regime of the free atmosphere, or to special local wind systems, such that enhanced advection effects occur. On tropical mountains the decrease in temperature and occurrence of cloud and fog belts must be of primary importance.

The irregular terrain and heterogeneous vegetation cover of mountains make areal assessments of evaporation based on point observations, or on theoretical grounds, difficult and of indeterminate accuracy. Analysis of evaporation rates in upland north Wales calculated by the Penman method using automatic weather station data for 1970–3 shows that spatial correlations between sites range from "strong" (0.76) to unacceptably poor (Ovadia and Pegg, 1979). Water budget calculations are commonly unreliable due to the problem of measuring precipitation accurately, while advection effects and other theoretical limitations make an aerodynamic approach inapplicable. An energy budget (or combination method) calculation seems likely to be most reliable, although the use of lysimeters, or snow pans in the case of a snow pack, may give the best results.

4.6.2 *Evaporation and water balance*

Mountaineers and botanists have long recognized the physiologically desiccating effect of low absolute humidity at high elevations and this, coupled with the commonly observed strong winds, has created a widespread impression of large evaporation losses in mountain areas. The occurrence of "penitent" forms of ice pinnacles on high altitude tropical glaciers (Figure 4.37) that arise through a

Fig. 4.37 **Penitents approximately 5 m
high, formed by differential
ablation on the Khumbu
Glacier (5000 m) in the Nepal
Himalaya. The ice fall of
the glacier where the Mt.
Everest base camp is located
is visible in the background
(K. Steffen).**

complex interaction of solar radiation, cold, dry air, and microscale airflows that
transport sensible heat, has also been interpreted in a like manner. Penitents may be
0.5–6 m high with a horizontal spacing comparable to their height and they tend to
tilt towards the elevation of the Sun at local noon. Betterton (2001) has developed a
basic numerical modeling approach to demonstrate the role of solar radiation,
multiple reflections from an irregular snow/ice surface, and the predominance of
sublimation in cold dry air. She concludes that sunlight drives the formation of
penitents in clean snow where multiple reflections of radiation into depressions
causes them to deepen. However, ablation is greatly altered in the presence of dirt
on the snow surface; a thin cover can increase ablation because of the lower albedo,
while a thick dirt layer insulates the snow and reduces ablation. Melting can occur
in the hollows between the ice pinnacles where the air is saturated and there is little
air movement (Schultz and de Jong, 2004).

Since the evaporation coefficient in equations of the Dalton type varies inversely
with atmospheric pressure, an increase in evaporation with elevation has been
argued on physical grounds, although Horton (1934) noted that theoretical and
empirical considerations contradict this view. There are many conflicting observa-
tional results in the literature on evaporation and an attempt must therefore be
made to select those where commonly accepted observational procedures were
employed. Slaughter (1970) provides a convenient review.

Remarkably, at first sight, more data have been obtained for evaporation/
sublimation losses from snow cover than from vegetated surfaces. That this is so
reflects the importance of mountain snow packs for water supplies in many parts of

the world. Careful studies of alpine snow packs in the central Sierra Nevada, California, and the Rocky Mountains of Colorado, indicate that direct evaporation/sublimation has a negligible role compared with melt followed by subsequent evaporation of the melt water (Martinelli, 1959, 1960; West, 1959, 1962; Hutchison, 1966). Martinelli, for example, reported that evaporation determined by Sverdrup's equation (p. 331) accounted for only 1–2 percent of the summer ablation of snowfields at 3500–3800 m in the Rocky Mountains, 39° N. Energy balance measurements for a few days in March 1964 at Fraser Experimental Forest, Colorado (2700 m), gave daytime sublimation amounts of 1.0–1.5 mm and nocturnal condensation of 0.2–0.3 mm (Bergen and Swanson, 1964), although work by Köhler (1950; Lauscher, 1978) at Haldde Observatory, Norway (70° N, 23° E, 893 m) and studies in southern Finland by Lemmela and Kuusisto (1974) suggest that evaporation and condensation on snow cover are more or less in balance in winter. In a forest opening at the Central Sierra Snow Laboratory (2100 m), California, West (1959, 1962) measured an annual average snow pack evaporation of only 25–35 mm (2–3 percent of the ablation) using small polyethylene pans sunk in the snow surface. In clearings and on exposed ridge top sites, amounts two to three times larger than in the forested areas were indicated. Similar results have been obtained in Russia. In the Krestovoi Pass in the central Caucasus, observed daily sublimation averaged 0.11 mm in mid-winter for coarse-grained snow (Kuvaeva, 1967). Slight condensation was observed at night. During 5 days in March 1965, the mean daily rate was only 0.21 mm from coarse-grained snow (0.11 mm for 7–10/10 cloud and 0.36 mm for 0–3/10 cloud) and 0.13 mm from fine-grained snow (0.10 mm for 7–10/10 and 0.23 mm for 0–3/10 cloud).

Few studies have specifically examined altitudinal differences in snow evaporation. Church (1934) reported figures two to four times greater on Mt. Rose, Nevada (3292 m) than from open meadow locations near Lake Tahoe (1897 m) and attributed the difference to wind conditions. More detailed measurements at the Weissflujoch, Switzerland, show a similar altitudinal increase during the daytime (de Quervain, 1951). Between 1300–1500 h on 9 March, 1950, for example, the snow evaporation was approximately $40 \, \mathrm{g \, m^{-2} \, h^{-1}}$ $(0.04 \, \mathrm{mm \, h^{-1}})$ at Davos (1550 m), $60–75 \, \mathrm{g \, m^{-2} \, h^{-1}}$ at the Weissflujoch (2670 m), and $90–110 \, \mathrm{g \, m^{-2} \, h^{-1}}$ at the summit (2850 m). Based on data for 20 days without precipitation in each month, a seasonal trend of evaporation was determined:

	Jan	Feb	March	April	May	June	Total
Sunny location	4	5	10	15	13	−5	42 mm
Shade	1	1	4	7	5	−6	12 mm

The figures show an increasing trend in spring, followed by condensation on the snow surface in summer. Again, the seasonal totals are quite modest. These results have been confirmed by other studies of evaporation from snow cover at altitudes of 2000–2500 m in the Alps (Lang, 1981).

Table 4.7 Snow evaporation (E), condensation (C) and the balance (mm) at the Sonnblick (3106 m), October 1969–September 1976.

	J	F	M	A	M	J	J	A	S	O	N	D	Year
E	5.5	4.2	3.5	2.5	3.6	2.3	1.8	2.1	5.2	17.9	8.9	10.3	67.8
C	−0.2	−0.2	−0.3	−0.1	−0.6	−4.9	−16.6	−20.1	−4.9	−0.4	−0.2	−0.1	−48.6
E + C	5.3	4.0	3.2	2.3	3.0	−2.5	−14.6	−18.1	0.3	17.4	8.7	10.1	19.0

Source: from Lauscher and Lauscher (1976).

Calculations by Lauscher and Lauscher (1976) using Kuz'min's equation (p. 330) and daily meteorological data for October 1969–September 1974 at the Sonnblick Observatory, Austria (3106 m), show that evaporation there is relatively constant from January through May and reaches a maximum in October (Table 4.7). Conversely, condensation values are large in July–August. The annual net evaporation is only 19 mm, compared with 270 cm of precipitation (90 percent of which falls as snow), although the October–January net evaporation totals 42 mm (Table 4.7). Lauscher and Lauscher also show that almost two-thirds of days during February–May have zero snow evaporation at each of the three daily observations (0700, 1400 and 1900 or 2100 h).

In contrast, other work has produced results indicating that evaporation from mountain snow cover is far from negligible. In the dry, high-radiation environment of the White Mountains, California (38° N, 118° W; 3800 m), springtime sublimation/evaporation exceeds melt by a factor of four for "fresh" snow and by 1.5 times for old drifts, according to Beaty (1975). In the central Rocky Mountains of Colorado, measurements and hydrological balance calculations led Santeford (1972) to the conclusion that, in the alpine area above the timberline, 80 percent of the winter snowfall must be removed by the sublimation of blowing and drifting snow, or by sublimation *in situ*. The first factor is dominant in early and mid-winter, but later in the season sublimation/evaporation becomes important and may account for about half of the observed storage change in ridgeline cornices according to Santeford. In (artificial) drift situations on Pole Mountain, Wyoming (2470 m), losses by evaporation–sublimation of 20–30 percent of the volume at the start of the ablation period are attributed to sensible heat advection from surrounding bare ground (Rechard and Raffelson, 1974). Nevertheless, this situation is unlikely to be common in much alpine terrain.

In many mid-latitude continental areas, forest cover extends to 3000–3500 m and sublimation–evaporation of snow intercepted in the crowns then becomes an additional complication (Miller, 1955). Again, however, Miller (1962) shows that the maximum daily evaporation rate from snow-covered trees would not exceed about 0.7 mm in the Sierra Nevada or on the Allegheny Plateau. The duration of

snow cover on tree canopies may be relatively limited, at least in dry sunny climates. At Fraser Experiment Station in the Colorado Rockies, a southeast facing slope in a valley location was snow-free 31 percent of the time between 1 December and 31 March and had $\geq 2/3$ cover during 55 percent of this time (Hoover and Leaf, 1967). It was also suggested that snowfall redistribution from tree crowns into openings would reduce evaporation losses from openings compared with forested sites since melt rates are higher in the former, but other work contradicts this. Measurements on the east slope of the Rocky Mountains, at Pingree Park, Colorado (2740 m), using evaporation pans designed to simulate snow pack conditions, indicate losses of 135 mm from a forest opening and 122 mm within lodgepole pine forest during a 5-month winter period (Meiman and Grant, 1974). This represents 45 percent of seasonal snowfall. For 83 observation periods during two winter seasons 1972–3, 1973–4, average hourly evaporation–sublimation rates in an opening and a forest site during the day were as follows:

	Morning	Afternoon	Night
Opening	0.048	0.070	0.024 (mm H_2O) h^{-1}
Forest site	0.039	0.039	0.029

Condensation on the surface was rarely observed. Meiman and Grant (1974) also note that calculated evaporation rates from on-site measurements of temperature, vapor pressure and wind using an aerodynamic formulation accounted for 83 and 76 percent of the observed variances for the opening and forest sites, respectively.

In semi-arid environments, sublimation losses are considerable. At El Laco (23.8° S, 67.5° W) in the southern Altiplano. Vuille (1996) modeled sublimation losses of 30 percent of seasonal SWE at 3000 m, 60 percent at 4000 m and 90 percent at 5000 m. In the southern High Atlas of Morocco (31.5° N, 6.5° W), winter season losses at a snow pillow at 2960 m altitude during 27 November–15 December 2003 were 22 mm (43 percent) by sublimation and 27 mm by melt (Schultz and de Jong, 2004).

Undoubtedly, sublimation losses from blowing snow are a major factor in the water balance of alpine catchments. Estimates of the return of seasonal snowfall to the atmosphere by sublimation of blowing snow range from 10–50 percent in prairie and tundra environments of North America according to Pomeroy and Essery (1999). For the alpine tundra of Niwot Ridge, Colorado, the data of Hood et al. (1999) give values within this range of 15 percent (Chapter 5, p. 406).

To summarize, evaporation/sublimation losses from mountain snowpacks seem to be a minor component of snow ablation in many environments. However, carefully conducted measurement programs are not numerous and in warm/dry and windy conditions important exceptions do occur. Usually in spring/summer warm air masses are also moist and the moisture and temperature gradients produce condensation on the snow surface. While blowing snow is subject to significant sublimation, it is not yet clear to what extent this may occur from

Fig. 4.38 **Estimated annual evaporation (cm) from water surfaces in central California based on pan measurements and meteorological data (after Longacre and Blaney, 1962).**
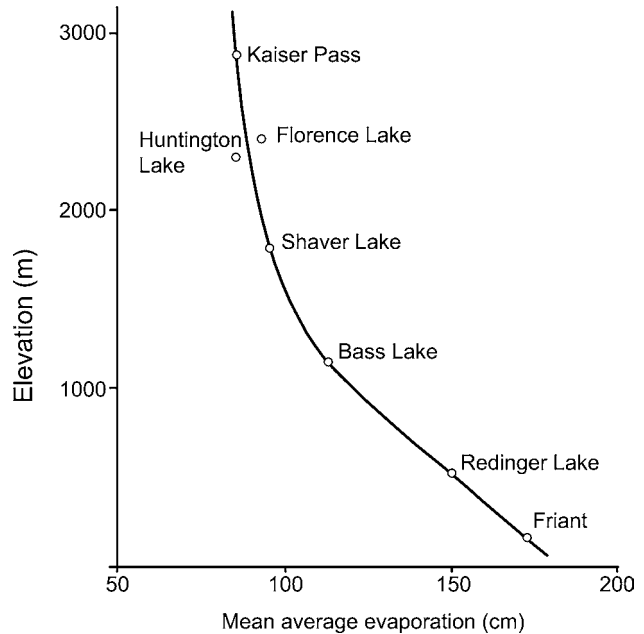
snow on ground. Many research studies of changes in the snow pack are unable to separate these two components. Nevertheless, the environment of snow-covered mountains in winter is one where there is sufficient energy available to vaporize the snow grains, despite the generally dry air.

Data on evaporation from mountain areas in summer are similarly indeterminate. Measurements in 1904 by F. Adams using sunken pans on the east slope of Mt. Whitney indicated that evaporation rates decrease with elevation to about 3000 m, thereafter becoming more or less constant to 4000 m (Horton, 1934). Estimates for water surfaces based on extensive meteorological data and pan measurements in the upper San Joaquin River basin of central California (37° N, 119° W) show a similar altitudinal pattern (Figure 4.38) (Longacre and Blaney, 1962). However, the derivation of pan coefficients to estimate evaporation for the winter half-year makes the calculated mean annual values in Figure 4.38 of uncertain reliability. Summer measurements, also using evaporation pans, in the Wasatch Mountains, Utah, show a greater complexity (Peck and Pfankuch, 1963). Mean daily wind speed and elevation together are shown to be more important, on a seasonal basis, than elevation or temperature alone.

Aspect must also play an important role. Peck and Pfankuch found higher evaporation rates on south-facing slopes, but attributed this to southerly airflow and increased instability effects rather than to excess radiation. Comparison of diurnal differences between a station on the canyon floor and one on a ridge top suggested that nocturnal drainage winds substantially augment evaporation rates. On lee slopes, föhn winds can be a major factor in enhancing evaporation.

Calculations of potential evaporation during winter chinook conditions in Alberta gave 1.2 mm day^{-1} for 19 days in 1975 and 2.0 mm day^{-1} for 20 days in 1976 (Golding, 1978).

Long-term evapotranspiration data in mountain areas are almost non-existent, yet it is these losses rather than potential evaporation, which are of most significance for vegetation growth. For alpine tundra at 3500 m on Niwot Ridge, Colorado, LeDrew (1975) estimated a rate of 1.9 mm day^{-1} in July 1973. This was obtained through an empirical formula based on measurements with a small weighing lysimeter and measured vertical profiles of temperature, humidity, and wind speed. As a result of strong advection at this exposed site, evapotranspiration continues through the night if soil moisture is available, although rates are low. Isard and Belding (1989) used a weighing lysimeter for the 1987 growing season together with energy budget and gradient measurements at four sites in a dry alpine meadow. They show that for three to five days after a precipitation event, evapotranspiration (ET) is controlled by energy availability, but thereafter water availability is a key factor. Average lysimeter data indicate an average evaporation rate of 2.2 mm day^{-1}, while turbulent transfer calculations gave 4.1 mm day^{-1}. This difference reflects the advection of cold, dry air from the Continental Divide. The increased sensible and latent heat fluxes reduce the ground heat flux and hence the surface temperature. Climatic estimates by Greenland (1989) of the water budget terms according to Thornthwaite's method indicate that actual evaporation is only about 28 percent of annual precipitation at Niwot Ridge (3750 m) compared with 47 percent at Como (3050 m). In summer, calculated actual evaporation slightly exceeds precipitation at both stations due to the implied use of soil moisture. Energy balance data from the Austrian Alps show a 30 percent decrease in summer evapotranspiration from a meadow site at 1960 m to alpine grassland at 2580 m (Staudinger and Rott, 1981).

In the Canadian Arctic, Ohmura (1982) measured the altitudinal variation in evapotranspiration during the snow-free period using small weighing lysimeters. The rate increased from 1.13 mm day^{-1} near sea level on Axel Heiberg Island (79.5° N, 91° W) to 1.65 mm day^{-1} at 750 m altitude (averaged over summers 1969 and 1970), in response to increasing wind speeds. However, the shorter snow-free period at the highest ridge site resulted in the seasonal total reaching a maximum of about 100 mm at 600 m compared with 85 mm at 750 m and at sea level. Precipitation, on the other hand, increased linearly with altitude from 60 mm to 110 mm for the snow-free period, so that precipitation exceeds evaporation above 500 m, whereas the opposite holds for this period at the lower elevations.

An energy balance study was carried out in August 1995 on a valley bottom meadow and at an upper slope with dwarf shrubs, bare patches and rocks, in the Dischma valley near Davos, Switzerland (Konzelmann et al., 1997). After five fine days, there was a succession of rain events during August. Net radiation is the only energy source, amounting to 81 W m^{-2} at the valley site (1680 m) and 98 W m^{-2} at the upper site (Stillberg, 2220 m). respectively. The difference mainly reflects the

different heights of the horizon, 23° at the valley site and 12° at Stillberg. The latent heat flux represents the most important energy sink, averaging $-70\,\mathrm{W\,m^{-2}}$ (86 percent of R_n) at the lower and $-63\,\mathrm{W\,m^{-2}}$ (64 percent) at the upper site. This is due to a significantly larger Bowen ratio at the upper location. The actual evapotranspiration was compared to the Penman estimate of the potential limit for saturated surface conditions and it was found that, even during wet periods, evapotranspiration is regulated by the moisture conditions in the soil (frequently saturated after rain at the valley site and well drained at Stillberg) and the physiological behavior of the vegetation with much higher transpiration rates from the meadow than the dwarf shrubs. In the Dischma valley, de Jong (2005) also installed lysimeters in the valley bottom at 2080 m and at the valley head (2361 m). Average daily sums of ET and condensation during a week of variable weather, with evening rainfall events, in early August 1999 were as follows:

	ET	Condensation	Total water loss (mm day^{-1})
2080 m	4.0	0.5	3.5
2361 m	1.6	0.5	1.1

However, altitudinal gradients are not simple linear ones since net ET is affected by vegetation cover, aspect and slope characteristics as well as by radiation and wind conditions. This is illustrated by Bowen ratio determinations of ET and condensation at three sites in the Dischma valley, Switzerland (Table 4.8).

During hot summers, de Jong (2005) finds that low altitude dwarf shrubs have the lowest overall evaporation, while high altitude dwarf shrubs evaporate more than the wet meadows (Fettwiesen, located on the valley floor). This result, contrary to that of Konzelmann et al. (1997), is based on several years of field measurements from many stations located in the lower and upper valley (de Jong et al., 2005). De Jong (pers. comm. 2005) considers that the findings of Konzelmann et al. (1997) may reflect the fact that their upper shrub site, just above the tree line, was atypical being in a north-facing depression behind lateral moraines.

Table 4.8 Day- and night-time Bowen ratio estimates of evaporation and condensation during 7–30 August 1998 at three sites (mm day^{-1}) in the Dischma Valley, Switzerland (from de Jong, 2005). Values in parentheses are the percentage contribution of condensation to total evaporation.

Location	Altitude (m)	DAY Evaporation	DAY Condensation	NIGHT Evaporation	NIGHT Condensation
Valley bottom	1960	54.2	4.7 (8.7%)	4.2	2.9 (69%)
Trough shoulder NW	2360	50.1	15.8 (35%)	7.8	1.9 (21%)
Trough shoulder NE	2360	55.5	7.7 (14%)	12.5	5.9(47%)

Fig. 4.39 **Altitudinal profiles of mean annual precipitation (P), evaporation (E) and runoff (D) for the Swiss Alps (after Baumgartner *et al.*, 1983). The plots of condensation, sublimation, fog precipitation and glacier mass loss are offset on the abscissa for clarity.**
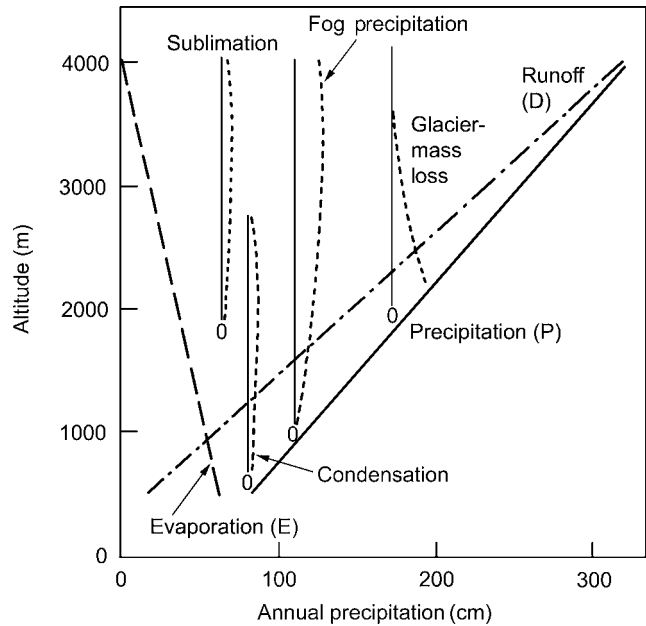
For the Alps, long-term regional evapotranspiration averages for 1931–60 have been determined on the basis of water balance calculations (precipitation minus runoff) for 1000 catchments, with checks using the empirical relationships of W. Wundt, C. W. Thornthwaite (see p. 329) and others (Baumgartner *et al.*, 1983). Averages for 500 m belts show a small approximately linear decrease with elevation (Figure 4.39). Between 500 and 2500 m asl, annual evapotranspiration (E_T) is given by:

$$E_T(mm) = 680 - 20h,$$

where *h* is the elevation in hundreds of meters. There is still considerable uncertainty as to the magnitudes of evapotranspiration determined from water balance calculations, even for basins in the European Alps. Lang (1981) cites a five-fold range in the rate of decrease of mean annual evaporation with altitude from 71 to 356 mm km^{-1}, according to difference sources. This range reflects uncertainties in the data rather than regional differences. Measurements on the Hintereisferner basin (Ötztal, Austria) over 2 years showed an average evaporation of 180 mm for the 58 percent ice-covered basin (mean altitude almost 3000 m); this represents only about 10 percent of the annual precipitation. Two years of water balance data for the Emerald Lake Basin (2800–3400 m) in the Sierra Nevada, California, which is 70 percent bare rock, show that total evaporation accounts for 19 to 32 percent of evaporation, the larger amount in the wetter year (Kattelman and Elder, 1991). Snowfall represents 95 percent of the precipitation and 80 percent of the evaporative losses are from snow cover. Sublimation averages about 50 mm month^{-1} during winter; during non-winter conditions actual evaporation is about 140 mm month^{-1}.

seventy-five to 90 percent of the peak spring snow pack (and subsequent rainfall) goes into streamflow.

As implied above, the effects of wind on snowfall and snow cover make the application of this hydrological method of limited value for evaporation estimates in many alpine locations (Santeford, 1972). The implications of decreasing evapotranspiration, but increasing precipitation with altitude in many mid-latitude mountain areas are that runoff increases with height. This is shown by Baumgartner *et al.* (1983) for the Alps and by Alford (1985) for Colorado. Nevertheless, different vertical patterns of runoff can be expected in other latitudes as a result of the profiles of precipitation and evaporation.

4.7 NOTES

(1) The temperature–entropy chart or tephigram ($T-\phi$ gram) is one version of adiabatic diagram for displaying and analyzing upper air sounding data. Values of air pressure, temperature (dry bulb, wet bulb, dew point), potential temperature (θ), air density and vapor pressure (humidity mixing ratio) can be plotted. The X-axis is temperature and the Y-axis is $\ln \theta$; isobars are slightly curved inclined lines. The adiabatic processes involved in air rising or sinking are represented by curves following the air parcels motion. Glickman (2000) lists eight different versions; on several of these charts, including the tephigram, the area enclosed by a closed curve showing a cyclic process is proportional to the work done in the process.

BIBLIOGRAPHY

Adams, J., *et al.* (2006) Correction of global precipitation for orographic effects. *J. Climate*, **19**, 15–38.

Aizenshtat, B. A. (1962) Nekotorye cherty radiatsonnogo rezhima, teplogo balansa, mikroklimata gornogo perevala (Some characteristics of the radiation regime, heat balance and microclimate of a mountain pass). *Met. Gidrol*., **3**, 273–82.

Alexeiev, J. K., Dalyrymple, P. C. and Gerger, H. (1974) *Instrument and Observing Problems in Cold Climates*. Geneva: World Meteorological Organization, No. 384.

Alford, D. (1985) Montain hydrologic systems. *Mountain Res. Devel*., **5**, 349–63.

Alpert, P. (1986) Mesoscale indexing of the distribution of orographic precipitation over high mountains. *J. Clim. Appl. Met*., **25**, 532–45.

Alter, J. C. (1937) Shielded storage precipitation gages. *Mon. Weather Rev*., **65**, 262–5.

Anderl, B., Altmanspacker, W. and Schultz, G. A. (1976) Accuracy of reservoir inflow measurements based on radar rainfall measurements. *Water Resources Res*., **12**, 217–23.

Anders, A. M., Roe, G. H. and Durran, D. R. (2004) Conference notebook orographic precipitation and the form of mountain ranges. *Bull. Amer. Met. Soc*., **85**, 498–9.

Andersson, T. (1980) Bergeron and the oreigenic (orographic) maxima of precipitation. *Pure Appl. Geophys*., **119**, 558–76.

Armstrong, C. F. and Stidd, C. K. (1967) A moisture-balance profile in the Sierra Nevada. *J. Hydrol.*, **5**, 252–68.

Atkinson, B. W. and Smithson, P. A. (1976) Precipitation. In T. J. Chandler and S. Gregory (eds), *The Climate of the British Isles*. London: Longman, pp. 129–82.

Aulitsky, H. (1967) Lage und Ausmass der "warmen Hangzone" in einen Quertal der Innenalp. *Ann. Met.*, **3**, 159–65.

Banta, R. M. (1990) The role of mountain flows in making clouds. Atmospheric processes over complex terrain. *Meteorol. Monogr.*, **23**(45), 229–83.

Baranowski, S. and Liebersbach, J. (1977) The intensity of different kinds of rime on the upper tree line in the Sudety Mountains. *J. Glaciol.*, **19**, 489–97.

Barry, R. G. (1973) A climatological transect along the east slope of the Front Range. Colorado. *Arct. Alp. Res.*, **5**, 89–110.

Barry, R. G. and Chorley, R. J. (2003) *Atmosphere, Weather and Climate*, 8th edn. London: Routledge, 421 pp.

Barstad, I. and Smith, R. B. (2005) Evaluation of an orographic precipitation model. *J. Hydromet.*, **6**, 85–95.

Basist, A., Bell, G. D. and Meentemeyer, V. (1994) Statistical relationships between topography and precipitation patterns. *J. Climate*, **7**(9), 1305–15.

Baumgartner, A. (1960–2) Die Lufttemperatur als Standortsfaktor am Grossen Falkenstein, 1. *Forstwiss. Centralblatt*, **79**, 362–73; 2. *Forstwiss. Centralblatt*, **80**, 107–20; 3. *Forstwiss. Centralblatt*, **81**, 17–47.

Baumgartner, A., Reichel, E. and Weber, G. (1983) *Der Wasserhaushalt der Alpen*. Munich: Oldenbourg.

Beaty, C. B. (1975) Sublimation or melting: observations from the White Mountains, California, and Nevada, U.S.A. *J. Glaciol.*, **14**(71), 275–86.

Benizou, P. (1989) Taking topography into account for network optimization in mountainous areas. In B. Sevruk (ed.), *Precipitation Measurement, WMO/IAHS/ETH Workshop on Precipitation Measurement*. Zurich: Swiss Federal Institute of Technology, pp. 307–12.

Berg, N. (1986) Blowing snow at a Colorado alpine site: Measurements and implications. *Arctic Alpine Res.*, **18**, 147–61.

Berg, N. H. (1988) Mountain-top riming at sites in California and Nevada, U.S.A. *Arct. Alp. Res.*, **20**, 429–47.

Berg, N. and Caine, N. (1975) Prediction of natural snowdrift accumulation in alpine areas, Final Report to Rocky Mountain Forest and Range Expt. Station (USFS 16–388-CA). Boulder, CO: Department of Geography, University of Colorado.

Bergen, J. D. and Swanson, R. H. (1964) Evaporation from a winter snow cover in the Rocky Mountain forest zone. In *Proc. 32nd Western Snow Conference*, pp. 52–8.

Bergeron, T. (1949) Problem of artificial control of rainfall on the globe. *Tellus*, **1**, 32–43.

Bergeron, T. (1960) Problems and methods of rainfall investigation. In *The Physics of Precipitation*. Geophysical Monograph No. 5. Washington, DC: American Geophysical Union, pp. 5–30.

Bergeron, T. (1961) *Preliminary results of Project Pluvius*. International Association of Scientific Hydrology, Publication No. 53, pp. 226–37.

Berkovsky, L. (1964) The fall-off with height of terrain-induced vertical velocity. *J. appl. Met.*, **3**, 410–14.

Berndt, H. W. and Fowler, B. W. (1969) Rime and hoarfrost in upper-slope forests of eastern Washington. *J. Forestry*, **67**, 92–5.

Betterton, M. D. (2001) Theory of structure formation in snowfields motivated by penitentes, suncups, and dirt comes. *Phys. Rev., E*, **63**, 056129, 1–12.

Bintanja, R. (2001) Snowdrift sublimation in a katabatic wind region of the Antarctic Ice Sheet. *J. appl. Met.*, **40**(11), 1952–66.

Bleasdale, A. and Chan, Y. K. (1972) Orographic influences on the distribution of precipitation. In *The Distribution of Precipitation in Mountainous Areas*, Vol. II. Geneva: World Meteorological Organization no. 326, pp. 322–33.

Bonacina, L. C. W. (1945) Orographic rainfall and its place in the hydrology of the globe. *Q. J. R. Met. Soc.*, **71**, 41–55.

Borzenkova, I. I. (1965) K metodike rascheta summarnoy radiatsii dlya uslovii gornogo plato. [The calculation of radiation total for mountain plateau conditions] *Trudy Glav. Geofiz. Obs.*, **179**, 98–107.

Borzenkova, I. I. (1967) K voprosy o vliyanii mestnikh faktorov na prikhod radiastsii v gornoi mestnosti. [On the influence of local factors on the radiation receipts in mountain locations] *Trudy Glav. Geofiz. Obs.*, **209**, 70–7.

Bosch, J. M. and Hewlett, J. D. (1982) A review of catchment experiments to determine the effect of vegetation change on water yield and evapotranspiration. *J. Hydrol.*, **55**, 2–23.

Bossert, J. E. and Cotton, W. R. (1994) Regional-scale flows in mountainous terrain. Part I: A numerical and observational comparison. *Mon. Wea. Rev.*, **122**, 1449–71.

Braham, R. R. (1968) Meteorological bases for precipitation development. *Bull. Amer. Met. Soc.*, **49**, 343–53.

Brazel, A. H. and Marcus, M. G. (1979) Heat exchange across a snow surface at 5365 meters, Mt. Logan, Yukon. *Arct. Alp. Res.*, **11**, 1–10.

Brown, M. J. and Peck, E. L. (1962) Reliability of precipitation measurements as related to exposure. *J. appl. Met.*, **1**, 203–7.

Browning, K. A. (1980) Structure, mechanism and prediction of orographically enhanced rain in Britain. In R. Hide and P. W. White (eds), *Orographic Effects in Planetary Flows*, GARP Publication Series No. 23. Geneva: WMO-ICSU Joint Scientific Committee, World Meteorological Organization, pp. 85–114.

Browning, K. A. (1985) Conceptual models of precipitation systems. *Wea. Forecasting*, **1**, 23–41.

Browning, K. and Harrold, T. W. (1969) Air motion and precipitation growth in a wave depression. *Q. J. R. Met. Soc.*, **95**, 288–309.

Browning, K. A. and Hill, F. F. (1981) Orographic rain. *Weather*, **36**, 326–9.

Browning, K. A., Hill, F. F. and Pardoe, C. W. (1974) Structure and mechanism of precipitation and the effect of orography in a wintertime warm sector. *Q. J. R. Met. Soc.*, **100**, 309–30.

Browning, K. A., Pardoe, C. W. and Hill, F. F. (1975) The nature of orographic rain at wintertime cold fronts. *Q. J. R. Met. Soc.*, **101**, 333–52.

Brunsdon, C., McClatchey, J. and Unwin, D. J. (2001) Spatial variations in the average rainfall–altitude relationship in Great Britain: An approach using geographically-weighted regression. *Int. J. Climatol.*, **21**, 455–66.

Bryson, R. A. and Kuhn, P. M. (1961) Stress-differential induced divergence with application to littoral precipitation. *Erdkunde*, **15**, 287–94.

Buchan, A. (1890) The meteorology of Ben Nevis. *Trans. R. Soc. Edin.*, **34**, xvii–lxi.

Budyko, M. I. (1974) *Climate and Life*. New York: Academic Press. 508 pp.

Caine, N. (1975) An elevational control of peak snowpack variability. *Water Res. Bull.*, **11**, 613–21.

Calder, I. R. (1990) *Evaporation in the Uplands*. Chichester: J. Wiley and Sons.

Carruthers, D. J. and Choularton, T. W. (1983) A model of the seeder-feeder mechanism of orographic rain including stratification and wind-drift effects. *Q. J. R. Met. Soc.*, **109**, 575–88.

Catterall, J. W. (1972) An a priori model to suggest rain gauge domains. *Area*, **4**, 158–63.

Cavelier, J. and Goldstein, G. (1989) Mist and fog interception in elfin cloud forests in Colombia and Venezuela. *J. Trop. Ecol.*, **5**, 309–22.

Cherry, J. E., *et al.* (2005) Solid precipitation reconstruction using snow depth measurements and a land surface hydrology model. *Water Resour. Res.*, **41**(9), W09401.

Chickering, J. W., Jr. (1884) Thermal belts. *Am. Met. J.*, **1**, 213–18.

Chidley, T. R. E. and Pike, J. G. (1970) A generalized computer program for the solution of the Penman equation for evapotranspiration. *J. Hydrol.*, **10**, 75–89.

Chuan, G. K. and Lockwood, J. G. (1974) An assessment of the topographic controls on the distribution of rainfall in the central Pennines. *Met. Mag.*, **103**, 275–87.

Church, J. E. (1934) Evaporation at high altitudes and latitudes. *Trans. Am. Geophys. Union*, **15**(2), 326–51.

Cline, D. W. (1997) Snow surface energy exchanges and snowmelt at a continental midlatitude alpine site. *Water Resour. Res.*, **33**(4), 689–702.

Collier, C. G. and Larke, P. R. (1978) A case study of the measurement of snowfall by radar: an assessment of accuracy. *Q. J. R. Met. Soc.*, **104**, 615–21.

Colton, D. E. (1976) Numerical simulation of the orographically induced precipitation distribution for use in hydrologic analysis. *J. appl. Met.*, **15**, 1241–51.

Conrad, V. (1935) Beiträge zur Kenntnis der Schneedeckenverhältnisse. *Gerlands Beitr. Geophys.*, **45**, 225–36.

Cosma, S., Richard, E. and Miniscloux, F. (2002) The role of small-scale orographic features in the spatial distribution of precipitation. *Q. J. R. Met. Soc.*, **128**, 75–92.

Costin, A. B. and Wimbush, D. J. (1961) Studies in catchment hydrology in the Australian Alps, IV. Interception by trees of rain, cloud and fog. Canberra: C.S.I.R.O., Australia Division of Plant Industry, Technical Paper 16.

Cotton, W. R., *et al.* (1983) A long-lived mesoscale convective complex. Part I: The mountain-generated component. *Mon. Wea. Rev.*, **111**, 1893–918.

Cox, H. J. (1923) Thermal belts and fruit growing in North Carolina. *Mon. Wea. Rev.*, **Suppl.**, 19.

Cressie, N. A. C. (1993) *Statistics for Spatial Data*. Hoboken, NJ: Wiley.

Daly, C., Nelson, R. P. and Phillips, D. L. (1994) A statistical-topographic model for mapping climatological precipitation over mountainous terrain. *J. appl. Met.*, **33**, 140–58.

Danard, M. B. (1971) A simple method for computing the variation of annual precipitation over mountainous terrain. *Boundary-Layer Met.*, **2**, 41–55.

Deems, J. S., Fassnacht, S. R. and Elder, K. J. (2006) Fractal distribution of snow depth from lidar data. *J. Hydromet.*, **7**, 285–97.

de Jong, C. (2005) The contribution of condensation to the water cycle under high-mountain conditions. *Hydrol. Processes*, **19**, 2419–35.

de Jong, C., Mundelius, M. and Migala, K. (2005) Comparison of evapotranspiration and condensation measurements between the Giant Mountains and the Alps. In C. de Jong, D. M. Collins and R. Ranzi (eds), *Climate and Hydrology in Mountain Areas*. New York: J. Wiley and Sons, pp. 161–3.

de Quervain, M. R. (1951) Zur Verdunstung der Schneedecke. *Arch. Met. Geophys. Biokl.*, B **3**, 47–64.

Déry, S. J. and Yau, M. K. (2002) Large-scale mass balance effects of blowing snow and surface sublimation. *J. Geophys. Res.*, **107 (D23)**, 4679 ACL 8-1–8-17.

Dettinger, M., Redmond, K. and Cayan, D. (2004) Winter orographic precipitation rates in the Sierra Nevada – large-scale atmospheric circulations and hydrologic consequences. *J. Hydromet.*, **5**, 1102–16.

Diem, M. (1955) Höchstlasten der Nebelfrostablagerungen am Hochspannungsleitungen im Gebirge. *Arch. Met. Geophys. Biokl.*, B **7**, 84–95.

Diodato, N. (2005) The influence of topographic co-variables on the spatial variability of precipitation over small regions of complex terrain. *Int. J. Climatol.*, **25**(3), 351–63.

Douglas, C. K. M. and Glasspoole, J. (1947) Meteorological conditions in heavy orographic rainfall in the British Isles. *Q. J. R. Met. Soc.*, **73**, 11–38.

Douguédroit, A. and Saintignon, F. F. de (1970) Methode de l'étude de la dècroissance des temperatures en montagne de latitude moyenne: exemple des Alpes françaises du sud. *Rev. Géog. Alp.*, **58**, 453–72.

Dreiseitl, E. (1988) Slope and free air temperatures in the Inn valley. *Met. Atmos. Phys.*, **39**, 25–41.

Dunbar, G. S. (1966) Thermal belts in North Carolina. *Geog. Rev.*, **56**, 516–26.

Dyunin, A. K. and Kotlyakov, V. M. (1980) Redistribution of snow in the mountains under the effect of heavy snow storms. *Cold Regions Sci. Technol.*, **3**, 287–94.

Elder, K., Dozier, J. and Michaelsen, J. (1989) Spatial and temporal variation of net snow accumulation in a small alpine watershed, Emerald Lake basin, Sierra Nevada, California. *Ann. Glaciol.*, **13**, 56–63.

Elliott, R. D. (1977) Methods for estimating areal precipitation in mountainous areas. Report 77–13. Goleta, CA: North American Weather Consultants (for National Weather Service, NOAA-77-111506) (NTIS:PB-276 140/IGA).

Elliott, R. D. and Shaffer, R. W. (1962) The development of quantitative relationships between orographic precipitation and air-mass parameters for use in forecasting and cloud seeding evaluation. *J. appl. Met.*, **1**, 218–28.

Erickson, T. A., Williams, M. W. and Winstral, A. (2005) Persistence of topographic controls on the spatial distribution of snow in rugged mountain terrain, Colorado, United States. *Water Resour. Res.*, **41**, W04014, 17 pp.

Erk, F. (1887) Die vertikale Verteilung und die Maximalzone des Neiderschlags am Nordhange der bayrischen Alpen im Zeitraum November 1883 bis November 1885. *Met. Zeit.*, **4**, 55–69.

Essery, R. (2001) Spatial statistics of windflow and blowing-snow fluxes over complex topography. *Boundary-Layer Met.*, **100**, 131–47.

Essery, R., Li. L. and Pomeroy, J. (1999) A distributed model of blowing snow over complex terrain. *Hydrol. Processes*, **13** (14–15), 2423–38. Sublimation and blowing

snow transport at six sites in the conterminous United States. *Proc. 61st Annual Western Snow Conference* (Portland, OR), pp. 15–26.

Fassnacht, S. R. (2004) Estimation alter-shielded gauge snowfall undercatch, snowpack.

Flenley, J. R. (1994) Cloud Forest, the Massenerhebung Effect, and Ultraviolet Insolation. In L. S. Hamilton, J. O. Juvik and F. N. Scatena (eds), *Tropical Montane Cloud Forests*. New York: Springer-Verlag, pp. 150–5.

Fliri, F. (1967) Uber die klimatologische Bedeutung der Kondensationshöhe im Gebirge. *Die Erde*, **98**, 203–10.

Fliri, F. (1975) *Das Klima der Alpen im Raume von Tirol*. Innsbruck: Universitãtsverlag Wagner.

Flohn, H. (1969) Zum Klima und Wasserhaushalt des Hindukushs und benachtbaren Gebirge. *Erdkunde*, **23**, 205–15.

Flohn, H. (1970) Comments on water budget investigations, especially in tropical and subtropical mountain regions. In *Symposium on World Water Balance*, pp. 251–62. IASH Publication, 93, Vol. 2. New York: UNESCO.

Flohn, H. (1974) Contribution to a comparative meteorology of mountain areas. In J. D. Ives and R. G. Barry (eds), *Arctic and Alpine Environments*. London: Methuen, pp. 55–71.

Fogarasi, S. (1972) *Weather Systems and Precipitation Characteristics over the Arctic Archipelago in the Summer of 1968*. Inland Waters Directorate. Technical Report No. 16. Ottawa: Environment Canada.

Föhn, P. M. B. (1977) Representativeness of precipitation measurements in mountainous areas. *Proceedings of the Joint AMS/SGBB/SSG Meeting on Mountain Meteorology and Biometeorology*. Geneva: Blanc et Wittwer, pp. 61–77.

Föhn, P. M. (1980) Snow transport over mountain crests. *J. Glaciol.*, **26**(94), 469–80.

Föhn, P. and Meister, R. (1983) Distribution of snowdrifts on ridge slopes: measurements and theoretical approximations. *Ann. Glaciol.*, **4**, 52–7.

Frére, M., Rijks, J. Q. and Rea, J. (1975) Estudio Agroclimatologico de la Zona Andina, Informe Technico. Rome: Food and Agricultural Organization of the United Nations.

Fu, B.-P. (1995) The effects of orography on precipitation. *Boundary-Layer Met.*, **75**, 189–205.

Fujita, T. (1967) Mesoscale aspects of orographic influences on flow and precipitation patterns. In E. R. Reiter and J. L. Rasmussen (eds), *Proceedings of the Symposium on Mountain Meteorology*, Atmospheric Science Paper No. 122. Fort Collins, CO: Colorado State University, pp. 131–46.

Fujita, T., Baralt, G. and Tsuchiya, J. (1968) Aerial measurement of radiation temperatures over Mt. Fuji and Tokyo areas and their application to the determination of ground- and water-surface temperatures. *J. appl. Met.*, **7**, 801–16.

Fulks, J. R. (1935) Rate of precipitation from adiabatically ascending air. *Mon. Weather Rev.*, **63**, 291–4.

Furman, R. W. (1978) Wildfire zones on a mountain ridge. *Ann. Ass. Am. Geog.*, **68**, 89–94.

Gangopadhyaya, M., Harbeck, G. E., Jr., Nordenson, T. J., Omar, M. H. and Uryvaev, V. A. (1966) *Measurement and Estimation of Evaporation and Evapotranspiration*. Geneva: World Meteorological Organization Technical Note No. 83.

Gauer, P. (2005) Numerical modeling of blowing and drifting snow in Alpine terrain. *J. Glaciol.*, **47**(156), 97–110.

Geiger, R. (1965) *The Climate near the Ground*. Cambridge, MA: Harvard University Press, pp. 417–18, 430–42, 453–4.

Geiger, R., Aron, A. H. and Todhunter, P. (2003) *Climate near the Ground*. Lanham, MD: Rowman and Littlefield, 584 pp.

Glazyrin, G. E. (1970) Fazovoe sostoyanie osadkov v gorakh v zavisimosti ot prizemnoy temperaturiy vozdukha (The phase condition of precipitation in mountains independence on surface air temperature). *Met. i Gidrol.*, 30–4.

Glickman, T. S. (ed.) (2000) *The Glossary of Meteorology*, 2nd edn. Boston, MA: American Meteorological Society.

Golding, D. L. (1978) Calculated snowpack evaporation during chinooks along the eastern slopes of the Rocky Mountains. *J. appl. Met.*, **17**, 1647–51.

Golubev, V. S. (1986) On the problem of standard conditions for precipitation gauge installation. In B. Sevruk (ed.), *Proceedings, International Workshop on the Correction of Precipitation Measurements, Instruments and Observing Methods*, Report no. 24 (WMO/TD no. 104). Geneva: World Meteorological Organization, pp. 57–9.

Goodin, D. G. and Isard, S. A. (1989) Magnitude and sources of variation in albedo within an alpine tundra. *Theoret. Appl. Climatol.*, **40**, 50–60.

Goodison, B. E., Sevruk, B. and Klemm, S. (1989) WMO solid precipitation measurement intercomparison: objectives, methodology, analysis. In J. W. Delleur (ed.), *Atmospheric Deposition*, International Association of Hydrological Sciences, Publication No. 179. Wallingford, UK: IAHS Press, pp. 59–64.

Goodison, B. E., Louie, P. Y. T. and Yang, D.-Q. (1998) *WMO Solid Precipitation Intercomparison*, WMO/TD-872. Geneva: World Meteorological Organization, 212 pp.

Goovaerts, P. (2000) Geostatistical approaches for incorporating elevation into the spatial interpolation of rainfall. *J. Hydrol.*, **228**, 113–29.

Greenland, D. (1978) Spatial distribution of radiation on the Colorado Front Range. *Climat. Bull.*, Montreal, **24**, 1–14.

Greenland, D. (1989) The climate of Niwot Ridge, Front Range, Colorado, USA. *Arct. Alp. Res.*, **21**, 380–91.

Greenland, D. E. (1991) Surface energy budgets over alpine tundra in summer, Niwot Range, Colorado Front Range. *Mountain Res. Devel.*, **11**, 339–51.

Greenland, D. (1993) Spatial energy budgets in alpine tundra. *Theor. Appl. Clim.*, **46**, 229–39.

Gregory, S. (1968) The orographic component in rainfall distribution patterns. In J. A. Sporck (ed.), *Mélanges de Géographie. I. Géographie Physique et Géographie Humaine*. Gembloux, Belgium: J. Duculot, S. A., pp. 234–52.

Grunow, J. (1952a) Nebelniederschlag: Bedeutung und Erfassung einer Zusatz- komponente des Niederschlags, *Berichte deutsch. Wetterdienst.-US Zone*, **7**(42), 30–4.

Grunow, J. (1952b) Kritische Nebelfroststudien. *Arch. Met. Geophys. Biokl.*, **B 4**, 389–419.

Grunow, J. (1960) *Ergebnisse mehrjähriger Messungen von Niederschlägen am Hang und im Gebirge*. International Association of Scientific Hydrology Publication No. 53, 300–16.

Grunow, J. and Tollner, H. (1969) Nebelniederschlag im Hochgebirge. *Arch. Met. Geophys. Biokl.*, **B 17**, 201–28.

Guan, H., Wilson, J. L. and Makhnin, O. (2005) Geostatistical mapping of mountain precipitation incorporating autosearched effects of terrain and climatic characteristics. *J. Hydromet.*, **6**, 1018–31.

Hanson, C. L. (1982) Distribution and stochastic generation of annual and monthly precipitation on a mountainous watershed in southwest Idaho. *Water Resour. Bull.*, **18**, 875–83.

Harrold, T. W. (1966) The measurement of rainfall using radar. *Weather*, **21**, 247–9, 256–8.

Hartman, M. D., *et al.* Simulations of snow distribution and hydrology in a mountain basin. *Water Resour. Res.*, **35**(8), 1587–604.

Hastenrath, S. L. (1967) Rainfall distribution and regime in central America. *Arch. Met. Geophys. Biokl.*, **B 15**, 201–41.

Hastenrath, S. L. (1978) Heat-budget measurements on the Quelccaya ice cap, Peruvian Andes. *J. Glaciol.*, **20**(82), 85–97.

Hauer, H. (1950) Klima und Wetter der Zugspitze. *Berichte d. Deutschen Wetterdienstes in der US-Zone*, **16**.

Havlik, D. (1968) Die Höhenstufe maximaler Niederschlagssummen in den Westalpen. *Freiburger Geogr. Hefte*, **7**.

Hay, L. E. and McCabe, G. J. (1998) Verification of the Rhea orographic-precipitation model. *J. Amer. Water Assoc.*, **34**, 1103–12.

Hennemuth, B. and Köhler, U. (1984) Estimation of the energy balance of the Dischma Valley. *Arch. Met. Geophys. Biocl.*, **B 34**, 97–119.

Hennessy, J. P., Jr. (1979) Comments on "Use of mesoscale climatology in mountainous terrain to improve the spatial representation of mean monthly temperatures." *Mon. Wea. Rev.*, **107**, 352–3.

Henning, D. and Henning, D. (1981) Potential evapotranspiration in mountain geo-ecosystems of different altitudes and latitudes, *Mountain Res. Devel.*, **1**, 267–74.

Henz, J. F. (1972) An operational technique of forecasting thunderstorms along the lee slope of a mountain range. *J. appl. Met.*, **11**, 1284–92.

Hess, M., Niedzwiedz, T. and Obrebska-Starkel, B. (1975) The methods of constructing climatic maps of various scales for mountainous and upland territories, exemplified by the maps prepared for southern Poland. *Geog. Polonica*, **31**, 163–87.

Hill, F. F. (1983) The use of average annual rainfall to derive estimates of orographic enhancement of frontal rain over England and Wales for different wind directions. *J. Climatol.*, **3**, 113–29.

Hill, F. F., Browning, K. A. and Bader, M. J. (1981) Radar and raingauge observations of orographic rain over south Wales. *Q. J. R. Met. Soc.*, **107**, 643–70.

Hill, S. A. (1881) The meteorology of the North-West Himalaya. *Ind. Met. Mem.*, Calcutta, **1**(VI), 377–429.

Hindman, E. E. (1986a) An atmospheric water balance over a mountain barrier. In Y.-G. Xu (ed.), *Proceedings of the International Symposium on the Qinghai-Xizang Plateau and Mountain Meteorology*. Beijing: Science Press, pp. 580–95.

Hindman, E. E. (1986b) Characteristics of supercooled liquid water in clouds at mountaintop sites in the Colorado Rockies. *J. Clim. Appl. Met.*, **25**, 1271–9.

Hjermstad, L. M. (1970) *The Influence of Meteorological Parameters on the Distribution of Precipitation across Central Colorado Mountains*. Atmospheric Science Paper No. 163. Fort Collins, CO: Colorado State University.

Hjermstad, L. M. (1975) *Final Comprehensive Operations Report 1970–75 Season*. Colorado River Basin Pilot Project, EG & G (Report AL-1200), Albuquerque, New Mexico.

Hobbs, P. V. (1975) The nature of winter clouds and precipitation in the Cascade Mountains and their modification by artificial seeding. Pt. 1. Natural conditions, *J. appl. Met.*, **14**, 783–804.

Hobbs, P. V. (1978) Organization and structure of clouds and precipitation on the mesoscale and microscale in cyclonic storms. *Rev. Geophys. Space Phys.*, **16**, 741–55.

Hobbs, P. V., Easter, R. C. and Fraser, A. B. (1973) A theoretical study of the flow of air and fallout of solid precipitation over mountainous terrain. Pt. II: Microphysics. *J. Atmos. Sci.*, **30**, 813–23.

Hobbs, P. V., Houze, R. A., Jr. and Matejka, T. J. (1975) The dynamical and microphysical structure of an occluded frontal system and its modification by orography. *J. Atmos. Sci.*, **32**, 1542–62.

Holmboe, J. and Klieforth, H. (1957) *Investigations of Mountain Lee Waves and the Air Flow over the Sierra Nevada*, Final Report, Contract AF19-(604)-728. Los Angeles: Meteorology Department, University of California.

Hood, E. W., Williams, M. W. and Cline, D. (1999) Sublimation from a seasonal snowpack at a continental, mid-latitude alpine site. *Hydrol. Processes*, **13**, 1781–97.

Hoover, M. D. and Leaf, C. E. (1967) Process and significance of interception in Colorado subalpine forest. In W. E. Sopper and H. W. Lull (eds), *Symposium on Forest Hydrology*. Oxford: Pergamon Press, pp. 213–24.

Horton, R. E. (1934) Water losses in high latitudes and at high elevations. *Trans. Am. Geophys. Union*, **15**(2), 351–79.

Hosler, C. L., Davis, L. G. and Booker, D. R. (1963) Modification of convective systems by terrain with local relief of several hundred metres. *Zeit. angew. Math. Phys.*, **14**, 410–18.

Houghton, J. G. (1979) A model for orographic precipitation in the north-central Great Basin. *Mon. Weather Rev.*, **107**, 1462–75.

Houze, R. A., Jr. and Medina, S. (2005) Turbulence as a mechanism for orographic precipitation enhancement. *J. Atmos. Sci.*, **62**(10), 3599–623.

Hovkind, E. L. (1965) Precipitation distribution round a windy mountain peak. *J. Geophys. Res.*, **70**, 3271–8.

Hrudicka, B. (1937) Zur Nebelfrosttage. *Gerlands Beitr. Geophys.*, **51**, 335–42.

Hutchison, B. A. (1966) A comparison of evaporation from snow and soil surfaces. *Bull. Int. Ass. Sci. Hydrol.*, **11**, 34–42.

Hutchinson, P. (1968) An analysis of the effect of topography on rainfall in the Taieri catchment. Otago. *Earth Sci. J.*, **2**, 51–68.

Isard, S. A. and Belding, M. J. (1989) Evapotranspiration from the alpine tundra of Colorado, U.S.A. *Arct. Alp. Res.*, **21**, 71–82.

Jackson, M. C. (1978) Snow cover in Great Britain. *Weather*, **33**, 298–309.

Jairell, R. L. (1975) An improved recording gage for blowing snow. *Water Resour. Res.*, **11**, 674–80.

James, C. N. and Houze, R. A., Jr. (2005) Modification of precipitation by coastal orography in storms crossing northern California. *Mon. Wea. Rev.*, **133**(11), 3110–31.

Jarvis, E. C. and Leonard, R. (1969) *Vertical Velocities induced by Smoothed Topography for Ontario and their Use in Areal Forecasting*. Meteorological Branch, Technical Memorandum 728. Toronto: Department of Transport.

Jevons, W. S. (1861) On the deficiency of rain in an elevated rain gauge as caused by wind, London. *Edinburgh and Dublin Phil. Mag.*, **22**, 421–33.

Jiang, Q.-F. and Smith, R. B. (2003) Cloud timescales and orographic precipitation. *J. Atmos. Sci.*, **60**(13), 1543–59.

Juvik, J. O. and Ekern, P. C. (1978) A climatology of mountain fog on Mauna Loa, Hawaii Island, University of Hawaii. *Water Resour. Res. Cen. Tech. Rep.* no. 118.

Kattleman, R. and Elder, K. (1991) Hydrologic characteristics and balance of an alpine basin in the Sierra Nevada. *Water Resour. Res.*, **27**, 1553–62.

Kirshbaum, D. J. and Durran, D. R. (2005) Observations and modeling of banded orographic precipitation. *J. Atmos, Sci.*, **62**(5), 1463–79.

Koch, H. G. (1961) Die warme Hangzone. Neue anschauungen zur nächtlichen Kaltluftschichtung in Tälern und an Hängen. *Zeit. Met.*, **15**, 151–71.

Köhler, H. (1950) On evaporation from snow surfaces. *Arkiv Geofis.*, **1**, 159–85.

Kolbig, J. and Beckert, T. (1968) Untersuchungen der regionalen Unterschiede im Auftreten von Nebelfrost, *Zeit. Met.*, **20**, 148–60.

Komarkova, V. and Webber, P. J. (1978) An Alpine vegetation map of Niwot Ridge, Colorado. *Arct. Alp. Res.*, **10**, 1–29.

Koncek, M. (1959) Schneeverhältnisse der Hohen Tatra. *Ber. dtsch. Wetterdienst*, **54**, 132–3.

Koncek, M. (1960) Zur Frage der Nebelfrostablagerungen im Gebirge. *Studia Geophys. Geodet.*, **4**, 69–84.

Konzelmann, T., *et al.* (1997) Energy balance and evapotranspiration in a high mountain area during summer. *J. appl. Met.*, **36**, 966–73.

Korff, H. C. (1971) Messungen zum Wärmehaushalt in den äquatorialen Anden. *Ann. Met.*, **N.F. 5**, 99–102.

Koster, R. D., *et al.* (2000) A catchment-based approach to modeling land surface processes in a general circulation model. *J. Geophys. Res.*, **105(D20)**, 24 809–22.

Kraus, H. (1967) Das Klima von Nepal. *Khumbu Himal*, **1**(4), 301–21.

Kraus, H. (1971) A contribution to the heat and radiation budget in the Himalayas. *Arch. Met. Geophys. Biokl.*, **A 20**, 175–82.

Krestoviskiy, O. I. (1962) The water balance of small drainage basins during the period of high water. *Soviet Hydrol.*, **1**, 362–411.

Kunz, M. and Kottmeier, C. (2006) Orographic enhancement of precipitation over low mountain ranges, Part I. Model formulation and idealized simulations. *J. Appl. Met. Climatol.*, **45**, 1025–45.

Kuo, J. T. and Orville, H. D. (1973) A radar climatology of summertime convective clouds in the Black Hills. *J. appl. Met.*, **12**, 359–73.

Kuroiwa, D. (1965) *Icing and Snow Accretion on Electric Wires*, CRREL Research Report 123. Hanover, NH: US Army.

Küttner, J. and Model, E. (1948) Verschlüsselungsschwierigkeiten auf Bergstationen. *Zeit. Met.*, **2**, 139–41.

Kuvaeva, G. M. (1967) Nekotorye resultaty nablyudeniy nad ispareniem s poverkhnosti snezhnogo pokrova v vysokogornoy zone tsentralnogo Kavkaza (Some results of observations on evaporation over snow surfaces in the high mountain zone of the Central Caucasus 1). *Trudy Vysokogornyi Geofiz. Inst.*, **12**, 40–6.

Kuz'min, P. (1970) Methods for the estimation of evaporation from land applied in the USSR. *Symposium on World Water Balance*, Vol. 1, International Association of Scientific Hydrology Publication No. 92. Paris: UNESCO, pp. 225–31.

Kuz'min, P. (1972) *Melting of Snow Cover*. Jerusalem: Israel Program of Scientific Translation.

Lamb, H. H. (1955) Two-way relationships between the snow or ice limit and 1000–500 mb thickness in the overlying atmosphere. *Q. J. R. Met. Soc.*, **81**, 172–89.

Landsberg, H. (1962) *Physical Climatology*. DuBois, PA: Gray Printing Co., Inc, p. 186.

Lang, H. (1981) Is evaporation an important component in high alpine hydrology, *Nordic Hydrol.*, **12**, 217–24.

Lang, H. (1985) Höhenabhängigkeit der Niederschläge. In B. Sevruk (ed.), *Die Niederschlag in der Schweiz* (Berträge zur Geologie der Schweiz – Hydrologie, No. 31). Bern: Kummerly and Frey, pp. 149–57.

Larson, L. W. (1971) *Shielding Precipitation Gages from Adverse Wind Effects with Snow Fences*. Laramie: University of Wyoming, Water Resources Ser. no. 25.

Lauer, W. (1975) Klimatische Grundzüge der Höhenstufung tropischer Gebirge. In *Tagungsbericht und wissenschaftliche Abhandlungen*. 40 Deutscher Geographentag, Innsbruck. Innsbruck: F. Steiner, pp. 76–90.

Lauscher, A. and Lauscher, F. (1976) Zur Berechnung der Schneeverdunstung auf dem Sonnblick, 72–73 *Jahresber. des Sonnblick-Vereines für die Jahre* 1974–1975. Vienna: Sonnblict-Verein, pp. 3–10.

Lauscher, F. (1976a) Weltweite Typen der Höhenabhängigkeit des Niederschlags. *Wetter u. Leben*, **28**, 80–90.

Lauscher, F. (1976b) Methoden zur Weltklimatologie der Hydrometeore. Der Anteil des festen Niederschlags am Gesamtniederschlag. *Arch. Met. Geophys. Biokl.*, **B 24**, 129–76.

Lauscher, F. (1977) Reif und Kondensation auf Schnee und die wahre Zahl der Tage mit Reif. *Wetter u. Leben*, **29**, 175–80.

Lauscher, F. (1978a) Eine neue Analyse von Hilding Köhler's Messungen der Schneeverdunstung auf dem Haldde-Observatorium aus dem Winter 1920/21. *Arch. Met. Geophys. Biokl.*, **B 26**, 193–8.

Lauscher, F. (1978b) Typen der Höhenabhängigkeit des Niederschlags bei verschiedenen Witterungslagen im Sonnblick Gebiet. *Arbeiten, Zentralanst. für Met. Geodynam.* (Vienna), **32**(95), 1–6.

LeDrew, E. F. (1975) The energy balance of a mid-latitude alpine site during the growing season, 1973. *Arct. Alp. Res.* **7**, 301–14.

LeDrew, E. F. and Emerick, J. C. (1974) A mechanical balance-type lysimeter for use in remote environments. *Agric. Met.*, **13**, 253–8.

LeDrew, E. F. and Weller, G. (1978) A comparison of the radiation and energy balance during the growing season for arctic and alpine tundra. *Arct. Alp. Res.*, **10**, 665–78.

Lemmela, R. and Kuusisto, E. (1974) Evaporation from snow cover. *Hydrol. Sci. Bull.*, **19**, 541–8.

Li, L. and Pomeroy, J. W. (1997) Estimates of threshold wind speeds for snow transport using meteorological data. *J. appl. Met.*, **36**(3), 205–13.

Light, P. (1941) Analysis of high rates of snow-melting. *Trans. Am. Geophys. Union*, **22**(1), 195–205.

Linsley, R. K. (1958) Correlation of rainfall intensity and topography in northern California. *Trans. Am. Geophys. Union*, **39**, 15–18.

Lloyd, C. D. (2005) Assessing the effect of integrating elevation data into the estimation of monthly precipitation in Great Britain. *J. Hydrol.*, **308**, 128–50.

Longacre, L. L. and Blaney, H. F. (1962) Evaporation at high elevations in California. *Proc. Am. Soc. Civ. Eng. J. Irrig. Drainage Div.*, **3172**, 33–54.

Longley, R. W. (1975) Precipitation in valleys. *Weather*, **30**, 294–300.

Lumb, P. E. (1983) Snow on the hills. *Weather*, **38**, 114–15.

Lundquist, J. D. and Cayan, D. R. (2007) Surface temperature patterns in complex terrain: Daily variations and long-term changes in the central Sierra Nevada, California. *J. Geophys. Res.*, **112(D11)** D11124, 1–15.

MacCready, P. B. (1955) High and low elevations as thermal source regions. *Weather*, **10**, 35–40.

Mahrt, L. (2006) Variation of surface air temperature in complex terrain. *J. Atmos. Sci.*, **45**, 1481–93.

Manley, G. (1971) The mountain snows of Britain, *Weather*, **26**, 192–200.

Marcus, M. G. and Brazel, A. J. (1974) Solar radiation measurements at 5365 meters, Mt. Logan, Yukon. In V. C. Bushnell and M. G. Marcus (eds), *Icefield Ranges Research Project, Scientific Results*, Vol. 4. New York: American Geographical Society, pp. 117–19.

Marcus, M. G. and LaBelle, J. C. (1970) Summertime observations at the 5360 meter level, Mount Logan, Yukon, 1968–1969. *Arct. Alp. Res.*, **2**, 103–14.

Marek, B., *et al.* (2002) Temporal and spatial variations of fog in the western Sudety Mts., Poland. *Atmos. Res.*, **64**(1–4), 19–28.

Martinec, J. (1985) Korrektur der Niederschlagsdaten durch Schneemessungen. In B. Sevruk (ed.), *Die Niederschlag in der Schweiz* (Beiträge zur Geologie der Schweiz-Hydrologie no. 31). Berne: Kummerly and Frey, pp. 77–96.

Martinec, J. (1987) Importance and effects of seasonal snow cover. In B. E. Goodison, R. G. Barry and J. Dozier (eds), *Large Scale Effects of Seasonal Snow Cover*. IAHS Publ. no. 166. Wallingford, UK: International Association of Hydrological Science, pp. 107–20.

Martinec, J. (1989) Hour-to-hour snowmelt rates and lysimeter outflow during an entire ablation period. *Snow Cover and Glacier Variations*. Wallingford, UK: JAHS.

Martinelli, M., Jr. (1959) Some hydrologic aspects of alpine snowfields under summer conditions. *J. Geophys. Res.*, **64**, 451–5.

Martinelli, M., Jr., (1960) Moisture exchange between the atmosphere and alpine snow surfaces under summer conditions. *J. Met.*, **17**, 227–31.

Martinelli, M., Jr. (1973) Snow-fence experiments in alpine areas. *J. Glaciol.*, **12**(65), 291–303.

Marwitz, J. D. (1974) An airflow case study over the San Juan Mountains of Colorado. *J. appl. Met.*, **13**, 450–8.

Marwitz, J. D. (1980) Winter storms over the San Juan Mountains. Part I. Dynamical processes. *J. appl. Met.*, **19**, 913–26.

Marwitz, J. D. (1987) Deep orographic storms over the Sierra Nevada. Part II. The precipitation process. *J. Atmos. Sci.*, **44**, 174–85.

McCulloch, J. S. G. (1965) Tables for the rapid computation of the Penman estimate of evaporation. *E. Afr. Agric. Forest J.*, **30**, 286–95.

McCutchan, M. H. (1976) Diagnosing and predicting surface temperature in mountainous terrain. *Mon. Wea. Rev.*, **104**, 1044–51.

Medina, S., *et al.* (2005) Cross-barrier flow during orographic precipitation events: Results from MAP and IMPROVE. *J. Atmos. Sci.*, **62**(10), 3580–98.

Meiman, J. R. and Grant, L. O. (1974) *Snow-Air Interactions and Management of Mountain Watershed Snowpack*, Completion Report Serial No. 57. Fort Collins, CO: Environmental Research Center, Colorado State University.

Meister, R. (1987) Wind systems and snow transport in alpine topography. In B. Salm and H. Gubler (eds), *Avalanche Formation, Movement and Effects*, IAHS. Publication 162. Wallingford, UK: International Association of Hydrological Sciences, pp. 265–7.

Mellor, M. (1965) *Blowing Snow* (Cold Regions Science and Engineering. Part III, Section A3c). Hanover, NH: US Army, Cold Regions Research Engineering Laboratory.

Mendonca, B. G. and Iwaoka, W. T. (1969) Trade wind inversion at the slope of Mauna Loa. *J. appl. Met.*, **8**, 213–19.

Migala, K. and Sobik, M. (2002) Rime in the Giant Mountains (the Sudetes). Poland. *Atmos. Res.*, **64**(1–4), 63–73.

Mikhel, V. M. and Rudneva, A. V. (1971) Description of snow transport and snow deposition in the European USSR. *Soviet Hydrol.*, **10**, 342–8.

Mikhel, V. M., Rudneva, A. V. and Lipovskaya, V. I. (1971) *Snowfall and Snow Transport during Snowstorms over the USSR*. Jerusalem: Israel Program of Scientific Translation.

Miller, D. H. (1955) *Snow Cover and Climate in the Sierra Nevada, California*. Berkeley, CA: University of California Press, Publ. in Geog., 11.

Miller, D. H. (1962) Snow in the trees – where does it go? In *Proceedings of the 30th Annual Western Snow Conference*, pp. 21–9.

Miller, J. F. (1972) Physiographically adjusted precipitation-frequency maps. In *Distribution of Precipitation in Mountainous Areas*, Vol. 2. Geneva: World Meteorological Organization no. 326, pp. 264–77.

Miller, J. F. (1982) Precipitation evaluation in hydrology. In E. J. Plate (ed.), *Engineering Meteorology*. Amsterdam: Elsevier, pp. 371–428.

Miniscloux, F., Creutin, J. D. and Anquetin, S. (2001) Geostatistical analysis of orographic rainbands. *J. appl. Met.*, **40**, 1835–54.

Mori, M. and Kobayashi, T. (1996) Dynamics interactions between observed nocturnal drainage winds and cold air lake. *J. Met. Soc. Japan*, **74**, 247–58.

Müller, H. (1984) *Zum Strahlungshaushalt im Alpenraum*. Mitteilungen der Versuchsanstalt fuer Wasserbau, Hydrologie und Glaziologie No. 71. Zurich: ETH, 167 pp.

Müller, H. (1985) On the radiation budget in the Alps. *J. Climatol.*, **5**, 445–62.

Murray, R. (1952) Rain and snow in relation to the 1000–700 mb and 1000–500 mb thickness and the freezing level. *Met. Mag.*, **81**, 5–8.

Myers, V. A. (1962) Airflow on the windward side of a ridge. *J. Geophys. Res.*, **67**, 4267–91.

Nagel, J. F. (1956) Fog precipitation on Table Mountain. *Q. J. R. Met. Soc.*, **83**, 452–60.

Nicholass, C. A. and Harrold, T. W. (1975) The distribution of rainfall over subcatchments of the River Dee as a function of synoptic type. *Met. Mag.*, **104**, 208–17.

Nickerson, E. C., Smith, D. R. and Chappell, C. F. (1978) Numerical calculation of airflow and cloud during winter storm conditions in the Colorado Rockies and Sierra Nevada mountains. In *Proceedings of the Conference on Sierra Nevada Meteorology*. Boston, MA: American Meteorological Society, pp. 126–32.

Nipher, F. E. (1878) On the determination of the true rainfall in elevated gages. *Proc. Am. Ass. Adv. Sci.*, **27**, 103–8.

Nullet, D. and McGranaghan, M. (1988) Rainfall enhancement over the Hawaiian Islands. *J. Climate*, **1**, 837–9.

Obrebska-Starkel, B. (1970) Uber die thermische Temperaturschichtung in Bergtälern. *Acta Climat.*, **9**, 33–47.

Ohmura, A. (1982) Regional water balance on the arctic tundra in summer. *Water Resour. Res.*, **18**, 301–5.

Ohmura, A. (1991) New precipitation and accumulation maps for Greenland. *J. Glaciol.*, **37**(125), 140–8.

Oke, T. R. (1987) *Boundary Layer Climates*, 2nd edn. London: Methuen, 435 pp.

Ono, S. (1925) On orographic precipitation. *Phil. Mag.*, 6th Ser., **49**, 144–64.

Orville, H. D. (1965a) A numerical study on the initiation of cumulus clouds over mountainous terrain. *J. Atmos. Sci.*, **22**, 684–99.

Orville, H. D. (1965b) A photogrammetric study of the initiation of cumulus clouds over mountainous terrain. *J. Atmos. Sci.*, **22**, 700–9.

Orville, H. D. (1968) Ambient wind effects on the initiation and development of cumulus clouds over mountains. *J. Atmos. Sci.*, **25**, 385–403.

Ovadia, D. and Pegg, R. K. (1979) An approach to calculating evaporation rates at remote sites. *Nordic Hydrol.*, **10**, 41–8.

Page, J. K. (1969) Heavy glaze in Yorkshire – March 1969. *Weather*, **24**, 486–95.

Parsons, J. (1960) "Fog drip" from coastal stratus, with special reference to California. *Weather*, **15**, 58–62.

Peak, G. W. (1963) Snow pack evaporation factors. In *Proceedings of the 31st Annual Western Snow Conference*, pp. 20–7.

Peck, E. L. (1964) The little used third dimension. In *Proceedings of the 32nd Annual Meeting of the Western Snow Conf.* (Nelson, British Columbia), pp. 33–40.

Peck, E. L. (1972a) Discussion of problems in measuring precipitation in mountainous Areas. In *Distribution of Precipitation in Mountainous Areas*, Vol. I. Geneva: World Meteorological Organization No. 326, pp. 5–16.

Peck, E. L. (1972b) Relation of orographic precipitation patterns to meteorological parameters. In *Distribution of Precipitation in Mountainous Areas*, Vol. II. Geneva: World Meteorological Organization No. 326, pp. 234–42.

Peck, E. L. and Brown, M. J. (1962) An approach to the development of isohyetal maps for mountainous areas. *J. Geophys. Res.*, **67**, 681–94.

Peck, E. L. and Pfankuch, D. J. (1963) *Evaporation Rates in Mountainous Terrain*. International Association of Scientific Hydrology, Publ. No. 62. Gentbrugge, Belgium: IASH, pp. 267–78.

Pedgley, D. E. (1967) The shape of snowdrifts. *Weather*, **22**, 42–8.

Pedgley, D. E. (1970) Heavy rainfalls over Snowdonia. *Weather*, **25**, 340–9.

Pedgley, D. E. (1971) Some weather patterns in Snowdonia. *Weather*, **26**, 412–44.

Penman, H. L. (1963) *Vegetation and Hydrology*. Commonwealth Bureau of Soils Technical Communication 53. Farnham Royal, Bucks: Commonwealth Agricultural Bureaux.

Phillips, D. L., Dolp, J. and Marks, D. (1992) A comparison of geostatistical procedures for spatial analysis of precipitation in mountainous terrain. *Agric. Forest Met.*, **58**, 1–21.

Phillips, P. E. (1956) Icing of overhead high-voltage power lines in the Grampians. *Met. Mag.*, **85**, 376–8.

Pielke, R. A. and Mehring, P. (1977) Use of mesoscale climatology in mountainous terrain to improve the spatial representation of mean monthly temperatures. *Mon. Wea. Rev.*, **105**, 108–12.

Pleško, N. and Sinik, N. (1978) The energy balance in the mountains of Croatia. *Arbeiten, Zentralanst. Met. Geodynam.*, Vienna, **31**(9), 1–9, 16.

Pockels, F. (1901) The theory of the formation of precipitation on mountain slopes. *Mon. Weather Rev.*, **29**, 152–9, 306–7.

Poggi, A. (1959) Contribution à la connaissance de la distribution altimétrique de la durée de l'enneigement dans les Alpes françaises du nord. *Ber. dtsch. Wetterd.*, **54**, 134–49.

Pomeroy, J. W. and Essery, R. L. H. (1999) Turbulent fluxes during blowing snow: Field tests of model sublimation predictions. *Hydrol. Processes*, **13**, 2963–75.

Pomeroy, J. W., Gray, D. M. and Landine, P. G. (1993) Prairie blowing snow model: characteristics, validation, operation. *J. Hydrol.*, **144**(1–4), 165–92.

Poulter, R. M. (1936) Configuration, air mass and rainfall. *Q. J. R. Met. Soc.*, **62**, 49–79.

Priestley, C. H. B. and Taylor, R. J. (1972) On the assessment of surface heat flux and evaporation using large-scale parameters. *Mon. Wea. Rev.*, **100**, 81–92.

Pugh, H. L. D. and Price, W. I. J. (1954) Snow drifting and the use of snow fences. *Polar Rec.*, **7**(47), 4–23.

Queney, P. (1948) The problem of airflow over mountains: a summary of theoretical studies. *Bull. Am. Met. Soc.*, **29**, 16–26.

Raddatz, R. L. and Khandekar, M. L. (1977) Numerical simulation of cold easterly circulations over the Canadian Western Plains using a mesoscale boundary-layer model. *Boundary-Layer Met.*, **11**, 307–28.

Radok, U. (1968) *Deposition and Erosion of Snow by the Wind*. CRREL Research Report 20, Hanover, NH: US Army, Cold Regions Research Engineering Laboratory.

Radok, U. (1977) Snow drift. *J. Glaciol.*, **19**(81), 123–39.

Rallison, R. E. (1981) Automated system for collecting snow and related hydrological data in mountains of the western United States. *Hydrol. Sci. Bull.*, **26**, 83–9.

Rangno, A. L. (1979) A re-analysis of the Wolf Creek cloud seeding experiment. *J. appl. Met.*, **18**, 579–85.

Rango, A., et al. (1989) Average areal water equivalent of snow in a mountain basin using microwave and visible satellite data. *IEEE Trans. Geosci. Remote Sensing*, **27**, 740–5.

Ranzi, R., Zappa, M. and Bachi, B. (2007) Hydrological aspects of the Mesoscale Alpine Programme; Findings from field experiments and simulations. *Q. J. Roy. Met. Soc.*, **133**(625), 867–80.

Rauber, R. M., et al. (1986) The characteristics and distribution of cloud water over the mountains of northern Colorado during winter-time storms. Part I. Temporal variations. *J. Clim. Appl. Met.*, **25**, 468–88.

Raymond, D. J. and Wilkening, M. H. (1980) Mountain-induced convection under fair weather conditions. *J. Atmos. Sci.*, **37**, 2693–706.

Rechard, P. A. (1972) Winter precipitation gauge catch in windy mountainous areas. In *Distribution of Precipitation in Mountainous Areas*, Vol. I. Geneva: World Meteorological Organization No. 326, pp. 13–26.

Rechard, P. A. and Raffelson, C. N. (1974) Evaporation from snowdrifts under oasis conditions. In Advanced Concepts and Techniques, *The Study of Snow and Ice Resources*. Washington, DC: National Academy Science, pp. 99–107.

Reid, I. (1973) The influence of slope aspect on precipitation receipt. *Weather*, **28**, 490–3.

Reinelt, E. R. (1970) On the role of orography in the precipitation regime of Alberta. *Albertan Geographer*, **6**, 45–58.

Reiter, R. and Sladkovic, P. (1970) Control of vertical transport of aerosols between 700 and 3000 metres by lapse rate and fine structure of temperature. *J. Geophys. Res.*, **75**, 3065–75.

Rhea, J. O. (1978) Orographic Precipitation Model for Hydrometeorological Use, Atmospheric Science Paper No. 287. Fort Collins, CO: Colorado State University.

Rhea, J. O. and Grant, L. O. (1974) Topographic influences on snowfall patterns in mountainous terrain. In *Advanced Concepts and Techniques in the Study of Snow and Ice Resources*. Washington, DC: National Academy of Science, pp. 182–92.

Riley, G. T., Landin, M. G. and Bosart, L. F. (1987) The diurnal variability of precipitation across the central Rockies and adjacent Great Plains. *Mon. Wea. Rev.*, **115**(6), 1161–72.

Rodda, J. C. (1967) The rainfall measurement problem. In *Geochemistry, Precipitation, Evaporation, Soil-Moisture, Evaporation*. IUGG General Assembly of Bern, pp. 215–30.

Roe, G. H. (2002) Modeling orographic precipitation over ice sheets: an assessment over Greenland. *J. Glaciol.*, **48**, 70–80.

Roe, G. T. (2005) Orographic precipitation. *Ann. Rev. Earth Planet. Sci.*, **33**, 645–71.

Rohrer, M. (1989) Determination of the transition air temperature from snow to rain and intensity of precipitation. In B. Sevruk (ed.), *Precipitation Measurement, WMO/IAHS/ETH Workshop on Precipitation Measurements*. Zurich: Swiss Federal Institute of Technology, pp. 475–82.

Rotach, M. W., *et al.* (2004) Turbulence structure and exchange processes in an alpine valley, The Riviera project. *Bull. Amer. Met. Soc.*, **85**(9), 1367–85.

Rott, H. (1979) Vergleichende Untersuchungen der Energiebilanz in Hochgebirge. *Arch. Met. Geophys. Biokl.*, **A 28**, 211–32.

Rotunno, R. and Houze, R. A. (2007) Lessons on orographic precipitation from the Mesoscale Alpine Programme. *Q. J. Roy. Met. Soc.*, **133**(625), 811–30.

Ryerson, C. C. (1988) *New England Mountain Icing Climatology*, CRREL Report 88–12. Hanover, NH: US Army.

Sabo, E. D. (1956) *Evaporation from Snow in the Ergeni District. Selected Articles on Snow and Snow Evaporation*. Jerusalem: Israel Program of Science Translations, pp. 14–21.

Sachs, P. (1972) *Wind Forces in Engineering*. Oxford: Pergamon Press, p. 270.

Saintignon, M. F. de (1976) Décroissance de températures en montagne de latitude moyenne: exemple des Alpes françaises du Nord. *Rev. Géog. Alp.*, **64**, 483–94.

Salter, M. de C. S. (1918) The relation of rainfall to configuration. *Brit. Rainfall*, **1918**, 40–56.

Santeford, H. S., Jr. (1972) Management of windblown alpine snows. Unpublished Ph.D. Thesis. Fort Collins, CO: Colorado State University.

Sarker, R. P. (1966) A dynamical model of orographic rainfall. *Mon. Weather Rev.*, **94**, 555–72.

Sarker, R. P. (1967) Some modifications in a dynamical model of orographic rainfall. *Mon. Weather Rev.*, **95**, 673–84.

Sato, T. and Kimura, F. (2005) Diurnal cycle of convective instability around the central mountains in Japan during the warm season. *J. Atmos. Sci.*, **62**(5), 1626–36.

Sawyer, J. S. (1956) The physical and dynamical problems of orographic rain. *Weather*, **11**, 375–81.

Schermerhorn, V. P. (1967) Relations between topography and annual precipitation in western Oregon and Washington. *Water Resour. Res.*, **3**, 707–11.

Schmidt, R. A., Jr. (1972) Sublimation of wind-transported snow – a model, USDA, Forest Service Research Paper RM-90. Fort Collins, CO: Rocky Mountain Forest and Range Experimental Station.

Schmidt, R. A. (1977) A system that measures blowing snow. USDA, Forest Service Research Paper RM-194. Fort Collins, CO: Rocky Mountain Forest and Range Experimental Station.

Schmidt, R. A. (1984) Transport rate of drifting snow and the mean wind speed profile. *Boundary-Layer Met.*, **34**, 213–41.

Schüepp, M. (1963) Bewölkung und Nebel. *Klimatologie der Schweiz*, Vol. 4, part H. Supplement, Annalen, Schweizerischen Meteorologischen Zentralanstalt, (Annual 1962), 68 pp.

Schultz, O. and de Jong, C. (2004) Snowmelt and sublimation: Field experiments and modelling in the High Atlas Mountains of Morocco. *Hydrol Earth System Sci.*, **8**, 1076–89.

Scorer, R. S. (1955) The growth of cumulus over mountains. *Arch. Met. Geophys. Biokl.*, **A 8**, 25–34.

Sevruk, B. (1972a) Precipitation measurements by means of storage gauges with stereo and horizontal orifices in the Baye de Montreux watershed. In *Distribution of Precipitation in Mountainous Areas*, Vol. 1. Geneva: World Meteorological Organization No. 326, pp. 86–95.

Sevruk, B. (1972b) Evaporation losses from storage gauges. In *Distribution of Precipitation in Mountainous Areas*, Vol. 1. Geneva: World Meteorological Organization No. 326, pp. 96–102.

Sevruk, B. (1974) The use of stereo, horizontal and ground level orifice gages to determine a rainfall-elevation relationship. *Water Resour. Res.*, **10**, 1138–42.

Sevruk, B. (1983) Correction of measured precipitation in the Alps using the water equivalent of new snow. *Nordic Hydrol.*, **14**, 49–58.

Sevruk, B. (1985) Schneeanteil am Monatsniederschlag. In B. Sevruk (ed.), *Die Niederschlag in der Schweiz* (Beiträge zur Geologie der Schweiz – Hydrologie No. 31). Bern: Kummerly and Frey, pp. 127–37.

Sevruk, B. (1986a) Correction of precipitation measurements. In B. Sevruk (ed.), *Proceedings of the International Workshop on the Correction of Precipitation Measurements, Instruments and Observing Methods*, Report No. 24 (WMO/TD No. 104). Geneva: World Meteorological Organization, pp. 13–23.

Sevruk, B. (1986b) Correction of precipitation measurements: Swiss experience. In B. Sevruk (ed.), *Precipitation Measurement*. Zurich: Swiss Federal Institute of Technology, pp. 187–93.

Sevruk, B. (ed.) (1989) *Precipitation measurement. WMO/IAHS/ETH Workshop on Precipitation Measurement*. Zurich: Swiss Federal Institute of Technology.

Sevruk, B. and Klemm, S. (1989) Types of standard precipitation gauges. In B. Sevruk (ed.), *Precipitation Measurement*. Zurich: Swiss Federal Institute of Technology, pp. 227–32.

Sharples, J. J., Hutchinson, M. F. and Jellett, D. R. (2005) On the horizontal scale of elevation dependence of Australian monthly precipitation. *J. appl. Met.*, **44**, 1850–65.

Shea, J. M., Marshall, S. J. and Livingston, J. M. (2004) Glacier distribution and climate in the Canadian Rockies. *Arct. Antarct. Alp Res.*, **36**(2), 272–9.

Sheaffer, J. D. and Reiter, E. R. (1987) Measurements of surface energy budgets in the Rocky Mountains of Colorado. *J. Geophys. Res.*, **92(D4)**, 445–62.

Sibley, A. (2005) Analysis of the heavy orographic rainfall over North Wales, 3 and 4 February 2004. *Weather*, **60**, 31–6.

Silverman, B. A. (1960) The effect of a mountain on convection. In C. E. Anderson (ed.), *Cumulus Dynamics*. New York: Pergamon Press, pp. 4–27.

Slatyer, R. O., Cochrane, P. M. and Galloway, R. W. (1984) Duration and extent of snow cover in the Snowy Mountains and a comparison with Switzerland. *Search*, **15**, 327–31.

Slaughter, C. W. (1970) *Evaporation from Snow and Evaporation Retardation by Monomolecular Films*, Special Rep. 130. Hanover, NH: Cold Regions Research Engineering Laboratory, US Army.

Smith, R. B. (1979) The influence of mountains on the atmosphere. *Adv. Geophys.*, **21**, 87–230.

Smith, R. B. (1982) A differential advection model of orographic rain. *Mon. Wea. Rev.*, **110**, 306–9.

Smith, R. B. (1985) Comment on "Interaction of low-level flow with the Western Ghat mountains and offshore convection in the summer monsoon" (Reply D. R. Durran and R. L. Grossman). *Mon. Wea. Rev.*, **113**, 2176–81.

Smith, R. B. (2003) A linear time-delay model of orographic precipitation. *J. Hydrol.*, **282**, 2–9.

Smith, R. B. and Lin, Y.-L. (1983) Orographic rain on the Western Ghats. In E. R. Riter, B.-Z. Zhu and Y.-F. Qian (eds), *Proceedings of the First Sino-American Workshop on Mountain Meteorology*. Beijing: Science Press, pp. 71–94.

Smith, R. B. and Barstad, I. (2004) A linear theory of orographic precipitation. *J. Atmos. Sci.*, **61**, 1377–91.

Smith, R. B., *et al.* (2003) Orographic precipitation and airmass transformation; An Alpine example. *Q. J. R. Met. Soc.*, **129**, 433–54.

Smith, R. B., Barstad, L. and Bonneau, L. (2005) Orographic precipitation and Oregon's climate transition. *J. Atmos. Sci.*, **62**, 177–91.

Smithson, P. A. (1970) Influence of topography and exposure on airstream rainfall in Scotland. *Weather*, **25**, 379–86.

Sporns, U. (1964) On the transportation of short duration rainfall intensity data in mountainous regions. *Arch. Met. Geophys. Biokl.*, **B 13**, 438–42.

Spreen, W. C. (1947) Determination of the effect of topography on precipitation. *Trans. Am. Geophys. Un.*, **28**, 285–90.

Stanev, S. (1968) Nebelfrostablagerungen an Freileitungen unter Gebirgsbedingungen. *Zeit. Met.*, **20**, 161–4.

Staudinger, M. and Rott, H. (1981) Evapotranspiration at two mountain sites during the vegetation period. *Nordic Hydrol.*, **12**, 207–16.

Steinacker, R. (1983) Diagnose und Prognose der Schneefallgrenze. *Wetter u. Leben*, **35**, 81–90.

Steinhauser, F. (1948) Die Schneehöhen in den Ostalpen und die Bedeutung der winterlichen Temperaturinversion. *Arch. Met. Geophys. Biokl.*, **B 1**, 63–74.

Steinhauser, F. (1967) Methods of evaluation and drawing of climatic maps in mountainous countries. *Arch. Met. Geophys. Biokl.*, **B 15**, 329–58.

Stewart, R. E. (1985) Precipitation types in winter storms. *Pure Appl. Geophys.*, **123**, 597–609.

Stigter, C. J. (1976) On the non-constant gamma. *J. appl. Met.*, **15**, 1326–7.

Stigter, C. J. (1978) On the pressure dependence of the wind function in Dalton's and Penman's evaporation equations. *Arch. Met. Geophys. Biokl.*, **A 27**, 147–54.

Storebö, P. B. (1968) Precipitation formation in a mountainous coast region. *Tellus*, **20**, 239–50.

Storr, D. and den Hartog, G. (1975) Gamma – the psychrometer non-constant. *J. appl. Met.*, **14**, 1397–8.

Strangeways, I. (2000) *Measuring the Natural Environment*. Cambridge: Cambridge University Press, 365 pp.

Struzer, L. R., Nechayer, I. N. and Bogdanova, E. G. (1965) Systematic errors of measurements of atmospheric precipitation. *Soviet Hydrol.*, **4**, 500–4.

Sugden, D. E. (1977) Reconstruction of the morphology, dynamics, and thermal characteristics of the Laurentide ice sheet at its maximum. *Arct. Alp. Res.*, **9**, 21–47.

Tabler, R. D. (1975a) Predicting profiles of snowdrifts in topographic catchments. In *Proceedings of the 43rd Western Snow Conference*, pp. 87–97.

Tabler, R. D. (1975b) Estimating the transport and evaporation of blowing snow. In *Snow Management on the Great Plains*, Publication 73. Lincoln, NE: University of Nebraska, Agriculture Experimental Station, pp. 85–104.

Takeuchi, M. (1980) Vertical profile and horizontal increase of drift-snow transport. *J. Glaciol.*, **26**(94), 481–92.

Tappenier, U. and Cernusca, A. (1989) Canopy structure and light climate of different alpine plant communities: analysis by means of a model. *Theoret. Appl. Climatol.*, **40**, 81–92.

Tepes, E. (1978) Ice depositions in Romanian mountainous regions. *Veröff, Schweiz. Met. Zentralanstalt*, Zurich, **40**, 308–12.

Tesche, T. W. (1988) Numerical simulation of snow transport, deposition and redistribution. In *Proceedings of the Western Snow Conference 56th Annual Meeting*, 93–103.

Thom, A. S. and Oliver, H. R. (1977) On Penman's equation for estimating regional evapo-transpiration. *Q. J. R. Met. Soc.*, **103**, 345–58.

Thompson, R. J. (1975) Energy budgets for three small plots – substantiation of Priestley and Taylor's large-scale evaporation parameter. *J. appl. Met.*, **14**, 1399–401.

Thornton, P. E., Running, S. W. and White, M. A. (1997) Generating surfaces of daily meteorological variables over large regions of complex terrain. *J. Hydrol.*, **190**, 214–51.

Tucker, D. F. and Reiter, E. R. (1988) Modeling heavy precipitation in complex terrain. *Met. Atmos. Phys.*, **39**, 119–31.

Tucker, G. B. (1954) Mountain cumulus. *Weather*, **9**, 198–200.

Turner, H. (1985) Nebelniederschlag. In B. Sevruk (ed.), *Die Niederschlag in der Schweiz*. (Beiträge zur Geologie der Schweiz – Hydrologie, No. 31). Bern: Kummerly and Frey, pp. 77–96.

Vogelman, H. W. (1973) Fog precipitation in the cloud forests of eastern Mexico. *BioScience*, **23**, 96–100.

Voloshina, A. P. (1966) *Teplovoy Balans Poverkhnosti Vysokogornykh Lednikov v Letnii Period* (Heat Balance of the Surface of Mountain Glaciers in Summer). Moscow: Nauka.

Vuille, M. (1996) Zur raumzeitlichen Dynamik von Schneefall und Ausaperung in Bereich des südlichen Altiplano. *Geographica Bernensia* (University of Bern), **G45**, 118 pp.

Wagner, A. (1930) Uber die Feinstruktur des Temperaturgradienten längs Berghängen. *Zeit. Geophys.*, **6**, 310–18.

Wagner, A. (1937) Gibt es im Gebirge eine Hôhenzone maximalen Niederschlages? *Gerlands Beitr. Geophys.*, **50**, 150–5.

Waibel, K. (1955) Die meteorologischen Bedingungen für Nebelfrostablagerungen am Hochspannungsleitungen im Gebirge. *Arch. Met. Geophys. Biokl.*, **B 7**, 74–83.

Waldemann, G. (1959) Schnee und Bodenfrost als Standortsfaktoren am Grossen Falkenstein. *Forstwiss. Centralblatt.*, **78**, 98–108.

Walker, E. R. (1961) *A Synoptic Climatology for Parts of the Western Cordillera*. Arctic Meteorology Research Group, Published in Met. No. 35. Montreal: McGill University.

Wanner, H. (1979) Zur Bildung, Verteilung und Vorhersage winterlicher Nebel im Querschnitt Jura-Alpen. *Geographica Bernensia*, G. **7**.

Warnick, C. C. and Penton, V. E. (1971) New methods of measuring water equivalent of snow pack for automatic recording at remote mountain locations. *J. Hydrol.*, **13**, 201–15.

Webster, R. and Oliver, M. A. (2001) *Geostatistics for Environmental Geoscientists*. Hoboken, NJ: Wiley, 286 pp.

Weckworth, I. M., *et al.* (1997) Horizontal convective rolls: Determining the environmental conditions supporting their existence and characteristics. *Mon. Wea. Rev.*, **125**, 505–26.

Weischet, W. (1969) Klimatologische Regeln zur Vertikalverteilung der Niederschlage in Tropengebirgen. *Die Erde*, **100**, 287–306.

Wendler, G. and Ishikawa, N. (1973) Heat balance investigations in an arctic mountainous area in northern Alaska. *J. appl. Met.*, **12**, 955–62.

West, A. J. (1959) Snow evaporation and condensation. In *Proceedings of the 27th Annual Meeting, Western Snow Conference*, pp. 66–74.

West, A. J. (1962) Snow evaporation from a forested watershed in the central Sierra Nevada. *J. Forest.*, **60**, 481–4.

Whiteman, C. D., *et al.* (2004) Comparison of vertical sounding and sidewall air temperature measurements in a small alpine basin. *J. appl. Met.*, **43**(11), 1635–47.

Willmott, C. J. (1977) WATBUG: A FORTRAN IV algorithm for calculating the climatic water budget. Newark, DE: Water Resources Center, University of Delaware.

Wilson, H. P. (1978) On orographic precipitation. In *Climatic Networks: Proceedings of the Workshop and Annual Meeting of the Alberta Climatological Association*. Inform. Rep., NOR-X-209. Edmonton, Alberta: Fisheries and Environment Canada, Northern Forest Research Centre, pp. 82–121.

Woods, C. P., *et al.* (2005) Microphysical processes and synergistic interactions between frontal and orographic forcing of precipitation during the 13 December 2001 IMPROVE-2 event over the Oregon Cascades. *J. Atmos. Sci.*, **62**(10), 3493–519.

World Meteorological Organization (1956) *International Cloud Atlas*, (abridged). Geneva: World Meteorological Organization.

World Meteorological Organization (1975) *Manual on the Observation of Clouds and Other Meteors: International Cloud Atlas*, Vol. I. Geneva: World Meteorological Organization, No. 407.

World Meteorological Organization (1984) *Guide to Hydrological Practices,* Vol. 1. *Data Acquisition and Processing* (4th edn). Geneva: World Meteorological Organization, No. 168.

World Meteorological Organization (1987) *International Cloud Atlas*, Vol. 2. Plates. Geneva: World Meteorological Organization, No. 407, 212 pp.

Yang, D.-Q., *et al.* (2000) An evaluation of the Wyoming gauge system for snowfall measurement. *Water Resour. Res.*, **36**(9), 2665–77.

Yang, D.-Q., *et al.* (2001) Compatibility evaluation of national precipitation measurements. *J. Geophys. Res.*, **106(D2)**, 1481–91,

Yoshino, M. M. (1975) *Climate in a Small Area: An Introduction to Local Meteorology*. Tokyo: University of Tokyo Press, 549 pp; pp. 429–34.

Yoshino, M. M. (1984) Thermal belt and cold air drainage on the mountain slope and cold air lake in the basin at quiet, clear night. *Geojournal*, **8**, 23–50.

Young, K. C. (1974) A numerical simulation of wintertime orographic precipitation. *J. Atmos. Sci.*, **31**, 1735–48; 1749–67.

Zängl, G. (2005a) The impact of lee-side stratification on the spatial distribution of orographic precipitation. *Q. J. R. Met. Soc.*, **131**, 1075–91.

Zängl, G. (2005b) Dynamical aspects of winter-time cold pools in an Alpine valley system. *Mon. Wea. Rev.*, **133**(9), 2721–40.

Zehnder, J., *et al.* (2006) Using digital cloud photogrammmetry to characterize the onset and transition from shallow to deep convection over orography. *Mon. Wea. Rev.*, **134**(9), 2527–46.

5 REGIONAL CASE STUDIES

The generalized view of the major climatic controls and characteristics provided in the preceding chapters obviously neglects many significant details and local anomalies, although the data are in many cases so sparse that the generalizations can only be preliminary and partial. As a counterbalance, therefore, it is worthwhile examining the climates of particular ranges via a series of complementary case studies. These include mountain systems in equatorial, tropical, mid-latitude (continental and maritime), and sub-polar regions, as well as high plateaus and ice sheets, which have been selected to illustrate both latitudinal and regional climatic differences. The selection is determined in part by the availability of data and adequate literature.

5.1 EQUATORIAL MOUNTAINS – NEW GUINEA AND EAST AFRICA

5.1.1 New Guinea

The central ranges of New Guinea form a backbone running through the length of the island. Except for the Owen Stanley Range in eastern Papua New Guinea, which is not considered here due to a total absence of information, the central ranges are orientated west-northwest–east-southeast. The mountains and highlands are most extensive between 143 and 145° E. The general summit level is about 3500–4000 m, but in Irian Jaya (Papua, or western New Guinea) peaks rise to over 4600 m with small ice bodies on Mt. Jaya (Mt. Carstenz) (4° S, 137° E), which have been studied by Australian expeditions (Hope *et al.*, 1976; Peterson *et al.*, 2002). The only other mountain area that has received climatological study is Mt. Wilhelm in the Bismarck Range (5° 40′ S, 145° 01′ E) (Hnatiuk *et al.*, 1976). The mountains are generally forested from the cultivation level around 2600 m to about 3500 m, with alpine tussock grassland above.

From May through October, New Guinea is under the influence of deep tropical easterly airflow while in December–March there are equatorial westerly winds at 700 mb and below, associated with the Indonesian–Australian summer monsoon circulation. In all seasons, the region is a frequent locus of air stream convergence and large-scale vertical motion. As a result, there is an average cloudiness of 5–6 oktas over Papua New Guinea and only slightly less further west. Humidity mixing ratio levels are high year round according to Prentice and Hope (2006).

For Merauke, sea level amounts average $15.5\,g\,kg^{-1}$ in July and $19\,g\,kg^{-1}$ in January. A mountain station at 4400 m near Mt. Jaya recorded $8–9\,g\,kg^{-1}$ in both months.

The seasonal circulation patterns exert a strong influence on precipitation regimes in the Highlands, except in the central part of the island where it is almost equally wet in all months. During the southeasterly season (May–September/October), the Eastern Highlands of Papua New Guinea (145–146° E) and the central ranges of Irian Jaya experience drier conditions with minimum amounts in June, July and August. The trade wind inversion, at about 2000 m south of the mountains, is a controlling factor for cloud development, but local convective circulations take on a dominant role at this season. Consequently there is a low inter-station correlation, even for annual precipitation amounts. During the southeast season, cloudiness shows a strong diurnal regime at Mt. Wilhelm. Skies are generally clear in the early morning, but convective build-up occurs from 0900–1000 h and cloud cover is complete by midday, often with afternoon precipitation, which may continue during the early part of the night. Sunset and sunrise, of course, vary little from the hours of 1800 h and 0600 h, respectively, in all months.

The "northwest season" (December–March) is almost continuously wet in all parts of the island and especially at high elevations. However, intensities are consistently modest. Annual amounts decrease above about 800 m on north and south slopes of the central range in Papua (Figure 5.1) (Barry, 1978). Along a transect on the southern side of Mt. Jaya, Prentice and Hope (2006) also show altitudinal maxima for average January and July conditions at 700 m elevation. The wettest locations in the upper Purari and Fly river basins receive over 7500 mm annually (Barry, 1980) and similar totals extend westward along the southern slopes of the Merauke Range according to Prentice and Hope. They report totals of 6000 and 7000 mm year^{-1} at 700 m asl and 1950 m asl, respectively, with no stations in between. Prentice *et al.* (2005; pers. comm., 2006) report a 1994–2003 annual average of 3150 mm for a weather station situated at 3750 m south of Mt. Jaya. In AD 2000, almost 4900 mm was recorded at 4400 m altitude.

Snow and graupel fall quite frequently on Mt. Wilhelm above 3800 m, in any month, and sleet or wet snow is the main precipitation form above 4400 m on Mt. Carstenz (Allison and Bennett, 1976). Occasional heavy falls of dry snow are reported even at the 4250 m level. The Merauke rawinsonde data indicate a freezing level, based on the standard atmosphere, at about 4900 m in January and July (Prentice and Hope, 2006).

The temperature regime in the mountains shows almost no seasonality, but the expected diurnal pattern is present (see p. 27). On Mt. Wilhelm, temperatures range between a mean minimum of 6 °C and a mean maximum of 10–11 °C except in the northwest season when maxima average 8–9 °C. Ground frost is not uncommon in the dry season, when skies usually clear before sunrise. Agriculturally devastating frost events occur periodically in the New Guinea highlands down to 2000–1500 m elevation in association with large-scale subsidence and reduced cloud cover.
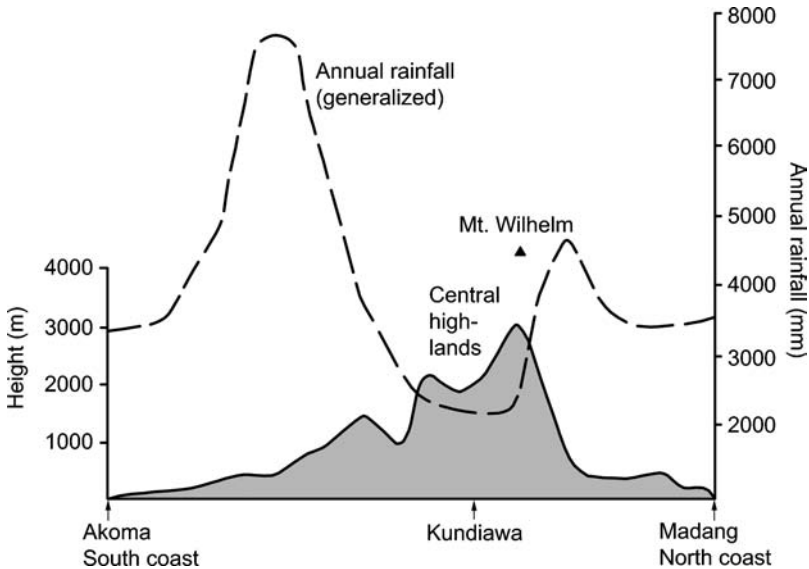
Fig. 5.1   Generalized topography and annual rainfall (cm) along a cross-section northward from Akoma on the
Gulf of Papua to Kundiawa (145° E, 6° S), then northeastward to Madang (from Barry 1978; based on a
rainfall map produced by the Snowy Mountain Engineering Corporation, 1975).

Such conditions are favored during El Niño/Southern Oscillation (ENSO) warm
events, when the normal area of deep convection over Indonesia–New Guinea
shifts eastward over the Pacific (Brookfield and Allen, 1989). Allen (1989) shows
that frost events in 1965, 1972, and 1982 were also dry years in New Guinea, but
the drought–frost/ENSO relationship is by no means definitively established.

A special feature of these equatorial mountains is the light winds. On Mt. Jaya,
(Mt. Carstenz), Allison and Bennett (1976) report an average speed of only
2.1 m s^{-1} for the period 22 December 1971–5 March 1972. Winds in the free air
are stronger in July–August with vector mean speeds of 6–7 m s^{-1} at 600 mb.
Occasional strong down-valley winds have been reported at Mt. Wilhelm during
dry spells (Hnatiuk *et al.*, 1976) and the highland valleys, generally, are subject to
mountain–valley wind systems.

A fuller review of the available material and literature on the climate of the New
Guinea mountains is published elsewhere (Barry, 1980). Other details may be found
in the cited references and McVean (1974).

5.1.2   *East Africa*

The isolated volcanic peaks of Mt. Kenya (5185 m) and Mt. Kilimanjaro (5895 m)
rise some 4000 m above the level of the high plains at around 800–1000 m in
equatorial East Africa. Farther west, the Ruwenzori Mountains – C. Ptolemy's
"Mountains of the Moon" (AD 150) – extend over 100 km southwest–northeast
along the Uganda–Zaire border, with 24 peaks rising above 4600 m. Many of the

peaks possess small remnant ice bodies that are rapidly waning (Boy and Allan, 1989; Young and Hastenrath, 1991; Kaser and Osmaston, 2002). In the Ruwenzori, Mt. Stanley (5100 m) has an icefield and several glaciers, with others on Mt. Speke and Mt. Baker.

The climatic setting involves a seasonal wind shift from tropical easterlies in the boreal winter to a south to north cross-equatorial monsoon flow over the western Indian Ocean in June–August. The East African mountains are under the influence of northeasterly monsoon flow from December–March and southeasterly monsoon flow from June–October. The southeasterly flow is often capped by an inversion around 4000 m asl with tropical easterlies above. On Mt. Kenya most precipitation falls in the inter-monsoon months of April and November when the equatorial trough is over or near the equator (Thompson, 1966). However, the relative contribution of precipitation in these months to the annual total diminishes with height. Annual precipitation at Embu (1477 m) at the eastern foot of Mt. Kenya averages 1040 mm and amounts increase to 2000 mm or more in a belt situated at around 2150 m on the east slope that rises to 2600 m elevation on the southeast slope (Thompson, 1966). His map shows maximum totals exceeding 2600 mm based on monthly measurements along the summit track in 1951–2. The summit area receives less than 1000 mm and Nanyuki on the northwest side at 1965 m measured barely 740 mm. Pedgley (1966) comments that two regimes are operating: (i) convective precipitation forced by anabatic winds during the inter-monsoon period; and (ii) drizzle associated with mechanical uplift on the upwind slopes during the monsoon periods. Amounts are largest on the mid-slopes as evaporation occurs below the cloud base. Winiger (1981) illustrates the role of slope heating and moisture advection on cloudiness and precipitation on Mt. Kenya (Figure 5.2). Precipitation totals show both vertical gradients and differences with aspect. Soil temperature measurements by Winiger in 1978 show that slope zones of heat surplus or deficit broadly agreed with the distribution of cloudiness and precipitation maxima/minima. On the east slope, maximum amounts of almost 2000 mm occur at the base of the mountain whereas on the south and east slopes the maxima are at higher elevations, 2200–2700 and 3200 m, respectively. Young and Hastenrath (1991) also show maximum annual totals exceeding 2500 m at about 2200 m on the south-southeast flanks of the mountain. Glaciers are best developed on the western upper slopes of the peaks as a result of the diurnal build up of cloud cover. The north slope is the driest (Figure 5.2).

Davies *et al*. (1977) describe the daily cycle of weather on Mt. Kenya as observed in July–August 1975. Clouds tend to move up the eastern side of Mt. Kenya in the late morning covering the summit area and then disperse in late afternoon. The diurnal temperature variation at 4750 m was between about $-3°$ and $1°C$ with extremes of $-7°$ and $5°C$ during the 2-week observation period. Wind speeds at 4750 m on Mt. Kenya were around $4 \, m \, s^{-1}$ at midday and $6 \, m \, s^{-1}$ in the evening, with some stronger winds at night. Diurnal katabatic and anabatic regimes are illustrated by direction changes.
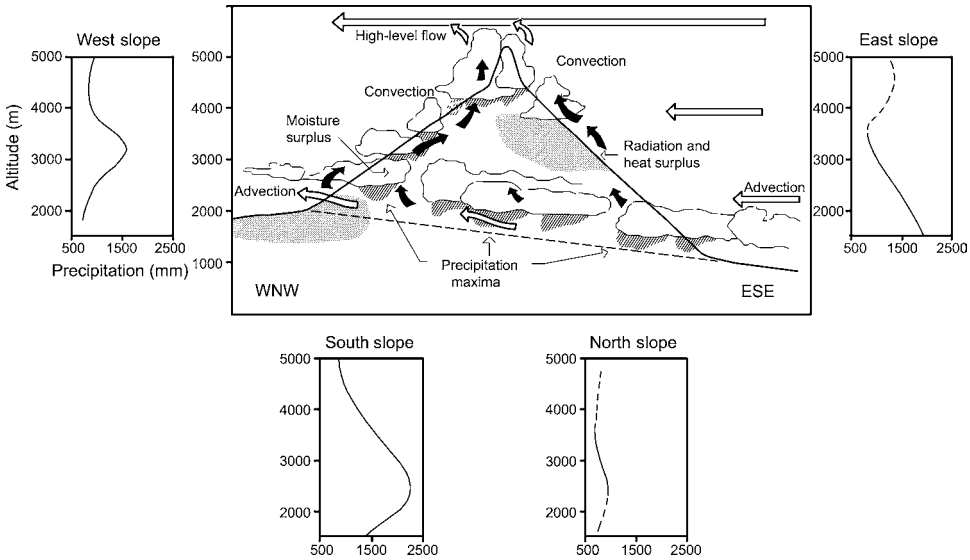
Fig. 5.2   Schematic view of daytime circulation, moisture advection, cloudiness and precipitation on Mt. Kenya (adapted from Winiger, 1981).

Coutts (1969) reported on the precipitation around Mt. Kilimanjaro (3.1°S, 37.35°E), and Mt. Meru, 65 km to the southwest. As with Mt. Kenya, 70–80 percent of the annual totals fall during the inter-monsoon transitions. On the southern slopes, April and May each receive over 400 mm with ∼100 mm or less in the other months. Maximum amounts in March, April and May exceeding 1500 mm are recorded between 1500 and 2500 m on the southern slopes, when there is often stratiform cloud with cloud top around 3000–3500 m. The pattern of annual totals (>2500 mm) is similar. Mt. Meru also receives 2000–2500 mm annually on its southern slope around 2500 m asl. There is a shorter rainy season in November–December with northeasterly flow. Totals of 500 mm occur on the northeastern slope of Mt. Kilimanjaro between 1500 and 2500 m. The northeasterly flow that is deflected by Mt. Kilimanjaro gives rise to a maximum on the southeast slope of Mt. Meru, in addition to the one from the direct monsoon flow on its northeast slope. During November–March 40 percent of the daily rainfall occurs between 1200 and 2100 h, whereas this convective regime is less evident in April–May when less than 25 percent of the rain falls at this time and even more so during June–September when the figure is less than 15 percent. The southeasterly flow at this season is deflected by the west-northwest–east-southeast elliptical out-line of the mountain, leading to convergence along the southern slope (Coutts, 1969). Amounts increase sharply with height, up to 2500 m on the southern slopes in April–May, whereas there is barely any increase in November–December.

An AWS has operated at 5794 m (∼506 mb) on Mt. Kilimanjaro (Kibo) since March 2000 (Mölg and Hardy, 2004; Hardy, pers. comm. 2006). The 12-monthly average air temperature is near −7 °C and the vapor pressure 2 mb. The mean

monthly maximum was $-1.8\,°C$ in April 2005 and the minimum $-10.7\,°C$ in February 2001. The mean wind speed was $6.6\,m\,s^{-1}$ in April and $4.7\,m\,s^{-1}$ in May with a resultant direction from about $100°$ except in June–July when it was variable from the northeast. There are about four snowfall events per month with monthly totals averaging $12\,cm$ and a variation from $0.4\,cm$ in August 2002 to $49\,cm$ in January 2001. The energy balance over 12 months at the site is included in Table 4.2. (p. 256).

The Ruwenzori have persistent cloud cover and year-round precipitation, with maxima in the transition seasons. On the eastern slopes, annual totals increase from about $1100\,mm$ at $1200\,m$ to $2500\,mm$ at $3000\,m$; above this level, values range between 1900 and $2790\,mm$ according to Livingstone (1967).

Pronounced glacier retreat on the East African mountains, documented since the beginning of the twentieth century, seems to be driven not by warming, as temperatures remain below $0\,°C$ on the summits, but by low humidity and sublimation. On Mt. Kilimanjaro, for example, the vertical faces of the residual ice patches are retreating laterally with little or no melting (Mölg and Hardy, 2004; Mölg et al., 2003).

5.2   THE HIMALAYA

The Himalaya are a 2500 km-long, arcuate system of mountain ranges, 250–400 km in width, that extends from 34–$36°\,N$, $27°\,E$ in the northwest to 27–$28°\,N$, $90°\,E$ in the east. They comprise three major ranges: the Great Himalaya, averaging $6000\,m$ and with peaks over $8500\,m$, bordering Tibet, the Lesser Himalaya (2000–$3300\,m$) in the middle and the outer Siwaliks (900–$1200\,m$) in the south. They are deeply dissected by large valleys. On the western margin they are flanked by the southwest–northeast Hindu Kush of Afghanistan–Pakistan. On the northern side there is the massive Tibet Plateau averaging around $4500\,m$ in elevation with numerous high mountain ranges within it. Ecologically, the Himalaya comprise an outer zone of monsoon forest, an inner zone of coniferous forest with heavy winter snows, and a Tibetan zone of arid steppe (Troll, 1972).

Interest in the meteorology of the Himalaya dates from the latter part of the nineteenth century. Hill (1881) provided a detailed compilation of early records for the northwestern Himalaya in Kashmir, although the principal station referred to is Leh ($3316\,m$) which is situated in the upper Indus valley between the Himalaya and Karakoram ranges. Climbing expeditions have provided most of the high-level observations (Somervell and Whipple, 1926; Bleeker, 1936; Wien, 1936; Reiter and Heuberger, 1960; Mitsudera and Numata, 1967; Raghavan, 1979) while, more recently, existing station data have been synthesized to give a more complete and up-to-date picture of conditions (Kraus, 1967; Flohn, 1968, 1970; Dittmann, 1970; Dobremez, 1976). Climatic observations have also been made, particularly in the Khumbu Himal, in connection with studies of glaciers (Higuchi, 1976) and average annual accumulation determined from ice cores taken from glaciers in the

Himalaya and ice caps in Tibet (Davis *et al.*, 2005) are other sources. In the last decade there has been renewed interest and research both in the field and using satellite data.

Despite the sub-tropical latitudes of the Himalaya, their weather is controlled by the low-level southwesterly Indian monsoon regime, overlain by tropical easterlies, from June through September. The autumn transition in the upper troposphere between the easterly winds and the re-establishment of the westerlies is unlike the gradual change in spring. Observations from the 1954 Austrian expedition showed that the westerly jet re-established itself at the end of September although föhn effects on the south side of the range maintained relatively warm conditions during October (Reiter and Heuberger, 1960). Persistent strong winds are to be expected on the high Himalaya once this wind shift has taken place. From October through May, the mountains are just north of the axis of the subtropical westerly jet stream in the upper troposphere and, steered by this system, disturbances travel eastward causing gales and blizzards on the peaks. These westerlies decrease markedly in strength from $\geq 25\,\mathrm{m\,s^{-1}}$ at 9 km to only about $10\,\mathrm{m\,s^{-1}}$ in late May (on average), and are replaced by easterlies a month later (Nedungadi and Srinivasan, 1964), as the summer high-level anticyclone develops over the Tibetan Plateau (Flohn, 1968). Monthly precipitation totals in fact show a two- to three-fold increase from May to June over Nepal (see Table 5.1), although there is no particular increase in precipitation activity at individual stations that can be distinguished from the

Table 5.1 Precipitation in eastern Nepal–Sikkim–southern Tibet, between approximately 86.5°–89° E.

Station	Latitude	Elevation (m)	Annual total (mm)	June–May ratio	June–September (% annual)	December–March (% annual)
Gyangtse	28° 56′ N	3996	271	3.2	90	1.5
Khumbu Glacier	27° 59′ N	5300	450	–	(73)	(16)
Pyramid, Lobuche	27° 58 N	5050	495	–	82	–
Lhajung (1974–6)	27° 53′ N	4420	527	–	(84)	(8)
Thanggu	27° 55′ N	3000	738	1.5	55	26
Namche Bazar	27° 50′ N	3400	939	3.2	75	11
Lachen	27° 43′ N	2697	1707	1.7	47	16
Wallungchung Gola	27° 42′ N	3048	1695	2.3	74	9
Chaunrikharka	27° 42′ N	2700	2284	3.0	86	2.5
Jiri	27° 38′ N	1895	2387	3.9	81	4
Gangtok	27° 20′ N	1764	3452	1.3	66	7
Darjeeling	27° 03′ N	2265	3082	2.6	80	3

Source: after Kraus (1967), Flohn (1968), 1970); Higuchi (1976); Yasunari and Inoue (1978); Bollasina *et al.* (2002).

pre-monsoonal showers. Nevertheless, an analysis of spatial coherence of rainfall at ten stations in southeastern Nepal shows that widespread rains occur only during June–September (Dittmann, 1970). Although of a convective nature, the "monsoon rains" in Nepal occur in spells (Ramage, 1971). There appears to be a major periodicity of about 10 days in monsoon "bursts" and "breaks" over the whole country associated with a general fluctuation in the monsoon regime or oscillations in the Tibetan anticyclone (Yasunari, 1976b). A secondary one of about 5 days, which is more pronounced in eastern Nepal is probably due to westward-moving depressions over northern India. The intervening days are relatively dry, apart from local convective showers. Even so, over the highlands of eastern Nepal, July and August typically have about 27 rain days (≥ 2.5 mm) with a mean intensity of about 20 mm. Totals and intensities decrease sharply in the higher valleys and at Namche Bazar (3400 m), for example, intensities are only 8 mm rain day^{-1} in summer. Identical intensities occur there in January (Dhar and Narayanan, 1965).

An analysis of precipitation regimes at 22 stations in Nepal illustrates three primary controls on precipitation. First is the duration of the southwest monsoon and the influence of topography (Kansaker et al., 2004). The onset of the monsoon is later going from east to west, and the earlier withdrawal of the monsoon in the west means a shorter rainy season. Second, precipitation in the northwestern Himalaya of Kashmir and western Nepal comes also from "Western Disturbances" in the winter season. Third, topography gives increases up to some limiting elevation and then amounts decrease northward and in lee-side rain shadows. Four seasonal patterns are identified by Kansaker et al. (2004).

(A) A July–August peak with rapid monsoon onset and ending, occurring in western Nepal and at low elevations in the Terai and Siwaliks.
(B) A July peak with gradual onset and ending found in the Lesser Himalayas
(C) A July peak with rapid onset and a gradual ending occurring in central Nepal and the eastern lowlands.
(D) A July–August peak and a secondary maximum in January–March, dry in September–December found in the higher western mountains.

In winter, precipitation in the Himalaya falls as snow and the snow line descends to about 1500 m in the western Himalaya and 3000 m in the eastern Himalaya (Mani, 1981).

Overall, precipitation amounts decrease westward along the Himalaya since most of the moisture is derived from synoptic systems moving westward from the Bay of Bengal. A network of 20 stations was operated in the Marsyandi River basin of central Nepal between 528 and 4435 m (ca. 28.5° N, 84° E) during summers 1999 and 2000 (Lang and Barros, 2002). Combining the records with satellite and radiosonde data, shows that monsoon onset occurs with monsoon depressions from the Bay of Bengal. Two-day events each contribute 10–20 percent of monsoon precipitation totals. There is a mixture of stratiform and convective precipitation.

A broad picture of precipitation characteristics in the Himalaya can be derived from the precipitation radar on the Tropical Rainfall Measuring Mission (TRMM). Bhatt and Nakamura (2005; 2006) analyzed hourly data, averaged for 0.5×0.5 degree cells, for 1998–2002. The data were separated into light and moderate–heavy for amounts above/below a threshold of $0.5\,\mathrm{mm\,h^{-1}}$. On south-facing slopes of the Himalaya, there is embedded convection in areas of light rain during afternoon–evening hours. Over Tibet and the northern subcontinent, most precipitation falls between 1200 and 1800 h LT and is concentrated over ridges. Strong, low-level meridional circulations probably enhance convection over the south-facing ridges. Intense precipitation may fall at night (0000–0600 h) over both ridges and valleys. Bhatt and Nakamura (2005; 2006) suggest that convergence may be aided by mountain-forced gravity waves and atmospheric instability. Pre-monsoon there is an afternoon precipitation maximum over the southern slopes of the Himalaya, which switches to a midnight–early morning maximum during the monsoon. A schematic model of nocturnal precipitation suggested by Barros and Lang (2003) is shown in Figure 5.3. Bhatt and Nakamura (2006) propose that mountain winds after midnight trigger moist convection, supported by radiative cooling from cloud tops. The precipitation associated with this moist convection sets up a cold pool that generates a downslope/down-valley density current and this leads to a southward displacement of the precipitation system by the morning.

The relative importance of "winter" precipitation increases with latitude and altitude although actual amounts are greatest in the northwest. In the late nineteenth century, Hill (1881) identified a maximum of annual precipitation at elevations of around 1200 m in the northwestern Himalaya of Kashmir. Schickoff (1994) provides climatic data for three stations in this area (35° N, 74° E) at 991, 2362 and 2670 m. Annual precipitation decreases with altitude from 1545 to 1210, and 1010 mm, respectively. The lowest station is monsoon-dominated with a July–August peak, whereas the upper station has precipitation during October–May, especially in February–April. This reflects the role in winter months of Western Disturbances. Each month, three to four disturbances from the Caspian Sea area bring precipitation to the western and central Himalaya. Lang and Barros (2004) suggest that when a trough in the upper westerlies moves eastward toward the Tibetan Plateau, it may split into a system moving eastward to the north of the plateau and another moving to the south of the northwestern Himalaya that may become terrain-locked in the notch formed by the Hindu Kush and Himalaya mountains.

North of the western Great Himalaya along the Kashmir–Pakistan–China border, are the Karakoram – Himalaya with extensive glaciers and high peaks (including K-2, 8611 m, 35.9° N, 76.5° E). Hewitt (2005) presents glacier data showing that precipitation here increases $\times 5$ to $\times 10$ between 2500 and 4800 m. He argues that maximum precipitation falls between 5000 and 6000 m although there are no high station records in this region. About two-thirds of the annual total falls as winter snowfall, while summer precipitation is related to the Indian monsoon.
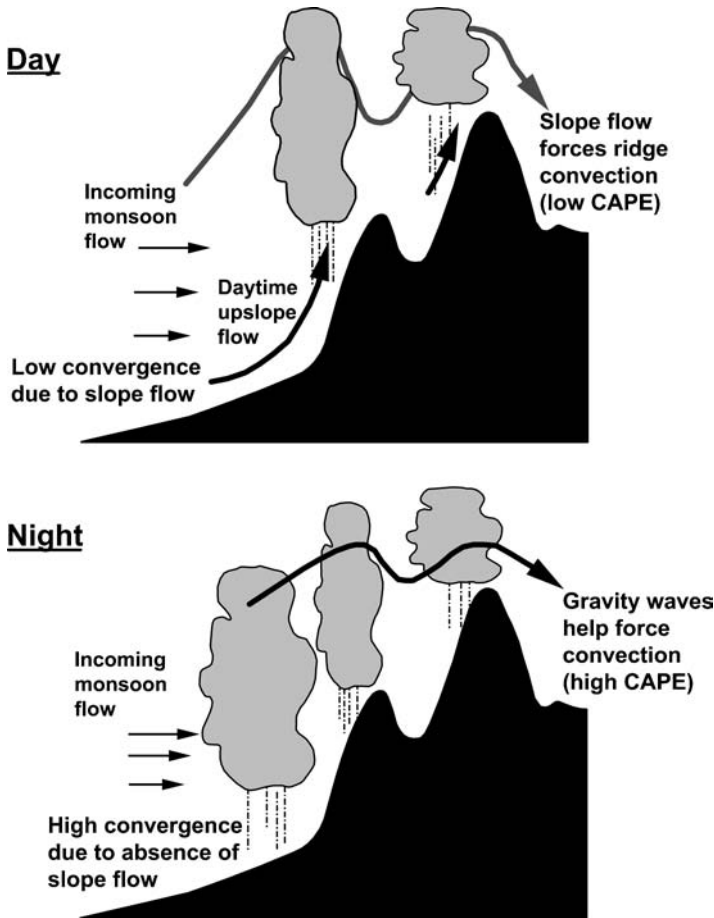
Fig. 5.3   Schematic illustration of nocturnal precipitation in the central Himalaya (from Barros and Lang, 2003).
Convectively available potential energy.

In the central section of the Himalaya there are more numerous data available.
Dhar and Rakhecha (1980) determined that there are two elevation zones of high
monsoon rainfall totals, one at the foot of the Siwaliks and one around 2000–2400 m
over the Lesser Himalaya. In the latter zone, June–October totals were two-thirds
greater than in the plains, averaging 2000–2200 mm. Along the outer ranges of the
Himalaya, the altitude of maximum precipitation during the monsoon season gen-
erally occurs at or a little below 2000 m (see Table 5.1). Reiter and Heuberger (1960)
note that this is the level of night and early morning cloud. From their data for
September 1954, relative humidity is ≥ 90 percent between 2 and 4 km. Relative
humidity values of 90–100 percent during the monsoon months are confirmed by
observations at Lhajung (4420 m) in the Khumbu Himal (Inoue, 1976). Stations in
the central Himalaya (Kosi) exhibit seasonal maxima in the foothills of the Siwalik
Range and around 2000–2400 m elevation in the Lesser Himalayan Range; further

northward amounts decrease towards the main Himalayan range (Dhar and Rakhecha, 1980). In the winter period of the upper westerly wind regime, however, precipitation may increase above 3000 m according to Flohn (1970).

Dhar and Nandargi (2005) identify three areas of high mean annual precipitation in the Nepal Himalaya. The greatest totals, exceeding 5000 mm, are observed at stations in the Nepal Meteorological Department network located between 1000 and 1700 m in altitude, 40–50 km south of the Annapurna Range. However, Putkonen (2004) provides year-round data from a local network of 14–19 stations installed across the Annapurna Range (ca. 28.4° N, 84.3° E) during 1999–2001. Rainfall during the summer monsoon peaks at around 3000 m altitude on the south side of the Himalayan Range, while winter precipitation increases monotonically to the highest gauge at 4400 m (Figure 5.4). Annual totals, which are dominated by the monsoon, reach 5030 mm during this short record. Amounts decrease to only 1100 mm year^{-1} on the northern side in the rain shadow of the main ranges. In the Mustang and Manang districts of central and northwest Nepal (27.7–30° N, 82.5–84.5° E) annual totals in the lee of the Annapurna Range are as low as 200–800 mm (Dhar and Nandargi, 2005). Based on estimated lapse rates, only snow falls above about 5880 m.

A hydrometeorological network, including some snow depth and SWE measurements, was operated in the Marsysandi River basin on the eastern slopes of the Annapurna Range for the winters of 1999–2002 (Lang and Barros, 2004). Snowfall accounted for 25–40 percent of the 1 May–30 April annual precipitation at elevations of 4000–4400 m, compared with about 5 percent at 3170 m. However, the relative importance of elevation versus topographic location is unclear, and there is large interannual and intraseasonal variability. A climatology of negative
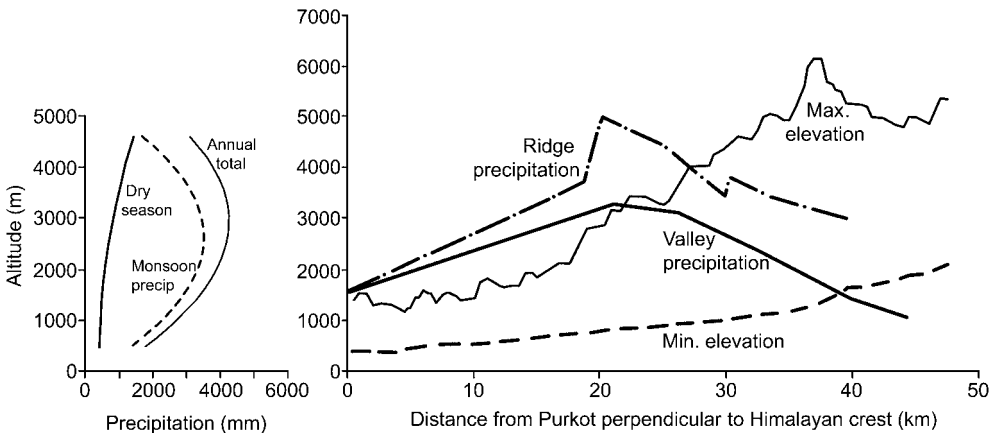
Fig. 5.4 Precipitation gradients in the Annapurna region (adapted from Putkonen, 2004). Left: Altitudinal profile of October–May (solid), June–September (dashed) and annual precipitation. Right: A south–north transect of total precipitation for 1 September 2000–31 August 2001 from Purkhot to the main crest of the Himalaya (after Putkonen, 2004).

anomalies of 500 mb heights over 30–32.5° N, 70–75° E for January–March 1973–2002 shows an average of around 15 days per season with such anomalies, but the numbers range from almost none up to 30. Snow events ($\geq$ 1 cm snow depth increase at three out of four stations with sonic depth gauges) occurred on 19 days in January–March 2000, but only 9 days in 2001. Lang and Barros show that, while Western Disturbances are required, heavy snowfalls tend to occur when a depression is trapped in the notch between the Hindu Kush to the west and the Himalayan ranges to the east. The airflow is southwesterly against the Himalaya and, based on a model simulation, this appears to give rise at low levels (below 4 km) to an easterly barrier jet.

At a temporary station at 5055 m on the northern (lee) side of Dhaulagiri Himal (28.4° N, 83.4° E.), major precipitation events in 1974 were associated with large-scale disturbances of the monsoon trough to the south (Shresta *et al.*, 1976). The July–August total (200 mm) exceeded amounts at lower stations in windward locations. Here, winter precipitation is minimal and the excess of potential evaporation over summer precipitation produces an arid environment.

South of the Langtang Himalaya, annual totals are around 3500 mm at elevations of 1600–2600 m (Dhar and Nadargi, 2005). At altitudes of 5350–5800 m in the Langtang region (28° N, 85° E), snow pits on three glaciers in 1991 provide a 10-year record of seasonal snow accumulation (Steinegger *et al.*, 1993). At 5580 and 5800 m the mean annual accumulation was about 830 mm w.e., with a range of 600–1300 mm. Five years of precipitation data at nearby Kyanjin (28.2° N, 85.6° E, 3880 m) at the foot of the Yala Glacier ranged from 500 to 850 mm (average $\sim$ 635 mm, or 25 percent less than on the glaciers) (Fujita *et al.*, 2006). Precipitation falls as snow down to 5400 m in the monsoon season which accounts for about 75 percent of annual net snow accumulation above 5000 m. The amounts exceed those in the Khumbu further east but are substantially less than around Annapurna to the west (5000 mm annually with 2000 mm in winter above 5500 m).

Based on summer measurements in the Langtang valley in 1987 and 1990, weekly precipitation totals show a linear increase with elevation along the valley (Ueno *et al.*, 1993). There are lower totals in the upper reaches, however, than in the middle reaches at the same altitude ($\sim$ 5000 m). In the lower valley precipitation mainly falls in the evening, whereas in the upper valley it peaks around midnight.

The characteristics of precipitation distribution further east, around Mt. Everest and Kanchenjunga (26.5–28° N, 86.5–88° E), are well documented (Dhar and Nandargi, 2000). The Kanchenjunga area has 1.2–1.7 times the amounts in the Everest area. The former area, which is further east, is wetter because Mt. Everest is screened by mountain ranges to the south. At about 27.5° N, 87° E, totals approach 2600 mm at 1400 m, decreasing to 1000–1200 mm around 4000 m. South of Mt. Everest at 2600 m, annual totals are 2300–2600 mm decreasing to 1000 mm or less at 3450–3850 m. At Namche Bazar (3450 m, 25 km southwest of Mt. Everest) the annual total is about 1000 mm while on the Khumbu Glacier it is only 450 mm

(Table 5.1). The southwest monsoon accounts for 65–75 percent of the annual totals south of Kanchenjunga and 75–85 percent south of Mt. Everest.

Several AWS have recently been operated in the Khumbu region of Nepal. A 6-year record, October 1994 to October 2000, from one at 27.8° N, 86.7° E, 3833 m (Ueno et al., 2001), shows annual precipitation totals ranged from 840–1010 mm with a strong maximum in July–August and very small amounts from December–April. In summer, peak rainfall was between 2000 and 0300 h whereas in spring it was during 1000–1300 h and in the autumn from 2100 to 0400 h. Winds at this location were weak and mainly of mountain–valley type.

The high-altitude Pyramid meteorological station (27.96° N, 86.81° E, 5050 m) was established in the Sagarmatha National Park, Nepal, by an Italian research group in 1990 (Natari et al., 1998; Stravisi et al., 1998; Bollasina et al., 2002). It is located in a secondary valley at the confluence of Lobuche Glacier with the main Khumbu Glacier, 12 km southwest of Mt. Everest and 8 km north of Lhajung. Annual precipitation at the station averaged only 465 mm for 1994–9, 82 percent of this precipitation fell during the monsoon season (Table 5.1), with rain on 85 percent of days. August is the rainiest month (147 mm), followed by July (132 mm), June (68 mm) and September (56.5 mm). Monsoon precipitation here falls as frequent light showers or drizzle, with sporadic heavier precipitation events (up to 10 mm day^{-1}). During "active" monsoon periods, light rain falls nearly all day, while in "break" periods (see Barry and Carleton, 2001; p. 197) it tends to occur between 1400–2400 h, peaking around 1800 h, and slowly decreasing during the evening and night. There are spectral peaks in the precipitation at around 5 and 10 days at Pyramid station, matching the finding of Yasunari (1976b) for the Nepal Himalya as a whole.

To the east of Bhutan, the Himalaya in Arunachal Pradesh (27° N, 91–95° E) bordering Tibet are generally lower than further west. Dhar and Nandargi (2004) describe the precipitation characteristic using records for 67 stations. There is a zone of maximum precipitation (3000–5000 mm) along the foothills north of the Brahmaputra River in Assam, but generally annual totals are around 2000–3000 mm with a small pocket below 1000 mm around 27.8° N, 93.8° E .

Precipitation varies considerably on a local scale in relation to location on windward/leeward slopes, and as a result of the local wind circulations. Large annual totals are observed on the southern slopes of the eastern Himalayan foothills, exposed to the southerly monsoon flow. The Khasi hills of Assam, which extend 300 km east–west and rise to about 1800 m, are exceptional in this respect. The annual rainfall at Cherrapunji, 1313 m altitude (25.3° N, 91.7° E) averaged 11 490 mm for 1931–60 (Chaggar, 1983), with 2500 mm or more falling in both June and July; in 1974 Cherrapunji received 24 400 mm. However, nearby Mawsyuram (1401 m) averaged 12 210 mm for 1941–69 while Cherrapunji averaged only 11 020 mm. Rao (1976) notes that the monsoon season amounts on the adjacent plains are only about 1600 mm compared with 8000–9000 mm around 1300–1400 m; corresponding amounts near the crest of the hills, however, are

around 2500 mm. Rao points out that the exceptionally wet middle slopes are partly attributable to a funnel-shaped catchment in the hills, opening at the south, that augments the airflow convergence. The overall slope from the plains is about 1:8.

Rainfall decreases northward and altitudinally along the major valleys in the Khumbu Himal (Ageta, 1976), for example, but there are local altitudinal increases. Yasunari and Inoue (1978) note that short-term records in the monsoon season of 1976 show totals around 5000–5500 m peaks and ridges were four to five times those at Lhajung in the main valley. They attribute this to orographically and thermally induced convection; radiative heating below the snow line may be an important trigger. In summer, convective cloud spreads northward up the main Imja Valley, reaching Lhajung by late afternoon on fine days and by 0900–1000 h on unstable days (Yasunari, 1976a). Much of the monsoon precipitation in the valley occurs nocturnally, associated with these up-valley motions.

During 21–31 August 1974, 70 percent of the precipitation (37 mm total) occurred at night at Lhajung (4420 m) compared with only 35 percent (of a total of 107 mm) at a glacier col at 5360 m, 10 km to the northwest (Ageta, 1976). The instability diminishes at night and stratiform clouds fill the valleys in the early morning. Middle and high level clouds may affect the highest peaks, especially in association with westerly disturbances in winter. A schematic view of these cloud systems is illustrated in Figure 5.5.

Studies in Langtang Valley, Nepal (28.1° N, 85.4° E) between 3920 and 5090 m show that, in winter, snowfall from the Westerly Disturbances increase with height. During the monsoon season it decreases with altitude from Kathmandu (60 km

Fig. 5.5   **Schematic cloud patterns in summer and winter in the Khumbu region, Nepal (after Yasunari, 1976a). Ac, altocumulus; As, altostratus; Ci, cirrus; Cc, cirrocumulus; Cu, cumulus; Cb, cumulonimbus; Cs, cumulostratus.**
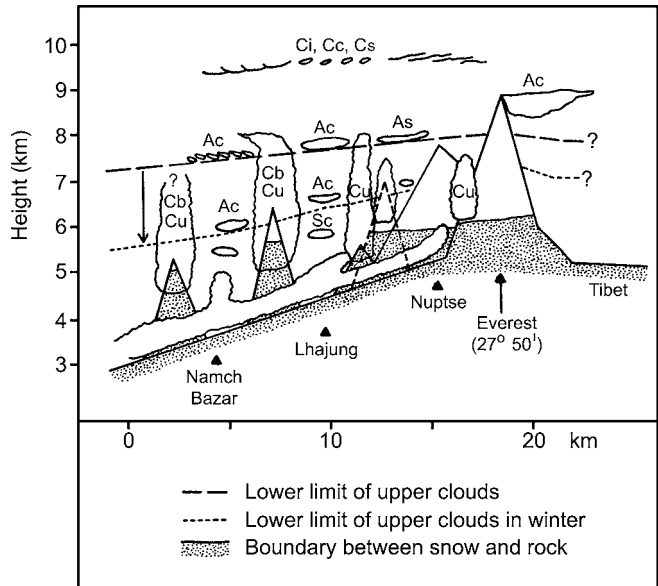
to the southwest) to 3920 m and then increases slightly to 5090 m as a result of convective activity over the ridges. During mid-August to October, however, there are distinct diurnal patterns (Ueno and Yamada, 1990). From 1600/1800 h to 2300/ 0200 h (local time) about half of the daily precipitation occurs simultaneously over the valley, in up-valley winds. During the night (midnight to 0500/0600 h) rain falls in the valley bottom from stratiform cloud, while in the morning hours to mid-afternoon it occurs over ridges and peaks associated with up-slope winds. In the northwestern Himalaya, the shower regime, which is strongly influenced by local wind systems, largely determines the distribution of summer precipitation since the role of monsoon depressions is much reduced in the far northwest.

Troll (1951), Schweinfürth (1956), Schickoff (1994) and Richter *et al.* (1999) have shown how the vegetation patterns in the major Himalayan valleys reflect the fact that it is much wetter on slopes and ridges and drier along the valley bottoms. This is attributed to the tendency for subsidence over the valleys in the slope wind circulation. Since many observing stations are located in valleys, such wind systems may result in serious underestimation of areally-averaged precipitation (sometimes referred to as the "Troll effect"). Flohn (1974) illustrates this for the Hindu Kush and Karakoram ranges. Annual totals at five stations in the valleys of the Karakoram are only 80–160 mm, whereas hydrological and glaciological estimates show that at least 2–3 m must fall annually over the surrounding mountains and glaciers. In the Himalaya, the up-valley wind system is continuous through the night (until about 0400 h) during the summer monsoon, whereas a normal diurnal mountain–valley wind regime is observed during the dry months, October–May (Ohata *et al.*, 1981). Flohn (1970) shows that this is due to the regional-scale circulation between the southern edge of the Tibetan Plateau and the Indo-Pakistan lowlands. As discussed on p. 66, the Plateau and Himalaya act as a major heat source, one component of which is the release of latent heat in cumulonimbus cells. This maintains the convective process, and thereby the regional-scale thermally driven circulation. Substantial local differences in the seasonal distribution of precipitation amounts can also occur due to the orientation of major drainage basins. Upper-level easterly airflow in summer and westerly airflow in winter may interact with the topography in different ways to affect the low-level cloud motion in the valleys.

To complete this brief overview of climatic conditions in the Himalaya, mean monthly temperatures versus altitude are summarized in Figure 5.6. Interestingly, there is no apparent decrease in seasonal range with altitude, probably due to the widespread significance of the monsoon regime (Dobremez, 1976), although the higher stations are sited in valley locations. The mean diurnal range is strongly site-dependent and with major seasonal differences. Mitsudera and Numata (1967) show that large diurnal variations occur in spring with a daily range of 21 °C between 1000 and 4000 m in April on Mt. Numbur, eastern Nepal, compared with only 2–4 °C range in late June. Inoue (1976) notes that solar radiation intensities reach a maximum in May at Lhajung and decrease with the beginning of the monsoon in June. The mean daily range at Lhajung (4420 m) is about 12 °C in

Fig. 5.6   The range of mean monthly temperatures versus altitude in the Nepal Himalaya (after Dobremez, 1976).
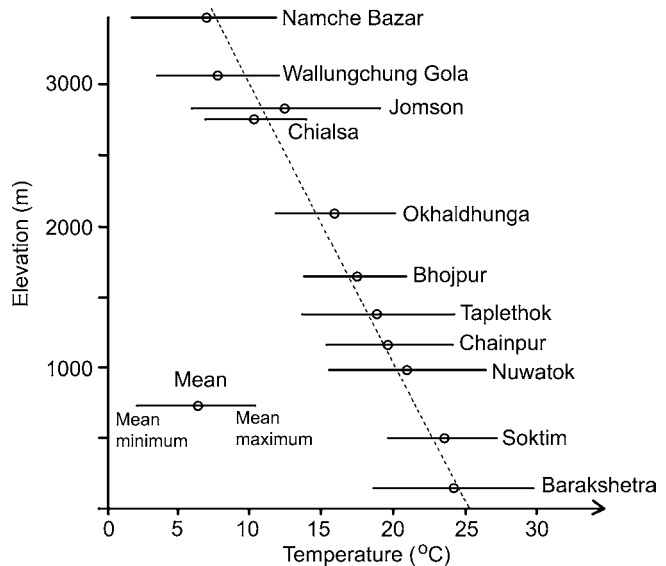
December–January compared with 5–6 °C in the monsoon months. An expedition temperature profile for the Cho-Oyu area (28° 06′ N, 86° 40′ E) in September 1954 showed conditions close to those in the free air over Calcutta and New Delhi (Reiter and Heuberger, 1960). In October and early November 1954, when the upper westerlies were re-established, temperatures were lower over the Himalaya and New Delhi than Calcutta, reflecting the normal latitudinal gradient (except for some pronounced föhn cases at 5700 m).

5.3   SUB-TROPICAL DESERT MOUNTAINS – THE HOGGAR AND TIBESTI

Two mountain massifs rise above the Saharan desert to elevations close to 3000 m. They are the Hoggar of southern Algeria and the Tibesti of northern Chad. The latter area was the site of scientific research organized by the Free University, Berlin, from 1966 to 1974 (Jäkel, 1977). Weather stations were established at Bardai (1020 m) and Trou au Natron (2450 m). Climatological studies are reported by Heckendorff (1972) and Indermühle (1972). The Hoggar massif exceeds 2000 m over an area some 20–30 km wide and about 100 km long; Atakor summit rises to 2918 m. The area was the location of considerable research in the 1950–60s by the Institut de Recherches Sahariennes, University of Algiers. This group established a first-order weather station at Asekreme (2706 m), 23° 16′ N, 50° 38′ E, in March 1955 and an autographic station at the Tahat summit (2900 m) in 1959 (Dubieff, 1963). Between 1959 and 1962 a network of 120 rain gauges was maintained on and around the mountains (Yacono, 1968). A long-term record, since 1925, is provided by the observatory at Tamanrasset (1376 m) to the southwest.

The climatic regime and its synoptic controls have been described in some detail by Yacono (1968) and the following account is based largely on her studies. The lapse rate of temperature averages $5\,^{\circ}C\,km^{-1}$ in January, increasing to $8\,^{\circ}C\,km^{-1}$ during the more unstable conditions of July. More interesting is the increase of days with minimum temperatures below $0\,^{\circ}C$, from 39 days year^{-1} at Tamanrasset to 114 days year^{-1} at Asekreme. Temperatures below $-5\,^{\circ}C$ have been observed at Asekreme in association with outbreaks of polar air in deep cold lows. July and August mean daily maximum temperatures are almost $35\,^{\circ}C$ at Tamanrasset but only $24\,^{\circ}C$ at Asekreme. The mean monthly minimum temperature in January is only $2\,^{\circ}C$ at Asekreme and $5\,^{\circ}C$ at Tamanrasset (Leroux, 1991).

There is a typical Sudan–Sahelian type of rainfall regime with about 60 percent of the annual total falling during August–September and another 25 percent in May–June. In the Hoggar, according to Leroux (1991), the annual precipitation totals increase from only 46 mm at Tamanrasset (1930–88), where 20 percent falls in September, to 116 mm at Asekreme (1955–88), with 30 percent falling in August–September. There is high interannual variability; Tamanrasset received 150 mm in 2 years and less than 10 mm in 11 years, Asekreme had totals over 200 mm in 4 years between 1955 and 1988 and only 1 year (1973) with less than 10 mm. Tibesti is considerably more arid than the Hoggar. Bardai (1020 m) to the north and Zouar to the south of the ridge topped by Peak Toussidé (3265 m), receive annual totals of only 5 mm and 46 mm, respectively (Leroux, 1991).

The altitudinal effect is strongly dependent on total amount. Figure 5.7 shows that, in a dry year, altitude has only a limited effect whereas in years with more depression rain there tend to be maximum amounts at about 2500 m. However, this
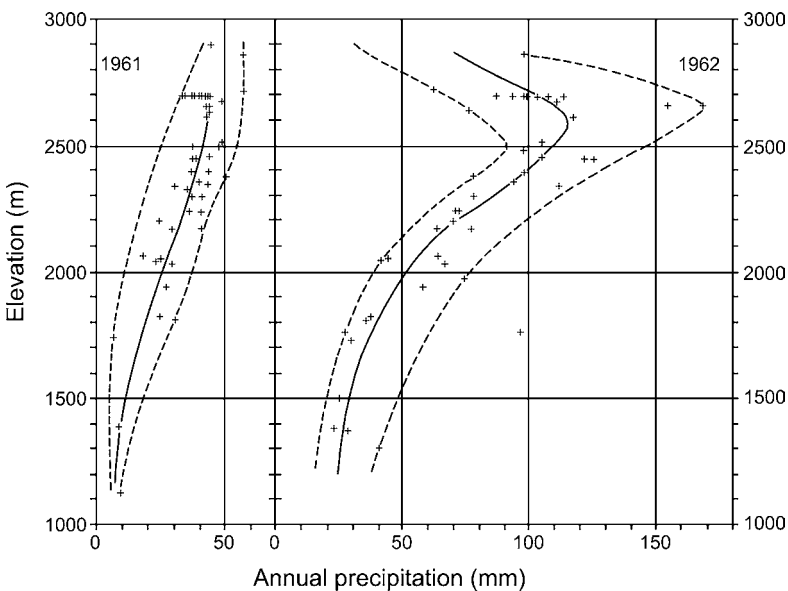
Fig. 5.7   Annual rainfall (mm) versus altitude in the Hoggar in a wet year and dry year (after Yacono, 1968).

is not simply a result of increased intensity, since there are more days with measurable rainfall, and also with traces of precipitation, at the higher stations.

The aridity of the area is primarily due to low humidity rather than to an absence of disturbances. The mean annual relative humidity at Tamanrasset is 23 percent, with little seasonal variation (Leroux, 1991). Relative humidity ranges from a mean of 30 percent in April and 46 percent in November at Segueika (2450 m) to between 17 and 29 percent, respectively, for the same months at Tamanrasset probably due to a tendency for downslope motion in the predominantly northeasterly flow. Yacono (1968) shows that cloud systems associated with westward-moving disturbances regularly affect the Hoggar. Analysis of satellite imagery and weather maps for 1968 by Winiger (1972) indicated that the Intertropical Convergence Zone (ITC), extending northward as a "cloud bridge" from Niger, was over or north of Hoggar on 42 days with mean monthly cloud cover exceeding 50 percent in May–July and September–October. Precipitation, however, is invariably light. Rare, exceptional rainstorms are usually caused by North African lows such as that which gave 111 mm at Asekreme on 25–26 November 1968. Moist, tropical maritime air in a southwesterly flow was drawn northward by a deepening depression over Morocco–Tunisia. In winter and spring, Sudano–Saharan depressions may affect the Hoggar after recurving northeastward, whereas in autumn they are usually too far west (Figure 5.8). Their movement is dependent on the flow around
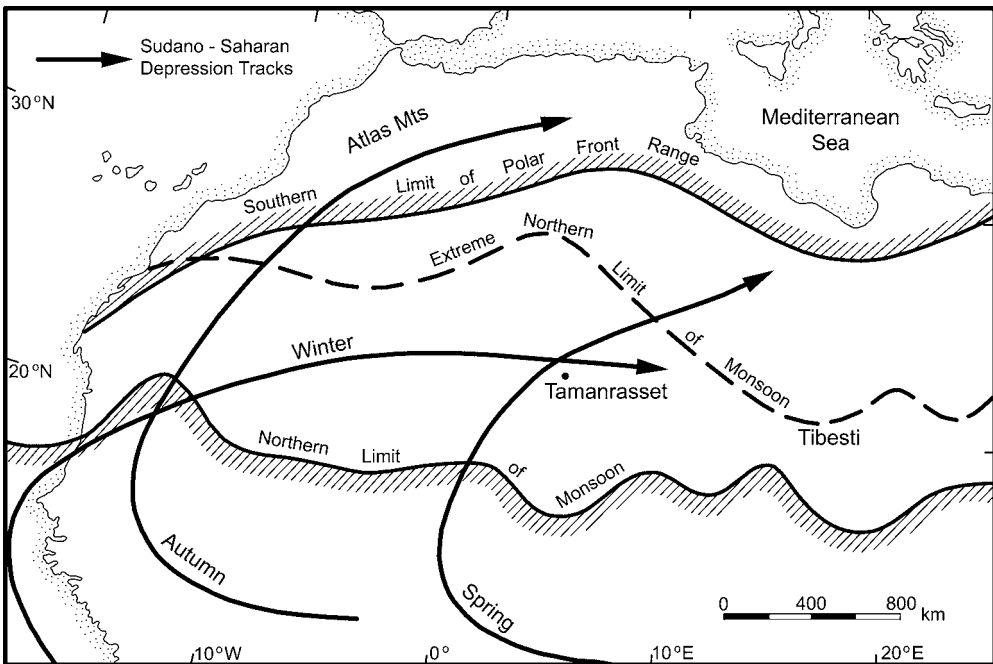
Fig. 5.8 Extent of precipitation systems affecting western and central North Africa and typical tracks of Sudano–Saharan depressions (after Dubief, 1962; Yacono, 1968).

the mean upper-level high-pressure cell over northern Africa. Yacono (1968; p. 111) notes that these systems are major sources of Saharan precipitation. Occasional winter precipitation is derived from polar front depressions or polar air advected southward on the western limb of an upper trough. Such incursions may produce light falls of snow at Asekreme averaging about one per year.

The Hoggar is rather windier than might be expected from its location with respect to the sub-tropical anticyclone and the predominance of subsiding air. Limited data cited by Yacono (1968) indicate a mean annual wind speed of $2\,\mathrm{m\,s^{-1}}$ at Tamanrasset, but $7\,\mathrm{m\,s^{-1}}$ at Asekreme for 10 months of observation in 1960. A southerly storm on 16 December 1960 gave winds of up to $54\,\mathrm{m\,s^{-1}}$ at Asekreme while the maximum at Segueika (2450 m) reached only $15\,\mathrm{m\,s^{-1}}$.

5.4   CENTRAL ASIA

Central Asia, as considered here, is a vast, mostly semi-arid region with extensive basins, plateaus and high mountain ranges. The principal mountain systems are the very extensive Tien Shan ranges, extending over 2000 km between 40–45° N, 67–95° E in Kyrgyzstan, Kazakhstan and Xinxiang, China, the east–west Pamir-Alai in southern Uzbekistan–Kyrgyzstan and the north–south Pamir of Tajikistan linking with the Hindu Kush of Afghanistan and the Karakorum further east. Here we focus on the Tien Shan and the Pamirs, where more data are available.

The Tien Shan of the former Soviet Union (fSU) are conventionally divided into western, northern, interior and central Tien Shan; the eastern Tien Shan are in Xinxiang. In the central part the mountains rise to 7400 m and have extensive ice cover. The ELA rises from 3500–3600 m in the north to 4400 m in the southern Tien Shan ranges (Solomina *et al.*, 2004) compared with 5200 m in the central and eastern Pamir.

The western Tien Shan comprise many complex ranges, including the Alatau ranges in the western part, which rise to around 5000 m. Records for the Abramov glacier station (Table 5.2) show relatively warm, dry summers with maximum precipitation in spring. In the central Tien Shan to the south of Almaty, Khazakstan, there are parallel east–west ranges to the north and south of Lake Issyk-Kul at 1600 m elevation. Merzlyakova (2002) shows that the precipitation regimes in the central Tien Shan contrast with those in the western Tien Shan and in the Pamir to the southwest. In the latter areas, summers are dry and there is a spring maximum, whereas in the central Tien Shan winters are dry and there is a clear summer maximum.

Table 5.2 **Mean monthly temperature ($T\,°C$) and precipitation (P, mm) for 1968–88 at the former Abramov Glacier moraine station, Alai Range, 37.6° N, 71.6° E, 3780 m (from Glazyrin *et al.*, 1993).**

	J	F	M	A	M	J	J	A	S	O	N	D	Year
T	−14	−14	−10	−4	−1	2.8	6.2	6.4	2.0	−4	−8	−12	−4.1
P	50	44	95	89	98	62	47	19	26	68	48	68	727

The climate in the central Tien Shan, the Ak-Shirak Range (about $42°$ N, $78°$ E), is typical of continental high-mountain regions: dry and cold. Annual precipitation is about 300 mm, with over 60 percent during June–September. Annual air temperature at the glacier termini is about $-8°$C; $-11°$C in winter and 3 to $4°$C in summer (June–August) based on data from the mountain meteorological station "Tien Shan" (3614 m) during 1930–98 (Khromova et al., 2003).

The northwestern Pamir has alpine relief with deep, narrow valleys and high peaks. The southeastern part of the Pamir is a vast high upland with peaks reaching 5000–5500 m and valleys at 3600–4000 m. The southwestern Pamir is heavily glacierized between 2500 m and 5000–6000 m. It includes the 75 km-long Fedtchenko Glacier ($38.7°$ N, $72.3°$ E). The ranges of the eastern Pamir ($38°$ N, $72°$ E) are mainly between 4800–5000 m and 5500–6000 m and have less ice cover. Voloshina (2002) notes that the accumulation zone descends to 4400 m in the northwestern Pamir compared with 5200 m in the southeast and attributes this to the wetter conditions in the west, where there are 229 days year^{-1} with precipitation, versus only 165 days in the eastern Pamir where most precipitation falls in summer. The Kara Kul meteorological station (3930 m) averages $-18°$C in winter and $5–8°$C in June–August. Precipitation records at the meteorological station on the Fedtchenko Glacier (4169 m) show that the driest months are November–December with June and July the wettest (see Table 5.3). The western Pamir is mainly influenced by cyclonic systems on the polar front. In spring these move eastward from Iran.

Getker (1985) shows that the fraction of annual precipitation falling during October–March decreases from 0.6–0.7 in the south and southwest of the region to 0.1–0.2 in the east and northeast. In addition, in the interior Pamir and Gissaro-Alai the winter fraction increases with altitude, suggesting high-level moisture penetration in winter cyclones, whereas in the Tien Shan there is little altitudinal change.

Mean summer temperatures at 4170 m on the Fedtchenko Glacier are $0°$C in June rising to less than $4°$C in July and August. Clear skies predominate in summer with 56 percent of days, compared with only 23 percent cloudy.

Getker (1985) provides an important, little known synthesis of information on altitudinal precipitation gradients in central Asian mountains, based on glaciological principles developed by Khodakov and Krenke (1980). They proposed that the ratio of annual precipitation at a given altitude z, (P_z), to the annual amount at the equilibrium line altitude (z_{ELA}) in glacierized basins, (P_{ELA}), is related to altitudinal variables as follows:

Table 5.3 **Mean monthly temperature (T), Sept. 1934–Dec. 1989 ($°$C) and precipitation (P), Jan. 1937– Dec. 1989 (mm) at the Fedtchenko Glacier station, Pamir, $38.8°$ N, $72.2°$ E, 4169 m (courtesy M. Dyurgerov).**

	J	F	M	A	M	J	J	A	S	O	N	D	Year
T	−17	−16	−13	−8	−4	−0.2	3.5	3.8	0	−7	−12	−15	−7.0
P	91	122	126	105	115	150	129	120	67	40	20	24	1068

Fig. 5.9 Vertical gradients of annual precipitation in the Tien Shan and Pamir ranges. The values are scaled relative to the annual totals at the equilibrium line altitude (ELA) as estimated from the climatic snow line (adapted from Getker and Shchetinnikov, 1992). Zones 1 and 2 have spring–summer maxima in peripheral basins and interior basins, respectively. Zones 3 and 4 have winter–spring maxima in the corresponding topographic locations.
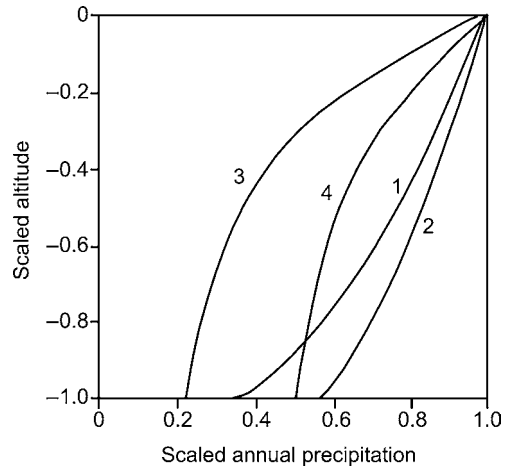
$$\frac{(P_z)}{(P_{\mathrm{ELA}})} = f\,\frac{\{z - z_{\mathrm{ELA}}\}}{\{z_{\mathrm{FL}} - z_{\mathrm{B}}\}},$$

where z_{B} is the minimum height in the basin, and z_{FL} is the altitude of the climatic snow line (the altitude above which net snow accumulation will occur on a plateau surface; approximately the firn line on glaciers). Getker (1985) uses this approach to determine the vertical precipitation gradients in the Tien Shan and Pamir-Alai for four macro-scale slope categories: (Figure 5.9). For zone (1) with a distinct winter–spring maximum of precipitation, annual totals increase, at a diminishing rate, from about 500–600 mm at lower elevations to 1500–2000 mm in higher zones. For zone (2) the corresponding increase is from 350–500 mm to 800–1000 mm. For zone (3) the increase is from 100–300 mm to 500–1000 mm and for zone (4) it is from 350–400 mm to 800–1200 mm.

Getker (1985; p. 12) shows that the fraction of mean annual precipitation falling in solid form (P_{s}) can be estimated from the expression:

$$P_{\mathrm{s}} = 0.78f + 0.004t - 0.43$$

where f is the fraction of total annual precipitation falling during the months October–March and t is the number of days with mean daily temperature below $0\,°\mathrm{C}$. Getker determined P_{s} and the maximum snow water equivalent in spring. Table 5.4 summarizes his results for the Pamir-Alai and the western and central Tien Shan, based on data for 510 meteorological stations and posts and 315 totalizing gauges. Both the annual precipitation and solid precipitation amounts are about half as large again in the Pamir-Alai as in the Tien Shan. Furthermore, these values of mountain snowfall are some eight times greater than in the lowlands. Table 5.4 shows that there is greater inter-annual variability in the Tien Shan than in the Pamir-Alai.

Table 5.4   Generalized amounts of solid precipitation and maximum snow water equivalent (SWE) in the mountains of Central Asia (from Getker, 1985).

Characteristics / region	Pamir-Alai	Tien Shan
Area (km^2)	128 000	191 000
Mean solid precipitation (mm) 50% probability	440	300
Range of solid precipitation for 5% and 95% probabilities	1650–100	1150–80
Mean snow depth (m)	1.1	0.7
Mean maximum SWE (mm)	350	180
50% probability SWE (mm) value	300	140
5% and 95% probability SWE (mm)	700–60	1400–80
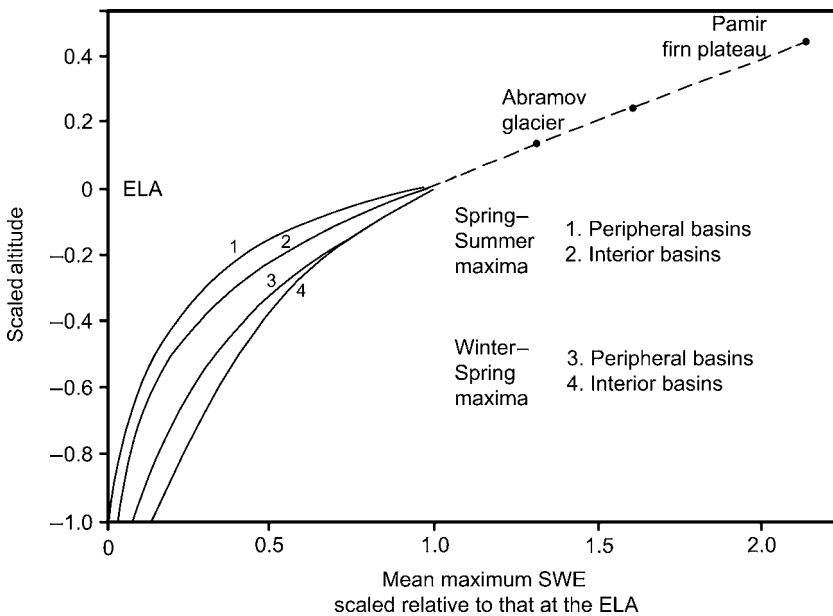
Fig. 5.10   Typical vertical gradients of maximum snow water equivalent (SWE) on macro-scale slopes in the Tien Shan and Pamir ranges (adapted from Getker, 1985).

The vertical gradients of maximum snow water equivalent (SWE), scaled in the same way as the precipitation gradients discussed above, are shown for the same four categories of macro-slope in Figure 5.10. Values on the firn plateau of the Pamir (∼5000 m altitude) are twice those at the equilibrium line altitude. The curves, based on data in 15 different river basins, are all basically the same. Values of maximum SWE are as follows: (1) northern periphery of the Tien Shan: 50–60 mm at 1000 m increasing to 300–450 mm at 3500–4000 m; (2) inner sheltered regions of the central Tien Shan: 15–50 mm in the valleys around 2000–2500 m
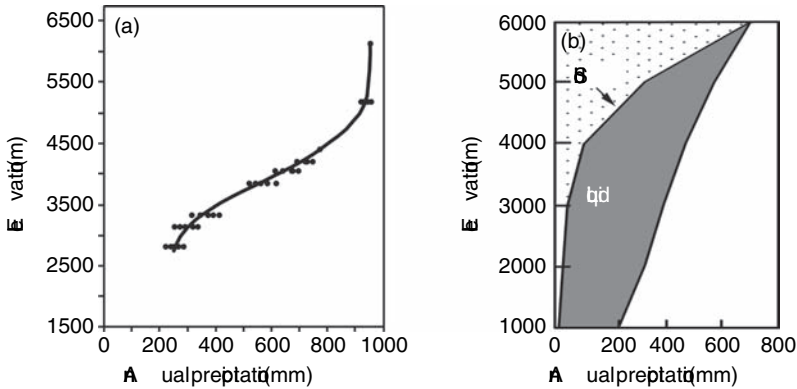
Fig. 5.11 Annual precipitation (mm) versus elevation (m) in the mountains of Central Asia. (a) Inylchek Glacier, Khan Tengry massif, central Tien Shan (ca. 42° N, 80° E) (Aizen *et al.*, 1997); (b) Hei He River basin, Qilian Shan, China (ca. 39° N, 100° E) (Kang *et al.*, 1999).

increasing to 200–300 mm around 4000–4500 m; (3) southwest-facing slopes of the Gissaro-Alai, western Pamir, and western Tien Shan: 60–100 mm at 1000 m increasing to 1000–1800 mm at 3500 m; (4) inner sheltered basins and northern periphery of the Pamir: only 20–40 mm in the valleys between 2000 and 4000 m, and 300–1500 mm on the peaks between 4000 and 6000 m.

In the northern Tien Shan, 75–80 mm of precipitation month^{-1} falls in April and May at > 3500 m and ~ 100 mm in May and June around 3000 m. In the central Tien Shan, 70–80 mm month^{-1} falls in May–August versus 40 mm month^{-1} in May and June around 1000–1500 m (Aizen and Aizen, 1997).

Estimates of the vertical gradients of annual precipitation in the Khan-Tengry massif of the central Tien Shan on the Kyrgystan–Chinese border (Aizen *et al.*, 1997) and further east in the Qilian Shan of western China (Kang *et al.*, 1999) are illustrated in Figure 5.11. The data in Figure 5.11a are based on records at the Tien Shan station (3614 m), correlated with records of snow-firn w.e. for 1969–89 at 6148 m, and calculations using field snow surveys on the Inylchek glacier; the northern and southern branches of the 65-km-long Inylchek glacier, are separated for 40 km by the Khan–Tengry massif, including Pobeda Peak which rises to 7440 m.

The Qilian Shan region is arid with less than 100 mm annual precipitation in the lowlands. For example, Jiuquan (39.8° N, 98.5° E, 1477 m) averaged 93 mm annually for 1961–90, with over half of this in the three summer months, and only occasional light snowfalls during November–February (source: Hong Kong Observatory: http://www.hko.gov.hk/wxinfo/climat/world/eng/asia/china). Heavier amounts fall in the mountains. Kang *et al.* (1999) provide results obtained from monthly altitudinal gradients of precipitation for six altitude zones from 1000 to 6000 m in the Hei He River basin, based on measurements at Zhangye (38.9° N, 100° E, 1483 m), corrected for gauge undercatch ($\times 1.3$ for solid and $\times 1.1$ for liquid precipitation)

(Figure 5.11b). The solid/liquid fractions are based on temperature data and a threshold temperature of 2 °C.

5.5   THE ALPS

The European Alps were the birthplace of mountain meteorology (see p. 6) and have been the location of so many meteorological studies that it is only feasible to give a general impression here of their variety and content. First, there are the climatological accounts for the major observatories – the Sonnblick in Austria, Hohenpeissenberg and the Zugspitze in Germany, and the Jungfraujoch in Switzerland (see Table 1.3, p. 8). Second, there are several syntheses – for the French Alps (Bénévent, 1926; Bezinge, 1974), the Tyrol (Fliri, 1962, 1975, 1977, 1982), the Hohe Tauern (Dobesch, 1983), French Switzerland (Bouët, 1972), as well as the entire area (Flohn, 1954; Fliri, 1974, 1984; Schüepp and Schirmer, 1977; Sevruk, 1985; Kerschner, 1989). The publications of the biennial *International Tagung für Alpine Meteorologie* (see Bibliography, p. 22) are a further major reference source. Recently, a climatic time series (HISTALP) comprising monthly pressure, temperature, precipitation, cloudiness and sunshine data for networks of stations in the Greater Alpine Region (*ca*. 43–49° N, 4–19° E) has been compiled. The records begin in the late eighteenth century for temperature and pressure, around 1800 for precipitation, and in the mid-nineteenth century for cloudiness and sunshine. Auer *et al.* (2005) describe the precipitation records and Matulla *et al.* (2005) analyze especially the temperature and pressure data.

A particular focus of research on weather and climate in the Alps has been the application of synoptic-climatological catalogs of pressure or airflow patterns (see Barry and Perry, 1973; Barry and Carleton, 2001). Fliri's (1962) analysis of the climatic characteristics in the Tyrol uses the system developed for the eastern Alps by Lauscher (1958), which was based on the *Grosswetterlagen* scheme of Hess and Brezowsky. Other classifications systems, developed by Schüepp (1959), and for the 500 mb level by Kirchhofer (1976, 1982), have been used in Switzerland. Kirchhofer analyzes temperature, precipitation, and sunshine data for Säntis, Davos and three lowland stations for each of 24 upper air circulation patterns. A further classification by Perret (1987) adopts elements of the *Grosswetterlagen*.

The Alps are arcuate in form at their western end where they extend some 250 km north–south. Winter snow cover as seen from space dramatically illustrates the extent and spatial character of the European Alps. Figure 5.12 clearly shows the main mountain ranges, the Po Valley and Maritime Alps to the southwest, the major Alpine valleys and the Jura to the northwest. Their orientation is almost west–east through Switzerland, where the ranges are less than 100 km in total width, and through Austria where they again broaden to 150 km, but are subdivided by pronounced longitudinal valleys such as the Inn and Drau. The Rhône and upper Rhine valleys in Switzerland are similar, but less extensive. The Alps accentuate

Fig. 5.12 Snow on the Alps (MODIS)
(NASA).
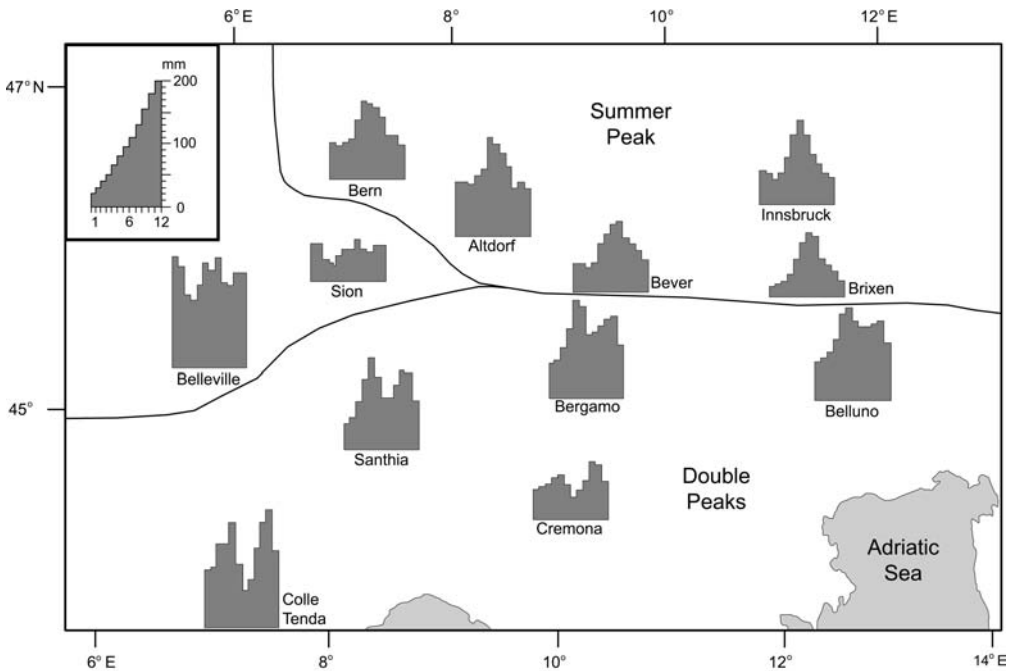
The annual cycle of precipitation in the Alps (1931-1960)

Fig. 5.13 Annual precipitation regimes at selected stations in the western Alps for 1931–60 (based on Fliri, 1974).

the climatic gradient between the Mediterranean and central Europe and the contrast between northern and southern slopes is pronounced in the vicinity of the St. Gotthard Pass. This effect is illustrated by the change in seasonal character-istics of Alpine precipitation (Figure 5.13). There is a summer convective maximum

east of a line from Locarno to Bern, while to the west there is year-round precipitation with no clear peak (Schaer *et al.*, 1998). In lowland Italy and the Alps Maritimes there is the classic Mediterranean pattern of maxima in May–June and October–November.

The large number of mountain stations in the Alps enables some estimate of station representativeness to be made. Beniston (2005) examines anomalies of winter daily maximum air temperatures for 1961–90 at ten Swiss climatological stations compared with those at the Säntis (2500 m) station in northeastern Switzerland. Correlations are 0.84 for all ten stations (including Zurich, 569 m) and reach 0.92–0.95 with Grand St. Bernard (2479 m), Jungfraujoch (3572 m) and Arosa (1847 m). Nevertheless, a regionalization of temperature patterns in the Greater Alpine Region, based on rotated empirical orthogonal functions (see Barry and Carleton, 2001; p. 78) identifies four major subregions: northwest–southwest of the main alpine crestline (NW–SW); northeast–east (NE–E), southeast (SE); and south-central (SC) (Matullo *et al.*, 2005). The north–south boundaries between NW–SW and NE, and between SE and SC are somewhat arbitrary as there are no major topographic features. There is also a group of high altitude stations. The significance of these regional differences will be noted in terms of long-term changes in Chapter 7.

Based on the various high-level stations and observatories in the Alps, early studies concluded that precipitation amounts increase with elevation to the highest levels (3000–3500 m). Steinhauser (1938; p. 96) showed this pattern on a local scale around the Sonnblick observatory while Baumgartner *et al.* (1983) argued for its generality based on 1000 Alpine catchments. Havlik (1968) demonstrates convincingly that most of this orographic effect is associated with cyclonic weather situations. For the French Alps, Bénévent (1926; p. 64) concluded that the elevation of maximum precipitation increases towards the Alps proper since it occurs around 2000 m in the Pre-Alps, 2500 m in the central massifs of the Dauphiné-Savoie, and 2500–3000 m in the mountains furthest into the intra-alpine zone, but no summit observatory data are available in this area. Only about 10 percent of the altitudinal increase in precipitation amount is attributable to more frequent rain days, according to Havlik (1968); differences in intensity are the primary factors. Nevertheless, variations in precipitation intensity are also attributable to location with respect to the entire mountain area and the orientation of particular ranges in relation to the major air currents (Bénévent, 1926).

Weingartner and Pearson (2001) point out that the pattern of precipitation across the European Alps is characterized by pronounced bands along the northern and southern edges of the area. These bands represent regions of high precipitation that converge in the central Swiss Alps. They are separated by internal drier zones (Tirol in Austria and Valais in the Swiss Alps), which are sheltered north and south by high mountain ranges (Schwarb *et al.*, 2001).

Work by Blumer (1994) around Säntis in northeastern Switzerland analyzed the effects of distance and direction from the mountains versus altitude effects and showed that annual totals are often weakly related to station elevation. In fact,
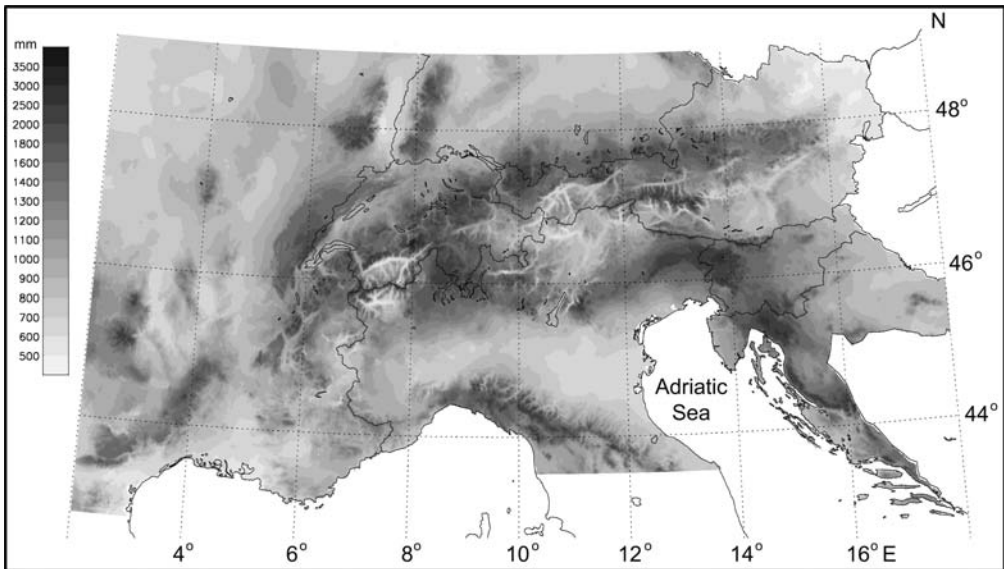
Fig. 5.14 **Annual precipitation over the Alps for 1966–95 based on a dense station network (see text) (simplified after Frei and Schär, 1998).**

precipitation gradients in Switzerland show large regional contrasts, particularly north and south of the main Alpine ridge, according to Sevruk (1997). North of the main ridge there is a strong correlation ($r^2 = 0.67$) for annual precipitation totals adjusted for known systematic errors (see p. 310) and altitude; from 500 to 2500 m the gradient is 866 mm km^{-1}. South of the ridge in contrast there is no correlation. On a regional basis, wide differences in gradient are noted, ranging from below 300 mm km^{-1} in Ticino and the Engadine in the southeast to 1580 mm km^{-1} in northeast Switzerland, although the value is close to 800 mm km^{-1} in most of Switzerland north of the main ridge. Sevruk also finds that the gradients are steeper above 1500 m, where a separate regression equation is preferable.

Recent studies in the Alps during the Mesoscale Alpine Program (MAP) in 1999 and subsequently show a much revised picture of the spatial and altitudinal distribution of precipitation from earlier work using only station data. Frei and Schär (1998) assembled a daily time series for 6700 locations for at least part of the interval 1966–95. On average there are 5000 stations corresponding to a spacing of 10–15 km. A simplified version of their climatology is shown in Figure 5.14. There are maxima over the northern and southern mountain ranges, with a connection between the two zones over the St. Gotthard pass. The southern zone extends southeastward from the Julian Alps to the Dinaric Alps. Totals are low in the interior east–west valleys and the driest region is in the southeast Tyrol (< 700 mm). In the Tyrol there is an "inner alpine province" with its own distinctive climatic characteristics (Fliri, 1975). Table 5.5, showing mean precipitation on rain days (≥ 1 mm), illustrates the dryness of this area, which is due to the dual sheltering

Table 5.5 District averages of seasonal precipitation characteristics for the Alps.

District	Mean elevation (m)	Winter			Spring			Summer			Autumn		
		p	spd	d_{30}	p	spd	d_{30}	p	spd	d_{30}	p	spd	d_{30}
N. Foreland	670	169	5.2	0.3	208	6.2	0.3	407	9.7	2.0	186	6.6	0.4
N. Edge (W)	953	412	10.8	2.1	388	10.7	2.0	681	13.7	4.8	384	11.1	2.3
N. Edge (E)	768	320	9.6	1.6	336	9.1	1.4	606	12.0	3.6	288	9.3	1.2
Central Inn	809	159	6.8	0.5	171	6.5	0.3	397	9.5	1.8	172	7.6	0.5
Silvretta	1541	261	9.6	1.5	214	7.5	0.4	448	9.8	2.0	236	9.0	0.8
Ötztal Alps	1619	160	7.1	0.7	143	5.7	0.3	301	7.2	0.9	163	7.1	0.4
Vintschgau	1130	95	6.8	0.3	98	6.0	0.2	236	7.9	0.9	151	8.2	0.6
Bolzano	809	91	7.0	0.2	143	7.2	0.1	302	9.4	0.8	164	8.9	0.6
Veltlin	1540	214	11.4	1.5	270	11.2	1.6	414	11.9	2.8	338	14.5	3.2
SE Dolomites	1315	209	11.0	1.6	269	9.3	1.0	412	10.0	1.9	321	13.3	2.6
Trentino	236	167	12.2	1.1	217	10.4	1.0	279	10.9	1.7	287	13.9	2.7

Notes: p = mean seasonal precipitation (mm); spd = specific precipitation density (mean precipitation per rain day, mm d^{-1}); d_{30} = number of days with $\geq$ 30 mm precipitation

Source: after Fliri (1962).

effect of the ranges to both the north and south. Precipitation amounts also generally decline eastward through the Alps; compare for example the western and eastern parts of the "northern edge"; also Silvretta and the Öztal Alps in Table 5.5. The inner alpine province is continental in character with a summer precipitation maximum and a winter or spring minimum. In contrast, the northern Alps have a primary maximum in summer and a secondary one in winter in the western section, while the southern slopes of the southern Alps have an autumn maximum and winter minimum, typical of the northern Mediterranean. Precipitation on the northern slopes of the Alps is mainly of cyclonic origin, enhanced by orographic effects, and of moderate intensity, but with summer convective precipitation (Table 5.5). The southern ranges more commonly experience showery precipitation, with thunderstorms and hail, particularly in summer and autumn. The central Alps have less thunderstorm activity (Bouët, 1972).

Interactions between orography and weather systems simultaneously lead to heavy precipitation on windward slopes of the Alps and much lesser amounts on lee slopes, as well as creating corresponding patterns of snow accumulation, or melt. Lang and Rohrer (1987) illustrate the atmospheric conditions for several cases with deeper snow cover on the northern slopes of the Alps, or south of the Alps. Southeasterly flows of Mediterranean air have higher humidity and temperature than the northwesterly flows, for example. However, these differences for individual storm events are largely canceled out when longer time intervals are considered.

A transect across the eastern Alps (averaged over $11°$–$13.5°$ E) between $45°$ and $49°$ N demonstrates that maximum amounts fall around 1100 m on the southern slope and as low as 750 m on the northern slope; minimum amounts are recorded above 2000 m (Figure 5.15) (Schwarb et al., 2001; also see Frei and Schär, 1998). The range of variability between different locations is greatest on the southern slope between 1000 and 1500 m.

The cross-sections in Figure 5.16 show differences between the western and central Swiss Alps. In the western Alps highest amounts tend to be over the higher terrain as proposed by Maurer and Lütschg (1931), for the Jungfrau massif, for example. In the central transect (Rhine–Maggia) the high inner Alps are drier. The location of the maxima follow the pattern pointed out by Frei and Schär (1998)

Fig. 5.15   **Mean annual precipitation (dashed) and elevation (solid line) for a south–north transect through the eastern Alps between the Gulf of Venice and Bavaria (based on Schwarb et al., 2001).**
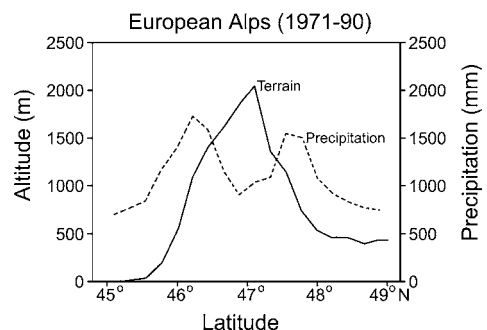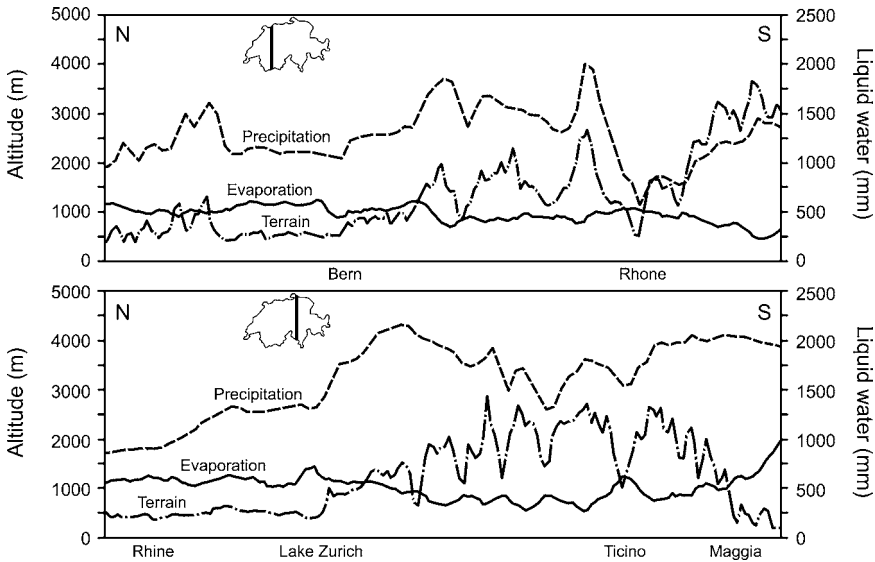
Fig. 5.16 **North–south transects of precipitation for 1971–90 and actual evaporation for 1973–92 across the Swiss Alps (after Spreafico and Weingartner, 2005).**

although on the southern side totals are consistently high from the foothills to the first crest. These maxima are a consequence of the blocking of humid northwesterly or southwesterly airflow (called "Staulage"). The first northern obstacles are in the region of central Switzerland – Wäggital and Säntis. In the south, it is the region of the southern Valais, the upper Maggia and Melezza valleys, or even the Poschiavo and Veltelina valleys, depending on the airflow coming from a southwesterly or southeasterly direction.

In summary, the detailed analyses by Sevruk (1997), Frei and Schär (1998) and Spreafico and Weingartner (2005) show that there is no unique relationship between precipitation amount and altitude in the Alps, and there is great variability in altitudinal gradients.

An episode of intense rainfall over the Alps in November 1994 resulted in disastrous floods in the Piedmont of Italy (Cassardo *et al.*, 2002). Totals exceeded 200–250 mm in the upper reaches of two river basins in the Maritime Alps and in a separate area of the northwestern Italian Alps. There was a stationary low over Western Europe and southerly upper level flow over northern Italy. The rainfall was caused by convergence between moist, low-level southeasterly flow moving over the mountains while stable, unsaturated air to the east was deflected westward by the terrain. An easterly jet of $40\,\mathrm{m\,s^{-1}}$ was observed at 900 mb over Milan on 5 November, for example. A further factor in generating high runoff was the snow line elevation at 2200–2400 m, 500 m above its seasonal average elevation (Cassardo *et al.*, 2002). The cul-de-sac shape of the Piedmont lowlands, with the southern Alps to the north, Maritime Alps, to the west and Apennines to the south acts as a natural trap for moist airflows from the southeast (Rotunno

and Ferretri, 2001). Potential vorticity banners in the lower stratosphere are a strong indicator (73 percent of cases) of heavy precipitation events on the southern side of the Swiss Alps (Martius *et al.*, 2006).

The greater continentality of the inner Alps is apparent in the greater sunshine duration −60 percent of possible on an annual basis – compared with only 45–50 percent on the northern and southern margins. As a result, the central zone has higher totals of absorbed global solar radiation and a larger annual range of mean daily maximum temperature; 23 °C in the inner zone compared with 20 °C at the edges at 500 m elevations and 17 and 15 °C, respectively, at 2000 m elevation. The various data and Fliri's (1975; pp. 139) analysis bear on the question of the so-called *Massenerhebung* (mass-elevation) effect discussed earlier (p. 65). Tollner (1949) demonstrated that, in the Alps, stations located on mountains, in high valleys, and in passes, are all colder than the free air on a mean annual basis at 0700 h. and there are ample observations to confirm this result. However, mountain temperatures have a tendency to exceed those in the free air, by a degree or so, on summer afternoons (see p. 63). The fact that vegetation boundaries extend to higher elevations in the central Alps is related primarily to the reduced snow cover duration, greater radiation income, and longer growing season. The Bernese Oberland, which on topographic grounds alone might be expected to show such a mass–elevation effect, in fact experiences a more "maritime" climatic regime as a result of its general windward location (H. Turner, personal communication, 1975). The relative dryness of the central Alps, together with the high radiation amounts, implies less energy going into latent heat and more into sensible heat to the atmosphere. However, this transfer is not the sole mechanism for raising atmospheric temperatures over the central Alps since the effect is already present in April when all of the higher elevations are still snow-covered (Fliri, 1975).

Snow cover in Switzerland has been examined in detail by Witmer *et al.* (1986) using the networks of the Swiss Meteorological Institute and the Federal Institute for Snow and Avalanche Research (ELSLF) for October–June, 1950–1 to 1979–80 (or sub-periods). The mean gradient of total new snowfall below 1100 m altitude for November–April (1970–1 to 1979–80) varies from 8 cm /100 m in the Valais (southwestern Alps) to 73 cm/100 m in the Bernese Alps (north slope of the Alps). Above 900 m, the mean gradients range from 26 cm/100 m in the southeastern Engadine (Grisons) to 107 cm/100 m in the northeast (Glarner Alps). Using data for 1960–1 to 1979–80, Witmer *et al.* show that snow depths above 900 m in April have a range of gradients (for median depth values) from 9 cm/100 m in the Valais to 26 cm/100 m in the Glarner Alps with values > 20 cm/100 m through the north slope of the Alps and in the southern Tessin (Gotthard area). There are also large differences between north- and south-facing slopes in winter and spring. Depth ratios compared with a horizontal surface are approximately 1.2/0.7 for 20 °N/S-facing slopes at 1800 m in early February, increasing to 2.0/0.3, respectively, in late March. The altitudinal variation of snow cover duration for 1960–1 to 1979–80 increases almost linearly for depths ≥ 30 cm, from 5 days at 400 m to

Table 5.6 Mean potential temperature (°C) during 12 cases each of north föhn and south föhn, 1942–5.

	Elevation (m)					
	Lugano 276	Airolo 1170	Gotthard 2096	Göschenen 1107	Altdorf 456	Zurich 493
S Föhn	8.3	11.2	12.8	14.3	15.7	12.4
N Föhn	13.8	10.5	9.5	6.2	4.8	5.1

Source: after Frey (1953).

Table 5.7 Characteristics of south föhn in the eastern Alps and Foreland.

	Elevation (m)					
	Lake Garda 90	Innsbruck 575	Partenkirchen 715	Hohenpeissenberg 994	Munich 528	Regensburg 343
θ_{14} (°C)	8.3	15.5	17.4	16.1	13.4	9.7
R.H.$_{14}$ (%)	69	39	33	40	49	56
Meancloud (%)	73	40	30	43	44	49

Notes: θ_{14} = Potential temperature (at 500 m) at 14 hours; R.H.$_{14}$ = Relative humidity at 14 hours.
Source: after von Ficker and de Rudder 1943.

160 days at 2000 m, whereas it is curvilinear for depths ≥ 1 cm, ranging from 25–50 days around 400 m to 175 days at 2000 m and above. The problem of mapping snow depths is overcome by the preparation of maps for all of Switzerland or the Alps at fixed levels (1000, 1500 and 2000 m).

Liang (1982) presents a general picture of altitudinal variations in moisture balance for Austria. Potential evaporation is calculated from Penman's method (p. 331); actual evaporation is determined using an empirical relationship proposed by Turc. Potential evaporation (PE) decreases rapidly and then more slowly with altitude while actual evaporation (AE) decreases nearly linearly. AE increases from 90 percent of PE between 500 and 1500 m to over 95 percent above 2000 m. AE accounts for about 45 percent of the annual precipitation between 500–1500 m, but only 25 percent around 2000 m. Actual evaporation on an annual basis is plotted on the transects in Figure 5.16. These show that evaporation is unrelated to the topography and that the P–E amounts are large in the mountains generally.

A major climatic characteristic of the alpine valleys and foothill locations is the occurrence of föhn winds. Numerous general and local studies have been made of their effects. Tables 5.6 and 5.7 illustrate profiles of mean potential temperature for 12 cases each of north and south föhn during the peak phases with valley föhn (Frey, 1953). It is notable that the warming is already apparent over the higher elevations (at St. Gotthard) implying subsidence effects. North föhn generally

occurs with a northerly flow of modified cold polar air behind a meridional trough. South föhn is typically associated with warm sector air. At Sierre, in the central part of the Valais of southwest Switzerland, the south föhn occurs on about 33 days per year, with a maximum in April (Bouët, 1972). The winds at summit level (4000 m) are usually southwesterly, but valley channeling causes them to be southerly in the lower Valais and northeasterly at Sierre where they have a mean speed of 6 m s^{-1}. In a third of the cases the maximum wind may exceed 15 m s^{-1}. At Innsbruck the south föhn has an average annual frequency of 60 days, with 40 percent of these in the spring. Other months each have 3–5 days with south föhn (Fliri, 1975). However, the greatest departures of daily temperature from normal ($+8\,°C$) at Innsbruck are experienced during autumn and winter cases.

In the 10-km wide, upper Rhine valley north of Lake Constance, there were on average 33 half-days with föhn during 7 September–15 November, 1989–98, the MAP Special Observation Period (Richner *et al.*, 2005), with a minimum of 19 and a maximum of 58 half-days. Prior work shows that south föhns occur almost equally in autumn, winter and spring. For the FORM project, the definition of föhn was a (reduced) pressure gradient of at least 5 mb between Lugano and Vaduz. The 12 cases had a mean duration of 20 h, ranging from 3 to 39 h. Six of the cases were pronounced and followed by a cold front, while the remainder were shallow and associated with a weak trough. The south föhn does not always penetrate to ground level in the major valleys and northern Foreland since shallow cold air lifts it above the surface. Occasionally, when the föhn wall extends across the crest of the Alps and winds are strong at summit level, the air is unable to follow the terrain and only reaches the ground where the valleys open out onto the lowlands. This is known as "dimmer-föhn," meaning blocked or damned-up föhn (Frey, 1953). Apart from the much-discussed but poorly understood symptoms of "föhn sickness" (see Chapter 6, p. 452), föhn occurrences in spring cause rapid snowmelt, with a risk of avalanche activity and also floods. Föhn gales may result in damage to forest through windfalls, as well as enhanced fire risk due to the low humidity. On 7–8 November 1982 a violent south föhn in the northern Alpine foreland of Switzerland brought peak gusts of 40 m s^{-1} at Jungfraujoch and 54 m s^{-1} at Gütsch near Altdorf (2282 m), associated with a south–north pressure gradient of 18 mb/100 km – the highest on record (Frey, 1984). Temperatures rose to 20 °C at Zurich compared with readings of 2 °C in the Po lowlands of Italy. This "100-year" event is an example of the persistent type of south föhn that occurs ahead of a deep, slow-moving upper trough, with strong southerly flow aloft (Schüepp, 1990). Short-lived south föhn events are associated with upper westerlies, when upper-level divergence generates surface pressure falls north of the Alps.

A local wind of importance in the northern and western Alps is the *bise*. Cold northerly flows of polar air in winter and spring are typically blocked and channeled by the Jura and Alps (Wanner and Furger, 1990). It occurs, on average, on 94 days per year at Lausanne. The speed of the bise averages 3–4 m s^{-1} at Lausanne with gale-force maxima in about 10 percent of cases. In the vicinity of Geneva, and

also in the sheltered Valais, these winds give dry fine weather, but further east the orientation of the ranges in the Pre-Alps and Alps produces heavy cloud, due to the forced uplift, with precipitation in about one-third of cases (Bouët, 1972). On the southern slopes of the Alps, of course, these situations usually give rise to north föhn, provided the flow is forced across the mountains.

Fog and low stratus is a significant feature of the winter climate of the Bernese Plateau. A detailed analysis by Wanner (1979) shows that fog occurs at least locally on 50 percent of mornings between September and March. There is clear distinction between seasonal fog regimes on the plateau, where there is a pronounced maximum in October–November and a summer minimum, and at summit stations which have a high frequency year-round, but with a spring maximum (Figure 5.17). In many alpine valleys, and in the Valais, however, the frequency of early morning fog in winter is less than 10 percent. An inversion top is frequently located about 800 m asl above Payerne corresponding to the typical fog limit reported by Wanner. It is also noteworthy that, at Montreux, stratus occurs on an average of

Fig. 5.17 **Diurnal fog frequency on the Bernese Plateau (a) and on an alpine summit (b) (from Wanner, 1979).**
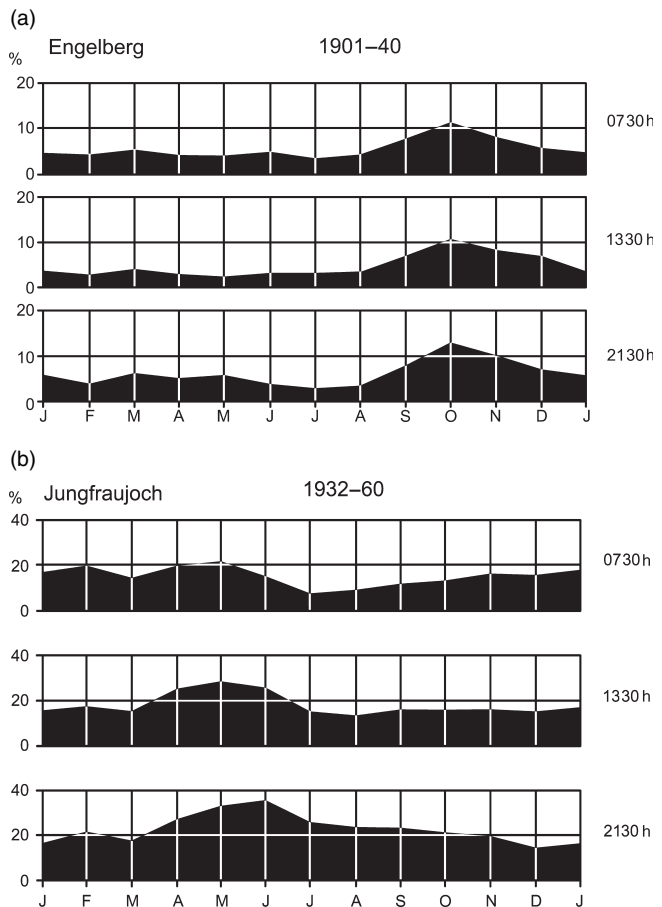
80 mornings between September and March, with its base between 700–900 m on 87 percent of occasions (Bouët, 1972). Low-level inversions and radiation fog are most common during weak anticyclonic situations, while cold northeasterly flow with anticyclonic patterns (bise) tends to give rise to high-level inversions and shallow high fog or stratus. Upslope fog, in contrast, usually occurs with cyclonic southwesterly airflows.

The final phenomenon to be discussed is common to all mountain systems with east–west valleys. It is the well-known *adret* (sunny) *ubac* (shaded) contrast between slopes, which has been most thoroughly investigated in the Alps. The differences are largest in winter when the solar angle is low and the period of radiation income is minimal. Bénévent (1926; p. 105) cites typical mean temperature differences of 0.5–1.0 °C, with up to 3 °C difference at 1300 h in appropriate locations. Bouët (1972) notes that snow-cover duration at 1500 m is 160 days on the shady slope, but 30 days less on the sunny slope. This difference finds expression in the pattern of land use and also in the preferred location of alpine settlement (Garnett, 1937).

5.6   THE MARITIME MOUNTAINS OF GREAT BRITAIN

The mountains of northwestern Europe are notable for their extremely maritime character. This is manifested in the limited seasonal variation of cloudiness, precipitation and temperature, in the high humidity, in the steep lapse rates, and in the low tree line (Manley, 1945; Green, 1955; Taylor, 1976). The most detailed observational material in the British Isles was provided by the Ben Nevis Observatories (McConnell, 1988). The records for 1883–1904 at Ben Nevis (1343 m), 6 km inland from the observatory at Fort William (13 m), are fully tabulated by Buchan (1890) and Buchan and Omond (1902, 1905, 1910), although Buchan's death in 1907 halted the planned thorough analysis of the data [von Hann (1912) summarized some of the data]. The maintenance of good observational records on the summit of Ben Nevis was a major problem due to frequent riming of instruments (see, for example, Curran *et al.*, 1977), summit cloud, and winter snowfall. (In addition, the cost was borne by private sources and the unwillingness of the government to provide assistance led to the eventual closure.) The thermometer screens were mounted on ladders and their height adjusted in relation to the snow surface, which could exceed 3 m. The site was adjacent to a steep 550 m drop on the north side of the mountain and the effect of this location on air motion caused frequent "pumping" of the barometer.

Currently, there are few meteorological stations in Britain above 400 m and no actual mountain stations (Taylor, 1976). Manley (1936, 1942, 1943, 1980) has summarized some records for the northern Pennines, but data for the mountains of Scotland, Wales and the Lake District are very fragmentary. Automatic stations can help to fill this gap, at least for the major weather elements. Barton (1984) describes the AWS that operated in the Cairn Gorm since 1977. The data since 1990 are available on line from Heriot-Watt University.

The western highlands of Britain have a high proportion of cloudy days. On Ben Nevis, for example, the mean cloudiness exceeds 80 percent in all months and in winter months only about 10 percent of the possible sunshine hours are recorded. The summit is clear of fog only 21 percent of the time from November to March, with the majority of clear weather occurring in spring (45 percent of the time). Buchanan (1902) showed that, during 1885–97, there were 185 spells, averaging 4.0 days in length, with *no* clear observations.

Glasspoole (1953) used data of R. C. Mossman (in Buchan and Omond, 1910; p. 444) to show that summit cloud around Ben Nevis during winter 1901–2, averaged almost 50 percent at 1000 m, 67 percent at the summit and only 20 percent at 700 m, whereas in the northern Pennines of England (Great Dun Fell, 847 m) and the Southern Uplands of Scotland (Lowther Hill, 725 m) the frequency was also approximately 60 percent.

As a result of cloud cover, solar radiation amounts in Wales and the Pennines decrease with elevation below 500 m asl by roughly 2.5–$3 \, \mathrm{MJ \, m^{-2} \, day^{-1} \, km^{-1}}$ (Harding, 1979b). However, this effect operates on a regional scale. Receipts are fairly uniform within a given upland area, regardless of altitudinal differences. Above 500 m, the higher summits in summer may have shallow cloud, or no cloud, above them. Harding notes that a 35 percent increase in solar radiation from Glenmore Lodge (341 m) to the Cairn Gorm Summit (1245 m) was observed between 25 May and 22 July 1977 (for 1000–1400 h).

Annual precipitation is high in northwest Britain due to the northeastward movement of frontal depressions from the Atlantic, and the location of the mountains causes large altitudinal increases. In the western highlands of Scotland, measurable precipitation falls more than 1500 h per year, although annual rates are only about $2.0 \, \mathrm{mm \, h^{-1}}$ (Atkinson and Smithson, 1976). Using data from more than 6500 stations over Britain, Bleasdale and Chan (1972) determine that average annual precipitation, R (mm) can be expressed:

$$R = 714 + 2.42 \, H$$

where H is the height (m). The line of zero anomaly from this regression closely approximates the main east–west water divide in Scotland, northern England and Wales. Positive residuals ≥ 600 mm occur in western Scotland, the Lake District and Wales with negative residuals ≥ 600 mm over the Cairngorms, where there are strong lee (sheltering) effects with the prevailing air flow. An annual total of 4084 mm was recorded on Ben Nevis for 1883–1904, although this is only 120 mm in excess of the "predicted" amount. The orographic effect is exhibited more in terms of increased intensity than duration. For example, the annual mean at Cwm Dyli, Snowdonia (101 m) is 3500 mm with a mean intensity of $2.7 \, \mathrm{mm \, h^{-1}}$ whereas at Holyhead (9 m) on the coast, the corresponding figures are 1000 mm and $1.4 \, \mathrm{mm \, h^{-1}}$ (Atkinson and Smithson, 1976). The total is increased 3.5 times with less than a doubling of the average hours with precipitation. "Exceptional" daily

falls, defined as totals of 125 mm (5 in) which account for at least 15 percent of the annual average at a given station, are most common in the western mountain districts of Britain in the winter half-year according to Bleasdale (1963), illustrating the importance of orographic intensification of precipitation in deep frontal depressions. Moreover, the Ben Nevis records (Buchan, 1890) show that most thunderstorms occur in the winter months, in associations with such systems, in contrast to the summer maximum over the European mountains.

Since surface temperatures are frequently slightly below freezing point on the mountains in winter, the occurrence of rainfall especially with warm front situations, quite commonly gives rise to freezing precipitation and glazed ice. On Ben Nevis, there were 198 cases of such "silver thaw" (Mossman, 1902) during 1885–90, with an average duration of 4.4 h. These cases occurred largely in the winter months with air temperatures between $0°$ and $-2.5°C$. In rare instances, ice build-up from such events, perhaps associated with heavy riming (freezing fog/cloud droplets), can set up severe stresses on structures (see p. 319 and Figure 4.34). The Cairn Gorm AWS uses a heated chamber to overcome the build up of glaze on the instruments (Barton, 1984).

General snowfall conditions in relation to altitude in the British mountains are discussed on p. 295. In connection with a survey of the possibilities for winter sports development at Fort William, Thom (1974) has analyzed the snowfall data for 1895–1904 at Ben Nevis. Figure 5.18 shows the percentage of the total precipitation in each month occurring as snow, and the extremes. In April the percentage does not fall below about 60 percent. At 750 m elevation, the ratio of rain to snow approaches 50 : 50 from January through April. Thom also shows that, on average, the snowfall fraction on Ben Nevis increases by 9 percent per $1°C$ decrease in mean monthly temperature. However, since the scatter is considerable, this relationship may be of limited value in assessing the snowfall fraction in relation to temperature for a particular month.

The climate of the Cairn Gorm summit (1245 m), where the mean annual temperature is near $0°C$, (and the western Scottish mountains, including Ben

Fig. 5.18 **Percentage of the monthly precipitation falling as snow on Ben Nevis (1343 m), 1895–1904. Average (solid) and extremes (fine lines) (after Thom, 1974).**
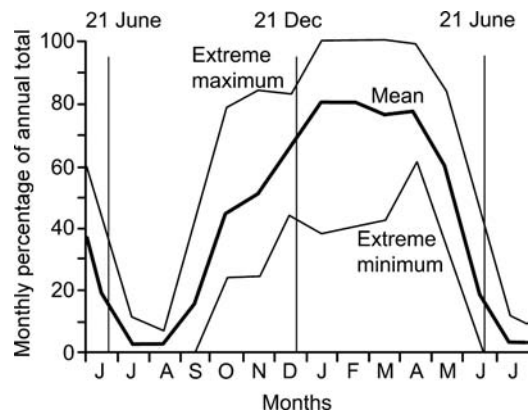
Nevis, see Table 2.1) is appropriately described as "sub-arctic" (Barton and Borthwick, 1982). The extremes recorded at the Cairn Gorm AWS are 18.6 °C and −15.5 °C. As already noted, lapse rates in Britain are steep due to the maritime air mass characteristics. Data from 14 pairs of lowland and upland stations show a mean gradient of about 8.5 °C km^{-1} for annual mean maximum temperature (Harding, 1978). As recognized earlier by Manley (1942), there is a clear winter minimum (6–7 °C km^{-1}) and spring maximum (8–10 °C km^{-1}) and this pattern seems to be general throughout northwestern Europe. The spring maximum apparently reflects a general increase in instability, rather than synoptic airflow patterns (Harding, 1978). The gradients of mean temperature and maximum temperature in Britain are closely similar in winter, when the short day-length and large cloud amounts lessen the diurnal variation of lapse rate. Pepin *et al.* (1999) present results from five AWS installed for 2 years between 170 and 847 m in northern England spanning a unique 700 m range for Great Britain. They note that there was a strong diurnal variation in lapse rates, especially in summer and on the lower slopes; for the latter sites values approach the DALR in early afternoon and fell to only −4.2 °C km^{-1} by 0500 h. Overall, the smallest lapse rates ($\sim$ −4.4 °C km^{-1}) occurred during south, southeast and anticyclonic circulation types. These results differ from those of Manley and Harding perhaps due to the more detailed data available to Pepin *et al.*

The diurnal temperature range (DTR) on British mountains appears to be remarkably small. The Ben Nevis records for 1883–7 show average departures of hourly temperatures from the daily mean of ± 1 °C in summer and only ± 0.2 °C in winter (Buchan, 1890). On Cairn Gorm (57° N, 3° W, 1245 m), observations during 16–31 August 1980 suggest that there are two types of weather. Either, there is hill fog, humidity > 95 percent and a DTR < 2 °C, or in clear conditions with light winds, the DTR is 8–10 °C. (Barton and Borthwick, 1982).

The gradient of maximum temperature, which is controlled mainly by radiational heating (Harding, 1979a), approximates the dry adiabatic lapse rate in sunny convective conditions, although higher rates may occur due to the existence of a shallow super-adiabatic layer at the lowland station. Omond (1910) reported 205 cases (0.2 percent of observations) with lapse rates > 10.5 °C km^{-1} at Ben Nevis between August 1890 and July 1903. They occurred predominantly on sunny afternoons or with dry southeasterly airflow during April–June. The gradient of minimum temperature is subject to local topographic effects, especially valley inversions, making general discussion of regional characteristics impossible.

The length of the frost-free season generally decreases with altitude, although, as shown by S. J. Harrison (cited by Taylor, 1976; p. 279), the use of screen temperatures greatly overestimates conditions at the ground surface. The difference between frost-free seasons, determined from readings of screen and grass minimum thermometers, for example, amounted to 18 weeks (35 versus 17) at sea level and 25 weeks (33 versus 8) at 450 m asl in western Wales in 1969.

An unexpected feature of British mountain climate is the occasional observation of very dry air. On Ben Nevis, 2.5 percent of days (1884–1903) had at least one hourly reading of relative humidity below 20 percent, based on recalculations using a more accurate hygrometric equation (Green, 1967). Most of the cases occurred in autumn and winter, apparently related to subsidence during spells with blocking anticyclones.

Wind data for the British uplands are extremely sparse. The annual mean on Ben Nevis averages $6.5\,\mathrm{m\,s^{-1}}$, with a range of 9.0 to $4.5\,\mathrm{m\,s^{-1}}$ between the means of January and July. In view of the fact that part of the motivation for the observatory was its location on the Atlantic storm track, these values are lower than might have been anticipated, although Thom (1974) shows good agreement between observed summit winds, estimated geostrophic values, and observed 900 mb soundings at Stornoway in the Hebrides. Winds on Ben Nevis exceeded $22\,\mathrm{m\,s^{-1}}$ about 9 percent of the time during November through to March. The AWS in the Cairngorms (1245 m) indicates that a high degree of gustiness may be expected, despite the smooth dome-shape of that summit (Curran *et al.*, 1977). During October 1978–May 1983 the annual mean speed was $13\,\mathrm{m\,s^{-1}}$ with a maximum monthly average of $24.5\,\mathrm{m\,s^{-1}}$ in January 1983 and maximum gust of $66\,\mathrm{m\,s^{-1}}$ (Barton and Borthwick, 1982, and web site).

5.7   THE ROCKY MOUNTAINS IN COLORADO

The Rocky Mountains extend from the Yukon Territory to New Mexico, but we are concerned only with their southern part in Colorado, at about latitude $40°\,\mathrm{N}$, where fairly extensive data are available. Here the mountains form a pronounced north–south barrier rising to 4000 m asl. To the east they front the high plains and to the west there are intermontane basins, both with elevations around 1500 m. The location, 1500 km from the Pacific coast, provides a continental climatic setting, although the Rockies create their own distinctive altitudinal climatic belts, to the extent that permafrost patches are present under windswept sites above about 3750 m a.s.l. (Ives, 1973). Here mean annual air temperatures are around $-4\,°\mathrm{C}$.

Despite the relative ease of access to the alpine zone above the tree line, located about 3500 m, there are no permanent mountain observatories. The Pike's Peak Observatory (4311 m) was operated in the 1870–90s (see Table 1.3, p. 8) (Diaz *et al.*, 1982), but recent high-level stations have been of a climatological nature (Judson, 1965, 1977; Marr, 1961). Four stations established for ecological purposes by J. W. Marr in 1952 along an altitudinal transect on the east slope of the Front Range west of Boulder, and subsequently maintained by the Institute of Arctic and Alpine Research at the University of Colorado, provide a valuable picture of year-round conditions in the mountains.

These, and other records collected in connection with avalanche studies and cloud-seeding programs, provide the basis for the present discussion.

Topics of special interest in the Rocky Mountain area are the precipitation characteristics, especially snowfall, and the wind regime. Analysis of the precipitation records from the four-station transect on the east slope of the Front Range demonstrates the importance of the large-scale atmospheric circulation and its interaction with the topography (Barry, 1973). In the winter months, westerly air circulation is dominant with Pacific storms affecting particularly the western side of the range and its higher elevations. Nevertheless, some meridional flow patterns cause upslope flow on the east slope. In spring, and also in autumn, meridional troughs and occasionally deep cut-off cold lows draw moist air northward from the Gulf of Mexico. The temperature structure is potentially unstable and forced ascent in upslope flow causes heavy precipitation, falling as snow at higher elevations and even in the foothills, on the east slope. On 14–15 April 1921, for example, a deep storm with this type of circulation established a US record of 193 cm for a 24-h snowfall at Silver Lake, Boulder County (3170 m). In summer, precipitation is mainly of a convective kind, although sufficient moisture must be transported into the area for the instability to be released by heating and orographic effects. At this season, patterns of equivalent potential temperature show sharp gradients paralleling the Rocky Mountains, with higher values indicating warm moist air to the east of the mountains, which act as a climatic divide (Mitchell, 1976).

Using SNOTEL data (see Chapter 4. p. 311), Serreze et al. (1999) show that in the western United States, snowfall accounts for 62–67 percent of annual precipitation in the mountain ranges of Colorado, northwestern Wyoming, western Montana, Idaho, and the Sierra Nevada. The ratio drops to 50 percent in the milder Pacific Northwest and 39 percent in the mountains of Arizona–New Mexico. Large snowfall events, lasting up to 72 hours, are found to contribute 10–23 percent of the annual snowfall totals [water equivalent (w.e.)] according to Serreze et al. (2001). While these events are mainly in midwinter in most of the western United States, they are more common in late winter–spring in the Rocky Mountains and in Utah.

On an annual basis there is a sharp transition across the Front Range from a Great Plains regime, with a spring precipitation maximum which is apparent up to at least 3000 m on the east slope (Como station, see Figure 5.19), to a west slope pattern, characterized by a winter maximum and autumn minimum, at Niwot Ridge (3750 m), located just 2.5 km east of the Continental Divide; the two stations are separated by a distance of only 7 km. At Berthoud Pass (3448 m) on the Continental Divide some 30 km further south, Judson (1977) reports a mean annual total of 930 mm, comparable to the figure of 1017 mm for Niwot Ridge (1952–2004), but there April receives the highest total. On the east slope, annual totals increase from less than 600 mm in the foothills (2200 to 2600 m) to about 740 mm at 3000 m and 1000 mm (75 percent occurring as snowfall) at 3750 m on Niwot Ridge where the gauge is screened by a modified Wyoming-type of snow fence (see p. 309).

A larger-scale study of winter storm precipitation across the Continental Divide from Grand Junction to Denver by Hjermstad (1970) shows the effects of

Fig. 5.19 Precipitation regimes on the east slope of the Front Range, Colorado (40° N, 105.5° W) expressed as monthly percentages of the annual total (based on Niwot Ridge LTER data). Niwot Ridge (3743 m) is 2.5 km east of the Continental Divide, Como (3022 m) is 9.5 km and Sugarloaf (2591 m) 22.5 km east of the Divide. The data for Niwot Ridge and Como are for 1952–2004, for Sugarloaf for 1952–1991.
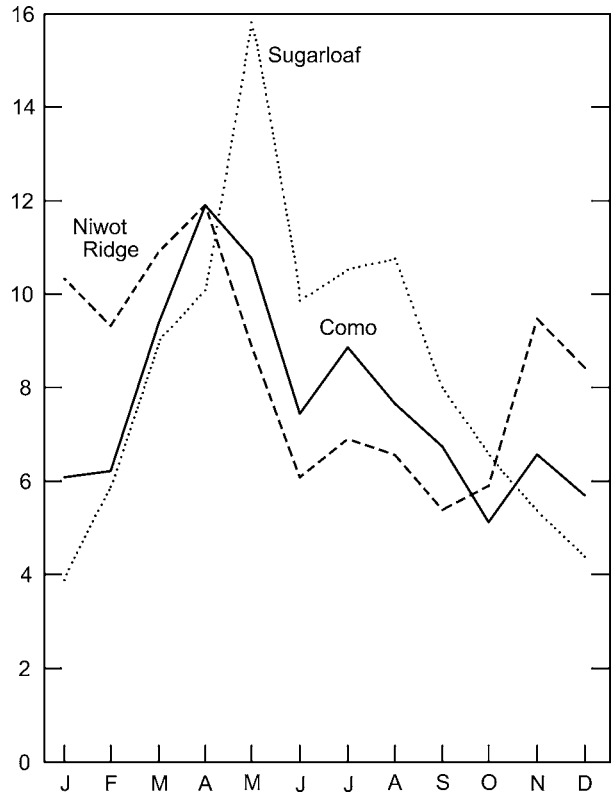
orography (Table 5.8). Altitudinal increases on the west slope are most pronounced between 2100 m and 3200 m, where there is, on average, a six-fold increase. Analysis by wind direction at 500 mb shows that the orographic effect is largest for north-westerly winds in excess of $25\,\mathrm{m\,s^{-1}}$. Table 5.8 shows that totals are 50 percent larger at the base of the east slope than at the same elevation on the west slope. This is attributable, in part, to cases of flow patterns with an easterly upslope component. Precipitation in these situations may not reach west of the Divide. However, even with westerly upper-level flow, storm systems give almost equal amounts of precipitation, on average, at Grand Junction and Denver. This may partly reflect carry-over effects and partly easterly components in the low-level flow ahead of the traveling storm systems. In this area, simple concepts of sheltering effects due to the mountains must be treated with caution.

The occurrence of extreme precipitation events and flooding is of considerable importance in the Rocky Mountains foothills for flood control planning purposes. In the eastern foothills of the Front Range, Colorado, rapid snowmelt accounts for peak discharges above an elevation of approximately 2300 m, whereas at lower elevations they are caused by extreme rainfall events according to Jarrett (1990b). His analysis of 97 intense rainstorms shows that 6-h totals decrease sharply from

Table 5.8 A profile of winter storm precipitation across the Colorado Rockies for 265 storms during winters 1960/1–1967/8.

	West Slope						East Slope					
	Grand Junction						Vail Pass					Denver
Height (m)	1525	1830	2135	2440	2745	3050	3200	3050	2590	2285	1830	1525
Precipitation (mm)	259	344	224	794	1120	1539	1513	1109	212	309	484	393
Ratio to Grand Junction	1.0	1.33	0.85	3.05	4.30	5.93	5.83	4.28	0.78	1.20	1.85	1.50

Source: from Hjermstad (1970).

Fig. 5.20 The relation between precipitation and elevation for large storms in Colorado (after Jarrett, 1990). Source: *Geomorphology* **3(2), 1990, R. D. Jarrett, p. 184, Figure 5. Elsevier, Amsterdam.**
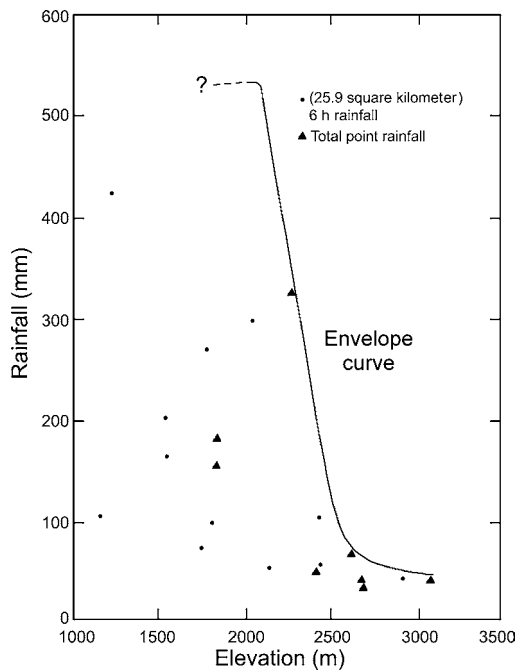
500 mm at elevations below 2100 m to barely 50 mm above 2400 m (Figure 5.20). The elevation limit on large-magnitude floods is confirmed by the contrasting types of erosional and depositional features in the river channels above and below a similar altitudinal threshold. The upper elevation of such rainstorm-producing floods decreases northward. In New Mexico, it is around 2400 m, in Wyoming 2000 m, and Idaho–Montana only 1600 m. This reflects the increasing distance from moisture-bearing air from the Gulf of Mexico. Myers and Norris (1991) confirm that extreme probabilities of maximum daily precipitation are less than

100 mm at elevations above 3000 m in the Rocky Mountains based on SNOTEL site data for June–September.

Maximum daily precipitation in Colorado above 2400 m during June–September has only a 0.01 percent probability of exceeding 100 mm according to Myers and Norris (1991). This contrasts strongly with earlier estimates of potentially large totals at 3000 m based on probable maximum precipitation (PMP) assessments that transposed such amounts over high terrain without taking orographic processes into account (see Chapter 4). Flooding in basins below 2300 m is caused by slow-moving summer thunderstorms, like that responsible for the Big Thompson flood in July 1976 (Maddox et al., 1978), or cut-off cold lows over Colorado in spring and autumn. A localized thunderstorm system on 31 July 1976 resulted in a major disaster in Big Thompson Canyon, northwest of Denver, Colorado (Maddox et al., 1978). A quasi-stationary thunderstorm complex with very high moisture contents $(14 \, g \, kg^{-1}$ at low levels) located over the mountains west of Loveland, Colorado produced rainfall totals of 250–300 mm between 1830 and 2230 h local time. A massive flood wall caused at least 139 deaths, mainly of tourists and campers along the canyon highway, and property damage of US $ 35 million (Maddox et al., 1978). Jarrett estimates from paleohydrological methods that the Big Thompson event had a recurrence interval of 10 000 years, compared with only 100–300 years estimated by conventional hydrologic analysis based on short stream flow records.

In other years, such as May 1969, more widespread flooding may occur in the Colorado foothills in association with a deep, quasi-stationary cold low. Such pressure systems draw moist air from the south and southeast into an upslope flow. Thunderstorms may also be generated within the low. An example of a strong cut-off low was recorded 24–26 October 1997 when strong, moist easterly upslope flow led to snowfall exceeding 1 m in the foothills west of Boulder, Colorado (Poulos et al., 2002).

Cloud and radiation conditions are also strongly influenced by the mountains, although fewer data are available to illustrate this. In winter, when westerly flow prevails, a crest cloud or föhn wall is commonly observed over the Continental Divide while the east slopes remain generally clear apart from occasional lee wave clouds. Under upslope conditions with an inversion, however, the lower slopes may be below stratiform cloud not reaching above 2800–3000 m, leaving the higher zones in sunlight. Clark and Peterson (1967) found this situation to be more prevalent than the crest cloud pattern in 1964–5, although their relative frequencies must vary from year to year. These regimes are apparent also from the radiation studies of Greenland (1978) (see p. 252). In summer, in contrast, towering cumulus rapidly develops over the mountains on most mornings, and spreads eastward. Radar studies indicate that convective build-up begins by mid-morning over the east slope of the Front Range, with preferred locations near Estes Park, Idaho Springs, and southwest of Pueblo, Colorado (Karr and Wooten, 1976). A further investigation using half-hourly GOES imagery for summer 1983–5 by Banta and Schaaf (1987) and Schaaf et al. (1988) extends the radar results. Thunderstorm

initiation is related both to isolated mountains such as Pike's Peak, lifting and channeling by the San Juan Mountains, and leeside convergence zones (see p. 222) along the eastern slopes of the Front Range and the Sangre de Cristo Mountains. The latter zone is well developed under northwesterly to southwesterly flows. For southeasterly flow, there is lee convergence west of the southern Sangre de Cristo Mountains. The results of numerical simulations of the effects of the Colorado Rocky Mountains on flow from directions between $180°$ and $315°$ are shown by Tucker and Crook (2005) and bear out their simulations of the effects of heated topography on airflow discussed in Chapter 2 (p. 79). Convective precipitation is more likely to occur downwind of ridges whose axis is parallel to the flow direction. For the Rocky Mountains of Colorado, the likelihood of precipitation is maximized for southerly and northwesterly airflows, especially in the presence of instability.

Wind conditions in the Colorado Rockies have received much attention, both in terms of intrinsic interest in the phenomena themselves and in view of their significance for sub-alpine vegetation and snow transport. The summits are exposed to high mean wind speeds during the winter half-year with prevailing westerly flow; the summer months are much less windy. Records on an 11.6 m tower on Mines Peak (3808 m) on the Continental Divide indicate a mean speed of $15.4\,\mathrm{m\,s^{-1}}$ in January 1968–75 (Judson, 1977), while just east of the Divide at Niwot Ridge (3750 m), the averages for October–March 1965–70 on a 2 m mast are 12–$14\,\mathrm{m\,s^{-1}}$ (equivalent to 15.6–$18.2\,\mathrm{m\,s^{-1}}$ at 11.6 m) (Barry, 1973). On a knoll (3608 m) 1 km further east on Niwot Ridge, short-term measurements on 117 days in winter 1975–6 showed that, at 6 m above the surface, winds exceeded $18\,\mathrm{m\,s^{-1}}$ during 50 percent of the time and exceeded $27\,\mathrm{m\,s^{-1}}$ for 16 percent of the time. The average daily maximum recorded at the knoll site was $39\,\mathrm{m\,s^{-1}}$ compared with $24\,\mathrm{m\,s^{-1}}$ (at the same height) at the Niwot Ridge station, and the extreme gust recorded on the knoll was $62\,\mathrm{m\,s^{-1}}$.

These high mean velocities and gust speeds are a basic result of the height and position of the Continental Divide in relation to the westerly wind belt. Wind speeds in the valleys are only about one-quarter of those at summit sites. However, in a narrow zone along the east slope and its foothills gust/mean speed ratios are well above average during downslope windstorm conditions. Figure 5.21 illustrates the results of Brinkman (1973) during 20 windstorms in the Boulder area. The occurrence and mechanisms of these winds are described in Chapter 3 (p. 179). The air stream parameters are occasionally such that downslope windstorm conditions occur at east slope locations up to at least 3050 m elevation.

One major consequence of the strong winter winds is the transport, redistribution and sublimation of snow. These aspects have been treated in Chapter 4 (pp. 325 and 337), but information on the frequency of blowing snow in the Colorado Rockies and its large-scale consequences for alpine snow hydrology seems to be lacking. Within the montane forest belt, winds serve mainly to redistribute snow and deposit it in clearings where it is subject to more rapid melt than in the forest (Hoover and Leaf, 1967). This has the potential for lessening the losses by sublimation and evaporation.
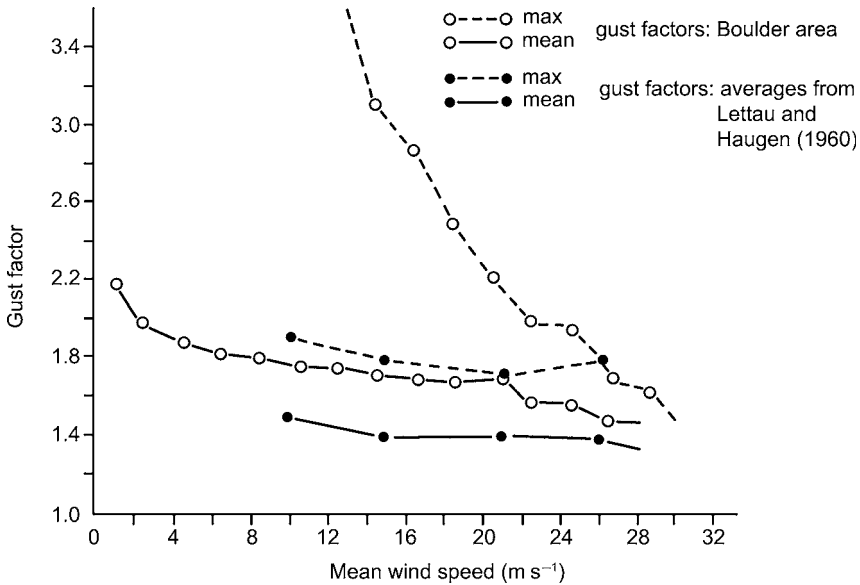
Fig. 5.21 Ratios of mean and maximum gust speeds to 5-min mean wind speeds in Boulder, Colorado, compared with averages cited by H. H. Lettau and D. A. Haugen (from Brinkmann, 1973).

5.8   THE SUB-POLAR ST. ELIAS MOUNTAINS – ALASKA/YUKON

Few mountain areas in high latitudes have received any study of their climatic characteristics. Consequently, the intensive investigations organized jointly by the American Geographical Society and the Arctic Institute of North America in the St. Elias Mountains are of special significance. These mountains border the Pacific Ocean, rising sharply to 2600 m some 60–180 km from the coastline, with the mass of Mt. Logan exceeding 6000 m. The results of the many diverse studies carried out under the Icefield Ranges Research Project and the related High Mountain Environment Project (Marcus, 1974a) are detailed in scientific reports (Bushnell and Ragle, 1969–72; Bushnell and Marcus, 1974) and other papers. A brief synopsis based on these studies is presented here.

The interactions of the large-scale circulation with the mountain range have been examined by Taylor-Barge (1969). She gives special attention to the role of the St. Elias Mountains in accentuating the normal climatic gradient between coastal maritime conditions and the interior continental regime in summer. At this season the mean circulation is weak westerly at the surface, to southwesterly at 700 mb, alternating between ridge situations and cyclones in the Gulf of Alaska.

Temperature soundings at Yakutat on the coast and Whitehorse, 275 km inland (see Figure 5.22) reveal that lapse rate profiles become closely similar at the 3 km level. The temperature regime at Seward Glacier southwest of the main divide, is similar to that at Yakutat, whereas stations on the Kaskawulsh Glacier
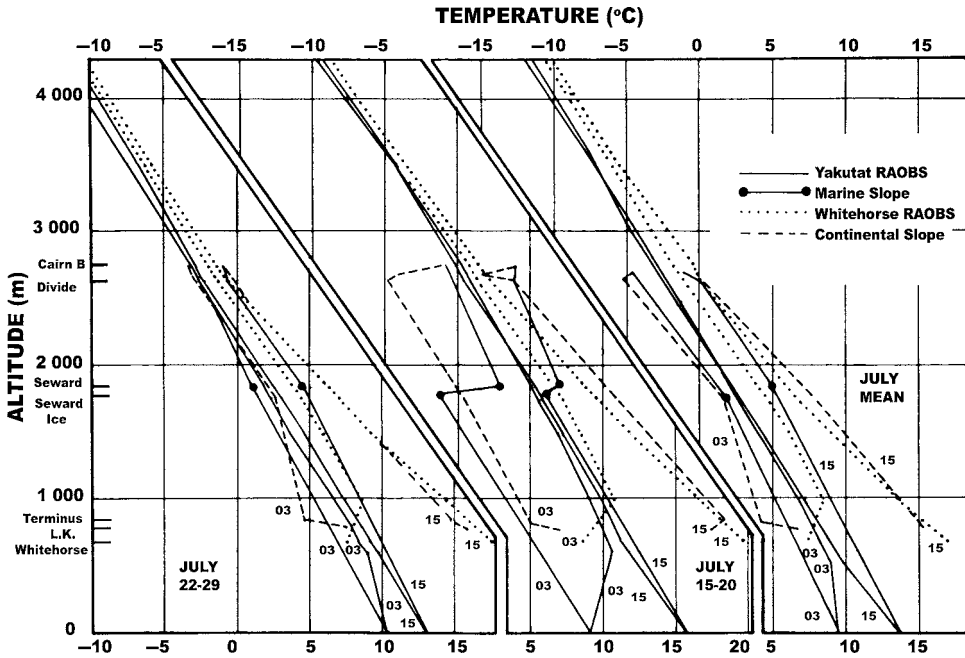
Fig. 5.22   Temperature soundings at Yakutat and Whitehorse and lapse rates in the St. Elias region, July 1964 (from Marcus, 1965).

(approximately 1768 m) and at Kluane Lake on the eastern side have a 10–11 °C diurnal range in the summer months, resembling Whitehorse (Table 5.9). Stations on the Divide at approximately 2560 m have intermediate temperature characteristics. However, since daily temperature trends are similar at all stations, Marcus (1965) suggests that the range is not a total barrier to the transference of air mass characteristics.

The degree of climatic similarity between the stations varies according to the parameter. Summer cloud conditions at the Divide resemble those at Seward Glacier, with a predominance of fog and stratus, and similar overall cloud amounts. The Kaskawulsh Glacier stations are more like Kluane Lake, on the east side, in having a summer predominance of cumuliform clouds. In view of this, it is not unexpected that afternoon convective showers occur on the eastern side of the range. These are not experienced at Divide, or stations further west, where most precipitation is of cyclonic origin. Precipitation probabilities and daily amounts decrease eastward in summer (Table 5.9), but observing problems and local variability prevent general inferences from being drawn.

From the available data, Taylor-Barge (1969) concludes that in summer the range acts as a transition zone rather than a sharp climatic divide. An average dividing line between coastal maritime and continental interior regimes can be located on the eastern side of the mountains between Divide station and the Kaskawulsh Glacier, but it shifts location according to synoptic conditions. Thus, an unusual

Table 5.9 Summer climatic data for the St. Elias Mountains.

Station	Elevation (m)	July 1963–5				June–August 1963–5	
		Mean daily temperature (°C)	Mean daily range (°C)	Vapor pressure (mb)	Solar radiation (W m^{-2})	Daily precipitation probability	Mean daily precipitation (mm day^{-1})
Yakutat	14	11.4	7.1	12.0	–	0.73	8.28
Seward Glacier[c]	c. 1860	2.6	8.2	6.6	(252)[f]	0.66	(1.36)
Mt. Logan[a]	5360	–18.2	11.3	1.1	360	–	–
Divide	c. 2650	–1.8	8.8	4.7	272[d]	0.66	1.21
Chittistone[b]	1779	5.2	6.6	7.6	198	–	–
Kaskawulsh[e]	c. 1768	4.7	7.2	6.4	249[f]	0.48	(0.15)[f]
Kluane Lake	786	11.9	10.8	10.1	212[b]	0.35	0.90
Whitehorse	698	13.8	12.3	8.9	–	0.43	0.92

Notes:
[a] 1968–70;
[b] 1967–9;
[c] 1964 and July 1965 only;
[d] 1969 only;
[e] 1964–6;
[f] 1965 only.

Source: after Taylor-Barge (1969); Marcus (1974a, b).

northeasterly flow pattern during 17–19 July 1965 produced cool rainy weather on the east side of the range with precipitation occurring up to the Divide stations, while föhn conditions associated with subsidence in the airflow affected the Pacific slope. This is more or less a mirror image of the normal summer pattern of weather across the range. The barrier seems effective up to about the 3 km level in the free atmosphere, but this level is only a few hundred meters above the Divide stations. On the other hand, upper fronts affect the higher parts of the range. As described in Chapter 3, p. 138, frontal systems may be deflected north or southward by the barrier, or become aligned parallel to it, with blocking of the air at lower levels. Thus, for example, the weather on the windward Pacific slope frequently fails to clear up after a cold front passage.

In winter, the climate of the Pacific slope is dominated by Aleutian–Gulf of Alaska low-pressure systems bringing onshore flow, cloudiness and large amounts of precipitation. The circulation of the interior, in contrast, is determined by the Yukon–Mackenzie high-pressure system. Few low-pressure systems cross the Divide, so that the range may act as a climatic divide to a greater degree than in summer (Taylor-Barge, 1969). Whereas the mean low-level flow is southerly, that at 500 mb is northwesterly, paralleling the valleys in the ranges.

There is no clear relationship between accumulation on Mt. Logan and regional precipitation, nor with large-scale circulation indices for the North Pacific. Correlations between accumulation at Mt. Logan (from ice core data) and precipitation records at nearby stations for 1949–97 are mostly weak and some are negative (Rupper *et al.*, 2005). The largest is −0.46 with coastal Seward. Accumulation amounts at Mt. Logan are greatest in September–November. High winter accumulation is experienced during positive Pacific North America pattern of circulation but the correlation is weak and there is no relationship for low-normal accumulation years.

Local effects will also be much less pronounced in winter due to the continuous snow cover. In summer, down-glacier winds occur 70 percent of the time over the Kaskawulsh Glacier, with a depth of 50–500 m or more above the surface (Marcus, 1974a). Indeed, the lower limit of geostrophic flow may lie above the local summits (Benjey, 1969), suggesting large-scale cold air drainage from the extensive high surfaces in the vicinity. On Mt. Logan (5360 m) itself, wind directions are similar to those over Yakutat at 500 mb, but speeds averaged only 3 m s^{-1} during July 1968. In other years, however, prolonged high winds have been observed in association with Pacific storms (Marcus and LaBelle, 1970).

Only a "tentative" profile of annual precipitation based on snow-pit data can be given (Figure 5.23). This shows an altitudinal maximum around 1800 m, in line with estimates for the Cordillera in British Columbia (Walker, 1961). The graph indicates a pronounced shadow effect in the lee of Mt. Logan and a subsidiary maximum at the Divide where, even at the relatively low elevation of 2650 m, only snowfall has been observed. During the 1960s, accumulation of the higher elevations was often unrelated to precipitation anomalies on the coast of Yakutat (Marcus and Ragle, 1970), suggesting the importance of upper-level disturbances
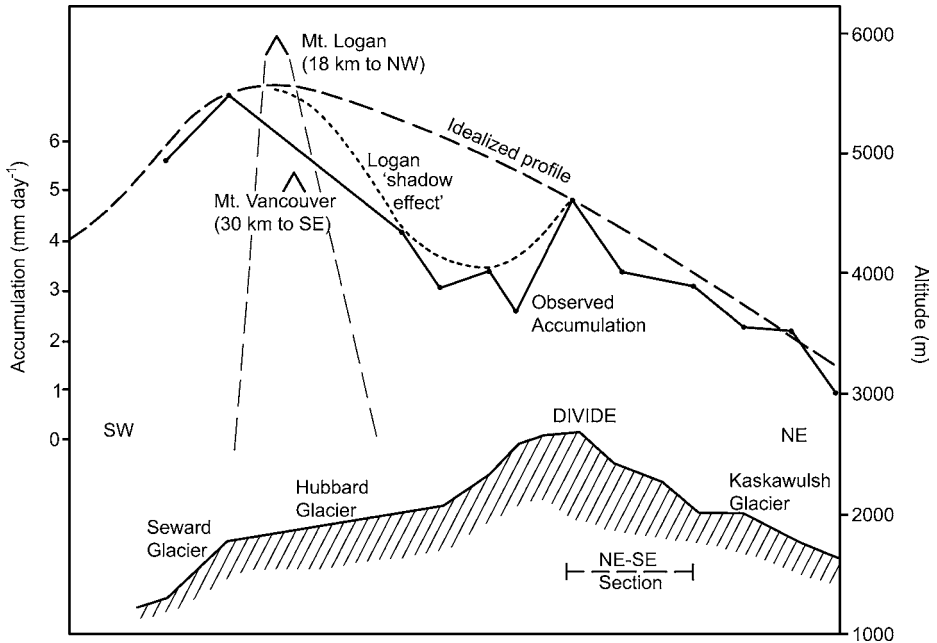
Fig. 5.23 Observed and idealized profiles of accumulation rate (mm day^{-1}) across the St. Elias Range based on snow-pit data (after Taylor-Barge, 1969).

and upper fronts for precipitation on the mountains. Such altitudinal differences are supported by observations of 2 m snow pack temperatures on Mt. Logan in 1965 (Alford and Keeler, 1969). These temperatures approximated the dry adiabatic lapse rate, apparently in response to prevailing katabatic drainage, except between 3000 and 3500 m where an *inverted* temperature lapse of 1.3 °C 100 m^{-1} occurred. In contrast, in 1969–70, an average lapse rate of 0.61–0.66 °C 100 m^{-1} was measured at 2 m in the snow and there was no local inversion zone (Marcus, 1974b). The weather regime of 1964–5 was dominated by southwesterly flow across the range from 850–500 mb, which would cause katabatic winds on the lee of Mt. Logan. The pressure pattern in 1969–70 was unusual in the presence of a ridge over the area giving northwesterly flow over the eastern slopes. Orographic lifting would account for the observed lapse rate and high accumulation about 4200 m.

5.9 HIGH PLATEAUS

On a global scale, the high plateaus have significant effects on the planetary circulation and wave structure, while locally they have their own unique climatic environments. The Tibetan (Qinghai–Xizang) Plateau is unique in its size (some 2.5 million km^2) and altitude – around 4–4.5 km. By contrast, the Altiplano of Bolivia–Peru covers only 100 000 km^2 with the Andean cordillera to the west and dissected mountains to the north and east (Ceverny, 1998). Some aspects of their

heating regimes have been treated earlier (Chapter 2, p. 67). Other smaller plateaus include those of Anatolia, Aldan, Anadyr, and Mexico. It is worth noting that several of them actually form a basin with high mountains around at least part of their perimeter. The ice plateaus of Greenland and Antarctica represent another category of elevated terrain although their basic topographical characteristics resemble those of Tibet. Tibet and the Altiplano have seasonal snow cover and Tibet also has extensive permafrost, while the ice surface of Greenland undergoes rare melting in the higher parts and Antarctica only at the margins.

5.9.1   *The Tibetan Plateau*

The Himalaya borders the Tibetan Plateau to the south and the Kunlun Mountains to the north. Other mountain ranges with peaks exceeding 6500 m are located within this vast region of complex terrain – the east–west Tanggula Mountains, and other ranges in southeastern Tibet. The plateau exceeds 5000 m in the western part (west of $\sim 90°$ E) and averages 3000–4000 m elevation to the east. On a global scale, it has significant effects on the planetary circulation and wave structure. The Tibetan Plateau sets up a downstream trough in the circumpolar westerlies over eastern Asia that plays a major role in the cold season climate of East Asia and the North Pacific sector. The westerlies are split by the plateau and the subtropical westerly jet stream is anchored south of the Himalayas over northern India from November through May, while to the north of the Plateau the polar front jet may vary widely in its latitudinal occurrence. In summer, the plateau heat source supports a shallow thermal low in the afternoon–early evening (Yanai and Li, 1994). At upper levels there is an anticyclonic circulation in summer and the equatorward thermal gradient supports the 150 mb easterly tropical jet stream at 15° N over India.

Energy budgets were measured at 14 stations on the plateau in 1997 (Xu and Haginoy, 2001). Net radiation exceeds $100 \, W \, m^{-2}$ at 4500–4700 m elevation in summer, due to low levels of water vapor content and high levels of solar radiation. Sensible heat is a maximum in May–June with values of $54–76 \, W \, m^{-2}$ while latent heat peaks in July–August with $41–83 \, W \, m^{-2}$. In winter, net radiation is about $25 \, W \, m^{-2}$ (Xu *et al.*, 2005).

The higher western parts of the plateau are some 10 °C colder than the eastern sector with summer (winter) temperatures around 0 °C (−25 °C) in the west and 10 °C (−15 °C) in the east according to Frauenfeld *et al.* (2005). Consequently there are large contrasts in summer between the plateau and the Taklimakan desert to the north, on the one hand, and the lowlands of the Indian subcontinent to the south, on the other. Much of the high plateau is underlain by permafrost. Zhang (2005) illustrates the distribution of permafrost and seasonally frozen ground in China. Mountain permafrost occurs in the Altai and Tian Shan, the Qilian Shan, the northern and eastern parts of the Tibetan Plateau and in the Himalaya. There is extensive continuous permafrost in the high, cold zone of the northern part of the

southern Qinghai and northern Tibetan Plateau with discontinuous and island permafrost in the southern part of the latter. The 1100-km-long Goldmud–Lhasa railroad, opened in 2006, has specially engineered embankments to avoid permafrost degradation, since it crosses 550 km underlain by permafrost, half of it "high-temperature" and over a third of it ice-rich permafrost, susceptible to thaw.

The South Asian summer monsoon affects the southern part of the Tibetan plateau during late June–August. At Tingri meteorological station (28.6° N, 87.1° E, $\sim$4300 m) on the northern slope of the Himalaya, there is a July maximum with an annual total of only 254 mm, whereas Nyalam, Tibet (28.2° N, 86.0° E, 3810 m) recorded an annual total of 620 mm (1967–83), 60 percent of which fell during June–September with a secondary maximum in February (Kang et al., 1999). Here July–August mean monthly temperatures are 10 °C. Some 20 km northwest of Nyalam, Aizen et al. (2002; Aizen and Aizen, 1985) reported a precipitation minimum of 300 mm on the northern slope of the Himalaya around 4500 m, increasing to over 600 mm at 6700 m and above. Their study area was a flat-topped glacier at 5600–6100 m, part of the 8000 m Xixibangma peak (28.4° N, 85.7° E). In the same massif, on the level surface of the Dasuopo Glacier, accumulation at 7200 m averages 1000 mm w.e., most of which falls during the southwest monsoon according to Davis et al. (2005). The ice-covered slopes generate katabatic flows that lead to strong evapo-sublimation on the glaciers although solar radiation is the main energy source for ablation, despite high cloudiness (Aizen et al., 2002).

The spatial distribution of δO^{18} and δD stable isotopes along a southwest–northeast transect across the plateau in July 1986 shows that whereas south of the Himalaya, moisture comes from the Indian monsoon circulation, between the Himalaya and Tanggula Mountains its source is the Bay of Bengal and northern India. This moisture is transported by southerly flow reaching the plateau through valleys like the Brahmaputra in the Himalaya (Tian et al., 2001). This confirms the findings of Huang and Shen (1986), based on an analysis of atmospheric water vapor flux and flux divergence. North of the Tanggula Mountains, over half of the moisture is from recycling over inland Asia. For example, on the Dunde ice cap in northeast Tibet (38° N, 86° E, 5325 m altitude) annual accumulation is about 440 mm w.e., and is derived from Eurasian sources (Davis et al., 2005).

Precipitation amounts decrease sharply north of the Himalaya (see Gyangtse in Table 5.1) and over the Tibetan Plateau they decrease steadily from southeast (500–600 mm) to northwest (50–100 mm) (Xu and Haginoya, 2001), as shown in Figure 5.24. However, in 1998 in the southeast, totals were 700–1000 mm at stations located between 28.5° and 31.4° N, 94.3° and 100° E, at around 2600–3300 m elevation (Xu et al., 2005). At the Gongga massif (29.6° N, 101.9° E), total precipitation is 2200–2300 mm from 3000 to 5500 m, compared with 1000 mm at 2600 m (Aizen et al., 1997).

Tibet has seasonal snow cover, but amounts are generally small (Figure 5.24). Naqu, for example at 31.4° N, 91.9° E, 4500 m altitude had a maximum SWE of 20 mm during 1994–2000 (Sato, 2001) and seasonal freezing of the ground
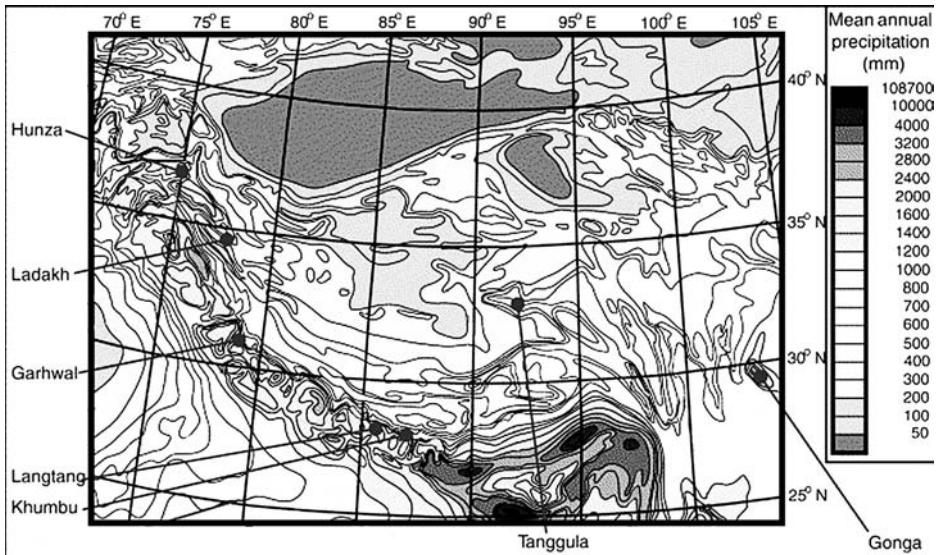
Fig. 5.24   **Annual precipitation (mm) over the Tibetan Plateau and adjoining areas (adapted from Owen *et al.*, 2006).**

penetrated to 1.6 to 2 m. As a consequence of the greater aridity, the snow line is 400–500 m higher on the north side of the Nangpa Pass (28.1° N, 85.6° E, 5500 m) than on the south side. Reiter and Heuberger (1960) contrast this situation with the Alps where the snow line is 200 m higher on the south side since radiation and temperature are the primary controls. Zhang *et al.* (2006) show that the snow line drops 97 m per degree of latitude moving northward in China. It is highest, almost 6000 m, around 32° N on the northern flank of the Himalaya.

Most precipitation falls in summer. Luo and Yanai (1983; 1984) found strong uplift over the plateau in early summer 1979. The 40-day (26 May–4 July) mean vertical velocity at 32.5° N, 93° E was 5 mb h^{-1} at 400 mb. The rainfall total for 31 May–4 July 1979 was 77 mm over the western plateau (including parts of the NW Himalaya) and 96 mm over the eastern plateau. The Qinghai–Xizang Meteorology Experiment (QPMEX) in summer 1979 showed that there is a super-adiabatic surface layer by day (Yanai and Li, 1994). Over the western–central Plateau there is a deep, well-mixed layer by evening, although the moisture is not well mixed. More detailed field experiments in 1998 and 2002 collected radar, sodar and profiler data near Naqu (Yang *et al.*, 2004). Dry shallow convection is common over the plateau in the dry season during the morning, driven by sensible heating, becoming deep moist convection in the afternoon when the boundary layer can extend up to 3 km. Shallow convection is organized by the horizontal scale of the hills, whereas the deep convection is less regular and generated over mountain slopes in late morning and over valleys from early afternoon.

Precipitation over the Tibetan Plateau is mostly convectional from large cumulonimbus cells and hail is not uncommon (Lu, 1939; Flohn, 1968). Three-hourly

geostationary satellite data for 1989–94 show two periods of maximum diurnal cloud activity (Fujinami and Yasunari, 2001). The first in March–April affects most of the plateau, especially the southern part (30° N, 90° E) and a region from 35° N, 80° E to 31° N, 102° E. This activity is related to cold air in upper westerly troughs and daytime heating. In June, warm humid air from the South Asian monsoon initiates diurnal cloud activity in the southeast and gradually this moves towards 30° N, 86° E where activity is concentrated during the monsoon season. In September it retreats southeastward again. In 1998, monsoon precipitation from mid-June to early September averaged over the Naqu basin (4500–5000 m) was 336 mm falling as rain or hail (Ueno *et al.*, 2001). The lowest altitude for snowfall (50 percent probability) was estimated to be 5000 m. Precipitation of > 0.25 mm occurred on 87 percent of monsoon season days with an average intensity of $1.27 \, \mathrm{mm \, h^{-1}}$. Heavier precipitation ($\geq 3 \, \mathrm{mm \, h^{-1}}$) events occurred at night associated with synoptic-scale cloud systems and widespread stratiform cloud. Shimizu *et al.* (2001) examined two cases of nocturnal stratiform precipitation in summer 1998 and showed that they were associated with meso-scale convergence. In the 7–8 July case there was a synoptic disturbance over the southern plateau while on 1–2 August this was not present.

Disturbances in summer over the plateau have received limited attention. Wang (1987) examined two cases of low-level warm cyclonic vortices of meso $- \alpha$ (few 100 km) scale. These developed in July 1979 over about 32–33° N, 92–93° E. Three mechanisms are involved: strong heating in a shallow layer, reduced static stability due to sensible heating, and sufficient moisture in the boundary layer from southerly inflow of monsoon air and local surface evaporation. Wang (1987) reports monthly mean specific humidity values for July 1981, averaged for Lhasa and Naqu at 1800 LST, of $8.4 \, \mathrm{g \, kg^{-1}}$ at 600 mb and $5.2 \, \mathrm{g \, kg^{-1}}$ at 500 mb. The lows generally move eastward and decay in the lee of the plateau, although some cause cyclogenesis and trigger severe weather downstream.

A study of precipitation over the eastern plateau during 1961–90, based on 66 stations above 2000 m (Liu and Yin, 2001), shows that during summers with a low index of the North Atlantic Oscillation (NAO), implying weak westerlies in the North Atlantic, summer cyclonic flows develop east of the Tibetan Plateau (TP). As a result, the southerly winds in the southeastern TP and the northerly winds in the northeastern TP are strengthened simultaneously. In this case, summer precipitation is usually above normal in the southeast but below normal in the northeast of the plateau. During summers of high NAO index values, the patterns are reversed.

5.9.2 *The ice plateaus*

The ice sheets in Antarctica and Greenland represent a special environment where the snow and ice cover create their own climates. They undergo melting only at the margins in the case of Antarctica, but more extensively in Greenland. The

topography of these ice sheets also affects the atmospheric circulation and weather systems – regionally in the case of Greenland, and for the southern hemisphere in the case of Antarctica. Despite expeditions in the early twentieth century, little was known in detail about the climate of their interiors until the 1930s in Greenland (Loewe, 1936) and the 1950s in the Antarctic. Inland stations were set up in Antarctica during the 1957–8 International Geophysical Year (IGY) with automatic weather station (AWS) networks being installed in the Antarctic (Bromwich and Stearns, 1993) and Greenland (Steffen and Box, 2001) in the 1980s–90s.

5.9.2.1 *Antarctica*

The Antarctic continent (including its floating ice shelves) has an area of 14 million km^2, of which 97.6 percent is ice covered with a mean elevation of 2400 m. In East Antarctica the ice dome rises to 4070 m elevation. The continent is also surrounded by pack ice that varies in extent from almost 4 million km^2 in late February to 19 million km^2 in late September.

The presence of permanent snow and ice cover leads to albedos exceeding 0.8 and emissivity values of 0.9 or more producing strong radiative cooling over these surfaces (Carroll, 1982), modifying the temperature structure of the lower troposphere and setting up intense ground-based inversions. Figure 5.25 illustrates the surface inversion observed during austral summer 1965–6 at Plateau station located at 79.25° S, 40.5° E at 3625 m (Kuhn, 2004). In winter the inversion strength over the eastern Antarctic Plateau averages 25 °C.

The climate is extreme in its degree of cold, and aridity. South Pole station, at 2800 m elevation, experiences mean temperatures of −29 °C in January and −59 °C
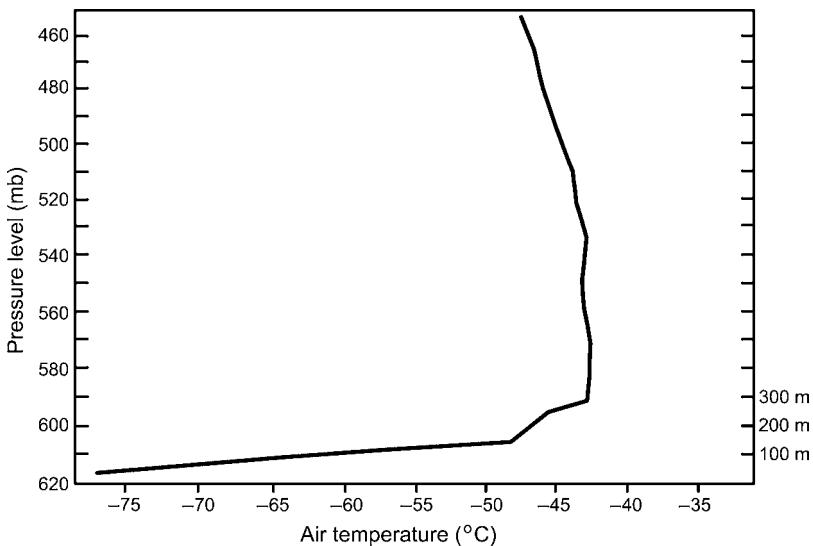
Fig. 5.25   The temperature in the lower troposphere in the austral summer, 2 July 1966, at Plateau Station (79° 15′ S, 40° 30′ E, 3625 m), East Antarctica (after Kuhn, 2004).

in July. Corresponding values at Vostok station (78.46° S, 106.86° E, 3488 m), on the higher, more extensive East Antarctic plateau, are −33 °C and −67 °C, respectively (Simmonds, 1998). Vostok station recorded a world record minimum at the surface of −89.2 °C in July 1983. The annual temperature regime at interior stations shows a well-known 6-month (March–August) period with near constant mean temperatures – the "coreless" (*kernlose* in German) winter (Bromwich and Parish, 1998). This is attributed to radiative cooling eventually diminishing as the temperature falls and the longwave radiation emitted by the surface decreases and is balanced by downward longwave radiation and the downward sensible heat transfer from the warmer air above the surface.

At South Pole station (2900 m elevation) during 1994–2003, temperatures ranged from −20° to −38 °C in "summer" and from −38° to −73 °C in winter (Hudson and Brandt, 2005). However, the annual cycle shows a clear "coreless" winter – with a flat pattern of minimum values around −60 °C – between April and September. Maximum values in summer are confined to December–January.

Where there is a snow or ice cover, radiative cooling over extensive high plateaus modifies the temperature structure of the lower troposphere setting up strong ground based inversions. Hudson and Brandt (2005) re-examined the surface-based inversion at South Pole and Dome C (3233 m). Lowest temperatures and the maximum inversion occur with a wind of 3–5 m s^{-1} rather than calms, probably due to an inversion wind. Cloud cover, leading to enhanced downward longwave radiation, can cause inversions to be broken up. In the mean, the surface cooling also leads hydrostatically to low tropospheric thickness with surface high pressure and an upper-level trough of low pressure.

In summer at Dome C (75.1° S, 123.4° E, 3233 m) there is a diurnal regime in temperature and wind speed. King *et al.* (2006) found a 10 °C diurnal temperature range and the growth of a convective boundary layer to 350 m due to daytime heating, based on data for 7 December 1999–2 February 2000. The energy budget terms (W m^{-2}) for 1200 and 0000 h are as follows:

Dome C	R_n	G	H	$R_n + H + G$
1200 h	49	−19	−16	14 ± 8
0000 h	−44	18	7	-19 ± 7

Positive values are directed towards the snow surface.

The sign of each term changes during the day. Latent heat was not measured at Dome C but its magnitude is indicated by the sum of the other three terms.

From studies of sublimation near Svea station (74.2° S, 10.2° W, 1250 m) during austral summer, Bintanja (2001) finds that surface sublimation and drifting snow sublimation each remove about 20 percent of annual precipitation representing a total latent heat transfer of 10–17 W m^{-2}.

Surface winds over
Antarctica (from Parish
and Bromwich, 1991).
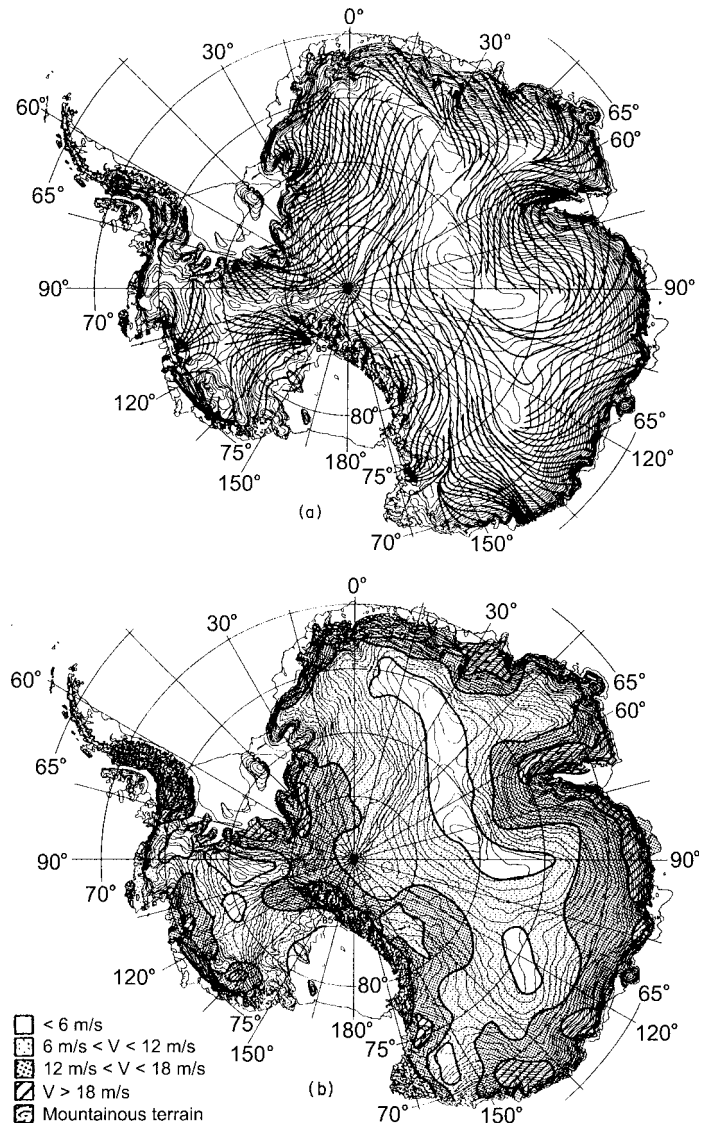
The katabatic wind regime of Antarctica has been discussed in Chapter 3 (p. 183) in terms of observations near the coast. Over the interior slopes, a combination of large-scale synoptic pressure gradients, Coriolis force, katabatic flow, the surface inversion, and friction influence surface winds.

There is high directional constancy throughout the year with, in most cases, the resultant wind orientated 20–50° to the left of the terrain fall line (Figure 5.26) (Bromwich and Parish, 1998). This implies that there is only Coriolis deflection acting on a pure gravity-driven flow. Current thinking suggests that the near-steady winds of the interior represent a balance between horizontal pressure gradient force
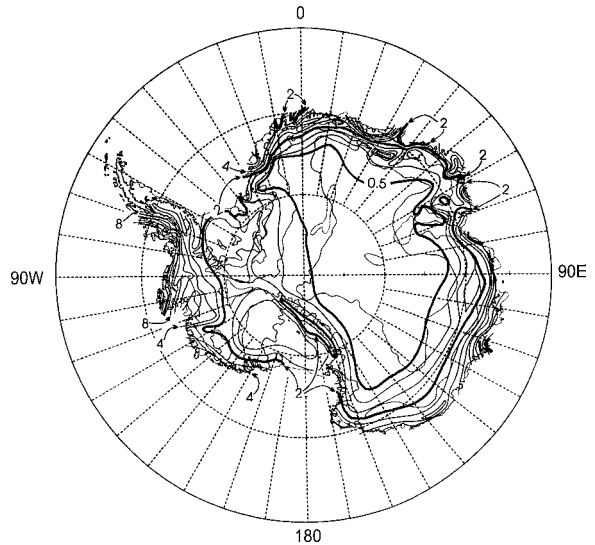
(PGF), Coriolis deflection, and friction. The PGF is itself determined by the terrain slope and the surface temperature inversion, which bring cold, dense air down slope (Parish, 1988). The air may also be cooled through sublimation of blowing snow (Gosink, 1989).

From modeling analyses, Parish and Casano (2003) conclude that the role of katabatic forcing in the boundary layer may be over-emphasized and that the adjustment process between the ice surface topography and the ambient pressure field may be the primary cause of Antarctic wind patterns.

Renfrew and Anderson (2006) provide katabatic flow profiles on moderate slopes over Coats Land (76–77° S, 25° W) from Doppler radar wind profilers. The shape and depth of the flow is related to wind speed. For relatively strong katabatic flow (maxima 8–10 m s^{-1}), there is a low-level jet 20–60 m above the surface extending to 200 m; with moderate flows, the jet is lower and shallower.

Precipitation is almost impossible to measure directly due to the winds and blowing snow. However, annual snow accumulation provides a good indication of the spatial pattern and amounts, because the net effects of sublimation and wind drifting are small on a continent-wide scale (Figure 5.27). Giovinetto and Bentley (1985) show annual totals below 50 mm over much of East Antarctica, increasing to around 200 mm in many coastal areas and up to 800 mm in narrow coastal zones of the Amundsen–Bellingshausen seas and on the west side of the Antarctic Peninsula. The annual cycle of net P–E derived from ECMWF analyses shows a summer minimum and a broad March–October maximum when monthly values above 2500 m elevation are around 5 mm (Bromwich and Parish, 1998).

5.9.2.2 Greenland

The Greenland ice sheet covers an area of 1.74 million km^2 (Weidick, 1995) and the highest dome reaches an elevation of over 3200 m at Summit (72.6° N, 37.6° W). However, the surface slope is barely 1°, except at the margins. The elevation has a strong control on temperature and precipitation, although distance inland and latitude are also involved (Krinner and Genthon, 1999). Near the coasts, the temperature decreases by 5 K km^{-1} increasing to 8 K km^{-1} on the plateau, based on a sensitivity study with an atmospheric GCM. Data for Greenland are available from several field programs. Since 1995, extensive climatic data have been collected by automatic weather stations on the ice sheet through the Program on Arctic Regional Climate Assessment (PARCA). An annual mean latitudinal temperature gradient of −0.78 °C (−0.82 °C) per 1° of latitude was derived from the AWS data for the western (eastern) slope of the ice sheet (Steffen and Box, 2001). Monthly mean slope lapse rates vary between −0.4 °C per 100 m in June and −1.0 °C per 100 m in November with an annual mean value of −0.71 °C per 100 m. Shuman et al. (2001) summarize 12 years of combined AWS and SSM/I brightness temperature data from sites close to Summit (∼ 3200 m) providing a picture of the annual cycle and its interannual variability. Monthly mean temperatures range between 225 and 263 K (Figure 5.28) and exhibit unexpectedly strong daily variability during October–March related to synoptic disturbances. There is alternation between katabatic downslope conditions and synoptic systems that bring cloud cover and, depending on the system's track and the local orography, may bring upslope winds. The daily data show an absolute range between about 214 and 270 K.

Surface melt is experienced around the margins of the ice sheet and the area affected, around 0.5 million km^2 (on at least one day during April–September), has been mapped using satellite passive microwave measurements since 1979 (Abdalati and Steffen, 2001). The records show an increasing trend punctuated by lesser amounts in summers following major volcanic eruptions. Record values were measured in 2002 (Steffen et al., 2004) and 2005.

Estimates of precipitation on Greenland have been based on annual accumulation measurements combined with coastal measurements and several modeling approaches (see Serreze and Barry, 2005; pp. 152–3; Chen et al., 1997; Ohmura
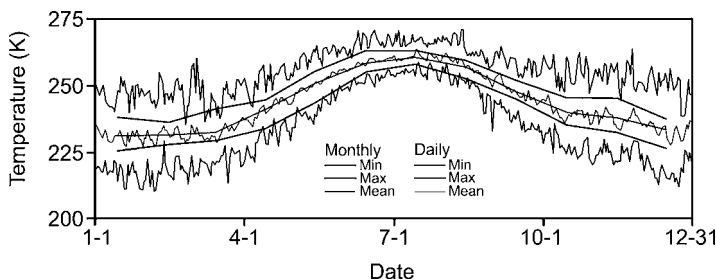
Fig. 5.28 **Temperatures at Summit, Greenland 1987–98 (after Shuman et al., 2001).**

et al., 1999). Maximum annual totals exceed 2000 mm near the coast in southeast Greenland. On the west and northwest slopes of the ice sheet there is a maximum of 600 mm. Lowest totals, below 100 mm. are found in the northern interior around 77–78° N. Losses by sublimation are calculated to be between 12 and 23 percent of annual precipitation using different formulations (Box and Steffen, 2001).

5.10   THE ANDES

The Andes extend more than 8000 km from Venezuela (10° N) to Patagonia and Tierra del Fuego (57° S). For most of their length there are two main ranges. Generally, the mountains are 100–300 km wide, much narrower than the cordilleras of North America. Their mean height is close to 4000 m with many peaks of 5000–6000 m or more, although they are lower in the south. In the northern section, the ranges are oriented northeast–southwest, while in Colombia they become mainly north–south. In Bolivia, there are widely separated ranges bordering the Altiplano, which has a mean altitude of 4000 m.

5.10.1   *Equatorial and tropical Andes*

In the Sierra Nevada de Merida of Venezuela (8–9° N, 70° W), the Venezuelan Air Force collected climatic data at four elevations. Pulwarty *et al.* (1998) examined these and other records of altitudinal gradients of precipitation. Figure 5.29 shows that on southwestern slopes, totals decrease with height (an equatorial pattern) while on the eastern slope in Tachira state, annual totals are a maximum (4000 mm) around 1200 m altitude (a tropical pattern). On the west-facing slopes of the River Chama valley, totals are constant ($\sim$2000 mm) from 1500 to 3500 m altitude and then decrease above to $\sim$1000 mm at Pico Espejo (4765 m).

In Colombia, from 1–10° N, there are three cordilleras orientated north-northwest–south-southeast; from west to east they are: the Cordillera Occidental, Cordillera Central, and Cordillera Oriental (the latter is a southward continuation

Fig. 5.29 **Precipitation versus elevation on different slopes of the Venezuelan Andes (from Pulwarty *et al.*, 1998).**
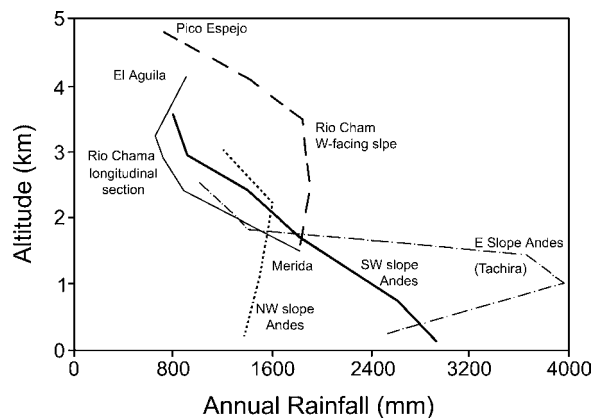
of the Sierra Nevada de Merida, Venezuela). There is also the Sierra Nevada de Santa Marta, a massif detached from the Cordillera Central, near the Caribbean coast. Snowfields and glaciers are restricted to the highest peaks of the Cordillera Central, Cordillera Oriental, and the Sierra Nevada de Santa Marta. Hourly data for 51 gauges, mainly between 1000 and 1700 m, with records over 22–28 years have been used to investigate the diurnal cycle of rainfall (Poveda et al., 2005). For all locations and seasons there are minimum amounts between 0900–1100 h. On the eastern flank of the Central Cordillera there is a peak around midnight, while in northeastern and western Colombia it occurs in the afternoon. On the western flank of the Central Cordillera the peak at individual stations may occur around midnight, in the afternoon, or at both times. Moreover, with only a few local exceptions, there is no evidence that altitude or aspect influences the diurnal cycle.

On the summit of Nevado Sajama, a volcano ($18.1°$ S, $68.9°$ W) in the dry western cordillera of Bolivia, an AWS with satellite telemetry via GOES was operated during 1996–7 (Vuille et al., 1998). While some data were not transmitted due to snowfalls, the overall performance and data recovery was good. Daily solar irradiance varied between about $1200 \, \text{W} \, \text{m}^{-2}$ in the austral summer and $800 \, \text{W} \, \text{m}^{-2}$ at the winter solstice. Maximum clear-sky values reached 85 percent of the extra-terrestrial direct irradiance on a horizontal surface. Generally, mornings are cloud free. Convective cloud builds up in the afternoon and maximum cloud cover occur around 1800 LST. Monthly mean temperature varied from $-7.5 °C$ in January to $-14.1 °C$ in June, whereas the daily range in April–May 1997 was twice as large (12–$13 °C$) as the annual value of $6.6 °C$. The mean specific humidity varied from $\leq 0.9 \, \text{g} \, \text{kg}^{-1}$ in the three winter months to $3.6 \, \text{g} \, \text{kg}^{-1}$ in summer (December–February) when vertical moisture transport and horizontal advection, mainly from the Amazon Basin, provide water vapor for the summit. In summer there are light east-southeast winds averaging $2.6 \, \text{m} \, \text{s}^{-1}$, whereas in winter there are strong north-northwest winds. Mean hourly speeds sometimes exceeded $20 \, \text{m} \, \text{s}^{-1}$.

The circulation over the Altiplano has been discussed earlier (Chapter 3, p. 224). In austral summer there is an anticyclonic circulation around the Bolivian high centered at $15°$ S, $65°$ W (Satyamurty et al., 1998). A convective cloud band occurs over the central Andes–Altiplano and during rainy periods on the Altiplano the Bolivian high shifts southward enhancing easterly flow from the lowlands of Amazonia (Garreaud, 1999; Garreaud et al., 2003). Over 70 percent of the annual precipitation falls in the austral summer and the moisture transport is strongest in the afternoon–evening hours and is a maximum around the 500 mb level. A study by Falvey and Garreaud (2005) for austral summer 2002–3 examines the role of the upper level flow on wet days. They show that, on days when the column precipitable water exceeds 10 mm over all the plateau, westward advection is observed at the same level from Amazonia. Daytime upslope flows from the east play only a minor role. Interestingly, dry conditions are not a result of dry advection from

the east. Rather the boundary layer dries out along the western mountains and over the southern Altiplano, while in the northern Altiplano the precipitable water content remains high. Convection and precipitation are strongly related to moisture along the Western Cordillera. Rainfall along the Zongo valley (16° S) in the Eastern Cordillera of Bolivia falls during October–April with maximum amounts near 2800 mm at 1200 m, diminishing to 800 mm at 4750 m (Ronchail and Gallaire, 2006).

5.10.2 The dry subtropical Andes

Subsiding air in the subtropical high pressure centered at 80–100° W, near 32° S in the austral summer and in the ridge about 28° S in austral winter, over the eastern South Pacific, dominates the year-round climate of this sector (Schwerdtfeger, 1976; Satyamurty *et al.*, 1998). Lliboutry (1998) terms the mountains between 17.5° and 31° S the *Desert Andes* because of the hyper-aridity. Vuille and Amman (1997) state that in northern Chile, from 18° to 28° S, there are no glaciers even above 6700 m due to the extreme aridity. However, Lliboutry (1998) tabulates 67 mountains and volcanoes rising to 5400–6800 m between 17.4° and 28.0° S that have permanent snow patches or glaciers. The snow line from 24° to 30° S is between 5500 and 6200 m according to Schwerdtfeger (1976); Lliboutry (1998) gives the same range for the glaciation level (see Note 5.1) and indicates that it declines to the east at 27° S but to the west at 29° S.

   North of about 22° S, snowfalls are observed only once or twice in winter even at 4500–5000 m, compared with three to five events further south (Vuille, 1996). West of the Altiplano at Rio Lauca (∼ 18.5° S, 69.4° W) below 4500 m, there were 10–15 days with snow cover in 1990–3 compared with 30–50 days below 4500 m on the volcanoes around Laguna Miscanti and Meñiques (∼ 23.7° S, 67.8° W) east of the Atacama Desert.

   Altitudinal and other influences on precipitation in the sector 18.5–24° S have been examined using data from 27 stations for 1977–91 (Houston and Harley, 2003). In the Cordillera and southern Altiplano, rain falls mostly in summer (December–March). There is a zone of maximum (about 1000 mm) on the eastern slopes at around 1000 m; above this altitude and across the Altiplano away from the Amazon moisture source, amounts decrease linearly with elevation. On the western slopes of the Western Cordillera, totals decrease exponentially below at least 5500 m down to 2300 m (Houston and Hartley, 2003). In the lower elevations of the Atacama Desert, stations receive some winter rainfall from trailing cold fronts.

   In the subtropical Cordillera, snow falls mainly in the austral winter. During May to September snowfall is linked to cut-off lows or Pacific cold air: cold fronts bring snowfall to the southernmost area and western (Chilean) side of the Andes, while cut-off cold lows give the most frequent snowfalls at 23–25° S (Vuille, 1996). Convective clouds in summer may give occasional snowfalls above 5000 m. However, at El Laco (23.8° S 67.5° W), for example, the freezing level is around

5200 m in January compared with 4000 m in July. Air temperatures at 5000 m here were below freezing on about four-fifths of days in June and July 1991–3. Nevertheless, even in winter average solar radiation at midday is around $1000 \, W \, m^{-2}$ at this location. Near El Laco, winds at a station at 5000 m were west-northwesterly in winter with speeds of 5–10 m s^{-1} but occasionally exceeding 20 m s^{-1}, with an observed record of 39 m s^{-1} in winter 1993. Typically, summer winds speeds are around 4–5 m s^{-1}(Vuille, 1996).

The highest mountains in the Andes are in this sector: the volcano Aconcagua (6960 m, 32.65° S, 70.2° E) lies in the Argentina, while Ojos del Salado (6880 m, 27.2° S, 68.65° W) is a dormant volcano east of the Atacama Desert.

South of 31° S the snow line drops steadily to only ~ 1200 m at 42° S (Schwerdtfeger, 1976). The central Andes, 31–35° S, have large glaciers at the heads of high valleys that have scarcely been visited due to their remoteness (Lliboutry, 1998). The glaciers are most commonly oriented to the southeast and their elevation increases from west to east. At Cristo Redentor in Argentina (32.8° S, 70.1° W, 3829 m) snow falls on almost one-third of days in the austral winter (Miller, 1976). Prevailing southwesterly winds exceed 12 m s^{-1} on 259 days/year at this station and occur almost daily from December to March. In winter storms, winds frequently exceed 40 m s^{-1} and may exceed 65 m s^{-1} according to Miller.

Air temperatures at high elevations in the central Andes have been published only for Paso de La Cumbre de Uspallata (32.8° S, 3827 m). There are also a few years of incomplete data for the Observatorio del Infiernillo (4320 m). A cold snowy season (May–October) and a cool dry season (November–April) are distinguished. Mean seasonal temperatures at Infiernillo are: snowy season −8.0 °C; dry season −1.1° C and year −4.5 °C. Based on data at Paso de La Cumbre, the environmental lapse rate is 5.6 °C km^{-1} in the snowy season and 8.9 °C km^{-1} in the dry season. Table 5.10 shows the temperatures of the warmest and coldest months of 1962–5 at Infiernillo. Air temperature depends on the weather conditions of a given month. The range of mean daily temperatures within a given month is slightly

Table 5.10 Mean daily maximum and minimum air temperatures (°C) at the Observatorio del Infiernillo for the warmest and coldest months of 1962–5 (33.2° S, 70.3° W, 4320 m) (from Lliboutry, 1998 and pers. comm. 2005).

		May–October	November–April
1962	T_{max}	− 3.7 °C August	5.3 °C December
	T_{min}	− 17.8 °C August	− 8.7 °C December
1963–4	T_{max}	− 6.7 °C June	8.2 °C January
	T_{min}	− 19.6 °C June	− 3.9 °C February, March
1964–5	T_{max}	− 7.2 °C June	6.0 °C March
	T_{min}	− 19.6 °C June	− 4.6 °C March

January–February 1963 and July 1964 missing.

larger than the range of monthly temperatures for the entire year (11 °C). However, both values are generally considerably smaller than the mean daily range in the cold snowy season, which is up to 14–19 °C. Mean air temperature during the dry season is near −2 °C, and for the entire year about −5 °C.

Since 1968, meteorological and mass-balance measurements have been made on Glaciar Echaurren Norte (33.6° S, 70.1° W, 3650 to 3880 m) in the upper Rìo Maipo, Chile. Summer is mainly cloud-free and ice melt is about 24 mm w.e. per day in January and 17 mm in May. However, there is day/night melt/refreeze in summer leading to superimposed ice formation. Thus the transient snow line is generally well above the equilibrium line. At the end of the melt season in normal years, only patches of firn remain on the glaciers, while in wet years the whole glacier may be in the accumulation zone (Lliboutry, 1998).

5.10.3   The wet Andes

South of about 35° S, the Andes are within the prevailing Southern Westerlies belt for much of the year and Lliboutry (1998) designates these as the Wet Andes. There is a Mediterranean regime between 33° and 39° S. Summers are dry north of about 37° S, but southward this dry season is less pronounced due to the westerlies. These occur 75 percent of the time along the coasts south of 39° S. The south coastal range becomes lower and discontinuous, allowing moisture to penetrate readily inland toward the Andes (Miller, 1976). The height of the Andes declines from about 5000 m at 34° S to only 2000 m at the Straits of Magellan (53° S). Only isolated volcanoes have ice bodies from 35–41° S. South of here cirque glaciers are present in the main range. South of about 45.5° S there are many glaciers and three major ice bodies spanning the Argentine–Chile frontier. The Northern Patagonia Icefield (∼ 47° S) covers some 4440 km^2 and is one-third the size of the much larger Southern Patagonia Icefield (13 500 km^2). The highest mountain in Patgonia, Mount San Valentin (3910 m), is located in the northeastern corner of the Northern Icefield. Just east of the Patagonian icefields, there are numerous bare granite rock spires such as Mount Fitz Roy (3375 m, 49.3° S, 73.1° W), Poincenot, Cerro Torre and Cerro del Paine (see Darack, 2002). There is also a smaller icefield, Cordilera Darwin, (2300 km^2) in southwestern Tierra del Fuego.

Annual precipitation on the coastal islands at 45–48° S exceeds 7000 mm according to Prohaska (1976) and Miller reports an annual average of 7300 mm at Guarelo at 50° S. Annual precipitation is 4000–4700 mm on the windward slopes and 6000–7500 mm on the Patagonian icefields according to Lliboutry (1998). The annual distribution is fairly even and in summer rain may fall on the icefields. Glaciological studies by Fujiyoshi et al. (1987) on the San Rafael Glacier (46.6° S, 73.9° W) suggest that annual totals on the Northern Icefield are almost three times those at the glacier terminus (3700 mm during 1983–6) or about 10 000 mm. Annual totals increase southward. At the San Rafael Glacier terminus more precipitation falls in summer than winter, while at western stations in Chile south of 46° S, winters receive more.

South of 48° S, annual rainfall in the western archipelagos is about 8000 mm, with little seasonality due to the persistent, strong westerly airflow, while east of the Andes amounts decrease to 250 mm or less. The west coast region south of 52° S is exceptionally cloudy and foggy with year-round precipitation. From a transect along 53° S, combining regular stations and AWS during October 1999–September 2002, Schneider *et al.*, (2003) show that precipitation at sea level on the Pacific coast is about 60 percent of that near sea level within the mountains. Here annual totals reach 6000–7000 m along the main divide decreasing to 1000 mm on the eastern slopes and 430 mm at Punta Arenas (53.2° S, 70.9° W). During this 2-year study, westerly flows occurred 60 percent of the time and northerly to easterly flows 26 percent.

5.11   NEW ZEALAND ALPS

The Southern Alps extend some 600 km from northeast to southwest in the South Island of New Zealand, rising sharply from the ocean to about 2200 m in the north and to 2700 m, with peaks over 3000 m, in the central section (Sturman and Wanner, 2001). The prevailing Southern Westerlies give rise to airflow that is predominantly from the west to northwest and the climatic regime is generally temperate, humid maritime. The west to northwest winds and the pronounced relief give rise to frequent föhn conditions in the lee of the Southern Alps There are also well-developed mountain–valley circulations (see Chapter 3). There is little seasonality of precipitation. Annual precipitation totals are 2000–3000 mm on the west coast, increasing sharply to over 10 000 mm just west of the Main Divide; Milford Peak registers 13 500 mm. Totals drop off sharply to around 1000 mm in the Canterbury Plains rain-shadow to the east (Wratt *et al.*, 2000; Weingartner and Pearson, 2001) and only 300 mm in central Otago.

Southerly and easterly airflows, during the passage of cyclones, are important sources of snowfall east of the Main Divide. Generally only 10–20 percent of the precipitation falls as snow, in contrast with the 60–80 percent figure in the European Alps. Nevertheless, large snowfall amounts on the high peaks supply snowfields and glaciers around Mt. Cook (3754 m). West of here the Franz-Joseph and Fox glaciers flow down into the West Coast lowlands. There are over 3000 glaciers in the Eastern Alps, Fiordland and Westland, with a total area of 115 000 km^2 (Chinn, 2001). In 1978, the snow line (on glaciers) averaged about 1600 m on the west side and 2200 m on the eastern side of the Alps. Variations in the annual end-of-summer snow line observed on 46 glaciers throughout the Southern Alps over 23 years show similar year-to-year behavior both across and along the mountains, indicating that they form a single climatic unit (Clare *et al.*, 2002). High (low) values of correlation between the snow line on individual glaciers and the Alps as a whole are associated with anomalous northerly (southerly) and weaker (stronger) westerly flows and positive (negative) sea surface temperature anomalies near New Zealand.

5.12 NOTE

(1) The *glaciation level* in a glacierized area is the average of the elevations of the lowest summits with ice and the highest summits without ice.

BIBLIOGRAPHY

Abdalati, W. and Steffen, K. (2001) Greenland ice sheet melt extent: 1979–1999, *J. Geophys. Res.*, **106** (D24), 33 983–9.

Ageta, A. (1976) Characteristics of precipitation during monsoon season in Khumbu Himal. *Seppyo*, **38**, Special Issue, 84–8.

Aizen, V. B. and Aizen, E. M. (1997) Hydrological cycle on north and south peripheries in mountain-glacial basins of Central Asia. *Hydrol. Processes*, **11**, 451–69.

Aizen, V., *et al.* (1997) Glacial regime of the highest Tien Shan mountain, Pobeda-Khan Tengry massif. *J. Glaciol.*, **43**(145), 503–21.

Aizen, V. B., Aizena, E. M. and Nikitin, S. A. (2002) Glacier regime on the northern slope of the Himalaya (Xixibangma glaciers) *Quatern. Int.*, **97–8**, 27–39.

Alford, D. and Keeler, C. (1969) Stratigraphic studies of the winter snow layer, Mt Logan, St. Elias Range. *Arctic*, **21**, 245–54.

Allen, B. (1989) Frost and drought through time and space, Part 1: The climatological record (*Frost and drought in the highlands of Papua New Guinea*, B. Allen and H. Brookfield (eds)), *Mountain Res. Dev.*, **9**, 252–78.

Allison, I. and Bennett, J. (1976) Climate and microclimate. In G. S. Hope, J. A. Peterson, I. Allison, and U. Radok (eds), *The Equatorial Glaciers of New Guinea*, Rotterdam: A. A. Balkema, pp. 61–80.

Atkinson, B. W. and Smithson, P. A. (1976) Precipitation. In T. J. Chandler and S. Gregory (eds), *The Climate of the British Isles*. London: Longman, pp. 129–82.

Banta, R. M. and Schaaf, C. L. B. (1987) Thunderstorm genesis zones in the Colorado Rocky Mountains as determined by traceback of geosynchronous satellite images. *Mon. Wea. Rev.*, **115**, 463–76.

Barros, A. P. and Lang, T. J. (2003) Monitoring the monsoon in the Himalayas: Observations in Central Nepal, June 2001. *Mon. Wea. Rev.*, **131**(7), 1408–27.

Barros, A. P. and Lettenmaier, D. P. 1994. Dynamic modeling of orographically induced precipitation. *Rev. Geophysics*, **32**, 265–94.

Barry, R. G. (1973) A climatological transect on the east slope of the Front Range, Colorado. *Arct. Alp. Res.*, **5**, 89–110.

Barry, R. G. (1978) Aspects of the precipitation characteristics of the New Guinea mountains. *J. Trop. Geog.*, **47**, 13–30.

Barry, R. G. (1980) Mountain climates of New Guinea. In P. Van Royen (ed.), *The Alpine Flora of New Guinea. Vol. 1. General Part*. Vaduz: J. Cramer, pp. 75–110.

Barry, R. G. and Carleton, A. M. (2001) *Synoptic and Dynamic Climatology*. London: Routledge, Ch. 7.

Barry, R. G. and Perry, A. H. (1973) *Synoptic Climatology: Methods and Applications*. London: Methuen.

Barry, R. G. and Seimon, A. S. (2000) Research for mountain area development: climate fluctuations in the mountains of the Americas and their significance. *Ambio*, **29**(7), 364–70. *Corrigendum. Ambio*, **30**(1), 69.

Barton, J. S. (1984) Observing mountain weather using an automatic station. *Weather*, **39**, 140–5.

Barton, J. S. and Borthwick, A. S. (1982) August weather on a mountain summit. *Weather*, **37**, 228–40.

Baudo, R., Tartari, G. and Munawar, M. (eds) (1998) *Top of the World Environmental Research: Mount Everest-Himalayan Ecosystem*. Leiden:Backhuys Publishers, Ecovision World Monograph Series: 290 pp.

Baumgartner, A., Reichel, E. and Weber, G. (1983) *Der Wasserhaushalt der Alpen*. Munich: Oldenbourg.

Bénévent, E. (1926) *Le Climat des Alpes Françaises*. Paris: Mémorial de l'Office Nationale Méteorologique de France, No. 14.

Beniston, M. (2005) Warm winter spells in the Swiss Alps: strong heat waves in a cold season? A study focusing on climate observations at the Saentis high-mountain site. *Geophys.Res. Lett.*, **32**, L01812, 5 pp.

Benjey, W. G. (1969) *Upper Air Wind Patterns in the St. Elias Mountains, Summer 1965*. Montreal: Arctic Institute of N. America, Research Paper No. 54. pp. 1–50.

Bezinge, A. (1974) Images du climat zur les Alpes. *Bull. de la Murithienne*, **91**, 27–48.

Bhatt, B. C. and Nakamura, K. (2005) Characteristics of monsoon rainfall around the Himalayas revealed by TRMM precipitation radar. *Mon. Wea. Rev.*, **133**, 149–65.

Bhatt, B. C. and Nakamura, K. (2006) A climatological-dynamical analysis associated with precipitation around the southern part of the Himalaya. *J. Geophys. Res.*, **111**, D02115, 1–13.

Bintanja, R. (2001) Snowdrift sublimation in a katabatic wind region of the Antarctic Ice Sheet. *J. appl. Met.*, **40**(11), 1952–66.

Bleasdale, A. (1963) The distribution of exceptionally heavy falls of rain in the United Kingdom, 1863 to 1960. *J. Instn. Wat. Engrs.*, **17**, 45–55.

Bleasdale, A. and Chan, Y. K. (1972) Orographic influences on the distribution of precipitation. In *Distribution of Precipitation in Mountainous Areas*, Vol. II. Geneva: World Meteorological Organization No. 326. pp. 161–70.

Bleeker, W. (1936) Meteorologisches zu den 3 holländischen Karakorum-Expeditionen. *Proc. R. Acad. Amsterdam*, **39**, 746–56, 839–45 and 962–70.

Blumer, F. P. (1994) Höhennabhängigkeit des Niederschlages im Alpenraum. Ph.D. Dissertation. Zurich: ETH, 242 pp.

Bollasina, M., Bertolani, L. and Tartari, G. (2002) Meteorological observations at high altitude in the Khumbu Valley, Nepal Himalayas, 1994–1999. *Bull. Glaciol. Res.*, **19**, 1–11.

Bouët, M. (1972) *Climat et Météorologie de la Suisse Romande*. Lausanne: Payot.

Box, J. E. and Steffen, K. (2001) Sublimation on the Greenland ice sheet from automated weather station observations. *J. Geophys. Res.*, **106(D24)**, 33 965–81.

Boy, G. and Allan, I. (1989) *Snowcaps on the Equator. The Fabled Mountains of Kenya, Tanzania, Uganda and Zaire*. London: Bodley Head, 192 pp.

Bradley, R., Yuretich, R. and Weingarten, B. (1991) Studies of modern climate. In R. Yuretich (ed.), *Late Quaternary Climatic Fluctuations of the Venezuelan Andes, Contrib.* No. 65. Amherst, MA: Dept. of Geology and Geography, University of Massachusetts, pp. 45–62.

Brazel, A. J. and Marcus, M. G. (1979) Heat exchange across a snow surface at 5365 metres, Mount Logan, Yukon. *Arct. Alp. Res.*, **11**, 1–16.

Brinkmann, W. A. R. (1973) *A Climatological Study of Strong Downslope Winds in the Boulder Area*, Institute of Arctic and Alpine Research, Occasional Paper No. 7. Boulder, CO: University of Colorado.

Bromwich, D. H. and Parish, T. R. (1998) Meteorology of the Antarctic. In D. J. Karoly and D. G. Vincent (eds), *Meteorology of the Southern Hemisphere*. Meteorological Monograph, **27**(49), pp. 175–200.

Bromwich, D. H. and Stearns, C. R. (eds) (1993) *Antarctic Meteorology and Climatology. Studies based on Automatic Weather Stations*. Antarctic Research Series 61. Washington, DC: Amer. Geophysical Union, 207 pp.

Brookfield, H. and Allen, B. (1989) High-altitude occupation and environment (Frost and drought in the Highlands of Papua New Guinea, B. Allen and H. Brookfield (eds), *Mountain Res. Dev.*, **9**, 201–9.

Buchan, A. (1890) The meteorology of Ben Nevis. *Trans. R. Soc. Edinb.*, **34**.

Buchan, A. and Omond, R. T. (1902) The meteorology of the Ben Nevis observations. Pt. II. Containing the observations for the years 1888, 1889, 1890, 1891 and 1892, with appendices. *Trans. R. Soc. Edinb.*, **42**.

Buchan, A. and Omond, R. T. (1905) ibid. Pt. III. Containing the observations for the years 1893, 1894, 1895, 1896 and 1897, with appendix. *Trans. R. Soc. Edinb.*, **43**.

Buchan, A. and Omond, R. T. (1910) ibid. Pt. IV. Containing the observations for the years 1898, 1899, 1900, 1901 and 1902 and Pt. V. Containing the observations for the years 1903 and 1904, with appendix. *Trans. R. Soc. Edinb.*, **44**.

Buchanan, J. Y. (1902) Abstract of paper on the meteorology of Ben Nevis in clear and in foggy weather. *Trans. R. Soc. Edinb.*, **42**, 465–78.

Bushnell, V. and Marcus, M. G. (eds) (1974) *Icefield Ranges Research Project. Scientific Results*, Vol. 4, New York: American Geographical Society and Montreal: Arctic Institute of North America.

Bushnell, V. C. and Ragle, R. H. (eds) (1969–72) *Icefield Ranges Research Project. Scientific Results*. New York: American Geographical Society and Montreal: Arctic Institute of North America.

Carrasco, J. F., Casassa, G. and Rivera, A. (2002) Meteorological and climatological aspects of the South Patagonian Icefield. In G. Casassa, F. Sepulveda and R. Sinclair, (eds), *The Patagonian Icefields: A Unique Natural Laboratory for Environmental and Climate Change Studies*. Dordrecht: Kluwer, pp. 29–41.

Carroll, J. J. (1982) Long-term means and short-term variability of the surface energy balance components at the South Pole. *J. Geophys. Res.*, **87**, 4277–86.

Cassardo, C., *et al.* (2002) The flood of November 1994 in Piedmont, Italy: A quantitative analysis and simulation. *Hydrol Processes*, **16**(6), 1275–99.

Ceverny, R. (1998) Present climates of South America. In J. E. Hobbs, J. A. Lindesay and H. A. Bridgman (eds), *Climates of the Southern Continents: Past, Present and Future*. Chichester, UK: J. Wiley and Sons., pp. 107–35.

Chaggar, T. S. (1983) Highest mean annual point rainfall in the world. *Weather*, **38**, 220–1.

Chen, Q. S., Bromwich, D. H. and Bai, L. (1997) Precipitation over Greenland retrieved by a dynamic method and its relation to synoptic activity. *J. Climate*, **10**, 839–70.

Chinn, T. J. (2001) Distribution of the glacial water resources of New Zealand. *J. Hydrol., New Zealand*, **40**(2), 139–87.

Clare, G. R., *et al*. (2002) Interannual variations in end-of-summer snowlines of the Southern Alps of New Zealand, and relationships with Southern Hemisphere atmospheric circulation and sea surface temperature patterns. *Int. J. Climatol.*, **22**, 101–2.

Clark, J. M. and Peterson, E. B. (1967) Insolation in relation to cloud characteristics in the Colorado Front Range. In H. E. Wright, Jr. and W. H. Osburn (eds), *Arctic and Alpine Environments*. Bloomington, IN: Indiana University Press, pp. 3–11.

Coutts, H. H. (1969) Rainfall of the Kilimanjaro area. *Weather*, **24**, 66–9.

Curran, J. C., *et al*. (1977) Cairngorm summit automatic weather station. *Weather*, **32**, 61–3.

Darack, E. (2002) Wild winds of the Andes. *Weatherwise*, **55**(4), 28–38.

Davies, T. D., Brimbecombe, P. and Vincent, C. (1977) The daily cycle of weather on Mount Kenya. *Weather*, **32**, 406–17.

Davis, M. E., *et al*. (2005) Forcing of the Asian monsoon on the Tibetan Plateau: Evidence from high-resolution ice core and tropical coral. *J. Geophys. Res.*, **110 (D4)**, D04101, 1–13.

Dhar, O. N. and Nandargi, S. (2000) An appraisal of precipitation distribution around the Everest–Kanchengjunga peaks in the Himalyas. *Weather*, **55**(7), 223–34.

Dhar, O. N. and Nandargi, S. (2004) Rainfall distribution over the Arunachal Pradesh Himalayas. *Weather*, **59**(6), 155–7.

Dhar, O. N. and Narayanan, J. (1965) A study of precipitation distribution in the neighbourhood of Mount Everest. *Ind. J. Met. Geophys.*, **16**, 229–40.

Dhar, O. N. and Rakhecha, P. R. (1980) The effect of elevation on monsoon rainfall distribution in the central Himalayas. In J. Lighthill and R. P. Pearce (eds), *Monsoon Dynamics*. Cambridge: Cambridge University Press, pp. 253–60.

Diaz, H. F., Barry, R. G. and Kiladis, G. (1982) Climatic characteristics of Pike's Peak, Colorado (1874–1888) and comparisons with other Colorado stations. *Mountain Res. Devel.*, **2**, 359–71.

Dirks, R. A. and Martner, B. E. (1982) The climate of Yellowstone and Grand Teton National Parks. National Park Service, Occasional Paper No. 6. Washington, DC: US Dept. of the Interior.

Dittmann, E. (1970) Statistische Untersuchungen zur Struktur der Niederschläge in Nepal. *Khumbu Himal.*, **7** (2), 47–60.

Dobesch, H. (ed.) (1983) *Die klimatologischen Untersuchungen in den Hohen Tauern von 1974–1980*, (Veröff. Òsterreich, MaB-Programs, Band 6). Innsbruck: Universitätsverlag Wagner.

Dobremez, J. F. (1976) Climatologie. In *Le Népal. Écologie et Biogéographie*, Paris: L C.N.R.S., pp. 31–91.

Dubieff, J. (1963) Résultats tirées d'enregistrements automatiques récents dans des stations élevées du Massif Central Saharien. *Geofis. Met.*, **11**, 119–25.

Erickson, T. A., Williams, M. W. and Winstral, A. (2005) Persistence of topographic controls on the spatial distribution of snow in rugged mountainous terrain, Colorado, United States. *Water Resour. Res.*, **41**, W04014, 1–17.

Erikson, W. (1984) Eco-climatological aspects of the Bolivian puna with special reference to frost frequency and moisture conditions. In W. Lauer (ed.) *Natural Environment and Man in Tropical Mountain Ecosystems*. Stuttgart: F. Steiner Verlag, pp. 197–209.

Falvey, M. and Garreaud, R. D. (2005) Moisture variability over the South American Altiplano during the South American Low Level Jet Experiment (SALLJEX) observing season. *J. Geophys. Res.*, **110(D22)**, D22105, 1–12.

Ficker, H. von and de Rudder, B. (1943) *Föhn und Föhnwirkung*. Leipzig: Akad. Verlag, Becker u. Erlerkom. Ges.

Finklin, A. I. (1983) *Weather and Climate of the Selway-Bitterroot Wilderness*. Moscow, ID: University Press of Idaho.

Finklin, A. I. (1986) *A Climatic Handbook for Glacier National Park – with data for Waterton Lakes National Park*. Forest Service, Intermountain Research Station, Technical Report INT-204. Ogden, UT: US Deptartment of Agriculture.

Fliri, F. (1962) *Wetterlagenkunde von Tirol*, Innsbruck: Universitäts-Verlag Wagner.

Fliri, F. (1968) Beiträge zur Hydrologie und Glaziologie der Cordillera Blanca/Peru. *Alpenkundliche Studien, Veröff. Univ. Innsbruck*, Vol. 1. Innsbruck: Universität, pp. 25–52.

Fliri, F. (1971) Neue klimatologische Querprofile der Alpen – ein Energiehaushalt. *Ann. Met.*, N.F. **5**, 93–7.

Fliri, F. (1974) *Niederschlag und Lufttemperatur im Alpenraum*. Innsbruck: Universitäts-Verlag Wagner.

Fliri, F. (1975) *Das Klima der Alpen im Raume von Tirol*. Innsbruck: Universitäts-Verlag Wagner.

Fliri, F. (1977) Das physiogeographische Regionen des Alpenraumes. In F. Wolkinger (ed.), *Natur und Mensch im Alpenraum*. Graz, Austria: Ludwig Boltzmann-Institute, pp. 13–26.

Fliri, F. (1982) *Tirol-Atlas, D. Klima*. Innsbruck: Universitätsverlag Wagner, 23 plates.

Fliri, F. (1984) *Synoptische Klimatographie der Alpen zwischen Mont Blanc und Hohe Tauern*, (with Schüepp, M. *Alpine Witterungslagen und europäische Luftdruck-verteilung*). Innsbruck: Universitätsverlag Wagner.

Flohn, H. (1954) *Witterung und Klima in Mitteleuropa*. Stuttgart: Forsch. dt. Landeskunde, p. 78.

Flohn, H. (1968a) *Contributions to a Meteorology of the Tibetan Highlands*. Atmospheric Science Paper No. 130. Ft. Collins, CO: Colorado State University.

Flohn, H. (1968b) Ein Klimaprofil durch die Sierra Nevada de Mérida (Venezuela), *Wetter u. Leben*, **20**, 181–91.

Flohn, H. (1970) Beiträge zur Meteorologie des Himalaya. *Khumbu Himal.*, **7**(2), 25–45.

Flohn, H. (1974) A comparative meteorology of mountain areas. In J. D. Ives and R. G. Barry (eds), *Arctic and Alpine Environments*. London: Methuen, pp. 55–71.

Frauenfeld, O. W., Zhang, T.-J. and Serreze, M. C. (2005) Climate change and variability using European Centre for Medium-range Weather Forecasting reanalysis (ERA-40) temperatures on the Tibetan Plateau. *J. Geophys. Res.*, **110**, D02101, 9 pp.

Frei C. and Schär, C. (1998) A precipitation climatology of the Alps from high-resolution rain-gauge observations. *Int. J. Climatol.*, **18**, 873–900.

Frey, K. (1953) Die Entwicklung des Sud- und des Nordföhns, *Arch. Met. Geophys. Biokl.*, A **5**, 432–77.

Frey, K. (1984) Der "Jahrhundertföhn" von 8 XI.81, *Met. Rdsch.*, **37**, 209–20.

Fujinami, H. and Yasunari, T. (2001) The seasonal and intraseasonal variability of diurnal cloud activity over the Tibetan Plateau. *J. Met. Soc. Japan*, **79** (6), 1207–27.

Fujita, K., *et al.* (2006) Thirty-year history of melting in the Nepal Himalayas. *J. Geophys. Res.*, **111**, D03109, 6 pp.

Fujiyoshi, T., *et al.* (1987) Characterisitics of precipitation and vertical structure of air temperature in northern Patagonia. *Bull. Glacier Res.* (Tokyo), **4**, 15–23.

Garnett, A. (1937) Insolation and relief. *Trans. Inst. Brit. Geog.*, **5**, 71 pp.

Garreaud, R. (1999) Multi-scale analysis of the summertime precipitation over the central Andes. *Mon. Wea. Rev.*, **127**, 901–21.

Garreaud, R., Vuille, M. and Clement, A. C. (2003) The climate of the Altiplano: observed current conditions and mechanisms of past changes. *Palaeogeog., Palaeoclimatol., Palaeoecol.*, **194**, 5–22.

Getker, M. I. (1985) *Snezhnye resursy gornykh territoii Srednei Azii* (Snow resources of the mountain regions of Middle Asia). Avtoreferat. D.Sc. Dissertation, Institute of Geography, Academy of Sciences, USSR, Moscow, 44 pp. (in Russian).

Getker, M. I. and Shchetinnikov, A. S. (1992) Kharakter raspredeleniya godovykh tverdykh osadkov i summarnyi akkumulatsii v gornykh rainov srednei Azii (Character of the distribution of annual solid precipitation and total accumulation in the mountains of Middle Asia). *Glatsiologiya Gornykh Oblastei TrudySredneaziatskogo Regional.Nauchno-Issled. Gidrometeorol. Inst.*, **146**(227): 23–35 (in Russian).

Glasspoole, J. (1953) Frequency of clouds at mountain summits, *Met. Mag.*, **82**, 156–7.

Glazyrin, G. E., Kamnyanskii, G. M. and Pertziger, F. I. (1993) *Rezhim Lednika Abramova* (The regime of the Abramov Glacier), St. Petersburg: Gidrometeoizdat, 228 pp. (in Russian).

Golubchikov, Yu. N. (1996) *Geografiya Gornykh i Polyarnykh Stran* (The Geography of Mountain and Polar Lands), Moscow: Moscow University Press, 304 pp.

Gosink, J. P. (1989) The extension of a density current model of katabatic winds to include the effects of blowing snow and sublimation. *Boundary-layer Met.*, **49**, 367–94.

Grabs, W. E. and Pokhrel, A. P. (1992) Establishment of a measuring service for snow and glacier hydrology in Nepal – conceptual and operational aspects. In G. Y. Young (ed.), *Snow and Glacier Hydrology*. International Association of Hydrological Science, Publ. No. 218, 3–16.

Green, F. H. W. (1955) Climatological work in the Nature Conservancy, *Weather*, **10**, 233–6.

Green, F. H. W. (1967) Air humidity on Ben Nevis. *Weather*, **22**, 174–84.

Greenland, D. (1978) Spatial distribution of radiation on the Colorado Front Range. *Climat. Bull., Montreal*, **24**, 1–14.

Greenland, D. (1989) The climate of Niwot Ridge, Front Range, Colorado, U.S.A. *Arct. Alp. Res.*, **21**, 380–91.

Hann, J. von (1912) The meteorology of the Ben Nevis Observatories. *Q.J.R. Met. Soc.*, **38**, 51–62.

Harding, R. J. (1978) The variation of the altitudinal gradient of temperature within the British Isles. *Geog. Ann.*, **A 60**, 43–9.

Harding, R. J. (1979a) Altitudinal gradients of temperatures in the northern Pennines. *Weather*, **34**, 190–201.

Harding, R. J. (1979b) Radiation in the British Uplands. *J. Appl. Ecol.*, **16**, 161–70.

Hardy, D. R., *et al.* (1998) Annual and daily meteorological cycles at high altitude on a tropical mountain. *Bull. Amer. Met. Soc.*, **79**(9), 1899–1913.

Hastenrath, S. (1971) Beobachtungen zur klimatologischen Höhenstufung der Cordillera Real (Boliven), *Erdkunde*, **25**, 102–8.

Hastenrath, S. (1981) *The Glaciation of the Ecuadorian Andes*. Rotterdam: A. A. Balkema.

Havlik, D. (1968) Die Höhenstüfe maximaler Niederschlagssummen in den Westalpen. *Freiburger Geogr. Hefte*, **7**, Freiburg.

Heckendorff, W. D. (1972) Zum Klima des Tibestigebirges. *Berlin. Geog. Abh.*, **16**, 165–6.

Heinemann, G. and Klein, T. (2002) Modelling and observations of the katabatic flow dynamics over Greenland. *Tellus*, **54A**(5), 542–54.

Herrmann, R. (1970) Vertically differentiated water balance in tropical high mountains – with special reference to the Sierra Nevada de Santa Marta/Columbia. In *World Water Balance*. Reading, UK: International Association of the Science of Hydrology, pp. 266–73.

Hewitt, K. (2005) The Karakoram anomaly? Glacier expansion and the "elevation" effect, Karakoram Himalaya. *Mountain Res Dev.*, **25**(4), 332–40.

Higuchi, K. (ed.) (1976) Glaciers and climate of the Nepal Himalayas. *Seppyo*, **38**, Special Issue.

Hill, S. A. (1881) The meteorology of the north-west Himalaya. *Ind. Met. Mem.*, **I**(VI), 377–429.

Hjermstad, L. M. (1970) *The Influence of Meteorological Parameters on the Distribution of Precipitation across the Central Colorado Mountains*. Atmospheric Science Paper No. 163. Fort Collins, CO: Colorado State University.

Hnatiuk, R. J., Smith, J. M. B. and McVean, D. N. (1976) *Mt Wilhelm Studies II. The Climate of Mt. Wilhelm*, Research School for Pacific Studies. Canberra: Australian National University, Publ. BG/4.

Hoover, M. and Leaf, C. (1967) Process and significance of interception in Colorado subalpine forest. In W. E. Sopper and H. W. Lull (eds), *Forest Hydrology*. Oxford: Pergamon Press, pp. 213–23.

Hope, G. S., Peterson, J. A., Allison, I. and Radok, U. (eds) (1976) *The Equatorial Glaciers of New Guinea*. Rotterdam: A. A. Balkema, 244 pp.

Houston, J. and Hartley, A. J. (2003) The central Andean west-slope rainshadow and its potential contributions to the origin of the hyper-aridity in the Atacama Desert. *Int. J. Climatol.*, **23**, 1453–64.

Huang, F.-J. and Shen, R.-J. (1986) The source of water vapor and its distribution over the Qinghai-Xizang Plateau during the period of summer monsoon. In *Proceedings of the International Symposium on the Qinghai-Xizang Plateau and Mountain Meteorology*. Beijing: Science Press, and Boston, MA: American Meteorological Society, pp. 5506–603.

Hudson, S. R. and Brandt, R. E. (2005) A look at the surface-based temperature inversion on the Antarctic plateau. *J. Climate*, **18**(11), 1673–96.

Hurni, H. and Stähli, P. (1982) Contributions to the climate. In H. Hurni (ed.), *Klima und Dynamik der Höhenstufung von der letzten Kaltzeit bis zur Gegenwart* (Hochgebirge von Semien-Äthiopien, Vol. II). *Geogr. Bernensia G13*. pp. 37–82.

Indermühle, D. (1972) Mikroklimatiche Untersuchung in Tibesti-Gebirge (Sahara). *Hochgebirgsforschung*, **2**, 121–42.

Inoue, H. (1976) Climate of Khumbu Himal. *Seppyo*, **38**, Special Issue, 66–73.

Inoue, J., *et al.* (1987) Summer climate of the Northern Patagonia Icefield. *Bull. Glacier Res.* (Tokyo), **4**: 7–14.

Ives, J. D. (1973) Permafrost and its relationship to other environmental parameters in a midlatitude, high-altitude setting, Front Range, Colorado Rocky Mountains. In *Permafrost: The North American Contribution to the Second International Conference*. Washington, DC: National Academy of Science, pp. 121–5.

Jäkel, D. (1977). The work of the field station at Bardai in the Tibesti Mountains. *Geog. J.*, **143**, 61–72.

Jarrett, R. D. (1990a) Paleohydrologic techniques used to define the spatial occurrence of floods. *Geomorphology*, **3**, 181–95.

Jarrett, R. D. (1990b) Hydrologic and hydraulic research in mountain rivers. *Water Resour. Bull.*, **26**, 419–29.

Judson, A. (1965) *The Weather and Climate of a High Mountain Pass in the Colorado Rockies*. Forest Service, Research Paper RM-16. Fort Collins, CO: US Department of Agriculture.

Judson, A. (1977) *Climatological Data from the Berthoud Pass Area of Colorado*. Forest Service, General Technical Report RM-42. Fort Collins, CO: US Department of Agriculture.

Kang, E.-S., *et al.* (1999) A model for simulating the responses of runoff from the mountainous watersheds of inland river basins in the arid area of northwest China to climatic changes. *Science in China*, **D42**, suppl., 52–63.

Kang, X.-Ch. and Xie, Y.-Q. (1989) The character of weather and climate in the west Kunlun Mountains area in summer, 1987, *Bull. Glacier Res.* (Tokyo), **7**, 77–81.

Kansaker, S. R., *et al.* (2004) Spatial pattern in the precipitation regime of Nepal. *Int. J. Climatol.*, **24**(13), 1645–59.

Karr, T. W. and Wooten, R. L. (1976) Summer radar echo distribution around Limon, Colorado. *Mon. Wea. Rev.*, **104**, 728–34.

Kaser, G. and Osmaston, H. (eds) (2002) *Tropical Glaciers*. Cambridge: Cambridge University Press, 206 pp.

Kaser, G., *et al.* (2004) Modern glacier retreat on Kilimanjaro as evidence of climate change: observations and fact. *Int. J. Climatol.*, **24**(3), 329–39.

Kenworthy, J. M. (1984) Climatic survey in the Kenya Highlands with particular reference to the needs of farmers. In W. Lauer (ed.), *Natural Environment and Man in Tropical Mountain Ecosystems*. Stuttgart: Steiner Verlag, pp. 23–39.

Kerschner, H. (1989) Beiträge zur synoptischen Klimatologie der Alpen zwischen Innsbruck und dem Alpenostrand. *Innsbrucker Geographische Studien*, **17**, 253 pp.

Khromova, T. E., Dyurgerov, M. B. and Barry, R. G. (2003) Late-twentieth century changes in glacier extent in the Ak-Shirak Range, Central Asia, determined from historical data and ASTER imagery. *Geophys. Res. Lett.* **30**(16), 1863, pp. HLS 2–1 to 2–5.

King, J. C., Argentini, S. A. and Anderson. P. S. (2006) Contrast between summertime surface energy balance and boundary layer structure at Dome C and Halley station, Antarctica. *J. Geophys. Res.*, **111**, D02105, 1–13.

Kirchhofer, W. (1976) Stationsbezogene Wetterlagenklassifikation. *Veröff. Schweiz. Met. Zentralanst.*, **34**.

Kirchhofer, W. (ed. in chief) (1982) *Klimaatlas der Schweiz*, Part 1. Zurich: Schweiz. Met. Anst. (Part 2, 1984; Part 3, 1987).

Kistemann, T. and Lauer, W. (1990) Lokale Windsysteme in der Charazani-Talung (Bolivien). *Erdkunde*, **44**, 46–59.

Konzelmann, T. and Ohmura, A. (1995) Radiative fluxes and their impact on the energy balance of the Greenland ice sheet. *J. Glaciol.*, **41**(139), 490–502.

Kraus, H. (1967) Das Klima von Nepal. *Khumbu Himal.*, **1**(4) 301–21.

Krinner, G. and Genthon, C. (1999) Altitude dependence of the ice sheet surface climate. *Geophys. Res. Lett.*, **26**(15), 2227–30.

Kuhn, M. (2004) Die Plateau Station in der Antarktis. In *100. Jahresbericht des Sonnblick-Vereinenes fuer das Jahr 2002*. Vienna: Sonnblick-Verein, pp. 87–90.

Lang, H. and Rohrer, M. (1987) Temporal and spatial variations of snow cover in the Swiss Alps. In B. E. Goodison, R. G. Barry and J. Dozier (eds), *Large-Scale Effects of Seasonal Snow Cover*, Publication No. 166, International Association for Hydrological Sciences. Wallingford, UK: IAHS Press, pp. 79–92.

Lang, T. J. and Barros, A. P. (2002) An investigation of the onsets of the 1999 and 2000 monsoons in central Nepal. *Mon. Wea. Rev.*, **130**, 1299–316.

Lang, T. J. and Barros, A. P. (2004) Winter storms in the central Himalayas. *J. Met. Soc. Japan*, **82**(3), 829–44.

Lauer, W. and Klaus, D. (1975) Geoecological investigations on the timberline of Pico de Orizaba, Mexico. *Arct. Alp. Res.*, **7**, 315–30.

Lauscher, F. (1958) Studien zue Wetterlagenklimatologie der Ostalpenlander. *Wetter u. Leben*, **10**, 79–83.

Lauscher, F. (1977) Ergebnisse der Beobachtungen an den nordchilenischen Hochgebirgsstationen Collahuasi und Chuquicamata. *74–75 Jahresbericht, Sonnblick-Vereines, Jahre 1976–1977*. Vienna: Sonnblick-Verein, pp. 43–66.

Leroux, M. (1991) La spécificité climatique des montagnes sahariennes. *Rev Geogr. Alp.*, **79**(1), 23–42.

Liang, G. (1982) Net radiation, potential and actual evapotranspiration in Austria. *Arch. Met. Geophys. Biokl.*, **B 31**, 379–90.

Liu, X.-D. and Yin, Z.-Y. (2001) Spatial and temporal variations of summer precipitation over the eastern Tibetan Plateau and the North Atlantic Oscillation. *J. Climate*, **14**(13), 2896–909.

Livingstone, D. A. (1967) Postglacial vegetation of the Ruwenzori Mountains in equatorial Africa. *Ecol. Monogr.*, **37**, 25–52.

Lliboutry, L. (1998) Glaciers of Chile and Argentina. In R. S. Williams, Jr. and J. G. Ferrigno (eds), *Glaciers of South America. Satellite Image Atlas of the World*, USGS Professional Paper 1386-I. Washington, DC: USGS, pp. I 109–I 206.

Lo, H. and Yanai, M. (1984) The large-scale circulation and heat sources over the Tibetan Plateau and surrounding areas during the early summer of 1979. Part II. Heat and moisture budgets, *Mon. Wea. Rev.*, **112**, 966–89.

Loewe, F. (1936) The Greenland ice cap as seen by a meteorologist. *Q. J. Roy. Met. Soc.*, **62**, 359–77.

Lu, A. (1939) A brief survey of the climate of Lhasa. *Q.J.R. Met. Soc.*, **65**, 297–302.

Luo, H.-B. and Yanai, N. (1983) The large-scale circulation and heat sources over the Tibetan Plateau and surrounding regions during the early summer of 1979. Part I. Precipitation and kinematic analysis. *Mon. Wea. Rev.*, **111**(5), 922–44.

Luo, H.-B. and Yanai, N. (1984) The large-scale circulation and heat sources over the Tibetan Plateau and surrounding regions during the early summer of 1979: Part II. Heat and moisture budgets. *Mon. Wea. Rev.*, **112**(5), 966–89.

Maddox, R. A., *et al.* (1978) Comparison of meteorological aspects of the Big Thompson and Rapid City flash floods. *Mon. Wea. Rev.*, **106**, 375–89.

Mani, A. (1981) The climate of the Himalaya. In J. S. Lall and A. D. Moddie (eds), *The Himalaya: Aspects of Changes*. New Delhi: Oxford University Press, pp. 3–15.

Manley, G. (1936) The climate of the northern Pennines. *Q.J.R. Met. Soc.*, **62**, 103–15.

Manley, G. (1942) Meteorological observations on Dun Fell, a mountain station in northern England. *Q.J.R. Met. Soc.*, **68**, 151–65.

Manley, G. (1943) Further climatological averages for the northern Pennines, with a note on topographical effects. *Q.J.R. Met. Soc.*, **69**, 251–61.

Manley, G. (1945) The effective rate of altitudinal change in temperate Atlantic climates. *Geog. Rev.*, **35**, 408–17.

Manley, G. (1980) The northern Pennines revisited: Moor House, 1932–78. *Met. Mag.*, **109**, 281–92.

Marcus, M. G. (1965) Summer temperature relationships along a transect in the St. Elias Mountains, Alaska and Yukon territory. In *Man and the Earth*, No, 3. Boulder, CO: University of Colorado Press, pp. 15–30.

Marcus, M. G. (1974a) Investigations in alpine climatology: The St. Elias Mountains, 1963–1971. In V. C. Bushnell and M. G. Marcus (eds), *Icefield Ranges Research Project, Scientific Results*. Vol. 4. New York: American Geographical Society and Montreal: Arctic Institute of North America, pp. 13–26.

Marcus, M. G. (1974b) A note on snow accumulation and climatic trends in the Icefield Ranges, 1969–1970. In V. C. Bushnell and M. G. Marcus (eds), *Icefield Ranges Research* Project, Scientific Results, Vol. 4. New York: American Geographical Society and Montreal: Arctic Institute of North America, pp. 219–23.

Marcus, M. G. and LaBelle, J. C. (1970) Summer climatic observations at the 5360 meter level, Mt Logan, 1958–1969. *Arct. Alp. Res.*, **2**, 103–14.

Marcus, M. G. and Ragle, R. H. (1970) Snow accumulation in the Icefield Ranges, St. Elias Mountains. *Arct. Alp. Res.*, **2**, 277–92.

Mark, A. F., *et al.* (2006) Two GLORIA long-term alpine monitoring sites established in New Zealand as part of a global network. *J. Roy. Soc. New Zealand*, **36**, 111–28.

Marr, J. W. (1961) *Ecosystems of the East Slope of the Front Range in Colorado*. In University of Colorado Studies Series, Biology 8, Boulder, CO: University of Colorado.

Martius, O., *et al.* (1931) Zur Meteorologie und Hydrologie des Jungfraugebietes. In *Jungfraujoch Hochalpine Forschungstation*, pp. 33–45, Zurich.

Martius, O., *et al.* (2006) Episodes of the Alpine heavy precipitation with an overlying elongated stratospheric intrusion: A climatology. *Int. J. Climatol.*, **26**, 1149–64.

Matulla, C., *et al.* (2005) *Outstanding Past Decadal-scale Climate Events in the Greater Alpine Region Analysed by 250 years Data and Model Runs*. GKSS 2005/4. Geesthacht, Germany: GKSS Forschungszentrum, 114 pp.

Maurer, J. and Luetschg, O. (1931) Zur Meteorologie und Hydrologie des Jungfraugebietes. In *Jungfraujoch Hochalpine Forschungsstation*. Zurich: pp. 33–45.

McConnell, D. (1988) The Ben Nevis Observatory log books. *Weather*, **43**, 356–62 and 396–401.

McVean, D. M. (1974) Mountain climates of the Southwest Pacific. In J. R. Flenley (ed.), *Altitudinal Zonation in Malesia*. Hull: University of Hull, Department of Geography, Miscellaneous Series 16, pp. 47–57.

Merzlyakova, I. (2002) The mountains of central Asia and Kazakhstan. In M. Shahgedanova (ed.), *The Physical Geography of Northern Eurasia*. Oxford: Oxford University Press, pp. 377–402.

Miller, A. (1976) The climate of Chile. In W. Scherdtfeger (ed.), *Climate of Central and South America, World Survey of Climatology*. Amsterdam: Elsevier, pp. 113–46.

Mitchell, V. L. (1976) The regionalization of climate in the western United States. *J. appl. Met.*, **15**, 920–7.

Mitsudera, M. and Numata, M. (1967) Meteorology of eastern Nepal. *J. Coll. Arts Sci, Chiba Univ.*, **5**, 75–83.

Mölg, T. and Hardy, D. R. (2004) Ablation and associated energy balance of a horizontal glacier surface on Kilimanjaro. *J. Geophys. Res.*, **109**, D16104.

Mölg, T., Georges, C. and Hardy, D. R. (2003) The contribution of increased incoming shortwave radiation to the retreat of the Rwenzori glaciers, East Africa, during the 20th century. *Int. J. Climatol.*, **23**, 291–303.

Monasterio, M. (ed.) (1980) *Estudios Ecologicos en los Paramos Andinos*. Mérida, Venezueka: Edic. Universidad de los Andes.

Moore, G. W. K. and Semple, J. L. (2004) High Himalayan meteorology: weather at the South Col. *Geophys. Res. Lett.*, **31**, L 18109.

Mossman, R. C. (1902) Abstract of paper on silver thaw at the Ben Nevis Observatory. *Trans. R. Soc. Edinb.*, **42**, 525–7.

Myers, V. A. and Norris, D. F. (1991) New techniques and data sources for PMP. In Darling, D. D. (ed.), *Waterpower '91*, Vol. 2. New York: American Society of Civil Engineers. pp. 1319–27.

Nedungadi, T. M. K. and Srinivasan, T. R. (1964) Monsoon onset and Everest Expeditions. *Ind. J. Met. Geophys.*, **15**, 137–48.

Niedzwiecky, T. (1992) Climate of the Tatra Mountains. *Mountain Res. Dev.*, **12**(2), 131–46.

Ohata, T., Higuchi, K. and Ikegami, K. (1981) Mountain-valley wind system in the Khumbu Himal, east Nepal. *J. Met. Soc. Japan*, **53**, 753–62.

Ohata, T., Kang, X.-Ch. and Takahasi, S. (1990) Full year of surface meteorological data at northwestern Tibetan Plateau using an automatic meteorological station. *Bull. Glacier Res.* (Tokyo), **8**, 73–86.

Ohmura, A., Calanca, P., Wild, M. and Anklin, M. A. (1999) Precipitation, accumulation and mass balance of the Greenland ice sheet. Z*eitschr. Gletscherkunde Glazialgeol.*, **35**, 1–20.

Omond, R. T. (1910) Large differences of temperature between the Ben Nevis and Fort William Observatories. *Trans. R. Soc. Edinb.*, **44**, 702–5.

Owen, L. A., *et al.* (2006) Climatic and topographic controls on the style and timing of Late Quaternary glaciation throughout Tibet and the Himalaya defined by 10Be cosmogenic radionuclide surface exposure dating. *Quatern. Sci Rev.*, **24** (12–13), 1391–411.

Parish, T. R. (1988) Surface winds over the Antarctic continent: A review. *Rev Geophys.*, **26**, 169–80.

Parish, T. R. and Bromwich, D. H. (1991) Continental-scale simulation of the Antarctic katabatic wind regime. *J. Climate*, **4**, 135–46.

Parish, T. R. and Cassano, J. J. (2003) The role of katabatic winds on the Antarctic surface wind regime. *Mon. Wea. Rev.*, **131**, 317–33.

Pedgley, D. E. (1966) Rainfall of Mount Kenya. *Weather*, **21**, 187–8.

Peterson, J. A., *et al.* (2002) Mountain environments in New Guinea, and the late Glacial maximum "warm seas/cold mountains" enigma in the West Pacific Warm Pool region. In A. P. Kershaw, *et al.* (eds), *Bridging Wallace's Line. Advances Geoecol.*, **34**, 173–87.

Poulos, G. S., *et al.* (2002) A Rocky Mountain snowstorm. Part I. The blizzard-kinematic evolution and the potential for high-resolution numerical modeling. *Wea. Forecasting*, **17**(5), 955–70.

Poveda, G., *et al.* (2005) The diurnal cycle of precipitation in the tropical Andes. *Mon. Wea. Rev.*, **131**(1), 228–40.

Prentice, M. L. and Hope, G. S. (2006) The climate of Papua and its recent changes. In A. J. Marshall and B. M. Beehler (eds), *The Ecology of Papua*. Singapore: Periplus Editions.

Prentice, M. L., *et al.* (2005) An evaluation of snowline data across New Guinea during the last major glaciation, and area-based glacier snowlines in the Mt. Jaya region of Papua. Indonesia, during the Last Glacial Maximum. *Quatern Int.*, **138/9**, 93–117.

Prohaska, F. (1976) The climate of Argentina, Paraguay and Uruguay. In W. Schwerdtfeger (ed.), *Climate of Central and South America, World Survey of Climatology*, Vol. 12. Amsterdam: Elsevier, pp. 112–13.

Pulwarty, R. S., *et al.* (1998) Precipitation in the Venezuelan Andes in the context of regional climate. *Met. Atmos. Phys.*, **67**, 217–38.

Putkonen, J. K. (2004) Continuous snow and rain data at 500–4400 m altitude near Annapurna, Nepal, 1999–2001. *Arct. Antarct. Alp. Res.*, **36**(2), 244–8.

Putnins, P. (1969) The climate of Greenland. In S. Orvig (ed.), *Climates of the Polar Regions World Survey of Climatology*, Vol. 14. Amsterdam: Elsevier, pp. 3–128.

Raghavan, K. (1979) Summer weather and climate of the Himalaya. *Weather*, **34**, 448–54.

Ramage, C. S. (1971) *Monsoon Meteorology*. New York: Academic Press, 296 pp.

Rao, Y. P. (1976) *Southwest Monsoon*. (Meteorol. Monogr., Synoptic Meteorology). Delhi: Indian Meteorological Department, 367 pp.

Rao, Y. P. (1981) The climate of the Indian subcontinent. In K. Takahashi and T. Arakawa (eds), *Climates of Southern and Western Asia. World Survey of Climatology*, Vol. 9. Amsterdam: Elsevier Sci. Publ., pp. 67–182.

Reiter, E. R. and Heuberger, H. (1960) A synoptic example of the retreat of the Indian summer monsoon. *Geog. Ann.*, **42**, 17–35.

Reiter, E. R., *et al.* (1987) Tibet revisited – TIPMEX-86. *Bull. Amer. Met. Soc.*, **68**, 607–15.

Renfrew, I. A. and Anderson, P. S. (2006) Profiles of katabatic flow in summer and winter over Coats Land, Antarctica. *Q. J. R. Met Soc.*, **132**, 772–809.

Richter, M., Pfeiffer, H. and Fickert, T. (1999) Differences in exposure and altitudinal limits as climatic indicators in a profile western Himalaya to Tian Shan. *Erdkunde*, **53**, 89–107.

Ronchail, J. and Gallaire, R. (2006) ENSO and rainfall along the Zongo Valley (Bolivia) from the Altiplano to the Amazon Basin. *Int. J. Climatol.*, **26**, 1223–36.

Rotunno, R. and Ferretti, R. (2001) Mechanisms of intense Alpine rainfall. *J. Atmos. Sci.*, **58**(13), 1732–49.

Rupper, S., Steig, E. J. and Roe, G. (2005) The relationship between snow accumulation at Mt. Logan, Yukon, Canada, and climate variability in the North Pacific. *J. Climate*, **17**(24), 4724–39.

Sarmiento, G. (1986) Los principales gradientes ecoclimaticos en los Andes tropicales. In *Ecologia de Tierras Altas*, Annales del IV Congreso Latinoamericano de Botanico Vol. 1 (Columbia), pp. 47–64.

Sato, T. (2001) Spatial and temporal variations of frozen ground and snow cover in the eastern part of the Tibetan Plateau. *J. Met. Soc. Japan*, **79**(1B), 519–34.

Satyamurty, P., Nobre, C. A. and Silva Dias, P. L. (1998) South America. In D. J. Karoly and D. G. Vincent, (eds), *The Meteorology of the Southern Hemisphere*, Meteorological Monographs, **27**(49), 119–39.

Schaaf, C. L. B., Wurman, J. and Banta, R. M. (1988) Thunderstorm-producing terrain features. *Bull. Amer. Met. Soc.*, **769**, 272–7.

Schär, C., Davies, H. C. and Wanner, H. (1998) Alpine climate. In P. Cebon, *et al.* (eds), *Views from the Alps: Regional Perspectives on Climate Change*. Boston, MA: MIT Press, pp. 171–223.

Scherrer, S. C. and Appenzeller, C. (2006) Swiss Alpine snow pack variability: major patterns and links to local climate and large-scale flow. *Clim. Res.*, **32**, 187–99.

Schickoff, U. (1994) Die Verbreitung der Vegetation im Kaghan-Tal (West Himalaya, Pakistan) und ihre kartographische Darstellung in Massstab 1:150,000. *Erdkunde*, **48**, 92–110.

Schneider, C., *et al.* (2003) Weather observations across the southern Andes at 53° S. *Phys. Geog.*, **24**, 97–119.

Schüepp, M. (1959) Die Klassifikation der Wetterlagen im Alpengebiet, *Geofis. Pura Appl.*, **44**, 242–8.

Schüepp, M. (1990) Der Einfluss des Appenines auf die Föhnströmung in den Alpen, *CIMA '88. 20° Congresso Internaz. di Meteorologia Alpina*. Servizio Meteorologico Italiano.

Schüepp, M. and Schirmer, H. (1977) Climates of central Europe. In Wallen, C. C. (ed.), *Climates of Central and Southern Europe*. Amsterdam: Elsevier, pp. 3–73.

Schwarb, M., Daly, C., Frei, C. and Schär, C. (2001) Mittlere jährliche Niederschlagshöhen im europäischen Alpenraum. In Gruppe für Hydrologie, Universität Bern: *Hydrologischer Atlas der Schweiz*. Berne: Landeshydrologie, Bundesamt für Wasser und Geologie, plate 2.6.

Schweinfürth, U. (1956) Uber klimatische Trockentäler in Himalaya. *Erdkunde*, **10**, 297–302.

Schwerdtfeger, W. (1976) Introduction. In W. Schwerdtfeger (ed.), *Climate of Central and South America, World Survey of Climatology*, Vol. 12. Amsterdam: Elsevier, pp. 1–12.

Seko, K. (1987) Seasonal variation of altitude dependence of precipitation in Langtang Valley, Nepal Himalayas. *Bull. Glacier Res*. (Tokyo), **5**, 41–8.

Serreze, M. C. and Barry, R. G. (2005) *The Arctic Climate System*. Cambridge: Cambridge University Press, 385 pp.

Serreze, M. C., *et al.* (1999) Characteristics of the western United States snowpack from arrowpack telemetry (SNOTEL data). *Water Resour. Res.*, **35**(7), 2145–60.

Serreze, M. C., Clark, M. P. and Frei, A. (2001) Characteristics of large snowfall events in the montane Western United States as examined using snowpack telemetry (SNOTEL) data. *Water Resour. Res.*, **37**(3), 675–88.

Sevruk, B. (ed.) (1985) Der Niederschlag in der Schweiz, *Beiträge, Geologie der Schweiz-Hydrologie*, 31. Bern: Kümmerly and Frey.

Sevruk, B. (1997) Regional dependency of precipitation-altitude relationship in the Swiss Alps. *Clim. Change*, **36**, 355–69.

Shahgedanova, M. (2002) Climate at present and in the historical past. In M. Shahgedanova (ed.), *The Physical Geography of Northern Eurasia*. Oxford: Oxford University Press, pp. 70–102.

Shahgedanova, M., Mikhailov, N., Larin, S. and Bredikhin, A. (2002) The mountains of Southern Siberia. In M. Shahgedanova (ed.), *The Physical Geography of Northern Eurasia*. Oxford: Oxford University Press, pp. 314–49.

Shimizu, S., *et al.* (2001) Mesoscale characteristics and structures of stratiform precipitation on the Tibetan Plateau. *J. Met. Soc. Japan*, **79**(1B), 435–61.

Shresta, M. L., Fujii, Y. and Nakawo, M. (1976) Climate of Hidden Valley, Mukut Himal, during the monsoon in 1974. *Seppyo*, **38**, Special Issue, 105–8.

Shuman, C. A., Steffen, K. and Stearns, C. R. (2001) A dozen years of temperature observations at Summit. Central Greenland automatic weather stations 1987–99. *J. appl. Met.*, **40**(4), 741–52.

Simmonds, I. (1998) The climate of the Antarctic region. In J. E. Hobbs, J. A. Lindesay and H. A. Bridgman (eds), *Climates of the Southern Continents: Past, Present and Future*. Chichester, UK: J. Wiley and Sons, pp. 137–60.

Singh, P. and Kumar, N. (1997) Effect of orography on precipitation in the western Himalayan region. *J. Hydrol.*, **199**, 183–206.

Singh, P., Haritashya, U. K. and Kumar, N. (2007) Meteorological study for Gangroti glacier and its comparison with other high altitude meteorological stations in central Himalaya region. *Nordic Hydrol.*, **38**, 59–77.

Smith, E. A. and Shi, L. (1996) Reducing discrepancies in atmospheric heat budget of Tibetan Plateau by satellite-based estimates of radiative cooling and cloud – radiation feedback. *Met. Atmos. Phys.*, **56**, 229–60.

Somervell, T. H. and Whipple, F. J. W. (1926) The meteorological results of the Mount Everest expedition. *Q. J. R. Met. Soc.*, **52**, 131–42.

Spreafico, M. and Weingartner, R. (2005) *The Hydrology of Switzerland. Selected aspects and results*. Reports, Bundesamt f. Wasser u. Geologie (BWG) Water Series No. 7, Bern, Switzerland: BWG, 139 pp.

Steffen, K. and Box, J. E. (2001) Surface climatology of the ice sheet: Greenland: Climate Network 1995–1999. *J. Geophys. Res.*, **106**, (D24), 33 951–64.

Steffen, K., Nghiem, S. V., Huff, R. and Neumann, G. (2004) The melt anomaly of 2002 on the Greenland Ice Sheet from active and passive microwave satellite observations. *Geophys. Res. Lett.*, **31**(20), L2040210.

Steinegger, U., *et al.* (1993) Assessment of annual snow accumulation over the past 10 years at high elevations in the Langtang region. In G. Young (ed.), *Snow and Glacier Hydrology*, IAHS publication no. 218, Wallingford, UK: IAHS, pp. 155–65.

Steinhauser, F. (1938) *Die Meteorologie des Sonnblicks, I. Teil*. Vienna; J. Springer.

Stravisi, F., Verza, G. P. and Tartari, G. (1998) Meteorology and climatology at high altitude in Himalaya. In R. Baudo, G. Tartari and M. Munawar (eds), *Top of the World Environmental Research: Mount Everest Himalayan Ecosystem*. Leiden: Backhuys Publishers, pp. 101–22.

Sturman, A. and Wanner, H. (2001) A comparative review of the weather and climate of the Southern Alps of New Zealand and the European Alps. *Mountain Res. Dev.*, **21**(4), 359–69.

Tartari, G., Verza, G. and Bertolami, L. (1998) Meteorological data at the Pyramid Observatory Laboratory (Khumbu Valley, Sagarmatha National Park, Nepal). In *Limnology of High Altitude Lakes in the Mt. Everest Region (Nepal)*. *Mem. Ist. Ital. Idrobiol.* **57**, 23–40.

Taylor, J. A. (1976) Upland climates. In T. J. Chandler and S. Gregory (eds), *The Climate of the British Isles*. London: Longman, pp. 264–87.

Taylor-Barge, B. (1969) *The Summer Climate of the St. Elias Mountain Region*. Montreal: Arctic Institute of North America, Research Paper No. 53.

Thom, A. S. (1974) Meteorological report. In B. K. Parnell (ed.), *Anonach Moor: a Planning Report on the Prospect of Winter Sport Development at Fort William*. Glasgow: Glasgow School of Art, Department of Planning, pp. 85–109.

Thompson, B. W. (1966) Mean annual rainfall of Mount Kenya. *Weather*, **21**, 48–9.

Thompson, L. G. and Hastenrath, S. L. (1981) Climatic ice core studies at Lewis Glacier, Mount Kenya. *Zeitschr. Gletscherkunde Glazialgeol.*, **17**, 115–23.

Tian, L., *et al.* (2001) Tibetan Plateau summer monsoon northward extent revealed by measurements of water stable isotopes. *J. Geophys. Res.*, **106** (D22), 28 081–8.

Tollner, H. (1949) Der Einfluss grosser Massenerhebungen auf die Lufttemperatur und die Ursachen der Hebung der Vegetationsgrenzen in den inneren Ostalpen. *Arch Met. Geophys. Biokl.*, **B 1**, 347–72.

Troll, C. (1951) Die Lokalwinde der Tropengebirge und ihr Einfluss auf Niederschlag und Vegetation. *Bonner Geog. Abh.*, **9**, 124–82.

Troll, C. (1968) The Cordilleras of the tropical Americas. Aspects of climatic phytogeographical and agrarian ecology. *Colloq. Geogr.* (Bonn), **9**, 15–56.

Troll, C. (1972) The three-dimensional zonation of the Himalayan system. In C. Troll (ed.), *Geoecology of the High-Mountain Regions of Eurasia*. Wiesbaden: F. Steiner, pp. 264–75.

Tucker, D. F. and Crook, N. A. (2005) Flow over heated terrain, Part II: Generation of convective precipitation. *Mon. Wea. Rev.*, **133**(9), 2565–82.

Ueno, K. and Yamada, T. (1990) Diurnal variations of precipitation in Langtang Valley, Nepal Himalayas. *Bull. Glacier Res.* (Tokyo), **8**, 93–101.

Ueno, K., Shiraiwa, T. and Yamada, T. (1993) Precipitation in the Langtang valley, Nepal Himalyas. In G. Young (ed.), *Snow and Glacier Hydrology*, IAHS publication No. 218. Wallingford, UK: IAHS, pp. 207–19.

Ueno, K., *et al.* (2001a) Weak and frequent monsoon precipitation over the Tibetan Plateau. *J. Met. Soc. Japan*, **79** (1B), 419–34.

Ueno, K., *et al.* (2001b) Meteorological observations during 1994–2000 at the Automatic weather Station (GEN-AWS) in Khumbu region, Nepal Himalayas. *Bull. Glacier Res.* (Tokyo), **18**, 23–30.

Van der Veen, C. J., Bromwich, D. H. and Castho, C. K. (2001) Trend surface analysis of Greenland accumulation. *J. Geophys. Res.*, **9106** (D24), 33 909–18.

Volodicheva, N. (2002) The Caucasus. In M. Shahgedanova (ed.), *The Physical Geography of Northern Eurasia*. Oxford: Oxford University Press, pp. 350–76.

Voloshina A. P. (2002) Meteorologiya goinykh lednikov (Meteorology of mountain glaciers). English summaries. *Materialy Glatsiol. Issled.*, (Institute of Geography, RAS, Moscow) **92**, 3–148.

Vuille, M. (1996) Zur raumzeitlichen Dynamik von Schneefall und Ausaperung in Bereich des südlichen Altiplano. *Geographica Bernensi*, University of Bern, G45, 118 pp.

Vuille, M. and Amman, C. (1997) Regional snowfall patterns in the high, arid Andes. *Clim. Change* **36**, 413–23.

Vuille, M. and Baumgartner, M. F. (1998) Monitoring the regional and temporal variability of winter snowfall in the arid Andes using digital NOAA/AVHRR data. *Geocarto. Internat.*, **13**, 59–68.

Vuille, M., *et al*. (1998) Atmospheric circulation anomalies associated with 1996/1997 summer precipitation events on Sajama Ice Cap, Bolivia. *J. Geophys. Res.* **103** (D10), 11 191–204.

Walker, E. R. (1961) *A Synoptic climatology for parts of the Western Cordillera*. Montreal: McGill University, Arctic Meteorological Research Group, Publication in Met. No. 35.

Wang, B. (1987) The development mechanism for Tibetan Plateau warm vortices. *J. Atmos. Sci.*, **44**(20), 2978–94.

Wanner, H. (1979) Zur Bildung, Verteilung und Vorhersage winterlicher Nebel im Querschnitt Jura-Alpen. *Geogr. Bernensia*, **G**, 7.

Wanner, H. (1992) Ein Nussgipfel im Westwind – zur Dynamik von Wetter Und Klima im Alpenraum. In J. P. Mueller and B. Gilgen (eds), *Dia Alpen – ein sicherer Lebensraum?* Bern: Schweizerische Akademie Naturwissenschaften, Publication No. 5: 50–60.

Wanner, H. and Furger, M. (1990) The Bise – climatology of a regional wind north of the Alps. *Met. Atmos. Phys.*, **43**, 105–15.

Weidick, A. (1995) *Greenland*. In R. S. Williams and J. G. Ferrigno (eds), *Satellite Image Atlas of Glaciers of the World*. US Geological Survey Professional Paper 1386-C, Washington, DC: US Geological Survey, 141 pp.

Weingartner, R. and Pearson, C. (2001) A comparison of the hydrology of the Swiss Alps and the Southern Alps of New Zealand. *Mountain Res. Devel.*, **21** (4). 370–81.

Wien, K. (1936) Die Wetterverhältnisse am Nanga-Parbat während der Katastrophe auf der deutschen Himalaja – Expedition 1934. *Met. Zeit.*, **53**, 26–32. (Bermerkungen, M. Rodewald, *Met. Zeit.*, **53**, 182–6).

Winiger, M. (1972) Die Bewölkungsverhältnisse der zentralsharischen Gebirge aus Wettersatellitenbildern. *Hochgebirgsforschung*, **2**, 87–120.

Winiger, M. (1981) Zur thermisch-hygrischen Gliederungs des Mount Kenya. *Erdkunde* **35**, 248–63.

Witmer, U., *et al*. (1986) Erfassung, Bearbeitung und Kartieren von Schneedaten in der Schweiz. *Geogr. Bernensia*, **G25**.

Wratt, D. S., *et al*. (2000) Relationships between air mass properties and mesoscale rainfall in New Zealand's Southern Alps. *Atmos. Res.*, **52**, 261–82.

Xu, J.-Q. and Haginoya, S. (2001) An estimation of heat and water balances on the Tibetan Plateau. *J. Met. Soc. Japan*, **79** (1B), 485–504.

Xu, J.-Q., *et al*. (2005) Heat and water balances over the Tibetan Plateau in 1997–1998. *J. Met. Soc. Japan*, **83**(4), 577–93.

Xu, Y.-G. (ed.) (1986) *Proceedings of the International Symposium of the Qinghai-Xizang Plateau and Mountain Meteorology*. Beijing: Science Press, and Boston, MA: American Meteorological Society.

Yacono, D. (1968) L'Ahaggar, Essai sur le climat de montagne au Sahara. *Travaux de l'Institut de Recherches Sahariennes*, 27, Université d'Alger.

Yanai, M. and Li, C.-F. (1994) Mechanism of heating and the boundary layer of the Tibetan Plateau. *Mon. Wea. Rev.*, **102**(2), 3305–23.

Yang, K., *et al*. (2004) The daytime evolution of the atmospheric boundary layer and convection over the Tibetan Plateau: Observations and simulations. *J. Met. Soc. Japan*, **82**(6), 1777–92.

Yasunari, T. (1976a) Seasonal weather variations in Khumbu Himal. *Seppyo*, **38**, Special Issue, 74–83.

Yasunari, T. (1976b) Spectral analysis of monsoonal precipitation in the Nepal Himalayas. *Seppyo*, **38**, Special Issue, 59–65.

Yasunari, T. and Inoue, J. (1978) Characteristics of monsoonal precipitation around peaks and ridges in Shorong and Khumbu Himal. *Seppyo*, **40**, Special Issue, 26–32.

Yasunari, T., Kanehira, A. and Koike, T. (2002) Seasonal and interannual variability of snow mass on the Tibetan Plateau and its impact on Asian summer monsoon. In Sh-Y. Tao, *et al*. (eds), *The Second Tibetan Plateau Experiment of Atmospheric Sciences*. Beijing: China Meteorological Press, pp. 70–6.

Yeh, D.-Z. and Gao, Y.-X. (1979) *Meteorology of Qinghai-Xizang (Tibet) Plateau* (in Chinese) Beijing: Science Press.

Young, J. A. T. and Hastenrath, S. (1991) The glaciers of East Africa. In R. S. Williams, Jr., and J. G. Ferrigno (eds), *Satellite Image Atlas of the World, Glaciers of the Middle East and Africa*. US Geological Survey Professional Paper 1386, G-3. Washington, DC: USGS, pp, G 48–70.

Zängl, G. and Chico, S. (2006) The thermal circulation of a grand plateau: sensitivity to the height, width and shape of the plateau. *Mon. Wea. Rev*., **134**, 2581–600.

Zhang, B.-P., *et al*. (2006) Integration of data on Chinese mountains into a digital altitudinal belt system. *Mt. Res. Dev*., **26**, 163–71.

Zhang, T.-J. (2005) Historical overview of permafrost studies in China. *Polar Geog*., **266**, 279–98.

6 MOUNTAIN BIOCLIMATOLOGY

6.1 HUMAN BIOCLIMATOLOGY

The high altitude environment is one of severe stress for humans. Air pressure is reduced from its sea level value by 30 percent at 3000 m and almost 50 percent at 5000 m (see Table 2.2, 32) and, on average, air temperatures decrease from sea level to the same elevations by about 18 and 30° C, respectively. Other factors include low humidity and increased ultraviolet radiation. Visitors to high altitudes, above about 3000 m, generally notice the oxygen deficiency as a slight breathlessness, especially when undergoing any exertion, and they frequently experience sleep-disordered breathing and/or apnea. Beneficial effects of altitude have also been noted among asthma sufferers due to reduced levels of air pollution and allergens (Hackett, 2001).

The consequences for permanent residents of high altitudes are quite different, however, since they acquire long-term acclimatization. In fact, low temperatures, snow cover and, therefore, limited food resources rather than oxygen deficiency are the dominant controls of human occupancy in the high mountains (Grover, 1974). We will consider first some basic physiological aspects relating to mountain environments in terms of short-term visitors.

6.1.1 Physiological factors and responses

6.1.1.1 Oxygen deficiency

The difficulties of breathing and symptoms of mountain sickness experienced by early travelers crossing high mountain passes is reported in many historical documents, but scientific explanations only began to be proposed in the late eighteenth century (Houston, 2001). De Saussure suggested that the symptoms he experienced on Mont Blanc were linked to the fact that the air density was only about half that in the lowlands, while Alexander von Humboldt, climbing Chimborazo in the Andes in 1802 considered that lack of oxygen caused his mountain sickness. However, in the 1870s Paul Bert discovered experimentally the role of the decrease of the oxygen partial pressure in hypoxia – rather than the total air pressure. Research in high altitude medicine was carried out by Angelo Mosso in a special laboratory on Monte Rosa, Italy in the 1890s and British and American scientists made studies of the cause of hypoxia and acclimatization on Pike's Peak, Colorado

in 1911, but it was another 20 years before the precise physiological mechanisms of hypoxia were established definitively (Houston, 2001).

Mountaineering expeditions, especially in the Himalayas, led to attempts in the 1930s to understand acclimatization and the great variation between individuals, and even day-to-day in the same individual. Even today, such differences are not completely understood.

A realistic relationship between air pressure and altitude was given by N. Zuntz and colleagues in 1906 (see West, 2001):

$$\log p_2 = \log p_1 - h/[72(256.4 + T)]$$

where p_1 is the barometric pressure at the lower altitude (mmHg $= 1$ torr $= 1.333$ mb); p_2 is the barometric pressure at the higher altitude; h is the altitude difference (m); and T is the mean air temperature of the column of height h ($^\circ$C).

By contrast, the standard atmosphere developed for international aviation and meteorology (see Table 2.2), which assumes a mean sea level pressure of 1013 mb and a constant lapse rate of 6.5 $^\circ$C km^{-1} up to 11 km, predicts pressures that are significantly too low in the high mountains as recognized by Pugh (1957) and West (1996). For the summit of Mt. Everest (8848 m), the standard atmosphere gives pressures that are 16–23 mb too low depending on season and weather conditions, which affect air temperature.

With increased altitude, there is a reduction in the capacity of the body to take in oxygen, which is distributed throughout the body by hemoglobin in the red blood cells. The proportion of oxygen in air remains a constant 21 percent by volume, but its partial pressure decreases in relation to the total pressure. The partial pressure of oxygen inspired into the lungs (P_1O_2) is determined by the ambient air pressure, reduced by the saturation water vapor pressure at body temperature (37 $^\circ$C), multiplied by the oxygen fraction (0.21). Thus, at sea level, $P_1O_2 = 0.21$ (1013–63) $= 200$ mb, whereas at 5000 m, $P_1O_2 = 0.21$ (540–63) $= 100$ mb. On Mt. Everest (8848 m asl) the mean P_1O_2 is 57 mb (Moore and Semple, 2006). The human limit of indefinite tolerance to oxygen deficiency, or *hypoxia*, occurs where P_1O_2 falls below one-half of its sea level value, but the effects of a hypoxic environment are physiologically significant above 3000 m, where P_1O_2 is 133 mb (Grover, 1974).

For a given altitude, say 4000 m (neglecting the small numerical difference between geopotential and geometric height), the corresponding standard atmosphere value of pressure is approximately 630 mb at latitudes equatorward of 30°, but at 60° N latitude ranges between 593 mb in January and 616 mb in July (see Table 2.2). Thus, at an equivalent height, the effect of reduced air pressure is substantially greater in middle and high latitudes, particularly in winter. The passage of a cyclonic system could further lower the pressure by some 20–30 mb, equivalent at the given altitude to a height difference of ≈ 250–375 m. Such latitudinal and seasonal effects may be important for climbers in high mountains, as well as in terms of high-altitude settlements and work enterprises in mid-latitudes.

The effects of extreme low pressure were graphically demonstrated during balloon ascents up to 8800 m by James Glaisher in the 1860s. On one ascent, he lost the use of his limbs and became unconscious, but fortuitously survived. The immediate response to oxygen deficiency is an increase in air volume inspired, or *hyperventilation*. This maintains the quantity of oxygen in the lungs but not in the blood, which is compensated for initially by an increase in the heart rate. The tendency to hyperventilate results in excessive elimination of carbon dioxide from the lungs, which inhibits respiration. This can be overcome temporarily by taking several breaths into and out of a container, such as a paper bag, to return some of the expired carbon dioxide. After a week or so at high altitude, the volume of blood plasma decreases, thereby increasing the concentration of red blood cells and hemoglobin and allowing more oxygen to be transported by a given volume of blood to the body tissues. Prolonged high altitude exposure leads to an increase in the total volume of red blood cells (polycythemia), which tends to increase oxygen transport, but the greater viscosity of the blood may impede its flow. Even so, the maximum amount of oxygen that the body can consume, which determines the "aerobic working capacity" (VO_2), declines 10 percent per kilometer above about 1500 m (Buskirk, 1969). Thus, persons at high altitude tire more rapidly, even if acclimatized. Moore and Semple (2006) note that a pressure drop of 10–14 mb during a storm in May 1996 on Mt. Everest led to a 6 percent decrease in P_IO_2 below the mean value for the summit (57 mb) and a resultant 14 percent decrease in VO_2. This, together with winds $> 30 \, \mathrm{m \, s^{-1}}$, air temperatures of $-32\,°C$, and the descent of ozone-rich stratospheric air (that is thought to decrease pulmonary function), is believed to have contributed significantly to the eight fatalities among the climbers near the summit.

The first laboratory for high-altitude research was established at 4560 m on Mt. Rosa, Italy, in 1901 and, about the same time, several studies of mountain sickness were published. Hypoxia can lead to mountain sickness, symptoms of which include headache, dizziness, nausea, loss of appetite, and insomnia. Cheyne–Stokes breathing at night, which is an irregular rhythm fluctuating between deep breathing (giving hyperventilation) and then a cessation of breathing (apnea) for perhaps 10 s, is also a common response to hypoxia. Chest pains, coughing and muscular weakness indicate severe mountain sickness. Although such severe symptoms rarely persist longer than a few days, full recovery may require a month of more for some individuals (Heath and Williams, 1977: p. 105). To avoid mountain sickness, a stop of about a week should be spent around 3000 m and at each 1000 m interval above, before proceeding higher. Dietary precautions include a low-fat, high-carbohydrate diet.

Symptoms of acute mountain sickness (AMS) include insomnia, headache, peripheral edema and low pulmonary rates; also vomiting and dizziness. Maggiorini *et al.* (1990) identified AMS occurrences (> 2 symptoms) among 466 recreational climbers using four Swiss mountain huts: at 2850 m there was a 9 percent incidence, at 3350 m -13 percent, at 3650 m -34 percent, and at 4559 m -53 percent. At 4559 m, five percent developed high altitude pulmonary edema (HAPE), cerebral edema or both. Pulmonary edema can result from a rapid move to high altitude

and over-exertion. Here, fluid accumulation in the lungs impairs the oxygen transfer into the blood. The symptoms – excessive fatigue, shortness of breath, and a cough – resemble pneumonia. Active young males at moderate altitudes between 3000–4000 m, who have not acclimatized, seem to be particularly at risk. Ward (1975; p. 284) notes that deaths have occurred, despite oxygen treatment, even in healthy individuals.

Renewed interest has been shown in medical and physiological research using high altitude facilities such as the Margherita hut on Monte Rosa for studies of HAPE susceptibility. Richalet (2001) describes similar work on Mont Blanc.

6.1.1.2 The human energy budget and cold effects

The body core, at a normal temperature of about 37 °C, transfers heat by conduction to the muscles and skin layers, and by blood circulation to the extremities which are usually some 8 °C cooler. The body surface then loses heat by radiation, conduction, convection and evaporation.

The energy budget of an upright person at high altitude has been studied in the White Mountains of California in July (Terjung, 1970). Two important results were demonstrated. First, it was shown that the environmental radiant temperature (determined from $T_c = 0.5 (T_{sky} + T_s)$, where T_{sky} represents an average radiant sky temperature and T_s an average terrain surface temperature, is subject to much greater extremes than the air temperature. Figure 6.1 compares the altitudinal and diurnal variation of these two parameters. Second, the net radiation on an erect figure was found to have a diurnal variation inverse to that of the ground surface, with minimal values around midday (and also in summer). Computed values of net radiation on the body were largest in spring as a result of the high surface albedo associated with snow cover.
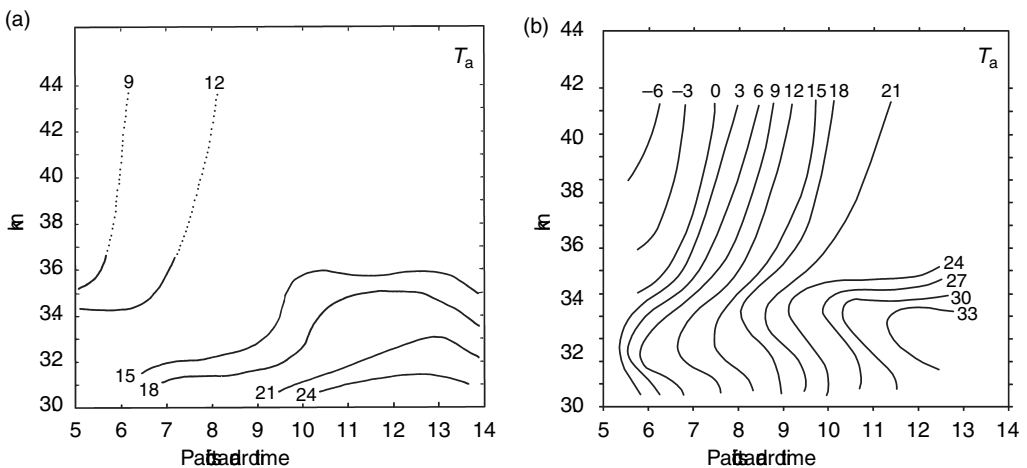
Fig. 6.1 Altitudinal and diurnal variations of (a) air temperature (°C) and (b) environmental radiant temperature in the White Mountains, California, mid-July (from Terjung, 1970).

The energy budget of a mountain climber in winter clothing, calculated for light winds and weakly positive air temperatures at 3100 m in the Alps, shows that 60 percent of the energy loss is by sensible heat; radiation, moisture loss and breathing make up the balance in nearly equal amounts (Hammer *et al.*, 1989). Nevertheless, in cold, dry conditions, heat loss by conduction and evaporation from the lungs can account for 20 percent of the total body heat loss (Steadman, 1971). Mitchell (1974) notes that the evaporative heat transfer coefficient is proportional to $(1/p)^{0.4}$ and thus it increases with altitude as the air pressure decreases. The dehydration effects of altitude were recognized and described by de Saussure in 1787. Wind augments the convective heat loss from the skin and this is measured by the *windchill* index of cooling power or by the windchill equivalent temperature. The latter measure, which is convenient to use, denotes the effect of a $2.2 \, \mathrm{m \, s^{-1}}$ wind on the skin. The original windchill equivalent temperature scale was proposed by Siple and Passel (1945) based on cold chamber experiments with unclothed individuals. Steadman (1971) has developed indices for clothed persons and Dixon (1991) provides a nomograph to relate these to categories of comfort.

Osczevski and Bluestein (2005) jointly developed a new index of windchill in 2001. It is based on a model of how fast a human face loses heat and the skin temperature under various conditions of wind and temperature. (Meteorological Service of Canada web site; Henson, 2002). The model, which has been validated through clinical trials, takes into account the lowering of skin temperature through the heat loss caused by wind and cold, and the effect of this lower skin temperature on the rate of heat loss. The index is given by:

$$W = 13.12 + 0.6215T - 11.37V^{0.16} - 0.3965T \times V^{0.16}$$

where W is the windchill equivalent temperature, based on the Celsius temperature scale; T is the air temperature ($^\circ$C); and V is the wind speed at 10 m height ($\mathrm{km \, h^{-1}} = 0.277 \, \mathrm{m \, s^{-1}}$).

Henson (2002) gives the corresponding equation for W in Fahrenheit units and mph. Figure 6.2 illustrates the new index.

Important features of the new index include the following items.

(1)   It uses wind speed calculated at 1.5 m, the average height of the human face, instead of at the standard anemometer height of 10 m. The speed at 1.5 m is obtained by multiplying the 10-m value by a factor of 0.667.

(2)   It is based on a model of the human face, and incorporates modern heat transfer theory on how much heat is lost by the body to its surroundings during cold and windy conditions. It also uses a consistent standard for skin tissue resistance to heat loss.

(3)   A wind threshold of $1.3 \, \mathrm{m \, s^{-1}}$ is chosen for calm based on observations of the speed of pedestrians at intersections.
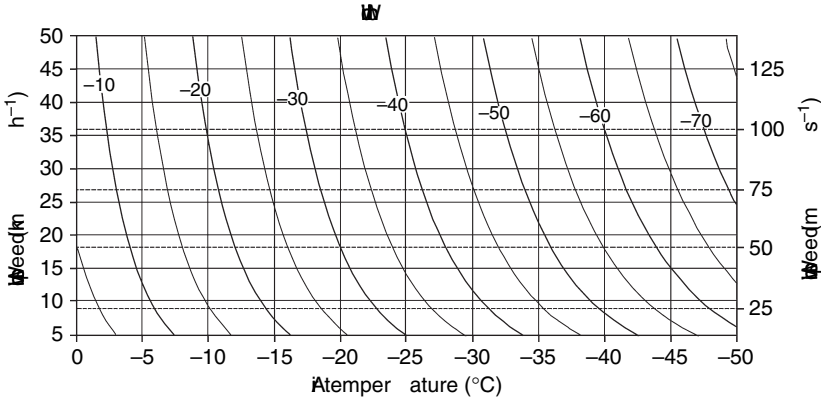
Fig. 6.2 **The index of windchill equivalent temperature versus air temperature and wind speed (based on Osczevski and Bluestein, 2005; and Meteorological Service of Canada, 2005).**

Currently, the index does not take into account any offsetting effect for wind-chill due to solar radiation although such a term may be added later. Shitzer and de Dear (2006) also point out that there are significant discontinuities in W at the assumed "calm" condition, and propose corrections to the formula to make the transitions gradual rather than abrupt.

Obviously, windchill is a highly significant factor in mountain environments. Smithson and Baldwin (1979) find a linear relation between mean annual windchill (based on the original formula expressed in $W\,m^{-2}$) and elevation (h in m) in upland Britain:

$$W = 0.456h + 394$$

Monthly averages in January are $1308\,W\,m^{-2}$ on Ben Nevis (1343 m) and $814\,W\,m^{-2}$ at Moor House (561 m), with corresponding hourly extremes of $3925\,W\,m^{-2}$ and $1907\,W\,m^{-2}$, respectively. In windy wet conditions, which are common at low elevations in maritime mountain areas, the cooling effects may be even greater (see below under *Clothing*). Greenland (1977) shows that at 3750 m on Niwot Ridge, Colorado, the windchill threshold associated with the freezing of exposed flesh ($-31\,°C$ old scale windchill equivalent temperature) occurs more than 50 percent of the time, December through February. For the new scale the thresh-old temperature is $-27\,°C$.

Cold-sensitive receptors are located primarily in the skin, and also in abdominal viscera, the spinal cord, and hypothalamus (Webster, 1974a). The last of these monitors cold signals and initiates body responses (Van Wie, 1974). Cold stress induces several body reactions in the attempt to maintain body temperature. A common and noticeable response is shivering, which serves to increase muscular heat production four- or five-fold (Carlson, 1964), although much of this is lost by convection from the skin. Another prompt reaction to cold exposure is the
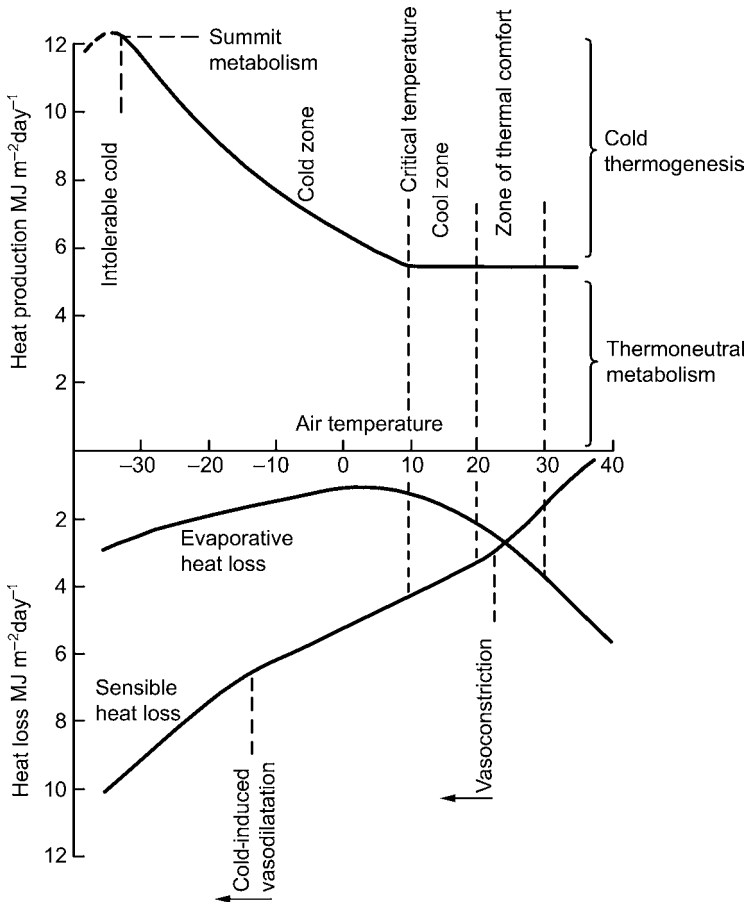
Fig. 6.3 Schematic illustration of the heat exchanges of a homeotherm for air temperatures between $-40°$ and $+40°C$ (from Webster, 1974a).

constriction of blood vessels (vasoconstriction) especially in the extremities. This is illustrated in the schematic temperature metabolism curve for homeotherms in general, shown in Figure 6.3. However, at air temperatures below 0 °C, blood vessels in the extremities must dilate in order to prevent freezing; this "cold-induced vasodilatation" [Webster (1974a: pp. 59–64) gives a general account of it in homeotherms] increases the sensible (conductive and convective) heat loss. Increases in evaporative loss at very low temperatures (see Figure 6.3) are a result of the increase in ventilation rate associated with the increased metabolic rate.

When the body cannot maintain its core temperature, the condition of *hypothermia* results. Unconsciousness occurs when the core temperature falls to about 30 °C and the heart generally ceases at 26 °C (Ward, 1975; p. 309), although a few exceptional survivals have been reported.

Recurring, or prolonged, exposure to cold, damp conditions commonly results in swelling and irritation of parts of the skin on the hands and feet, forming chilblains or

in more severe cases, immersion foot. If the skin temperature locally drops below freezing, the tissues freeze ("frostbite") (Smith, 1970). Following an initial localized burning sensation the affected area goes numb. If untreated, the area may turn black and develop gangrene. Various medical studies indicate that *rapid* re-warming minimizes tissue loss. Ward (1975) recommends that generalized warming, for example by intake of hot liquids, be combined with local warming to the injury. The latter could take the form of 20-min applications of a container of water at 44 °C, or body contact with another individual. He emphasizes also that surgery is seldom necessary, although complete recovery of an affected part may take from 6 to 12 months.

6.1.1.3 Combined influence

High altitudes, especially in winter in middle and high latitudes, combine the problems of cold, dry air and hypoxic environment. Exposure of newborn infants to such stresses may be a special hazard although little is known about this. Ward (1975; pp. 296–9) states that cold injury appears to be more common, for equivalent temperatures, at high altitude. For example, fatigue due to hypoxia, and weight loss if a high-altitude stay is prolonged, decrease the heat that can be produced by activity; greater ventilation augments heat loss from the lungs, and hypoxia may impair judgment with regard to critical behavioral adjustments (such as clothing worn, etc.). However, the cold, dry atmosphere at high altitudes does facilitate the removal of body heat generated by physical exercise and this allows a higher work rate (Lahiri, 1974).

Another combined effect at high altitude results from the presence of a snow cover together with the augmented ultraviolet component of solar radiation. The high surface albedo causes intense glare, which can lead to snow blindness, as well as severe facial sunburn, unless protected. Blowing snow, which can reduce visibility to < 50 m and exacerbate white-out conditions, may lead to disorientation and losing one's direction, increasing the risk of exposure and hypothermia.

6.1.2 Clothing

The thermal insulation available to a clothed individual comprises three components due to skin tissue, the air, and clothing. The scientific study of cold-weather clothes was given a considerable boost by military needs during the Second World War. Polar expeditions and the growth of high-altitude climbing and winter sports have also contributed to this interest.

The insulation provided by clothing is commonly expressed in units of "clo." One clo maintains a seated person at a comfortable temperature indefinitely in an environment of 21 °C, air movement of 10 cm s^{-1}, and a relative humidity below 50 percent (assuming a basal metabolic rate of 58 W m^{-2} (50 kcal m^{-2} h^{-1}). Polar or alpine expedition clothing may have a clo value of 3 or more, while the wool garments (excluding poncho or hat) of the Quechua Indians on the Altiplano have a clo value of 1.2–1.4 (Hanna, 1976). Calculated requirements at 3100 m for

climatic conditions in the Alps at 1300 m range from 2.5 clo in summer to 4.5 clo in winter for moderate activity (climbing 260 m altitude h^{-1} with $1 \, km \, h^{-1}$ wind; 140 W energy); to 2.0 clo in summer to 2.5 clo in winter for vigorous activity (climbing $520 \, m \, h^{-1}$ with $2 \, km \, h^{-1}$ wind; 273 W energy) (Hammer *et al.*, 1989). For comparison, the clo value of skin tissue may range from 0.3 when exercising, to 0.55 at rest, and that of the air from 0.1 in strong winds to 1.0 when the air is still (Pugh, 1966). Weather conditions have a major effect on the insulative properties of clothing. Pugh notes that the insulation of a wind-proof parka may be reduced 30–40 percent with winds of $12 \, m \, s^{-1}$. Clothing with a normal insulation of 1.5 clo may have a value of only 0.2–0.5 when wet.

Apart from the thickness of clothing it is also worth considering its distribution in relation to body heat production and loss. When man is active, the skin and muscles generate 73 percent of the body's heat, the chest and abdomen 22 percent, and the brain 3 percent (van Wie, 1974). However, when resting, the brain produces 16 percent of the total and the chest and abdomen 56 percent. Clearly, the head and trunk especially should be well protected when an individual is inactive (or injured).

6.1.3   Weather and human comfort

There is a long literature, especially in European countries, on physiological reactions to föhn conditions in and around the Alps (Schmidt, 1930). One of the few well-documented investigations of such weather-sensitive reactions was carried out by Richner (1979) in and around Zurich, Switzerland, during south-föhn events. Typically, warm southerly flow crossing the Alps overrides a pool of cold air on the north side creating a sharp temperature discontinuity and wind shear at the interface. Gravity wave propagation sets up pressure fluctuations of about 1 mb with periods of 4–30 min. Based on correlation analysis of such events (detected with microbarographs), and of physiological responses for groups of individuals who believed in or disbelieved such effects, Richner (1979) showed an increase in specific ailments and a corresponding decrease in an index of "well-being" as the amplitude of the pressure fluctuations increased. At the same time, no relationships were found with shorter period ($< 4 \, min$) acoustic infra-sound waves. Headaches (the most frequent ailment) also showed no weather relationships. The survey showed the effects to be stronger for women than men, and stronger for workers in air-conditioned buildings, where the pressure fluctuations are also found to be present. The link between pressure fluctuations and human physiology is still hypothetical, but may involve an instability in the normal physiological control system that enables humans to adjust to temporal and altitudinal variations in ambient pressure.

6.1.4   Adaptations

It is appropriate to begin with some definitions. *Adaptation* – morphological, physiological and behavioral – denotes an adjustment that is beneficial to well-being

and to survival in a particular environment (Webster, 1974b; Little, 1976). *Acclimatization* is a phenotypic adjustment to a complex of climatic conditions that may or may not be reversible. (*Acclimation* is restricted to changes induced by *one* environmental factor in a controlled experiment (Hart, 1957).) While the effects of low pressure and low temperature are not wholly separable in high altitude environments, it is convenient to discuss them in turn.

6.1.4.1 *High altitude*

The special capabilities of native populations, such as the Himalayan Sherpas and the Andean Quechua Indians, to live and work effectively at altitudes in excess of 4000 m has been a topic of physiological interest since the 1920s. The available evidence indicates that these peoples develop special features by acclimatization during a lifetime spent at high altitude (Baker, 1969; Hock, 1970; Baker and Little, 1976; Reeves *et al.*, 1981). Mountain peoples tend to have a high breathing rate, and high concentrations of red blood cells and hemoglobin. In the Andes, they also have a large chest and lung volume, although this may be a racial trait. According to Grover (1974), their physiology resembles that of lowland athletes; the native likewise having a slow heartbeat and a high aerobic working capacity. Lahiri (1974) emphasizes that Andean Quechua ventilate *less* than acclimatized lowlanders and that this hyposensitivity persists for at least several years if they move to sea level. He cites data for natives in the Andes and Himalaya, which indicate that hypoxic insensitivity develops in childhood, but studies at Leadville (3100 m), Colorado, suggest that this trait increases with duration of high altitude residence, especially beyond 10–12 years. There appears to be no evidence of this occurring in high altitude animals, however. Baker (1976) notes that the Quechua of Nuñoa in southern Peru have almost no cardiovascular diseases, although respiratory diseases are common. Furthermore, it is now well established that the high-altitude environment of the Altiplano is a cause of reduced fertility in Nuñoa women and of slow rates of physical maturation in the children (Little and Baker, 1976). Nevertheless, the work capacity of Andean natives is identical to that of lowland natives and substantially higher than that of European newcomers, even after a year's acclimatization (Baker, 1976; Little, 1981). The question of a genetic adaptation is still not fully proven and Heath and Williams (1977; p. 227) favor the view that the Quechua have natural acclimatization with partial adaptation (voluminous chests).

From archeological, genetic and linguistic research, it seems that the peoples of Tibet have occupied the high plateau since the Paleolithic. It is uncertain how long the Andean populations have lived on the Altiplano, since over 90 percent of the indigenous population died following the Conquest in the 1500s. The genetic make-up of Amerindian people may or may not include traits derived from high altitude settlement according to Niermeyer *et al.* (2001).

Established effects of high altitude include low birth weight. Data from Tibet, South America and North America show mean birth weights decreasing by 100 g

(about 0.3 percent) per 100 m increase in altitude (Moore *et al.*, 1994). However, the reduction, which is attributed to retarded intrauterine growth as a result of insufficient oxygen delivery for the fetus, is greatest in North America and least in Tibet. Lower birth weight can lead to subsequent decreases in neonatal and infant survival, particularly in the absence of adequate health care. Andean and Tibetan children and adolescents show delayed and reduced growth compared with lowland groups, but nutritional and socio-economic factors seem to be involved. Quechua and Aymara high-altitude residents have enlarged chest dimensions, but it is lung volume and vital capacity that assists gas exchange and alveolar–arterial oxygen diffusion. Total lung capacity is found to be 25–40 percent greater in Andean and Tibetan residents at 3600–4500 m than is predicted for sea level (Niermeyer *et al.*, 2001). Aerobic capacity in Aymara and European children living in La Paz (3750 m) is about 10 percent less than in their lowland counterparts. However, those born and raised in La Paz have greater aerobic capacity than persons who only moved there as adults according to Frisancho *et al.* (1995).

Recent studies confirm Buskirk's (1969) finding that aerobic working capacity declines 10–11 percent per kilometer increase in altitude. Nevertheless, it is greater in lifelong residents at high altitudes than in acclimatized newcomers. Niermeyer *et al.* (2001) state that for native residents it is 16 percent higher in the Andes and 12 percent higher in the Himalayas than for acclimatized newcomers. The causes of higher levels of aerobic capacity among high-altitude residents are attributed to better oxygen transport. This is achieved partly by higher effective alveolar ventilation among Himalayan (but not Andean) natives, giving rise to increased ventilatory response to hypoxia. The alveolar–arterial oxygen difference is also lower in high-altitude residents in the Rocky Mountains, Andes and Himalayas than in acclimatized migrants. Another possible factor is increased tissue oxygen utilization by higher arterial oxygen content, blood flow, or tissue oxygen extraction (Niermeyer *et al.*, 2001).

Even permanent residents of high altitudes can sometimes lose their ventilatory acclimatization to the hypoxic environment. Severe arterial hypoxia develops, causing low oxygen pressure in the lungs, and stimulating excessive polycythemia. This state, known as chronic mountain sickness (CMS) (*soroche* in the Andes), can lead to congestive symptoms and heart failure if the individual remains at high altitude. About 80 cases have been documented, three-quarters of them in males, with a 12 percent mortality rate (Ward, 1975; p. 270). Common symptoms of CMS include headaches, dizziness, fatigue, sleep disturbances, and dilation of veins in the hands and feet (Monge *et al.*, 2001). Since many recorded cases are from the Andes, Heath and Williams (1977; p. 150) consider that the disease may be a clinical syndrome rather than a pathological entity. Other cases are recorded, however, from Leadville, Colorado (R. F. Grover, pers. comm., 1980).

A study of mestizo residents of Cerro de Pasco, Peru (4300 m), found excessive polycythemia (indicative of CMS) in 16 percent of 2875 males and 9 percent of 152 females between 30 and 54 years of age. For males aged 60–69 years, the figure rose

to 34 percent (Leon-Vallarde *et al.*, 1993). In Tibet, Xie and Pei (1981) reported CMS in 13 percent of male migrant Han workers compared with 1 percent of male native workers in Lhasa (3650 m); the corresponding figures were 32 and 5 percent in Gyangze (4040 m) and 38 and 14 percent in Naqu (4500–4700 m). In each case, the incidence of CMS was much less among women workers and also among native farmers and herders.

6.1.4.2 *Sub-freezing temperatures*

Acclimatization to cold has been most studied in the polar regions and experimental situations. It is a controversial subject, but a detailed review by Webster (1974b) argues that certain adaptations are observed. He specifies the different criteria that must be met to establish some type of cold acclimatization. The three major ones are: (1) a reduced heat loss by increased tissue insulation; (2) a reduced susceptibility of the extremities to pain or cold injury; and (3) a reduced cutaneous sensory threshold. There seems to be no firm evidence that the thermoneutral metabolic rate (TMR) can be modified by acclimatization. This rate is raised approximately 10 percent above the basal metabolic rate by food intake and activity (Webster, 1974a). While it has been claimed that the Eskimo show metabolic acclimatization, their high metabolic rates (e.g. Folk, 1966) are due to their large food intake.

Australian aborigines and Kalahari bushmen can sleep in the open even when night temperatures cause the body heat loss to exceed the TMR. Heat production is increased by shivering, while heat losses are reduced as a result of the high tissue insulation and generalized vasoconstriction. Nevertheless, they can tolerate some degree of hypothermia as shown by the nocturnal decrease of rectal temperature (Webster, 1974b). This response may be called hypothermic acclimatization, although Webster prefers the term metabolic habituation. (Habituation is a gradual (quantitative) decrease in physiological response due to a repeated stimulus (Webster, 1974b).) Tromp (1978) suggests that exposure to (simulated) high altitude, above 2000 m, can improve thermoregulatory efficiency in asthmatic and rheumatic patients.

Much more common, and of greater interest from the viewpoint of mountain environments, is the tolerance of severe local cooling of hands of feet. This has been identified in Eskimos, Arctic Indians, polar explorers, groups of fishermen, and Quechua Indians of highland Peru. Research with the last group (Little, 1976) suggests the maintenance of a high heat loss by enhanced blood flow to the extremities (and perhaps a 5 percent increase in basal metabolism). Gloves and footwear are not worn and Hanna (1976) considers that adaptation must occur during childhood. Toe temperatures as low as 20 °C were recorded in children, who often spend long hours watching and herding the animals. Webster (1974b) refers to this response as vasomotor habituation since the usual vasoconstriction response is diminished.

The Quechua also display behavioral adaptations to their environment. Air temperatures in the coldest month fall several degrees below zero at 4000 m and

indoor temperatures in the unheated stone houses may be only 4 °C. Families usually sleep in groups of two or more to combat the cold. However, Hanna (1976) notes that some cold stress appears to affect children in the early evening before they go to bed.

6.2   WEATHER HAZARDS

Many features of the mountain climatic environment present a hazard to the unwary or inexperienced. Apart from the obvious problems caused by fog due to orographic cloud, strong winds and low temperatures, the general rapidity of weather changes in mountains is a factor not always taken into account. Snow and hail showers can occur on most mid-latitude mountains in the summer months to the surprise of casual tourists from the lowlands. Here, however, we consider two specific weather-related hazards characteristic of different seasons.

6.2.1   Lightning

Lightning is both an individual hazard to hikers and climbers in summer and a major cause of forest fires. Approximately 70 percent of all forest fires in the western United States are attributed to lightning, and in a 20-year period in the thirteen western states and Alaska, there were 132 000 lightning-caused fires (Fuquay, 1962). Based on studies in Montana (Fuquay, 1980), the US Forest Service has developed a guide to identify and forecast lightning activity level (LAL) in connection with fire hazard. This is shown in abbreviated form in Table 6.1.

Table 6.1 US Forest Service guide to lightning activity level (LAL).

LAL cloud conditions	Average cloud–ground lightning rate (min^{-1})	Cloud–ground lightning density (6500 km^2)$^{-1}$	Maximum radar echo height (m asl)
1 No thunderstorms	–	–	–
2 Few towering Cu	≤ 1	20	< 8500
3 Scattered Cu, occasional Cb	Max. 1–2	40	7900–9700
4 1–3/10 Cu, Cu congestus	Max. 2–3	80	9100–11 000
5 Extensive Cu congestus, moderate–heavy rain with Cb	Steady flashes at some place during storm; max. > 3	160	$> 11 000$
6 Scattered towering Cu, high bases; virga common	≤ 0.5	–	–

Source: after Fuquay (1980). Cu, cumulus; Cb, cumulonimbus.

The unit of area considered is a square approximately 80 km on a side, corresponding to the largest area over which lightning activity can be effectively monitored from a fire lookout point. Storms become more intense up to LAL 5, although the area covered by the storm does not increase at the same rate; even with LAL 5, measurable precipitation usually affects less than half of a forecast area. The relationship between lightning and precipitation is not well documented, but Table 6.1 indicates that lightning activity is related to cloud development, as measured by the maximum height of radar echoes. In western Montana, cloud tops need to be above about 6500 m for thunderstorms to occur.

Lightning density (or risk) increases geometrically with LAL-value, LAL 6 is a special category for dry storms which create a high risk of lightning-caused fires. Cloud-to-ground (C–G) flashes occur in an approximately 1:4 ratio to total lightning activity.

In the Rocky Mountains near the Montana–Wyoming border, there are about 44 days with thunderstorms in July–August. This gives rise to 6 C–G flashes per 10 km^2 near Helena decreasing northward to 2 per 10 km^2 at Missoula and only 0.25 per 10 km^2 in Glacier National Park (Fuquay, 1962). The average frequency of LAL classes on thunderstorm days in western Montana during summers 1965–7 was 35 percent each for classes 3 and 4, 18 percent LAL 5, 10 percent LAL 2, and 2 percent LAL 6 (Fuquay, 1980). Cloud-to-ground strikes in the western United States increase four-fold between 500 and 1700 m, but then show little change up to 3000 m altitude, based on two summers' data analyzed over 2200 km^2 grid blocks (Reap, 1986).

Radar studies in Colorado show that on the large scale there are preferred areas for convective cells to develop (Karr and Wooten, 1976; and see p. 222). In the morning, such areas are over the east slopes of the Front Range, with subsequent growth taking place over the mountains. In the late afternoon, development takes place over ridges that extend eastward from the Rocky Mountains into the plains.

On a local scale, lightning strikes are strongly related to the terrain profile. Exposed ridges and summits are widely recognized to be dangerous localities due to their build-up of charge and the usually preferred path of lightning to the nearest high point. Protruding objects sometimes release streamers of current, referred to as coronal discharge (St. Elmo's fire), and in the case of a standing person, this may be dramatically illustrated by the hair literally standing on end! Buzzing or hissing sounds may result from ionization currents from protruding objects. If thunderstorms are nearby, this is a clear and imminent hazard warning. Any slope convexity is more prone to a direct lightning strike than a level or concave surface; but even in such sites, ground currents also pose other less well-known dangers. (Peterson, 1962; Taylor, 1975). When a projection is struck by lightning, the current seeks the path of least electrical impedance. On rock, this path is generally over the surface and downward. Short gaps and crevices tend to be jumped so that it is dangerous to shelter in narrow, vertical gullies or small holes or beneath rock overhangs. These can act as "spark gaps," which the body bridges for the current

path. Large isolated rocks should also be avoided. Gullies and crevices with flowing water are also paths of low resistance for electrical current. The recommended procedure for anyone caught out in a thunderstorm is to crouch down in an open slope concavity. One should be at least the body height away from any adjacent cliff or large rock (Peterson, 1962; Herry and Foray, 1994). The zone of protection from direct strikes at the base of a 20 m high rock wall is between 2 and 20 m from the cliff. Insulation between the body and the ground can be obtained by sitting on a rucksack, coil of rope, folded dry clothing or a small *loose* rock.

The hazards of lightning in mountains to structures, individuals and livestock have been addressed at multidisciplinary conferences held in Chamonix–Mont Blanc, France (Comité de Foudre et Montagne, 1994). The results of a survey in the Swiss Alps show that accidents due to lightning account for less than 1 percent of all mountaineering emergencies. Durrer *et al.* (1994) report that during July–August 1991–3 there were 23 cases: 40 percent hikers, 25 percent rock climbers and 35 percent mixed climbers, and 30 percent of those involved died. In alpine accidents in Austria, during May–September, 1986–92, there were 63 individuals involved in lightning accidents with 12 deaths (Nachbauer, 1994). Lightning accounted for only 1.2 percent of alpine fatalities overall, compared with over 40 percent each for falls and cardiac arrest, but the risks due to lightning injury on storm days exceed those due to the other causes. Lightning risk prevention primarily involves awareness of thunderstorm development through attention to weather forecasts, direct observation of cumulus cloud build-up, and avoidance of dangerous terrain, huts without lightning protection and climbing routes with wire ropes. The body can receive a direct lightning strike, or a side flash, for example from a nearby tree. The main outcomes to humans are: failure of the respiratory system, burns, temporary paralysis, loss of consciousness and ruptured eardrums (Taylor, 1975). First aid for lightning injury involves treatment for burns and electric shock. External chest massage may be necessary in cases of heart fibrillation, and mouth-to-mouth artificial respiration if breathing has ceased.

6.2.2   Snow avalanches

For anyone adequately clothed against windchill effects, the most serious wintertime hazard in mountain areas is the snow avalanche. Most alpine countries operate some form of warning service, based on weather forecast information and snow survey data, for mountain travelers on roads or cross-country ski trails. In the European Alps protective structures such as fences and snow sheds are a prominent feature of the mountain landscape. Even so, property damage and deaths result each year in mountainous areas from avalanche occurrences. Austria, Japan and Switzerland each report an average yearly death toll of between 25 and 36 victims. Property damage in the United States in 1967–71 was US\$ 250 000 per year (Williams, 1975) and these figures are increasing with more

winter sports activity, the development of mountain areas and higher property values.

Avalanches form when the snow pack resting on a slope undergoes failure. New dry snow can cling to 40° slopes, whereas wet slushy snow may slide even on 15° slopes. The critical angle of repose depends on the temperature and density of the snow, which determine its texture and wetness. Overloading due to newly fallen or wind-blown snow deposition, or to the weight of a skier, may cause the critical angle on a particular slope to be exceeded. Alternatively, physical processes in the snow pack may lead to changes in its structure and cohesion. Failure can occur near the surface, in which case a small mass of snow slips downslope leaving an inverted V-shaped scar. This gives rise to a *loose-snow avalanche*. Most of these are relatively minor "sluffs," but even so they may be hazardous to an individual skier or mountaineer. The second type of failure involves the fracture of a slab perhaps 1 m or more thick on slopes of 20–45°. *Slab avalanches* may involve dry or wet snow, but both are associated with shear stresses in the snow exceeding the shear strength in some underlying layer. Dry snow falling at $30 \, \mathrm{m \, s^{-1}}$ over a long path may generate an airborne *powder avalanche* ahead of the sliding snow. This powder avalanche travels at high velocities as an atmospheric turbidity current, and causes damage by wind blast up to 100 m beyond the limit of the run-out zone. Details and illustrations of these processes may be found in Mellor (1968), Perla and Martinelli (1975), and Perla (1980).

An avalanche track comprises an upper starting zone, the main track itself, which is often clearly delimited by a swath of grassy or shrubby vegetation running down below the tree line into the montane forest, and a lower run-out zone, which may have a more or less well-marked debris fan at the foot of the slope. Defense structures include snow fences and nets in the starting zone, to help maintain the stability of the snow pack, and deflecting structures (walls and snow sheds) as well as energy-absorbing structures such as concrete or earth mounds, in the run-out zone (Frutiger, 1977). In areas of high risk, walls of buildings must be designed to withstand perpendicular pressures of $3 \, \mathrm{t \, m^{-2}}$ (Aulitsky, 1978). Avalanche mapping and land-use zoning is now being applied in many mountain areas to minimize these problems, but the hazard remains for skiers and other back-country travelers.

Interest here is primarily with the weather phenomena that favor avalanche situations and this aspect is less well understood than the snow mechanics. For the San Juan Mountains of southwest Colorado, Bovis (1977) identified different key meteorological variables for dry- and wet-snow avalanches by discriminant analysis. Dry-snow avalanches are particularly associated with high snowfall amounts over the preceding 4 days and with wind redistribution of the snow 12–24 h before the event. Wet-snow slides, which mainly occur in spring, are associated with the antecedent air temperature values. Another situation, which is common in dry continental interiors, such as the Rocky Mountains, but less usual in the maritime coastal ranges of North America, is the formation of depth hoar by temperature-gradient metamorphism in the snow. The existence of steep temperature gradients

in a snow pack during clear cold weather causes upward transfer of water vapor producing larger and weaker grains. New snow deposition on such an unstable base may cause collapse in the depth hoar layer triggering a slab avalanche. In the San Juan Mountains, Colorado, the large diurnal range of winter radiation and temperature regimes creates a distinctive "radiation snow climate," where temperature-gradient metamorphism is a factor in most major observed avalanches (LaChapelle and Armstrong, 1976).

A climatology of avalanche conditions in mountain ranges of the western United States has been prepared by Mock and Birkeland (2003) based on the categorization of snow climatic types by Sturm *et al.* (1995). In essence, thresholds of temperature, SWE, and snowfall are used to separate coastal (Pacific Northwest), interior/transitional (Idaho, Utah, and Montana) and continental regions (Colorado Rocky Mountains). The coastal zone has high values of precipitation, snow density and temperature, whereas the continental zone has correspondingly low values of these, high temperature gradients in the snow and the presence of depth hoar leading to unstable snow packs.

Avalanche forecasting is based on information on existing snow pack characteristics and on weather conditions – particularly air temperature in the starting zones, wind speeds over the ridge crests, and precipitation amounts and rates. In Colorado, orographic precipitation is now predicted using the numerical model developed by J. O. Rhea, described on p. 299, adapted for 12-h intervals (Judson, 1976, 1977). Critical total water equivalents for snow accumulation for avalanche occurrence are of the order of 2.0–2.5 cm (Perla and Martinelli, 1975). Snow loading on slopes is also associated with wind transport, although this factor is mainly important in association with precipitation events. For lee slopes, winds of $5\,\mathrm{m\,s^{-1}}$ are required according to Perla and Martinelli (1975), although this figure seems low compared with theoretical values of the threshold speed for blowing snow transport by turbulent diffusion (p. 324). The development of cornices, where air motion decelerates immediately in the lee of a ridge crest, is an important feature of the snow cover, since cornice collapse will often trigger an avalanche if the mass of snow falls onto the slopes below.

6.3 AIR POLLUTION IN MOUNTAIN REGIONS

It is ironic that early in the twentieth century sanatoria were located in alpine areas because of the purity of mountain air. Today, many mountain valleys face problems of air pollution associated with the development of residential and tourist settlements, industrial establishments and power stations. Emissions from such sources are concentrated by valley inversions at night and more persistently in winter months. Major disasters, as a result of intense valley air-pollution episodes in the Meuse valley, Belgium, in December 1930 that caused 63 deaths, and at Donora, Pennsylvania, in late October 1948 (21 deaths) were among some of the catalysts of research on pollutant transport. Until recently, most studies of effluent

dispersion had been carried out in level open country where simple diffusion theories are readily applicable, but measurements of pollution transport from sources in mountain valleys show the necessity for more complex models in order to make reliable predictions relating to proposed new developments.

6.3.1 Pollution characteristics

Pollutants may originate from a point source (a chimney), a line source (a highway) or an area (a city, a forest fire). They may occur as gases (carbon monoxide, nitrogen dioxide, ozone, sulfur dioxide) or particles (dust, smoke) of both natural and anthropogenic origin. The term aerosol refers to a colloidal system of very fine particles dispersed in the air, as in smoke and dust storms. There are also primary pollutants emitted into the atmosphere and secondary pollutants produced by transformations, such as chemical reactions, in the atmosphere. Deposition can occur by gravitational settling (dry deposition), impaction and adsorption on surfaces, or due to scavenging by precipitation.

Pollutant plumes are subject to dispersion by the wind and dilution by mixing with cleaner air. Such mixing is produced by plume stretching by the wind and turbulent eddies resulting from free (thermal) and forced convection; the latter may arise through vertical and horizontal wind shear or from terrain-induced eddies. In fine weather over land the depth of the atmospheric boundary layer that is well mixed typically deepens during the day. It is shallow in the early morning as a nocturnal inversion breaks down, and is generally capped by a stable layer. By late morning, heating causes the top of the mixed layer to rise and a 1–2-km-deep convective boundary layer builds. On a regional scale, the topography may greatly influence the mixing depth (Holzworth, 1967) while synoptic weather regimes determine atmospheric stability and the likelihood of inversion conditions. Daly et al. (2002) develop a knowledge-based system, based on PRISM (see p. 290), to define regions in the conterminous United States where the terrain typically rises above the level of winter inversions, should they form. Almost all of the area so defined is in the montane western United States. The frequency of anticyclonic conditions is also of special importance in pollution climatology due to the light winds and stable atmosphere (Holzworth, 1962). The scope of air pollution is immense and only the effects of mountain terrain on pollutant transport and dispersal, and pollution conditions in mountains, are discussed here.

The effect of altitude on pollution concentrations is being addressed in several localities. In the Alps, Li et al. (2005) find that *hydrocarbon* concentrations are generally much greater at Arosa (2010 m) than Jungfraujoch (3680 m). Furthermore, the diurnal rise of the boundary layer over the Alps leads to differences in timing of peak concentrations; and an increase in concentrations in the morning at Arosa and in the afternoon at Jungfraujoch. At the latter site, summer aerosol values are 10 times those in winter according to Baltensperger et al. (1997). There

are peak concentrations in late afternoon in summer associated with a stable atmosphere. Slope/valley winds within a certain valley–plains catchment area appear to account for the transport to high elevations since the local slopes are snow and ice covered.

There is a lack of basic long-term data on the altitudinal variation of aerosols and trace gases in mountain regions. A monitoring program in southern Bavaria provides illustrative results, however (Reiter *et al.*, 1987; Reiter, 1988). The measurements show that NO_x levels at Wank Peak (1780 m) are 3–5 ppbv compared with 5–15 ppbv at Garmisch (740 m). SO_2 levels in winter at the mountain site (3–5 ppbv) are also about half those in the valley (5–10 ppbv), but during April–September SO_2 levels are similar (~ 3 ppbv) at both stations, apparently as a result of comparable long-distance transport and convective mixing. An observed positive correlation between SO_2 amounts and concentrations of cloud nuclei, as well as higher levels of sulfate ion during fog conditions at Wank Peak, leads Reiter to point out the possibility that the greater acidity of cloud droplets, compared with rainfall, may accentuate tree damage in zones of fog deposition.

6.3.2   Controls of atmospheric diffusion in complex terrain

The dispersion of pollutants in mountain areas is influenced by the thermal structure of the atmosphere, as well as by the terrain-induced air motion. The following factors are involved to a greater or lesser degree in most locations (Barr *et al.*, 1977; Greenland, 1979).

(1)   The deformation and channeling of the streamlines over and around obstacles.
(2)   The separation of the airflow from the surface over a break of slope or an obstacle (Scorer, 1978; p. 107).
(3)   Lee waves and rotors and internal gravity waves at an inversion interface.
(4)   Slope winds and mountain/valley wind systems.
(5)   The pattern of inversion break-up.
(6)   Enhanced convection due to differential slope heating.

Hanna and Strimaitis (1990) recognize four situations where rugged terrain may exacerbate pollution problems from sources in valleys or basins.

(1)   Plumes impinging on valley sides and hills in stable conditions.
(2)   Cold air pools in valleys and basins where vertical diffusion is minimized.
(3)   Nocturnal drainage flows concentrating pollutants in valleys and basins.
(4)   Valley channeling of gradient winds.

The characteristics of topographically and thermally induced airflows, discussed in Chapter 3, are clearly relevant to the problem of pollutant dispersal, but existing theories seldom prove adequate to make predictions in complex terrain. Special

observation programs are beginning to provide new insights into airflow and pollutant behavior in particular locations and, although it is too early to generalize such results, it is nevertheless worth illustrating some of the findings.

Studies of katabatic flow over a simple slope in the Geysers area, California (Nappo *et al.*, 1989), show that pollutants released at the ground can spread through the depth of the flow, especially over shallow slopes. When releases are elevated above the drainage layer they can be entrained into the layer and so diffused to the ground. Surface concentrations can be high near the source, if a stack releases within the drainage flow, as a result of subsidence in the flow.

Observations with tracers (perfluorocarbon, sulfur hexafluoride) in the Brush Creek Valley, Colorado (see Chapter 3, p. 209 also) show how pollutants are transported and dispersed in valley wind systems. Tracers released at the floor and at 200 m from a balloon, showed well-defined plumes when entrained into the down-valley flow. The external winds appeared to have little effect (Gudiksen and Shearer, 1989). Within minutes of sunrise on the valley wall, upslope flows cause ventilation out of the valley to begin (Orgill, 1989; Whiteman, 1989). This may continue for 2 to 3 h.

It is usual for the base of inversions to rise during the day. The role of surface heating and entrainment of air from the stable layer above the inversion base into the convective boundary layer was first described by Ball (1960) and subsequently modeled by Carson (1973) and Tennekes (1973). The height of the inversion base is calculated as a function of the sensible heat flux at the surface. Models of the rise of inversions have been incorporated into "box models" of pollution in mountain valleys (Tennekes, 1976; Howard and Fox, 1978; Greenland, 1979). Such models ignore the details of plume behavior and examine the total changes in the valley air. Since the walls of the valley prescribe the sides of the box and an elevated inversion is the lid, these simple models have found some success. Greenland (1979) reports that the Tennekes model of inversion rise agreed well with observations made with an acoustic sounder during December 1975–March 1976 at Vail, in the Gore Valley, Colorado. Within this period, observations using a tethered-balloon system demonstrated some unusual features of inversion break-up on 10 December, 1975. Whiteman and McKee (1977) describe how the top of a nocturnal inversion layer descended into the valley, lowering from about 450 m at 0800 h to 100 m at 1130 h. They hypothesize that slope heating forms a thin super-adiabatic layer from which convective plumes penetrate into the cold stable air above. Entrainment of this valley air is initiated by the plumes along the valley slopes, and as the cold air is removed up the slopes, mass continuity causes the top of the inversion layer to descend. Up-valley winds above the inversion deepen into the valley and assist in eroding the top of the cold air until the inversion finally dissipates (cf. Davidson and Rao, 1963). The mechanism of inversion break-up will have important effects for pollutant dispersion (Whiteman and McKee, 1978). Assuming that an elevated source has concentrated pollutants in the stable air over the valley floor, growth of the convective boundary layer leads to *fumigation*, or downward transport, of

these pollutants to the valley floor through convective mixing of the boundary layer and the stable air above. This sequence is probable in wide shallow valleys where slope flows are less effective in removing air from the center of the valley. If the convective boundary layer grows slowly, the pollutants sink as the core of the stable layer descends, producing high concentrations at ground level. This pattern is likely over snow-covered terrain. Once the pollutants are entrained into the boundary layer, in this second case, they are advected up the valley sides and dispersed into the air above.

In a study of Huntingdon Canyon, Utah, tracer releases (oil fog and sulfur hexafluoride gas) were used to assess the nature of atmospheric transport and diffusion (Start *et al.*, 1974, 1975). The canyon is steep-walled and 400–500 m deep. Releases were made from the 183 m stack of the power plant in the canyon entrance, during lapse to neutral stability conditions, and from sites on the canyon floor or walls during inversions. It was found that in every case of stack release, samples from the canyon floor and walls are 1.5–3 times more dilute than concentrations from the plume center line and that the plume concentrations are less than those expected theoretically over flat terrain (Pasquill, 1961; Scorer, 1978; Chapter 2). Under inversion conditions, turbulent mixing produces nearly uniform concentrations along the canyon floor and these concentrations are closer to those expected over flat terrain. Start *et al.* (1975) also examined the characteristics of plume impaction on the canyon walls. They conclude that filament-like plumes are unlikely to occur in steep-walled canyons. The evidence for enhanced mechanical turbulence provided by these observations suggests three special airflow phenomena. These are: turbulence generated around the adjacent summits, with roll eddies which transport momentum down into the canyon; helical circulations triggered by the interaction between katabatic slope winds and air drainage from side canyons; and small-scale wake turbulence associated with airflow around and over protrusions of the canyon walls (see Figure 6.4) (cf. Davidson, 1963). The occurrence of roll eddies with cross-canyon flows has also been reported by Clements and Barr (1978) in Los Alamos Canyon.

Other investigations have been carried out by Start *et al.* (1974) at the Garfield copper smelter near the south shore of the Great Salt Lake, Utah, and adjacent to the rugged Oquirrh Mountains. The ground rises 600–1000 m, within 3 km south of the smelter. Gas tracer studies again show dilutions two to four times greater than would be estimated for flat terrain in the elevated plume center lines. Lateral plume spreading is also about twice as great as over flat terrain. Under lapse conditions, plumes are deflected aloft over the ridges and ground-level concentrations are much smaller than those measured aloft. With a strong stable layer just above the ridge tops, a pollution plume may flow in a shallow layer over the mountains. Rapid vertical mixing leads to nearly uniform vertical concentrations downwind, but ground-level concentrations may be up to twice those in the air layer due to ground reflection effects (Zone 4 in Figure 6.5).

(a)   (b)
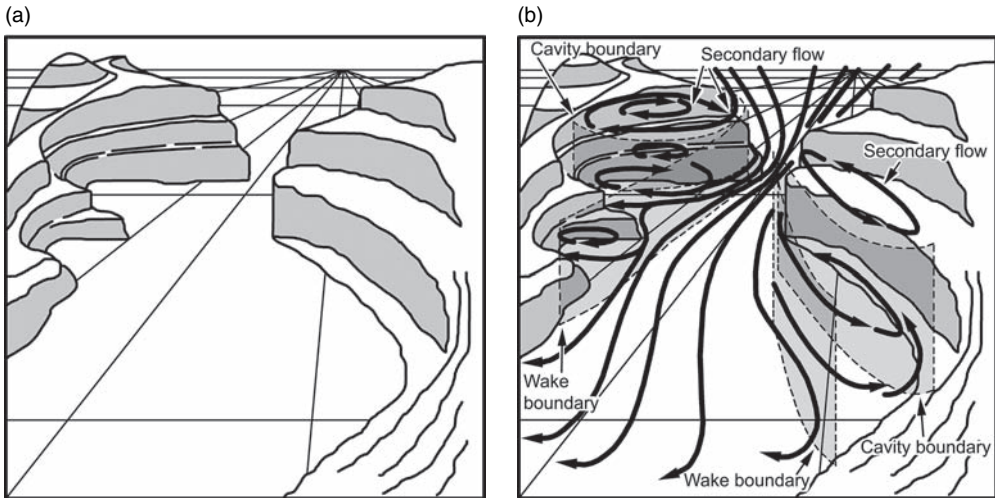
Fig. 6.4 **Schematic model of turbulent wake effects associated with airflow along a canyon: (a) oblique view of canyon; (b) airflow along the canyon (from Start *et al.*, 1975).**
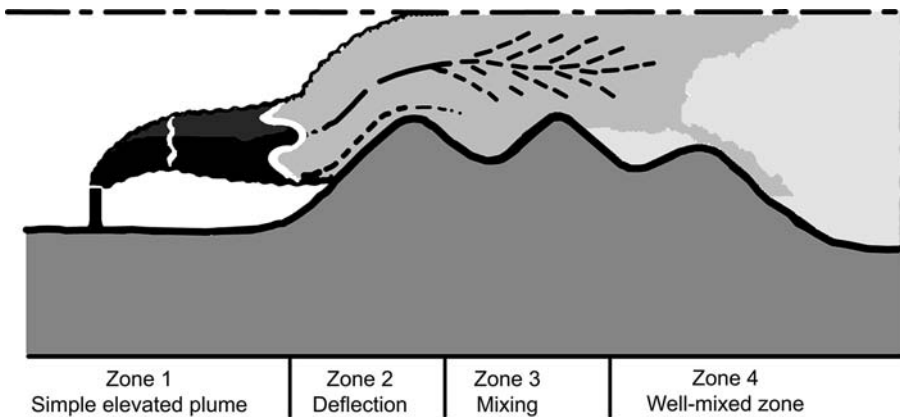
Fig. 6.5 **The dilution of an airborne plume flowing across nearby elevated terrain. Four zones of plume behavior and predicted vertical mass distribution are shown (after Start *et al.*, 1974).**

Whether a pollutant plume will impact on the front surface of terrain downwind, as sketched in Figure 6.4, or whether it crosses the hilltop, depends on the height of the "dividing streamline," where the flow crosses the barrier, rather than being deflected around it or blocked (Chapter 2, p. 76). Experiments with a laboratory model indicate that if the source is below the dividing streamline height, then the plume does impact on the mountain front. If the source is above this critical height, the plume crosses the barrier and surface concentrations vary inversely with the height of the source (Snyder and Hunt, 1984).

Regional-scale pollutant dispersal and deposition is now being analyzed using two- and three-dimensional meso-scale models (see Chapter 3, p. 236). Mass

conserving models, such as that described by Sherman (1978) have been used to model the effects of varying atmospheric conditions on pollutant distribution (Lange, 1978).

Atmospheric deposition in high mountain regions that have a seasonal snow pack has received increased attention since it was recognized that the accumulated chemical pollutants are released during the short snowmelt interval in spring–early summer. In the United States, the National Atmospheric Deposition Program (NADP)/National Trends Network (NTN) provide atmospheric deposition data for major acid anions and base cations, as well as ammonium and hydrogen ions. However, there are few high-elevation stations. Fortunately, snow pack samples for nitrates and sulfates in the Rocky Mountains (2400–3500 m) compare closely with winter volume-weighted mean values from paired NADP/NTN sites for 1992–9 (Clow et al., 2002). Nanus et al. (2003) combined weekly NADP/NTN wet deposition data from 27 sites and annual snow pack data from 71 sites near the Continental Divide from northern New Mexico to northern Montana, with estimates of precipitation at 1-km resolution based on PRISM (see Chapter 4) to generate maps for the Rocky Mountain region. Concentrations of nitrate and sulfate show a general increase from northwest to southeast. Nitrate (sulfate) concentrations range from 3.2–21.5 (3.1–19.3) μeq. l^{-1}. Average annual deposition reaches 2–3 kg ha^{-1} for nitrate and 8–12 kg ha^{-1} for sulfate with maxima in the Park Range of northwest Colorado, the Front Range, and the Wasatch Front in northeast Utah; the last two areas are adjacent to major urban corridors.

Meso-scale primitive equation models in one and two dimensions have been available for a number of years (see Pielke, 1985, 2002). Micro-scale processes that affect the dispersion of pollutants are now being incorporated into such models. A two-stage approach to modelling pollutant transport can be employed, where estimates of wind components and their departures obtained from a mesoscale model are combined with micro-scale turbulence statistics and used as input to a Lagrangian (i.e. trajectory following) model of particle dispersion (Pielke et al., 1987). However, sufficient field data to validate such models fully is seldom available. A specific regional study for the Swiss Jura is described by Beniston (1987). A meso-scale model is developed for an area 20 km × 20 km, with a horizontal resolution of 500 m and vertical resolution of 250 m. This is coupled to a micro-scale model for the city of Bienne (4 km × 4 km) with corresponding resolutions of 100 and 10 m, respectively. Plume trajectories are calculated and Beniston shows the effects of channeling by the Jura on synoptic flow directions, as well as the influence of cloud cover and the urban heat island.

The modeling of pollutant dispersal in the boundary layer over complex terrain follows one of three general approaches. Gaussian plume models, mass conservation (box) models, and three-dimensional numerical models based on the diffusion equations (Deardorff, 1978; Greenland, 1979). The plume model is applicable for the determination of pollutant concentration downwind from a source (at the

ground, or elevated). Its application depends on the determination of low-level stability, which is a function of cloud cover, solar radiation and wind velocity. The mass conservation model assumes that surface emissions over an area are fully mixed in a specified air volume or box (Venkataram, 1978). Concentration changes in the box, typically prescribed by the valley sides and an inversion lid, are determined in terms of an emission rate, mean wind speed, a mixing depth, and the air volume flowing through the box. This approach has been applied to simple mountain valley cases (Greenland, 1979) and in complex regional models.

In a broad-scale study for Switzerland, Furger *et al*. (1989) utilize information on the height, depth, intensity and duration of inversions, and 850 mb winds for selected weather situations to map typical patterns of low-level airflow during conditions of anticyclonic circulation, bise, föhn, cold front passages and westerly airflow. Low-level air trajectories were determined by equivalent potential temperature analyses.

A regional air quality model (LIRAQ) using the mass conservation equations integrated vertically to the base of the boundary layer inversion has been developed particularly for use in the San Francisco Bay area by MacCracken *et al*. (1978). Two versions treat the transport and dispersion of photochemical species (non-reactive and reactive). The model requires topographic data, source emission rates, initial and lateral boundary pollution concentrations, and meteorological information (wind, inversion base height, diffusion coefficients and radiative flux). The motion and inversion information are supplied via the MASCON model of Dickerson (1987). Sensitivity studies show that emissions, meteorological factors and vertical boundary conditions are significant for regional scale pollutant concentrations, while initial and horizontal boundary conditions, as well as sub-grid scale effects, are very important for local air quality prediction (Duewer *et al*., 1978).

A recent three-dimensional modeling system described by Lu *et al*. (1997) has the following model components: a meso-scale meteorological model incorporating turbulent diffusion, condensation and precipitation over complex terrain, radiative transfers, and ground surface processes; tracer transport treating emission sources, dispersion of gases and aerosols, and dry and wet deposition; and a chemical and aerosol microphysical model that includes gas-phase photochemistry and aerosol chemistry and microphysics. Aerosol nucleation, coagulation, condensational growth, evaporation, sedimentation, chemical equilibrium and aqueous chemistry are treated. Photodissociation rates, heating/cooling profiles, and boundary visibilities are determined.

An important consideration in any pollutant modeling is the availability of emissions data for settlements, industries and traffic in mountain valleys. Additionally, information on winds and mixing depths in the valley must be obtained from observations or modeled, based on comparable studies elsewhere.

Existing regulatory models of the Environmental Protection Agency (EPA) in the United States typically consider "worst-case" scenarios using simple dispersion formulae such as the Gaussian plume. Hanna and Strimaitis (1990) provide a useful

summary of EPA-approved models and the results of field and laboratory experiments to evaluate them. These have been performed for hills (Cinder Cone Butte, Idaho), ridges (Hogback, New Mexico) and narrow valleys (Brush Creek, Colorado, and the Geysers area, California). The dividing streamline concept (p. 76) has been tested in these experiments and good agreement shown with theory. The various investigations suggest that the modeling of pollutant diffusion is satisfactory (within ± 30 percent of mean and maximum observed concentrations) *only* for simple terrain situations (Hanna and Strimaitis, 1990). Moreover, the accuracy is heavily dependent on the availability of suitable input data (e.g. 12 months of hourly observations of wind speed and direction, mixing depth, and cloudiness). Typically, only the first impact of a plume is modeled and separation zones in the lee of a hill are not treated.

BIBLIOGRAPHY

Aulitsky, H. (1978) State in the avalanche-zoning methods today. *Mitt. Forstl. Bundes - Versuchsanstalt*, **125**, 129–43.

Baertsch, P. (2002) The Western European perspective on high altitude medicine. *High Alt. Med. Biol.*, **7**(3), 249–51.

Baker, P. T. (1969) Human adaptation to high altitude. *Science*, **163** (3872), 1149–56.

Baker, P. T. (1976) Work performance of highland natives. In P. T. Baker and M. A. Little (eds), *Man in the Andes: A Multidisciplinary Study of the High-Altitude Quechua*, Vol. 1. Stroudsburg, PA: Dowden, Hutchinson & Ross, Inc., pp. 300–14.

Baker, P. T. and Little, M. A. (eds) (1976). *Man in the Andes: A Multidisciplinary Study of the High-Altitude Quechua*, Vol. 1. Stroudsberg, PA: Dowden, Hutchinson & Ross, Inc.

Baldwin, H. and Smithson, P. A. (1979) Wind chill in upland Britain. *Weather*, **34**, 294–306.

Ball, F. K. (1960) Control of inversion height by surface heating. *Q.J.R. Met. Soc.*, **86**, 483–4.

Baltensperger, U., *et al.* (1997) Aerosol climatology at the high-alpine site Jungfraujoch, Switzerland. *J. Geophys. Res.*, **102**(**D16**), 19, 707–15.

Barr, S., *et al.* (1977) *Workshop on Research Needs for Atmospheric Transport and Diffusion in Complex Terrain*. Albuquerque, NM: Department of Energy Research and Development Administration, Division of Biomedical and Environmental Research.

Beniston, M. (1987) A numerical study of atmospheric pollution over complex terrain in Switzerland. *Boundary-Layer Met.*, **41**, 75–96.

Bovis, M. J. (1977) Statistical forecasting of snow avalanches, San Juan Mountains, southern Colorado, U.S.A. *J. Glaciol.*, **18**(78), 87–99.

Buskirk, E. R. (1969) Decrease in physical work capacity at high altitude. In A. H. Hegnauer (ed.), *Medical Climatology*. Baltimore, MD: Waverly Press, pp. 204–22.

Carlson, L. D. (1964) Reactions of man to cold. In E. Licht (ed.), *Medical Climatology*. Baltimore, MD: Waverly Press, pp. 196–228.

Carson, D. J. (1973) The development of a dry inversion-capped convectively unstable boundary layer. *Q.J.R. Met. Soc.*, **99**, 450–7.

Clements, W. E. and Barr, S. (1978) Atmospheric transport at a site dominated by complex terrain. *Fourth Symposium on Turbulence, Diffusion and Air Pollution*. Boston, MA: American Meteorological Society, pp. 430–5.

Clow, D. W., *et al.* (2002) Comparison of snow pack and winter wet deposition chemistry in the Rocky Mountains, USA. *Atmos. Environ.*, **36**, 237–48.

Comité de Foudre et Montagne. (1994) *Foudre et montagnes*. Paris: Soc. Electriciens Electroniciens et Club Alpin Français, 425 pp.

Daly, C., *et al.* (2002) A knowledge-based approach to the statistical mapping of climate. *Clim. Res.*, **22**(2), 99–113.

Davidson, B. (1963) Some turbulence and wind variability observations in the lee of mountain ridges. *J. appl. Met.*, **2**, 463–2.

Davidson, B. and Rao, P. K. (1963) Experimental studies of the valley–plain wind. *Int. J. Air Water Poll.*, **7**, 907–23.

Deardorff, J. W. (1978) Different approaches toward predicting pollutant dispersion in the boundary layer, and their advantages and disadvantages. In *WMO Symposium on Boundary Layer Physics Applied to Specific Problems of Air Pollution*. Geneva: World Meteorological Organization, WMO no. 510, pp. 1–8.

Dickerson, M. H. (1987) MASCON, a mass-consistent atmospheric flux model for regions with complex terrain. *J. appl. Met.*, **17**, 241–53.

Dixon, J. C. (1991) Wind chill – it's sensational. *Weather*, **46**, 141–4.

Duewer, W. H., MacCracken, M. C. and Walton, J. J. (1978) The Livermore Regional Air Quality Model: II. Verification and sample application in the San Francisco Bay Area. *J. appl. Met.*, **17**, 273–311.

Durrer, B., Hasler, R. and Mosssiman, U. (1994) Lightning accidents in the Swiss Alps, 1991–1993. *Foudre et montagnes*. Paris: Soc. Electriciens Electroniciens et Club Alpin Français, pp. 337–40.

Folk, G. E., Jr. (1966) *Introduction to Environmental Physiology*, 2nd edn. Philadelphia: Lea & Febiger, pp. 77–136.

Frisancho, A. R., *et al.* (1995) Developmental, genetic and environmental components of aerobic capacity at high altitude. *Amer. J. Physical Anthopol.*, **96**, 431–42.

Frutiger, H. (1977) Avalanche damage and avalanche protection in Switzerland. In *Avalanches, Glaciol. Data Rep. GD-5*. Boulder, CO: World Data Center-A for Glaciology, pp. 17–32.

Fuquay, D. M. (1962) Mountain thunderstorms and forest fires. *Weatherwise*, **15**, 149–52.

Fuquay, D. M. (1980) *Forecasting Lightning Activity Level and Associated Weather*. Forest Service Research Paper INT-244, International Forest and Range Experimental Station. Ogden, UT: US Dept. of Agriculture.

Furger, M., *et al.* (1989) Zur Durchluftung der Täler und Vorlandsenken der Schweiz. *Geogr. Bernensia*, P20. Bern: University of Bern.

Greenland, D. (1977) Living on the 700 millibar surface: The Mountain Research Station of the Institute of Arctic and Alpine Research. *Weatherwise*, **30**, 233–8.

Greenland, D. E. (1979) *Modelling Air Pollution Potential for Mountain Resorts*. Institute of Arctic and Alpine Research, Occasional Paper No. 32. Boulder, CO: University of Colorado.

Grover, R. F. (1974) Man living at high altitudes. In J. D. Ives and R. G. Barry (eds), *Arctic and Alpine Environments*. London: Methuen, pp. 817–30.

Gudiksen, P. H. and Shearer, D. L. (1989) The dispersion of atmospheric tracers in nocturnal drainage flows. *J. appl. Met.*, **28**, 602–8.

Hackett, P. H. (2001) High altitude and common medical conditions. In T. F. Hornbein and R. B. Schoene (eds), *High Altitude: An Exploration of Human Adaptation*. New York: M. Dekker Inc., pp. 839–85.

Hammer, N., Koch, E. and Rudel, E. (1989) Klimagerechte Bekleidung im Hochgebirge. *Wetter u. Leben* **41**, 235–41.

Hanna, J. M. (1976) Natural exposure to cold. In P. T. Baker and M. A. Little (eds), *Man in the Andes: A Multidisciplinary Study of the High-Altitude Quechua*, Vol. 1. Stroudsburg, PA: Dowden, Hutchinson & Ross, Inc., pp. 315–31.

Hanna, S. R. and Strimaitis, D. G. (1990) Rugged terrain effects on diffusion. In W. Blumen (ed.), *Atmospheric Processes over Complex Terrain*. Meteorological Monograph 23 (45). Boston, MA: American Meteorological Society, pp. 109–43.

Hart, J. S. (1957) Climate and temperature-induced changes in the energetics of homeotherms. *Rev. Can. Biol.*, **16**, 133.

Heath, D. and Williams, D. R. (1977) *Man at High Altitude*. Edinburgh: Churchill Livingstone.

Hebertson, E. G. and Jenkins, M. J. (2003) Historic climate factors associated with major avalanche years on the Wasatch Plateau, Utah. *Cold Reg. Sci. Technol.*, **37**, 315–32.

Henson, R. (2002) Cold rush. *Weatherwise*, **55**, 14–19.

Herry, J.-P. and Foray, J. (1994) Accidents de foudre en montagnes: prévention et premiers soins. *Revue générale de l'électricité* 1994, No. **6**, 67–72.

Hock, R. J. (1970) The physiology of high altitude, *Sci. Am.*, **222**, 52–62.

Holzworth, G. C. (1962) A study of air pollution potential for the western United States. *J. appl. Met.*, **1**, 366–82.

Holzworth, G. C. (1967) Mixing depths, wind speed and air pollution potential for selected locations in the United States. *J. appl. Met.*, **6**, 1039–44.

Hornbein, T. F. and Schoene, R. B. (eds) (2001) *High Altitude; An Exploration of Human Adaptation*. New York: M. Dekker Inc., 982 pp.

Houston, C. S. (2001) The growth of knowledge about air, breathing, and circulation as they relate to high altitude. In T. F. Hornbein and R. B. Schoene (eds), *High Altitude: An Exploration of Human Adaptation*. New York: M. Dekker Inc., pp. 1–23.

Howard, E. A. and Fox, D. G. (1978) Modeling mountain valley airsheds. In *Fourth Symposium on Turbulence, Diffusion and Air Pollution*. Boston, MA: American Meteorological Society, pp. 182–8.

Judson, A. (1976) Colorado's avalanche warning program. *Weatherwise*, **29**, 268–77.

Judson, A. (1977) The avalanche warning program in Colorado. In *Proceedings of the 45th Annual Meeting Western Snow Conference*, pp. 19–27.

Karr, T. W. and Wooten, R. L. (1976) Summer radar echo distribution around Limon, Colorado. *Mon. Weather Rev.*, **106**, 728–34.

LaChapelle, E. and Armstrong, R. L. (1976) Nature and causes of avalanches in the San Juan Mountains. In R. L. Armstrong and J. D. Ives (eds), *Avalanche Release and Snow Characteristics, San Juan Mountains, Colorado*, Institute of Arctic and Alpine Research Occasional Paper No. 19, pp. 23–40. Boulder, CO: University of Colorado.

Lahiri, S. (1974) Physiological responses and adaptations to high altitude. In D. Robertshaw (ed.), *Environmental Physiology*, Vol. 7. London: Butterworths, pp. 271–311.

Lange, R. (1978) ADPIC – a three-dimensional particle-in-cell model for the dispersal of atmospheric pollutants and its comparison to regional tracer studies. *J. appl. Met.*, **17**, 320–9.

Leon-Vallarde, F., *et al.* (1993) Aging at high altitudes and the risk of chronic mountain sickness. *J. Wilderness Med.*, **4**, 183–8.

Li, Y.-S., *et al.* (2005) Hydrocarbon concentrations at the Alpine mountain sites Jungfraujoch and Arosa. *Atmos. Environ.*, **39**(6), 1113–27.

Little, M. A. (1976) Physiological responses to cold. In P. T. Baker and M. A. Little (eds), *Man in the Andes: A Multidisciplinary Study of the High-Altitude Quechua*, Vol. 1. Stroudsburg, PA: Dowden, Hutchinson & Ross, Inc., pp. 332–62.

Little, M. A. (1981) Human population of the Andes: The human science base for research planning. *Mountain Res. Dev.*, **1**, 145–70.

Little, M. A. and Baker, P. T. (1976) Environmental adaptations and perspective. In P. T. Baker and M. A. Little (eds), *Man in the Andes: A Multidisciplinary Study of the High-Altitude Quechua*, Vol. 1. Stroudsburg, PA: Dowden, Hutchinson & Ross, Inc., pp. 405–28.

Lu, R., Turco, R. P. and Jacobsen, M. Z. (1997) An integrated air pollution modeling system for urban and regional scales. I. Structure and performance. *J. Geophys. Res.*, **102(D5)**, 6063–79.

MacCracken, M. C., *et al.* (1978) The Livermore Regional Air Quality Model I: concept and development. *J. appl. Met.*, **17**, 254 –72.

Maggiorini, M., *et al.* (1990) Prevalence of acute mountain sickness in the Swiss Alps. *Brit. Med. J.*, **301**, 853–5.

Mellor, M. (1968) *Avalanches*, Cold Reg. Sci. and Eng., Part. III-A3d. Hanover, NH: US Army, Cold Reg. Res. and Eng. Lab.

Meteorological Service of Canada (2005) Windchill index. http://www.mscsmc.ec.gc.ca/education/windchill/chill_graph_e.cfm

Mitchell, D. (1974) Physical basis of thermoregulation. In D. Robertshaw (ed.), *Environmental Physiology*, Vol. 7. London: Butterworths, pp. 1–32.

Mock, C. J. and Birkeland, K. W. (2003) Snow avalanche climatology of the western United States mountain ranges. *Bull. Amer. Met. Soc.*, **81**(10), 2367–92.

Monge, C. C., Leon-Velarde, F. and Arregui, A. (2001) Chronic mountain sickness in Andeans. In T. F. Hornbein and R. B. Schoene (eds), *High Altitude: An Exploration of Human Adaptation*. New York: M. Dekker Inc., pp. 815–38.

Moore, G. W. K. and Semple, J. L. (2006) Weather and death on Mount Everest. *Bull. Amer. Met. Soc.*, **87**(4), 465–80.

Moore, L. G., *et al.* (1994) Genetic adaptation to high altitude. In S. C. Wood and R. C. Roach (eds), *Sports and Exercise Medicine*. New York: M. Dekker Inc., pp. 225–62.

Nachbauer, W. (1994) Characteristics of alpine accidents caused by lightning. In *Foudre et montagnes*. Paris: Soc. Electriciens Electroniciens et Club Alpin Français, pp. 341–3.

Nanus, L., *et al.* (2003) Atmospheric deposition maps for the Rocky Mountains. *Atmos. Environ.*, **37**, 4881–92.

Nappo, C. J., Shankar Rao, K. and Herwethe, J. A. (1989) Pollutant transport and diffusion in katabatic flow. *J. appl. Met.*, **28**, 617–25.

Niermeyer, S., Zamudio, S. and Moore, L. G. (2001) The people. In T. F. Hornbein and R. B. Schoene (eds), *High Altitude: An Exploration of Human Adaptation*. New York: M. Dekker Inc., pp. 43–100.

Orgill, M. M. (1989) Early morning ventilation of a gaseous tracer from a mountain valley. *J. appl. Met.*, **28**, 636–51.

Osczevski, R. and Bluestein, M. (2005) The new wind chill equivalent temperature chart. *Bull. Amer. Met. Soc.*, **86** (10), 1453–8.

Pasquill, F. (1961) The estimation of the dispersion of windborne material. *Met. Mag.*, **90**, 33–49.

Perla, R. I. (1980) Avalanche release, motion and impact. In S. C. Colbeck (ed.), *Dynamics of Snow and Ice Masses*. New York: Academic Press, pp. 397–462.

Perla, R. I. and Martinelli, M., Jr. (1975) *Avalanche Handbook*. Fort Collins, CO: US Department of Agriculture Forestry Service.

Peterson, A. E. (1962) Lightning hazards to mountaineers. *Am. Alp. J.*, **13** (36), 143–54.

Pielke, R. A. (1985) The use of mesoscale numerical models to assess wind distribution and boundary-layer structure in complex terrain. *Boundary-Layer Met.*, **31**, 217–31.

Pielke, R. A. (2002) *Mesoscale Meteorological Modeling*, 2nd edn. Orlando, FL: Academic Press, 676 pp.

Pielke, R. A., *et al.* (1987) Mesoscale numerical modeling of pollutant transport in complex terrain. *Boundary-Layer Met.*, **41**, 59–74.

Pugh, L. G. C. E. (1957) Resting ventricular and alveolar air on Mount Everest: with remarks on the relation of barometric pressure to altitude in mountains. *J. Physiol.* (London), **135**, 590–610.

Pugh, L. G. C. (1966) Clothing insulation and accidental hypothermia in youth. *Nature*, **209**, 1281–6.

Reap, R. M. (1986) Evaluation of cloud-to-ground lightning data from the western United States for the 1983–84 summer seasons. *J. Clim. Appl. Met.*, **25**, 785–99.

Reeves, J. T., Grover, R. F., Weil, J. V. and Hackett, P. (1981) Pulmonary ventilation in peoples living at high altitude. In *Geoecological and Ecological Studies of Qinghai-Xizang Plateau*, Vol. 2. Beijing: Science Press, pp. 1377–83.

Reiter, R. (1988) Messreihen atmosphärische Spurenstoffe an alpinen Station Südbayerns zwischen 0.7 und 3 km Höhe. *Wetter u. Leben*, **40**, 1–30.

Reiter, R., Sladkovic, R. and Kanter, H.-J. (1987) Concentrations of trace gases in the lower troposphere simultaneously recorded at neighbouring alpine stations. Part III. Sulfur dioxide, nitrogen dioxide and nitric oxide. *Met. Atmos. Phys.*, **37**, 114–28.

Richalet, J. P. (2001) The scientific observations on Mont Blanc. *High Alt. Med. Biol.*, **2**, 57–8.

Richner, H. (1979) Possible influences of rapid fluctuations in atmospheric pressure on human comfort. In S. W. Tromp and J. J. Bouma (eds), *Biometeorological Survey*, Vol. 1, Part A. London: Heyden, pp. 96–102.

Schmidt, W. (1930) *Föhnerscheinungen und Föhngebiete*. Innsbruck: Lindauer Verlag.

Scorer, R. S. (1978) *Environmental Aerodynamics*. Chichester, UK: Ellis Horwood.

Sherman, C. A. (1978) A mass-consistent model for wind fields over complex terrain. *J. appl. Met.*, **17**, 312–19.

Shitzer, A. and de Dear, R. (2006) Inconsistencies in the "new" wind chill chart at low wind speeds. *J. Appl. Met. Climatol.*, **45**, 787–90.

Siple, P. A. and Passel, C. F. (1945) Measurements of dry atmospheric cooling in subfreezing temperatures. *Proc. Am. Phil. Soc.*, **89**, 177–99.

Smith, A. U. (1970) Frostbite, hypothermia and resuscitation after freezing. In A. U. Smith (ed.), *Current Trends in Cryobiology*. New York: Plenum Press, pp. 181–208.

Smithson, P. A. and Baldwin, H. (1979) The cooling power of wind and its influence on human comfort in upland areas of Britain. *Arch. Met. Geophys. Biokl.* **B27**, 361–80.

Snyder, W. H. and Hunt, J. C. R. (1984) Turbulent diffusion from a point source in stratified and neutral flows around a three-dimensional hill. *Atmos. Environ.*, **18**, 1069–2002.

Start, G. E., Dickson, C. R. and Wendell, L. L. (1974) *Effluent Dilutions over Mountainous Terrain*, NOAA Technical Memorandum ERL ARL-51, Idaho Falls, Idaho: NOAA.

Start, G. E., Dickson, C. R. and Wendell, L. L. (1975) Diffusion in a canyon within rough mountainous terrain. *J. appl. Met.*, **14**, 333–46.

Steadman, R. G. (1971) Indices of windchill of clothed persons. *J. appl. Met.*, **10**, 674–83.

Sturm, M., Holmgren, J. and Liston, G. E. (1995) A seasonal snow cover classification system for local to global applications. *J. Climate*, **8**, 1261–83.

Taylor, C. (1975) Alpine thunderstorms. *Alp. J.*, **80** (324), 173–83.

Tennekes, H. (1973) A model for the dynamics of the inversion above a convective boundary layer. *J. Atmos. Sci.*, **30**, 558–66.

Tennekes, H. (1976) Observations on the dynamics and statistics of simple box models with a variable inversion lid. In *Proceedings of the Third Symposium on Atmospheric Turbulence, Diffusion and Air Quality*. Boston, MA: American Meteorological Society, pp. 397–402.

Terjung, W. H. (1970) The energy budget of man at high altitudes. *Int. J. Biomet.*, **14**, 13–43.

Tromp, W. S. (1978) Biological effects of high altitude climate and its therapeutic applications. *Veröff. Schweiz. Met. Zent.*, **40**, 100–3.

Van Wie, C. C. (1974) Physiological responses to cold environments. In J. D. Ives and R. G. Barry (eds), *Arctic and Alpine Environments*. London: Methuen, pp. 805–16.

Venkataram, A. (1978) An examination of box models for air quality simulation. *Atmos. Environ.*, **12**, 1243–9.

Ward, M. (1975) *Mountain Medicine: a Clinical Study of Cold and High Altitudes*. New York: St. Albans.

Webster, A. J. F. (1974a) Physiological effects of cold exposure. In D. Robertshaw (ed.), *Environmental Physiology*, Vol. 7. London: Butterworths, pp. 33–69.

Webster, A. J. F. (1974b) Adaptation to cold. In D. Robertshaw (ed.) *Environmental Physiology*, Vol. 7. London: Butterworths, pp. 71–106.

West, J. B. (1996) Prediction of barometric pressures at high altitudes using model atmospheres. *J. Appl. Physiol.*, **81**, 1850–4.

West, J. B. (2001) The atmosphere. In T. F. Hornbein and R. B. Schoene (eds), *High Altitude: An Exploration of Human Adaptation*. New York: M. Dekker Inc., pp. 215–42.

Whiteman, C. D. (1989) Morning transition tracer experiments in a deep narrow valley. *J. appl. Met.*, **28**, 626–35.

Whiteman, C. D. and McKee, T. B. (1977) Observations of vertical atmospheric structure in a deep mountain valley. *Arch. Met. Geophys, Biokl.*, **A 26**, 39–50.

Whiteman, C. D. and McKee, T. B. (1978) Air pollution implications of inversion descent in mountain valleys. *Atmos. Env.*, **2**, 2151–8.

Williams, K. (1975) *The Snowy Torrents. Avalanche Accidents in the United States, 1967–71*, Rocky Mountains Forest Range Experimental Station, Technical Report RM-8. Fort Collins, CO: US Department of Agriculture, Forest Service.

Xie, C. F. and Pei, S. X. (1981) Some physiological data of sojourners and native highlanders at three different altitudes in Xizang. In D. S. Liu (ed.) *Geological and Ecological Studies of Qinghai–Xizang Plateau*. New York: Gordon and Breach, pp. 1449–52.

7 CHANGES IN MOUNTAIN CLIMATES

Throughout the description and analysis of climatic regimes in mountain areas, the question of climatic change has so far been ignored. There is now overwhelming evidence of important climatic fluctuations on time scales of human significance and, since the mountain environment is, in many respects, marginal for human activities, it is necessary to understand and take account of such fluctuations (Barry, 1990).

The documented increases in greenhouse gases (carbon dioxide, methane, chlorofluorocarbons and nitrous oxide) since 1958 represent a global increase in heating of just over $1\,\mathrm{W\,m^{-2}}$ and the accumulated increases since the beginning of the Industrial Revolution ($c.$ AD 1800) have contributed in excess of $2\,\mathrm{W\,m^{-2}}$ i.e. 1 percent of the average absorbed solar radiation of $240\,\mathrm{W\,m^{-2}}$ (Hansen $et\ al.$, 1990). Some offsetting cooling may have occurred during the 1970s–80s as a result of increasing levels of tropospheric aerosols, predominantly sulfur dioxide; these represent a net cooling effect through the increase in planetary albedo, particularly over the oceans. The period from about 1950–90 saw a reduction in solar radiation at the Earth's surface, especially in northern mid-latitudes and in urban areas, averaging $0.5\,\mathrm{W\,m^{-2}}$ per year, or 2.7 percent per decade. This has been referred to as "global dimming" (Gilgen $et\ al.$, 1998; Stanhill and Cohen, 2001). The effect is attributed to both increased aerosol load blocking sunlight, and increased cloud reflectivity caused by the increase in condensation nuclei provided by the aerosols (Crutzen and Ramanathan, 2003). An opposite signature was found in solar radiation amounts in the tropical Indian Ocean where there is little industrial pollution. However, the dimming trend has now reversed according to Wild $et\ al.$ (2005), which will exacerbate the greenhouse warming contribution.

Fundamental work on changes in radiation balance components is sorely needed and a start has been made with the Baseline Surface Radiation Network (BSRN). The importance of this work is illustrated by the finding that ultraviolet radiation measurements (0.29–0.33 μm) at the Jungfraujoch Observatory, Switzerland, showed a 1 percent increase during 1981–9. This was initially interpreted as a response to the observed 3–4 percent depletion of stratospheric ozone since 1969 (Blumthaler and Ambach, 1990), but it seems to be a result of changes in synoptic conditions and cloudiness.

Changes in atmospheric composition and projected trends, based on various scenarios of emissions, population growth and energy use, are fairly well established. There is now a general consensus that the increased concentrations of greenhouse gases account for a significant part of the observed twentieth-century global warming, especially during the last few decades, although twentieth-century fluctuations have both natural and anthropogenic components. In previous centuries, forcing by solar variability and volcanic eruptions appears to account for most of the observed changes, but this is not the case for the second half of the twentieth century, particularly since the 1980s.

7.1.1   Temperature trends

Global mean annual temperature rose by just over 0.6 °C in the twentieth century (Jones *et al.*, 1999) with accelerated warming in the last decade. Global temperatures are at their highest level for at least the last two millennia (Mann and Jones, 2003). Observations at mountain observatories in Europe (Barry, 1990) and elsewhere (Diaz and Bradley, 1997), indicate that mean temperatures have generally risen by amounts comparable with those observed in the lowlands, although there are some differences in the altitudinal patterns of seasonal and diurnal change. The 114-year record of the Sonnblick Observatory, Austria (Auer *et al.*, 2005) shows the well-known, two-stage twentieth-century warming with a rise from the 1890s to 1940–50, followed by a leveling off, or slight cooling, and a further rise to the 1990s (Figure 7.1). The increase of about 1.5 °C is twice that of the corresponding increase in the surface air temperature in the northern hemisphere. In contrast to many other parts of the world, including mountain stations like the Pic du Midi in the Pyrenees (Dessens, 2004), there is no increase in the diurnal temperature range at Sonnblick (Auer *et al.*, 2005).

In the Italian Alps, 22 stations in high valley and piedmont stations in Liguria, the western Piedmont and the coastal region of the Gulf of Genoa, show mean temperature increases over 1865–2003 of 1.0 °C in spring and summer, 1.2 °C in winter and 0.8 °C in autumn (Brunetti *et al.*, 2006). A compilation of 87 early temperature records for the European Alps, with documentary and narrative reports and gridded reconstructions, for AD 1500–2000 demonstrates that the years 1994, 2001, 2002 and 2003 were the warmest recorded during those five centuries (Casty *et al.*, 2005). Beniston (2005) attributes the 1990s warming in Switzerland to a positive winter mode of the North Atlantic Oscillation (NAO) that generated anomalous high pressure over the Alpine region.

On Mt. Washington, NH, the air temperature record for the 1935–2003 period shows a statistically significant increase in mean temperature of 0.3 °C, while the diurnal temperature range has decreased by 0.15 °C (Grant *et al.*, 2005). In contrast with North American trends, the summit experienced lower temperatures in the 1940s, while in agreement with North American decadal trends the late 1980s–early 1990s were relatively warm.

Fig 7.1   **Time series of (a) summer half-year and (b) winter half-year air temperatures (°C) at Sonnblick Observatory, 1887–2000 (after Auer *et al.*, 2000). (Courtesy Zentralanstalt für Meterologie und Geodynamik, Vienna.)**
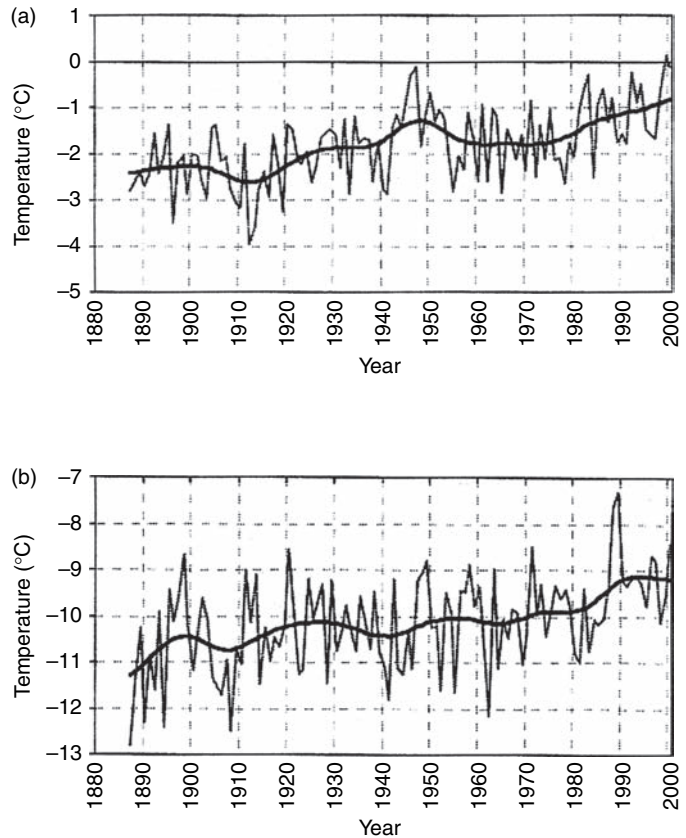
Diaz and Bradley (1997) present changes in zonally-averaged temperatures for 1951–89 between 30°–70° N, versus elevation. Mean maximum temperatures increased slightly between 500 and 1500 m, with minor changes at higher elevations, while minimum temperatures rose by about 0.2 °C/decade at elevations from 500 m to above 2500 m. In the tropical Andes, mean annual temperature trends for 268 stations between 1° N and 23° S during 1939–98 (Vuille and Bradley, 2000) show an overall warming of about 0.1 °C/decade and the rate tripled to + 0.32–0.34 °C/decade over the last 25 years. They find generally reduced warming trend with elevation, especially on the Pacific slopes of the Andes. In Switzerland, anomalies of minimum temperature (1979–93) increase (decrease) with altitude in mild (cold) winters (Beniston and Rebetez, 1995). There is a widespread tendency for diurnal asymmetry; increases in nocturnal minimum temperatures exceed those for daytime maxima. The latter may even have decreased. Thus, the diurnal temperature range (DTR) has diminished (Weber *et al.*, 1994). Globally, the decrease in DTR is attributed to increased cloud cover, locally augmented by changes in precipitation and soil moisture (Dai *et al.*, 1999). In the Rocky Mountains, Pepin (2000)

documents altitudinal differences in the Colorado Front Range since 1952, with overall cooling at 3750 m but warming between 2500 and 3100 m. This results in complex changes in lapse rate. An analysis in the Pennines of northern England indicates that atmospheric temperature and moisture level; cloudiness/solar radiation, and wind speed determine lapse rates. Thus, changes in lapse rate can result from changes in the frequency of cyclonic/anticyclonic circulation regimes. A shallower/steeper lapse rate may be expected under warmer, moister atmospheric conditions/increased solar radiation (Pepin et al., 1999).

For the United States west of 100° W, Diaz (2005) reports overall warming during 1950–2000, with an increase of 0.5–0.6 °C up to about 2100 m. At higher elevations, the station density seems inadequate for reliable assessments. At Aspen, Colorado (2488 m), air temperatures have risen 1.7 °C in the last 25 years, the number of frost-free days has increased by 20 and the annual precipitation falling as snow has declined by 16 percent (Aspen Global Institute, 2006). In a further study of changes during 1982–99, Pepin et al. (2005) compare trends in surface temperatures over the western United States at sites above 500 m with free-air trends. They note that free-air temperature trends should be spatially smoother than those of surface stations. They use records from 296 Global Historical Climate Network (GHCN) and Climate Research Unit (CRU) stations and about 600 SNOTEL sites. The free-air temperatures are consistently higher than the surface data and their trend is positive, The station data show generally positive trends, as do the SNOTEL data at night; however, the latter show daytime cooling of ~ 0.5 °C. The sign and magnitude of the surface temperature trends is variable. Possible causes may involve changes in energy balance related to clouds and snow cover, and changes in wind speed and direction. These factors are examined in a further study by Pepin and Norris (2005) who find that regression modals incorporating cloud cover, snow cover and wind speed can account for 20–40 percent of the annual temperature variability at high elevation stations, and more on a seasonal basis. They suggest that residual trends during 1971–96 in the daytime may be attributed to surface radiative cooling due to increases in atmospheric aerosols, but consider that the night-time residual trends are of uncertain origin.

Monitoring of ground temperatures in mountains has begun. In the northern Tien Shan, permafrost temperatures have risen by 0.2–0.3 °C over the last 25 years (Gorbunov et al., 2000). The depth of seasonal freezing has not changed significantly in the low mountains, but there has been a decrease in the depth between 1400 and 2700 m, while above 3000 m it is increasing. In the Swiss Alps, permafrost warmed by about 1 °C between 1880 and 1950, then stabilized, before accelerated warming during the late 1980s –1994 (Vonder Mühl et al., 1998). Borehole data (Harris et al., 2003) indicate that at the Murtel-Corvatsch rock glacier in the Engadine, the ground surface temperature increased steadily from about −3.3 °C to −2.3 °C during 1987–94 and since then has fluctuated around the lower level. Low values in 3 years are attributed to late snow cover formation that allows

Fig 7.2 **Changes from 1928–32 to 1968–72 in annual totals of sunshine hours at four stations in the Austrian lowlands (above) and at three mountain stations (below), plotted as a 5-year moving average (from Steinhauser, 1973).**
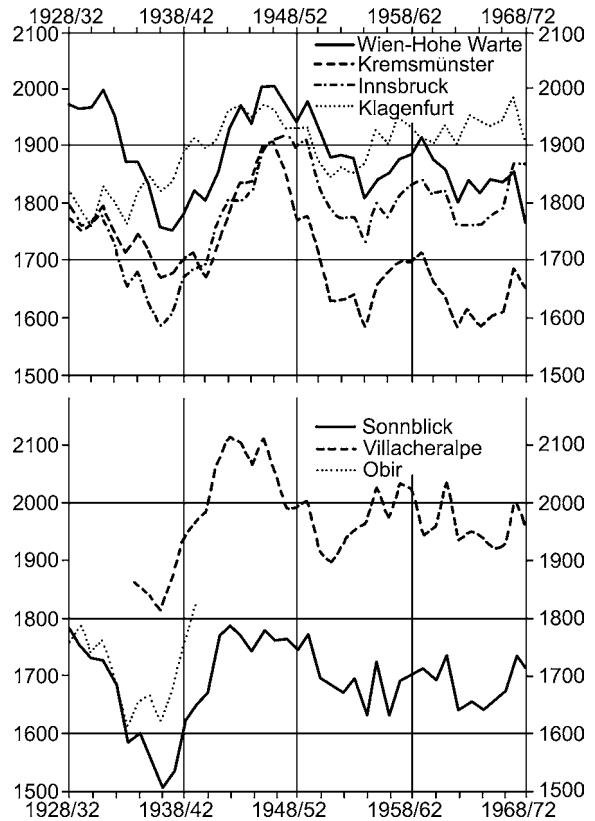
bedrock cooling. 2003 saw the warmest summer on record in the Swiss Alps with significant impacts on frozen rock faces.

The records from mountain observatories also enable us to compare the degree of parallelism and relative amplitudes of trends in the mountains and on the adjacent lowlands. Analyses illustrating trends of sunshine and snowfall in lowland and mountain regions of Austria (Steinhauser, 1970, 1973) are among the most complete such records available. Annual sunshine totals at Sonnblick (3106 m) and Villach (2140 m) show fluctuations similar in timing and amplitudes to those at four lowland stations (Figure 7.2). This agreement holds also on a seasonal basis, except in winter as a result of inversions associated with lowland fog and stratus. Variations in snow cover duration in Austria since 1900 show inter-regional differences with stations in western Austria and the southern Alps displaying patterns that are different from those in the northern Alpine Foreland and northeastern Austria (Figure 7.3). Temperature trends at Sonnblick for 1887–1979, compared with Hohenpeissenberg (994 m) and lowland stations in the surrounding region suggest that differences between them reflect spatial gradients rather than altitudinal contrasts (Lauscher, 1980).

Fig 7.3 Secular trends from 1900–1 to 1965–6 in the number of days with snow cover and total new snowfall as a percentage of the 1900–1 to 1959–60 mean value for four regions in Austria: western Austria, northern Alpine Foreland, northeast Austria, and southern Alps (from Steinhauser, 1970).
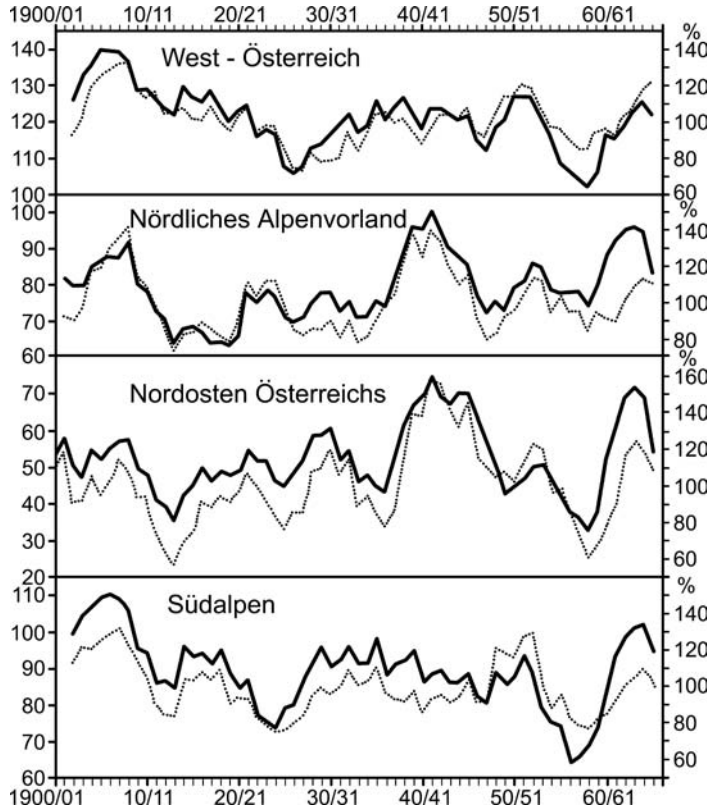
7.1.2 Precipitation and snow pack

Changes in precipitation are difficult to determine due to changes in gauge characteristics, movement of stations, and inadequate spatial coverage. These problems are exacerbated in the mountains, where much of the precipitation falls as snow, for which the under-catch may be 20–50% (see p. 310). More reliable precipitation assessments over mountain basins are often best made from hydrological budget estimates via runoff.

Mountain snow packs in western North America show substantial decreases since 1950 according to Mote *et al*. (2005) with April 1 SWE declining by 50–75 percent in western Washington and Oregon, and in northern California. Here, warming outweighs some increases in precipitation. In the northern Rockies decreases over this interval were of the order of 15–20 percent. Nevertheless, in some parts of the southwest (New Mexico and the southern Sierra Nevada of California) snow pack SWE has increased as a result of greater total precipitation.

For the Alps, contrasting trends are found in autumn and winter (Schmidli *et al.*, 2002). Decreases in mean precipitation of up to 20–30 percent per century occurred in the southern and eastern Alps in autumn, while in the winter season corresponding increases were found the northwestern Alps.

There are few long time series of snow depth, even in the Alps. At Claridenfern (in the Glarus, Swiss Alps) winter snow accumulation recorded since 1915 shows no significant change (Glaciological Commission of the Swiss Academy of Science, 2002). In the Wägital basin of the northern Swiss Alps, Gurtz *et al.* (2005) show there has been lower snow depths since 1989 compared with 1962–88, for transects from 900–1500 m and 1500–2300 m. However, depths were generally low from 1943–61 on the lower transect.

At Col de Porte (1320 m), near Grenoble in the pre-Alps, snow depth in mid-February has decreased from around 1.5 m in 1960 to below 1 m in 2000 and snow cover duration was also less after 1989 compared with around 1975–85 (Martin and Etchevers, 2005). Changes in snow cover duration and accumulation in the Swiss Alps are found to depend on altitude and the type of winter (Beniston *et al.*, 2003). Mild winters lead to more rainfall at lower elevations, but heavier snowfall above about 1700–2000 m. Time series show a shorter snow cover season since the early 1970s, but also high interannual variability. At Chateau d'Oex (980 m) in the southwestern Alps, the total seasonal snowfall decreased 451 percent between the 1960s and 1990s. Davos (1590 m) in eastern Switzerland showed a 12 percent decrease while Säntis (2500 m) in the northeast recorded a 35 percent increase. Beniston *et al.* (2003) also point out that a 3 °C warming, projected by AD 2050, would reduce the area in the Swiss Alps having a significant winter snow pack from 18 000 to 14 000 km^2. This, coupled with receding glaciers (see below), raises severe concern for water resources for consumption, irrigation and hydropower. Liniger *et al.* (1998) characterize mountains as the "water towers" of the twenty-first century, because of their importance for water supply in many mountain regions of the world. Hence, the growing attention being paid to projected changes in precipitation, evaporation, seasonal snow pack, and perennial ice cover.

Temporal changes of climate variables in the Alps show some interesting contrasts with altitudinal effects. At Sonnblick (3106 m) the average number of days with snow cover during May–September decreased from 82 days for 1910–25 to only 53 days for 1955–70 (Böhm, 1986). During the same interval, mean summer temperatures rose about 0.5 °C. However, if we compare the difference in days with snow cover over an altitude difference of 100 m (corresponding to a mean lapse rate of 0.5 °C per 100 m), a decrease of only 10–11 days, rather than 29 days, would be expected in the eastern Alps. Evidently, non-linearity associated with snowmelt effects and summer snowfalls must be involved. Snow-cover duration at high and low elevations is often poorly correlated (Pfister, 1985). A network of five snow stakes operated from 1927 at Sonnblick shows a maximum depth in May around 1950, a minimum about 1970 and then a slight recovery through 2000 (Auer *et al.*, 2002).

7.1.3   Proxy data

As a consequence of the limited observational data, climatic proxy sources have to be used to assess conditions over the last millennium. Proxy evidence of decadal–centennial climate change is available from changes in glacier size dated by lichenometry and ^{14}C, from tree-ring series indicating growing season temperature and moisture, from δO^{18} and δD stable isotopes in polar and high-elevation ice cores, and from temperature profiles in deep boreholes, *inter alia* (see Jones and Mann, 2004). Accounts from various mountain regions exemplify such work (Luckman, 1997: Kaser, 1999; Solomina, 2000; Luckman and Villaba, 2001). These sources become even more important in mountain regions that lack direct records, or where these are of short duration. Diaz and Graham (1996) report a rise of 100–150 m in the altitude of the freezing level in the atmosphere over the inner tropics (10° N–10° S) between 1970 and 1986 that is correlated with a warming in the sea-surface over the eastern tropical Pacific. Diaz *et al.* (2003) show that the freezing level and the annual totals of melting degree-days over the American Cordilleras correlate significantly with the Niño-3 region sea-surface temperatures during 1948–2000. The 20° N−20° S freezing level height rose 53 m from 1958–2000 and the Niño-3 SST increased by 0.5 °C accounting directly for half of the Cordilleran rise in freezing level.

One such line of evidence is provided by the occurrence of tree stumps and logs above present timberlines. In southern California and Nevada, dead tree remains are found up to 150 m above the present upper timberlines, indicating more favorable growing season conditions in the past (LaMarche and Mooney, 1972; LaMarche, 1973). Wood material can be dated by ^{14}C techniques and by cross-dating of the tree ring chronology with other trees. A detailed account of dendroclimatic methods of reconstructing past climates is given in Fritts (1976).

Remnants of bristlecone pine (*Pinus longaeva* Bailey) on Mt. Washington in eastern Nevada show a 100 m downward shift of the upper tree line zones from their positions between about 4000 and 2000 years ago (LaMarche and Mooney, 1972). This can be interpreted as reflecting cooler summers, more moist summers, or both. Summer moisture plays a significant role in reducing the preconditioning of these trees to winter desiccation stress. For the White Mountains, California, LaMarche (1973) demonstrates three times of timberline lowering: 3500 BP, 2500 BP and 850–450 BP. By comparing changes in different locations, he argues that the first and last change represent primarily cooling, whereas the one around 2500 BP was related to drier conditions.

In the North Island of New Zealand there is evidence for an upward migration of *Nothofagus menziesii* (beech) into the sub-alpine scrub and alpine grassland belts during the last 100 years or so, suggesting warmer and sunnier conditions recently (Burrows and Greenland, 1979). However, these authors also note that in other parts of North Island, trees near their upper altitudinal limit are predominantly old and show signs of imminent decline, with little indication that regeneration is occurring. In South Island, the recent rise in snow line has allowed some migration

of trees into gullies where seedlings were formerly unable to establish themselves (Wardle, 1973). Yet at the same time, a less reliable snow cover encourages frost heaving of soils and vegetation and this instability may be responsible in part for an observed lowering of the upper limit of continuous alpine grassland (Burrows and Greenland, 1979). Clearly, botanical evidence for climatic fluctuations must be interpreted with care since independent or inter-related biotic and pedological factors may also affect tree growth and regeneration.

In the Himalaya, tree ring studies by Brauning and Mantwill (2004) indicate an increasing influence of the Indian monsoon in August–September since 1980 that is unprecedented over the preceding 350 years.

Alpine glaciers provide the most widely available evidence of climatic change in mountains. Change in glacier length represents an intuitively understood and easily observed phenomenon to illustrate the reality and impacts of climate change. Overall, there are some 800 glaciers where terminus location is monitored every 5–10 years and about 100 of these are time series spanning 50–100+ years. Terminus location provides a strongly enhanced and easily measured signal of climate change, but at the same time it is indirect, filtered by glacier morphometry, and time delayed. Nevertheless, Oerlemans (1994) was able to derive an estimate of global warming (0.62 K per 100 years) from changes in the length of 46 glaciers in nine regions over the period 1884–1978, in quite good agreement with observational findings of 0.42–0.53 K per 100 years. The average length change in relation to temperature was $1.88 \, \mathrm{km \, K^{-1}}$.

Snow accumulation and ablation represent more direct responses to climatic parameters than do changes in length, but there are nevertheless considerable problems in developing a precise climatic interpretation of changes observed in glaciers.

Out of 290 locations with mass balance observations, reflecting the balance of long-term accumulation and ablation, there are only 48 series with records spanning more than 20 years worldwide (Dyurgerov, 2001; Haeberli, 1998). Moreover, they are principally in the northern hemisphere and for small valley glaciers. The relationship between mass balance changes and glacier extent is itself complex, involving the bedrock profile, ice thickness and ice flow properties (Paterson, 1994; see Barry, 2006).

Greene *et al.* (1999) develop a relationship between glacier equilibrium line altitude (*ELA*) and meteorological data. Using 52 mid-latitude glacier records in both hemispheres, a best-fit linear model was derived based on warm-season freezing level height (Z_{FL} in meters) and cold season precipitation (P_{wi} in mm):

$$ELA = 68 + 1.02Z_{\mathrm{FL}} - 0.90P_{\mathrm{wi}}$$

They obtained a coefficient of explained variance of 0.93 and showed a reasonable fit with observed changes in climatic variables and *ELA* changes since the mid-nineteenth century in the Swiss Alps.

Changes in glacier mass balance are caused by the *net* effect of changes in winter accumulation (involving snow fall and wind drifting) on the one hand, and summer ablation by sublimation and melt (involving the length and warmth of the thaw season, radiation conditions, and wind, humidity and temperature conditions above the glacier) on the other. A glacier's mass is therefore determined by the local micro- and topo-climatic conditions and there is no necessary simple relationship between these and the large-scale climate. On ice bodies where there is no summer melt, the long-term accumulation can be determined from ice cores. For Quelccaya Ice Cap at 5670 m in the Peruvian Andes (14° S), the mean annual temperature is $-3\,°C$ and there appears to have been no melt or evaporation until the 1990s. Thompson *et al.* (1985) identified extended dry regimes during AD 570–610, 1250–1310, and 1720–1860; the periods AD 1500–1720 and to a lesser degree 1870–1984 were wet. At present the wet season, which accounts for about 80 percent of the annual total, occurs between November and April with convective activity from an easterly direction. Later work by Thompson *et al.* (1993) shows that on Quelccaya, melt water penetration had obliterated the upper part of the climatic record provided by the ice core collected earlier. A new core was, however, obtained in 2004 and below the firn the record is intact.

Rapid glacier recession is underway in this and most other mountain regions (Dyurgerov and Meier, 2005). Comparison of AD 2000 high-resolution satellite images with ground surveys carried out in Central Asia in the 1940s–70s, shows substantial reductions in ice area in the Ak-Shirak range of the central Tien Shan (Khromova *et al.*, 2003; Alzen *et al.*, 2007) and in the eastern Pamir (Khromova *et al.*, 2006), as well as in the Caucasus (Shahgedanova *et al.*, 2007). In the Ak-Shirak ($\sim 43°$ N, 75° E), the reduction is a response to increases in summer and annual air temperature and decreases in annual precipitation. Similar factors seem to be at work in the eastern Pamir (38° N, 72° E) where the area of five glaciers and the terminus of 44 glaciers show accelerated decrease since 1970. The glacier area shrank 7.8 percent during 1978–90 and 11.6 percent during 1990–2001 (Khromova *et al.*, 2006). Solomina *et al.* (2004) report that, since the Little Ice Age, glaciers in the Tien Shan have retreated almost a kilometer. Temperatures have risen steadily, especially in winter, but in the northern Tien Shan (north of Lake Issyk-Kul), summer temperatures increased $0.012\,°C\,year^{-1}$ between 1935–85.

Glaciers in the European Alps have been objects of scientific interest since the late eighteenth century and in many localities documentary records and landscape paintings provide a means of determining glacier extent and thickness during earlier times. Figure 7.4 for example, illustrates the fluctuations of the Lower Grindelwald Glacier since 1590. While care must be taken in interpreting such a record, as discussed above, in this case it is possible to compare the evidence with temperature observations at Basel from 1755 onward. Messerli *et al.* (1978) show that the post-1860 retreat is correlated with increasing temperatures in spring and autumn. Shorter-term fluctuations in summer temperatures are also involved,
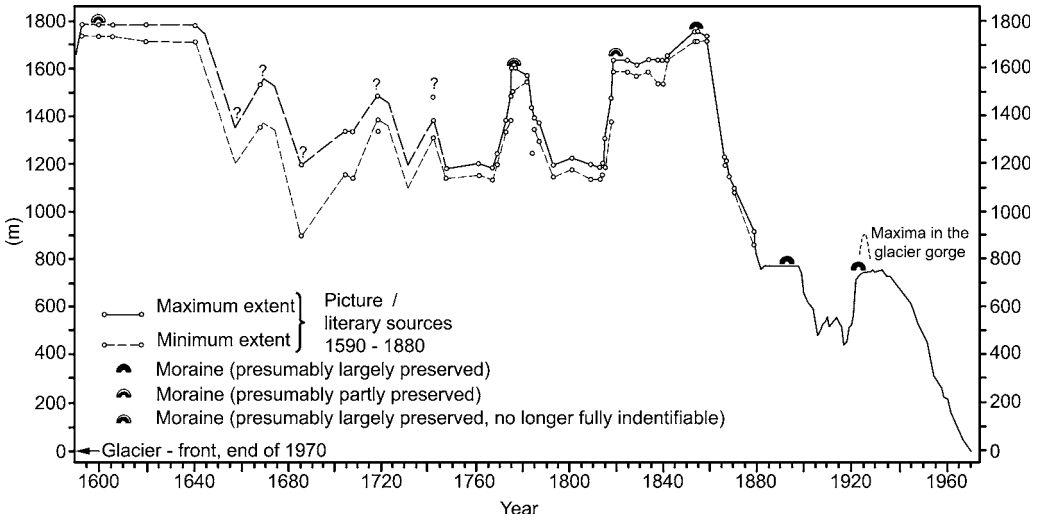
Fig 7.4   **Variations in the front of the Lower Grindelwald Glacier, Switzerland, 1590–1970, relative to the 1970 terminal position (after Messerli *et al.*, 1978).**
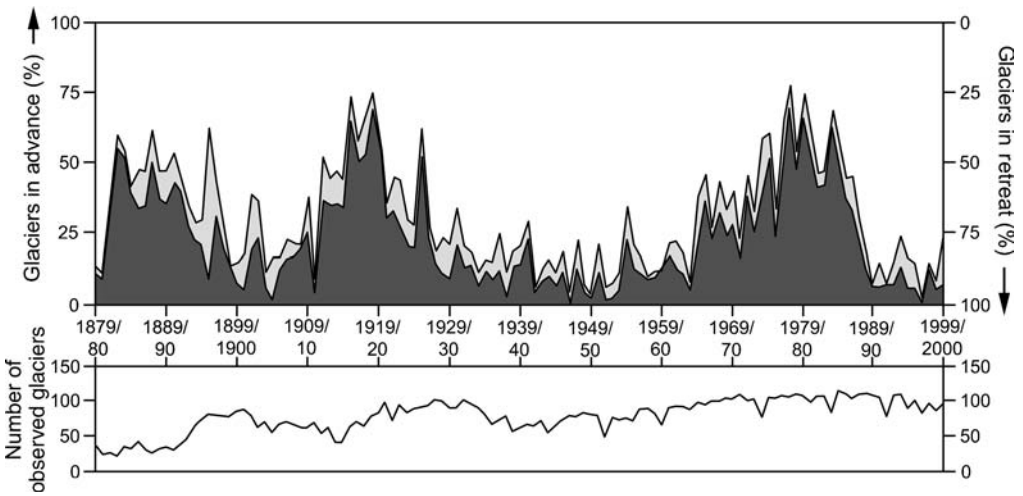
Fig 7.5   **Percentage of Swiss glaciers showing advance (hatched) or retreat (white) of the terminus, 1879–80 to 1999–2000 (based on data provided by the World Glacier Monitoring Service, Zurich).**

especially post-1935. Data on winter accumulation are required to complete the interpretations, but these are unfortunately not available.

Since the 1890s, numerous Swiss glaciers have been monitored. The percentage advancing, stationary, or retreating shows distinct differences over the last nine decades (Figure 7.5). Advances in the 1890s are attributed to cool cloudy summers, which diminish ablation, whereas the advances during 1912–20 also represent the

effect of a number of winters with heavy accumulation (Hoinkes, 1968). The maximal recession during the 1945–54 decade was associated with higher temperatures, increased sunshine duration and reduced precipitation at Alpine stations according to Rudloff (1962). The re-advances during the late 1960s–early 1980s were a result of slightly cooler summers, but these advances which affected small glaciers, have ceased, being replaced by general retreat and thinning (Maisch *et al.*, 1999). Similar sharp decreases in the rate of recession of glaciers in the Canadian Rocky Mountains during the 1970s–early 1980s also match the records of cooling at neighboring valley stations (Luckman, 1990). It is important to note, however, that the larger number of small glaciers biases summary statistics of glacier terminus fluctuations, such as those provided in Figure 7.5. In terms of glacier mass, which is dominated by large valley glaciers, the twentieth-century downward trend is essentially uninterrupted except in some maritime coastal ranges where accumulation temporarily increased in the 1980s (Haeberli *et al.*, 1989).

The various records for the Alps enabled LeRoy Ladurie (1971) to characterize the last millennium as follows: a brief cooling with glacier advances took place between about AD 1200–1300, followed by a pronounced cool interval and glacier maximum between about AD 1550 and 1850. This period, known as the Little Ice Age appears to have been a global phenomenon, although it was perhaps not entirely synchronous. In Norway, floods, landslides, avalanches and glacier encroachment on farms also reached a peak between AD 1680 and 1750, according to Grove (1972). However, in the Southern Alps of New Zealand, glacier maxima have been recognized in the thirteenth, fifteenth, seventeenth, mid-eighteenth and late-nineteenth centuries (Burrows and Greenland, 1979). The glacier fluctuations since the seventeenth century suggest quasi-periodic climatic fluctuations of 30–60 years duration. Grove (2004) provides an updated synthesis of the Little Ice Age and its earlier counterparts.

Extensive subsequent work has documented changes over the last millennium much more comprehensively, using multiple proxies. Although the exact amplitude of the fluctuations is still being debated it is evident that the global temperature levels since 1990 exceed those during the last two millennia (Jones and Mann, 2004).

The glacier recession in New Zealand, which began about 1900 and still continues, is the most substantial for at least 1800 years. It appears to be associated with a temperature rise of 1 °C, implying that the earlier fluctuations were of similar or lesser magnitude (Burrows and Greenland, 1979). In the Himalayan area, Mayewski and Jeschke (1979; Mayewski *et al.*, 1980) also find that a general glacial retreat has taken place since AD 1850, but with local differences according to regional and topo-climatic influences. Calculated changes in the dimensions of the small equatorial glaciers of Mt. Jaya (Mt. Carstenz) at 4° S in western New Guinea (Irian Jaya) have been used in conjunction with a glacier mass balance model by Allison and Kruss (1977) to estimate recent climatic changes there. The calculations indicate a temperature rise of $0.6\,°C\,100\,\text{years}^{-1}$ since the glacial maximum of the mid-nineteenth century.

7.2   SIGNIFICANCE

The interdisciplinary studies reported above remind us of the temporal dimension of climate in mountains. Scenarios of climatic conditions for the predicted warmer Earth resulting from the continued increase in greenhouse gases are numerous. Experiments with GCMs commonly compare the standard concentration of carbon dioxide (nominally 300ppm) with changes as greenhouse gas concentrations increase up to a doubled amount of CO_2 or a future time (AD 2100). The Intergovernmental Panel on Climate Change (IPCC) uses a range of scenarios for emissions, population growth, and economic growth to estimate conditions in the twenty-first century. Most GCM experiments suggest an associated $3\,°C \pm 1.5\,°C$ increase in mean global surface air temperature, with an approximate two- to three-fold amplification in polar latitudes (Schlesinger and Mitchell, 1987). The corresponding values at about 3 km (700 mb) in middle latitudes imply that in summer, the lower tropospheric lapse rate is more or less unchanged, whereas in winter it is steeper due to greater warming at the surface. It is, however, uncertain what the temperature changes are likely to be at the ground surface in mountain regions. Moreover, the anticipated changes in moisture balance and snow cover are even less certain. Comparison of GCM simulations, station data and field measurements in July 1988 in the mountains of Ladakh and Kashmir by Brazel and Marcus (1991) illustrate the discrepancies and problems of interpreting GCM results in mountain areas. These arise from the coarse resolution and topographic smoothing in the model simulations, as well as regional and local heating effects over arid surfaces that are not captured by the models. Possible approaches to resolve this problem involve either statistical downscaling of GCM results for a specific region based on the modern spatial distribution of climatic variables or using a regional meso-scale model forced at the boundaries by GCM output. (see Chapter 3. p. 229).

Calculations of the effect of specified changes on Alpine glaciers by Kuhn (1989), based on a scenario of a $3\,°C$ summer warming and an increase in annual accumulation of $100\,kg\,m^{-1}$ for AD 2050, show an expected rise in altitude of the mean equilibrium line by 190 m (to 3000 m). This would translate into a reduction of almost 50 percent in ice-covered area in Austria. Haeberli *et al.* (2000) project the loss by 2025 in the Alps of ~ 30 percent of the ice area that existed in 1970–80 and 50 percent of the corresponding ice mass. By 2100 these values will have risen to 80–90 percent and 90–95 percent, respectively.

Such changes in mountain climate regimes may be of considerable practical significance. In countries like New Zealand, Norway, and Switzerland where hydro-electric power is the primary energy source, changes in snowfall and glacier runoff could have serious economic implications. Shortening of the snow-cover season or drastic glacier retreat could also have long-term consequences for the skiing "industry" and tourism in alpine countries. Maisch *et al.* (1999) estimate that the snow line has risen 90 mm between 1850 and 1973. Direct information on snow cover conditions at Weissflujoch (2540 m), Switzerland, since 1940 indicates that

the disappearance of spring snow cover has got later as a result of cool spring weather and late season snowfalls (Föhn, 1989). There is also no long-term trend in snow depth on January 1 since 1935 at Weissflujoch, nor at Davos (1540 m) since 1892. However, Föhn notes that the last 5 to 7 years suggest a diminution in January 1 snow depth, as a result of a delay in onset of winter snowfalls. Such a trend if it persists could be serious for the ski-industry due to the loss of business over Christmas–New Year. Scherrer et al. (2004) find decreasing snow days in the Swiss Alpine area below 1300 m in the late twentieth century, attributed to increasing temperatures.

Assessments of such impacts heve been made by Breiling and Charanza (1999) and Elsaesser and Buerkli (2002). The latter show that while 85 percent of Alpine resorts, for a snow line at 1200 m altitude, have reliable skiing, warming could reduce this to 63 percent for a rise of snow line to 1550 m and only 44 percent for a rise to 1800 m. The delay in snow ablation in spring could impact Alpine agriculture by curtailing the early growing season. It would also delay the peak runoff in Alpine river basins, although this could have beneficial effects. Changes in other climatic elements could also have practical implications. Warmer sunnier conditions, as well as favoring tree growth at higher altitudes, could reduce conventional heating costs for buildings and perhaps make solar installations more cost-effective.

As a general outcome of the increasing international concern about climatic variability and change, various climatic "bench mark" monitoring programs have been established. The much-cited record of carbon dioxide trend obtained at Mauna Loa Observatory, Hawaii, is one illustration of the value of permanent mountain stations and of the difficulty in initiating and sustaining long-term monitoring programs (Keeling et al., 1976; Keeling, 1998). Monitoring of other trace gases and aerosol levels is also necessary, however, on both a local and global basis. Likewise, for energy assessments, better networks of solar radiation and wind measurements are essential in many mountainous countries. Pairs of mountain and lowland reference stations, where all climate variables are monitored, need to be established (Cehak, 1982). This has become an even more pressing concern in the context of international programs such as that for a Global Climate Observing System (GCOS) and Global Terrestrial Observing System (GTOS) (see http://www.fao.org/gtos/). The latter addresses observations of snow cover, glaciers, frozen ground, hydrology and vegetation. In many respects, the future for mountain weather and climate studies seems bright, but a resurgence of mountain meteorology will hopefully be accomplished via long-term commitments instead of short-term programs and experiments. The 2002 International Year of the Mountain had limited success in this regard, although worldwide awareness of mountain studies was increased.

It would also be regrettable if new technologies such as automatic stations and remote sensing techniques were allowed to replace rather than complement conventional station observations in remote mountain locations. The histories

of the Ben Nevis Observatories in Scotland and the Pike's Peak Observatory in Colorado demonstrate the impossibility of re-establishing mountain facilities once they are closed. Accordingly, it is appropriate to close this book with an expression of appreciation for the commitment of the mountain weather observers in many countries, who have so diligently maintained records under the trials of severe environments, isolation, and sometimes of bureaucratic disinterest.

BIBLIOGRAPHY

Aizen, V., *et al.* (2007) Glacier changes in the Tien Shan as determined from topographic and remotely sensed data. *Global Planet Change*, **56**, 328–40.

Allison, I. and Kruss, P. (1977) Estimation of recent climatic change in Irian Jaya by numerical modeling of its tropical glaciers. *Arct. Alp. Res.*, **9**, 49–60.

Aspen Global Change Institute (2006) Climate change and Aspen. An assessment of impacts and potential responses. Aspen, CO: Aspen Global Change Institute, 147 pp.

Auer, I., Böhm, R. and Mohnl, H. (1990) Die troposphärische Erwarmungsphase die 20 Jahrhunderts im Spiegel der 100-jährigen Messreihe des alpinen Gipfelobservatoriums auf dem Sonnblick. *CIMA '88 Proceedings of the 20th International Tagung für Alpine Meteorologie* Rome: Italian Meteorological Service.

Auer, I., *et al.* (2002). *Das Klima des Sonnblicks Österreich*. Beiträge Meteorologie u. Geophysik, 28. Zentralansalt Meteorologie u. Geodynamik, Vienna, 305 pp. and CD.

Auer, I., *et al.* (2005) A new instrumental precipitation dataset for the Greater Alpine Region for the period 1800–2002. *Int. J. Climatol.*, **25**(2), 139–66.

Auer, I., *et al.* (2007) HISTALP – historical instrumental climatological surface time series of the Greater Alpine Region. *Int. J. Climatol.*, **27**(1), 17–46.

Barry, R. G. (1990) Changes in mountain climate and glacio-hydrological responses. *Mountain Res. Devel.*, **10**, 161–70.

Barry, R. G. (2006) The status of research on glaciers and global glacier recession: a review. *Progr. Phys. Geog.*, **30**, 285–306.

Barry, R. G. and Seimon, A. (2000) Research for Mountain Area Development: Climate fluctuations in the mountains of the Americas and their significance. *Ambio*, **29**, 364–70. Corrigendum: *Ambio*, **30**, 69.

Beniston, M. (2005) Warm winter spells in the Swiss Alps: Strong heat waves in a cold season? *Geophys. Res. Lett.*, **32**(1), L01812.

Beniston, M. and Rebetez, M. (1995) Regional behavior of minimum temperatures in Switzerland for the period 1979–1993. *Theoret. Appl. Climatol.*, **53**, 233–43.

Beniston, M., Keller, F. and Goyette, S. (2003) Snow pack in the Swiss Alps under changing climatic conditions: An empirical approach for climate impacts studies. *Theoret. Appl. Climatol.*, **74**(1–2), 129–31.

Blumthaler, M. and Ambach, W. (1990) Indication of increasing solar ultraviolet-B radiation flux in alpine regions. *Science*, **248**, 206–8.

Böhm, R. (1986) *Der Sonnblick. Die 100 jährige Geschichte des Observatoriums und seiner Forschungstätigkeit*. Vienna: Osterreichischer Bundesverlag.

Braithwaite, R. J., Zhang, Y. and Raper, S. C. B. (2002) Temperature sensitivity of the mass balance of mountain glaciers and ice caps as a climatological characteristic. *Zeitschrift fuer Gletscherkunde und Glazialgeologie*, **38**, 63–9.

Brauning, A. and Mantwill, B. (2004) Summer temperature and summer monsoon history on the Tibetan plateau during the last 400 years recorded by tree rings. *Geophys. Res. Lett.*, **31**(24), L24205.

Brazel, A. J. and Marcus, M. G. (1991) July temperatures in Kashmir and Ladakh, India: Comparisons of observations and general circulation model simulations. *Mountain Res. Devel.*, **11**, 75–86.

Breiling, M. and Charanza, P. (1999) The impact of global warming on winter tourism and skiing: a regional model for Austrian snow conditions. *Regional Environ. Change*, **1**, 4–13.

Brown, T. J., Barry, R. G. and Doesken, N. J. (1992) An exploratory study of temperature trends for paired mountain–plains stations in Colorado. In *Proceedings of the Sixth Conference on Mountain Meteorology*. Boston, MA: American Meteorological Society, pp. 181–4.

Brunetti, M., *et al.* (2006) Temperature and precipitation variability in Italy in the last two centuries from homogenized instrumental time series. *Int. J. Climatol.*, **26**(3), 345–81.

Burrows, C. J. and Greenland, D. E. (1979) An analysis of the evidence for climatic change in the last thousand years: evidence from diverse natural phenomena and from instrumental records. *J. R. Soc. New Zealand*, **9**, 321–73.

Carrivick, J. and Brewer, T. R. (2004) Improving local estimations and regional trends of glacier equilibrium line altitudes. *Geogr. Annal.*, **86A**, 67–78.

Casty, C., *et al.* (2005) Temperature and precipitation variability in the European Alps since 1500. *Int. J. Climatol.*, **25**(14), 1855–80.

Cehak, K. (1982) Alpenklimatologie – ein Statusbericht. *Wetter u. Leben*, **34**, 227–40.

Chase, T. N., *et al.* (1999) Potential impacts on Colorado Rocky Mountain weather due to land use changes in the adjacent Great Plains. *J. Geophys. Res.*, **104**(16), 673–90.

Chen, J.-Y. and Ohmura, A. (1990) On the influence of Alpine glaciers on runoff. In H. Lang and Musy, (eds), *Hydrology in Mountain Regions I. Hydrological Measurements, The Water Cycle*, IAHS Publication No. 193. IAHS, Wallingford, UK, pp. 117–25.

CIRMOUNT Committee (2006) *Mapping New Terrain: Climate Change and America's West*. Report of the Consortium for Integrated Climate Research in Western Mountains (CIRMOUNT) , Misc. Publ. PSW-MISC-77. Pacific Southwest Research Station: Forest Service, US Dept of Agriculture, 29 pp.

Crutzen, P. J. and Ramanathan, V. (2003) The parasol effect on climate. *Science*, **302**, 1679–81.

Dai, A., Trenberth, K. E. and Karl, T. R. (1999) Effects of clouds, soil moisture, precipitation and water vapor on diurnal temperature range. *J. Climate*, **12**, 2451–73.

Dessens, J. (2004) Meteorological observations since 1882 at the Pic du Midi, central Pyrenees. In *100. Jahresbericht des Sonnblick-Vereines fur das Jahr 2002*. Vienna: Sonnblick-Verein, pp. 16–18.

Diaz, H. F. (ed.) (2003) *Climate Variability and Change in High Elevation Regions: Past, Present and Future*. Dordrecht: Kluwer. 282 pp.

Diaz, H. F. (2005) Monitoring climate variability and change in the western United States. In U. Huber, M. Reasoner and H. Bugmann (eds), *Global Change and Mountain Regions: a State of Knowledge Overview*. Dordrecht: Kluwer Academic Publishers, pp. 267–74.

Diaz, H. F. and Bradley, R. S. (1997) Temperature variations during the last century at high elevation sites. *Clim. Change*, **36**, 253–80.

Diaz, H. F. and Graham, N. E. (1996) Recent changes of tropical freezing heights and the role of sea surface temperature. *Nature*, **383**, 152–5.

Diaz, H. F., *et al*. (2003) Variability of freezing levels, melting season indicators, and snow cover for selected high-elevation and continental regions in the last 50 years. *Clim. Change*, **59**, 33–52.

Dyurgerov, M. B. (2001) Mountain glaciers at the end of the twentieth century: Global analysis in relation to climate and water cycle. *Polar Geog*., **26**(4), 241–336.

Dyurgerov, M. D. (2003) Mountain and subpolar glaciers show an increase in sensitivity to climate warming and intensification of the water cycle. *J. Hydrol*., **282**, 164–76.

Dyurgerov, M. D. and Meier, M. D. (2005) *Glaciers and the Changing Earth System: A 2004 Snapshot*. INSTAAR Occas. Paper, No. 5. Boulder, CO: University of Colorado. 117 pp.

Efthymiadis, D., *et al*. (2007) Influence of large-scale atmospheric circulation on climate variability in the Greater Alpine Region of Europe. *J. Geophys. Res*., **112(D12)** D12104, 1–19.

Elsaesser, H. and Buerkli, R. (2002) Climate change as a threat to tourism in the Alps. *Clim Res*., **20**(3), 253–7.

Föhn, P. M. B. (1989) Climatic change, snow cover and avalanches. In *Landscape Ecological Impact of Climatic Change on Alpine Regions with emphasis on the Alps*. Wagenigen, The Netherlands: Agricultural University of Wagenigen, pp. 27–40.

Fritts, H. C. (1976) *Tree Rings and Climate*. London: Academic Press.

Gilgen, H., Wild, M. and Ohmura, A. (1998) Means and trends of shortwave irradiance at the surface estimated from global energy balance archive data. *J. Climate*, **11**, 2042–61.

Gorbunov, A. P., Marchenko, S. S. and Seversky, E. V. (2000) Permafrost and seasonally frozen ground response to climate changes in the northern Tien Shan. *Krisfera Zemli*, **4**, 11–17.

Grant, A. N., Pszenny, A. A. P. and Fischer, E. V. (2005) The 1935–2003 air temperature record from the summit of Mount Washington, New Hampshire. *J. Climate*, **18**(21), 4445–53.

Greene, A. M., Broecker, W. S. and Rind, D. (1999) Swiss glacier recession since the Little Ice Age: Reconciliation with climate records. *Geophys. Res. Lett*., **26**(13), 1909–12.

Grove, J. M. (1972) The incidence of landslides, avalanches and floods in western Norway during the Little Ice Age. *Arct. Alp. Res*., **4**, 131–8.

Grove, J. M. (2004) *Little Ice Ages, Ancient and Modern*, 2nd edn. London: Routledge, 2 volumes, 718 pp.

Gurtz, J., *et al*. (2005) The use of hydrological models for the simulation of climate change impacts on mountain hydrology. In U. M. Huber, H. K. M. Brugman and M. A. Reasoner (eds), *Global Change and Mountain Regions. An Overview of Current Knowledge*. Dordrecht: Springer, pp. 343–54.

Haeberli, W. (1994) Accelerated glacier and permafrost changes in the Alps. In M. Beniston (ed.), *Mountain Environments in Changing Climate*. London: Routledge, pp. 91–107.

Haeberli, W. (1998) Historical evolution and operational aspects of worldwide glacier monitoring. In W. Haeberli, M. Hoelzle and S. Suter (eds), *Into the Second Century of World Glacier Monitoring – Prospects and Strategies*. Paris: UNESCO Publishing, pp 35–51.

Haeberli, W., *et al*. (1989) Glacier changes following the Little Ice Age – a survey of the international data base and its perspectives. In J. Oerlemans (ed.), *Glacier Fluctuations and Climate*. Dordrecht: Reidel, pp. 77–80.

Haeberli, W., Cihlar, J. and Barry, R. G. (2000) Glacier monitoring within the Global Climate Observing System. *Ann. Glaciol.*, **31**, 241–6.

Hansen, J., Rossow, W. and Fung, I. (1990) The missing data on global climate change. *Issues Sci. Technol.*, **7**(1), 62–9.

Harris, C., *et al.* (2004) Warming of permafrost in European mountains. *Global Planet. Change*, **39**, 215–25.

Hastenrath, S. and Greischar, L. (1998) Glacier recession on Kilimanjaro, East Africa, 1912–1989. *J. Glaciol.*, **43**(145), 455–9.

Hoinkes, H. (1968) Glacier variation and weather. *J. Glaciol.*, **7**, 3–21, 129–30.

Jones, P. D. and Mann, M. E. (2004) Climate over past millennia. *Rev. Geophys.*, **42**, RG2002.

Jones, P. D., *et al.* (1999) Surface air temperature and its changes over the past 150 years. *Rev. Geophys.*, **37**, 173–99.

Kaser, G. (1999) A review of the fluctuations of modern tropical glaciers. *Global Planet. Change*, **23**, 93–103.

Kaser, G. (2001) Glacier–climate interaction at low latitudes. *J. Glaciol.*, **47**(157), 195–204.

Kaser, G. and Noggler, B. (1996) Glacier fluctuations in the Ruwenzori Range (East Africa) during the 20th century. A preliminary report. *Zeitschr. Gletscherk. Glazialgeologie*, **32**, 109–17.

Keeling, C. D. (1998) Rewards and penalties of monitoring the Earth. *Annual Rev. Energy Environ.*, **23**, 25–82.

Keeling, C. D., *et al.* (1976) Atmospheric carbon dioxide variations at Mauna Loa Observatory, Hawaii. *Tellus*, **28**, 538–51.

Khromova, T. E., Dyurgerov, M. B. and Barry, R. G. (2003) Late-twentieth century changes in glacier extent in the Ak-Shirak Range, Central Asia, determined from historical data and ASTER Imagery. *Geophys. Res. Lett.*, **30**(16), 1863, pp. HLS 2–1 to 2–5.

Khromova, T. E., *et al.* (2006) Changes in glacier extent in the eastern Pamir, Central Asia, determined from historical data and ASTER imagery. *Remote Sens. Environ.*, **102**, 24–32.

Kuhn, M. (1989) The effects of long-term warming on alpine snow and ice. In *Landscape Ecological Impact of Climatic Change on Alpine Regions with Emphasis on the Alps*. Wagenigen, The Netherlands: Agricultural University of Wagenigen, pp. 10–20.

LaMarche, V. C. (1973) Holocene climatic variations inferred from treeline fluctuations in the White Mountains, California. *Quat. Res.*, **3**, 632–60.

LaMarche, V. C. and Mooney, H. A. (1972) Recent climatic change and development of the Bristlecone Pine (*P. longaeva* Bailey) krummholz zone, Mt. Washington, Nevada. *Arct. Alp. Res.*, **4**, 61–72.

Lauscher, F. (1980) Die Schwankungen der Temperatur auf dem Sonnblick seit 1887 im Vergleich zu globalen Temperaturschwankungen. In *16 International Tagung für Alpine Meteorologie (Aix-les Bains)*. Boulogne-Billancourt: Soc. Météorol. de France, pp. 315–19.

Lemke, P. and Ren, J.-W. (2007) Observations: Changes in snow, ice and frozen ground. In S. Solomon, and D. Qin (eds), *Climate Change 2006: The Physical Science Basis*. IPCC WG1, Fourth Assessment Report. Cambridge: Cambridge University Press. 337–83.

LeRoy Ladurie, E. (1971) *Times of Feast, Times of Famine: A History of Climate since the Year 1000 (transl. B. Bray)*. Garden City, NY: Doubleday & Co.

Liniger, H., Weingartner, R. and Grosjean, M. (eds) (1998) *Mountains of the World. Water Towers of the 21st Century*. Bern: Mountain Agenda, 32 pp.

Luckman, B. H. (1990) Mountain areas and global change: a view from the Canadian Rockies. *Mountain Res. Devel.*, **10**, 183–95.

Luckman, B. H. (1997) Developing a proxy climate record for the last 300 years in the Canadian Rockies – some problems and opportunities. *Clim. Change*, **36**, 455–76.

Luckman, B. H. and Villalba, R. (2001) Assessing the synchroneity of glacier fluctuationa in the western Cordillera of the Americas during the last millennium. In V. Markgraf (ed.). *Interhemispheric Climate Linkage*. San Diego, CA: Academic Press, pp. 119–40.

Maisch, M. (1987) Die Gletscher an "1850" und "Heute" im Bündnerland und in den angrenzden Gebieten: Untersuchungen zur Höhenlage, Veränderungen und räumlich Struktur von Schneegrenzen. *Geogr. Helvet.*, **42**, 127–45.

Maisch, M., *et al.* (1999) *Die Gletscher der Schweizer Alpen: Gletscherschwund 1850, aktuelle Vergletscherug, Gletscherschwund-Szenasrien 21. Jahrhundert*. Zurich: Hochschulverlag AG ETH, NFP 31.

Mann, M. E. and Jones, P. D. (2003) Global surface temperatures over the past two millennia. *Geophys. Res. Lett.*, **30**(15), 1820.

Martin, E. and Etchevers, P. (2005). Impact of climatic changes on snow cover and snow hydrology in the French Alps. In U. M. Huber, H. K. M. Brugman and M. A. Reasoner (eds), *Global Change and Mountain Regions. An Overview of Current Knowledge*. Dordrecht: Springer, pp. 235–42.

Matullo, C., *et al.* (2005) *Outstanding Past Decadal-scale Climate Events in the Greater Alpine Region Analysed by 250 years Data and Model Runs*. GKSS 2005/4. Geesthacht, Germany: GKSS Forschungszentrum, 114 pp.

Mayewski, P. A. and Jeschke, P. A. (1979) Himalayan and Trans-Himalayan glacier fluctuations since AD 1812. *Arct. Alp. Res.*, **11**, 267–87.

Mayewski, P. A., *et al.* (1980) Himalayan and Trans-Himalayan glacier fluctuations and the South Asian monsoon record. *Arct. Alp. Res.*, **12**(2), 171–82.

Messerli, B., *et al.* (1975) Die Schwankungen des Unteeren Grindelwaldgletschers seit den Mittelalter. *Zeit. Gletscherkumde Glazialgeologie*, **11**(1), 3–110.

Messerli, B., *et al.* (1978) Fluctuations of climate and glaciers in the Bernese Oberland, Switzerland, and their geoecological significance, 1600 to 1975. *Arct. Alp. Res.*, **10**, 247–60.

Mote, P. W., *et al.* (2005) Declining mountain snowpack in western North America. *Bull. Amer. Met. Soc.*, **86**, 39–49.

Oerlemans, J. (1994) Quantifying global warming from the retreat of glaciers. *Science*, **264**, 243–5.

Paterson, W. S. B. (1994) *The Physics of Glaciers*, 3rd edn. Oxford: Pergamon, 480 pp.

Pepin, N. (2000) Twentieth century change in the climate record for the Front Range, Colorado, USA. *Arct. Antarct. Alp. Res.*, **32**, 135–46.

Pepin, N., Benham, D. and Taylor, K. (1999) Modeling lapse rates in the maritime uplands of northern England: Implications for climate change. *Arct. Antarct. Alp. Res.*, **31**, 151–64.

Pepin, N. C. and Norris, J. T. (2005) An examination of the differences between surface and free-air temperature trends at high-elevation sites: relationships with cloud cover, snow cover and wind. *J. Geophys. Res.*, **110 (D24)**, D24112, 19 pp.

Pepin, N. C., *et al*. (2005) A comparison of SNOTEL and GHCN/CRU surface temperatures with free-air temperatures at high elevations in the western United States: Data compatibility and trends. *J. Climate*, **18**(12), 1067–85.

Pfister, C. (1985) Snow cover, snowlines and glaciers in central Europe since the 16th century. In M. J. Tooley and G. M. Sheail (eds), *The Climate Scene*. London: G. Allen and Unwin, pp. 155–74.

Pfister, C. (1995) Monthly temperature and precipitation in central Europe from 1529–1979; Quantifying documentary evidence on weather and its effects. In R. S. Bradley and P. D. Jones (eds), *Climate since A.D. 1500*. London: Routledge, pp. 118–42.

Pounds, J. A., Fogden, M. P. I. and Campbell, J. H. (1999) Biological response to change on a tropical mountain. *Nature*, **198**, 611–15.

Price, M. F. and Barry, R. G. (1997) Climate change. In B. Messerli and J. D. Ives (eds), *Mountains of the World. A Global Priority*. New York: Parthenon Publishing, pp. 409–45.

Rango, A. S. and Martinec, J. (1998) Effects ofglobal warming on runoff in mountain basins representing different climatic zones. In H. Weater and C. Kirby (eds), *Hydrology in a Changing Environment, Vol. 1*. Chichester, UK: John Wiley, pp. 133–9.

Rudloff, H. (1962) Die Klimaschwankungen in den Hochalpen seit Beginn der Instrumenten-Beobachtungen. *Arch. Met. Geophys. Biokl.*, **B 13**, 303–51.

Scherrer, S. C., Apenzeller, C. and Laternser, M. (2004) Trends in Swiss Alpine snow days: The role of local- and large-scale climate variability. *Geophys. Res. Lett.*, **31**, 10.1029/2004GL02055.

Schlesinger, M. E. and Mitchell, J. F. B. (1987) Climate model simulations of the equilibrium climatic response to increased carbon dioxide, *Rev. Geophys.*, **25**, 760–98.

Schmidli, J., *et al*. (2002) Mesoscale precipitation variability in the region of the European Alps during the 20th century. *Int. J. Climatol.*, **22**, 1049–74.

Shahgedanova, M., *et al*. (2007) Long-term change, inter-annual and intra-seasonal variability in climate and glacier mass balance in the central Greater Caucasus. *Ann. Glaciol.*, **46**, 355–61.

Solomina, O. N. (2000) Retreat of mountain glaciers of northern Eurasia since the Little Ice Age maximum. *Ann. Glaciol.*, **31**, 26–9.

Solomina, O. N. (2006) Glacier and climate variability in the former Soviet Union during the last 1000 years. In U. M. Huber, H. K. M. Bugmann, and M. A. Reasoner (eds), *Global Change and Mountain Regions. An Overview of Current Knowledge*. Dordrecht: Springer, pp. 61–72.

Solomina, O., Barry, R. G. and Bodnya, M. (2004) The retreat of Tien Shan glaciers (Kyrgyzstan) since the Little Ice Age estimated from aerial photographs, lichenometric and historical data. *Geograf. Annal.*, **86A(2)**, 205–15.

Solomon, S., *et al*. (eds), (2007) *Climate Change 2006. The Physical Science Basis*, IPCC WG1, Fourth Assessment Report. Cambridge: Cambridge University Press, 996 pp.

Stanhill, G. and Cohen, S. (2001) Global dimming: a review of the evidence for a widespread and significant reduction in global radiation with discussion of its probable causes and possible agricultural consequences. *Agric Forest Met.*, **107**, 255–78.

Steinhauser, F. (1938) *Die Meteorologie des Sonnblicks, Teil I*. Vienna: J. Springer.

Steinhauser, F. (1970) Die säkularen Änderungen der Schneedeckenverhältnisse in Osterreich. 66–7, *Jahresbericht des Sonnblick-Vereines, 1968–1969*. Vienna: Sonnblick-Verein, pp. 1–19.

Steinhauser, F. (1973) Die Änderungen der Sonnenscheindauer in Osterreich in neurer Zeit. 68–69, *Jahresbericht des Sonnblick-Vereines, 1972–1973*. Vienna: Sonnblick-Verein, pp. 41–53.

Thompson, L. G., *et al.* (1985) A 1500-year record of tropical precipitation in ice cores from the Quelccaya Ice Cap, Peru. *Science*, **229**, 971–3.

Thompson, L. G., *et al.* (1993) Recent warming: Ice core evidence from tropical ice cores with emphasis on central Asia. *Global Planet. Change,* **7**, 145–56.

Trenberth, K. E. and Jones, P. D. (2007) Observations: Surface and atmospheric climate change. In Solomon, S. and Qin, D. (eds). *Climate Change 2006: The Physical Science Basis*. IPCC WG1, Fourth Assessment Report. Cambridge: Cambridge University Press, pp. 235–336.

van de Schrier, G., *et al.* (2007) European Alpine moisture variability for 1800–2003. *Int. J. Climatol.*, **27**(4)L, 415–27.

Vonder Mühll, D. S., Stucki, T. and Haeberli, W. (1998) Borehole temperatures in alpine permafrost: a ten-year series. In A. G. Lewcowitz and M. Allard (eds), *Proceedings of the 7ᵗʰ International Permafrost Conference*. Quebec: University of Laval, pp. 1089–95.

Vuille, M. and Bradley, R. S. (2000) Mean annual temperature trends and their vertical structure in the tropical Andes. *Geophys. Res. Lett.*, **27**, 3885–8.

Wanner, H., *et al.* (2000) Interannual to century scale climate variability in the European Alps. *Erdkunde*, **54**, 62–9.

Wardle, P. (1973) Variations of the glaciers of Westland National Park and the Hooker Range, New Zealand. *N.Z. J. Bot.*, **11**, 349–88.

Weber, R. O., Talkner, P. and Stefanicki, G. (1994) Asymmetric diurnal temperature change in the Alpine region. *Geophys. Res, Lett.*, **21**, 673–76.

Wild, M., *et al.* (2005) From dimming to brightening: Decadal changes in solar radiation at Earth's surface. *Science*, **308**, 847–850.

Zumbühl, H. J. (1988) Der Rhonegletscher in den historischen Quellen. *Die Alpen*, **64**, 186–233.

APPENDIX

SYSTÈME INTERNATIONAL (SI) UNITS

Quantity	Dimensions	SI	cgs metric	British
Length	L	m	10^2 cm	3.2808 ft
Area	L^2	m^2	10^4 cm^2	10.764 ft^2
Volume	L^3	m^3	10^6 cm^3	35.314 ft^3
Mass	M	kg	10^3 g	2.205 lb
Density	ML^{-3}	$kg\,m^{-3}$	10^{-3} g cm^{-3}	
Time	T	s	s	
Velocity	LT^{-1}	$m\,s^{-1}$	10^2 cm s^{-1}	2.24 mph
Acceleration	LT^{-2}	$m\,s^{-2}$	10^2 cm s^{-2}	
Force	MLT^{-2}	newton (N or $kg\,m\,s^{-2}$)	10^5 dynes (10^5 g cm s^{-2})	
Pressure	$ML^{-1}T^{-2}$	pascal ($N\,m^{-2}$)	10^{-2} mb	
Energy, work	ML^2T^{-2}	joule (J or $kg\,m^2\,s^{-2}$)	10^7 ergs (10^7 g cm^2 s^{-2})	
Power	ML^2T^{-3}	watt(W or $kg\,m^2\,s^{-3}$)	10^7 ergs s^{-1}	1.34×10^{-3} hp
Temperature	θ	kelvin (K)	°C	1.8 °F
Heat energy	ML^2T^{-2} (or H)	joule (J)	0.2388 cal	9.47×10^{-4} BTU
Heat/radiation flux	HT^{-1}	watt(W or $J\,s^{-1}$)	0.2388 cal s^{-1}	3.412 BTU h^{-1}
Heat flux density	$HL^{-2}T^{-1}$	$W\,m^{-2}$	2.388×10^{-5} cal cm^{-2} s^{-1}	

ENERGY CONVERSION FACTORS

4.1868 J $= 1$ calorie

$J\,cm^{-2}$ $= 0.2388$ cal cm^{-2}

watt $= J\,s^{-1}$

kW h $= 3.60 \times 10^6$ J

$W\,m^{-2}$ $= 1.433 \times 10^{-3}$ cal cm^{-2} min^{-1}

697.8 W m^{-2} $=$ cal cm^{-2} min^{-1}

2.5 MJ m^{-2} $= 1$ mm of evaporation.

For time sums.

Day: $1 \, \mathrm{W \, m^{-2}}$ $\quad\quad\quad = 8.64 \, \mathrm{J \, cm^{-2} \, day^{-1}} = 8.64 \times 10^4 \, \mathrm{J \, m^{-2} \, day^{-1}}$

$\quad\quad\quad\quad\quad\quad\quad\quad\quad\quad\quad\quad\quad\quad\quad\quad\quad = 2.064 \, \mathrm{cal \, cm^{-2} \, day^{-1}}$

Month: $1 \, \mathrm{W \, m^{-2}}$ $\quad\quad\quad = 2.592 \, \mathrm{MJ \, m^{-2} \, (30 \, day)^{-1}}$

$\quad\quad\quad\quad\quad\quad\quad\quad\quad\quad\quad\quad\quad\quad\quad\quad\quad = 61.91 \, \mathrm{cal \, cm^{-2} \, (30 \, day)^{-1}}$

Year: $1 \, \mathrm{W \, m^{-2}}$ $\quad\quad\quad = 31.536 \, \mathrm{MJ \, m^{-2} \, year^{-1}} = 753.4 \, \mathrm{cal \, cm^{-2} \, year^{-1}}$

Gravitational acceleration (g) $\quad = 9.81 \, \mathrm{m \, s^{-2}}$

Latent heat of vaporization $\quad\quad = 2.47 \times 10^6 \, \mathrm{J \, kg^{-1}}$
(288 K)

Latent heat of fusion (273 K) $\quad = 3.34 \times 10^5 \, \mathrm{J \, kg^{-1}}$

Dry adiabatic lapse rate (Γ) $\quad = 9.8 \, \mathrm{K \, km^{-1}}$

INDEX